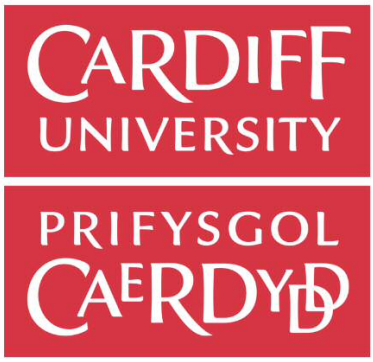

Caveolin-1: a mediator of Glioblastoma cell invasion and an independent negative biomarker of Glioblastoma patient survival

A thesis submitted in accordance with the conditions governing candidates for the degree of

Philosophiae Doctor in Cardiff University

Chiara Moriconi

Supervisor: Prof. Mark Gumbleton

Supervisor: Prof. Geoffrey Pilkington

September 2018

Cardiff School of Pharmacy and Pharmaceutical Science

Cardiff University

Acknowledgements

My acknowledgments go to all the people that made this four years possible:

First, my supervisors, Prof Mark Gumbleton and Prof Geoff Pilkington, who believed in me and my potential and chose me among many. They gave me invaluable gifts and contributed to the person I am now.

Second my funding charity, Cancer Research Wales, for their support.

To Ed Evans, who died in October 2007 from an inoperable brain tumour and who started to raise the money that partly became my scholarship. I hope I made his family proud.

To Dr Lee Campbell, whose help was invaluable. He helped me in so many ways with his wisdom, his expertise, his engagement activities and his support.

Third to the people that helped my experimental achievements.

First of all, Dr Valentina Palmieri, for her extraordinary help with the ImageJ software, for starting my first successful collaboration and my most important publication so far and for her friendship in the last 13 years now. She's my rock.

Thanks to Dr Giusy Tornillo, for her help with the lentiviral transfections and her willingness to help in any moment. I wish her an amazing future with her international family.

To Dr Christopher Von Ruhland, for his expertise with the immunohistochemistry sections preparation. I learned a lot from him and I wish him all the best.

To Dr Jack Sim, Dr Jenny Wymant and Dr Ed Sayer, as well as Prof. Arwyn Jones, for sharing their wisdom with me during all my immunofluorescences attempts. Not once I found them too busy to help.

To Mr Matthew Summers and Mr Marcin Kosiński, for opening me the doors of R.

To Miss Catia Neto, for letting me test my hypothesis on her freshly produced CRISPR cell lines.

To my family in Cardiff.

To Dr Robert Gutteridge and Dr Valentina Ferrari, for being the cornerstone of my life in Cardiff for so long. I really miss you, guys.

To Dr Michaela Serpi and Dr Fabrizio Pertusati, as well as the Pupetta, for being always present when I needed them and for letting me help them when they needed me,

Then to my real family, for being patient and supportive of this daughter/ sister/ granddaughter/ auntie/ sister-in-law that chose a different path for herself. I missed you every day.

Finally, to Daniel, who transformed my life, gave me a second family, gifted me with new purposes and decided to create a team together. I believe there is nothing that we can’t accomplish together.

I dedicate these four years of work to Ed Evans, to Daniele Frioni and to Marco Frioni, to all the ones we loved and who are not with us anymore but whose lives left a mark in so many people.

Dedico questi quattro anni di lavoro a Ed Evans, Daniele Frioni e Marco Frioni, a tutti coloro che abbiamo amato e che non sono più con noi ma le cui vite hanno lasciato un segno in così tanti.

ABSTRACT

Glioblastoma multiforme (GBM) is a malignant and highly aggressive form of brain tumour, with extremely poor prognosis. One of its features is the ability of the tumour to invade through normal brain resulting in tumour relapse.

Our hypothesis was that Caveolin-1 (Cav-1), a major component of the caveolae and recognized to be involved in a number of signalling pathways, has a key pro-invasive role in GBM.

We pursued our hypothesis by inhibiting the expression of Cav-1 in different adult GBM cell lines using different genetic techniques (liposome shRNA, lentiviral shRNA and CRISPR).

We found that Cav-1 drives clonogenicity (CHAPTER 3) and invasion in a combination of two- and three-dimensional models (CHAPTER 5). We focused our research on the invasion phenomenon and, in order to provide a robust quantification approach to study invasion in 3D spheroid assays, we developed (CHAPTER 4) a open-source semi-automated script, INSIDIA, available for all researchers in the community to use. This tool was used to quantify the impact of Cav-1 on invasive capacity.

In *in-vitro* systems, we explored the impact of Cav-1 expression upon molecules associated with the invasion phenomenon (CHAPTER 5). We found Cav-1 to be associated with CTSB, MMP1 and UPA and receptors like UPAR and CD44, as well as AKT activation.

Interrogating the “The Cancer Genome Atlas” (TCGA) database, we confirmed that Cav-1 is an independent biomarker of poor prognosis in GBM patients (CHAPTER 6). This clinical data also found association of genes that may cooperate with Cav-1, including CD44, ITGA3, VIM, CTSB, CTSL, TSP-1, TIMP1 and MT1MMP.

Collectively this thesis provides strong *in vitro* and clinical data supporting that Cav-1 as a key molecule promoting GBM invasion, and further identifying Cav-1 as a potential drug discovery target in GBM.

Contents

LIST OF ABBREVIATIONS **1**

1 CHAPTER 1. GENERAL INTRODUCTION **3**

1.1 CAVEOLINS AND CAVEOLAE 4

1.2 CAV-1 CELL SIGNALLING PATHWAYS 7

1.3 CAV-1 INVOLVEMENT IN CANCER 8

1.4 BRAIN TUMOURS 10

WHO 2007 CLASSIFICATION *11*

GLIOMAS MOLECULAR PROFILING *15*

WHO 2016 CLASSIFICATION *17*

CURRENT THERAPEUTICAL OPTIONS FOR GBM *20*

CAV-1 AND GBM AGGRESSIVENESS *21*

1.5 STEMNESS IN CANCER 24

CLONOGENICITY *28*

1.6 THE STUDY OF PROTEIN FUNCTION THROUGH EXPRESSION MODULATION 53

1.7 SCOPE OF THE PROJECT 67

2 CHAPTER 2- MATERIALS AND METHODS **69**

2.1 CELL LINES 70

2.2 GENERAL CONSUMABLES AND REAGENTS 72

2.3 ROUTINE CELL CULTURE 72

2.4 WESTERN BLOT 72

2.5 STATISTICAL ANALYSIS 74

3 CHAPTER 3- CAV-1 GENETIC KNOCK-DOWN/OUT APPROACHES **75**

3.1 INTRODUCTION 76

3.2 SCOPE OF THE CHAPTER 78

3.3 MATERIALS AND METHODS 79

CELL LINES *79*

RNAi *79*

CRISPR/Cas9 ..... *82*

CELL PROLIFERATION - MICROSCOPY; *84*

CELL PROLIFERATION - FLUORESCENCE *85*

SELF-RENEWAL CLONOGENIC ASSAYS *86*

SCRATCH ASSAY *87*

CELL CYCE ANALYSIS *88*

3.4 RESULTS AND DISCUSSION 89

LIPOSOME-MEDIATE SHRNA KNOCKDOWN *91*

'PANEL OF GLIOMA CELL LINES' – PROLIFERATIVE CAPACITY AND CAV-1 STATUS *109*
LENTIVIRAL TRANSFECTION *113*
CRISPR *122*
CAV-1 GENE MANIPULATION IMPACT ON MIGRATION *126*
3.5 SUMMARY OF KEY FINDINGS 128
Cell lines and experimental plan *129*
RNAi knockdown vs. CRISPR knockout *129*
Proliferation and cell cycle *130*
Clonogenicity *133*
3.6 CONCLUSIONS 134
4 CHAPTER 4- THE STUDY OF INVASION IN BRAIN TUMOURS 136
4.1 INTRODUCTION 137
4.2 SCOPE OF THE CHAPTER 149
4.3 MATERIALS AND METHODS 150
CELL LINES AND TREATMENTS *150*
METHODS- INVASION ASSAY (3D CELL SPROUTING ASSAY) *150*
4.4 RESULTS AND DISCUSSION 152
ASSAY SETTINGS *152*
INSIDIA *152*
GLIOMA CELL LINES INVASION INHIBITION MEDIATED BY SRC INHIBITOR, SARACATINIB *162*
4.5 CONCLUSIONS 165
5 CHAPTER 5- MOLECULAR SIGNALING INVOLVED IN CAV-1 ROLE IN INVASION 166
5.1 INTRODUCTION 167
5.2 SCOPE OF THE CHAPTER 169
5.3 MATERIAL AND METHODS 170
EXPERIMENTAL CONDITIONS USED FOR EACH APPLICATION *170*
PROTEIN ARRAY *171*
WESTERN BLOT ANALYSIS *175*
RT-PCR FOR GENE EXPRESSION ANALYSIS *177*
IMMUNOFLUORESCENCE *184*
IMMUNOHISTOCHEMISTRY *187*
5.4 RESULTS AND DISCUSSION 191
CAV-1 DRIVES INVASIVE PHENOTYPE ON 3D INVASION ASSAY MODEL *191*
RT-PCR ANALYSIS FOR GENES ASSOCIATED WITH INVASION *208*
WESTERN BLOT AND IMMUNOFLUORESCENCE OF SELECT MOLECULES FROM THE RT-PCR ANALYSIS *211*
PROTEIN ARRAY ON CELLS INTERACTING WITH MATRIGEL: BUILDING A PUTATIVE SIGNALLING PATHWAY *226*

PROTEIN ARRAY PATHWAY VALIDATION *232*
5.5 SUMMARY AND CONCLUSIONS 242
6 CHAPTER 6- THE CLINICAL IMPACT OF CAV-1 AND ASSOCIATED SIGNAL MOLECULES IN GBM 249
6.1 INTRODUCTION 250
The study of survival in GBM- The Cancer Genome Atlas (TCGA) *250*
Cav-1 and GBM clinical samples *251*
6.2 SCOPE OF THE CHAPTER 251
6.3 MATERIALS AND METHODS 252
The Cancer Genome Atlas (TCGA) *252*
R2 Genomic platform for the analysis of TCGA database *252*
R project *253*
Kaplan Meyer survival visualization and analysis *253*
COX regression and survival analysis *254*
Median Survival *254*
6.4 RESULTS AND DISCUSSION 255
GBM survival and The Cancer Genome Atlas (TCGA) *255*
Impact of Cav-1 on GBM survival *256*
Invasion-associated genes, Cav-1 expression and GBM *264*
Level 1 analysis *316*
Level 2 and 3 analysis *316*
Biological implications of the survival analysis *318*
6.5 CONCLUSIONS 325
7 CHAPTER 7- SUMMARISING DISCUSSION 327
APPENDIX 336
APPENDIX 1: BUFFERS AND SOLUTIONS 337
PBS (PHOSPATE BUFFER SALINE), 10mM *337*
LYSIS BUFFER *337*
ELCTROPHORESIS RUNNING BUFFER *338*
BLOTTING BUFFER *338*
WESTERNBLOT WASHING BUFFER *338*
BLOCKING BUFFER *339*
ANTIBODY DILUENT FOR WESTERN BLOT *339*
PONCEAU *339*
IMMUNOHISTOCHEMISTRY REAGENT DILUENT *339*
IMMUNOHISTOCHEMISTRY SODIUM CITRATE BUFFER *340*
IMMUNOHISTOCHEMISTRY ACTIVE DAB SOLUTION *340*
IMMUNOFLUORESCENCE BLOCKING BUFFER *340*
IMMUNOFLUORESCENCE WASHING BUFFER *340*

APPENDIX 2: SCRATCH ASSAY ANALYSIS PROCEDURE 341
APPENDIX 3: IF SECONDARY ANTIBODIES 342
APPENDIX 4: PRIMERS VALIDATION 343
APPENDIX 5: INSIDIA CODE 347
APPENDIX 6: R CODE 364
SURVIVAL SINGLE GENE *364*
SURVIVAL DOUBLE POSITIVE VS OTHER *367*
SURVIVAL FOUR GROUPS *370*
APPENDIX 7: TOP 500 GENES POSITIVELY CORRELATED TO CAV-1 IN GBM 373
APPENDIX 8: CAV-1/TARGET GENES EXPRESSION CORRELATION 379
APPENDIX 10: COPYRIGHT PERMISSIONS 398
APPENDIX 11: LIST OF PUBLICATIONS, ORAL PRESENTATIONS AND AWARDS 399
PUBLICATIONS *399*
AWARDS *399*
CONFERENCES *400*
BIBLIOGRAPHY 336

LIST OF ABBREVIATIONS

ADAM	A Disintegrin And Metalloproteinase	**MT1MMP**	Membrane-Type 1 MMP
ADAMT	A Disintegrin And Metalloproteinase With Thrombospondin Motifs	**mTOR**	Mechanistic Target Of Rapamycin Kinase
BEHAB	Brain-Enriched Hyaluronic Acid Binding Protein	**MYC**	Avian Myelocytomatosis Viral Oncogene Homolog
bFGF	basic Fibroblast Growth Factor	**MYCN**	Neuroblastoma MYC Oncogene
BMP	Bone Morphogenetic Protein	**NF1**	Neurofibromin 1
BRAF	V-Raf Murine Sarcoma Viral Oncogene Homolog B	**NPC**	Neural Progenitor Cells
Cas-9	Caspase-9	**ODZ3**	Teneurin Transmembrane Protein 3
Cav-1	Caveolin-1	**P2Y2R**	G Protein-Coupled P2Y2 Nucleotide Receptor
Cav-2	Caveolin-2	**PAI**	Plasminogen Activator Inhibitor
Cav-3	Caveolin-3	**PBS**	Phosphate Buffer Saline
CD44	Cluster of Differentiation 44	**PDGF**	Platelet-Derived Growth Factor
CHI3L1 or YKL40	Chitinase-3-Like Protein 1	**PDGFRA**	Platelet-Derived Growth Factor Receptor
CRISPR	Clustered Regularly Interspaced Short Palindromic Repeats	**PI3K**	Phosphatidylinositol-4,5-Bisphosphate 3-Kinase
CSC	Cancer Stem Cell	**PK**	Phospho Kinase
CSD	Caveolin-Scaffolding Domain	**PKC**	Protein Kinase C
CTS	Cathepsin	**PTEN**	Phosphatase And Tensin Homolog
ds	double strand	**PVRL4**	Poliovirus Receptor-Related Protein 4
ECAD	E Cadherin	**RISC**	RNA-Interfering Silencing Complex
ECM	Extracellular Matrix	**RNAi**	RNA Interference
EGF	Estrogen Growth Factor	**SHH**	Sonic Hedgehog
EGFR	Estrogen Growth Factor Receptor	**siRNA**	small interfering RNA
EMT	Epithelial To	**SNP**	Single-Nucleotide

	Mesenchymal Transition
eNOS	Endothelial Nitric Oxide Synthase
MMP	Matrix Metallo Protease
ERK	Extracellular Signal-Regulated Kinase
GFR	Growth Growth factorReduced
GPI	glycosyl-phosphatidylinositol
GSC	Glioma Stem Cells
HA	Hyaluronic Acid
HR	Hazard Ratio
IDH	Isocitrate Dehydrogenases
INI1	Integrase Interactor 1
ITGA	Integrin alpha subunit
ITGB	Integrin beta subunit
KD	Knock Down
KO	Knock Out
MGMT	Methyl Guanine Methyl Transferase
MIB-1	Mindbomb Homolog 1
miRNA	micro RNA
	Polymorphisms
SPARC	Secreted Protein Acidic And Rich In Cysteine Or Osteonectin
ss	single strand
STAT3	Signal Transducer and Activator of transcription-3
TCGA	The Cancer Genome Atlas
TGFB	Transforming Growth Factor Beta Receptor I
TGFBRI	Transforming Growth Factor Beta
TIMP	Metallopeptidase inhibitor
TMZ	Temozolomide
TNF	Tumor Necrosis Factor
TP53	Tumor Protein 53
TSP-1	Thrombospondin-1
uPA	Urokinase-type Plasminogen Activator
uPAR	Urokinase-type Plasminogen Activator Receptor
VEGF	Vascular-Endothelial Growth Factors
VIM	Vimentin
WHO	World Health Organization
WNT	Wingless-Type MMTV Integration Site Family
WT	Wild Type

1 CHAPTER 1. GENERAL INTRODUCTION

In this chapter, we reported a background introduction to the main themes that are recurrent in the present study. They are:

1. Caveolin 1
2. High-grade gliomas
3. Stemness markers
4. Markers of aggressiveness
5. Genetic knockdowns and knockouts

Specific information regarding single chapters is reported also in the introduction of each chapter.

1.1 CAVEOLINS AND CAVEOLAE

Caveolae are defined as flask-shaped plasma membrane domains of 60-100 nm (Goetz, Lajoie, Wiseman, & Nabi, 2008) in diameter that were first observed by electron microscopy in the 1950s (Palade, 1953; Yamada, 1955). The cytoplasmic face of these vesicles is coated by a protein termed Caveolin (Figure 1.1) which is responsible for many of their functional attributes (Parat, 2009).

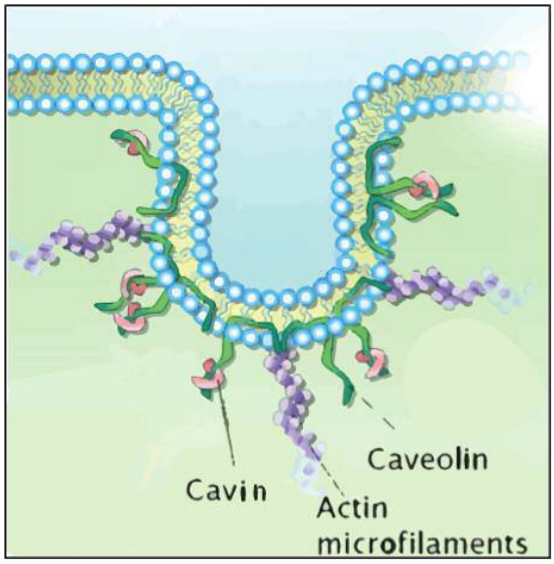

Figure 1.1 Caveolae structure and major components.

There are principally three caveolins that form the Caveolin family – Caveolin-1 (Cav-1), Caveolin-2 (Cav-2), and Caveolin-3 (Cav-3). Cav-1 is expressed in a

variety of tissues and cells (among these epithelial, endothelial and brain glial cells) and is mostly co-expressed in hetero-oligomers with Cav-2. 22kDa Cav-1 binds cholesterol (Murata et al., 1995) within the plasma membrane and forms higher-order oligomers (Monier, Dietzen, Hastings, Lublin, & Kurzchalia, 1996) (Figure 1.2) which are important for the generation of the characteristic caveola structure (Pelkmans & Zerial, 2005). While Cav-2 requires Cav-1 for its stabilisation and plasma membrane localization (Parolini et al., 1999), Cav-1 can exist independently and is the unequivocal marker for caveolae. Cav-3 expression is mostly limited to the muscle cells where it forms homo-oligomers or hetero-oligomers with Cav-1. Embryonic genetic ablation of Cav-1 or Cav-3, although not fatal, abolishes caveolae formation, leading to vascular, pulmonary and muscular defects in mice (Drab et al., 2001; Galbiati, Engelman, et al., 2001; Razani et al., 2001).

Among the other components of the Caveolin family, Cavin-1 is a soluble protein shown to be an abundant caveolar coat protein and to be required for caveolae stabilisation and probably for the interaction with the cytoskeleton (Gupta, Toufaily, & Annabi, 2014; Hill et al., 2008; Inder et al., 2012; L. Liu & Pilch, 2008). Cav-1 and Cav-3 recruit Cavin-1 to the plasma membrane where it also binds to cholesterol, phosphatidylserine and oligomerises with caveolins (Burgener, Wolf, Ganz, & Baggiolini, 1990). The membrane curvature of caveolae is stabilized by the binding of Cavin-1, leading to the characteristic flask-shape of the caveolae. Cavin-1 and Cav-1 appear not to interact directly but through microtubules and actin filaments (Hill et al., 2008).

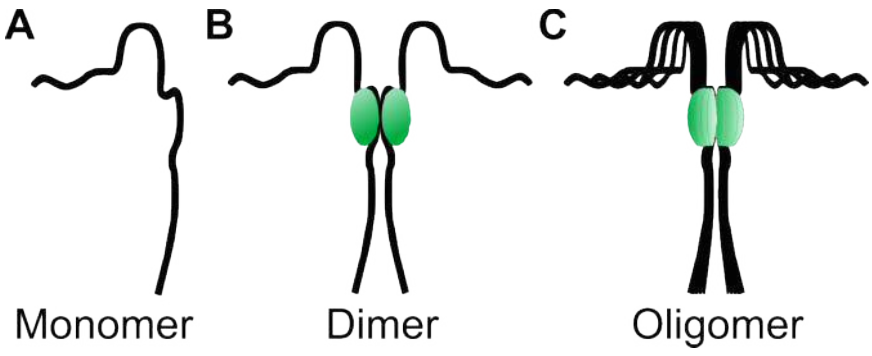

Figure 1.2 Caveolin-1 structure showing single molecule (a), dimer with Cavin-1 (b) and oligomer (c).

Located on chromosome 7, the Cav-1 gene consists of 3 exons (respectively 30, 165 and 342 bp long) separated by two introns of 1.5 kb and 32 kb (Figure 1.3). Two isoforms of Cav-1 have been identified: Caveolin-1α (residues 1-178) and Caveolin-1β (residues 32-178). These two isoforms of Cav-1 are generated by alternative initiation of the same mRNA translation (Kogo & Fujimoto, 2000; Shatz & Liscovitch, 2008).

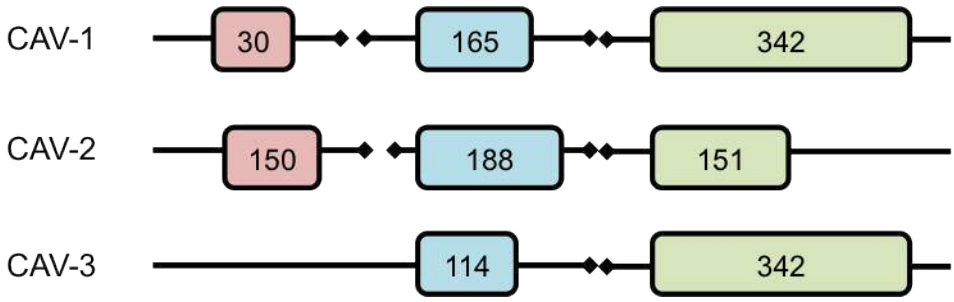

Figure 1.3 Caveolin gene structure with Cav-1 and Cav-2 located on chromosome 7 and Cav-3 located on chromosome 3.

Cav-1 is an integral membrane protein but has both the N'- and C'-terminals facing the cytoplasm (Figure 1.4). The protein comprises several domains including two membrane-compassing domains (residues 82–101 and 135–150) (Schlegel, Schwab, Scherer, & Lisanti, 1999; Woodman, Schlegel, Cohen, & Lisanti, 2002), an oligomerization domain (residues 61–101) (Sargiacomo et al., 1995; Song, Tang, Li, & Lisanti, 1997), and a Caveolin-scaffolding domain (CSD) (residues 82–101) (Schlegel et al., 1999); each of these domains display a specific functionality.

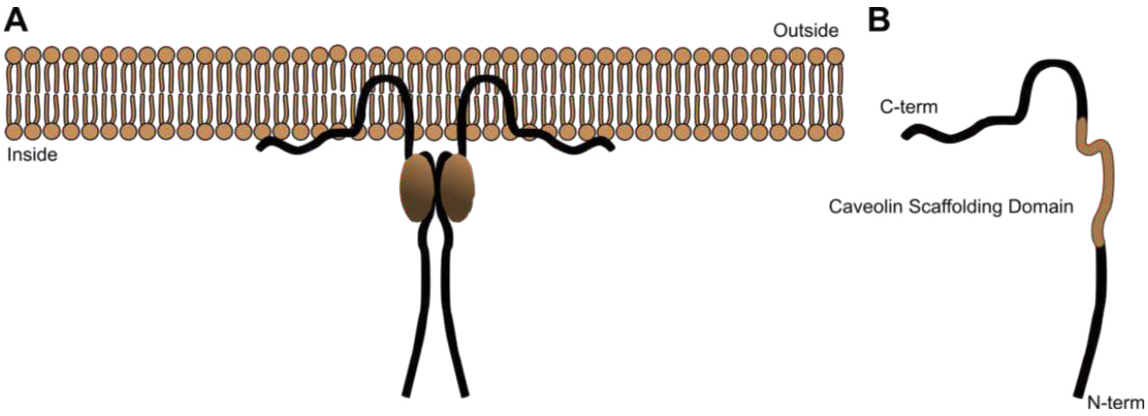

Figure 1.4 Caveolin-1 membrane topology and protein domains.

1.2 CAV-1 CELL SIGNALLING PATHWAYS

Cav-1 was first identified as one of the main tyrosine-phosphorylated proteins in Rous sarcoma virus-transformed fibroblasts (Glenney & Soppet, 1992). Further studies reported that Cav-1 can be phosphorylated at Tyr14 or Ser80 in a cell type-specific manner, following stimulation by, for example, the mitogens Epidermal growth factor (EGF), the Platelet-Derived growth factor (PDGF) and insulin (Fielding, Chau, Liu, Spencer, & Fielding, 2004; H Lee et al., 2000) or cellular stress signals (Sanguinetti & Mastick, 2003; Volonté, Galbiati, Pestell, & Lisanti, 2001); Cav-1 phosphorylation may be important in determining overall Cav-1 functionality. Mediated primarily through the CSD, Cav-1 has been shown to regulate the function of a wide variety of signalling molecules, including glycosyl-phosphatidylinositol (GPI)-linked proteins, Src-family tyrosine kinases, H-Ras, heterotrimeric G-protein subunits, protein kinase C (PKC) isoforms, and endothelial nitric oxide synthase (eNOS). These findings led to the proposal of the “Caveolae Signalling Hypothesis” whereby caveolae function as compartmentalisers of signalling molecules and regulators of signal transduction (Lisanti, Scherer, Tang, & Sargiacomo, 1994).

1.3 CAV-1 INVOLVEMENT IN CANCER

Cav-1 is known to directly interact via its scaffolding domain with multiple signalling proteins and to regulate their activity. These proteins include important regulators of cell transformation and growth (van Golen, 2006). Furthermore, whilst the signal regulatory actions of Cav-1 are mostly recognised as resulting from its plasma membrane location, there is evidence that its soluble and secreted forms are also involved in modulating cancer cell growth and metastasis (Parat, 2009).

In a number of tumour types, Cav-1 expression has been found to be associated with tumour grade and stage (Senetta et al., 2013). Depending upon the tumour type and the particular point in tumour development, Cav-1 has been shown to act variously as both a tumour suppressor and tumour promoter. There is evidence both *in vitro* and *in vivo* of the variable role of Cav-1 in cancer initiation and progression (Lloyd & Hardin, 2011). For example:

- Cav-1 expression has been found to be inversely associated with the transformation of breast cancer cell lines (S. W. Lee, Reimer, Oh, Campbell, & Schnitzer, 1998). Overexpression of human Cav-1 represses the transformed phenotype, in terms of a decrease in proliferation, reduced anchorage-independent colony formation in soft agar, reduced matrix invasion, and inhibition of matrix metalloproteinase (MMP)-2 collagenolytic activity (Engelman et al., 1997; Fiucci, Ravid, Reich, & Liscovitch, 2002). Consistent with this, Cav-1 appears to increase apoptosis of breast cancer cells *in vitro* (Sloan, Stanley, & Anderson, 2004), and the recombinant expression of murine Cav-1 in the breast cancer metastatic cell line, Met-1, suppresses experimental metastasis *in vivo*, with the CSD peptide alone sufficient to inhibit invasion (Williams et al., 2004).
- In renal cell carcinoma, the expression of Cav-1 in clinical tumour samples has been repeatedly observed to positively correlate with aggressive disease and represents a poor prognostic marker for patient

survival. *In vitro* studies in renal cancer cells has shown the expression of Cav-1 to drive tumour cell invasion and promotion of angiogenesis (Campbell et al., 2013). Moreover, RNA interference-directed Cav-1 knockdown sensitises renal carcinoma cells to doxorubicin-induced apoptosis and reduces metastasis to lung (Park et al., 2010).

- In prostate cancer, Cav-1 expression positively correlates with advanced disease in both human tumours and in experimental *in vivo* models of prostate cancer (Gould, Williams, & Nicholson, 2010). Cav-1 is released from tumour cells and acts in an autocrine and paracrine manner upon tumour and endothelial cells, respectively to promote cell proliferation and angiogenesis, *in vitro*, and lung metastases, *in vivo* (Tahir et al., 2006). In an *in vivo* prostate cancer model, lung metastases displayed increased expression of Cav-1. Furthermore, secreted Cav-1 levels has been found significantly higher in men with prostate cancer than in men with benign prostatic hyperplasia (Tahir et al., 2006) and elevated pre-operative levels of secreted Cav-1 predict a decreased time to cancer recurrence after radical prostatectomy (Tahir et al., 2006).
- Cav-1 levels are also increased in drug-resistant carcinomas, such as *in vitro* lung carcinoma cells, (Engelman et al., 1997; Ho et al., 2002) with Cav-1 also recognised to promote chemoresistance in lymph node metastasis of non-small cell lung cancer (M. Li et al., 2010), and with Cav-1 silencing arresting the proliferation of metastatic lung cancer cells through the inhibition of signal transducer and catalyst of transcription (STAT)-3 signalling (Pancotti, Roncuzzi, Maggiolini, & Gasperi-Campani, 2012).
- In human astrocytoma cell line 1321N1, G protein-coupled P2Y2 nucleotide receptor (P2Y2R) interaction with Cav-1 in membrane-raft caveolae has been reported to modulate the receptor coupling to its downstream signalling machinery (Martinez et al., 2016). P2Y2R is a mediator of pro-inflammatory responses, neurotransmission, apoptosis, proliferation, and cell migration (Abbracchio & Ceruti, 2006).

The above data indicate a complex role for Cav-1 in tumorigenesis and progression with Cav-1 expression pattern (Parat & Riggins, 2012) and function appearing to vary with cell oncogenic stage (Figure 1.5); it could be possible that

during the first stages of the oncogenic transformation Cav-1 may be downregulated in order to promote proliferation and anchorage-independent growth, whilst in the later stages, when a tumour has to adapt to the environment, e.g. increased interstitial pressure, hypoxia and challenge with chemo- and radio-therapies, Cav-1 is overexpressed (Quest et al., 2013).

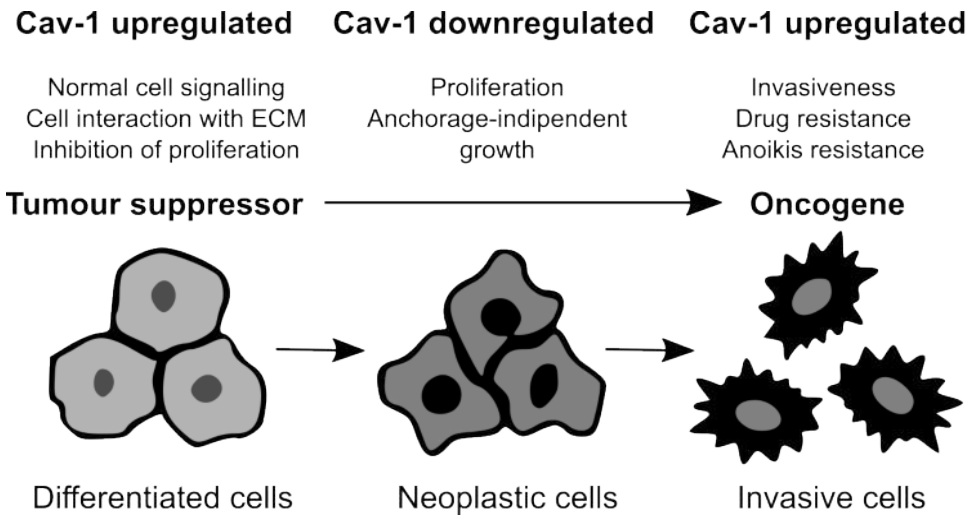

Figure 1.5 Caveolin-1 (Cav-1) may function both as a tumour suppressor and as an oncogene, depending on the stage of oncogenic transformation and the extent of tumour progression.

1.4 BRAIN TUMOURS

There are a variety of different types and grades of brain tumours (approximately 130 different types) (D. N. Louis et al., 2007). Up to 2016, brain tumours have been classified according to their cellular origin, the tumour growth pattern and whether they are benign or malignant. In 2016, a new classification system has been proposed, that takes into consideration clusters of genetic and molecular markers for the new stratification system. This classification is currently under review by the scientific community so, for this work, the 2007 classification will be firstly described. The World Health Organization (WHO) 2016 classification will be discussed in 1.4.3. Between the two classifications, a further approach was adopted with the molecular profiling, which will be described in 1.4.2.

1.4.1 WHO 2007 CLASSIFICATION

According to the WHO 2007 classification, a brain tumour is graded by its ability to grow and spread. The grade is most commonly defined by the criteria of the World Health Organization (WHO)(D. N. Louis et al., 2007) (Table 1.1). Such criteria include atypia (similarity to normal cells), mitotic index (rate of growth), indications of uncontrolled growth, necrosis (mostly in the centre of a tumour), infiltration ability (reflecting invasiveness and/or ability to migrate), margins (diffuse or focal) and vascularity.

Table 1.1 Criteria used to define brain tumours by the WHO 2007 (D. N. Louis et al., 2007) grading classification

World health Organization grading system	
Grade I tumour	• Benign • Slow growing • Cells look almost normal under a microscope • Usually associated with long-term survival • Rare in adults
Grade II tumour	• Relatively slow-growing • Sometimes spread into nearby normal tissue and recurs • Cells look slightly abnormal under a microscope • Sometimes comes back as a higher grade
Grade III tumour	• Malignant • Actively reproduces abnormal cells • Tumour spreads into nearby normal parts of the brain • Cells look abnormal under the microscope • Tends to come back, often as a higher grade tumour
Grade IV tumour	• Most malignant • Grows fast • Easily spreads into nearby normal parts of the brain • Actively reproduces abnormal cells • Tumour forms new blood vessels to mantain rapid growth • Tumours have necrotic area in their centres.

A tumour whose origin is in the brain, i.e. from brain cells, is termed a primary brain tumour and can be distinguished as either benign (low-grade) or malignant (high-grade). Benign tumours are characterised by a slow growth rate, a distinct border (which helps surgical resection) and a rare propensity to spread. In contrast, malignant tumours usually grow very fast and display the ability to invade surrounding tissue thus impairing the correct functioning of the brain with

physical and psychological consequences; malignant brain tumours are also called brain cancers. Secondary brain tumours can be defined as primary brain tumours which have progressed to a more malignant grade. Most typically, these are grade II gliomas which progress to GBM and are distinguished from *de novo* GBMs. Secondary brain tumours can be also the result of a peripheral tumour that has metastasised into the brain. The most common peripheral primary cancers metastasising to the brain origin from lung (50%), breast (15%–20%), unknown (10%–15%), melanoma (10%), and colon (5%) (Mehta M, Vogelbaum MA, Chang S, 2011; Patchell, 2003). Approximately 80% of brain metastases occur in the cerebral hemispheres, 15% occur in the cerebellum, and 5% occur in the brain stem (Mehta M, Vogelbaum MA, Chang S, 2011). Metastases to the brain are multiple in more than 70% of cases (Patchell, 2003).

A particular note should be reserved for paediatric brain tumours, which are rare but represent the most common form of solid tumour in patients less than 15 years of age. They display some different characteristics to adult tumours in that they have the propensity to arise from different cellular origins and exhibit different behaviours. The therapeutic approaches can also be quite different and depend not only on the tumour type but also on patient age (Karajannis, Allen, & Newcomb, 2008).

Primary brain tumours are named after the cellular origin from which they arise, as shown in (D. N. Louis et al., 2007) and Figure 1.6.

Gliomas include a range of different tumour types, arising from glial cells in the brain, i.e. gliomas include astrocytomas, oligodendrogliomas and ependymomas (Table 1.2). They are the most common type (86%) of primary malignant brain tumours (McKinney, 2004) with a combined five-year survival for the high-grade tumours (III and IV) that only approximates to 14.5 % for men and 16.1 % for women (Goggins & Wong, 2009).

Table 1.2 Brain tumours classification

No.	Brain tumour hystological type	Malignancy WHO grade
	Astrocytic tumours	
1	Pilocytic astrocytoma	I
2	Diffuse astrocytoma	II
3	Anaplastic astrocytoma	III
4	Glioblastoma	IV
	Oligodendroglial tumours	
5	Oligodendroglioma	II
6	Anaplastic oligodendroglioma	III
	Oligoastrocytic tumours	
7	Oligoastrocytoma	II
8	Oligoastrocytoma	III
9	Anaplastic oligoastrocytoma	III
	Ependymal tumours	
10	Subependymoma	I
11	Ependymoma	II
12	Anaplastic ependymoma	III
	Neuronal and mixed neuronal-glial tumours	
13	Dysembrioplastic neuroepithelial tumour	I
14	Ganglioglioma	II
15	Anaplastic ganglioglioma	III
16	Central neurocytoma	II

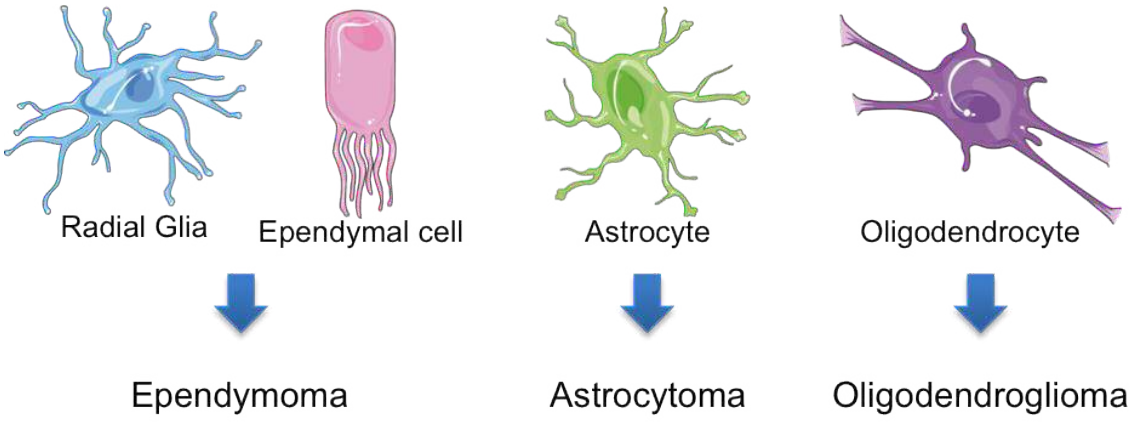

Figure 1.6 Glial cells include several cell types, which give rise to distinct brain tumour types, all of which are classified as gliomas.

Specifically, the following are the major types of glioma recognised:

Astrocytomas are derived from astrocytes, star-shaped glial cells the general function of which includes the provision of support for neurons, e.g. in the supply of nutrients and removal of neuronal waste products or cellular material (S. K.

Kim, Nabekura, & Koizumi, 2017). Astrocytes are key mediators of brain development, function, and plasticity (Guizzetti, Zhang, Goeke, & Gavin, 2014). They coordinate neuronal development and synapse formation and function through the release of trophic factors and synthesis of extracellular matrix (ECM) (Christopherson et al., 2005; Pascual et al., 2005). Moreover, astrocytes express numerous receptors, such as receptors for neurotransmitters and neuromodulators, that allow inter-cellular communication with neurons (Clarke & Barres, 2013) and other cell types. Astrocytomas represent the most frequent type of glioma in both adults and children (34% of the brain tumours) (D. N. Louis et al., 2007). They can initially form in any part of the brain or spinal cord, they can be focal (mostly diagnosed in children) or diffuse. Anaplastic astrocytoma (or Grade III astrocytoma) and glioblastoma multiforme (GBM or Grade IV astrocytoma) are the most common in adults and represent high-grade gliomas reflective of their malignant characteristics, such as the ability to spread to other parts of the brain. Glioblastomas' cell types are all highly malignant and characterized by an abnormal vascularization and a high proliferative rate. In the centre of the tumour, it is possible to find necrosis, surrounded by a pseudostratified layer (pseudo-palisading). Glioblastomas are most commonly found in the cerebral hemispheres, but they can arise also in other parts of the brain and the spinal cord. Primary GBM defines a grade IV glioblastoma that lacks any clinical or histological evidence of a lower grade malignant precursor, whilst secondary GBM displays clinical or histologic evidence of having progressed from low-grade (grade II) diffuse astrocytoma or grade III anaplastic astrocytoma (Parat, 2009).

Oligodendrogliomas are derived from oligodendrocytes, which are specialised glial cells that provide support and insulation to axons in the central nervous system. Oligodendrocytes create the myelin sheath around nerve axons providing axonal protection and improving the speed of the electrical signals (action potentials) within the axons (Jäkel & Dimou, 2017). Only the 3% of brain tumours are oligodendrogliomas (D. N. Louis et al., 2007). They are most often found in the cerebrum, in the temporal or frontal lobes where they can be fast or slow growing. They are more frequent in adults although they do occur also in

young children. Oligodendrogliomas sometimes display the ability to spread within the central nervous system towards the cerebrospinal fluid.

Ependymal cells constitute a polarised epithelial-like cellular barrier lining the ventricles of the brain and lining the central canal of the spinal cord (Jiménez, Domínguez-Pinos, Guerra, Fernández-Llebrez, & Pérez-Fígares, 2014). Their function is to separate the cerebrospinal fluid from brain parenchyma. Ependymal cells give rise to ependymomas which are relatively rare low-grade tumours (J. Wu, Armstrong, & Gilbert, 2016).

1.4.2 GLIOMAS MOLECULAR PROFILING

Several attempts of molecular profiling have been proposed since 2006 for diffuse gliomas (gliomas with diffuse infiltrative nature, such as astrocytomas and oligodendrogliomas) (Huse, Phillips, & Brennan, 2011). They were inspired by the successful advancement in lung cancer clinical trial results of adjuvant Gefitinib after selection of patients with tumours bearing a mutation of epidermal growth factor receptor (EGFR) (Giaccone et al., 2004; Herbst et al., 2004; Sequist et al., 2008). The authors believed that a molecular stratification would allow bringing to light the therapeutic potential of some of the small molecule kinase inhibitors tested for glioma and rejected in clinical trials (De Witt Hamer, 2010).

The first attempt was published in 2006 with three subgroups, proneural, proliferative and mesenchymal (Phillips et al., 2006). This study associated molecular markers with the patients' survival. It included previously reported markers, such as the Chitinase-3-like protein 1 (CHI3L1 or YKL40) and vascular endothelial growth factor (VEGF), that were used to discriminate between GBM and lower-grade tumours, and new ones like Mindbomb homolog 1 (MIB-1). In the same time, the classification has been enriched by other studies (Karcher et al., 2006; Tso et al., 2006).

The proneural group is the one with the highest survival rate and thus the better prognosis, while the mesenchymal one is the most aggressive and characterized by worst outcome (Huse et al., 2011).

Four years later, Verhaak et al. used the data from The Cancer Genome Atlas Project (TCGA) to identify markers for the sub-classification of four GBM subtypes, Proneural, Neural, Mesenchymal, and Classic (Verhaak et al., 2010a). According to this classification, the proneural group this time is the one that does not benefit from a more aggressive therapeutical approach. This group is composed by tumours with Isocitrate dehydrogenases (IDH) mutations or Platelet Derived Growth Factor Receptor Alpha (PDGFRA) amplification, the classical subtype exhibits EGFR mutation and/or amplification whilst the mesenchymal one loss and/or mutation of Neurofibromin 1 (NF1). This study, in particular has received some critical comments (Huse et al., 2011) since it used "an unsupervised approach to classify data" and it presented a "lack of methodological uniformity" between studies.

Anyway, the distinction between the proneural and mesenchymal group in both studies seems to be robust enough to allow a legitimate stratification. In Figure 1.7 it is reported a schematic comparison between the two studies, the WHO classification and other marker-related studies previously reported.

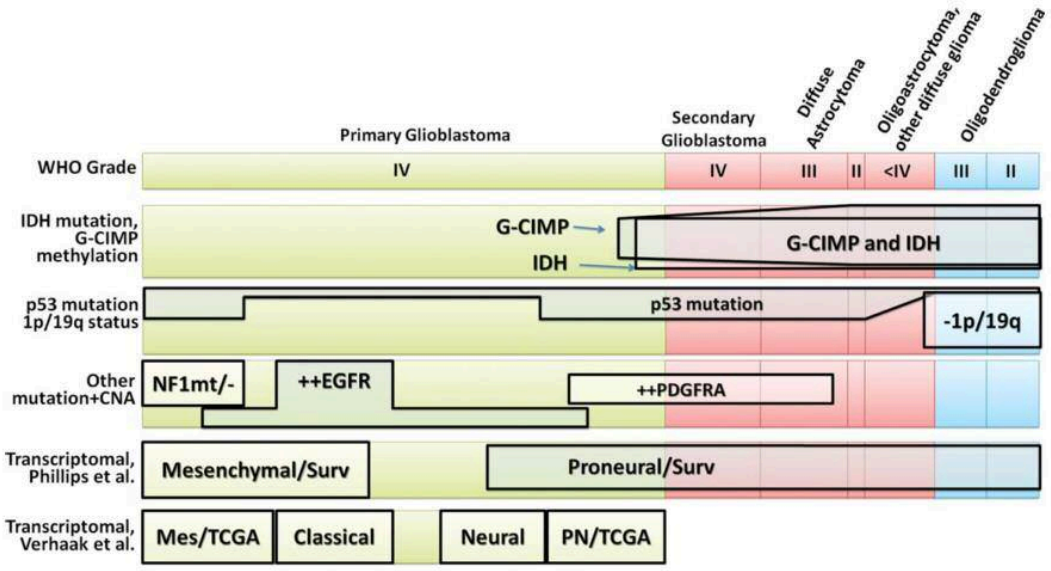

Figure 1.7 Schematic representation of the relationships between genetic markers and expression subgroups in diffuse gliomas. The areas are indicative of the incidence in adults (Central Brain Tumor Registry of the United States). Adapted from (Huse et al., 2011) with permission.

1.4.3 WHO 2016 CLASSIFICATION

Recent technological advancements and the consequent reduction in genomic sequencing costs made the shifting from a histological to molecular-based brain tumours classification a reality. In the last ten years, a variety of large-scale molecular profiling efforts have highlighted possible new biomarkers that allow the distinction of tumours similar form a microscopic point of view into more reproducible and objective subgroups.

Many of these efforts have been used to update the new WHO CNS 2016 classification (Louis, 2016). The new classification indeed is not based solely on tumours microscopic similarities with different putative cells of origin and their presumed levels of differentiation (Louis et al., 2016b). Despite the advances of this new system, like the increased objectivity given by the integration of genotypic and phenotypic parameters (Table 1.3), the authors still auspicate a further classification based only on the genetic characteristics, when a better stratification will be possible.

Table 1.3 The WHO CNS 2016 classification (D. N. Louis et al., 2016b)

Diffuse astrocytic and oligodendroglial tumours		Papillary glioneuronal tumour	I
Diffuse astrocytoma, IDH-mutant	II	Rosette-forming glioneural tumour	I
Anaplastic astrocytoma, IDH-mutant	III	Central neurocytoma	II
Glioblastoma, IDH-wildtype	IV	Extraventricular neurocytoma	II
Glioblastoma, IDH-mutant	IV	Cerebellar liponeurocytoma	II
Diffuse midline glioma, H3 K27M-mutant	IV	Tumours of pineal region	
Oligodendroglioma, IDH-mutant and 1p/19q-codeleted	II	Pineocytoma	I
Anaplastic oligodendroglioma, IDH-mutant and 1p/19q-codeleted	III	Pineal parenchymal tumour of intermediate differentiation	II or III
Other astrocytic tumours		Pineoblastoma	IV
Pilocytic astrocytoma	I	Papillary tumour of the pineal region	II or III
Subependymal giant cell astrocytoma	I	Embryonal tumours	
Pleomorphic xanthoastrocytoma	II	Medulloblastoma (all subtypes)	IV
Anaplastic pleomorphic xanthoastrocytoma	III	Embryonal tumour with multilayered rosettes, C19MC-altered	IV
Ependymal tumours		Medulloepithelioma	IV
Subependymoma	I	CNS embryonal tumour , NOS	IV
Myxopapillary ependymoma	I	Atypical teratoid/rhabdoid tumour	IV
Ependymoma	II	CNS embryonal tumour with rhabdoid features	IV
Ependymoma, RELA fusion-positive	II or III	Tumours of the cranial and paraspinal nerves	
Anaplastic ependymoma	III	Schwannoma	I
Other gliomas		Neurofibroma	I
Angiocentric glioma	I	Perineurioma	I
Chordoid glioma of third ventricle	II	Malignant peripheral nerve sheath tumour (MPNST)	II, III or IV
Choroid plexus tumours		Meningiomas	
Choroid plexus papilloma	I	Meningioma	I
Atypical choroid plexus papilloma	II	Atypical meningioma	II
Choroid plexus carcinoma	III	Anaplastic (malignant) meningioma	III
Neuronal and mixed neuronal-glial tumours		Mesenchymal, non-meningothelial tumours	
Dysembryonic neuroepithelial tumour	I	Solitary fibrous tumour/haemangiopericytoma	I, II or III
Gangliocytoma	I	Haemangioblastoma	I
Ganglioglioma	I	Tumours of the sellar region	
Anaplastic ganglioglioma	III	Craniopharyngioma	I
Dysplastic gangliocytoma of cerebellum (Lhermitte-Duclos)	I	Granular cell tumour	I
Desmoplastic infantile astrocytoma and ganglioglioma	I	Pituicytoma	I
		Spindle cell oncocytoma	I

The main genetic markers involved in this new classification are the IDH status and the 1p/19q deletion. Among other markers, there are Alpha-Thalassemia/Mental Retardation Syndrome, Non-deletion Type, X-Linked (ATRX) and tumour protein 53 (TP53).

In this work, only glioblastoma characteristics will be discussed.

Glioblastoma has been divided into two subgroups (Table 1.4), the IDH wild-type and the IDH mutant. The first one is mostly comprised by the *de novo* GBMs and represents the majority (90%) with an incidence more common in the age range >55 years old, whilst the second one represents around 10% of the cases, is more common in young people and is secondarily derived mostly by lower

grade gliomas. A third group is represented by those GBMs whose IDH status was not assessable.

The somatic IDH mutations correspond basically to the point mutation R132H of IDH1, or the mutually exclusive analogous residue in IDH2 (R172). These are enzymes part of the Krebs cycle, therefore relevant for the metabolic activity of the cells. Both the mutations affect the catalytic activity of the enzymes, leading to a decreased metabolic activity and a relatively better prognosis.

Table 1.4 Glioblastoma WHO 2016 classification (D. N. Louis et al., 2016b)

	IDH-wildtype glioblastoma	IDH-mutant glioblastoma
Synonym	Primary glioblastoma, IDH-wildtype	Secondary glioblastoma, IDH-mutant
Precursor lesion	Not identifiable; develops de novo	Diffuse astrocytoma Anaplastic astrocytoma
Proportion of glioblastoma	~90%	~10%
Median age at diagnosis	~62 years	~44 years
Male-to-female ratio	1.42:1	1.05:1
Mean length of clinical history	4 months	15 months
Median overall survival surgery + radiotherapy surgery + radiotherapy + chemotherapy	 9.9 months 15 months	 24 months 31 months
Location	Supratentorial	Preferentially frontal
Necrosis	Extensive	Limited
TERT promoter mutations	72%	26%
TP53 mutations	27%	81%
ATRX mutations	Exceptional	71%
EGFR amplification	35%	Exceptional
PTEN mutations	24%	Exceptional

Other genetic markers not reported in Table 1.4 are v-Raf murine sarcoma viral oncogene homolog B, (BRAF) V600E mutation, loss of Integrase Interactor 1 (INI1) expression, chromosome 10 loss, hemizygous deletions of Teneurin

Transmembrane Protein 3 (ODZ3) and Avian Myelocytomatosis Viral Oncogene Homolog (MYC) or Neuroblastoma MYC Oncogene (MYCN) amplification.

1.4.4 CURRENT THERAPEUTICAL OPTIONS FOR GBM

Even with advanced surgical procedures and treatment regimens involving radiation therapy and chemotherapy (Stupp et al., 2005), high-grade malignant gliomas display a poor prognosis. This is due to the diffuse infiltrative capacity of any residual tumour cells remaining after incomplete surgical resection, with the ability to spread to distant sites within the brain and undergo self-renewal and growth. High-grade tumours can also display resistance to chemo- and radiotherapy. The most aggressive form of glioma, GBM (grade IV), displays a median survival of two years (Parker, Khong, Parkinson, Howell, & Wheeler, 2015). Even the lower-grade gliomas that appear less aggressive at the time of diagnosis eventually progress into a malignancy. In addition, the destructive effect of such tumours on brain function often leads to cognitive and emotional deficits for patients. The treatment of high-grade gliomas represents a truly unmet medical need with improved genetic diagnosis and curative therapeutic strategies needed that target the cell of origin (Zong, Verhaak, & Canoll, 2012).

Upon initial diagnosis of GBM the standard treatment (Olar & Aldape, 2014) consists of maximal surgical resection, radiotherapy, and concomitant and adjuvant chemotherapy with Temozolomide (TMZ), an oral alkylating agent that was found to extend median survival to 15 months and with a 2-year survival in 26% of patients (Furnari et al., 2007; Stupp et al., 2009). This survival increase is, however, restricted to patients with tumours displaying an epigenetic silencing of the DNA repair gene methyl guanine methyl transferase (MGMT). Only when MGMT is methylated the survival is extended (Stupp et al., 2009). Another example is represented by MutS Homolog 6 (MSH6) gene mutations, which are not present in untreated GBM but are induced by TMZ treatment causing resistance to the therapy (Cahill et al., 2007; Yip et al., 2009).

Despite the new advances in target discovery and molecular classification described in glioma, very few markers passed the trial phase and are used in clinical practice. Indeed, apart from MGMT (which incidentally is not included in

the new classification but is already part of the routine diagnostic carnet), the only molecular marker in clinical practice for diffuse gliomas is the combined loss of chromosomes 1p and 19q, which is routinely tested in many centres as a prognostic and therapeutic indicator (Huse et al., 2011).

In the UK, the National Institute for Health and Care Excellence (NICE) (2007) guideline for newly diagnosed high-grade gliomas still advises Temozolomide as primary drug treatment, with the possible association of Carmustine implants, if more than 90% of a tumour has been removed (Price, Whittle, Ashkan, Grundy, & Cruickshank, 2012). Carmustine implants are biodegradable polymers impregnated with the alkylating agent Carmustine, that are implanted in the resection cavity at the time of the surgery. As an alkylating agent, Carmustine is able to bind DNA and prevent cell proliferation. The implants are in addition to surgery and radiation therapy.

1.4.5 CAV-1 AND GBM AGGRESSIVENESS

Cav-1 biology in glioma, by comparison to other tumour types, is poorly understood. There are a few limited studies of Cav-1 expression in clinical samples. These have reported positive correlations between Cav-1 expression and increased tumour grade (Barresi et al., 2009; Cassoni et al., 2007). Cav-1 expression has also been reported to independently predict shorter survival in oligodendrogliomas (Senetta et al., 2013), although this finding is not consistent with other studies that found no difference in Cav-1 expression in oligodendrogliomas or anaplastic astrocytomas (Barresi et al., 2009). It is clear however that Cav-1 positive and negative tumour cells co-exist in high-grade glioma. The potential role of Cav-1 in GBM has been reviewed by Parat (Parat & Riggins, 2012).

Whilst there are several possible single-nucleotide polymorphisms (SNPs) in the Cav-1 gene, only one has been related to cancer. Specifically in breast cancer (Hyangkyu Lee et al., 2002) in an *in vitro* and in a preclinical *in vivo* model, but there seems to be no clinical evidence of the association of Cav-1 mutations and brain tumours. Clearly, this is an area that needs further investigation.

In preclinical models, the work of Li and colleagues (Y. Li et al., 2011) has shown Cav-1 expression to promote astroglial differentiation of neural progenitor cells (NPCs), an outcome mediated through increased Notch1 signalling; the same workers showing Cav-1 to inhibit neuronal differentiation from NPCs (Y. Li et al., 2011) via inhibitory effects on VEGF, phosphor-Extracellular Signal-Regulated Kinase (pERK), AKT, Signal Transducer and Activator of transcription-3 (STAT3) pathways. Annabi and co-workers (Borhane Annabi, Thibeault, Moumdjian, & Béliveau, 2004) have proposed plasma membrane caveolae domains in glioma cells to serve as sites for the positive regulation of Cluster of Differentiation-44 (CD44) functional activity in respect to pro-invasive characteristics. Similarly, Strale's group (Strale et al., 2012) showed sequestration of Connexin43 in Cav-1 rich domains increased the invasive and clonogenicity of U251 glioma cells. Stanimoirovic's laboratory (Abulrob et al., 2004) reported Cav-1 in U87MG to serve as a molecular break for EGF receptor (EGFR) signalling, diminishing aggressive features of U87MG cells.

Cav-1 effects upon the glioma microenvironment have been studied: Régina et al. (Régina et al., 2004) reported angiogenic factors and hypoxia to downregulate Cav-1 in tumour brain microvasculature and to be associated with a less differentiated endothelial cell type. Kucharzewska et al. (Kucharzewska et al., 2013) reported hypoxia to induce Cav-1 levels in glioma cells and with Cav-1, amongst other molecules, to be secreted in exosomes from the glioma cells leading to promotion of angiogenesis during tumour development. Shimato et al (Shimato et al., 2013) reported that Cav-1 expression in brain tumour monocyte/microglia cells populations suppresses their immune-stimulatory functions and thus undermines immunotherapeutic strategies.

The more rigorously conducted studies focusing on Cav-1 biology in glioma are represented by three papers that have come from the laboratory of Sophie (Cosset et al., 2012; Martin et al., 2009) and from the one of Micheal Lisanti (Quann et al., 2013).

The group of Sophie Martin published two papers (Cosset et al., 2012; Martin et al., 2009) about Cav-1 and GBM, both using the astroglial cell line U87MG as the model of interest. They silenced Cav-1 with a shRNA approach and determined the genes affected by Cav-1 silencing. In particular, they focused on

integrins, more specifically on integrin α5β1; they found its expression increased with a knockdown of Cav-1, i.e. negative regulation of α5β1 by Cav-1. Cav-1 knockdown was also associated with an increase in cell proliferation, clonogenicity and adhesion to fibronectin. The tumour suppressor effects of Cav-1 were found to be integrin α5β1-mediated, as partly evidenced by the enhancement of Cav-1 silencing using an integrin antagonist.

They went on to explore how the expression of α5β1 integrin increased after the depletion of Cav-1. They found that Cav-1 caused transcriptional repression of α5β1 integrin. They showed that depletion of Cav-1 led to the activation of the Transforming growth factor (TGF) β/ TGFβ Receptor 1 (TGFBRI)/Smad2 pathway, which in turn induced the expression of α5β1 integrins.

They also examined human glioma biopsies and were able to identify isolated subgroups with either low levels of Cav-1/high levels of α5β1 and TGFβRI or high levels of Cav-1/low levels of α5β1 and TGFβRI. There were, however still a proportion of tumours in which Cav-1 and α5β1 expression were not inversely related. They concluded the status of Cav-1/α5β1 integrins/TGFβR1 axis might be a useful marker of the tumour evolution/prognosis in GBM as well as a predictor of the effectiveness of anti-TGFβ or anti-α5β1 integrin therapies.

The laboratory of Micheal P. Lisanti focused on the overexpression of Cav-1 in an in-vivo model. Using U87MG overexpressing Cav-1 through a lentiviral-based system, they observed a decrease of tumorigenicity (in an ectopic xenograft mouse model) with Cav-1 overexpression and an increase in Temozolomide sensitivity, the most commonly used chemotherapy agent for GBM. These effects (included Cav-1 overexpression) were associated with a decrease in the activity of the Phosphatidylinositol-4,5-Bisphosphate 3-Kinase (PI3K)/ Mechanistic Target Of Rapamycin Kinase (mTOR) pathway, metalloproteases and Cyclin D1, and an increase of P53, Phosphatase And Tensin Homolog (PTEN) (both negative modulators of the PI3K/mTOR pathway), factors responsible for cell cycle and transcription stop (FOXN3, HDAC, VHL and CDKN1C) and apoptosis-involved players.

Together the data indicate that Cav-1 serves as a putative tumour suppressor in GBM.

1.5 STEMNESS IN CANCER

There are multiple theories and models about tumour evolution and heterogeneity (Figure 1.8) (Parker et al., 2015). One of these is the “clonal evolution theory”, according to which somatic alterations occurring in the initial cell of origin lead to multiple cancer cell clones of differing chemo-sensitivities, survival and proliferative ability. These genetically unstable clones undergo successive genetic alterations and tumour cells with the most aggressive phenotype are selectively enriched.

In contrast, the “cancer stem cell theory” views that a tumour comprises a small percentage of the cells, known as cancer stem cells (CSC), which display the classic stem properties such as the ability to self-renew, to continuously proliferate, to give rise to genetically different clones, and display resistance to therapy. It is the sustained survival of these CSC that affords the persistence of the primary and secondary tumours.

Finally, the “theory of inter-clonal cooperativity” suggests that tumour evolution and heterogeneity is induced by interactions between tumour cell clones and the microenvironment.

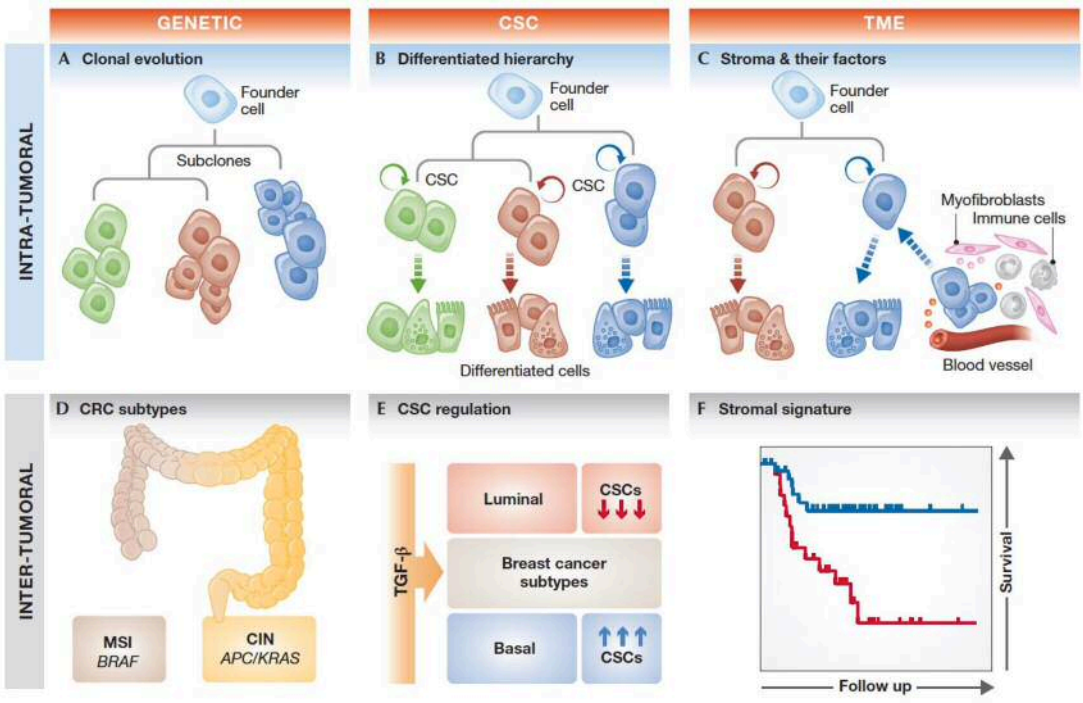

Figure 1.8 **Models for the origin of intra- (A-C) and inter- (D-F) tumour heterogeneity. A. Clonal evolution model.** From a common founder cell, different subclones emerge due to selection and distinct mutations. B. Cancer Stem Cells (CSCs) model. According to this model clonal evolution only happens for the CSCs. Different lienages are able to arise from different CS clones. C. Interclonal cooperativity model. The interaction with the microenvironment drives the phenotype of plastic cancer cells. D. Different subtypes of cancer can arise from different mutations occurring in different parts of the same organ. E. signals from the microenvironment can trigger the activation of specific CSCs clones. F. Gene expression can be used to identify patients with different survival probability. **Adapted from** (De Sousa E Melo et al. 2013) with permission.

While Figure 1.8 shows the three theories (Inda, Bonavia, & Seoane, 2014), Figure 1.9 shows how these three theories may give rise to GBM (Parker et al., 2015). The significant clonal diversity within tumours may explain the lack of effectiveness of the molecular target therapies in GBM patients. According to the theory of clonal evolution, one single cell affected by somatic alterations can give rise to multiple cancer clones each one displaying a different sensitivity to therapy and behaviour, such as the ability to survive and proliferate. These clones are genetically unstable and undergo successive waves of genetic alterations, and the ones with the most aggressive phenotype are advantaged. For example, cells displaying inhibiting methylation of the promoter in the MGMT gene (i.e. suppressing MGMT functional repair of damaged DNA) are more sensitive to the alkylating agent Temozolomide (TMZ) (Figure 1.9A). On the other hand, with the cancer stem cell theory, only a single subset of cells (CSCs) display the ability to self-renew, to endlessly proliferate and to give rise

to genetically variable clones, that are intrinsically resistant to therapy (Figure 1.9B). The theory of interclonal cooperativity views that the evolution and the heterogeneity of tumours are promoted by the interaction between tumour cell clones and the microenvironment with which they are in contact, including both immune and stromal factors (Figure 1.9C). Indeed, the reality will be more complex and likely involve elements of at least all three models.

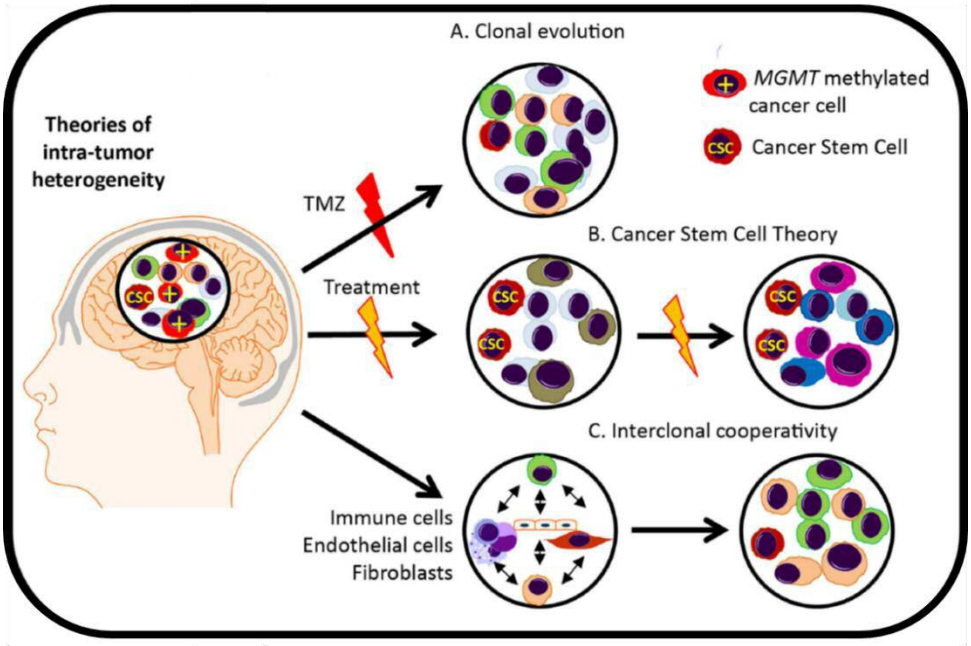

Figure 1.9 Glioblastoma tumour heterogeneity theories: tumour evolution and tumour heterogeneity may be promoted by clonal evolution (A), cancer stem cells (B) and interclonal cooperativity (C). Adapted from (Parker et al., 2015).

The properties that tumour cells are characterised by in terms of stem-like properties are:

Self-renewal (Figure 1.10A) – the ability of cells to continuously self-renew through symmetrical (both daughter cells the same as parent cell) and asymmetrical (daughter cells differing with only one daughter exactly the same as the parental one) cell divisions. Self-renewal is considered a characteristic of crucial importance for stem cells because it is the only way to ensure that at least one of the progenies display the same molecular characteristics as the parental stem cell. In terms of cancer, it is the mechanism that sustains over

multiple generations the cells whose characteristics underpin CSC populations (Suksuphew & Noisa, 2015).

Multipotency (Figure 1.10B) - the property of cells to retain the potential for cell differentiation to give rise to specialized and/or terminally differentiated cells. Stem cell plasticity is progressively restricted as differentiation advances, such that whilst the early stem cell generation(s) can give rise to a broad range of cell types, the latter more differentiated progeny have a more limited capacity, for example, able to give rise to only one or two different, but more closely related, cell types (Suksuphew & Noisa, 2015).

Tumorigenicity (Figure 1.10C)- the property of a cell or collection of cells to give rise to tumours. It does not, however, mean that tumorigenicity is explained only by the cancer stem cell theory (Sampetrean & Saya, 2013).

Chemo- and radio-resistance (Figure 1.10D)- this is the ability of tumour cells to possess or develop mechanisms that reduce the effectiveness of therapies and has direct clinical relevance. For example, the expression of efflux transporters in tumour cells, like P-glycoprotein, that export cytotoxic agents from the cell (Filatova, Acker, & Garvalov, 2013), or the expression of enzymes that repair DNA alkylation damage e.g. the enzyme MGMT removing methylation of DNA induced by TMZ.

Invasion and metastatic ability (Figure 1.10E) - invasion is the ability to overcome the ECM and the microenvironment to migrate and invade through tissue, to escape the confines of the primary tumour. This translates into metastasis when the invading cells reach blood or lymphatic vessels, overcome the vessel barrier and travel through the blood or lymphatic system to establish as a secondary tumour within a new microenvironment at a distant site. This ability requires the cells to display the property of plasticity to adapt its functions to meet changing needs and changing environments, a property that makes cells extremely aggressive (Beck & Blanpain, 2013). The same processes are also observed in a variety of physiological conditions, such as in development where differentiated cells may dedifferentiate, move towards a distant site, and differentiate again to form a new structure. This phenomenon is known as epithelial-mesenchymal transition (EMT) and is a natural physiologic characteristic, that can be observed during development but also in adult life

whilst e.g. wound healing is necessary (Kerosuo & Bronner-Fraser, 2012; Savagner, 2010); EMT is currently studied for the onset of cancer cell migration, invasion and metastatic spread (Yilmaz & Christofori, 2009).

Neo-angiogenesis (Figure 1.10F) - the ability of parenchymal cells to sense a decrease in the oxygen tension of their microenvironment and activate mechanisms that lead to the secretion of molecular signals stimulating the formation of new blood vessels. This ability is also connected to the theory of interclonal cooperativity, since newly-formed blood vessels may represent an ideal niche for cancer cells, particularly for GMB, whose cells in contact with the endothelial perivascular cells can exchange growth and survival factors (Folkins et al., 2007; Persano, Rampazzo, Basso, & Viola, 2013).

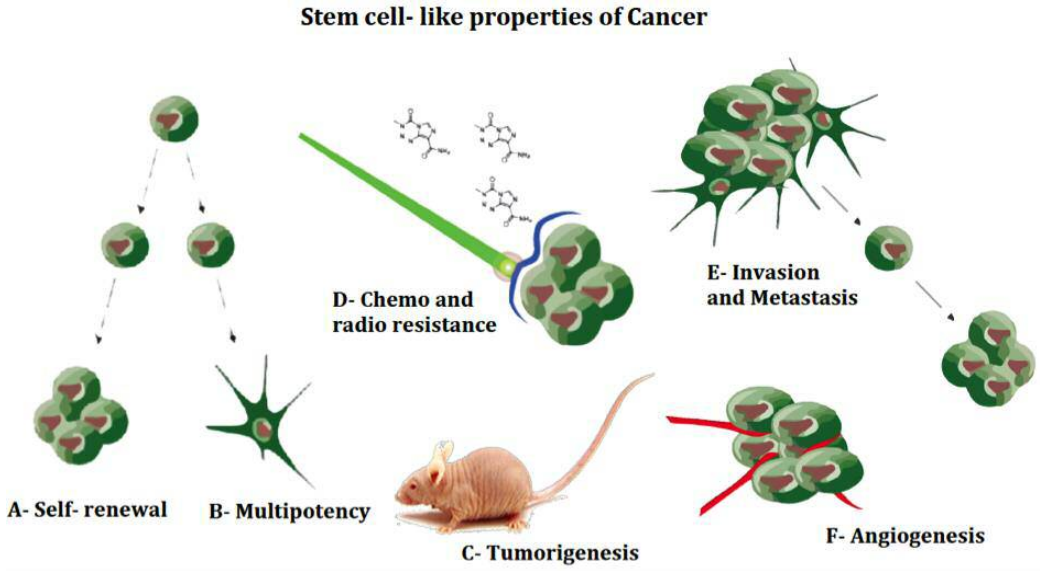

Figure 1.10 Stem cell-like properties of cancer: A- self-renewal, B- Multipotency, C- Tumorigenesis, D- Chemo- and radio-resistance, E- Invasion and metastasis, F- Angiogenesis.

1.5.1 CLONOGENICITY

1.5.1.1 CLONOGENICITY AND STEM CELL PROPERTIES

Clonogenicity is a stem cells property that can be distinguished in two and interconnected capabilities (Lewis & Petritsch, 2013). Stem cells, under physical and/or molecular stimuli, can start proliferating and undergo symmetrical or asymmetrical division. As a result of the symmetrical division, the daughter cells are exactly identical to the parental one. After the asymmetrical division, on the

contrary, the resulting daughter cells are different from each other. One of them is exactly the copy of the parental cell (according to the self-renewal ability principle). The other, on the other hand, is different from the previous two, reflecting a more committed phenotype; it will be potentially able to differentiate in all the different phenotypes that the committed cell is able to give rise to (in this case we can refer to the multipotency ability principle).

It can be thus inferred that clonogenicity is an essential property in stem cells that have to repair tissues damages. They need to differentiate and to give rise to new specialized cells but, in the meantime, it is important to maintain the stem phenotype for future needs.

Clonogenicity is of course also tightly connected to proliferation since the latter represents the first responder to the stimulation of the stem cell and it is also necessary for the generation of enough specialized cells for the complete repairing of the damage. Furthermore, clonogenic cells can proliferate whilst, e.g., invasive cells stop their proliferation and activate their motility mechanisms. Molecularly this is reflected in the passage between different phenotypes, among which the EMT is the most studied (De Sousa E Melo et al., 2013).

1.5.1.2 CLONOGENICITY AND CANCER

According to the CSC theory, within a tumour, most cells are non- tumorigenic and are characterized by limited self- renewal ability. The only subpopulation able to self-renew and initiate tumours is the one represented by the CSCs, also called tumour- initiating cells. This small group of cancer cells are believed to be able to hibernate during radiotherapy and chemotherapy, saving in this way their genetic and structural integrity (chemo- and radio-resistance), and to re-activate when the environmental conditions change, displaying both self- renewal and multipotency ability, in order to recapitulate a tumour (relapse and metastatic potential).

1.5.1.3 CLONOGENICITY AND GLIOMA

There are several signalling pathways that have been identified as shared between stem cells and Glioma stem cells (GSCs.) Among these, the most important are the Notch, Sonic Hedgehog (Shh), Bone morphogenetic proteins (BMPs) and Wingless-Type MMTV Integration Site Family (Wnt) signalling

pathways (Figure 1.11), that are believed to be essential for the maintenance of multipotency and self-renewal (Liebelt et al., 2016). In particular Notch signalling is important for regulating multiple cellular processes, including proliferation, differentiation, apoptosis, and cell lineage commitment in neural stem cells (NSCs), (Lasky & Wu, 2005). Recent studies have reported the implication of Notch signalling to be highly active in GSCs in the suppression of differentiation and in the maintenance of stem-like properties. Downregulation of Notch and its ligands, i.e. Delta-like-1 and Jagged-1, determines a decrease of the GSC oncogenic potential, implicating that Notch plays an important role in GSC survival and proliferation (Purow et al., 2005).

BMPs participate to the regulation of proliferation, differentiation, and apoptosis in NSCs through their interaction with various signalling molecules among which, for example, the hypoxia-inducible factor-1 (HIF-1) (Pistollato et al., 2009). Wnt signalling induces BMP expression, which redirects NSCs toward an astroglial lineage (Kasai, Satoh, & Akiyama, 2005). In the same way, BMPs expression is shown to play an important role in directing glioma stem cells (GSCs) astroglial differentiation, inhibiting in this way their tumorigenic potential (Piccirillo et al., 2006). Moreover, BMP-2 reduces GSCs proliferation and sensitizes them to TMZ through destabilization of HIF-1 (Persano et al., 2013), while *in vivo* delivery of BMP-4 decrease brain tumour growth with a consequent reduction in mortality (Piccirillo et al., 2006). Finally, a BMP antagonist, Gremlin1, prevents differentiation of GSCs confirming the role of endogenous BMP in the maintenance of GSC self-renewal and tumorigenic potential (Yan et al., 2014).

As mentioned, Wnt signalling is important for the regulation of neural stem cells expansion and the promotion of astroglial lineage differentiation (Pei et al., 2012). Downstream -Catenin is a critical factor for proliferation and differentiation of GSCs. An aberrant activation of Wnt signalling in GSCs induces tumour growth through nuclear localization of stabilized -Catenin. FoxM1/ -Catenin interaction induces the transcription of Wnt target genes like c-

Myc promoting glioma formation (N. Zhang et al., 2011). Finally, Wnt/ -Catenin signalling influences the expression of PLAGL2 leading to the suppression of GSCs differentiation and the maintenance of their stem phenotype (Zheng et al., 2010).

The EGFR signalling pathway influences NSCs proliferation, migration, differentiation, and survival (J. Wang & Yu, 2013). EGFR activation promotes GSC proliferation and tumorigenesis by transactivation of -Catenin, whilst its overexpression increases the self-renewal capability of GSCs and consequently their tumorigenic potential (W. Yang et al., 2011).

Sonic hedgehog (Shh) signalling is essential for proliferation, differentiation, and survival of NSCs in the subventricular zone (SVZ). Recent studies reported that the Shh pathway is highly important in the maintenance of self-renewal and the induction of tumorigenesis through the regulation of stemness genes (Ihrie et al., 2011). Suppression of Shh signalling impairs *in vitro* self-renewal and *in vivo* tumorigenicity, confirming the dependency of GSCs on Shh signalling for their survival.

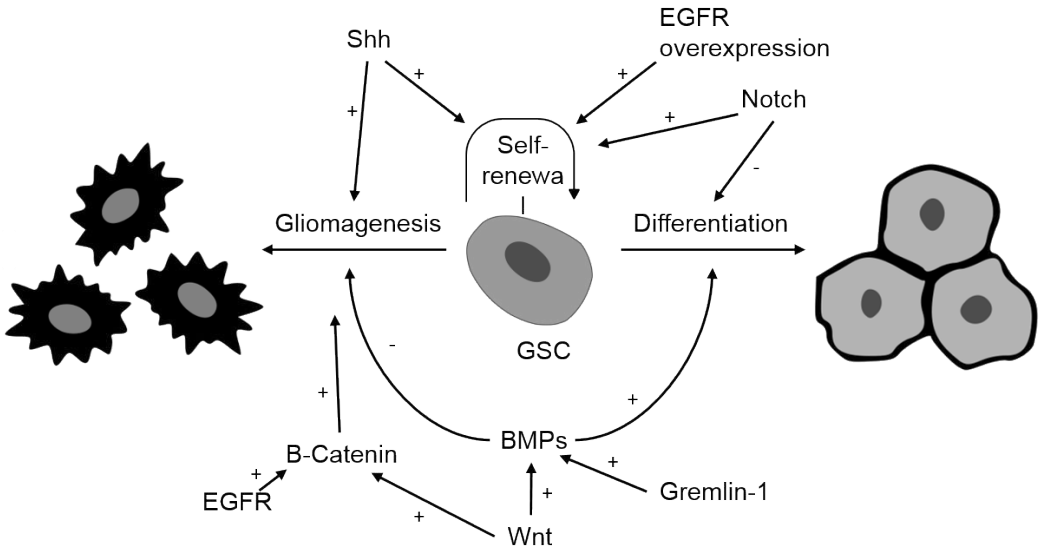

Figure 1.11 Key molecular pathways regulating steps in glioma stem cell self-renewal, differentiation, and gliomagenesis (Liebelt et al., 2016)

1.5.1.4 CAV-1 GLIOMA AND CLONOGENICITY

As previously discussed in 1.4.5, the group lead by Sophie Martin reported that, after manipulation of the levels of Cav-1 in a GBM cell line (U87MG), they observed that its reduction shifted cells towards a more aggressive phenotype whilst the forced expression of caveolin-1 slowed down not only proliferation and invasion but also clonogenicity (Martin et al., 2009). They then related this phenotype to the interference with a mechanism driven by secreted TGFβ (Cosset et al., 2012).

INVASION

1.5.1.5 INVASION AND STEM CELL PROPERTIES

Adult stem cells usually reside in the so-called stem cell niche, a physical environment, composed of cellular and non-cellular components, which provide nutrients and soluble factors and allow stem cells to maintain their quiescent status. In the brain, the stem cell niche has been demonstrated to reside in the perivascular environment, where NSCs can, in physiological conditions, receive nutrients and maintain their undifferentiated and quiescent status. In pathological conditions, they can instead receive activating signals in a prompt manner if their contribution is required for the production of new neurons or new macroglia components (astrocytes and oligodendrocytes) (Ottone et al., 2014). Adult stem cell niche effectors originate from the vascular endothelium, the molecules that are carried by the circulation, the ECM deposition, and the perivascular cell types (Figure 1.12) (Goldberg & Hirschi, 2013).

In the striatum it has been demonstrated that astrocytes are able not only to give rise to other astrocytes but also to de-differentiate in neural stem cells and produce new neurons, in response to injuries like stroke (by the downregulation of Notch signalling) or injury (by downregulation of Notch-mediated transcription factor Rbpj or overexpression of Sox2) (Magnusson & Frisen, 2016).

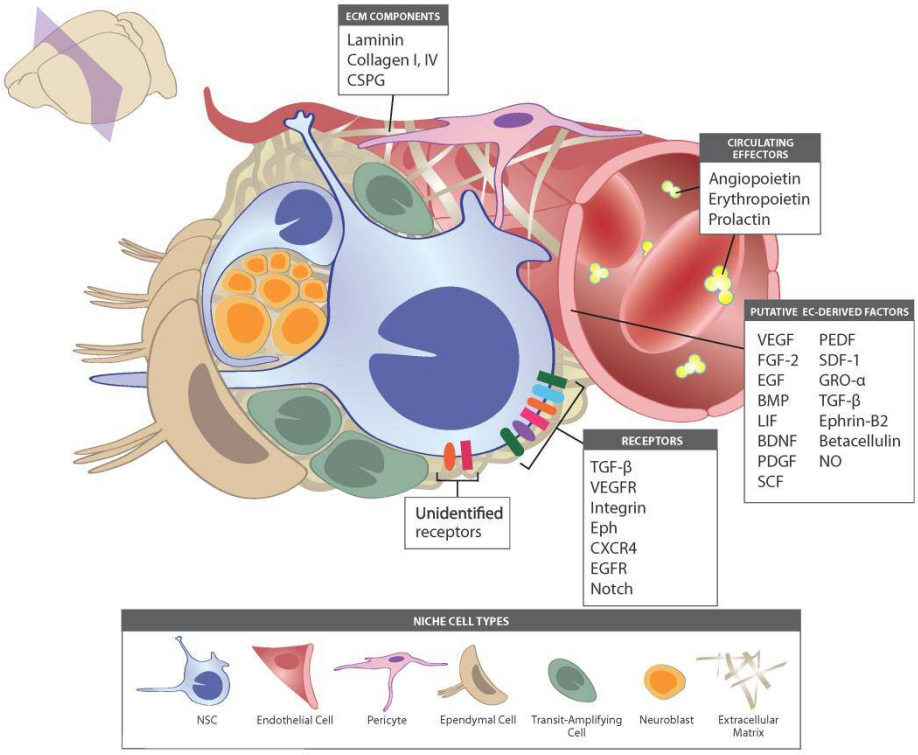

Figure 1.12 Putative vascular–derived regulators of the adult neural stem cell niche in a brain cross-section. With the permission of (Goldberg & Hirschi, 2013).

1.5.1.6 INVASION AND CANCER

Invasion in cancer is tightly related to EMT. EMT concept has been defined in chick embryos for the first time in 1968 by Elizabeth Hey, from Harvard Medical School (Hay, 1995). She defined it as a process, essential in embryos, during which cells with an epithelial phenotype loose contact with the surrounding cells and acquire a mesenchymal phenotype, which enables them to break through the basement membrane that separates the different tissues of the embryo, allowing the formation of new sub-tissues and, later on, organs (J. Zhang et al., 2015). Subsequently, researchers connected aberrant reactivation of EMT to tumour cell migration and invasion.

Several distinct molecular processes are required in order to initiate an EMT. These include activation of transcription factors for the expression of specific cell-surface proteins, cytoskeletal proteins and ECM-degrading enzymes. Some of these factors are often used as biomarkers to demonstrate the passage of a cell through an EMT, like for example the loss of E-Cadherin and the expression

of N-Cadherin, Vimentin, the nuclear localization of β-Catenin and the expression of transcriptional markers (summarized in Figure 1.13) (J. M. Lee, Dedhar, Kalluri, & Thompson, 2006).

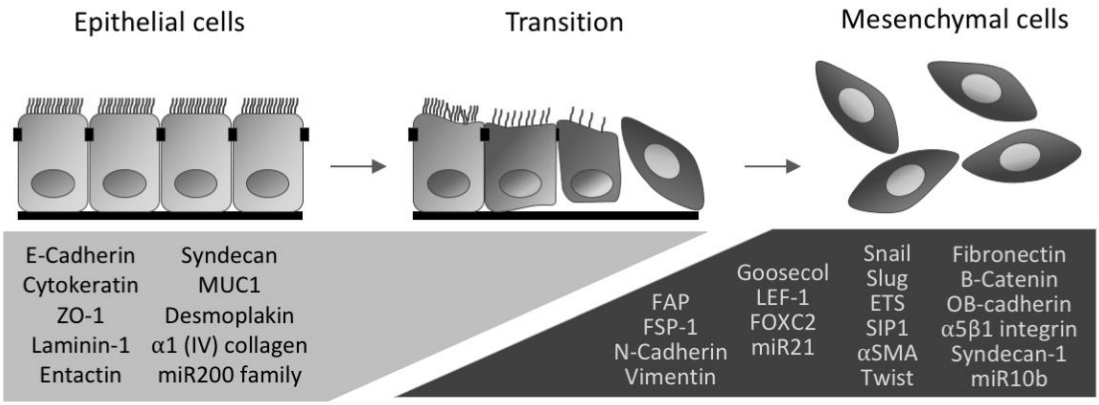

Figure 1.13 EMT markers

1.5.1.6.1 PATTERNS OF INVASION

The different tumours histological patterns and their behaviour in experimental conditions suggest that tumour cells can employ different ways of invasion. These molecular mechanisms translate then in cellular mechanisms, depending on the cell type and on the interaction with the local microenvironment.

Tumour cell invasion can be distinguished by two mechanisms: single and collective migration (Figure 1.14) (Friedl, Locker, Sahai, & Segall, 2012). Single-cell migration pattern includes the amoeboid and the mesenchymal sub-patterns. Amoeboid-like cells can invade as single cells, without interacting with the environment, but simply modulating their cytoskeleton in order to adapt their shape and access to the available parts of the surrounding tissue. Mesenchymal-like cells have a more defined shape and so need to interact with the ECM and the other cellular components, through the expression of adhesion and proteolytic molecules. They can invade as single cells or as strains, with the leading cells creating a path for the other cells.

The collective migration is typical of mesenchymal-like cells crossing the tissue in an organized manner, with the cells in front degrading the matrix and interacting with the other elements and the cells in the middle creating a supra-

cellular contractility system that allows a group of cells to move in a concerted manner (Friedl et al., 2012).

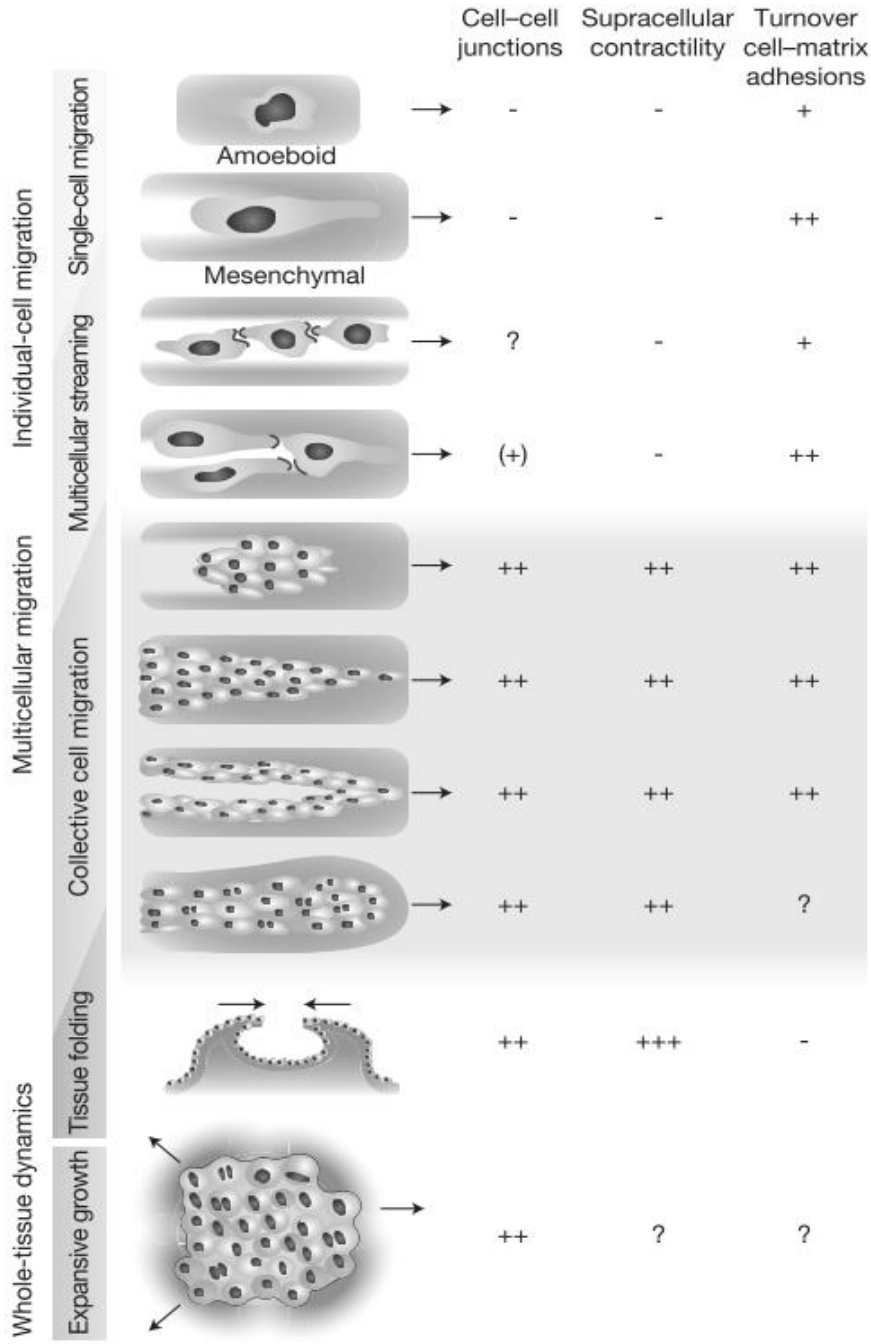

Figure 1.14 Patterns of Cancer Cell Invasion. Adopted from (Friedl et al., 2012) with permission.

1.5.1.7 INVASION AND GLIOMAS

Invasive behaviour is a critical prognostic factor for primary brain tumours. Glioma cells display a highly invasive behaviour that leads to the quick spreading of a tumour throughout both hemispheres (Brösicke & Faissner,

2015). This feature causes a dramatically shortening of glioma patients lifespan (Adamson et al., 2009).

The peculiarity of glioma cells invasion is their ability to migrate as single cells even to distant parts of the brain. Despite precise and accurate surgical procedures, the removal of all malignant cells is impossible and the relapsing tumours exhibit high resistance to chemotherapy and radiation approaches (Bao et al., 2006; Giese, Bjerkvig, Berens, & Westphal, 2003).

Regarding migration pathways, tumour cells display a tendency for blood vessel basement membranes, white matter tracts (such as the corpus callosum) and sub-ependymal layers as leading structures (Claes, Idema, & Wesseling, 2007). Although their migration along blood vessels, primary brain tumours are not able to invade into blood vessel walls. Neither do they invade into the braincase (Esiri, 2000). The vascular invasion capacity is a primary requisite for wide haematogenous metastasis of malignant neoplasms. This explains the very low propensity of primary brain tumours to metastasize outside of the brain to systemic organs (Bellail, Hunter, Brat, Tan, & Van Meir, 2004).

Usually, malignant cell types follow a three-step model of invasion. At the invasive front, tumour cells:

1. detach from the growing primary tumour bulk,
2. adhere, via specific receptors, to the ECM and
3. degrade the local ECM components progressively forming a pathway for the migration into adjacent tissues.

Brain tumours follow this model in some ways, even if their peculiar histologic pattern of invasion and the unique brain ECM composition, suggest that some glioma-specific mechanisms might also be involved (Bellail et al., 2004).

1.5.1.7.1 ECM IN GLIOMAS

The intercellular space occupies the 20% of the adult brain volume. This volume is filled for a further 20% with ECM (Nicholson & Syková, 1998). It is organized differently according to the three principal compartments: the basement membrane, the perineural nets and the neural interstitial matrix (Figure 1.15)

(Lau, Cua, Keough, Haylock-Jacobs, & Yong, 2013). The basement membrane is a layer that surrounds and is part of the vasculature and serves as a bridge between the endothelial cells and the brain parenchyma; it is composed by laminin-nidogen complexes (or entactin), collagen, fibronectin, dystroglycan complexes and perlecan. The perineural nets surround neuronal cell bodies participating in the maintaining of cellular health and synaptic plasticity; they are composed by proteoglycans, tenascins ad other link proteins. The neural interstitial matrix is formed by ECM molecules that are dispersed in the parenchyma, not associated with basal membranes nor perineural nets; it is composed by proteoglycans, hyaluronan, tenascins and link proteins associated in a dense network together with small amounts of collagen, elastin and adhesion molecules (like laminin and fibronectin).

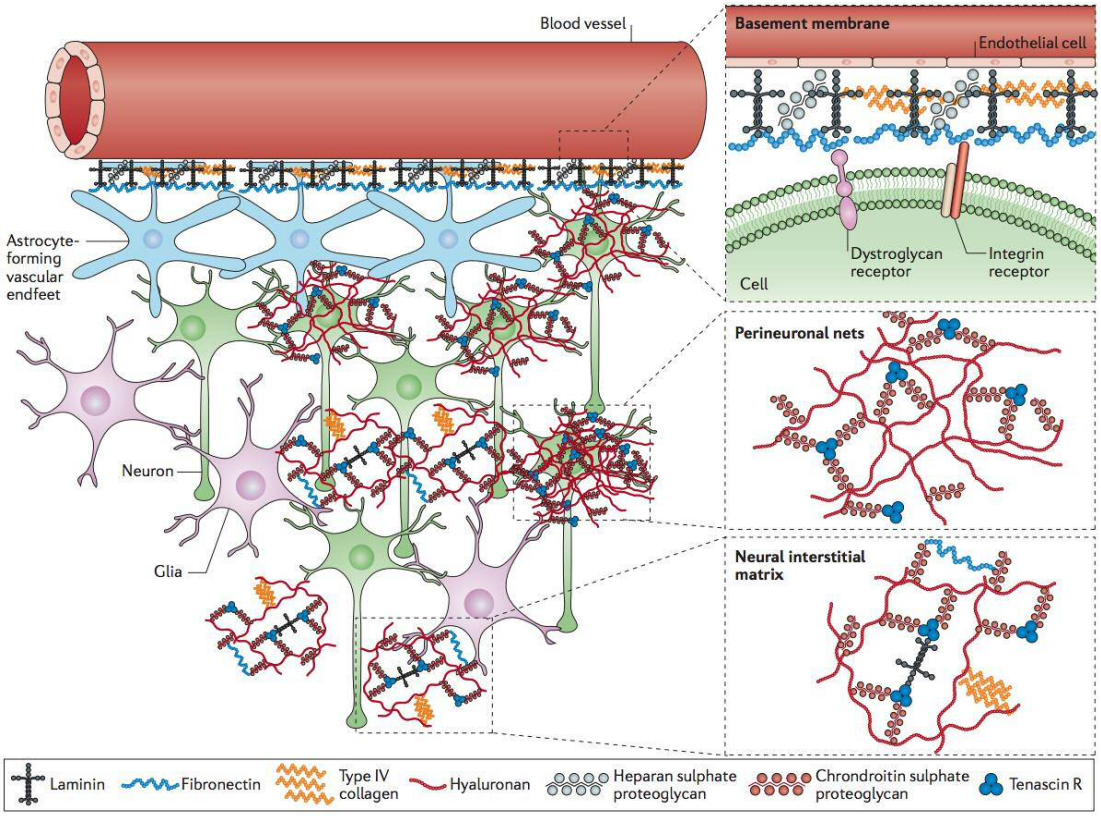

Figure 1.15 The three major compartments of the ECM in the CNS. Adopted from (Lau et al., 2013) with permission.

Hyaluronan (or hyaluronic acid, HA, Figure 1.15) is the major component of the brain ECM. Its high anionic property allows attracting high levels of cations,

which bring a high osmotic flux, ensuring an environment rich in water (Alberts et al., 2002). Through specific receptors, HA is non-covalently bound to other components of ECM, like the proteoglycans belonging to the family of lecticans (versican, aggrecan, neurocan, brevican) (Bignami, Hosley, & Dahl, 1993). HA is upregulated in tumour stroma and in the advancing edges of a tumour within the brain parenchyma. Interestingly, HA has been implicated in the stimulation of tumour proliferation and invasion and inhibition of apoptosis (S. H. Cho et al., 2012), but apparently according to his molecular weight. Indeed, Hirose et al. reported that, following Stabili-2 inhibition, HA levels were increased, and tumour metastasis was inhibited. However, this tumour suppressor function was limited only on small-sized HA (about 40kDa) suggesting a differential role of the different sizes of HA (Hirose et al., 2012). Proteoglycans consist of a protein core that can be chondroitin-, heparin-, keratin- or dermatan-sulphate. Up to now, 25 different proteoglycans have been identified, some of which exclusively present in the brain (like the brain-enriched hyaluronic acid binding protein or BEHAB, which is expressed only in malignant brain tumours). Important ECM components for brain tumour invasion are SPARC (Secreted Protein Acidic And Rich In Cysteine Or Osteonectin), that normally works as de-adhesive protein and cell cycle inhibitor, Thrombospondin-1 (TSP-1) that has a role in migration, invasion, adhesion, angiogenesis inhibition and activation of TGF- β and Tenascin C (TN-C), normally present in the white matter, that is upregulated in tumour (with increased expression associated to the increase of tumour grade) as well as in embryogenesis and wound healing. It is also inversely correlated with the expression of fibronectin (Higuchi, Ohnishi, Arita, Hiraga, & Hayakawa, 1993).

The lack of fibrillar components, such as collagen (with the exception of the perivascular niche), makes brain ECM softer in consistency, in comparison with other tissues ECM. (Bellail et al., 2004)

Hyaluronan has been proven to promote primary brain tumour invasion *in vivo* and migration *in vitro* through its binding to its two cellular receptors, CD44 and RHAMM (Akiyama et al., 2001). Further investigations anyway seem necessary, since glioma has been proven to invade along blood vessels, where hyaluronan is not present (Bellail et al., 2004).

Vitronectin, Osteopontin, REHAB, Tenascin C, Thrombospondin-1 and SPARC are upregulated in gliomas, and the last three have been suggested to play a role in the promotion of angiogenesis (Higuchi et al., 1993).

Versican is downregulated in some primary brain tumours and it seems to inhibit brain development, even if its mechanisms are unknown (Paulus, Baur, Dours-Zimmermann, & Zimmermann, 1996).

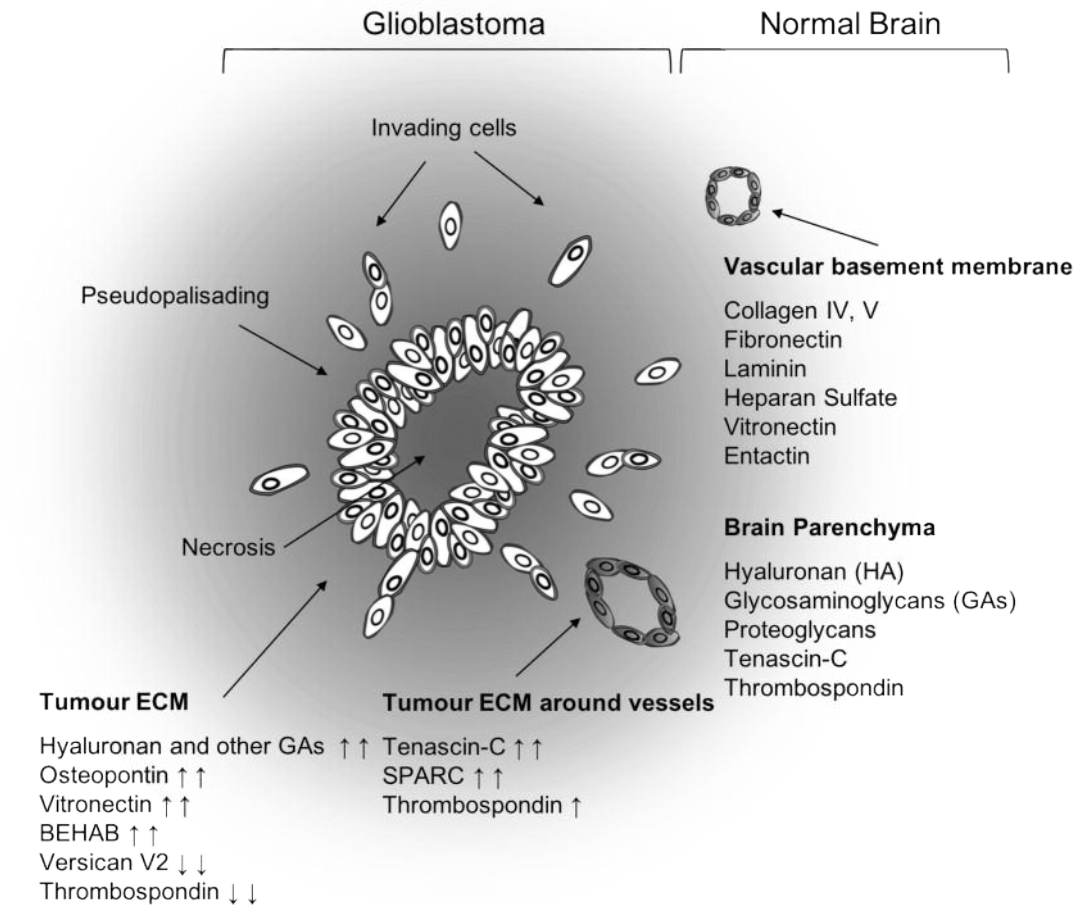

Figure 1.16 Schematic representation of the heterogeneity of the distribution of the various matrix proteins in normal brain ECM and in glial tumours

1.5.1.7.2 PROTEASES IN GLIOMAS

Proteases are secreted by glioma cells, glioma-associated macrophages or endothelial cells. They can degrade brain ECM or blood vessels basal lamina allowing glioma cell invasion through the brain parenchyma or along blood

vessels. They can also regulate growth and chemotactic factors (or their receptors) produced in the normal brain tissue or within a tumour (Mentlein, Hattermann, & Held-Feindt, 2012).

Proteases can be classified according to their mechanism of catalysis (e.g. metallo-, serine and cysteine proteases) or according to their molecular structure (e.g. the Metzincin proteases share a conserved Met at their active site and a Zinc ion at their enzymatic domain). They may be also distinguished, according to their protein target, in endopeptidases, specific in targeting internal peptide bonds, and exopeptidases, which target the last amino acids of the protein chains (aminopeptidases for the N-terminal and carboxypeptidases for the C-terminal). Whilst cysteine, serine and threonine proteases are named according to their target amino acid, matrix metalloproteinases (MMPs) are named after their localization (they are secreted in the ECM) and the presence of the Zinc ion (they are part of the Metzincin family) in their enzymatic domain, surrounded by the three Hys residues that contribute to their function (Nagase et al., 2006).

Proteases can be also distinguished according to their localization (Figure 1.17): intracellular proteases are located in the cytoplasm and intracellular organelles and can modulate the cytoskeleton and the intracellular responses; the extracellular cell surface-bound proteases are attached to the cell membrane and are able to activate receptors (like Notch, ErbB4 and Angiopoietin receptor Tie-1) (Gridley, 2007; Sato et al., 1995), cleave adhesion molecules (like MT1-MMP for CD44), release cytokines or growth factors (like MMP7 for pro-tumour necrosis factor- (TNF-) α) and activate other proteases (like plasminogen) (Nagase et al., 2006); extracellular secreted proteases in gliomas include MMPs, ADAMTS (a disintegrin and metalloproteinase with thrombospondin motifs) and serine proteases (like the urokinase/plasmin-type) and Cathepsins; they can be secreted as their active form or in a pro-active form that has to be activated by other proteases, to consequently cleave and activate other pro-proteases (typical of the MMPs) (Nagase et al., 2006).

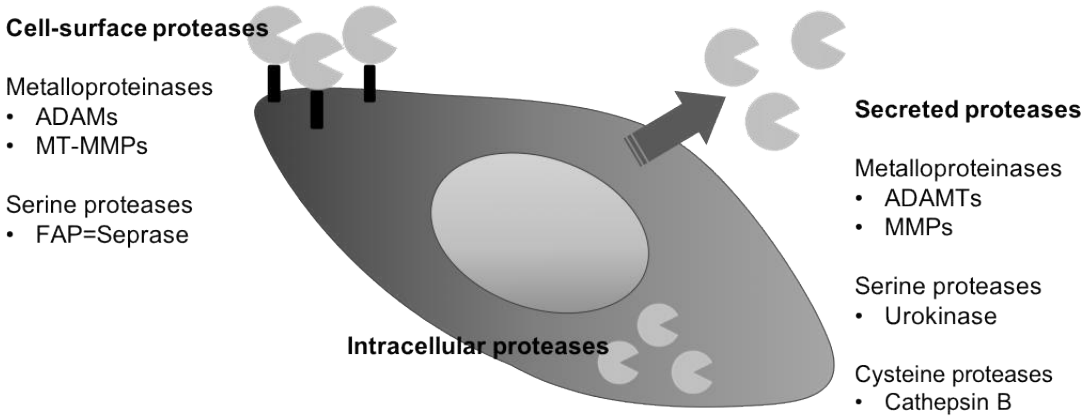

Figure 1.17 Example of different types of proteases on tumour (or tumour-associated) cells. (Mentlein et al., 2012)

MMPs (Table 1.5) are distinguished in collagenases, stromelysins, gelatinases (according to their substrate) and MT-MMPs (bound to the external cell surface). Interstitial collagenases cleave preferentially different interstitial collagen subtypes. Stromelysins digest basement membrane proteins as substrates, whereas gelatinases process primarily cleaved matrix proteins into smaller fragments (Herouy, 2004). While the first three categories are secreted as inactive forms and then activate by other proteases, the MT-MMPs are cleaved and activated into the Golgi and then expressed as functional on the cell membrane (Rivera, Khrestchatisky, Kaczmarek, Rosenberg, & Jaworski, 2010).

Table 1.5 Selected substrates of different matrix metalloproteinases (MMPs).(Herouy, 2004)

Subtypes of MMPs	MMP no.	Substrates and function
Collagenases		
Interstitial Collagenase	MMP-1	Type I, II, III, VI and X collagens, entactin and aggrecan
Neutrophil-collagenase	MMP-8	Type I, II and III collagens, aggrecan
Collagenase-3	MMP-13	Type I, II and III collagens
Gelatinases		
Gelatinase A	MMP-2	Type I, IV, V, VII, X, XI collagens, fibronectin, laminin, aggrecan, elastin, tenascin C and vitronectin
Gelatinase B	MMP-9	Type I, IV, XIV collagens, aggrecan, elastin, entactin and vitronectin
Stromelysin		
Stromelysin-1	MMP-3	Aggrecan, fibronectin, laminin, type III, IV, IX amd X collagens, tenascin C and vitronectin
Stromelysin-2	MMP-10	Aggrecan, fibronectin and type IV collagen
Stromelysin-3	MMP-11	Fibronectin, laminin, type IV collagen, aggrecan
Membrane-type MMPs		
MT1-MMP	MMP-14	Activator of proMMP-2, type I, II, III collagens, fibronectin, laminin-1 and vitronectin
MT2-MMP	MMP-15	Activator of proMMP-2, fibronectin, tenascin and aggrecan
MT3-MMP	MMP-16	Activator of proMMP-2, type III collagen and fibronectin
MT4-MMP	MMP-17	Unknown
MT5-MMP	MMP-24	Activator of proMMP-2
MT6-MMP	MMP-25	Type IV collagen, fibronectin, gelatin, fibrin
Other MMPs		
Matrilysin-1	MMP-7	Aggrecan, fibronectin, laminin, type IV collagen, elastin, entactin, tenascin and vitronectin
Matrilysin-2	MMP-26	Type IV collagen, fibronectin, fibrinogen and gelatin
Metalloelastase		
Metalloelastase	MMP-12	Elastin, type IV collagen, fibronectin, laminin, vitronectin and proteoglycan
Enamelysin	MMP-20	Aggrecan, cartylage oligomeric matrix protein (COMP)
Epilysin	MMP-28	Unknown
No trivial name	MMP-19	Aggrecan, cartylage oligomeric matrix protein (COMP)

The remodelling of the ECM as result of the action of MMPs is actually due to the balance between the action of the MMPs and their endogenous counterparts, α_2-macroglobulin and the tissue inhibitors of metalloproteinases (TIMPs). The first one is a big plasma glycoprotein (725 kDa) composed of 4 identical subunits, that adsorbs and entraps the proteinases, carrying them with itself during its specific endocytosis process; the action of this protein is mostly carried out in the fluid compartments. TIMPs bind to MMPs and inhibit them. They can have different affinity for each MMP but generally, they can inhibit all

MMPs. Other proteins that have been reported to inhibit MMPs but their mechanisms are not clear yet and sometimes their action is controversial (Nagase et al., 2006).

ADAMs (a disintegrin and metalloproteinases) are members of a family of cell-surface metalloproteinases. They have to be activated by cleavage and they can digest and activate cell surface receptors (Edwards, Handsley, & Pennington, 2008). An example is ADAM10 that is able to cut and activate HER2 (P. C. C. Liu et al., 2006).

ADAMTs (a disintegrin and metalloproteinases with thrombospondin motifs) are able to process procollagen and von Willebrand factor, but also cleave versican, aggrecan, brevican and neurocan, thus contributing to the remodelling of the ECM (Kelwick et al., 2015). They act basically like members of the ADAM family but they have in their structure also the presence of a thrombospondin motif (Le Goff & Cormier-Daire, 2011).

Urokinase-type plasminogen activator (uPA) is a serine-protease produced and secreted in the extracellular compartment, where it binds its receptor uPAR (uPA Receptor) and is activated by plasmin (J. S. Rao, 2003). uPA is able to activate plasminogen in plasmin and to inhibit its inhibitor PAI-1 (plasminogen activator inhibitor-1) and consequently is able also to start a positive feedback loop of its activation (Mentlein et al., 2012). uPA and Plasmin promote tumour growth and invasion through the activation of growth factors, the conversion of other proteases (especially MMPs) and by direct degradation of the ECM components. It is believed that their action is regulated by growth factors bFGF, TGF-α and -β, or chemokines (Mori et al., 2000; Oh, Olman, & Benveniste, 2009).

Cathepsin B is a lysosomal cysteine protease that has been showed in glioma to degrade laminin and collagen, thus influencing invasion (Natasa Levicar et al., 2002). High levels of Cathepsin B has been found in both *in vitro* cell lines and tumour samples, with an increased expression according to the tumour grade (and consequently it is inversely related to the patient's overall survival) (Demchik, Sameni, Nelson, Mikkelsen, & Sloane, 1999; Strojnik, Kos, Zidanik, Golouh, & Lah, 1999). Downregulation of Cathepsin B inhibits invasiveness and tumorigenicity of human GBM cell lines (Lakka et al., 2004; Mohanam et al.,

2001). At the present Cathepsin B is considered as a strong prognostic factor in malignant gliomas (Verbovšek, Van Noorden, & Lah, 2015).

Cathepsin D is an aspartic-protease that has been shown to be linked to glioma invasion. Pro-cathepsin D, which is found in the Golgi complex, is enzymatically inactive, whilst the intermediate and mature forms are enzymatically active and are found in the endosomes and lysosomes, respectively. The latter are involved in autophagy and apoptosis pathways, thus playing a crucial role in the control of cell and tissue homeostasis (Tan, Peng, Lu, & Tang, 2013). It has been showed in glioma that an inhibition of lysosomes exocytosis does not allow its excretion of Cathepsin D in the ECM, thus inhibiting invasion (Y. Liu, Zhou, & Zhu, 2012).

Cathepsin K is primarily responsible for the degradation of bone matrix by osteoclasts and plays a key role in osteoporosis (Tan et al., 2013). Like Cathepsin D it is expelled by the cells through lysosomes. It has been reported also that Cathepsin K is able to cleave SDF-1α, thus inhibiting it and promoting migration of GBM stem-like cells out of their niche (Verbovšek et al., 2015). At last, Cathepsin K has been shown to be stimulated by cytokines communications, like IL-1α (Verbovšek et al., 2015).

1.5.1.8 INVASION AND CAV-1

As previously mentioned, Cav-1 is believed to interact with several proteins, regulating directly or indirectly their function. These proteins interact with Cav-1 and with each other in a very articulate manner leading to completely different phenotypes, according to nuances in their expression or activation (Goetz, Lajoie, et al., 2008). For example (Figure 1.18) (Parat & Riggins, 2012), integrins, EGFR and uPA bind Cav-1, that compartmentalizes them into the caveolae. Cav-1 –mediated endocytosis regulate the presence of EGFR on the surface, but in the same time EGFR is activated by EGF when it is located in the caveolae (Senetta et al., 2013), and Cav-1 is phosphorylated by EGF induction (Y. N. Kim, Wiepz, Guadarrama, & Bertics, 2000). uPA is activated by the interaction of Cav-1, through β1-integrin, with uPAR, regulating both cell adhesion and signalling (Src and FAK, members of the Focal adhesion

signalling pathway). The formation of these complexes is relevant for migration and invasion in glioma. pCav-1 is able also to interact with MT1-MMP, inhibiting it, thus controlling its action in the direct ECM degradation and the activation of proMMP2.

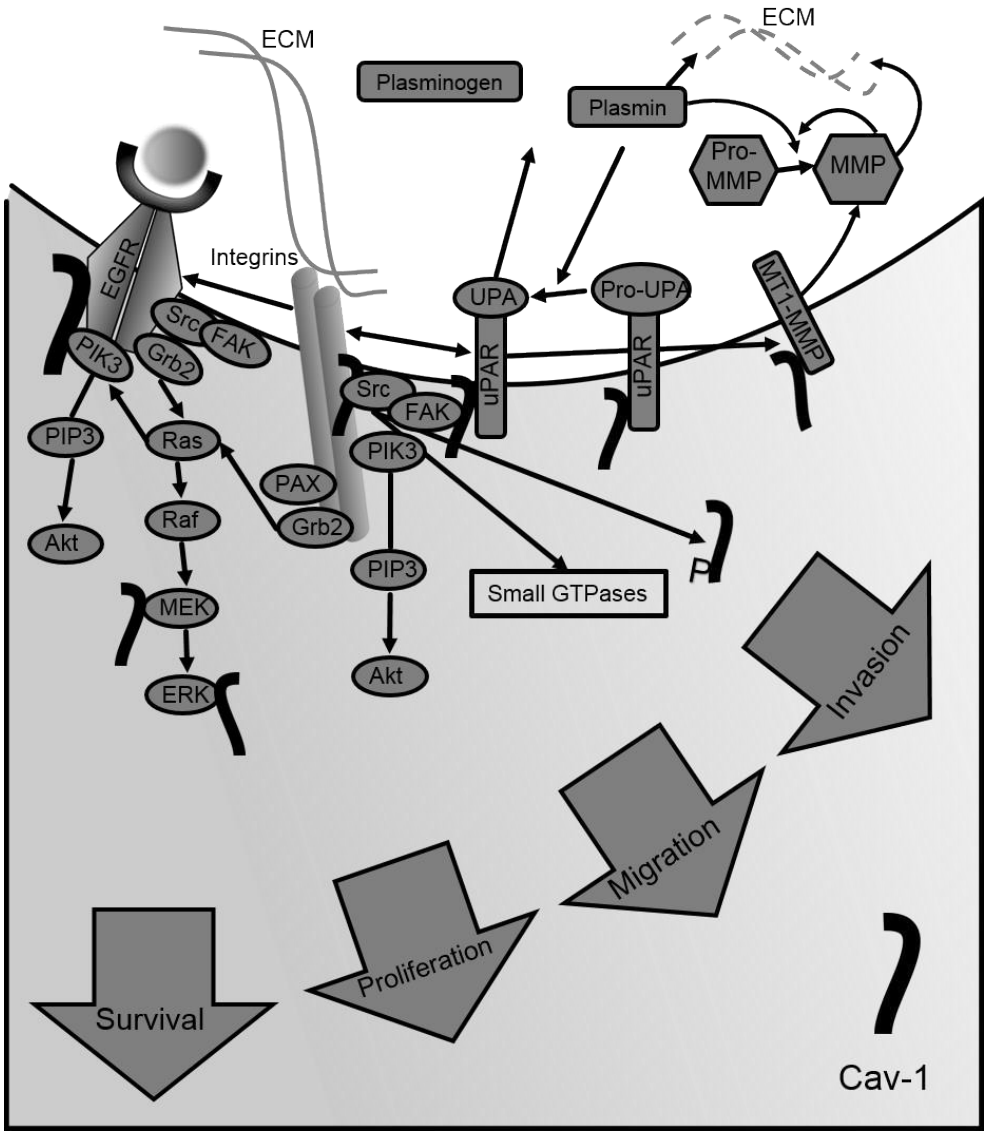

Figure 1.18 Multiple signalling pathways essential to GBM growth and invasion are controlled by Caveolin-1. Adapted from (Parat & Riggins, 2012).

Src is able to phosphorylate Cav-1, in particular when cells are expressing mutant or high levels of EGFR (Y.-N. Kim, Dam, & Bertics, 2002). Cav-1 phosphorylation has been associated also with EGF-mediated anchorage-independent growth and migration (H Lee et al., 2000).

1.5.1.9 INVASION, BIOLOGICAL CONSIDERATIONS FOR ANALYSIS

A wide range of animal models (zebrafish, mouse, rat) have been developed for the study of primary and metastatic tumours; those models included human tumour xenografts in immunocompromised mice, environmentally-induced models and genetically-engineered ones (Cekanova & Rathore, 2014; Denayer, Stöhr, & Van Roy, 2014; Katt, Placone, Wong, Xu, & Searson, 2016). While the advantage of the *in vivo* models is that they capture the complexity of the metastatic process in a living system (Figure 1.19), they present the obvious difficulty in visualizing the individual steps, making the extraction of quantitative mechanistic data very difficult. On the other hand, *in vitro* models recapitulate the physiological reality with less accuracy, with only limited aspects of the tumour microenvironment in evidence but make the control of the experimental variables easier and allow quantitative analysis. Another advantage of *in vitro* assays is that they are relatively easy handling and highly reproducible. They can be used to test cells invasive ability in correlation with genetic manipulation and with the interaction with their cellular, chemical, structural and metabolic environment (Hulkower and Herber, 2011; Wirtz et al., 2011; Infanger et al., 2013; Vidi et al., 2013). They can also be used for high-throughput drug screening and drug delivery (Friedrich, Seidel, Ebner, & Kunz-Schughart, 2009; Weigelt, Ghajar, & Bissell, 2014), being easier (from a technical and bureaucratic point of view), cheaper and less controversial than the *in vivo* studies.

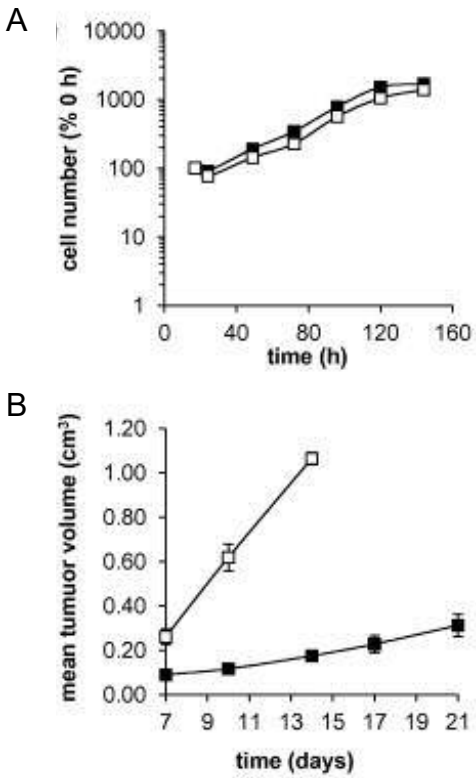

Figure 1.19 Different outcomes in the study of tumour growth *in vitro* vs *in vivo*. Cal^S and Cal^R cell lines growth *in vitro* (A) and *in vivo* (B). Adapted from (Box *et al.*, 2013) with permission.

1.5.1.9.1 IN VITRO INVASION ASSAYS

Several *in vitro* invasion assays have been developed. They differ in several aspects (economic, easy, representative of physiological condition) and they are summarized in Figure 1.20 (Kramer et al., 2013):

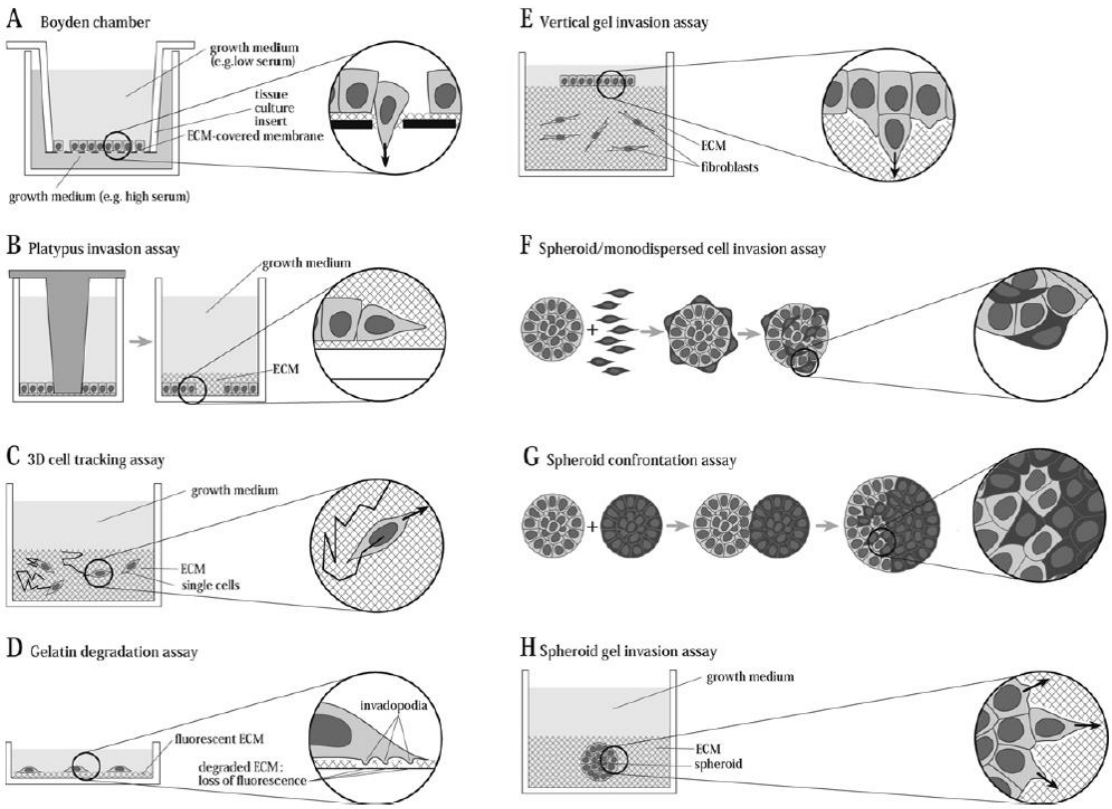

Figure 1.20 Schemes of commonly used invasion assays. An overview of the technical setup is schematically drawn for each assay and a close-up view is given on its right (inside the circles). Arrows indicate the direction of cell movement. Hatched areas symbolize ECM Adapted from (Kramer et al., 2013) with permission.

Figure 1.20A: Transwell invasion assay (or Boyden chamber assay). A thin ECM coating occludes the pores of the filter membrane. Cells are seeded on the top and their ability to overcome it and pass on the other side of the membrane is measured.

Figure 1.20B: Platypus invasion assay. Cells are seeded on top of a thin ECM coated surface. In the centre, a silicone plug creates a cell-free exclusion zone. After the plug is removed, cells are overlaid by a second thicker layer of ECM. The ability of cells to migrate from an outer ring towards the centre is measured.

Figure 1.20C: 3D cell tracking assay. An automated software coupled with optical microscope tracks cells moving through the ECM. The routes through 3D space can be recorded and measured.

Figure 1.20D: Gelatine degradation assay. Cells are seeded onto a thin fluorescently-labelled gelatine layer. Loss of gelatine fluorescence is an indirect measure of matrix degradation at the sites of invadopodia formation.

Figure 1.20E: Vertical gel invasion assay (organotypic skin model). Cells are cultured on top of a collagen gel. Cells invading vertically into the collagen matrix are counted.

Figure 1.20F: Spheroid/monodispersed cell invasion assay. A single cell suspension of a certain cell type is incubated with preformed non-invasive spheroids. Cells are tested for their ability to attach to and eventually invade into the spheroid.

Figure 1.20G: Spheroid confrontation assay. Spheroids from different cell types are separately fluorescently labelled and placed next to each other. If one of the spheroids presents invasive nature, it will penetrate into the cell clusters of the non-invasive cells.

Figure 1.20H: Spheroid gel invasion assay. Cellular spheroids are embedded into ECM gels. Invasive cells can detach from the spheroid and emerge to give rise to astral outgrowing structures.

1.5.1.9.2 3D CELL SPROUTING ASSAY

Of the assays just mentioned, the last one is the one that seems to have more potential and therefore it has been chosen for this work. When multicellular spheroids are embedded into a 3D ECM (Figure 1.20H), non-invasive cells remain compact spheroids with a border at the interphase with the ECM and with no sign of invasion even after 2 weeks of culture (Dolznig et al., 2011). Invasive cell lines, on the contrary, start to invade into the surrounding matrix and display astral outgrowth from the spheroid (Korff & Augustin, 1999). Invasion can be followed in time by live imaging. The gels with the invading structures can be fixed and processed for immunofluorescence staining and confocal microscopy (Sabeh, Shimizu-Hirota, & Weiss, 2009; Wolf et al., 2007; Ylivinkka et al., 2017). Alternatively, the gels can be enzymatically degraded, and the cells isolated for flow cytometry analysis or to make protein lysates and

perform Western blot analysis, but those two are subject to the quantity of cellular material that can be recovered. The main advantage of the 3D assay is that cells moving through a 3D matrix replicate invasion *in vivo* (Figure 1.21), not only because cells move through the ECM, but mostly because invasion occurs from a cell spheroid with well-established cell-cell interactions instead of single cells, as it is the situation in human cancers. A variety of different ECM gels (Matrigel, collagen I, other BMEs, fibrin, etc) can be commercially purchased as liquid forms able to quickly solidify both chemically and/or physically. Different substrates can then be chosen according to the study aim. Even without fluorescent labelling, the invasion can be followed since the outer border of spheroids placed in the gel can be easily detected in a standard inverted light microscope allowing kinetic measurements of cell invasion. Some researchers embed the spheroids at the gel-medium interface or at the bottom in contact with the tissue culture plate. In this case, care must be taken to distinguish real invasion from cell movement on the surface of the gel or on the bottom of the plate, which are the routes of least resistance preferred by the cells. This can falsely give the impression of rapid invasion. Furthermore, the assay requires a confident manual skill and some pre-acquired experience with 3D gel systems. This system has already been used to confirm essential molecular pathways during 3D invasive growth (Sabeh et al., 2009; Wolf et al., 2007) or to measure TGFβ induced invasion (H. P. H. Naber, Wiercinska, Ten Dijke, & van Laar, 2011). So far there is no spheroid invasion assay commercially available.

Spheroid formation proceeds from the initial seeding of single cells to aggregation. Due to the 3D nature of the growing aggregates, internal chemical gradients start building up. This leads to a typical stratification or zonation from the core to the spheroid surface as observed in growing tumours *in vivo* (M. Wu et al., 2014). An example can be the developing hypoxia gradient (Mueller-Klieser, 1984). Due to the limited diffusion of oxygen, a hypoxic area forms at the centre of the spheroids, which can then turn into necrosis in larger diameter spheroids (Freyer & Sutherland, 1986; Mueller-Klieser, Freyer, & Sutherland, 1986). When spheroids are small, for a low proliferation rate or at the initial formation stages, chemical factors can diffuse freely, and no zonation is observed. Further in the growth from small to medium-sized spheroids (with diameters of about 150–300 μm), a zonation starts to appear, with the surface to

the core being proliferative, the middle being normoxic and quiescent and the centre being hypoxic (Khaitan, Chandna, Arya, & Dwarakanath, 2006). The core of the hypoxic zone is in large spheroids can become, upon further growth, a necrotic zone (Figure 1.21) (Khaitan & Dwarakanath, 2006). From this, it is natural to derive that generating the optimal size, to investigate determinants of tumour biology, needs careful study of the growth properties and spheroid characteristics, considering also cell-type variables (Vinci et al., 2012). Indeed a small tight spheroid (200 μm) may already be hypoxic, whilst a loosely aggregated one (400-500 μm) may not (Hirschhaeuser et al., 2010). Comparative gene expression studies in cells from melanoma grown in 2D and 3D confirmed the appearance of a hypoxic core through upregulation HIF pathway (Sourabh Ghosh et al., 2005). Furthermore, different studies show that an induction of secreted factors could potentially contribute to cross-talk between more zones within the spheroid (Eckes et al., 1992; Enzerink, Salmenperä, Kankuri, & Vaheri, 2009; Klapperich & Bertozzi, 2004).

Tight control of spheroid size is, of course, necessary to obtain reproducible results. The choice of the size of the spheroid can depend also on the scientific question. For example, if the aim is the study of tumour initiation, small well-oxygenated spheroids with a diameter of about 200 μm may be desirable, while for studies related to tumour enlargement, where the presence of the hypoxic/necrotic core is desirable for the study of the poorly vascularized regions, large spheroids are preferred (Thoma, Zimmermann, Agarkova, Kelm, & Krek, 2014).

The field of 3D spheroid technology is rapidly advancing and is beginning to be important for both discovery and translational research related to cancer. Moreover, spheroids have the potential to become a superior system for drug target identification and validation and in general for drug development.

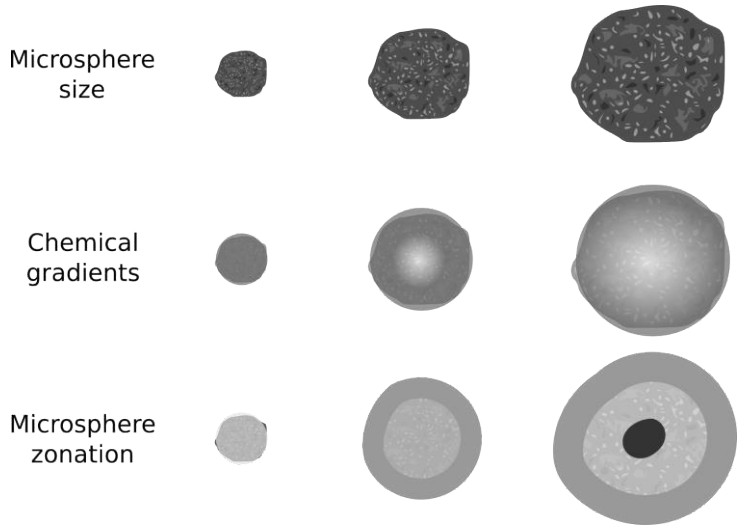

Figure 1.21 3D tumour spheroid size, chemical gradients and biological/phenotypical zonation: schematic of 3D tumour spheroid monoculture models illustrating how spheroid growth (top) generates gradients (middle; e.g. O_2) followed by typical zonation (bottom; yellow: proliferative zone, black: necrotic zone).

1.6 THE STUDY OF PROTEIN FUNCTION THROUGH EXPRESSION MODULATION

The key of cancer insurgence is in altered genes (D. D. Rao, Vorhies, Senzer, & Nemunaitis, 2009), in sequence (genomics) or in expression (epi-genomics), and in the percentage of neoplastic cells displaying such aberrations. The variety of possible genes that can be altered in neoplastic conditions increase the number of possible therapeutical targets that can be powerful tools for cancer treatment. Over the last decade, several new therapeutical approaches have been approved, that target aberrantly amplified genes or overexpressed proteins.

The goal of the study of gene and protein expression is to push the characterization towards a stratification where groups of patients present altered groups of genes and a specific therapeutic sensibility, and ideally towards the personalized medicine, according which the stratification is so narrowed that every single patient can be associated with a specific therapeutical cocktail.

Several tools are available for the study of genetic and epigenetic abnormalities (C. A. Stein & Cohen, 1988). One of them is based on the inhibition of the transcription of specific genes. This can be achieved in different ways.

Each patient's tumour genetics can be analysed in a variety of ways. The analysis' goal is to quantitatively determine both gene and protein over- or under-expression. Furthermore, functional pathways can be tested and integrated into a collaborative network allowing for the identification of new key molecular indicators and targets. Such information can potentially allow medical carers to prioritize and optimize treatment for cancer patients, and to validate alternative biomarkers for prognosis, and therapy. The recent discovery of RNA interference (RNAi) presents an invaluable tool for personalized cancer therapy. RNAi is basically a natural process through which the expression of a targeted gene can be reduced in a highly specific and selective way.

The idea of using antisense oligo-deoxy-nucleotides as modulators of gene expression in research and in cancer gene therapy development was introduced more than 30 years ago (Cech, 1986). It is based on the discovery of an evolutionarily conserved mechanism of gene silencing, consisting in small sequences of double-strand (ds) or single-strand (ss) RNA that recognize and complementary bind freshly transcribed mRNAs. This can result in an inhibition of the mRNA translation (siRNA) or in its total suppression (miRNA).

The main steps of the process are summarized in Figure 1.22. miRNAs are genomically encoded and are transcribed as long primary double-stranded transcripts (pre-miRNAs). The dsRNA is recognized and loaded onto the RNase III enzyme Dicer to form the RNA-interfering silencing complex (RISC) (Ichim et al., 2004) that cut them in 65nt pre-miRNA first and 22nt miRNA then (H. Wu et al., 2011). The non-guide strand is then removed, and the RISC complex recognizes the mRNA target through the guide-strand complementarity. The target mRNA is finally cleaved at a single site at ca 10 nucleotides from the 5′ end of the antisense siRNA sequence and then degraded, whilst the released RISC complex is able to recognize a new sequence (Elbashir et al., 2001; J. Liu et al., 2004).

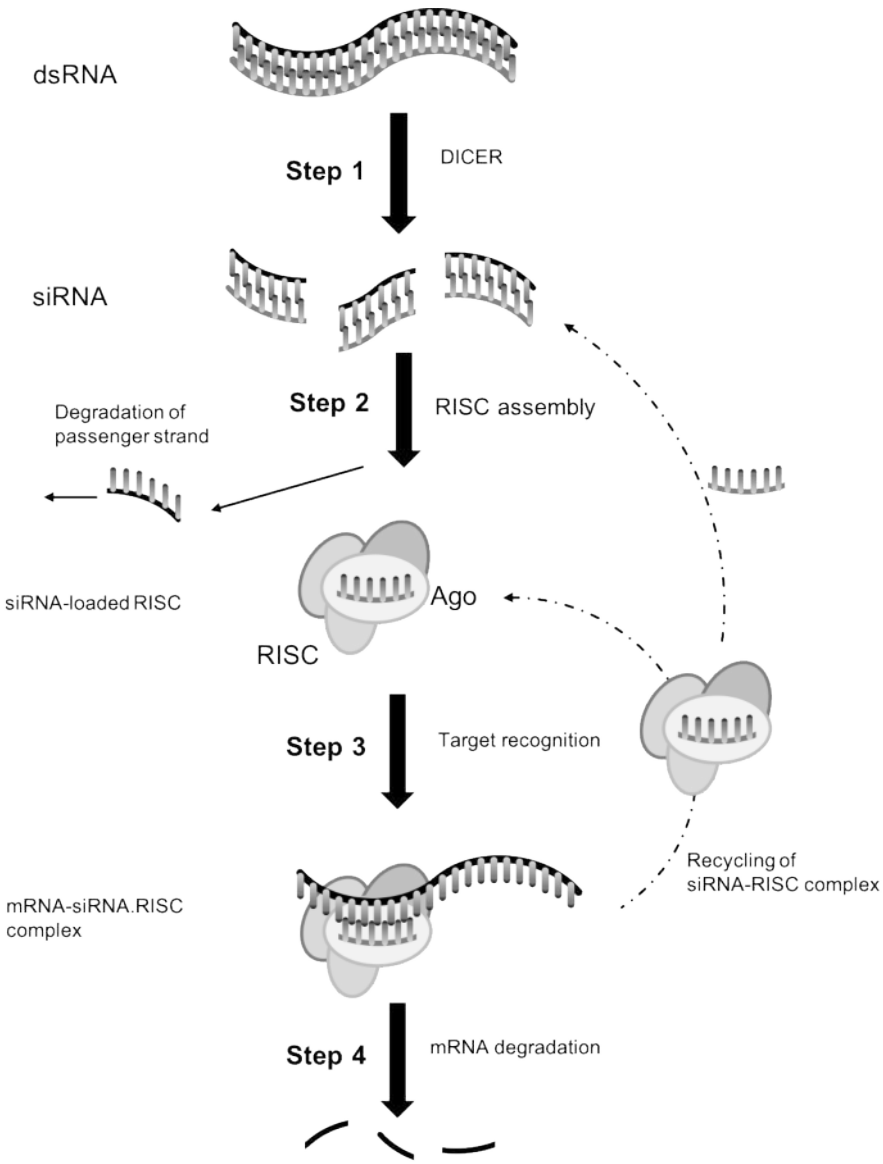

Figure 1.22 The RNA interference process in mammal cells.

The RNAi process is well studied and generally considered reliable. The application of the system to research purposes though encountered some challenges, like the delivery way and the efficiency of gene silencing. While the first one led to the development of several delivery techniques with different degrees of complexity, reliability and effectiveness (that will be discussed further on in 1.6.1.3), the latter has been improved through the insertion of mismatches that increased the rapidity and the degree of degradation (H. Wu et al., 2011) and the developing of two different kind of miRNA precursors, a dsRNA that can be directly loaded in the RISC complex (siRNA) and a plasmid vector codifying for an hairpin that can be subsequently cleaved and loaded onto RISC. A

graphical summary of the different structures and approaches is reported in Figure 1.23.

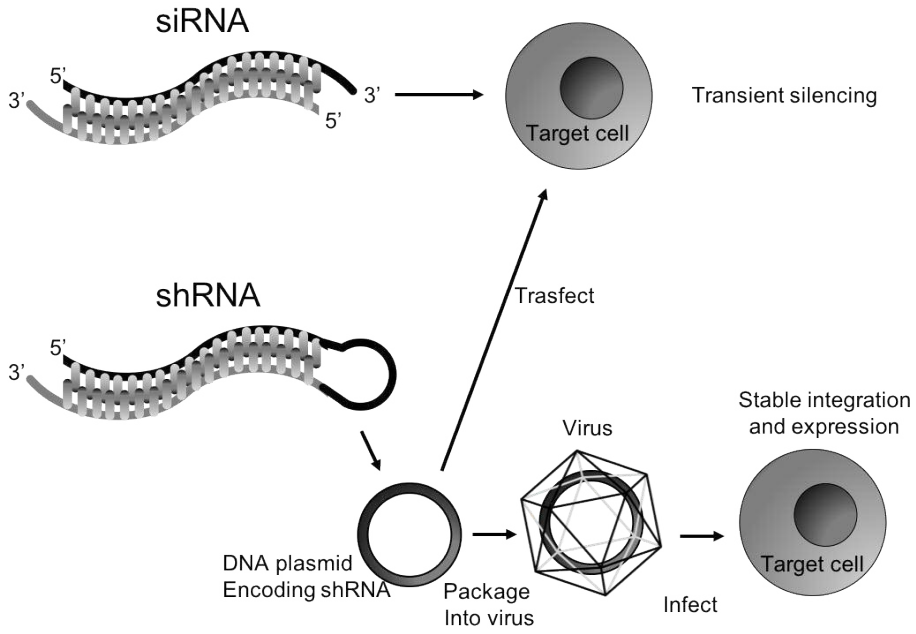

Figure 1.23 siRNA and shRNA approaches.

1.6.1.1 siRNA KNOCKDOWN

In fluorescence-mediated experiments, the intact siRNA was observed to pass into the nucleus within 15 min after the delivery and then to disseminate into the perinuclear region of the cytoplasm (Chiu, Ali, Chu, Cao, & Rana, 2004) within the next 4 hours. It is not clear however the mechanism that allows the siRNA to translocate into the nuclei (D. D. Rao et al., 2009).

At 48h post-delivery, the majority of siRNA appeared to be degraded with only 1% fluorescence remaining in the cell. This confirmed the siRNA methodology according which the effectiveness of the treatment reaches its peak at 24hours post-delivery and decreases after another 24 (Hammond, Caudy, & Hannon, 2001).

Duplex siRNA in association with the RISC complex. In the RISC complex, the two strands of the duplex are separated, resulting in the departure of the passenger strand. The RISC with single-stranded guide strand siRNA is then able to execute multiple rounds of RNA interference (Robb & Rana, 2007).

1.6.1.2 shRNA KNOCKDOWN

shRNAs, unlike siRNAs, are synthesized in the cell nucleus, where they are also processed and transported to the cytoplasm for the incorporation into the RISC complex for activity. The shRNA design aim is to create a template that is compatible with the cellular machinery in order to be processed in the microRNA maturation pathways (D. D. Rao et al., 2009).

shRNA is transcribed by the endogenous RNA polymerase II or III in the nucleus. The primary transcript contains a hairpin-like stem-loop structure that is processed by a complex containing Drosha, an RNase III and the double-stranded RNA-binding domain protein DGCR8 (Y. Lee et al., 2003). The complex processes the long primary transcripts into individual shRNAs with an extra 2 nucleotides overhanging at the 3' extremity (H. Zhang, Kolb, Brondani, Billy, & Filipowicz, 2002). The processed primary transcript is the pre-shRNA molecule which is transported to the cytoplasm by Exportin 5 (Cullen, 2004; Y. Lee, Jeon, Lee, Kim, & Kim, 2002). In the cytoplasm, the pre-shRNA is loaded onto Dicer and TRBP/PACT for the loop of the hairpin to be processed off to form a double-stranded siRNA the 2nt overhanging (Y. S. Lee et al., 2004; Lund, Güttinger, Calado, Dahlberg, & Kutay, 2004; Yi, Qin, Macara, & Cullen, 2003). The Dicer-containing complex then coordinates loading onto the Ago2 protein containing RISC as described earlier for siRNA. After loading onto RLC and passenger strand departure; both siRNA and shRNA in the RISC, in principle, should behave the same.

The advantage of shRNA is in efficiency of the loading onto the RISC complex, which is approximately 10x more efficient than the siRNA system (Sano et al., 2008). Further on the gene silencing resulting from transfected synthetic siRNAs are usually transient whilst the shRNA sequence can be inserted in a plasmid carrying a drug resistance. In this way, the addition of the drug allows the survival only of cells that contain and are actually transcribing the plasmid and therefore the cells that express the shRNA sequences, making this a step towards a more durable silencing effect. Of course, on the other hand, the continuous pharmacological stimulus of the cells can induce phenotypes that are dissimilar from the normal physiological conditions, so it's important to plan

carefully a negative control, whose aim is to exclude every phenotypical change that doesn't derive from the silencing.

1.6.1.3 RNAI DELIVERY METHODS

Not only the efficiency of processing of the siRNA/shRNA and their chemical and biological stability is important, but also the efficiency in the entry of the molecules into the target cells. Nucleic acids, indeed, have a net negative charge and, in order to enter the cell, they must come into contact with a lipid bilayer of the cell membrane, whose head groups are also negatively charged (Dalby et al., 2004). Three major technologies have been established to introduce siRNA into target cells.

1.6.1.3.1 TRANSFECTION

The siRNA molecules can be complexed with carriers that allow them to cross cell membranes in a process called transfection. Typical carriers are packaging particles called liposomes, that facilitate the cellular uptake of siRNA, through cationic lipids mimicking the physical characteristics of natural phospholipids. The siRNA-lipid complexes protect siRNA from enzymatic degradation and allow efficient endocytosis by the cell (W. J. Kim, Chang, Lee, & Kim, 2007; Love, Moffett, & Novina, 2008).

Recently, they have been introduced synthetic cationic polymer-based nanoparticles, with a size of ~ 100nm. They have been developed to enhance the transfection efficiency with the combined reduction of cytotoxicity, in comparison with the liposomes used so far (Aigner, 2006). They are composed of more than one layer of lipid molecules, each with different physical and chemical characteristics which allow a better fusion with the cell membrane and entry into the cell, an enhanced release of RNAi molecules inside the cell, and a reduced intracellular degradation of RNAi-nanoparticle complexes (Dalby et al., 2004). A further advantage of polymer nanoparticles consists in their ability to be modified with certain ligands for the increased stability *in vivo*, the reduce

immunogenicity and the delivery to specific cell types, (Aigner, 2006; Behlke, 2006).

siRNA/shRNA can be conjugated also with other hydrophobic molecules, such as cholesterol, that seems to improve *in vitro* cellular uptake and *in vivo* pharmacological properties of siRNA (C. Zhang et al., 2006). Another method involves the use of cationic cell-penetrating peptides (CPPs), such as MPG, transportan or penetratin, to the siRNA by covalent or electrostatic interactions. The strong positive charge on these peptides promotes the condensation of negatively charged siRNA, allowing their delivery with high efficiency and minimal toxicity (C. Zhang et al., 2006). Highly branched histidine-lysine polymer peptides, dedrimer molecules and artificial virus particles, have also been applied for the self-assembly of siRNA into nanoscale particles that are able to transport siRNA into the cells with high efficiency, low cell toxicity and enhanced cellular internalization (Patil et al., 2008).

1.6.1.3.2 ELECTROPORATION

Cell membranes, with their negatively charged phospholipids both outside and inside the bilayer, are susceptible to influence by an applied electric field. A brief but powerful electric pulse can reorient the lipid molecules and provoke a thermal phase transition, that creates transient hydrophilic pores. The temporary loss of the semi-permeability of cell membranes allows the escape of intracellular ions and metabolites, and the simultaneous uptake of drugs, molecular probes, and nucleic acids from the outside.

The cell delivery of siRNA based on electroporation has been developed to resolve some limitations of the liposome-based transfection associated with the specific cell line, such as primary and suspension cells. Despite the high efficiency of nucleic acid transfer, electroporation can induce high cell death (Tsong, 1991). Therefore, the individual parameters of electroporation (such as voltage, length of the electric pulse, and the number of pulses) must be optimized for each cell types.

1.6.1.3.3 VIRAL GENE TRANSFER

As reported earlier on, the gene silencing resulting from transfected synthetic siRNAs is usually transient. To increase the effect of the gene silencing and allow semi- and long-term experiments, an RNAi approach based on DNA expression plasmids (shRNA) can be used to stably express siRNA in cells. (Rutz & Scheffold, 2004).

The delivery of siRNA from DNA templates can be carried out by both liposomes and electroporation. However, the most efficient way seems to be the use of several recombinant viral vectors based on retrovirus, adeno-associated virus, adenovirus, and lentivirus. These vectors have been engineered and optimized to allow the easy entry of siRNA into cells that are difficult to transfect. Also, some synthetic viral vectors, like the lentiviral and adenoviral ones possess an ability to integrate the shRNA into the cell genome, thereby leading to stable siRNA expression and long-term knockdown of a target gene, with virtually no need for a continuous pharmacological treatment (Y. Shi, 2003).

One of the most popular is the lentiviral system, which aims to integrate anti-target gene shRNA coding DNA into the genetic patrimony of the cellular host. The sequences are inserted together with a puromycin resistance-carrying gene that allows the selection of the successfully transfected cells. (see map in Figure 1.23).

The plasmid is packaged into viral particles by lipo-transfecting the plasmid into so-called packaging cells, together with other plasmids necessary for the assembly of the viral particles. The plasmid carrying the shRNA sequence is replication incompetent, if not together with the other plasmids, making it “self-inactivating” once it is integrated. The lentiviral systems still used derive from the HIV-1 genome and are the 2nd and the 3rd generation ones. In both systems, the lentiviral genome has been split in separate plasmids, to neutralize the uncontrolled-replication risk.

In the 2nd generation vectors, a single packaging plasmid encodes Gag and Pol (for the viral structure) and Rev and Tat (essential regulatory elements) genes. The transfer plasmid contains the viral LTRs (long-term repeats that allow the insertion in the genome) and psi packaging signal. Unless an internal promoter

is provided, gene expression is driven by the 5'LTR, which is a weak promoter and requires the presence of Tat to activate expression. The envelope protein Env (usually VSV-G due to its wide infectivity) is encoded on a third, separate, envelope plasmid.

After the packaging of the viral particles containing the transfer vector, they are released into the medium and collected. When added to the target cell culture (or *in vivo* system) they penetrate the cells with high efficiency and release the transfer plasmid that is then able to integrate into the genome of the cells. The plasmid is carrying a resistance for puromycin, which allows the selection of the cells whose genome contains the integrated transfer vector. After the selection, the puromycin administration is suspended, the CMV promoter allows a high transcription of the inserted DNA and cells are tested for the expression of the silencing-targeted protein.

1.6.1.4 CRISPR KNOCKDOWN/KNOCKOUT

Concomitant to the development of RNAi, several other techniques for stable gene expression modifications have also been developed, in the branch so-called “gene editing techniques” (Boettcher & McManus, 2015). One of these approaches is based on the use of prokaryotes Clustered Regularly Interspaced Short Palindromic Repeats (CRISPR)/CRISPR-associated protein 9 (Cas9) systems for nucleic acid editing. The application of CRISPR/Cas9 was established very recently (2012–2013), but it has revolutionized the entire field (Cong et al., 2013; Jinek et al., 2012; Mali et al., 2013), starting replacing the RNAi system, that dominated the mammalian gene manipulation field for more than 15 years (Unniyampurath, Pilankatta, & Krishnan, 2016).

The CRISPR/Cas systems is a natural immune defence strategy in prokaryotes against the invasion of non-self-DNA, like viruses and plasmids and it occurs in a sequence-specific manner (Barrangou et al., 2007; Sorek, Kunin, & Hugenholtz, 2008).

The CRISPR/Cas system (Figure 1.24) is composed by several DNA repeats fragmented by spacers derived from foreign DNA, and multiple Cas genes, that can be nucleases or not (Haft, Selengut, Mongodin, & Nelson, 2005). The

spacer represents the code for the recognition of the foreign genetic element, and so for the identification of foreign DNA entering the host cell.

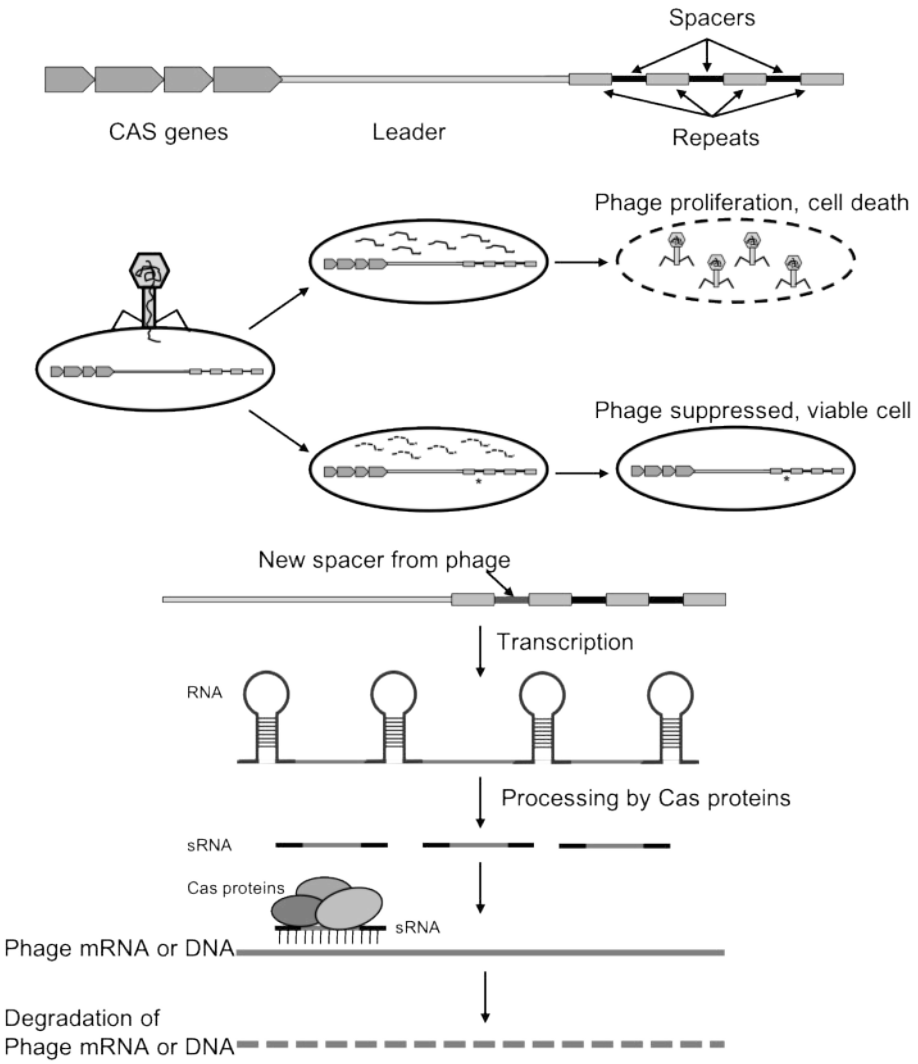

Figure 1.24 CRISPR structure and function (Sorek et al., 2008).

In the CRISPR/Cas system can be distinguished three steps (Jiang & Marraffini, 2015; van der Oost, Jore, Westra, Lundgren, & Brouns, 2009). During the "spacer acquisition" step, the cell recognises foreign DNA and incorporates it among the CRISPR loci to for the spacers (Garneau et al., 2010). Then, during the "crRNA maturation" step, the prokaryotic organism will transcribe and generate mature CRISPR RNA (crRNA) containing the CRISPR repeats integrated with the spacers (Brouns et al., 2008; Carte, Wang, Li, Terns, & Terns, 2008; Deltcheva et al., 2011; Gesner, Schellenberg, Garside, George, & MacMillan, 2011). Finally, in the "target interference step", the crRNA will detect

homologous DNA sequences when newly introduced, for example during the infection of another virus having the same sequence. Once the foreign DNA is recognized by the crRNA, the extra genetic material will be degraded by a cellular machinery, determining protection against the foreign DNA (Barrangou et al., 2007; Garneau et al., 2010; Semenova et al., 2011; Wiedenheft et al., 2011).

The 10 superfamilies of Cas proteins participate differently in all the steps of the CRISPR/Cas system (Makarova et al., 2011). Cas1 and 2 are involved in the spacer acquisition (Datsenko et al., 2012; Yosef, Goren, & Qimron, 2012), Cas6 and 5d in the crRNA maturation (Carte et al., 2008; Haurwitz, Jinek, Wiedenheft, Zhou, & Doudna, 2010; Naito & Ui-Tei, 2013), while several others are part of the interference complex.

The classification of the CRISPR/Cas systems has been structured in three types according to the conservation and composition of the Cas genes (Makarova et al., 2011; Tsui & Li, 2015). Type II is only present in bacteria, whilst types I and III are present in both bacteria and archaea. The two main differences between the three types of CRISPR/Cas systems are:

- the target: Type I targets only DNA while Type II and III can target both DNA and RNA;
- and the subunit composition: Type II system has two different RNA subunits in complex with a single Cas9 protein whilst Type I and III have multiple Cas proteins in complex with a single RNA.

Since Type II is the simplest of the three systems, with for instance only Cas9 necessary for the recognition and the incorporation of the foreign DNA into the spacers, it is the one that has been widely adapted for eukaryotic gene editing (Cong et al., 2013; Jiang & Marraffini, 2015; Mali et al., 2013). Furthermore, the type II CRISPR/Cas system requires only the tracrRNA cofactor, the crRNA and Cas9 to induce gene editing, while all others need multiple components, whose regulatory mechanisms are still not fully understood (Haft et al., 2005; Sorek et al., 2008; Tsui & Li, 2015).

1.6.1.4.1 CRISPR EFFICIENCY

Different technologies can be used to insert the CRISPR/Cas9 system into the target cells/tissues (Figure 1.25). DNA codifying for all the components can be transfected in a plasmid vector. The DNA must be transported in the nucleus, transcribed (for the tracrRNA and the crRNA) and translated for the Cas9 and the machinery has to be assembled to achieve its active function. Due to its length and articulation, this process is not very efficient, with only 1% of the cells targeted successfully, and can lead to off-targets. This has led to the development of systems that can allow the skipping of some of those steps. In particular, it is possible to transfect cells with mRNA codifying for the Cas9 protein and the other components, so to jump the transcription system, and also to introduce (generally by electroporation) the Cas9 protein ready to work into the cells associated already with the tracrRNA and the crRNA in ribonucleoproteins (RNPs), in order to allow its immediate functionality. Of course, those systems have as an advantage a higher efficiency and specificity in the gene manipulation but also a higher cost, as shown in Figure 1.25.

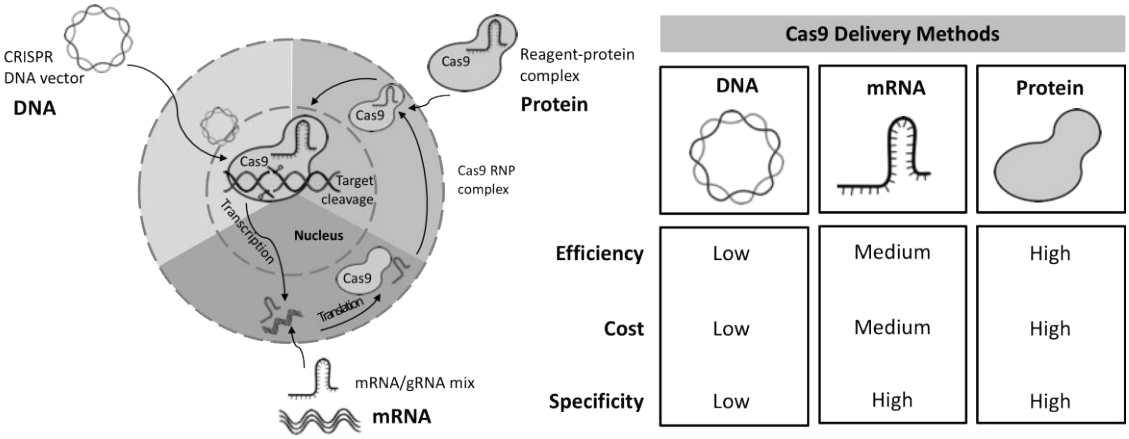

Figure 1.25 CRISPR/Cas9 delivery systems.

1.6.1.5 RNAI VERSUS CRISPR

The CRISPR/Cas9 system has been recently and widely accepted as a reliable and powerful tool for gene editing, both because of its simplicity and wider potential. So far, RNAi has been the major tool for several genetic applications requiring gene expression modulation, but the rapid growth and use of

CRISPR/Cas9 in mammalian systems certainly implies the possibility for this system to integrate, if not replace, the RNAi technology.

RNAi represented a revolution for reverse genetic screens, leading to an explosion of gene-function studies number and variety, including cell signalling, host-pathogen interactions, immune response, and cancer mechanisms. Many reports indicate now that a CRISPR/Cas9 based technology could also be used for this purpose (Parnas et al., 2015; Shalem, Sanjana, & Zhang, 2015; T. Wang et al., 2015; Tim Wang, Wei, Sabatini, & Lander, 2014). However, there are still several advantages to RNAi over CRISPR/Cas9 that makes the latter in need of further development.

Even if both technologies have comparable delivery efficiency for *in vitro* cell culture systems, in terms of efficiency in altering gene expression, both may perform differently. RNAi has a relatively very high transfection efficiency in suppressing gene expression with >70% knockdown of the intended target mRNAs. CRISPR/Cas9 efficiency is instead in the range of 1% to 79% (Duda et al., 2014; Liang et al., 2015; Swiech et al., 2014). Such a heterogeneous efficiency means that CRISPR/Cas9 transfected cells should be selected according to their gene modification before application for genetic screens.

RNAi has another advantage, which is that it can be used for genetic screening in both immortalized cell lines, and short-living primary cells (that often do not live longer than a week ex vivo), whilst the use CRISPR/Cas9 systems in short-living primary cells will be less practical because there may not be enough time for selecting the modified-gene population before performing the phenotypic assays.

Furthermore, another limitation of CRISPR/Cas9 system is that both the alleles in the targeted cells must be targeted in order to completely modify the expression of one gene, which reduces the efficiency of the process. If one considers that most of the widely used immortalized human cell lines are aneuploidy (with more than two alleles) gene deletion process becomes even more complex. RNAi instead targets transcripts, so it can cause a uniform and efficient gene repression.

Also, the time both techniques need for the displaying of the intended effect varies greatly, and this may lead to different choices regarding specific applications. RNAi exhibits rapid effects on gene expression. RNAi treatment can result in significant attenuation of gene expression in around 24h. However, the need for a selection step for cells treated with CRISPR/Cas9 may take up to a month or more depending on the specific needs, the gene effect on cells proliferation and the cells proliferation tendency per se (Gilbert et al., 2013).

The big advantage of CRISPR over RNAi is that the first induces an absolute null phenotype that is irreversible (Jiang & Marraffini, 2015), while the second produces a reversible and incomplete modification of gene expression (Bosher & Labouesse, 2000; Gilbert et al., 2014; Konermann et al., 2014; Qi et al., 2013). From this point of view, CRISPR/Cas9 seems to be ideal for the systematic study of gene function.

Moreover, the selection step of CRISPR allows an unequivocal phenotype to be studied whilst with the RNAi a polyclonal population is produced. This may mean different off-targets. Anyway, the basic CRISPR technology is not off-target risk-free, as we discussed previously.

The design of RNAi sequences need only information about the sequence of the gene transcript, with lower regard for information about the corresponding gene, whilst CRISPR, on the contrary, requires a full understanding of the gene sequence information, with exons and intron alternating and often promoters sequences (Cong et al., 2013; Jiang & Marraffini, 2015).

Furthermore, the RNAi system can be literally used to target any protein-coding gene, whilst the CRISPR/Cas9 system requires a short proto-spacer-adjacent motif at the target gene site, that makes the application of CRISPR/Cas9 bound to the presence of this sequence (Jinek et al., 2012).

As mentioned before, it is widely agreed that RNAi has off-target effects (Ui-Tei, 2013). Even if the new design principles that have been elaborated have greatly reduced off-target effects, there is still no methodology that can completely eliminate the RNAi-induced off targets (Naito & Ui-Tei, 2013). Unfortunately, the CRISPR/Cas9 system in mammalian cells has not overcome the issue. There are indeed several reports that have recently identified the off-target potential of

the CRISPR technology (S. W. Cho et al., 2014; Frock et al., 2014; Fu et al., 2013; Lin et al., 2014). The scientific community, both academy and companies, have modified the methodology in order to minimize the potential off-target risks (Ran et al., 2013). For instance, as mentioned earlier, Cas9 has been proposed to be delivered directly as mRNA, or coupled as gRNA-Cas9 in form of ribonucleoprotein complex; those systems should reduce off-target since they have a shorter cellular life in comparison to plasmid-based delivery (Chang et al., 2013; S. Kim, Kim, Cho, Kim, & Kim, 2014; Schumann et al., 2015). Moreover, a recent study reported a minimal off-target effect achieved through the generation of a mutant Cas9 (Kleinstiver et al., 2016).

All of this indicates that the CRISPR/Cas9 system has room for technology implementation and refinement in order to reduce the disadvantages and improve the advantages that differentiate it from the RNAi approach.

1.7 SCOPE OF THE PROJECT

As mentioned in 1.4.5, there still a lack of understanding about the role of Cav-1 in high-grade glioma. In light of the increasing molecular stratification, having a better understanding of the caveolae major component may contribute to the future classifications, with impact on both research and clinical practice.

The hypothesis of the present work is that Cav-1 serves as a modulator of the functional properties of cancer stemness in high-grade glioma, grade IV astrocytomas, either in a suppressor or promoter manner dependent upon context.

Specifically, that in sub-populations of glioma cells Cav-1 has a critical role in interplay with other pro-stemness molecules to impart cancer stem cell–like activity, including the ability for self-renewal and increased clonogenicity and the ability to migrate and invade tissue; particular attention is focused upon the impact of Cav-1 on invasion. The results may reveal Cav-1 protein to be a potential candidate target for therapy. The hypothesis will be tested through the following experimental objectives:

Objective 1. Create stable Cav-1 knockouts and knockdowns of established glioma cell lines. Here we created a series of stably transfected

shRNA anti-Cav-1 glioma cell lines (shRNA plasmid and lentiviral transfection) and genetic knockouts (CRISPR technology) which allowed explicit understanding of the role of Cav-1 biology in glioma stem-cell phenotype and function (Chapter 3).

Objective 2. Examine the impact of Cav-1 upon functional characteristics of cancer cell aggressiveness *in vitro*. Stem-like functionality has been analysed, which includes: self-renewal and clonogenicity (Chapter 3), and the ability to migrate and invade (Chapter 4 and 5).

Objective 3. Explore the molecular mechanism involved in Cav-1-driven changes in invasion of cancer cells. This has been achieved through the study of molecular pathways in Cav-1 expressing and non-expressing cell lines, and in aggressive and non–aggressive samples (Chapter 5).

Objective 4. Study the impact of Cav-1 expression in GBM patients within online dataset. The role of Cav-1 in GBM has been explored by accessing one of “The Cancer Genoma Atlas” datasets for GBM. The association between Cav-1 and molecules involved in GBM invasion have been also explored. This could be used to get an insight into mechanisms and confirm *in vitro* data. (Chapter 6).

2 CHAPTER 2- MATERIALS AND METHODS

This represents a brief summary of methods common across a number of chapters. Appendiced also provide detailed procedures and materials. When relevant, each chapter will also describe unique materials and methods pertinent to that work.

2.1 CELL LINES

Eight human GBM cell lines have been used in this project (Table 2-1). Specifically, the human adult GBM cell lines from Uppsala, U87Uppsala (=U87) and U373MG (=U373) (Pontén & Macintyre, 1968), three are adult GBM-derived cell lines isolated in SEBTA (South of England Brain Tumour Alliance) facility provided by Professor Geoff Pilkington, from Portsmouth University, UP007, UP019 and UP029, while the other three have been provided by the SEBTA facility and correspond to infra-tentorial paediatric brain tumours, IN699 (Ward et al., 2010), SF188 (Trent et al., 1986) and KNS42 (Iwao et al., 1987).

Table 2-1- Cell lines under examination

	Cell Line	Origin	Patient details	Type (Grade)	Genetic information available	Source
1	U87	U. Uppsala (SE)	Adult	Adult GBM (IV)	TP53 wt/ PTEN mut/ p16 del/ p14ARF del/CDKN2A mut	ECACC
2	U373	U. Uppsala (SE)	Adult	Adult GBM (IV)	TP53 wt/ PTEN null/ p16 wt/ p14ARF wt	ECACC
3	UP007	SEBTA	Adult	Adult GBM (IV)		SEBTA
4	UP019	SEBTA	Adult	Adult GBM (IV)		SEBTA
5	UP029	SEBTA	Adult	Adult GBM (IV)		SEBTA
6	IN699	Institute of Neurology (London, UK)	Adolescent (15-year-old male)	Supratentorial paediatric GBM		SEBTA
7	SF188	U. Arizona (AZ, USA)	Child (8-year-old male)	Frontal paediatric GBM (IV)	TP53 wt/ PTEN wt/ p16 wt/ p14ARF wt	SEBTA
8	KNS42	U. Kyushu (JP)	Adolescent (15-year-old male)	Frontoparietal anaplastic astrocytoma (IV)	TP53 mut/ PTEN wt	SEBTA

2.2 GENERAL CONSUMABLES AND REAGENTS

Unless otherwise stated tissue culture plastics were purchased from Corning Costar (Hemel Hempstead, UK); liquid materials for cell culture such as media, serum and antibiotics from Invitrogen Life Technologies, Thermo Fisher (Paisley, UK); chemicals and reagents of the highest grade from Fisher Scientific (Loughborough, UK) or Sigma (Poole, UK).

2.3 ROUTINE CELL CULTURE

All cell lines were grown on tissue-culture treated plastic in Dulbecco's Modified Eagle Medium (DMEM) (supplemented with 10% Foetal Bovine Serum (FBS) and 1% antibiotics Penicillin/Streptomycin). Cells were seeded with a density comprised between 5,000 and 10,000 cells/cm^2 and cultures were maintained in a humidified 5% CO_2 atmosphere. Cells were passaged twice each week with a protocol that foresees Phosphate Buffer Saline (PBS) washing, trypsinization (1x Trypsin-EDTA for 5min at 37°C), inactivation by FBS addition, centrifugation at 200g for 5 min and cell resuspension in an appropriate volume of medium for cell counting (Disposable FastRead Counting Slides - Immune Systems Ltd, Paignton UK) prior to re-seeding onto new plastic ware.

2.4 WESTERN BLOT

To generate cell lysates, pellets were first washed twice with PBS and an opportune volume of lysis buffer (see APPENDIX 1) was added and kept for 30 min with vortexing steps every 5 min. At the end of the incubation, the mixture was centrifuged at 4°C for 7 min (10,000g). The supernatant was aliquoted and stored at -20°C until required.

Total protein content in the cell lysates was quantified using the Coomassie Plus Protein Assay Reagent (Thermo Scientific cat. 1856210) The same procedure was followed for the construction of the BSA calibration curve (Albumin Standard- Thermo Scientific, cat. 23209).

All samples were incubated at 37°C and the absorbance of the resultant reaction at 30 min was measured at 495 nm with a LT5000MS ELISA reader (Labtech International Ltd, Uckfield UK). Using the calibration curve, the unknown protein concentrations were calculated.

Gel electrophoresis was undertaken using the Mini-protean II apparatus (BIORAD, Hertfordshire, UK) and 10% precast Mini-PROTEAN® TGX™ Gels. Each gel was placed in the apparatus submerged in running buffer (see APPENDIX 1) and electrophoresed at 90V for 15 min and then at 150V for 2 h.

Gel markers were added to monitor the run and to verify the bands molecular weight during the reading (Figure 2.1).

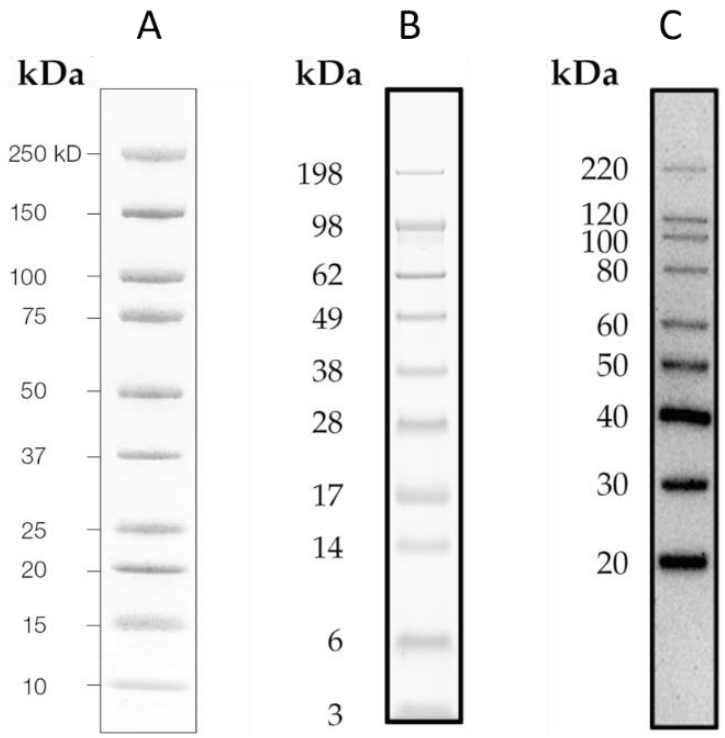

Figure 2.1 Molecular weight markers used for the execution and the analysis of western blots. A: Bio-Rad Precision Plus Protein Kaleidoscope Standard (BIORAD- cat. 161-0375) B: SeeBlue® Plus2 Pre-Stained Protein Standard (Life Technologies- cat. LC5925). C: MagicMark™ XP Western Protein Standard (Life Technologies- cat. LC5602). A and B were interchangeably used for the monitoring of the execution of the Western Blot, while C for the reading and the following analysis.

The blotting was undertaken using a semi-dry blotting approach (Bio-Rad Transblotting system). All the components had previously been submerged in

blotting buffer (see APPENDIX 1) and positioned into the chamber, in contact with the nitrocellulose membrane. The blotting was performed at 25V for 30 minutes.

The nitrocellulose membrane was then removed and washed in washing buffer (see APPENDIX 1) before being submerged in blocking buffer (see APPENDIX 1) for 1 hour. The membrane was then washed briefly and incubated, with shaking, for 16 hr at 4°C in the presence of the primary antibody, following specifications of manufacture. After the incubation with primary antibody the membrane was washed three times for 10 minutes at room temperature and then incubated for 1 hr at room temperature with the HRP-linked anti-rabbit or anti-mouse IgG secondary antibody (#7074S or #7076P2, Cell Signalling) at a dilution of 1:10,000 in blocking buffer. Subsequently, the membrane was washed three times for 10 minutes each and the signal detected using SuperSignal™ West Dura Extended Duration Substrate (Life Technologies Ltd, Paisley UK) and imaged and quantified on a ChemiDoc XRS+ (BIORAD, Hertfordshire, UK). A mouse anti-human β-actin monoclonal antibody (#A1978, SIGMA) has been used as housekeeping to normalize the expression of the target protein.

2.5 STATISTICAL ANALYSIS

For comparisons between two experimental groups, a Student's T-Test (unpaired two-tailed) was employed with statistical significance set at $P < 0.05$. For comparisons involving more than two experimental groups, a one-way ANOVA statistical analysis followed by an appropriate *post hoc* test was applied. When all possible pairwise comparisons have been made and the group sizes are equal then a Tukey's multiple comparison test has been performed. If the groups are of unequal size a Tukey-Kramer test was used. When multiple groups were compared to a single control treatment, a Dunnett test was applied.

3 CHAPTER 3- CAV-1 GENETIC KNOCK-DOWN/OUT APPROACHES

3.1 INTRODUCTION

The study of gene and protein expression in cancer allows the determination and characterization of sub-groups of patients presenting altered sets of genes and a specific therapeutic sensitivity. This could potentially stimulate specific therapeutical approaches that do not refer only to the broad diagnosis but also to the specific gene set and heterogeneity of the single patients.

Several tools are available for the study of genetic and epigenetic abnormalities (C. A. Stein & Cohen, 1988). One of them is based on the inhibition of the transcription of specific genes. This can be achieved in different ways, among which we selected, for this work, the RNAi-mediated gene knockdown and the CRISPR-mediated knockout.

Both took inspiration from physiological cellular processes. The RNAi is an evolutionarily conserved mechanism of gene silencing (Cech, 1986), consisting in small sequences of double-strand (ds) or single-strand (ss) RNA that are able to recognize and complementary bind freshly transcribed mRNA. This can result in an inhibition of the mRNA translation (siRNA) or in its total suppression (miRNA).

The RNAi process is well studied and generally considered reliable, with a variety of challenges that have been addressed and overcome in the past, like the delivery way and the efficiency of gene silencing. Several delivery techniques with different degrees of complexity, reliability and effectiveness (discussed in Chapter 1) have been developed, and the efficiency has been improved by the insertion of mismatches that increased the rapidity and the degree of degradation (H. Wu et al., 2011). Two different kinds of miRNA precursors can be used, a dsRNA that can act directly once inserted in the cell, and a plasmid vector codifying for a sequence that can be then cleaved and be functional.

The delivery of siRNA from DNA templates can be carried out by both liposomes and electroporation. However, the most efficient way seems to be the use of several recombinant viral vectors based on retrovirus, adeno-associated virus, adenovirus, and lentivirus. These vectors have been engineered and optimized

to allow the easy entry of siRNA into cells that are difficult to transfect. Also, some synthetic viral vectors, like the lentiviral and adenoviral ones possess an ability to integrate the shRNA into the cell genome, thereby leading to stable siRNA expression and long-term knockdown of a target gene, with virtually no need for a continuous pharmacological treatment (Y. Shi, 2003).

One of the most popular is the lentiviral system, which aims to integrate anti-target gene shRNA coding DNA into the genetic patrimony of the cellular host. The sequences are inserted together with a puromycin resistance-carrying gene that allows the selection of the successfully transfected cells.

CRISPR, on the other hand, is based on the use of prokaryotes Clustered Regularly Interspaced Short Palindromic Repeats (CRISPR)/CRISPR-associated protein 9 (Cas9) systems for nucleic acid editing. This system is a natural immune defence strategy in prokaryotes against the invasion of non-self-DNA, like viruses and plasmids and it occurs in a sequence-specific manner (Barrangou et al., 2007; Sorek et al., 2008).

The principle of the technology is that DNA sequences corresponding to the target gene are inserted among the spacers, so that the exogenous Cas9 can recognize it as foreign DNA and cut the genomic sequence, leading to a genetic knockout.

Again, like for the RNAi, the sequences can be inserted in different ways, like as DNA plasmids codifying for Cas9, or mRNA ready to be translated or the Cas9 protein itself. The last delivery methods allow increased efficiency and specificity.

Once the genetic knockdown/knockout has been assessed, generally via Western Blot or Real-Time PCR, cell properties can be tested to determine if the genetic modification had an impact on the phenotype of the cells under examination. Basic tests include cell cycle and cell proliferation, but also a change in morphology can indicate a change in the phenotype. For example, if cells pass from a mesenchymal to an epithelial shape, it may mean that some pathways related to EMT have been indirectly manipulated.

In terms of stem cell properties in cancer, clonogenicity is one of the main properties tested (Suksuphew & Noisa, 2015). As discussed in Chapter 1, this

property represents the ability of single cells to give rise to a new tumour *in vitro* or *in vivo* (Franken, Rodermond, Stap, Haveman, & van Bree, 2006). In case of high-grade gliomas, this would be particularly important since brain tumour cells display the ability to invade as single cells and to give rise to new tumours in other sides of the brain (Brösicke & Faissner, 2015).

3.2 SCOPE OF THE CHAPTER

The hypothesis of this thesis is that Cav-1 serves as a cancer stem cell tumour modulator able to influence cancer stem cell functions either in a suppressor or promoter manner dependent upon context. Ultimately the first milestone in the project was to evaluate in a panel of glioma cell lines (eight cell lines) the impact of a Cav-1 knockout (or Cav-1 knockdown) on cancer stem cell functions.

The selection of a glioma cell panel and the establishment of the requisite assays underpin this milestone. Method development initially involved the commonly used U87 glioma cell line and two of its shRNA transformed derivatives.

As extensively described in the General Introduction (Chapter 1), RNAi and CRISPR/Cas9 technologies both present advantages and disadvantages.

In different moments of the project, different technologies were available. This allowed us to test their ability to inhibit Cav-1 expression on the same cell lines and to discriminate the impact of Cav-1 on cell phenotype, aside from the changes induced by the technologies.

The effect of genetic modulation has been explored not only through the expression of the target protein but also cell line characterization, such as morphological changes, proliferation rate, cell cycle profile, clonogenic potential (both in 2D and in 3D format) and migration.

3.3 MATERIALS AND METHODS

3.3.1 CELL LINES

These have been described in Chapter 2.

3.3.2 RNAi

3.3.2.1 Lipid-based shRNA

U87 have previously been transfected for the silencing of Cav-1 by using a FUGENE-based technique. The Cav-1 knockout, U87 shRNA CAV and the non-target positive control counterpart, U87 shRNA CTRL were kept in the same culture condition but with the addition of puromycin 0.5μg/ml for the maintenance of the selection pressure.

3.3.2.2 Lentiviral-mediated shRNA (pLKO.1)

The Cav-1 knockdown, mediated by a lentiviral vector, has been obtained through the pLKO1 system (Figure 3.1), purchased from SIGMA-ALDRICH (MISSION® shRNA, SIGMA ALDRICH, Irvine, UK).

Table 3.1 The five sequences used for Cav-1 lentiviral-mediated shRNA knockdown.

NAME	SPECIFICATIONS	SEQUENCE
CAV(+) NT	SHC002-SIGMA MISSION® pLKO.1-puro Non-Mammalian shRNA Control Plasmid DNA	Targets no known mammalian genes
CAV(-) seq.1	TRCN0000007999- SIGMA Clone ID:NM_001753.3-2510s1c1	CCGGGCTTTGTGATTCAATCTGTAACTCG AGTTACAGATTGAATCACAAAGCTTTTT
CAV(-) seq.2	TRCN0000008000- SIGMA Clone ID:NM_001753.3-547s1c1	CCGGCCACCTTCACTGTGACGAAATCTCG AGATTTCGTCACAGTGAAGGTGGTTTTT
CAV(-) seq.3	TRCN0000008001- SIGMA Clone ID:NM_001753.3-441s1c1	CCGGGACCCTAAACACCTCAACGATCTCG AGATCGTTGAGGTGTTTAGGGTCTTTTT
CAV(-) seq.4	TRCN0000008002- SIGMA Clone ID:NM_001753.3-462s1c1	CCGGGACGTGGTCAAGATTGACTTTCTCG AGAAAGTCAATCTTGACCACGTCTTTTT
CAV(-) seq.5	TRCN0000011218- SIGMA Clone ID:NM_001753.3-747s1c1	CCGGGACCCACTCTTTGAAGCTGTTCTCG AGAACAGCTTCAAAGAGTGGGTCTTTTT

Five different active-predicted sequences have been selected on the Sigma website for the insertion in the plasmid (Table 3.1). One extra sequence, designed not to target any mammalian gene, was used as negative control for the silencing.

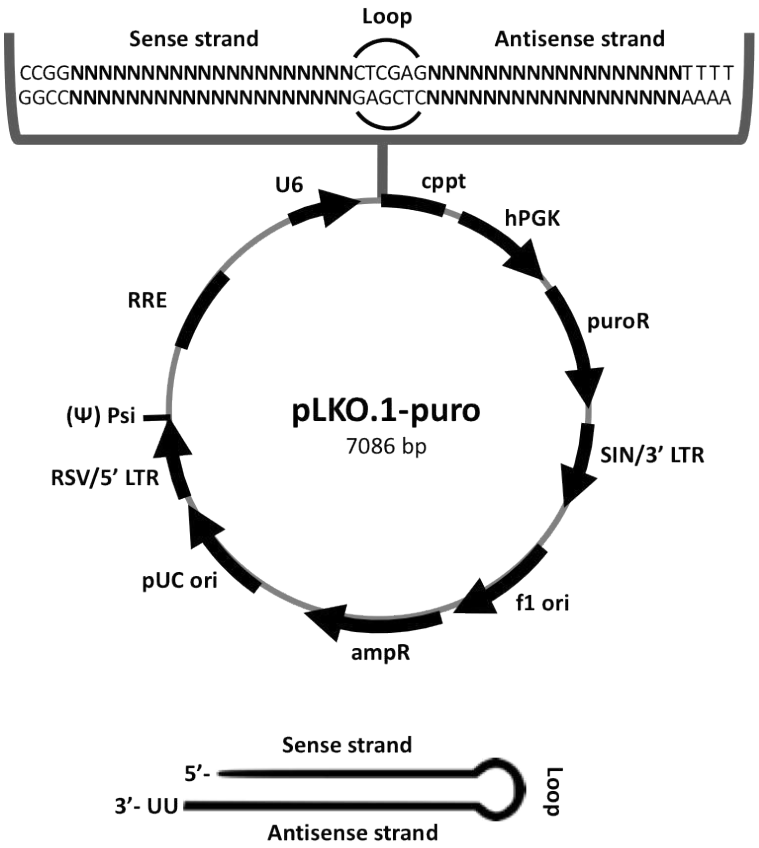

Figure 3.1 pLKO.1 vector map showing the insertion point of the custom sequences (top) and the resulting shRNA hairpin.

The pLKO.1 vector, however, is classified as third-generation since its safety is improved in key ways. First, the packaging plasmid is split into two separate plasmids, one encoding for Gag and Pol and the other for Rev. Tat is eliminated and replaced by a chimeric 5' LTR fused with a CMV promoter.

The five shRNA sequences (Table 3.1) from the SIGMA website were blasted on the whole human transcript to check if they were not interfering with the expression of other genes and subsequently tested (example in Table 3.2) (Altschul, Gish, Miller, Myers, & Lipman, 1990).

Table 3.2 BLAST of three sequences on the whole human transcript.

BLAST							
SEQUENCE	mRNA blasted	score	expect	identities	identities perc	gaps	strand
LKO1	(CAV1), transcript variant 3, mRNA	42.1	0.006	21/21	100	0/21	+/+
	(CAV1), transcript variant 2, mRNA	42.1	0.006	21/21	100	0/21	+/+
	(CAV1), transcript variant 1, mRNA	42.1	0.006	21/21	100	0/21	+/+
	zinc finger, matrin-type 1 (ZMAT1), transcript variant X1-7, mRNA	30.2	21	18/19	95	0/19	+/-
	N(alpha)-acetyltransferase 35, NatC auxiliary subunit (NAA35), transcript variant X1-6, mRNA	30.2	21	18/19	95	0/19	+/-
	G protein-coupled receptor 19 (GPR19), transcript variant X1-4, mRNA	30.2	21	18/19	95	0/19	+/+
	uncharacterized LOC105377025 (LOC105377025), ncRNA	30.2	21	15/15	100	0/15	+/+
	mRNA blasted	score	expect	identities	identities perc	gaps	strand
LKO2	(CAV1), transcript variant 4, mRNA	42.1	0.006	21/21	100	0/21	+/+
	(CAV1), transcript variant 3, mRNA	42.1	0.006	21/21	100	0/21	+/+
	(CAV1), transcript variant 2, mRNA	42.1	0.006	21/21	100	0/21	+/+
	(CAV1), transcript variant 1, mRNA	42.1	0.006	21/21	100	0/21	+/+
	GRB2-associated binding protein family, member 4 (GAB4), transcript variant X1-6, misc_RNA	30.2	21	15/15	100	0/15	+/+
	mRNA blasted	score	expect	identities	identities perc	gaps	strand
LKO4	(CAV1), transcript variant 4, mRNA	42.1	0.006	21/21	100	0/21	+/+
	(CAV1), transcript variant 3, mRNA	42.1	0.006	21/21	100	0/21	+/+
	(CAV1), transcript variant 2, mRNA	42.1	0.006	21/21	100	0/21	+/+
	(CAV1), transcript variant 1, mRNA	42.1	0.006	21/21	100	0/21	+/+
	proteasome (prosome, macropain) 26S subunit, non-ATPase, 5 (PSMD5), transcript variant X2, mRNA	28.2	85	14/14	100	0/14	+/-

The transfection procedure was performed by Dr Giusy Tornillo in the School of Bioscience, Cardiff University.

After the lipo-transfection into 293T cell lines, maintained in DMEM 10% FBS and 1% PS, the plasmid was packaged into viral particles, to be released from the packaging cells. The supernatant was replaced after 14-16 hours with new medium, which was collected after 8-9 hrs. It then was centrifuged for 5 min at 1500 rpm to remove cell debris, filtered (0.22μm) and transferred on the culture of target cells to allow the viral particles to infect the cells and release and integrate the plasmid carrying the shRNA sequences. Cells with the integrated plasmid and expressing the shRNA containing DNA sequence were selected by Puromycin administration after 24 hrs, at a concentration (Table 3.3) established

a the puromycin killing curve, that was performed on each target cell line (puromycin concentration 50nM-100μM, timepoints 72 and 120 hrs- see Figure 3.21).

Table 3.3 Puromycin concentrations for Lentiviral transfection selection and maintenance

	Cell Line	Puromicin Concentration Selection and Maintenance (μg/ml)
1	U87	0.4
2	U373	0.4
3	UP007	0.3
4	UP019*	0.4
5	UP029	0.8
6	IN699*	0.3
7	SF188	0.5
8	KNS42	0.5

Cell lines after selection were cultured in normal medium or in medium supplemented with half of the selecting concentration of Puromycin and Cav-1 expression was tested by Western Blot.

3.3.3 CRISPR/Cas9

CRISPR engineering was performed by Miss Catia Neto as part of her PhD project.

3.3.3.1 Plasmid delivery

Plasmids U6gRNA-Cas9-2A-GFP (Figure 3.2) were bought from Sigma-Aldrich, already engineered with the sequences for the recognition of CAV-1 target sequences (Table 3.4).

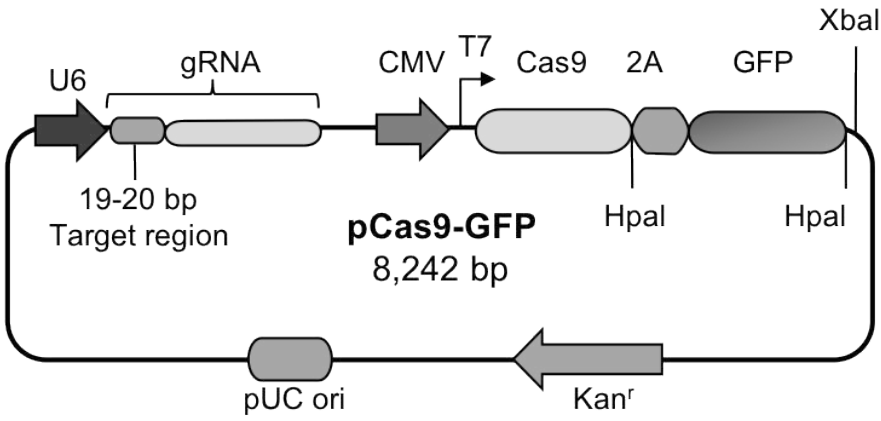

Figure 3.2 U6gRNA-Cas9-2A-GFP map (Sigma-Aldrich).

They were replicated into MAX Efficiency® DH5α competent cells (Invitrogen-Thermo Fisher Scientific- Waltham, MA, USA).

Table 3.4 Sequences for the targeting of CAV-1 with CRISPR knockout system.

Target ID	Target site	Blast CAV-1 gene
HS0000173746	TTTAGGGTCGCGGTTGACCAGG	6860-6881
HS0000173749	CATCCCGATGGCACTCATCTGG	39311-392990
HS0000173747	AAACACCTCAACGATGACGTGG	6879-6900

48 hours after the transfection with Oligofectamine, cells were sorted for GFP as single cells into 96-well plates and clones were expanded and checked for the expression of Cav-1 by Western Blot.

3.3.3.2 RNP (Alt-R®)

The RNP system was purchased from IDT (Integrated DNA Technologies-Coralville, Iowa USA). The system is based on a pre-assembly of the three components (crRNA, tracrRNA and fluorescent Cas9, Figure 3.3). The RNPs assembled were then delivered inside the cells' nucleus by electroporation and sorted after 48hrs into 96-well plates for the selection and the assessment of Cav-1 expression via Western Blot.

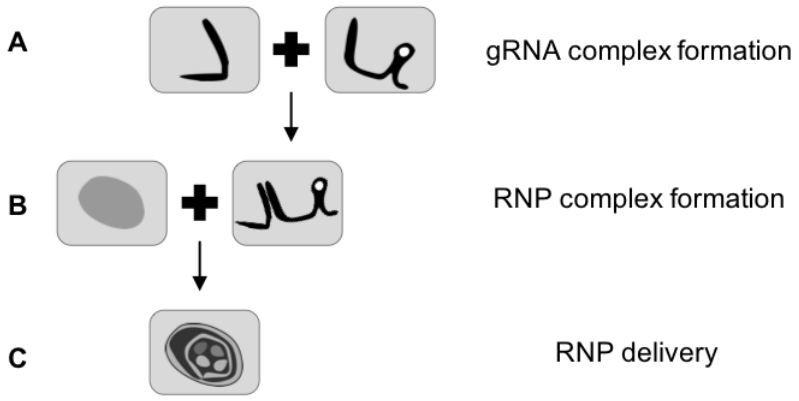

Figure 3.3 RNP assembly steps for the ALT-R CRISPR system.

3.3.4 CELL PROLIFERATION - MICROSCOPY;

U87 cells were seeded at three different seeding concentrations (5,000, 15,000 and 50,000 cells/cm^2) in a 24-well plate format (Figure 3.4). This included the non-transfected wild-type cells (U87-WT), the plasmid shRNA scrambled control cells (U87- shRNA CTRL) and the plasmid shRNA Cav-1 knockdown cells (U87-shRNA CAV). These transfectants were previously established in the laboratory by Ms Fang Zhang [between 2013 and 2014]. Together we refer to the different U87 cell lines described above as U87 shRNA.

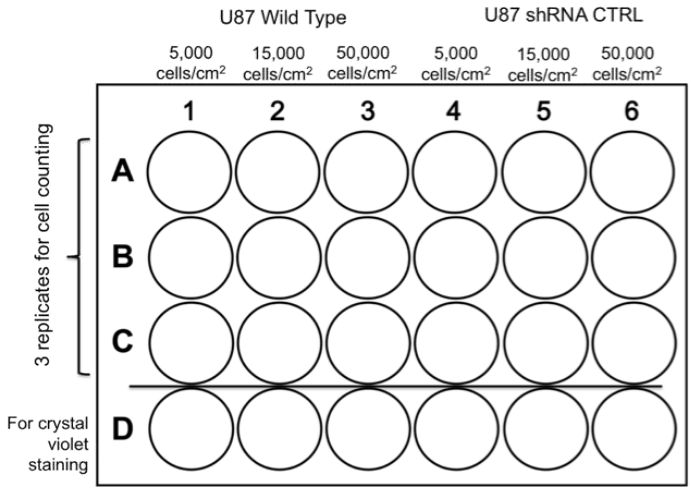

Figure 3.4 Cell growth seeding scheme for U87-WT and U87-shRNA CTRL. With a separate plate created for U87-shRNA CAV.

In each plate, three wells were used as replicates for the cell counting while a fourth well was reserved for staining with Crystal Violet (0.5% in Met OH) to allow the morphological characterization. Cells were counted and stained every day for seven days by haemocytometer-based methods. The cell counts were plotted as cells/cm^2 by GraphPad Prism 5 (GraphPad Software, Inc., La Jolla, CA USA).

3.3.5 CELL PROLIFERATION - FLUORESCENCE

Cell growth was assessed for all cell lines. Cells were seeded at the density of 5,000-15,000 cells/cm^2 in a 96 well-plate format and maintained in normal cell culture medium. At discrete time points for 144 hrs (6 days) cell counting was undertaken using the CyQUANT® Direct Cell Proliferation Assay Kit (Invitrogen, Life Technologies Ltd, Paisley UK). This assay quantifies DNA content and involves the addition of a nucleic stain, CyQuant® Direct nucleic acid stain, to the cells for an incubation period of 60 min at 37^{o}C. It does not require the prior washing of the cells in culture. The fluorescence was read at 480/535 nm with detection on a FLUOstar OPTIMA plate reader (BMG LABTECH Ltd, Bucks UK). For each cell line, at least 12 replicates were tested.

The doubling time was analysed by using the viability data corresponding to the log phase of the plots and an online tool for the calculation of the doubling time (Roth V., 2006).

3.3.6 SELF-RENEWAL CLONOGENIC ASSAYS

Three clonogenic assays were explored (Figure 3.5).

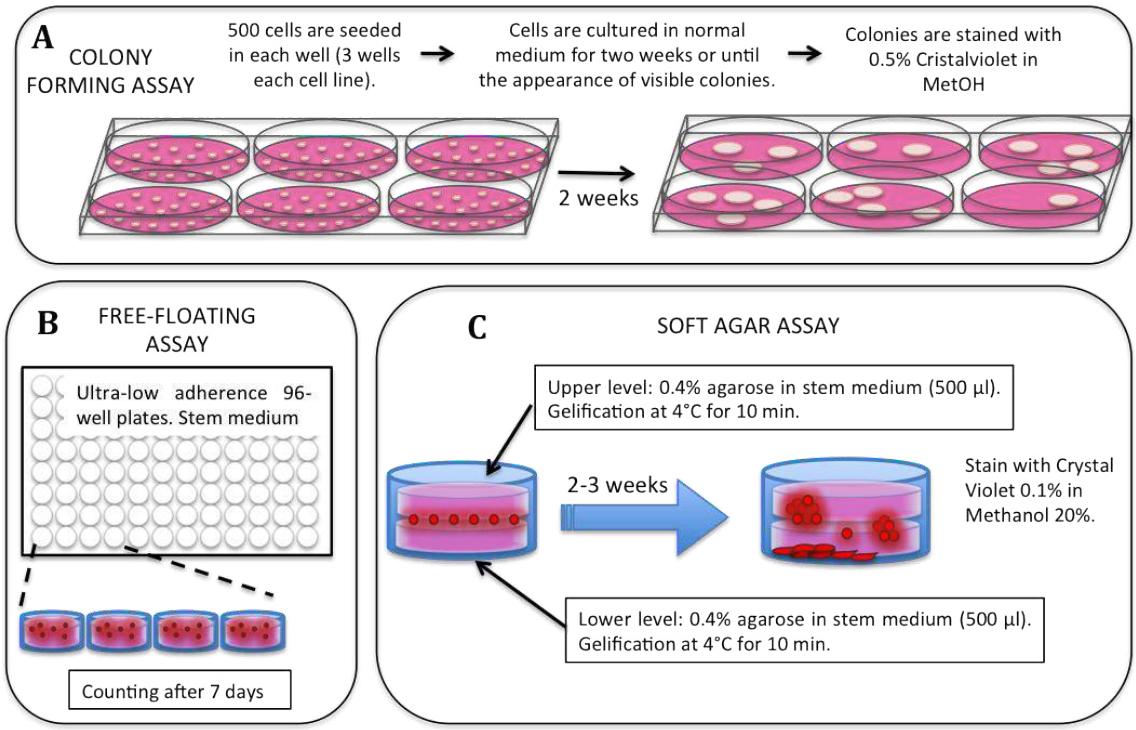

Figure 3.5 Graphical representation of the three-clonogenic assays. A. Colony-forming assay. B. Free-floating assay. C. Soft agar assay.

3.3.6.1 2D Colony-forming assay (Figure 3.5.A)

Cells from normal culture conditions were seeded at a density of 500 cells in each well (6 well-plate format) in normal culture medium and left to form cell colonies in 5% CO2 at 37°C, over 14 days, but with the culture medium replenished at 7 days. At the end of the experiment (day 14), the medium was removed, the cells briefly washed (PBS) and the colonies stained with 500µl solution of Crystal Violet (0.5% w/v in Met OH 20% v/v). After 2 minutes of submersion of plates in tap water, the staining was terminated. The dried plates were imaged, and colonies captured on a ChemiDoc XRS+ (BIORAD, Hertfordshire, UK), using a modified copper staining protocol from the machine standard software, and a cell culture microscope. Colonies were counted with the Cell Counter plugin of FIJI (Schindelin et al., 2012a).

3.3.6.2 3D Free-floating assay - materials (Figure 3.5.B)

Stem cell medium used was DMEM-F12 (Gibco, Life Technologies Ltd, Paisley UK); 2% B27 (Gibco, Life Technologies Ltd, Paisley UK); 1% Penicillin/Streptomycin; 20ng/ml EGF (Gibco, Life Technologies Ltd, Paisley UK); 20ng/ml bFGF (Gibco, Life Technologies Ltd, Paisley UK).

Cells were seeded at a density of 1000 cells/well (flat-bottomed-96 well-plate format) suspended in 100 µl of stem medium. After 7 days, the number of cellular spheres in each well were counted using a standard inverted light microscope. These spheres, when used in the context of a self-renewal clonogenicity assay, will be termed “neurospheres” in the following sections.

The same assay was performed as above but seeding a single cell into each well using the FACSaria III (BD Biosciences, Oxford UK) in Central Biotechnology Services (Cardiff University).

3.3.6.3 3D Soft agar assay (Figure 3.5.C)

Soft agar colony-forming assays were carried out by seeding 1000 cells between two layers of agar with a 24-well plate format. The top layer of agar comprised 0.3% v/v agar (SeaPlaque Agarose, Basel, Switzerland) in stem medium (as described before), while the bottom layer comprised 0.4% v/v agar in stem medium. Cells were incubated at 37 °C for up to 21 days. Colonies from at least 8 replicate wells were stained with Crystal Violet (0.01% in 20% Met OH), visualised and quantified as above (see 2D Colony-forming assay).

3.3.7 SCRATCH ASSAY

After trypsinization of normal cell culture, 100,000 single cells were counted and seeded in a 24-well plate and grown until confluent (on average two days). Wells were then scratched with a 200µl tip in both horizontal and vertical directions (see Figure 3.6). Wells were then washed to eliminate the floating scratched cells. Pictures were taken on cell culture microscope immediately after the scratch (0 hrs) and after 8 hours (8 hrs). The pictures were taken at the centre of the crossing, to replicate as much as possible to the position of the picture at 0 hrs.

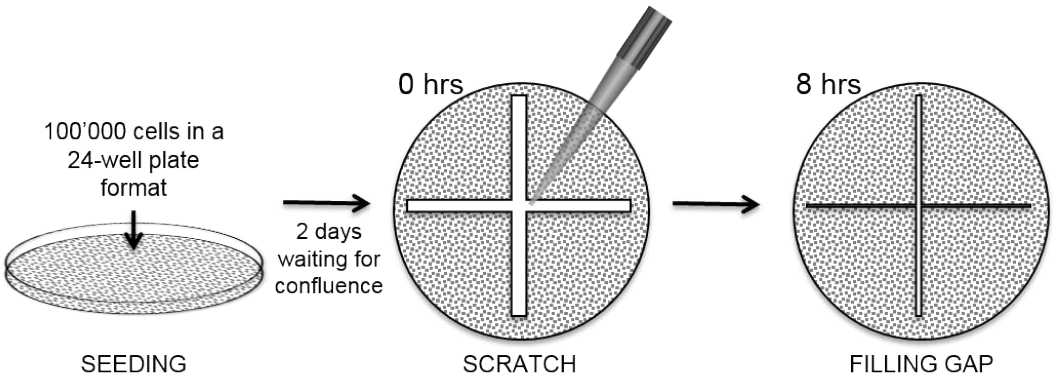

Figure 3.6 Graphical representation of the scratch assay methodology.

For the quantification, wells' pictures were loaded on ImageJ FIJI software and analysed with a procedure reported in detail in Appendix. Briefly, images were sharpened to highlight contrast and binarized, to allow the selection of the area not covered in cells.

After the analysis of all the areas (A), the A_{t8} were normalized on the A_{t0} (set as 100). The result is the percentage of area occupied by the migrated cells.

3.3.8 CELL CYCE ANALYSIS

1 million cells were resuspended in 1ml ice-cold PBS and then added delicately to 9 ml ice-cold Ethanol 70% for fixation.

Cell suspension was centrifuges and and supernatant discarded. After a was with PBS 5%FBS cells were resuspended in 5ml of PI staining solution (PBS, 0.1% Triton X-100, 2% PI 1mg/ml, 0.02% RNase) and incubated at RT for 30 min in the dark.

After resuspension and eventual filtering to eliminate clusters cells were analysed by flow citometry according to PI spectrum of excitation (536nm) and emission (617nm).

Cell cycle analysis was performed with FlowJo univariate analysis.

3.4 RESULTS AND DISCUSSION

In the table below (Table 3.5), all the cell lines under examination and the genetic modification are reported.

U87 and U373 were commercially obtained by ECACC, while the other cell lines were gently provided by Professor Geoff Pilkington, from the University of Portsmouth, School of Pharmacy and Biomedical Sciences. Among them three cell lines, UP007, UP019 and UP029 were isolated in Professor Pilkington's lab (Brain Tumour Research Centre).

In total 5 adult and 3 paediatric GBM cell lines were obtained. For some of them, it was possible to retrieve from the literature some genetic information, like the TP53 and the PTEN status.

After the first experiments, unfortunately, it was acknowledged that IN699 was indeed not derived from GBM but from rhabdomyosarcoma, while the UP019 cell line was cross-contaminated with UP007 before the aliquot was shipped to the group. Instead of manipulating the images of the first panel experiments containing those two cell lines, a choice was made of keeping them in (with an asterisk indicating them) and they were not furtherly part of the experimental plan.

Table 3.5 Cell lines under examination with available information and genetic modifications

	Cell Line	Origin	Patient details	Type (Grade)	Genetic information available	Source	shRNA	Lentiviral knockdown	CRISPR knockout
1	U87	U. Uppsala (SE)	Adult	Adult GBM (IV)	TP53 wt/ PTEN mut/ p16 del/ p14ARF del/CDKN2A mut	ECACC	✓	✓	✓ (plasmid)
2	U373	U. Uppsala (SE)	Adult	Adult GBM (IV)	TP53 wt/ PTEN null/ p16 wt/ p14ARF wt	ECACC		✓	
3	UP007	SEBTA	Adult	Adult GBM (IV)		SEBTA		✓	✓ (RNP)
4	UP019*	SEBTA	Adult	Adult GBM (IV)		SEBTA		✓	
5	UP029	SEBTA	Adult	Adult GBM (IV)		SEBTA		✓	✓ (RNP)
6	IN699*	Institute of Neurology (London)	Adolescent (15-year-old male)	Supratentorial paediatric GBM		SEBTA			
7	SF188	U. Arizona (AZ, USA)	Child (8-year-old male)	Frontal paediatric GBM (IV)	TP53 wt/ PTEN wt/ p16 wt/ p14ARF wt	SEBTA		✓	
8	KNS42	U. Kyushu (JP)	Adolescent (15-year-old male)	Frontoparietal anaplastic astrocytoma (IV)	TP53 mut/ PTEN wt	SEBTA			

3.4.1 LIPOSOME-MEDIATE SHRNA KNOCKDOWN

The U87 glioma cell line has been extensively used by the research community, including two laboratories in their study of the impact of Cav-1, as previously mentioned (Cosset et al., 2012; Martin et al., 2009; Quann et al., 2013). Preliminary studies were undertaken with this cell line served for methodological development prior to use a wider panel of glioma cell lines.

The laboratory held stocks of the U87 cell line (U87WT) (Cav-1 +) and derivative cells that had been stably transduced (lipid-based system) with: a shRNA anti-Cav-1 sequence generating a Cav-1 protein knockdown cell line (U87 shRNA CAV) (Cav –); and a parallel line transduced with a scrambled shRNA sequence (U87 shRNA CTRL) (Cav+) [Work of Ms Fang Zhang– Visiting Scholar in Gumbleton laboratory 2013-14]. The use of U87 within the pilot methodological experiments was decided also to allow initial testing of the impact of Cav-1 status upon function and further comparison to already-published work.

A western blot analysis of the U87 cells showed that the shRNA knockdown was intact with no Cav-1 protein expression observed in the shRNA Cav-1 cell line while expression was evident in the U87WT and shRNA CTRL cell lines (Figure 3.7).

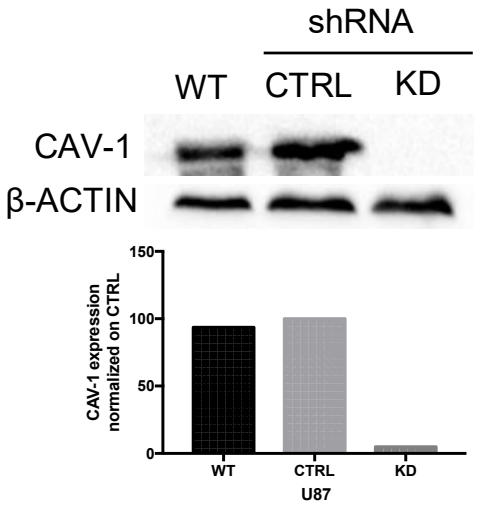

Figure 3.7 shRNA (plasmid) mediated Cav-1 silencing. Densitometry analysis of bands corresponding to Cav-1 molecular weight, 22 kDa, was performed and compared to the corresponding band density of the housekeeping gene β-Actin (46 kDa). The resulting folds were normalized on the shRNA CTRL, in order to evaluate the knockdown efficiency. Experiment was repeated once.

The pattern of growth (Figure 3.8B) of the U87 revealed that all three-cell lines (even when growing in standard cell culture medium) were able to establish sphere-like outgrowths of cells distinct from the adherent cell monolayer. This capacity to establish sphere-like cellular outgrowths may be regarded as a crude measure of clonogenicity. During the cell proliferation assay, where the actual cell count was monitored by microscopy and haemocytometer (Figure 3.8C-manual count), it was noted that the U87 cells not expressing Cav-1 protein (shRNA Cav) were always the first to form spheres, and these spheres were consistently smaller in size (qualitative assessment) compared to those seen in U87 CTRL and U87 WT cell lines. In the entire U87 a proportion of these spheres detached from the monolayer retaining the ability to grow while floating free in suspension. Figure 3.8C shows growth on a semi-log plot with a lag phase for all three U87 lines of 1-2 days. The exponential phase of cell growth indicated that the knockdown of Cav-1 had no impact upon U87 cell proliferation rate, with the rate of cell growth appearing to plateau at around day 8. This method of cell counting by microscopy did, however, require the initial washing of the cultures, which inevitably caused the release of some of the attached spheres. Figure 3.8D (linear scale) and Figure 3.8E (semi-log scale) show the growth pattern of the U87 as assessed over 6-days by a fluorescence DNA based assay. Here the assay did not involve a washing step of the cells, but simply the addition of the cell-permeable fluorescent label. The transfected cell lines, shRNA CTRL and shRNA Cav-1, are associated with a higher Level of fluorescence than the WT cells which is an expected outcome given that they bear additional recombinant DNA from the transformation shRNA process. However, the overall rate of proliferation across the cell lines appears to be unchanged by the loss of Cav-1, a consistent finding between the microscopy and fluorescence-based approaches to cell counting.

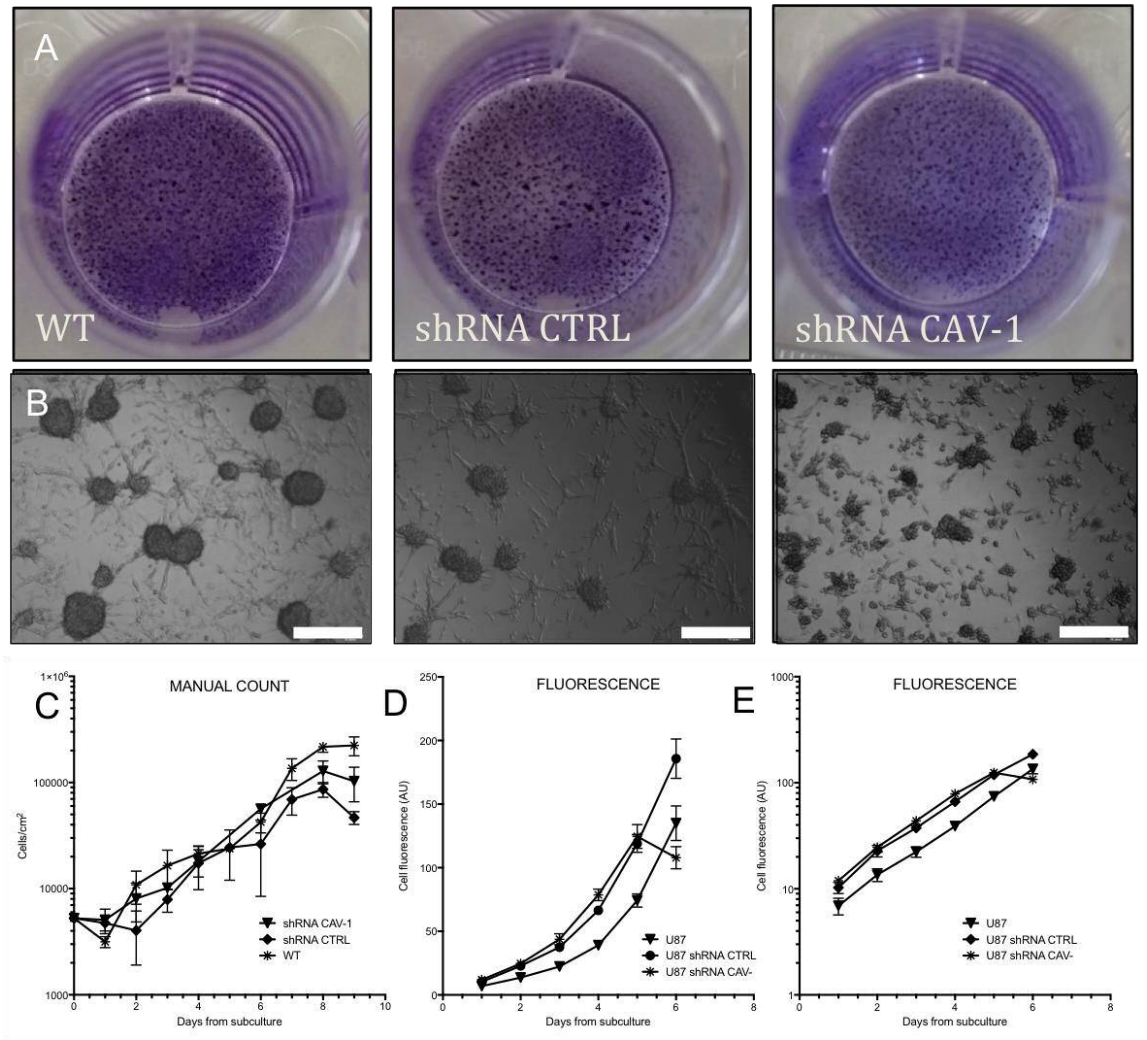

Figure 3.8 Growth pattern of U87: A non-magnified images of the U87 grown in a 24-well format and stained with crystal violet which highlights the size of the cellular spheres. B: 4x magnification of the spheres. C Cell counting-based proliferation assay (semi-log plot). The arrows indicate the time to the first appearance of the spheres/aggregates in the culture. D DNA content-based proliferation assay (linear plot) and E (semi-log plot). The transfected cell lines display an increased DNA content, but the Cav-1 knockdown appears not to have affected U87 cell growth rates.

3.4.1.1 U87 SELF-RENEWAL AND CLONOGENICITY: FREE-FLOATING NEUROSPHERE ASSAY

Using the U87, a method was developed to establish a clonogenic assay. A clonogenic assay assesses the capacity for a single cell to undergo a process of self-renewal giving rise to a distinct cell population. This population may or may not contain members that have the capacity to undergo further differentiation, but the point is that a self-renewal process must have occurred to initiate the population. The ability to survive and undergo a self-renewal process under

environmental pressure is one of the characteristics of cancer stemness and an aggressive cancer phenotype.

The clonogenic assay initially chosen was the 'free-floating' assay (Table 3.6 below). It is a relatively quick (7-days) suspension-based assay testing the ability of an individual cell to undergo self-renewal in an environment where anchorage-dependent growth is prevented (i.e. using cell culture plasticware that prevents cell adhesion) and where the culture medium is minimal, i.e. lacking serum but comprising select 'stem cell' growth factors. It is termed 'free-floating' as the cells that survive are literally free to float in suspension, i.e. they are not embedded in any matrix, and as they divide they will give rise to 'tumour-like' cellular neurosphere.

A set of criteria was used to count the neurospheres at the end of the 7-day assay:

- a mass of cells has been considered a neurosphere if it contained at least 50 cells (evaluated by optical microscopy). This criterion sets a certain demand on the replicative capacity of the cells comprising the neurosphere, e.g. discounting 'neurospheres' that may contain only a handful of cells after 7 days of culture– here the assay conditions will have imposed a significant challenge to particular cells in their capacity to undergo self-renewal and proliferation;
- to be considered as a neurosphere derived from a common initiator cell then the neurosphere must have a rounded and compacted structure (judged qualitatively by microscope). This criterion is aimed at distinguishing between a 'true' neurosphere and an aggregate of cells. This is particularly important in a 'free-floating' assay design as while it is easy to implement, the individual neurospheres that form have the potential to adhere to each other to form larger aggregates. An outcome not truly reflective of self-renewal capacity.

To establish an appropriate cell number for seeding into the low adherence 96-well format an initial cell seeding study was undertaken using U87 WT cells, with cell seeding varied between 100 to 1000 cells per well. Figure 3.9A shows after 7 days the number of neurospheres that had grown per well. Figure 3.9B shows the same data but expressing neurosphere growth as a % of original cell

seeding. While this pilot study represents only a single experiment the coefficient of variations for any of the seeding was no greater than 22%. The outcome of the pilot determined that 500 cells per well to be the basis for future U87 'free-floating' clonogenicity assays. This choice was based on the minimum cell seeding number associated with the maximal observed % neurosphere formation.

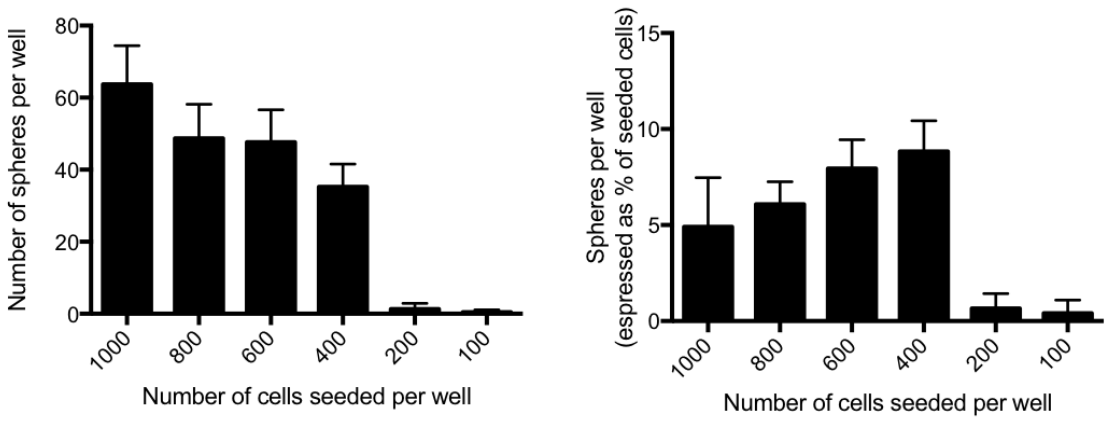

Figure 3.9 Establishing the seeding concentration for the free-floating assay for the U87. A: absolute number of neurospheres per well; B: number of neurospheres per well expressed as a % of original seeding number. Data represent a single experiment (mean ± SD) with n=10 wells for each seeding density

The pilot experiment above allowed application of the 'free-floating' clonogenic assay to the U87 of cells. Figure 3.10 shows the results of a free-floating clonogenic assay on the U87 across three different independent experiments. Despite what was considered careful adherence to the methodology, the outcome of each experiment produced entirely different findings with no consistent pattern. It was also noted that the yield of neurospheres was considerably reduced in these latter series of experiments (e.g. U87 WT ca. 0.5 to 1.6% neurosphere growth when expressed as % of the 500 cells seeded) compared to the pilot investigation (U87 WT ca. 7%, Figure 3.9). Nevertheless, despite the high variable outcomes in terms of the number of neurospheres formed, one consistent finding was that Cav-1 negative cells, (U87 shRNA CAV-1) displayed neurospheres that were smaller in size, indicating that the expression of Cav-1 expression is important for the growth of the neurosphere in the context of this self-renewal assay.

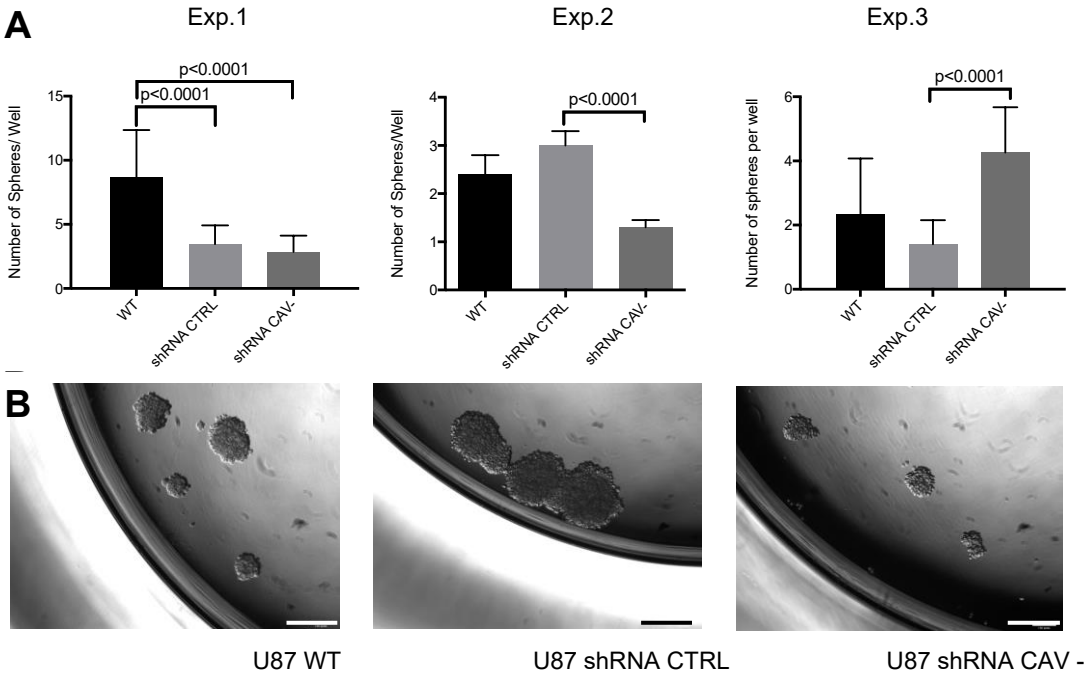

Figure 3.10 Free-floating assay on U87: U87 wild-type (U87 WT) cells, U87 shRNA CTRL cells and U87 shRNA Cav-1 cells. 500 cells seeded into each well of a 96-well format. A. shows three separate experiments (mean ± SD with n=10 replicates within each experiment). Statistical analysis by one-way ANOVA with Tukey's multiple comparison test. B. Representative images (4x magnification) of spheres formed for each cell line.

Although the 'free-floating' neurosphere culture has been widely used there are several limitations to the method. In particular, it is highly sensitive to cell density, different constituents or concentrations of factors in the media as well as the very real problem of distinguishing aggregates of cells from 'true neurospheres'. Further, when the repeated passages undertaken influence the composition of the individual passaged dissociated neurospheres themselves (e.g. differentiation status) and naturally lead to different outcomes. As a consequence of this, the cellular sphere formation saw in the U87 grown in standard 2D- culture conditions (Figure 3.8) might reflect the extent of the spheres present in the cells harvested from the standard 2D- cultures. Once harvested to seed into the self-renewal assay, they may represent a significant source of variation contributing to the findings in Figure 3.9 and Figure 3.10. Further, the U87 cells in such spheres maybe functionally/phenotypically different to those that had grown as part of the monolayer 'carpet' attached to the plastic.

3.4.1.2 'U87 CELL PANEL'- VARIABLE CELL PHENOTYPES WITHIN STANDARD 2D CELL CULTURE

The above data led to a series of experiments aimed at testing if in standard 2D-cultures the U87 cells growing within spheres behaved differently from the cells growing as part of the monolayer 'carpet' attached to the plastic. Figure 3.11 shows the experimental scheme for the harvesting of U87 cells that effectively represented sub-populations of cells from within a standard 2-D culture. The sub-populations tested were: adherent to the plastic in a monolayer culture; both adherent cells and cells weakly attached to the monolayer as spheres; and finally, as spheres or cell aggregates floating freely in suspension. The cells harvested under the different conditions were subjected to cell cycle analysis, Western Blot for Cav-1 and a self-renewal clonogenic assay.

The U87 cells were all seeded at a density of $5x10^3$ cells/cm^2 and were collected at three different time points, either prior to sphere formation (day 3) or at a sufficient time (day 7) that allowed the cell spheres/aggregates to detach from the monolayer and exist in sufficient numbers in suspension. The cells harvested as a monolayer only were easier to handle in comparison to the mixed population and the floating aggregates. Specifically, the cellular aggregates were difficult to dissociate especially as they became more compact.

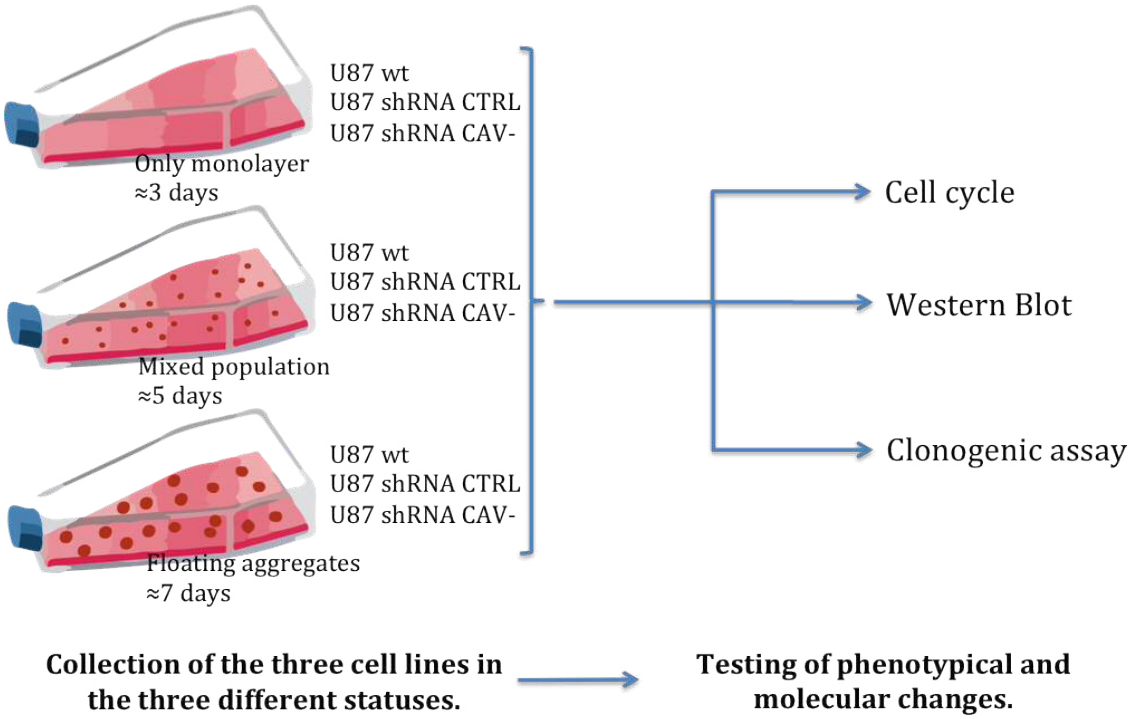

Figure 3.11 Experimental scheme within the standard 2-D culture to test if subpopulations of U87 cells were functionally different. Use was made of the U87 (U87 WT, U87 shRNA CTRL and U87 shRNA CAV-1. Cells were seeded at 5 x 10^3 cells/cm^2 onto standard tissue culture plastic containing full medium replete with serum. In total 9 T-flasks were seeded. The U87 cultures were harvested at different time points, specifically: Day 3 post-seeding– a time point at which the only cells present were those adhering to the plastic in a monolayer culture; Day 5 post-seeding– a time point where both adherent cells and cells contained in weakly attached spheres could be found; Day 7 post-seeding- a time point that allowed harvesting of spheres or cell aggregates floating in suspension.

Figure 3.12 shows the Western blot of the various sub-populations. The blots were difficult to conduct for the free-floating suspension spheres alone, reflecting a relatively low Level of protein material. These cell aggregates were difficult to process for the Western Blot being less susceptible to mechanical disruption and osmotic and chemical lysis. The resulting protein lysate was very poorly concentrated, and its consistency was jelly-like indicating nucleic acid contamination. Nevertheless, but not surprisingly, the expression of Cav-1 is maintained in the WT and CTRL cells for both the monolayer and mixed populations, and at least for the WT cells the expression of Cav-1 appears to be relatively stable.

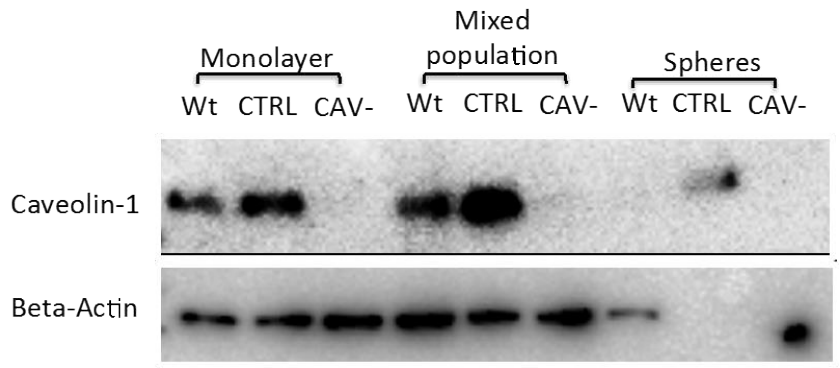

Figure 3.12 Cav-1 Western blot analysis of the three sub-populations. Image of bands corresponding to Cav-1 molecular weight, 22 kDa, was compared to the corresponding image of the housekeeping gene β-Actin (46 kDa).

Cell cycle analysis of the individual populations is shown in Figure 3.13. The cell cycle methodology essentially quantifies the amount of DNA each cell line possessed against a mathematical model. The method requires cells to be stained with a fluorescent dye, propidium iodide (PI), which binds to DNA in a manner that reflects directly and accurately the amount of DNA present; a flow cytometer is used to analyse the amount of fluorescence associated with each cell. As the cells start replicating (S-phase of the cell cycle) the amount of DNA increases to become double (at the point of cell division G2/M) that observed in the non-replicative phase of the cell cycle (G0/G1). The staining of the DNA allows calculation of the proportions of cells that are in the G0/G1 phase (first peak, the DNA content is defined as 1n), G2/M phase (second peak, the DNA content is now 2n) and in S phase (the transition between the two peaks) – see Figure 3.18 for an example. The modelling of the cell cycle is undertaken by flow cytometer software, FlowJo.

The cell cycle analysis (Figure 3.13) was able to model all the data for the monolayer sub-populations. However, the shRNA transfection process appeared to modify the cell cycle profiles, apparent from the comparison of the WT data to that of the shRNA CTRL (both Cav-1 +); this is likely a reflection of the additional DNA that the transfectants bear. When comparing the transfectants alone the shRNA CTRL (Cav-1 +) displayed a higher percentage of cells in the G0/G1 phase in comparison to cells with the shRNA Cav-1 (Cav-1-ve) knockdown. This result is consistent with previous studies reporting that the expression of Cav-1 induces G0/G1 arrest in breast and lung cells through a p53-dependent

mechanism (Galbiati, Volonté, et al., 2001; Torres et al., 2006). The shRNA Cav-1 (Cav-1–) cells (monolayer subpopulation) displayed a reduced G2/M phase compared to the shRNA CTRL, i.e. Cav-1 +ve cells have a longer duration G2/M phase. This is consistent with Quann et al. (Quann et al., 2013) who reported that Cav-1 expression inhibits cyclin D1, a factor promoting the cell to cycle rapidly through G2/M phase, i.e. high Cav-1 extends residence time in G2/M phase. Cell cycle analysis of the other sub-populations was more challenging. Specifically, the shRNA Cav-1 cells could not be adequately modelled. Again, the shRNA CTRL cells showed a different profile to the WT cells. Interestingly the cell cycle for the WT cells was modelled across all three subpopulations with the cells in the isolated spheres showing a distinctly lower fraction of cells in the resting phase (Go/G1) and a greater number in the S-phase.

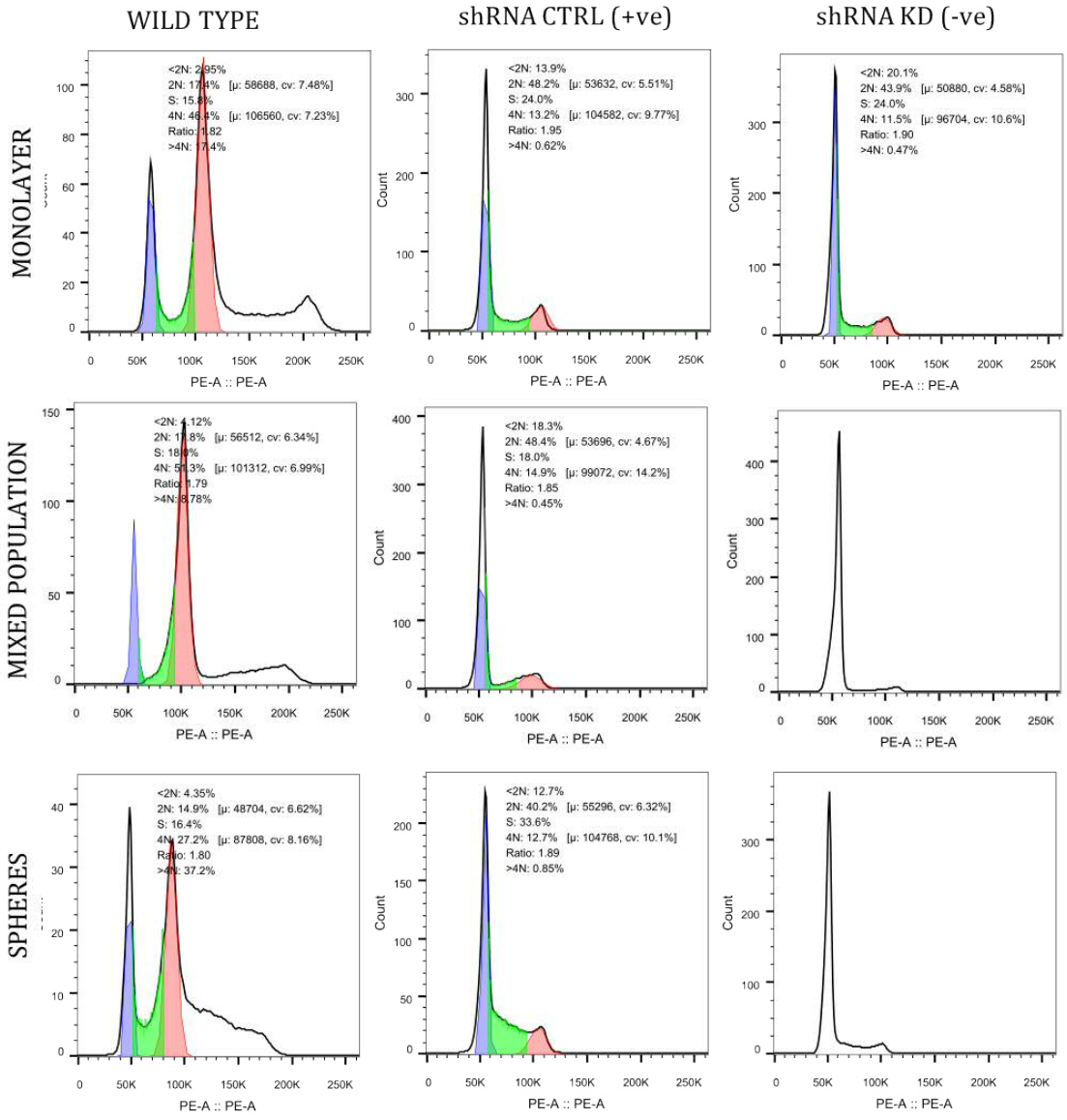

Figure 3.13 Cell cycle univariate analysis of the three sub-populations. Cells harvested for cell cycle from the monolayer state only; from a mixed state comprising monolayer and spheres attached to the monolayer, and finally, just spheres floating freely in suspension. Experiment was repeated once.

With regards to the self-renewal clonogenicity assay, it was determined that due to the continuing lack of reliability of the neurosphere free-floating assay to adopt an alternative self-renewal clonogenic assay based on a matrix approach with soft-agar, the 'Soft agar assay' (Table 3.6 below.) In this assay colonies of neurospheres are formed between two layers of agar within a 24-well plate format. With this approach, the issue of the aggregate formation between neurospheres is decreased significantly.

Figure 3.14 shows the results of the sub-population analysis using the 'soft agar' neurosphere assay. The same cell seeding was applied to each of the three different types of sub-population and it was clear that irrespective of the particular U87 cell line, i.e. either WT, CTRL or Cav-1 knockdown, that the monolayer adherent cell populations were always the most clonogenic with a significant difference observed between the other sub-population types. This was not a reflection of the cell viability at the point of seeding as all cells whether from the adherent monolayer or from the mixed or floating sphere populations displayed cell viability > 95% based on trypan blue exclusion microscopy conducted in parallel with cell counting. The differences in clonogenic capacity between the different sub-populations indicate that the composition of the cells used to seed any self-renewal assay will be an important consideration, at least for the U87 cell line which displays sphere formation even in standard 2D-culture – an observation not previously made in the literature. The U87 cells in the spheres while viable may be in a more differentiated state with less plasticity to adopt a phenotype able to survive the clonogenic assay.

It was also noted that within any given sub-population (e.g. adherent monolayer, mixed or suspension cells) that the Cav-1 knockdown cells showed the trend for the lowest self-renewal capacity, i.e. Cav-1 may be a mediator of neurosphere self-renewal.

Nevertheless, the above experiments suggested that any self-renewal assay involving U87 cells should be conducted only with cells from the adherent monolayer sub-population, i.e. strict consideration given to the point of harvest in the feeder cell cultures, i.e. the 2D standard cultures used as the source of cells.

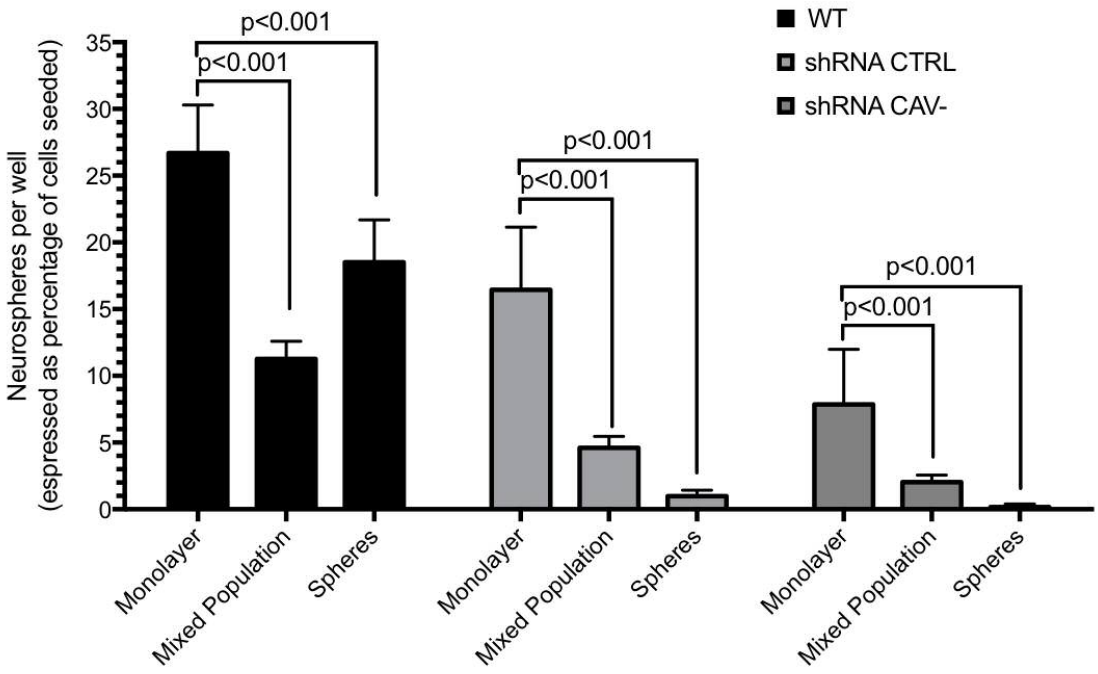

Figure 3.14 Soft agar neurosphere assay on the three subpopulations. U87 wild-type (U87 WT) cells, U87 shRNA CTRL cells and U87 shRNA Cav- cells. 1000 cells seeded between two layers of soft agar within a 24-well plate format. Data represent mean±SD with n=8 replicates from a single experiment. Statistical analysis is represented by one-way ANOVA with Tukey's test between each sample and the respective monolayer counterpart * p≤0.05, § p≤0.01, ¶ p≤0.001].

3.4.1.3 'U87 CELL PANEL' SELF-RENEWAL AND CLONOGENICITY: SOFT AGAR ASSAY AND COLONY FORMATION

As mentioned in the Introduction, Cav-1 knockdown in U87 cells has previously been associated with an increase clonogenicity using an *in vitro* 2D colony forming assay (Cosset et al., 2012; Martin et al., 2009), i.e. expression of Cav-1 serving as a tumour suppressor. Adopting 'soft-agar' clonogenic assay (Figure 3.5) we explored the capacity for neurosphere formation in U87 cells where the seeding cells were all obtained from the adherent monolayer cell populations. Figure 3.15 shows the outcome of this assay across four independent experiments. A consistent finding was that Cav-1 knockdown in the soft-agar assay decreased clonogenic potential, i.e. expression of Cav-1 mediates neurosphere self-renewal in the soft-agar assay with approximately half the capacity for self-renewal lost when Cav-1 is knocked down (shRNA CTRL vs. shRNA Cav-1; Figure 3.15A-B). Another finding from this study and one consistent to the qualitative findings of the free-floating assay (Figure 3.10B) is that the neurospheres formed in the Cav-1 knockdown cells were always greatly

reduced in size (Figure 3.15D) compared to the U87 cells expressing Cav-1, i.e. Cav-1 expression is important for the growth of a neurosphere in soft-agar self-renewal assay. Further, in the Cav-1+ve cells (notably shRNA CTRL) an increased migration of cells away from the formed neurosphere, i.e. Cav-1 may appear to promote cell migration.

The results of clonogenicity assay based in soft agar are in contrast with the clonogenic data reported by Martin et al. (Martin et al., 2009) who used an *in vitro* 2D colony-forming assay, where they reported Cav-1 in U87 cells to serve as a suppressor of clonogenic capacity.

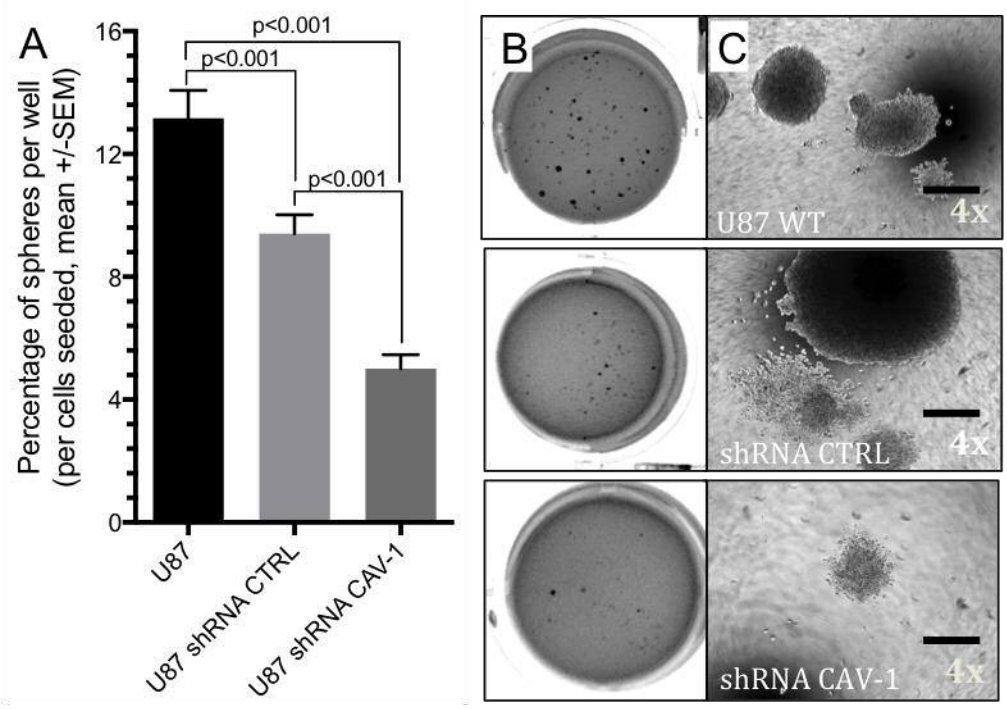

Figure 3.15 Soft agar assay neurosphere assay on U87. A. Cumulative graph of four separate experiments (means±SEM). B. Non-magnified images of the U87 grown in a 24-well format and stained with crystal violet which highlights the size of the cellular neurospheres C 4x magnification of the neurospheres. One-way ANOVA statistical analysis with Tukey's multiple comparison test has been performed.

In Figure 3.16 the results of an *in vitro* 2D colony-forming assay, similar to that undertaken by Martin et al. (Martin et al., 2009), are shown. The results of this type of assay are more difficult to interpret as demonstrated in the images in Figure 3.16C; it should be noted that the work of Martin et al. (Martin et al., 2009) did not publish images of their colony-forming assay.

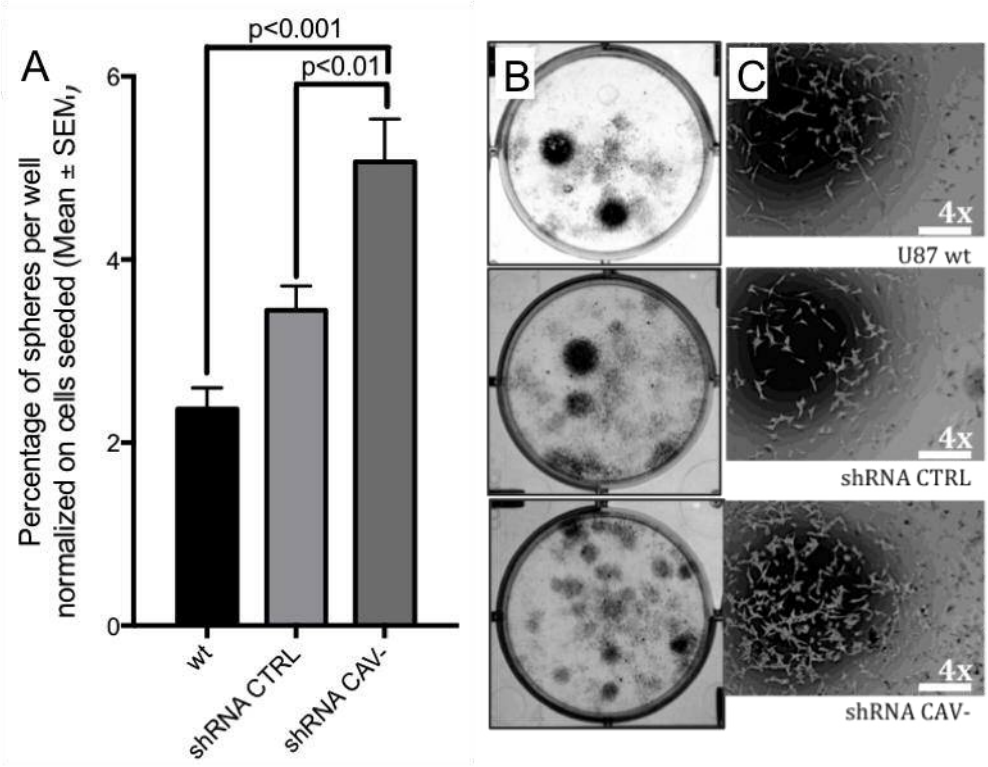

Figure 3.16 Colony-forming assay on the U87. A. Cumulative graph of the three separate experiments (means±SEM). B. Non-magnified images of the U87 grown in a 24-well format and stained with crystal violet, which highlights the size and number of colonies formed. C. Representative 4x magnification images of the colonies. One-way ANOVA statistical analysis with Tukey's multiple comparison test has been performed.

Specifically, we found the U87 cells displayed a tendency to spread across the plastic surface merging in instances with cells from an adjacent colony (Figure 3.16C). Nevertheless, the quantitation of colony formation in this study was undertaken based upon observing a regular concentric pattern of cell growth surrounded by what appeared to be a belt of clear plastic bearing no attachment of cells. We found that in contrast to our soft agar assay (Figure 3.15), but in agreement with the report of Martin et al. (Martin et al., 2009), that Cav-1 appears to serve as a suppressor of clonogenicity in the 2D colony-forming assay. Consistent with our free-floating and soft agar data we noted that the colonies formed in the Cav-1 knockout cells were always more defined and reduced in size (Figure 3.16C, D) compared to the U87 cells expressing Cav-1, i.e. in the context of the 2D assay Cav-1 expression is important for the growth of a colony or the migration of cells away from the colony.

Clearly, each of the three clonogenic assays is able to challenge different aspects of cellular biology.

The colony-forming assay is a very simple and cheap assay that tests the ability of an isolated cell to survive, and for such a cell to undergo division under normal cell culture conditions including the presence of a plastic support for cell adherence and generally with media comprising rich in mitogenic stimuli, i.e. containing FBS. It is the assay that least resembles physiological tumour growth.

The free-floating assay is also relatively easy to undertake. The isolated cells need to survive and proliferate in the absence of a plastic substratum for cell adherence (use is made of ultra-low attachment tissue culture plates), and in media that generally lacks FBS but contains specific growth factors in “Stem Media”(Dontu, Al-Hajj, Abdallah, Clarke, & Wicha, 2003), which is a basic medium deprived of FBS but containing EGF, bFGF and B27(Gu, Y., Fu, J., Lo, P-K., Wang, S., Wang, Q., Chen, 2011) as growth stimuli. The isolated cells need to adapt to the poor growing conditions and then proliferate within progressively expanding spheres, which float freely in suspension. Here the survival and expansion of the floating colony will depend upon anchorage-independent survival and cell-cell interactions.

The soft agar assay is complex and time-consuming, but it also is the one that more closely resembles physiological tumour growth. The isolated cells are placed between two layers of agarose gel prepared in ‘stem medium’. The cells need to survive in stem conditions and also to overcome the physical barrier imposed by the gel matrix surrounding if the colony is to expand in size. Here cell-cell interactions and the ability to migrate or invade through the matrix will be important. The principal characteristics of each of the three assays are highlighted in Table 3.6.

Table 3.6 Three clonogenic assays and their characteristics

	COLONY FORMING ASSAY	FREE-FLOATING ASSAY	SOFT AGAR ASSAY
Conditions	Culture medium	Stem medium	Stem medium
Type of growth	Adherence	Suspension	Semi-solid matrix (3D)
Testing	Ability to undergo "unlimited" divisions in normal culture conditions	Ability to undergo "unlimited" divisions in a deprived medium and without the assistance of an anchorage surface.	Ability to undergo "unlimited" divisions in a deprived medium, without the assistance of an anchorage surface and inside a 3D system that subject cells to external pressure.
Advantages	Easy Chip	Quite easy Quick: only 7 days Deprived medium and non-adherent conditions make it more similar to physiology.	More similar to physiology thanks to the medium and to the presence of the 3D environment. Cells are stuck inside the matrix, so they cannot aggregate. Useful to study also invasion ability.
Disadvantages	In vitro culture conditions (less physiological) Low seeding density can decrease the colony-forming ability.	Since cells are free to move inside the well, aggregation may occur, thus altering the result (high intra and inter-experimental variability).	Not all cell lines grow in this kind of assay.

The divergent outcome between the 2D colony forming assay (Figure 3.16) and the 3D soft agar assay (Figure 3.15) leads to the question of the differing biology that these two assays depend upon to assess self-renewal capacity.

The 2D colony-forming assay essentially addresses the ability of the cells to initially (however transiently) survive in the absence appropriate cell-cell interactions but where extracellular matrix (ECM) interactions are more readily established and in a medium promoting cell proliferation. Using a 2D colony forming assay Martin et al (Cosset et al., 2012; Martin et al., 2009) reported the increased clonogenicity of U87 cells when cellular Cav-1 levels were knocked

down. This reflected an increased U87 cell attachment to fibronectin ECM via α5β1 integrin, the expression of which was upregulated in the U87 cells as the Cav-1 protein was downregulated. Both the expression of β1 integrin, important in adhesion and mesenchymal-type cellular movement (Friedl, 2004), and the reported formation of co-operative plasma membrane complexes (Preissner, Kanse, & May, 2000) comprising Cav-1, the GPI-anchored urokinase receptor (uPAR) and β1 integrins, are consistent with the Cav-1 positive cells displaying greater adhesion and colony formation in the 2D assay and with the observation that the respectively formed colonies showed a more widespread migration of cells.

The 3D soft-agar assay while also testing the above is also examining the ability of the cells to overcome the process of anoikis (or cell-detachment-induced apoptosis) and it does so in a 'nutrient-poor' environment, i.e. one deficient in serum but supplemented with 'stem media'. Only cells possessing high plasticity will be able to survive and proliferate to form neurospheres. The soft agar assay requires the cells to survive the external pressure represented by the matrix and be able to break down the surrounding matrix in order that the neurosphere can expand through by proliferation (Friedl, 2004).

The process of anoikis eliminates cells that are not receiving the correct signals from the ECM (Grossmann, 2002). If the cells are able to adapt to their 'new environment' then anchorage-independent growth (AIG) is possible and is indeed one of the hallmarks of cancer. Resistance to anoikis and the ability of tumour cells to display AIG allows them to expand and potentially invade adjacent tissues. The ability to avoid anoikis is a critical transformation that a tumour cell undergoes during malignancy (Guadamillas, Cerezo, & Del Pozo, 2011; Paoli, Giannoni, & Chiarugi, 2013). Overcoming anoikis and exhibiting AIG ultimately requires a bypass of integrin-mediated signals, which in the absence of ECM would trigger cell death. This bypass may be through a variety of mechanisms including the cell adaptation such as undergoing EMT or an alteration in expression of the cell's integrin repertoire of proteins. There may also be compensatory mechanisms such as activation of pro-survival pathways such as PI3K, Ras-ERK etc. The role of Cav-1 in AIG has not been shown to be

consistent with studies in the lung cancer, reviewed in (Chunhacha & Chanvorachote, 2012). These studies reported that Cav-1 levels positively correlate with increased AIG, while in breast cancer (Fiucci et al., 2002) and indeed in transformed fibroblasts (Cerezo et al., 2009) decreased levels of Cav-1 favour AIG. Mechanistic studies are clearly needed, and future experimentation of self-renewal would use both assays as they clearly can reflect different biology.

3.4.2 'PANEL OF GLIOMA CELL LINES' – PROLIFERATIVE CAPACITY AND CAV-1 STATUS

As mentioned in the Introduction, one of the early milestones in the project is to evaluate in a panel of glioma cell lines (six cell lines) the impact of a Cav-1 knockdown (or Cav-1 knockdown) upon classical cancer stem cell functions, specifically with a focus upon self-renewal (clonogenicity). This milestone is underpinned by the selection of a glioma cell panel and the establishment of the requisite assays. The U87 studies described above in this report contributed to method development for self-renewal (clonogenicity) outcomes. Next step was to apply these methods to a selected panel of glioma cell lines.

Next, the Cav-1 status and proliferative capacity of the cell lines in the panel was assessed before the establishment of stable Cav-1 knockdowns.

Figure 3.17A shows the expression of Cav-1 with all cell lines displaying a relatively high expression of Cav-1 with the exception of IN699 that displayed negligible expression and also happened to have the highest rate of proliferation. The Western blot confirmed that seven of these cells are suitable for shRNA Cav-1 knockdown whereas a knock-in strategy might have been more appropriate for the IN699 cells. The cell doubling times for the panel of the six selected glioma cell lines are shown in the Figure 3.17B, where the doubling times were determined by monitoring cell proliferation rates using both the microscopy cell counting procedure and by the fluorescence-based assay; the latter is shown in Figure 3.17C. Importantly the microscopy approach allows

confirmation that from the six cell lines panel only the U87 cells formed the previously described spheres in 2D standard culture conditions.

The high proliferative rate of the IN699 is reflected also in the cell cycle analysis (Figure 3.18) where the G2/M phase of the IN699 is too small to allow a cell cycle profile to be adequately fit the data.

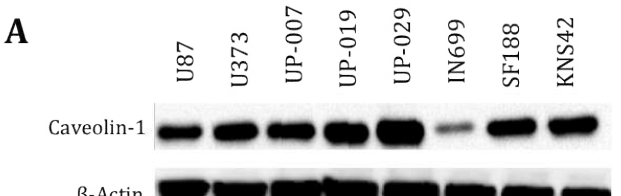

B

	Cell lines	Type	Doubling Times (hrs)
1	U87	Adult GBM	30
2	U373	Adult GBM	36
3	UP007	Adult GBM	60
* 4	UP019	Adult GBM	30
5	UP029	Adult GBM	43
* 6	IN699	Paediatric supratentorial GBM	25
7	SF188	Frontal paediatric GBM	28
8	KNS42	Frontoparietal anaplastic astrocytoma	61

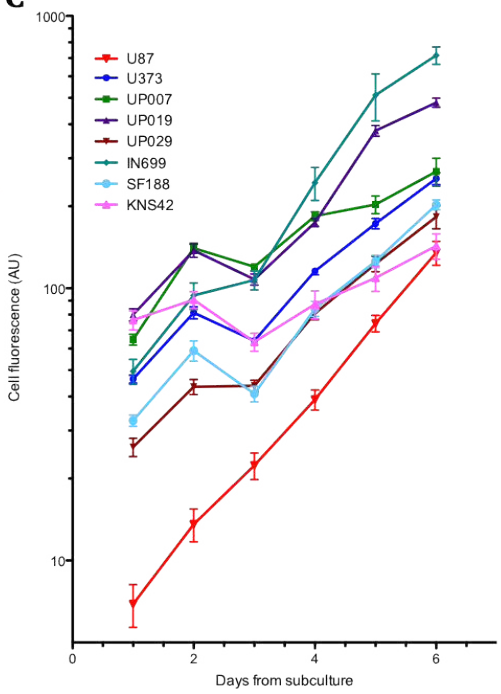

Figure 3.17 Panel of glioma cell lines'. A Protein expression of Cav-1 in the six glioma cell lines. β-Actin has been used as the housekeeping gene. B Characteristics of the six cell lines including doubling time derived from proliferation assays, an example of which is shown in C. Asterisks indicate cell lines that were subsequently excluded from the experimental plan for cross-contamination of the original stocks.

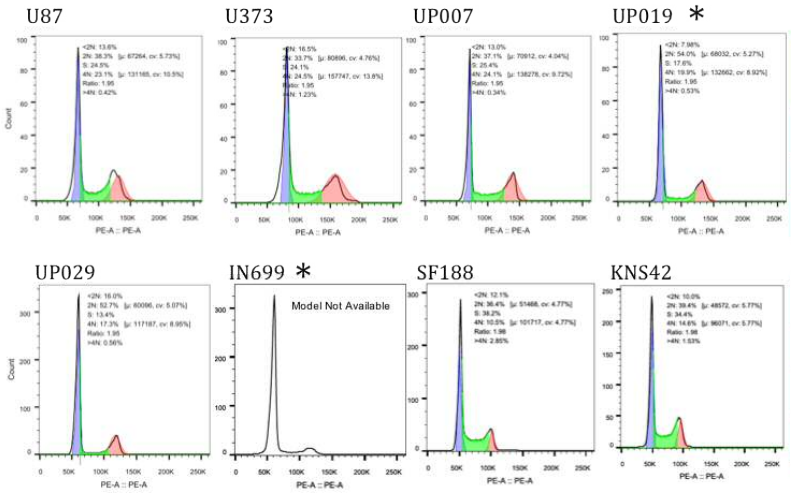

	G0/G1	S	G2/M
U87	38.3	24.5	23.1
U373	33.7	24.1	24.5
UP007	37.1	25.4	24.1
UP019	54	17.6	19.9
UP029	52.7	13.4	17.3
IN699	NA	NA	NA
SF188	36.4	38.2	10.5
KNS42	39.4	34.4	14.6

Figure 3.18 Panel of glioma cell lines', cell cycle analysis. Cells have been harvested, fixed and stained with Propidium Iodide. The DNA staining profiles have been obtained by flow cytometry and then analysed by FlowJo v10, using the Watson model (except for the IN699 whose G2/M peak was too low for the model). Asterisks indicate cell lines that were subsequently excluded from the experimental plan for cross-contamination of the original stocks.

3.4.2.1 'PANEL OF GLIOMA CELL LINES' – SELF-RENEWAL AND CLONOGENICITY: SOFT AGAR ASSAY AND COLONY FORMATION

Shown in Figure 3.19 are the results of soft agar self-renewal and clonogenicity assay. The capacity to form neurospheres varied from SF188 (highest capacity ca. 16% of cells seeded were able to give rise to neurospheres) to UP029 (lowest capacity < 1% of cells seeded giving rise to neurospheres). The UP029 cell line may simply be usable in this experiment without seeding a higher number of cells, which is not a desirable approach for such an assay.

The results of the 2D colony-forming assay are shown in Figure 3.20. The IN699 and the SF188 still retain the highest clonogenic potential (in agreement with the soft agar assay) while the UP007 and U87 cells now display the lowest clonogenic potential.

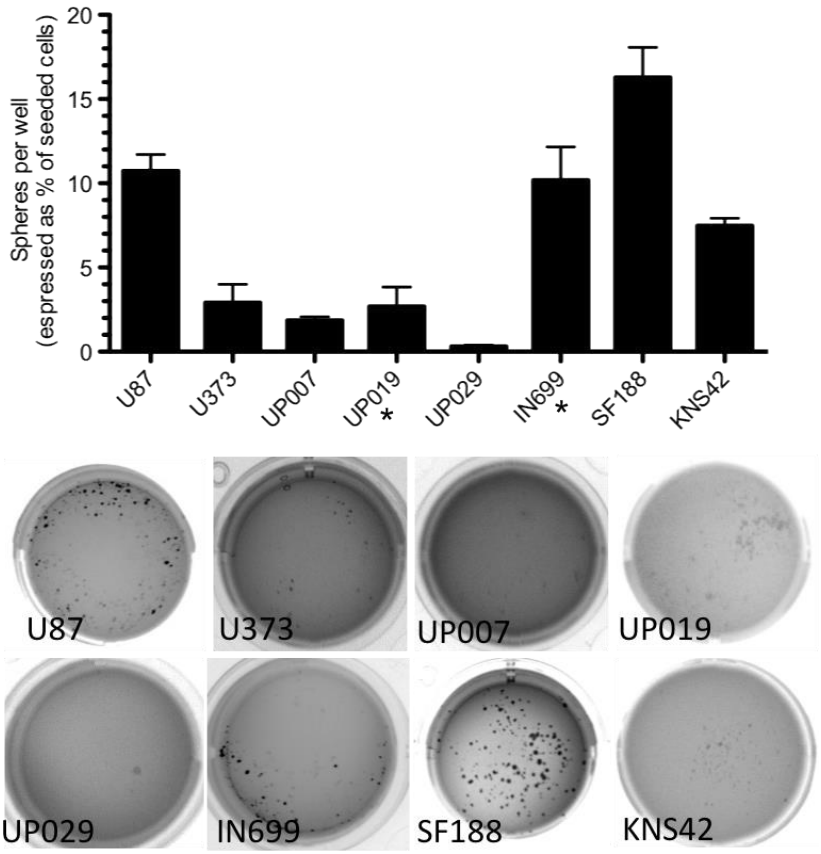

Figure 3.19 Panel of glioma cell lines'. 3D Soft agar neurosphere clonogenicity assay. The plot graph neurosphere growth per well expressed as a % of cells seeded (1000 cells seeded per well) for the six cell lines in the expanded glioma panel. The data represent means±SEM of at least three experiments with n=8 replicates in each experiment. Surrounding the plot is the non-magnified images of the glioma panel neurospheres grown in a 24-well format and stained with crystal violet which highlights the size of the cellular neurospheres. Asterisks indicate cell lines that were subsequently excluded from the experimental plan for cross-contamination of the original stocks.

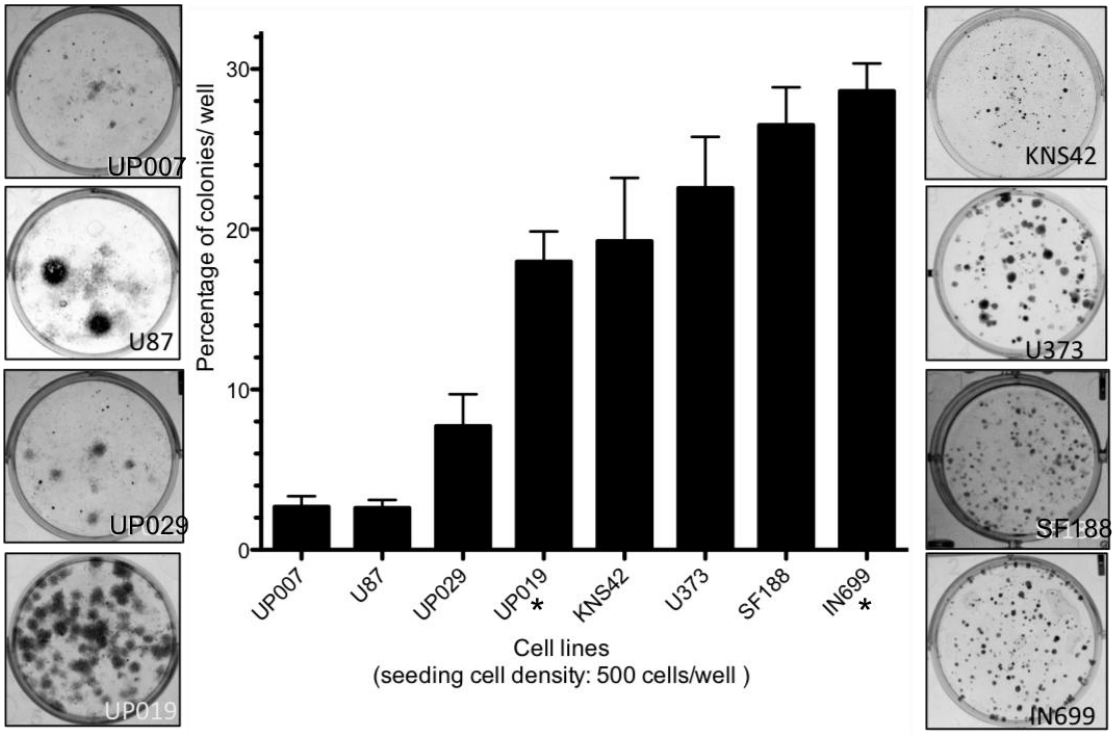

Figure 3.20 Panel of glioma cell lines'. 2D Colony-forming assay Plot shows outcome for three separate experiments for colony formation per well expressed as a % of cells seeded (500 cells per well seeded). The data represent means± SEM of at least three experiments with n=6 replicates in each experiment. Surrounding the plot is the non-magnified images around the graph the non-magnified images of the glioma panel colonies formed in 6-well format and stained with crystal violet, which highlights the size of the cellular colonies. Asterisks indicate cell lines that were subsequently excluded from the experimental plan for cross-contamination of the original stocks.

3.4.3 LENTIVIRAL TRANSFECTION

To test the effect of Cav-1 on the cell line panel, a lentiviral-based shRNA approach was adopted. The system is more stable and doesn't require the addition of puromycin to the culture medium, except for the initial selection stage.

To avoid misinterpreting a transfection-related phenotype with a knockdown-related one, another transfection was taken in parallel with a vector containing shRNA unable to target any mammalian gene.

Cell lines were tested first for their sensitivity to Puromycin (50ng/ml-100µg/ml) in order to determine the concentration to be used for the subsequent selection (Figure 3.21 and Table 3.3).

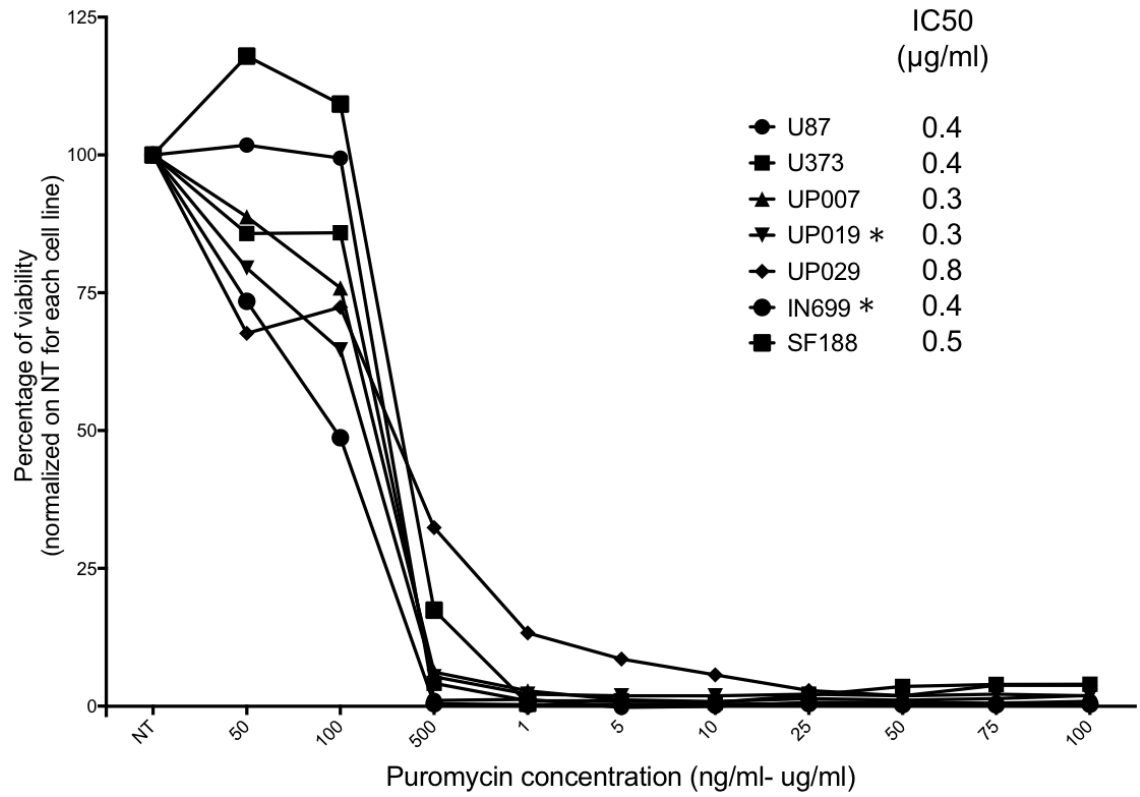

Figure 3.21 Viability curve for all the cell lines under examination (see legend) at different doses of Puromycin (50nM-100µM) after 120 hours post-treatment in order to establish the IC50 and then the puromycin concentration ideal for the selection of every cell line transfected. Asterisks indicate cell lines that were subsequently excluded from the experimental plan for cross-contamination of the original stocks.

The first cell line to be transfected was SF188, one of the paediatric cell lines. Among the five sequences tested, sequence number 5 was not producing cells able to survive, while sequence number 3 was not producing Cav-1 knockdown so they were not used for the transfection of the other cell lines (Figure 3.22). Three sequences, 1, 2 and 4 produced a substantial knockdown on SF188, so they were used for the lentiviral transfection of other cell lines (Figure 3.23). Unfortunately, a western blot for the SF188 cell line was repeated and this time the expression of Cav-1 for sequence number 1 was restored (if not increased in comparison with the positive control).

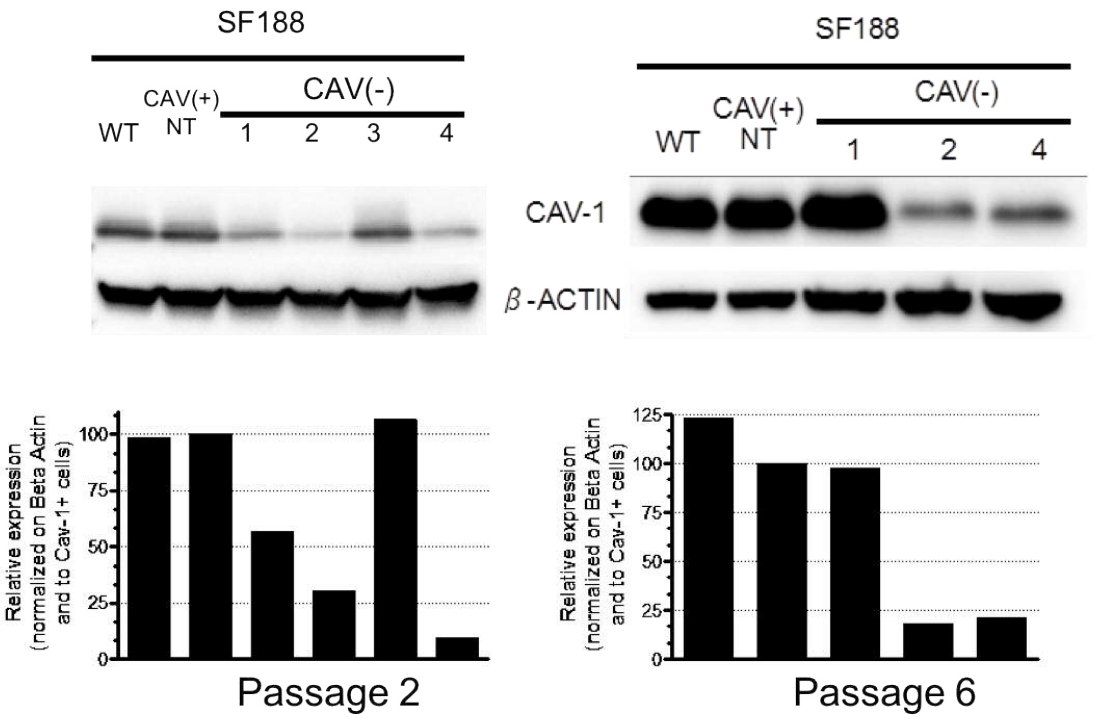

Figure 3.22 SF188 Lentiviral-mediated Cav-1 KD, following the transfection and after 4 passages in culture. Densitometry analysis of bands corresponding to Cav-1 molecular weight, 22 kDa, was performed and compared to the corresponding band density of the housekeeping gene β-Actin (46 kDa). The resulting folds were normalized on the shRNA CTRL, in order to evaluate the knockdown efficiency.

That is why only sequence 2 and 4 were used for the transfection of UP007 and UP029. Sequence 4, however, showed a residual expression of Cav-1, that kept the interpretation of further experiments doubting, and it was excluded too. This left only one sequence-derived knockdown to be analysed. Furthermore, due to the re-expression of Cav-1 by the sequence 1-mediated knockdown, it was decided to keep the puromycin-selecting presence in the culture medium. This allowed more reliability in the knockdown maintenance during further experiments but cast also the same doubts about the reliability of the phenotype as the previous genetic modification approach.

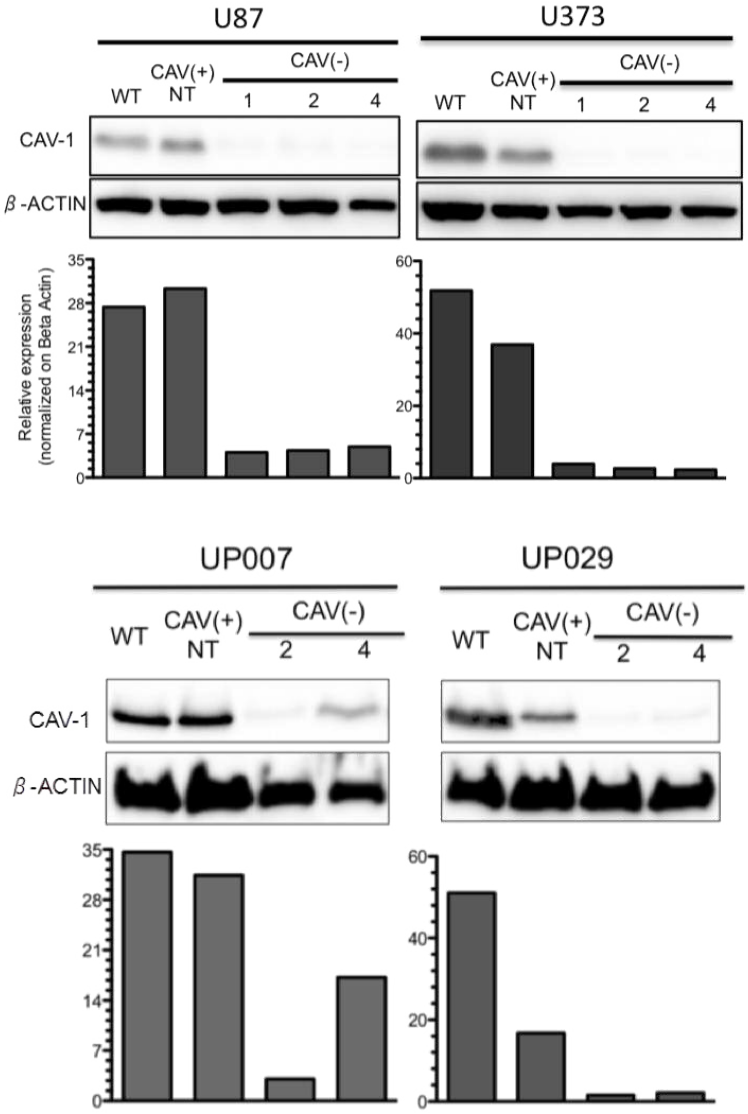

Figure 3.23 Quantification of Cav-1 expression after lentiviral transfection. U87, U373, UP007 and UP029 were transfected for the lentiviral-mediated knockdown of Cav-1. On the top the Western Blot bands with Cav-1 expression in wild-type cells, in the positive control (CAV+-NT) and in three of the 5 sequences. Densitometry analysis of bands corresponding to Cav-1 molecular weight, 22 kDa, was performed and compared to the corresponding band density of the housekeeping gene β-Actin (46 kDa). The resulting folds were normalized on the shRNA CTRL, in order to evaluate the knockdown efficiency.

After the assessment of the knockdown achievement, cells were tested for phenotypical changes, first of all, proliferation. As shown in Figure 3.24, when Cav-1 is knocked-down, U87, UP007 and UP029 reach the same Level of fluorescence as their control, while the U373 reach the plateau at a lower Level. On the other hand, while the U87 and the U373 do not display a significant difference in both proliferation rate and doubling time, UP007 and UP029

knockdowns are able to proliferate faster than their controls, suggesting that Cav-1 may be involved in limiting the proliferation mechanisms.

A

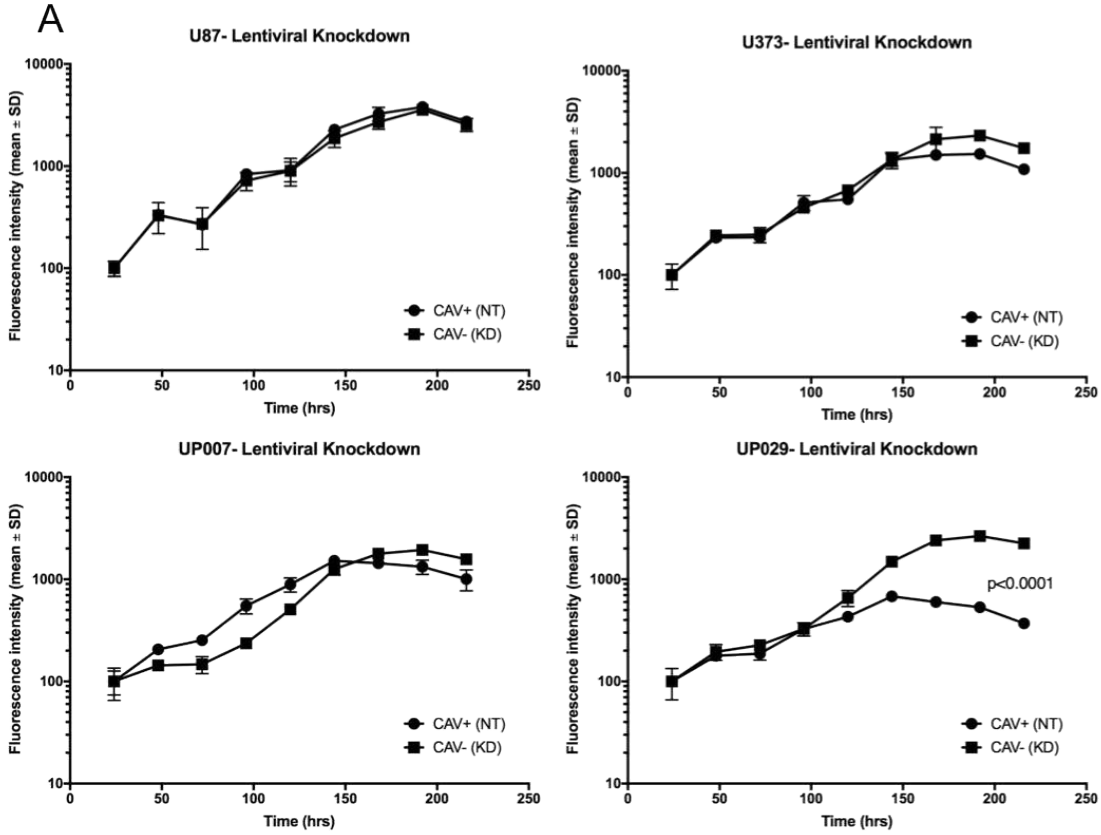

B

DOUBLING TIME (hrs)		
	CAV+ (NT)	CAV- (KD)
U87	30.66	32.57
U373	34.17	33.49
UP007	31.11	21.48
UP029	45.07	29.39

Figure 3.24 Effect of Cav-1 Knockdown on proliferation. A. proliferation plots for U87 (red), U373 (blue), UP007 (green), and UP029 (brown), after transfection for Cav-1 knockdown. The black lines refer always to the control (CAV+) samples. B Doubling time derived from the proliferation plots analysed on viability values corresponding to the log phase. Statistical analysis was performed with T-TEST and p value was reported when significant.

As for the cell cycle analysis (Figure 3.25), the transfected UP007 displayed no significant change in the portions of cells belonging to each cell cycle subpopulation (G0/G1, S and G2/M phases) in comparison with the wild-type reference, except for an increase of cells in S phase. The U87 and UP029, on the contrary, displayed a peculiar change. The control cells, like the UP007, were composed by an increase in the cells in S phase. The CAV-1 knockdown displayed three peaks, each one localized at the double of the previous one on the PI axis, indicating the double of the DNA. This may be due to the presence of different clonal subpopulations, some with a diploid and a quadruploid asset.

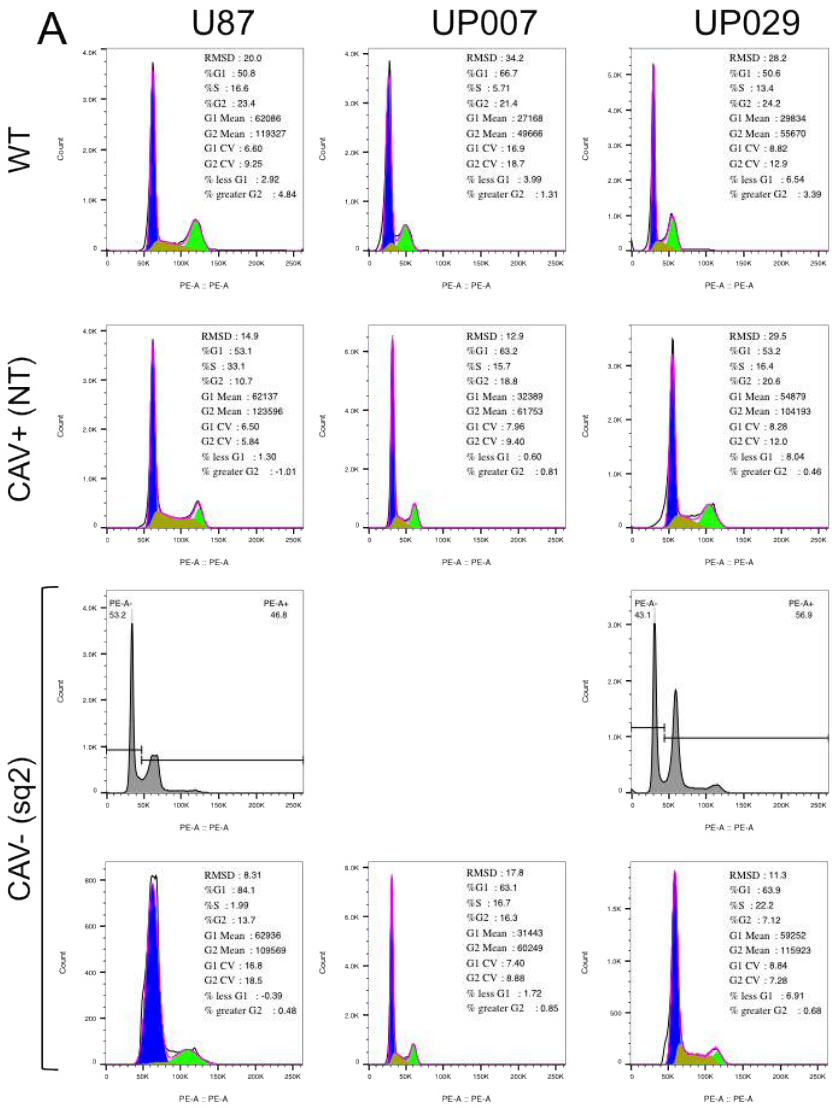

B Cell cycle **analysis**

Cell lines	G0/G1	S	G2/M
U87 WT	50.8	16.6	23.4
U87 CAV+ (NT)	53.1	33.1	10.7
U87 CAV- (KD)	54.1	1.99	13.7
UP007 WT	66.7	5.71	21.4
UP007 CAV+ (NT)	63.2	15.7	18.8
UP007 CAV- (KD)	63.1	16.7	16.3
UP029 WT	50.6	13.4	24.2
UP029 CAV+ (NT)	53.2	16.4	20.6
UP029 CAV- (KD)	63.9	22.2	7.12

Figure 3.25 Effect of Cav-1 knockdown on cell cycle. A. Plots of U87, UP007 and UP029 WT, CAV+(NT) and CAV-(KD) with highlighted cell cycle subpopulations. B. Table reporting, for each cell line, the percentages of cells belonging to each cell cycle subpopulation.

In terms of clonogenicity, cells have been tested for colony formation (U87 in Figure 3.26, U373 in Figure 3.27 and UP007 and UP029 in Figure 3.28A) and for soft agar clonogenic assay (U87 in Figure 3.26, U373 in Figure 3.27 and UP007 and UP029 in Figure 3.28B). For all the cell lines the loss of Cav-1 (sq.2) resulted in a decrease of the ability of the cells to form colonies.

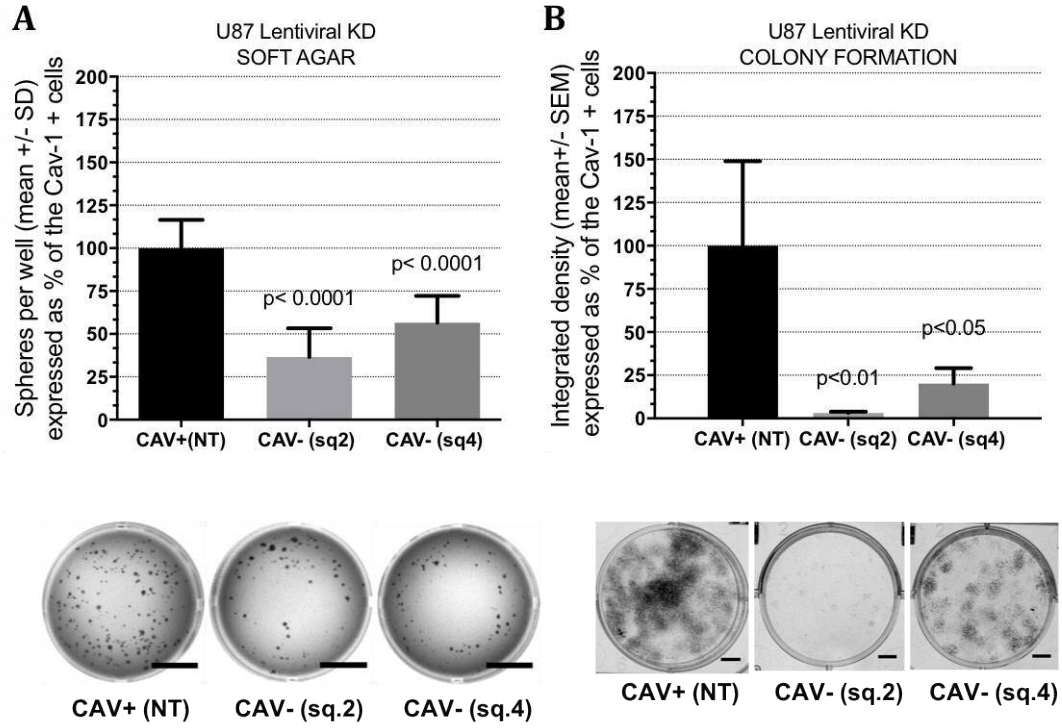

Figure 3.26 Effect of U87 Cav-1 knockdown on clonogenicity. Plots show the outcome of Soft agar assay (A) and colony formation assay (B). Data were expressed as a percentage of Cav+ cells (NT) and represent mean ±SD of at least three experiments with n=8 replicates for soft agar and n=6 replicates for colony formation in each experiment. Representative pictures for each sample on the bottom.

CAV-(sq.4) on the other hand, determined a decreased spheres formation only for the U87 cell lines. As mentioned before, the sq.4 did not produce a complete knockdown. One hypothesis is that this could be the reason why the clonogenic phenotype is not absolute for all the cell lines.

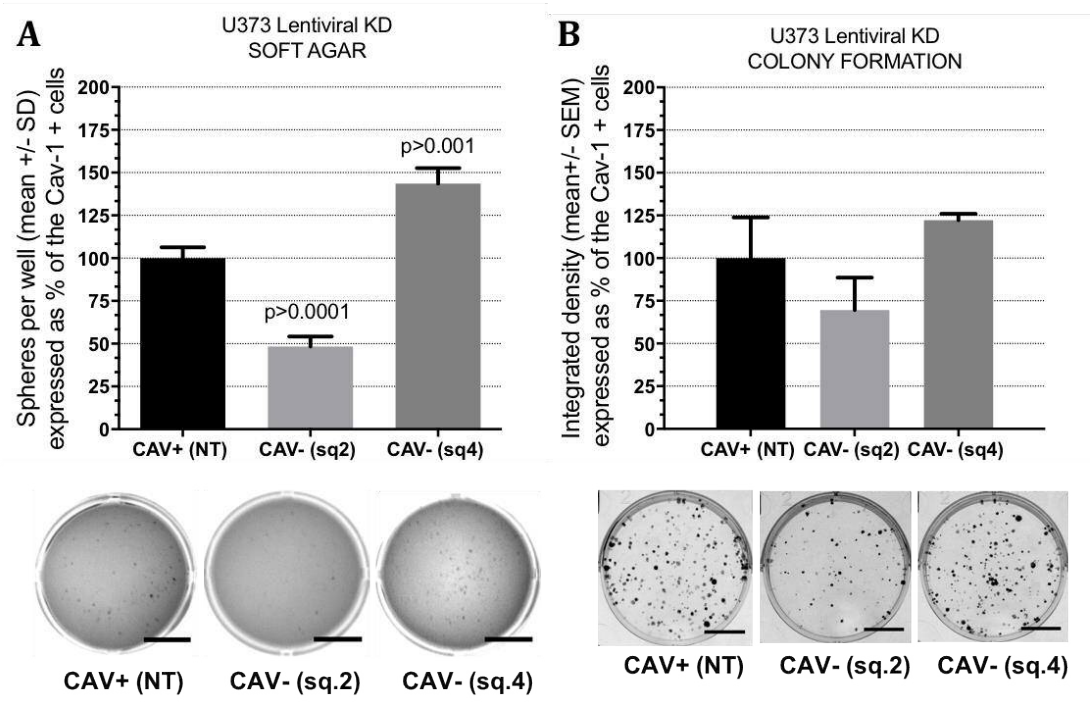

Figure 3.27 Effect of U373 Cav-1 knockdown on clonogenicity. Plots show the outcome of Soft agar assay (A) and colony formation assay (B). Data were expressed as a percentage of Cav+ cells (NT) and represent mean ±SD of at least three experiments with n=8 replicates for soft agar and n=6 replicates for colony formation in each experiment. Representative pictures for each sample on the bottom.

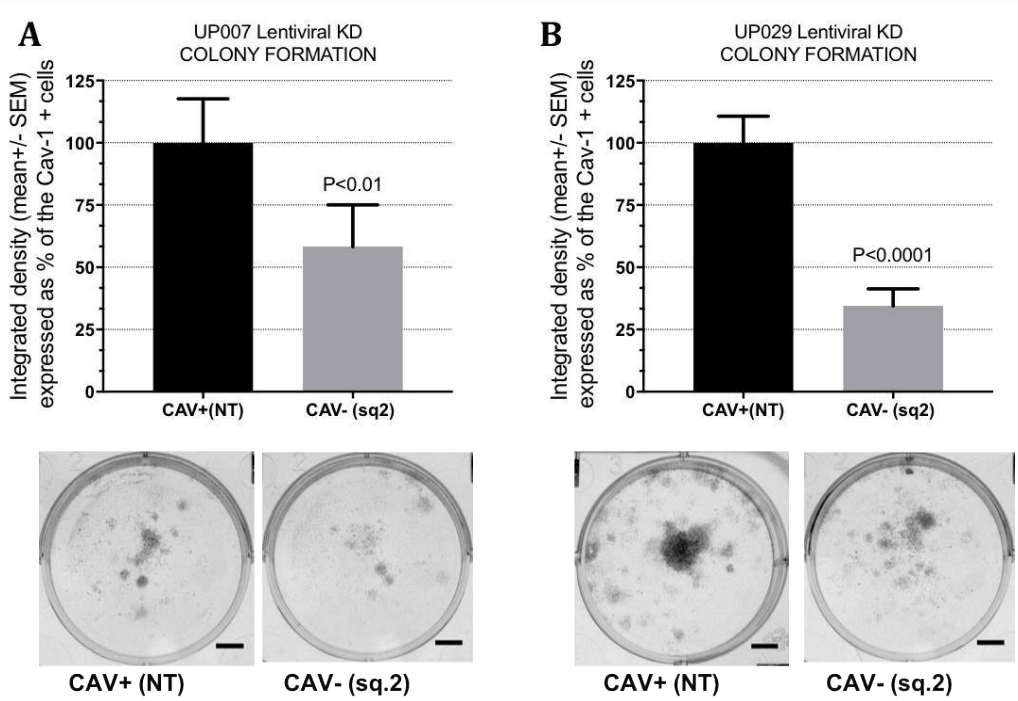

Figure 3.28 Effect of UP007 and UP029 Cav-1 knockdown on clonogenicity. Plots show the outcome of colony formation assay on UP007 (A) and UP029 (B). Data were expressed as a percentage of Cav+ cells (NT) and represent mean ±SD of at least three experiments with n=6 replicates in each experiment. Representative pictures for each sample on the bottom.

The use of puromycin for normal cell culture conditions cast a doubt of the validity of those assays and a confirmation was necessary. This came through the use of CAV-1 knockouts (KO).

3.4.4 CRISPR

3.4.4.1 Plasmid CRISPR-Cas9 System

Cav-1 CRISPR KO for the U87 has been obtained through a plasmid system described in materials and methods (3.3.3.1). After obtaining and testing the CRISPR U87 cell lines, we obtained also the CRISPR UP007 and UP029, with a ready RNP system as described in Materials and Methods (3.3.3.2). Together with the CAV-(KO) a positive control was produced and named CAV+(BB). Cav-1 expression was tested via Western Blot (

Figure 3.29).

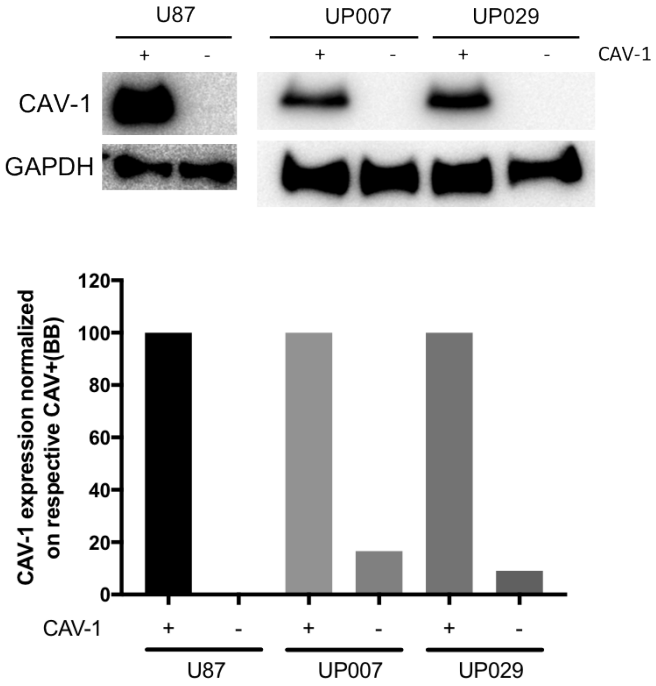

Figure 3.29 CRISPR-mediated Cav-1 Knockout of U87, UP007 and UP029. Densitometry analysis of bands corresponding to Cav-1 molecular weight, 22 kDa, was performed and compared to the corresponding band density of the housekeeping gene GAPDH (37 kDa). The resulting folds were normalized on the CAV+(BB) cells, in order to evaluate the knockout efficiency.

In terms of proliferation (Figure 3.30), U87 and UP029 show no difference between the CAV+(BB) and the CAV-(KO) while the plateau of the UP007 CAV-(KO) was reached at a lower fluorescence Level than the CAV+(BB) counterpart, leading to a longer doubling time.

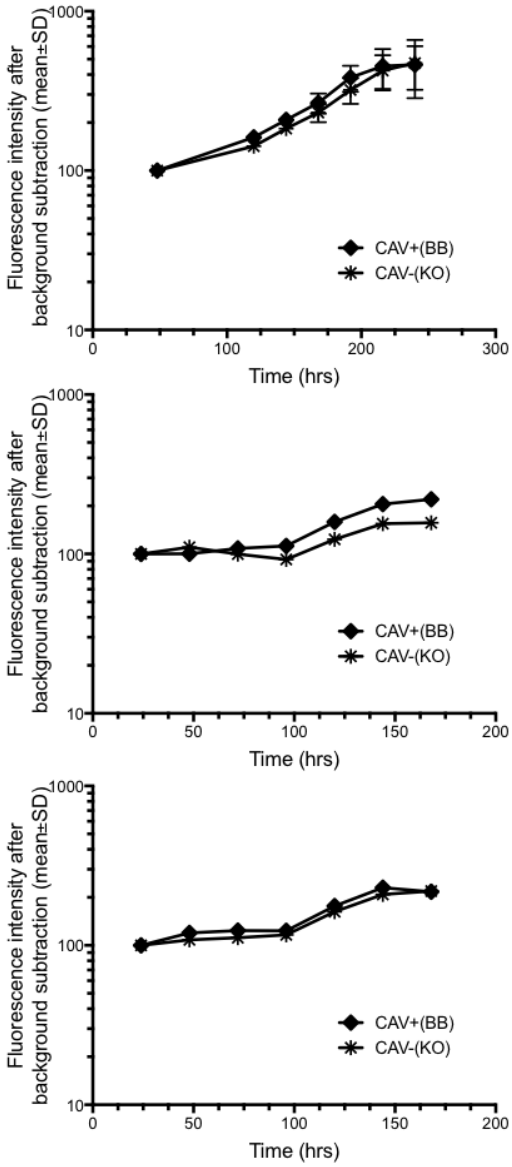

Doubling time (hrs)		
	CAV+ (BB)	CAV- (KO)
U87	47.20	48.30

Doubling time (hrs)		
	CAV+ (BB)	CAV- (KO)
UP007	56.02	65.14

Doubling time (hrs)		
	CAV+ (BB)	CAV- (KO)
UP029	54.25	57.86

Figure 3.30 CRISPR U87 cell line proliferation assay. Cell fluorescence intensity was followed in time and plots were obtained for the calculation of the doubling time during the exponential phase, reported in the tables.

The cell cycle analysis, on the contrary, showed an increased portion of cells in the G0/G1 phase when Cav-1 is knocked out (Figure 3.31). As for the cell cycle,

on the other hand, UP007 do not show any significant difference with the wild-type and positive. Control, while both Cav-1 KO and CRISPR control display a shift in PI intensity and the presence of additional peaks.

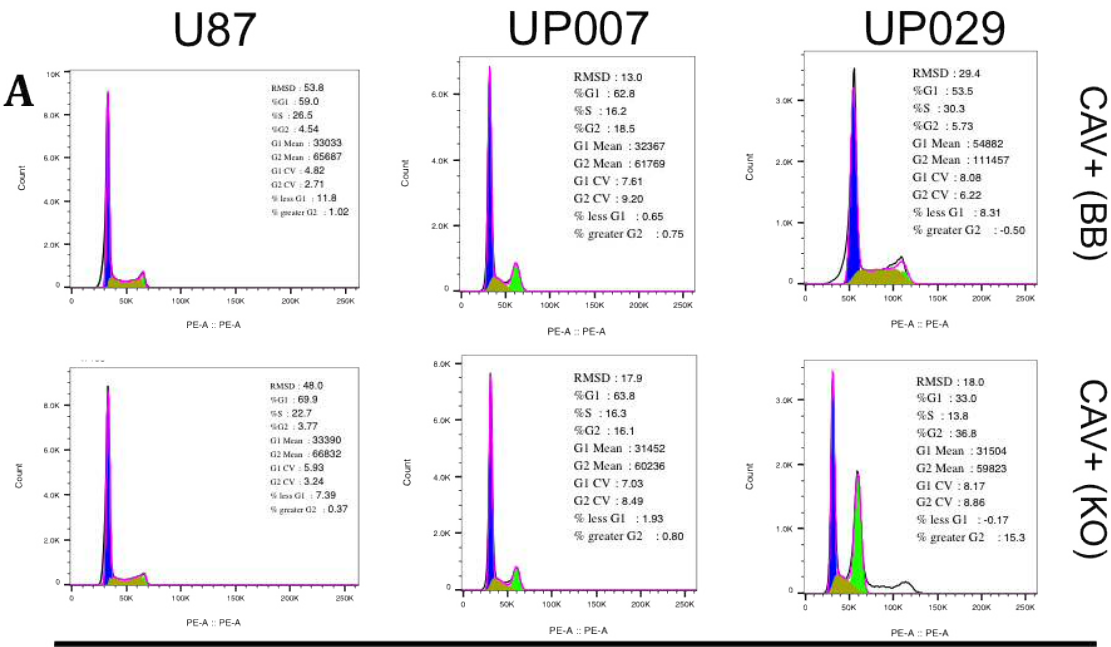

B

Cell Cycle				
		G0/G1	S	G2/M
U87	CAV+ (BB)	59.0	26.5	4.35
	CAV- (KO)	69.9	22.7	3.77
UP007	CAV+ (BB)	62.8	16.2	18.5
	CAV- (KO)	63.8	16.3	16.1
UP029	CAV+ (BB)	53.5	30.3	5.73
	CAV- (KO)	33	13.8	36.8

Figure 3.31 CRISPR cell lines cell cycle assay. A. Plots of U87, UP007 and UP029 CAV+(BB) and CAV-(KO) with highlighted cell cycle subpopulations. B. Table reporting, for each cell line, the percentages of cells belonging to each cell cycle subpopulation.

A colony formation was chosen as a phenotypical assay to test whether the new Cav-1 manipulation was able to confirm the results of the lentiviral-mediated shRNA. For both U87 and UP029, the number of colonies was decreased when Cav-1 was knockdown, while the UP007 CAV-(KO) displayed a significant increase in the number of colonies.

In particular, again for the U87 colonies were reduced visually in number but especially in colony density, indicating that not only fewer cells are able to start a colony, but that also the number of divisions that cells undergo are less.

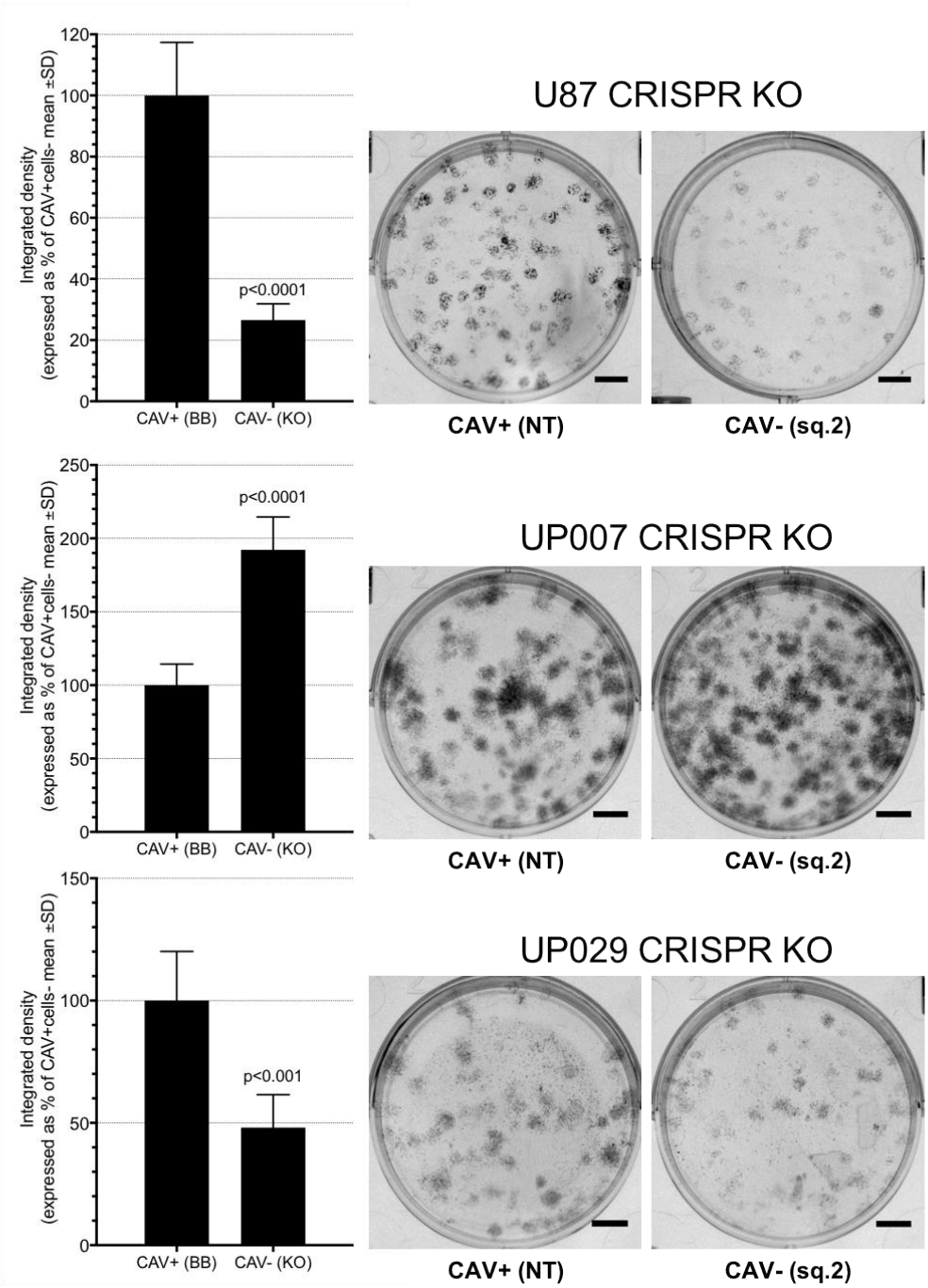

Figure 3.32 CRISPR cell lines colony formation assay. Plots show the outcome of colony formation assay on U87, UP007 and UP029. Data were expressed as a percentage of Cav+ cells (BB) and represent mean ±SD of at least three experiments with n=6 replicates in each experiment (Statistical analysis: T-test). Representative pictures for each sample on the side.

3.4.5 CAV-1 GENE MANIPULATION IMPACT ON MIGRATION

A second assay was performed to test whether Cav-1 was impacting on GBM cell lines phenotype, namely the scratch assay. This assay was chosen after the observation that U87 CAV+ cells in soft agar start to leave the neurospheres and to spread within the matrix (Figure 3.15D). cells tested were the lentiviral-mediated shRNA UP007, UP029 and U373. The U87 could not have been used since, as mentioned before, they do not grow in a carpet until confluency (which is essential for the scratch assay since cells must feel pressure to fill up only the gap left by the scratch) but start forming spheres that tend to float.

Both UP007 and UP029 displayed a significant decrease in migration velocity, while the U373 displayed a poor migration capacity in the CAV+ cells, thus not allowing a comparison with the CAV- counterpart.

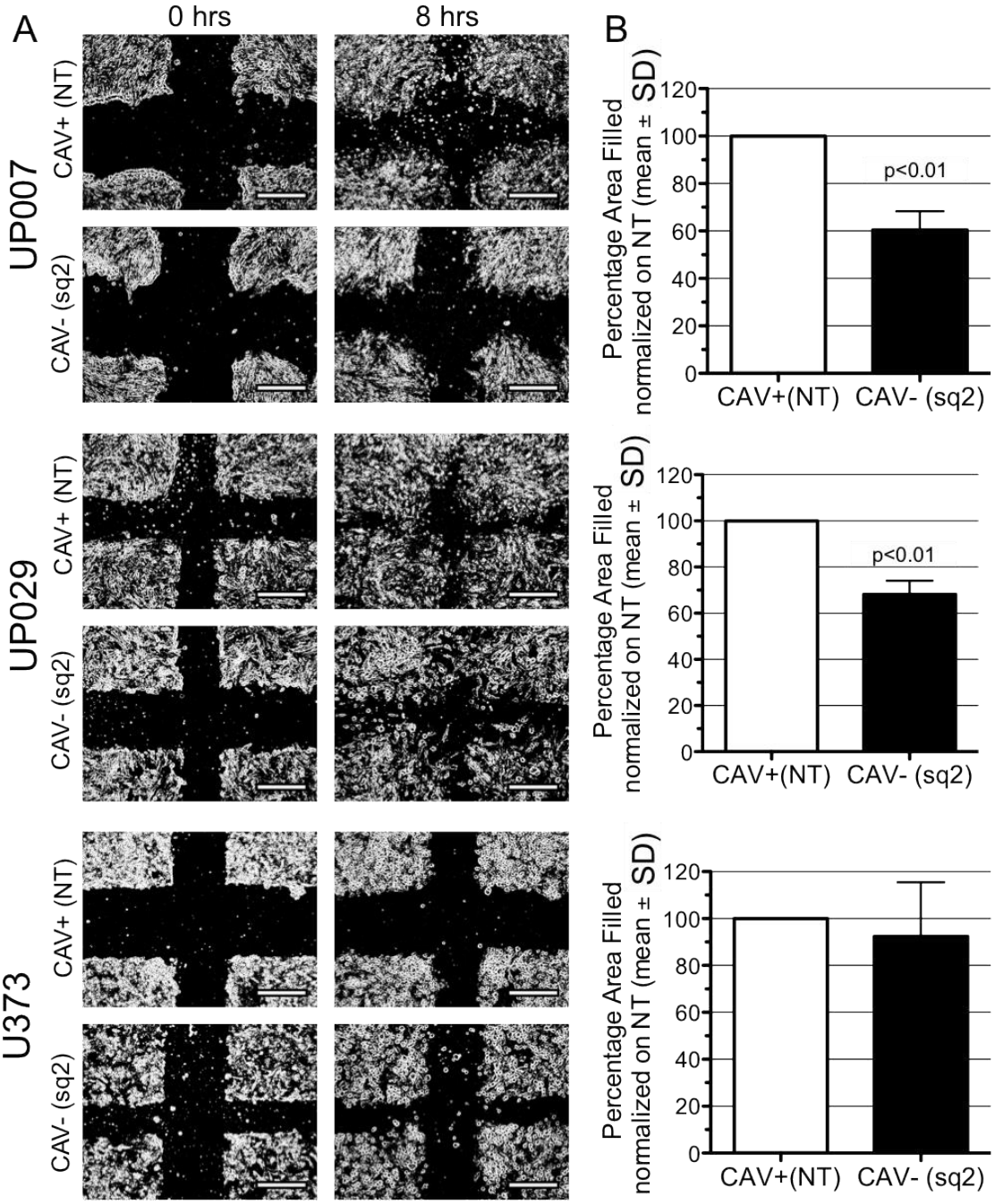

Figure 3.33 Scratch migration assay on UP007, UP029 and U373. A. Representative pictures of samples at 0 and 8 hours after the scratch. The area non-occupied by cells after eight hours from the scratch was quantified and normalized on the corresponding area immediately after the scratch. Plots represent one example experiment (mean ± SD). A T-test was used to compare the samples.

3.5 SUMMARY OF KEY FINDINGS

In this chapter, we focused on the creation of stable cell lines bearing a downregulation of Cav-1. These cell lines would serve for the evaluation of Cav-1's role in terms of a cancer stem cell modulator. Several genetic modifications have been used for the obtaining of the modified cell lines, and the confirmation of the genetic manipulations was evaluated via Western Blot assay. The impact of a Cav-1 knockout (or Cav-1 knockdown) was investigated upon morphological changes, proliferation, cell cycle and classical cancer stem cell functions, such as self-renewal (clonogenicity) and migration.

Distinct approaches for the stable suppression of Cav-1 gene expression were explored (RNAi and CRISPR/Cas9 technologies, as discussed in Chapter 1).

Table 3. 7 reports a summary of all the cell lines used for the perfomed assays.

Table 3. 7 Experimental plan

	shRNA Knockdown		**CRISPR Knockout**
	Liposome	Lentiviral	
Proliferation	U87	U87, U373, UP007, UP029	U87, UP007, UP029
Cell Cycle	U87	U87, U373, UP007, UP029	U87, UP007, UP029
Clonogenicity 2D	U87	U87, U373, UP007, UP029	U87, UP007, UP029
Clonogenicity 3D	U87	U87, U373,	
Migration		U373, UP007, UP029	

3.5.1 Cell lines and experimental plan

In the beginning of this project, the lab had already produced genetic knockdowns of Cav-1 in at least one cell line, through the liposome-mediated transfection of a plasmid codifying for shRNAs directed against the Cav-1 transcript. Initial studies have been performed with this technology, which required the persistent presence of puromycin to drive Cav-1 knockdown.

However, the necessity for antibiotic for the continuous selection of the cells expressing the plasmid can modify the cells phenotype in unpredictable ways (Llobet, Montoya, López-Gallardo, & Ruiz-Pesini, 2015). Our own inconsistent results reported after replicate experiments led to the decision of finding a more stable system for the study of Cav-1 function in GBM cell lines.

A lentiviral system for the transfection and the stable insertion of shRNA codifying sequences in the genome of the target cells was chosen. However, after a period in culture without puromycin, some of the cell lines started expressing Cav-1 again. This forced the reintroduction of the puromycin in culture.

Later the development of Cav-1 knockouts by CRISPR/Cas9 technology allowed the use of an alternative technology that was able to confirm the findings.

With the exclusion of one of the three paediatric cell lines (IN699), a decision of focusing only on the adult GBM-derived cell lines have been made, leaving in the experimental plan the U87, U373, UP007 and UP029.

3.5.2 RNAi knockdown vs. CRISPR knockout

As previously discussed in Chapter 1, RNAi modifications result in a genetic knockdown (reduction of protein expression), while CRISPR technology allows also to obtain genetic knockouts (total protein production suppression) (Unniyampurath et al., 2016). It is possible, as a result of that, to understand that CRISPR technology allows linking a particular phenotype unequivocally to the genetic knockout (Bosher & Labouesse, 2000; Gilbert et al., 2014; Jiang & Marraffini, 2015; Konermann et al., 2014; Qi et al., 2013). The use of the RNP

system reduces drastically the off-target risk and there is no need for selection antibiotics, that could induce further cellular modifications. CRISPR efficiency though is much lower than shRNA since both alleles have to be targeted and require the clonal selection of the modified cells. This means that after the treatment, single cells are isolated and allowed to grow. The few, if any, clones succeeding in starting a colony then have to be tested for the knockout. This results in a time-consuming process that can take up to several months. shRNA, on the contrary, is quite quick, and cells can be started to be stored and tested for the genetic knockdown a couple of weeks from the transfection (both lipid-based and lentiviral transfection). On the other hand, though, the shRNA technology relies on antibiotics for the selections, that can be virtually removed from the medium once the culture is started, but that in reality have to be maintained in order to preserve the genetic selection. In fact, for the SF188 cell line (Figure 3.22) a genetic knockdown that looked successful after two weeks after the transfection (less than 50% reduction in comparison with the control), after a further month was not only not significant anymore, but even reverted. This led to the necessity of having to select the best knockdown (sequence 2 was chosen) and to keep the puromycin selective presence in culture.

3.5.3 Proliferation and cell cycle

Both the Knockdown (KD- lentiviral shRNA) and knockout (KO- CRISPR) systems produced cell lines with a slightly reduced or equivalent proliferation rate to their respective Cav-1 positive controls. At the same time they produced cell lines with a different distribution of cell cycle sub-populations. Specifically, for:

- U87: both knockdown and knockout approaches did not change U87 proliferation profiles or rates, while at the same time increasing the G0/G1 subpopulations (Figure 3.24 and Figure 3.30 for proliferation and Figure 3.25, Figure 3.31 for cell cycle),
- UP029: this cell line presented a mixed picture, with the shRNA knockdown producing a cell line with delayed proliferation start and reduced G0/G1 population (Figure 3.24 and Figure 3.30), while the

CRISPR knockout did not present any difference in terms of both proliferation and cell cycle (Figure 3.25 and Figure 3.31).

- UP007: this cell line also presented a mixed picture, with the shRNA knockdown producing a cell line with delayed proliferation start and increased G0/G1 population (Figure 3.24 and Figure 3.30), while the CRISPR knockout did not present any difference in proliferation and cell cycle (Figure 3.25 and Figure 3.31).

It is possible that differences between KD and KO derived from the intrinsic nature of the two technologies. The knockdown produces a reduction of the protein expression while the KO approach aim to completely cancel the expression of the target. At the same time, the lentiviral KD technology stably insert the shRNA-codyfing plasmid in random regions in each cell targeted, creating a polyclonal population that can interact with other genes' expressiona dn regulation. The CRISPR system aim to inibit block the expression of the mRNA, acting on the gene promoter, thus creating potentially no cross-interactions.

Overall with the CRISPR technology,little to no effect of Cav-1 KO was seen in cell proliferation profiles or rates, nor in cell cycle. The comments below represent the integrationof results from both platforms.

The general proliferation results contrast with the work of Quann et al (Quann et al., 2013) who found, overexpressing Cav-1 *in vivo*, that it inhibit proliferation in the U87. As mentioned in the General Introduction (Chapter 1), Cav-1 role in cancer has been associated with different phenotypes, tissues, and stages of cancer development (Parat & Riggins, 2012; Senetta et al., 2013). As such, the differences in the impact of Cav-1 on cellular proliferation rate may be due to distinct molecular GBM subtypes associated with the cell lines.

In more than one cell line anyway the typical observation was that Cav- cells tend to delay their proliferation log phase, but then reach the same Level of the plateau than the Cav+ counterparts. This may be because, when Cav-1 is not expressed, the cell-cell and cell-environment communication is not efficient, and single cells may take more time to realize if the space around them has to be filled, resulting in a slower proliferation. At the same time, when the number of cells increases, and cell-cell communications focal points are increased too,

cells can trigger the proliferation pathway and start expanding quickly, filling in this way the gap with the Cav+ samples. Indeed, if Cav-1 is involved in cell-cell and cell-matrix interactions, it can also lead to a more committed phenotype, resulting in a reduced proliferation, like for the UP007 KO.

In previous reports, Cav-1 has been associated with induction of apoptosis and promotion of cell cycle arrest (Quann et al., 2013). In the same year Quest et al reported that Cav-1 promotes cell cycle arrest and decrease the number of cells going through the S phase by inhibiting the expression of Cyclin D1 (Quest et al., 2013). But also, as explored in the introduction, Cav-1 expression is thought to have a double role as both a tumour suppressor and an oncogene according to the tumour stage (Senetta et al., 2013).

Generally speaking, an increase in the G0/G1 cell fraction is generally associated with a delay of the proliferation and possibly the induction of differentiation (Zarrilli et al., 1999). Anyway, other reports indicate that the block of G0/G1 phase can be unrelated to a decrease of proliferation. For example, Perna et al reported that a block in the cell cycle was not accompanied for their cell lines by a reduction in the proliferation rate (Perna et al., 2017). In their case, in fact, a DNA damage caused by therapeutical treatment was altering the cell cycle plot.

It is then possible to hypothesize that a change in the cell cycle can be due, as for the proliferation, to a defect of the communication systems, due to the absence of Cav-1. Nuclei not receiving straightforward signals are not able to activate their cell cycle machine in a synchronized way, resulting in a delay in the cell cycle progression and in an accumulation of cells in the G0/G1 phase.

It has also to be noted the presence of three peaks in the Cav- UP029 cell lines (both KO and KD, but not the positive controls) and U87 KD. In the beginning, we considered the possibility of a contamination. However, we then realized that the peaks are localized on three positions on the x-axis that are each one the double of the previous one. This corresponds to a cell line with a mixture of diploid and polyploid cells (Kuo et al., 2014). This may be correlated to the defect of communication derived from the absence of Cav-1. The cells fail to receive all the right stimuli and the activation of a new DNA replication may start before the previous cycle is completed.

Finally, we can't fail to consider that the presence of three peaks makes it difficult to analyse the cell cycle status, and this may have led to the striving in the interpretation of the results.

3.5.4 Clonogenicity

In terms of clonogenic analysis, both the KD and KO produced cell lines with a reduced capacity of colony formation in 2D colony forming assay and neurosphere formation in 3D soft agar assay. Specifically, for:

- U87: both the shRNA KD and CRISPR KO produced a cell line with a reduced clonogenic potential (Figure 3.26 and Figure 3.32);
- UP007: this cell line presented a mixed picture, with the shRNA knockdown producing a cell line with a reduced clonogenic potential and the CRISPR KO producing a cell line with and increased clonogenic potential(Figure 3.28 and Figure 3.32);
- UP029: as for the U87, both the shRNA KD and CRISPR KO produced a cell line with a reduced clonogenic potential (Figure 3.28 and Figure 3.32);

In Table 3.8 the summary of the effects of Cav-1 expression modification in the three major cell lines upon clonogenicity.

Table 3.8 Effects of Cav-1 genetic Knockdown and knockout on GBM cell lines clonogenicity.

Effect of Cav-1 suppression in clonogenicity		
	Lentiviral shRNA KD	**CRISPR KO**
U87	Reduced	Reduced
UP007	Reduced	Increased
UP029	Reduced	Reduced

The general positive effect of Cav-1 on clonogenic potential (the reduction of Cav-1 expression correlates with a reduction in the clonogenic potential) may suggest that Cav-1 has an oncogenic role. These results included both the plastic condition (colony forming assay) and the 3D stem system (soft agar assay), meaning that the effect of Cav-1 expression on clonogenicity is not dependent on the cells environmental conditions. Moreover, in every assay, it is possible to observe that spheres/colonies produced by Cav+ cells are always consistently larger than the negative counterpart, and the colonies are also always less dense. This could confirm the hypothesis of Cav-1 absence as a difficulty for cells that have to start proliferating. In this sense, cells may start proliferating later and produce smaller and sparser colonies when Cav-1 is depleted.

It is possible to infer that the negative modulation of Cav-1 leads to a disrupted signal communication, resulting in cells delaying their proliferation rate with smaller colonies and sphere resulting in the clonogenicity assays, and cell cycle un-synchronicity which may lead to the reduced clonogenic potential of the Cav- cells.

Lastly, the Cav-1+ cells appeared to display increased migration of cells away from the formed neurosphere, i.e. Cav-1 appeared to promote cell migration. This observation would be important and concordant with the *in vitro* invasion studies reported in the next chapters.

3.6 CONCLUSIONS

The hypothesis of the work is that Cav-1 serves as a modulator of the functional properties of cancer stemness in high-grade glioma, grade IV astrocytomas, either as a suppressor or promoter. Specifically, that in sub-populations of glioma cells Cav-1 has a critical role in interplay with other pro-stemness molecules to impart cancer stem cell (CSC)–like activity, including the ability for self-renewal and increased clonogenicity and the ability to migrate and invade tissue.

The first objective was to create a series of stable glioma Cav-1-depleted cell lines, to understand the role of Cav-1 biology in glioma stem-cell phenotype and function. The initial lentiviral knockdown (KD) was compared to the newly developed technology CRISPR knockout (KO). The conclusion of the study is that they both present advantages and disadvantages. The RNAi KD is easier, cheaper and quicker to achieve and can be applied to a variety of difficult conditions (i.e. primary cell cultures) but it still produces only a reduction of the protein expression; moreover, its dependence on antibiotic selection contribute to its reduced reliability. The CRISPR KO produces straightforward phenotypes that can be related directly to the protein absence and doesn't need antibiotic selection; on the other hand, it is more complicated to achieve, it's expensive and not very efficient, and requires a clonal selection that is slow to achieve and must be confirmed by more than one clone. In the end, we must conclude anyway that, we feel more comfortable with the results of the cell lines derived by CRISPR KO than the RNAi technique.

The knockdown/knockout techniques partially showed that Cav-1 has a positive impact on glioma cell lines clonogenicity and enhance cell cycle progression. From the study, however, it was not possible to observe consistent results across the cell lines. This may be due to cell lines heterogeneity. Some cell lines may have indeed other activated/suppressed pathways that attenuate the impact of Cav-1 on the cell lines phenotype.

In the future, Cav-1 could be confirmed as driver of clonogenicity with *in vivo* tumourigenicity. Orthotopic injection of Cav+ and – cells could help understanding if Cav-1 is relevant for the tumour formation in vivo, thus confirming the clonogenicity results.

4 CHAPTER 4- THE STUDY OF INVASION IN BRAIN TUMOURS

4.1 INTRODUCTION

Cancer invasion is a complex process that needs *in vitro* and *in vivo* assays able to capture all its features. Among all the possible *in vitro* invasion assays available, the 3D invasion assay most likely captures the complexity of the phenomenon. Cells are first grown in a spheroidal state, under non-adherent conditions, and then surrounded by a matrix recalling the ECM. Invasion through the matrix can be followed in time by optical microscopy, or other imaging techniques.

It is clear from the literature that the 3D spheroid technology is taking the place of the classic transwell-based invasion assay, and the field is rapidly advancing and expanding toward both discovery and translational cancer research, with potential in drug development and testing.

However, when the project was started, there was a lack of a tool for the unequivocal quantification of the assay.

Spheroid integrity and cellular invasion in the 3D invasion assay system can easily be visualized by phase-contrast imaging (manual or automated), which can be applied for recording spheroid volume growth and invasion kinetics.

If from a qualitative point of view the interpretation of the 3D invasion assay is mainly straightforward and allows several kinds of studies and considerations, a quantitative point of view is also necessary to establish the reproducibility and the statistical significance of the qualitative observations. Many steps have been made in order to produce a satisfactory methodology for this necessity, but up to now, there is no standard system that is approved and shared among the scientific community.

Two main difficulties to overcome for an effective invasion analysis of 2D bright field greyscale images, which can be inferred by observing Figure 4.1 were addressed. The first problem is intrinsic of the quality of pictures from inverted phase-contrast microscopes; in this kind of images the object, i.e. the spheroid with its invasive protrusions must be distinguished from the background. When the spheroid is compact and intact (like during the spheroid formation, before the embedding in the 3D matrix, or if the spheroid is formed by non-invading

cells) the compactness of the cellular material results in an optical dense aggregate, which can be distinguished easily from the background (Figure 4.1A) even if the latter is dark. When the spheroids are invading (Figure 4.1), on the contrary, the finger-like projections are not uniformly dense anymore (Figure 4.1C) and are lighter than the background. While the operator can easily understand between the background and the invading structures, an automated software that uses pixel density to distinguish the background from the cellular material will start including outside pixels before including the finger-like projections' ones.

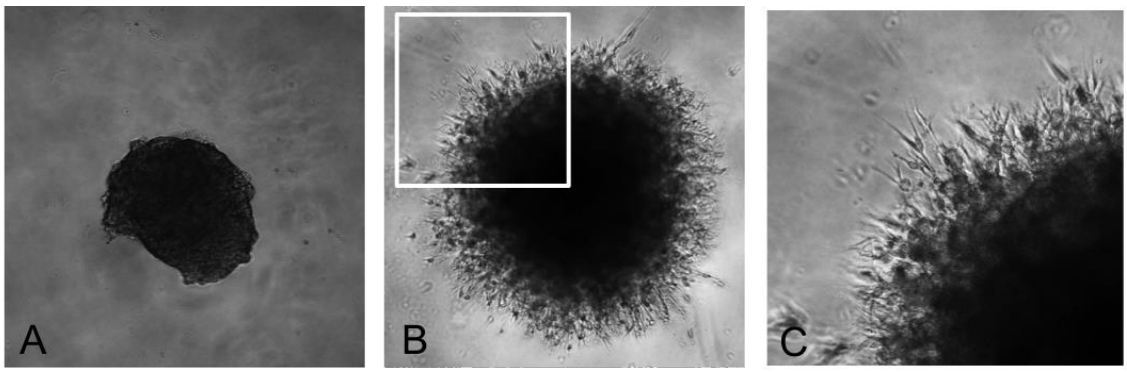

Figure 4.1 2D greyscale images of 3D spheroids embedded in BME. A- Day 0, after embedding. B- Day 2 after the invasion. C- Enhanced image of field of view highlighted in B.

The second problem is the need to distinguish the core of the spheroid from the invasive edges. Figure 4.2 reports three exemplified spheroids with the same invasive ability (traced by the red line and the number 100). On the other hand, the three spheroids occupy three different areas of the total image. This is because their cores, which are the parts of the spheroids that are not invading, behave differently in time. They, in fact, start all with the same size at Day 0 but then evolve differently. The first one increases in size more rapidly than the others (rapid proliferation), the second one is maintaining more or less the same size (the cells abandoning the core for the invasion process are replaced by cells proliferating at a lower rate than the ones of the first spheroid) and the third one is shrinking (cells are not proliferating enough/at all). This means that the invasion ability of the three spheroids is the same, while other processes are active or not, and they have to be taken into consideration. This results in

operators classifying spheroids invasion differently even if their net extent of protrusions is the same.

This important aspect is often underestimated since few image analysis algorithms can distinguish the spheroid core (i.e. the original cellular mass that may have undergone varying extents of proliferation) and the spheroid invasive edge (representing motile cells invading the ECM).

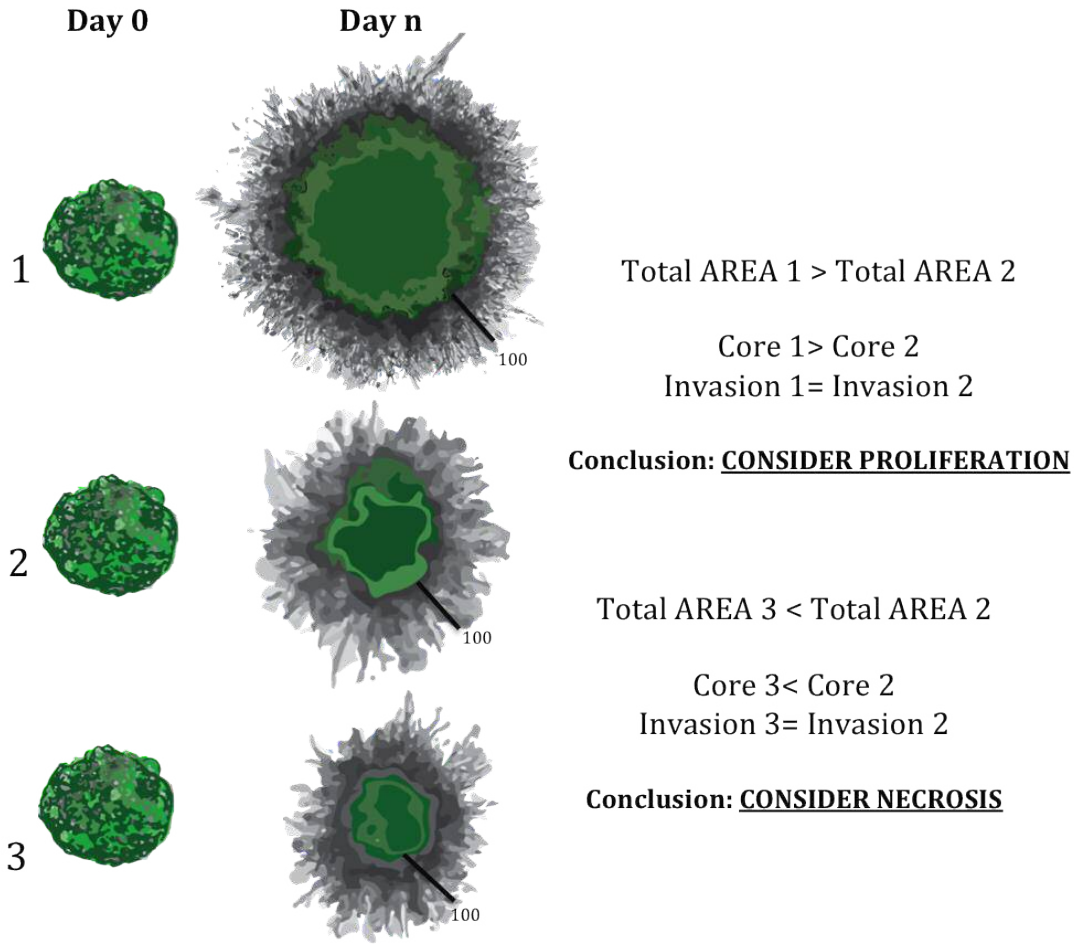

Figure 4.2 Considerations about the influence of the Core area over the total invading spheroid area. 1- Spheroid with high proliferation rate. 2- Spheroid with low or non-proliferating Core. 3- Spheroid with reducing core over time. The schematic comparisons are referred to a Day n spheroids.

In the next part the main attempt at a quantification of the 3D invasion assay based on 2D grayscale phase-contrast images. The studies are summarised schematically in Table 4.1.

Table 4.1 Methods for quantifying 3D spheroids and invasion in literature, with a preview of INSIDIA ability.

Reference	Geometric Parameters	Isolation of Core and Invasion	Specific Surface	Open Source Software	Semi-/Automated Image Processing
Stein 2007	✓	✓			
Friedrich 2009	✓		✓		✓
De Wever 2010	✓		✓	✓	
Naber 2011	✓				
Vinci 2012	✓				
Blacher 2014	✓	✓			✓
Vinci 2015	✓				
Solomon 2016	✓				
Ivanov 2014	✓			✓	✓
INSIDIA	✓	✓	✓	✓	✓

The first one is by an American group, led by Andrew M. Stein. Their mathematical model consists in quantifying the radius of the invasion in an image I. They calculated the magnitude of the gradient of the image, G =|∇I| and averaged it over the azimuthal angle to find $\overline{G}(r)$. Then they defined the radius of invasion to be the distance farthest from the centre where $\overline{G}(r)$ was half its maximum. The radius of the core was scored attributing at the darkest pixel (centre of the spheroid) the value 0 and the lightest pixel (background) value 1. The core was identified as the set of pixels with an intensity of <0.12. They chose this value because it corresponds to a region of the image where the pixel density is still high, but it is also rapidly decreasing, as for the passage from the core to the invasive edges, and also because it corresponded the core boundaries established by an operator in an experimental situation. Typical results are reported in Figure 4.3

The system is interesting even if not reproducible without the software. Moreover, it is important to point out, even from the representative results (Figure 4.3) that the algorithm seems not to be able to capture the total extent of the cells invading, which can result in an underestimation of the invasion process.

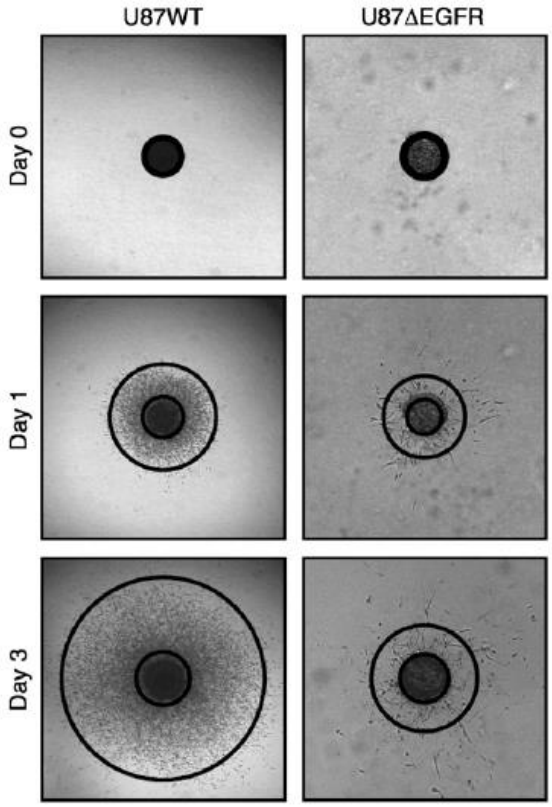

Figure 4.3 Mathematical model that quantifies the distance of the invasion from the Core. Adopted from (A. M. Stein, Demuth, Mobley, Berens, & Sander, 2007) with permission.

The second work reported is from a Friedrich et al, published in 2009 (Friedrich et al., 2009). They didn't actually quantify invasion but only the spheroids in suspension. Anyway, their important work provides multi-parameters for the interpretation of the assay outcome and also in a context of the semi-automated environment, not only in terms of image analysis but also for the setting of the assay (Figure 4.4). The group used a collaboration with Zeiss (Echingen, Germany) to image the spheroids and then to analyse them, through image processing algorithms implemented in the Zeiss AxioVision 4.5 Software. They reported that the software allows reliable and reproducible area selection to determine spheroid diameter and volume. Among the generated data there was

morphometric information, such as spheroid area, mean spheroid diameter, spheroid volume, minimum diameter, maximum diameter, circularity.

They then focused on the analysis of tumour volume in different cells lines. Even if not relevant for the discussion of the invasion analysis it seems important to point out their observation that a certain size has to be reached by all spheroids to allow a drug treatment that can be reproducible and comparable within a range of different samples.

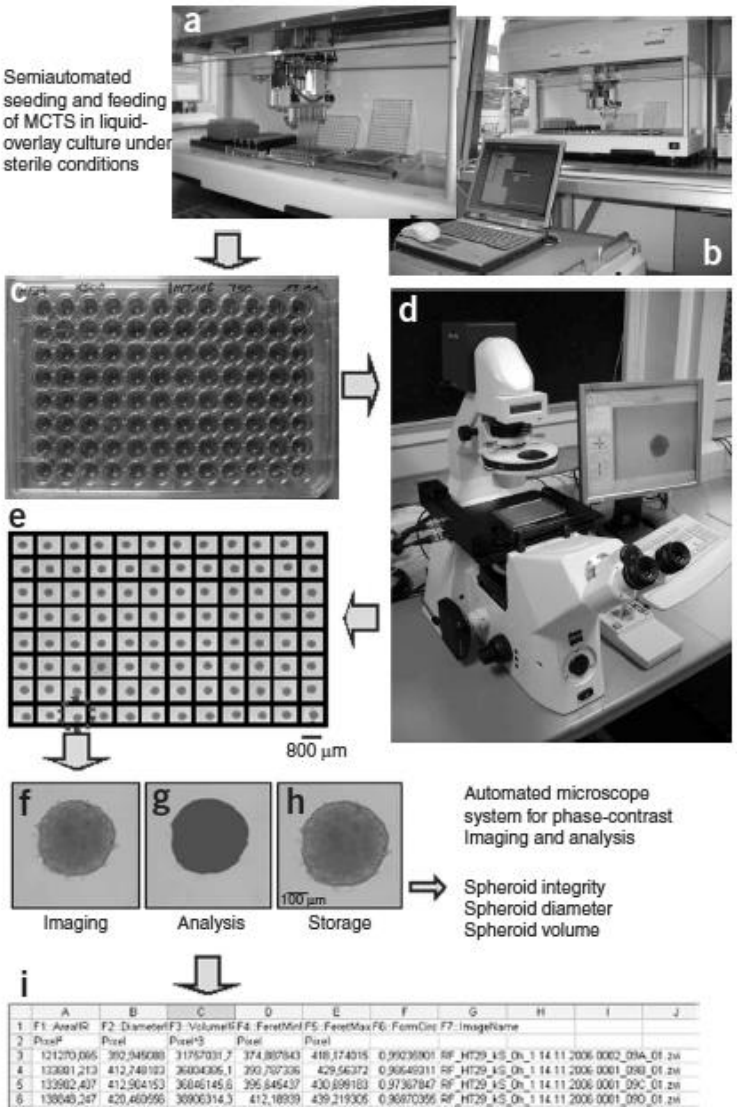

Figure 4.4 Spheroid assay setting and analysis by. Adopted from (Friedrich et al., 2009) with permission.

The third work reported is from a Belgian group, that analysed invasion in Collagen 3D matrices, by the use of ImageJ (NIH, Bethesda, MD, USA), an open-source software for image analysis (De Wever et al., 2010).

After converting the image in 8-bit type, they used ImageJ manual threshold to highlight the areas interest and convert them into black areas (Figure 4.5B) for a resulting binary (black/white) image. They subsequently manually “cleaned up” the images by excluding all particles less than three pixels in size and removing any artefacts (by comparison of the binary image with the phase-contrast pictures). At this point, they used the analyse particle to measure all remaining particles in the images in terms of area and perimeter of individual particles and recorded the area of the sum of individual particles. Other parameters (Figure 4.5C) included the shape factor, which refers to the ratio between perimeter and area and gives an idea of how the shape of the spheroid is close to a perfect circle (shape factor equal to 1) and the percent fragmentation, which is calculated as the percent of single or clustered cells released from the total spheroid area.

This system is interesting for its use of ImageJ as image analysis software. However, all the work on every single picture is manual and laborious. Moreover, the manual threshold of ImageJ, being operator-dependent, is not precise and does not discriminate all the cellular material present in the image (see Figure 4.1).

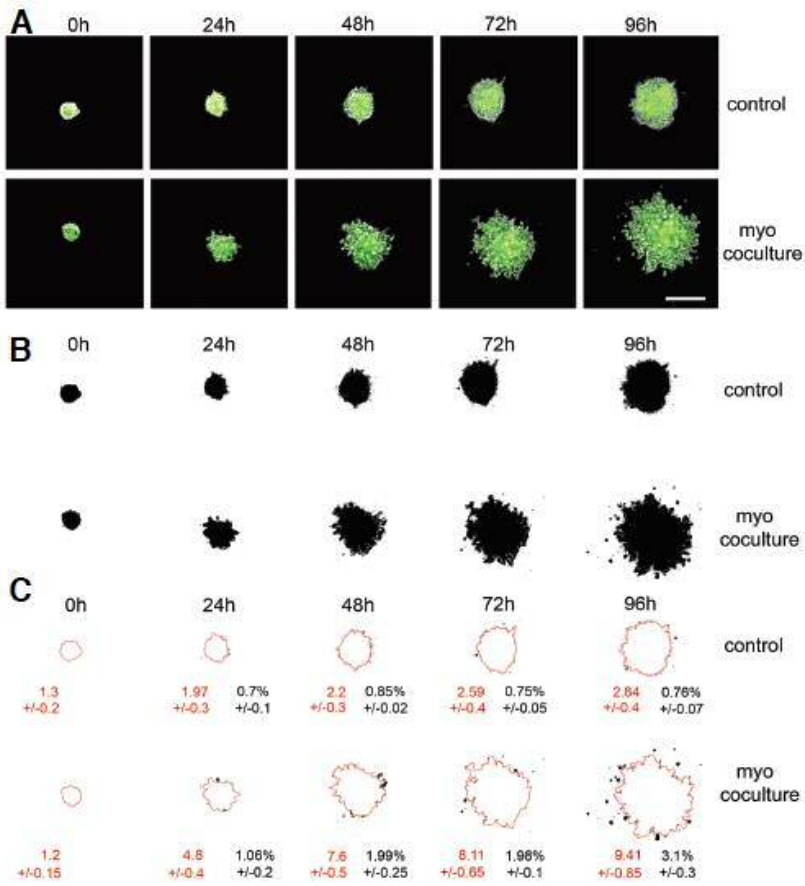

Figure 4.5 Representative data of a heterotypic spheroid collagen invasion assay. (A) GFP-phase contrast pictures of a representative GFP-colon cancer cell spheroid followed at different time intervals under control conditions and myofibroblast coculture conditions. (B) Computerized binary image processing of GFP-phase contrast pictures. (C) Factor shape (S) is calculated from perimeter2/4π area and is shown in red +/-SEM. A higher number means a more irregular, infiltrating spheroid structure. Fragmentation (%) is calculated from released cells or clusters/total area x100 and is shown in black +/-SEM. Adopted from (De Wever et al., 2010) with permission.

Further on, a group from Leiden (Netherlands) in 2011 used Adobe Photoshop Extended (San Jose, CA, USA) and its “quick selection tool” to manually select the area occupied by the cellular material, and then measure the total area and subtract the area at Day 0 (Figure 4.6). This method (H. Naber, Wiercinska, ten Dijke, & Laar, 2011) is straightforward and easy for the user to understand, and can reach a high Level of accuracy. Anyway, it is also extremely laborious, especially when cells are invading in highly ramified projections and when a lot of replicates and time points have to be analysed at once. The fact that the Photoshop software is not free-licenced is another disadvantage, even if it is possible to do the same process with the drawing tool in ImageJ. The laboriousness, however, would force the users to look for other solutions.

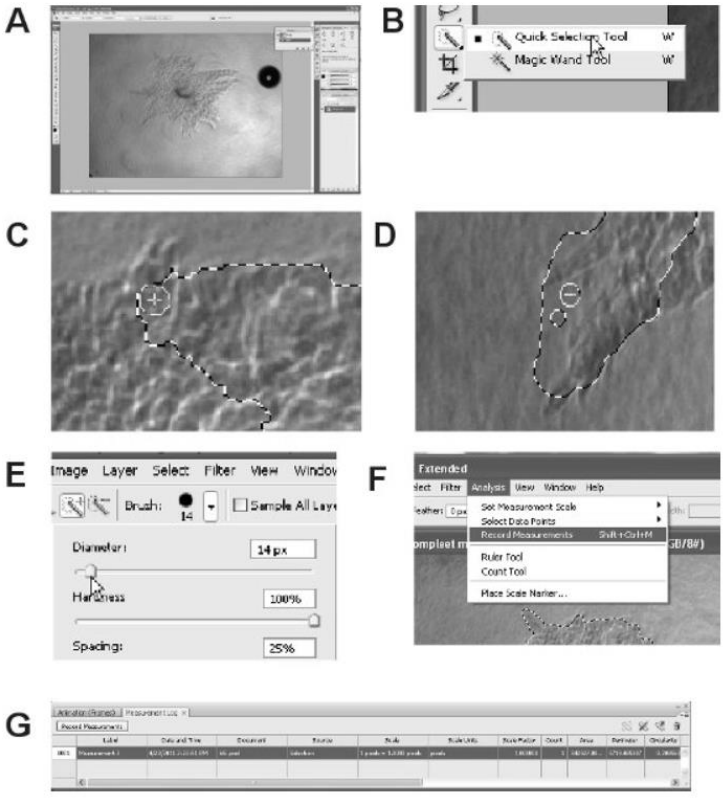

Figure 4.6 Quantification of the area of the spheroids using Adobe Photoshop Extended. (A) The picture of the spheroid is opened in Adobe Photoshop Extended (B) Selection of the Quick Selection tool (C) Dragging the cursor over the spheroid to select the area of the spheroid (D) Removal of a wrongly included area using the negative Quick Selection tool (E) Adjustment of the brush size of the Quick Selection tool to more accurately select the area (F) Selection of the measurement command to record (G) Example of a measurement record. Adopted from (H. Naber et al., 2011) with permission.

In 2012 a group from London (Vinci et al., 2012) published a paper for the high throughput study of spheroids, both in terms of drug screening and invasion.

Image analysis is performed this time on a Celigo cytometer (Nexcelom, Lawrence, MA, USA) by using the Cell Counting Confluence application, which calculates the area occupied by individual or groups of cells, after manual image segmentation around the invading cells (Figure 4.7). Even here, apart from the advantage of using a high-throughput machine that allows the automatic record of each time point and replicates, the segmentation (the drawing of the interphase between the cellular material and the background) can be done with a licenced software or manually if a free-tool is the only one available.

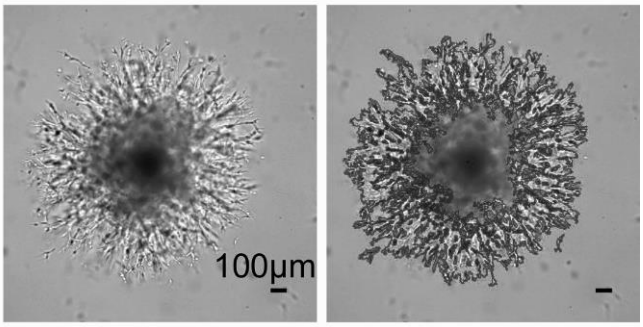

Figure 4.7 Schematic overview of 3D tumour spheroid invasion assay analysis. On the left U87 invading in the surrounding BME. On the right the same image after segmentation by Image Pro Analyser software (Vinci et al., 2012).

Moreover, Vinci decided to calculate invasion by simply reporting the total area occupied by the cellular material, without taking into consideration different densities of invasion (few cells creating an extensive net are not the same as many more cells invading altogether) or any change in the core.

One of the works that appear to be more accurate among the so far published ones, is the one of a Belgian group, led by Agnès Noel (Blacher et al., 2014). The group smartly recognised the importance of good segmentation and core thresholding (distinguishing the core from the invasive edge). They decided to use an algorithm developed for the highlight of blood vessels in angiograms, so-called Frangi filter (Frangi, Niessen, Vincken, & Viergever, 1998), for a spheroid segmentation that allows the accurate reconstructions of all the finger-like projections emanating from the spheroid (Figure 4.8D and E). Plus, they used pixel density, like Stein (A. M. Stein et al., 2007), to distinguish the Core from the invasive edges. They essentially drew a sequence of concentric circles, starting from the centroid (Figure 4.8K), and recorded the average pixel density along the circles and then plotted them against the distance from the centroid (Figure 4.8M). They then use the resulting profile to select the average distance from the centroid to the end of the Core (as the one where the pixel density is arriving at 0.8, where 1 is the darkest pixel and 0 the lightest). From that they could calculate the radius of the Core and the extension of the invasive edges plus, through integrals, they could take into consideration also the density of the cells invading and the spheroids proliferating. The system is very clever and potentially perfect for quantifying invasion in a 3D context, if it were not for the fact that the software that they used is a MATLAB-based script, not provided

with the paper, so virtually not useful for the common average operators. Plus, MATLAB (MATLAB and Statistics Toolbox Release 2012b, The MathWorks, Inc., Natick, Massachusetts, United States) is not only a licenced tool, but also a software that requires a certain amount of experience in programming and in script composition, with its specific language, which is not applicable in projects that are not purely models but includes an extensive experimental plan other than the 3D invasion assay.

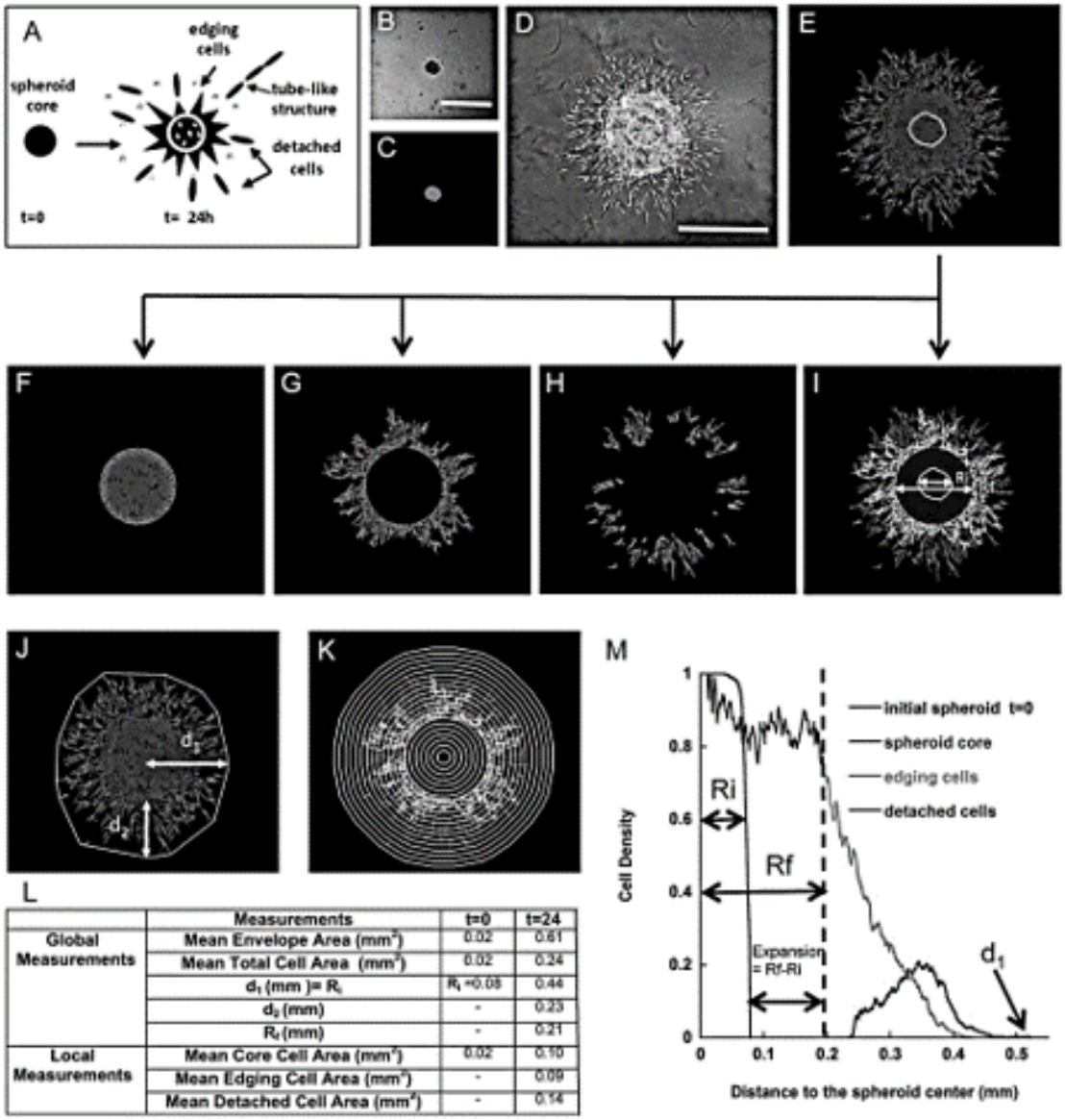

	Measurements	t=0	t=24
Global Measurements	Mean Envelope Area (mm^2)	0.02	0.61
	Mean Total Cell Area (mm^2)	0.02	0.24
	d_1 (mm)= R_i	R_i +0.05	0.44
	d_2 (mm)	-	0.23
	R_f (mm)	-	0.21
Local Measurements	Mean Core Cell Area (mm^2)	0.02	0.10
	Mean Edging Cell Area (mm^2)	-	0.09
	Mean Detached Cell Area (mm^2)	-	0.14

Figure 4.8 Description of the spheroid assay and the method of quantification (Blacher et al., 2014). (a) Schematic representation of spheroid evolution during cell culture. (b-e) Spheroid Day 0-n, greyscale and segmented. (f–i) Decomposition of the binarized image into spheroid core (f), edging cells (g) and detached cells (h) and composite (i). (j) Illustration of the parameters used for global measurements: convex envelope (green) and the total distance of cell invasion starting from the spheroid centre (d1) or border (d2). (k) The grid used for local measurements: a circular grid is superimposed on the coloured spheroid representation. (l) Comparison of global and local measurements at t = 0 and t = 24 h. (m) Graph representing the cell density distribution measured from the image. The colours of the curves correspond to the different spheroid components described in the other panels (a, i and k). Bars = 500 mm.

Finally, in 2014 a group composed a macro on FIJI (Schindelin et al., 2012b) platform for the segmentation of spheroids in suspension and the computation of geometrical parameters (Ivanov et al., 2014). Their segmentation was obtained by the Yen thresholding algorithm (Jui-Cheng Yen, Fu-Juay Chang, & Shyang Chang, 1995), present in the FIJI package, while the geometrical

parameters include Area and Ferret min and max diameter. The measured area was then used to retrospectively calculate the radius and volume of an equivalent sphere, and consequently to compare volumes of different time points.

The advantage of this approach is their effort to automatize the analysis process in a FIJI macro (the updated version of ImageJ) that they make public for the scientific community. On the other hand, the Yen segmentation algorithm is not as accurate as the manual outline performed by the other group. This is of course still acceptable for the Nottingham's group because they are analysing spheroids in suspension, and not invading ones.

4.2 SCOPE OF THE CHAPTER

In this chapter, cell lines characterized in the previous chapter have been analysed for their invasion ability, through the use of the 3D invasion assay.

An optimization of the protocol has been performed, as well as an effort for a reproducible, efficient and easy to use tool for the analysis. In fact, while image analysis software capable of detailed quantitative analysis of 3D spheroid assays are available, they are mostly licensed for a particular microscope platform, or are limited in terms of calculable parameters and not customisable by the end-user, for this reason we developed a new tool, based on ImageJ, for invasion assay analysis.

4.3 MATERIALS AND METHODS

4.3.1 CELL LINES AND TREATMENTS

U87, U373, UP007 and UP029 transfected for the lentiviral-mediated shRNA silencing of Cav-1, have been used for the analysis of *in vitro* invasion, as well as U87, UP007 and UP029 genetically modified by CRISPR technique.

4.3.2 METHODS- INVASION ASSAY (3D CELL SPROUTING ASSAY)

4.3.2.1 ASSAY SETTING

The invasion assay was performed according to Vinci et al (Vinci et al., 2012) and is summarized in Figure 4.9. Cells were seeded in a 96-well plate, treated to obtain ultra-low adherence conditions (ULA) and round-bottomed (COSTAR-ref. 7007). The optimal seeding concentration was established experimentally as 1000 cells/well for the U87 and 5000 cell/well for the other cell lines. After the seeding, cells were gently centrifuged (300g - 1 min) and incubated for four days at 37° C 5%pCO_2 to allow the formation of tight aggregates. After that half of the medium was replaced with growth growth factorreduced MATRIGEL™ (Corning, ref. 354230) on ice and the plate was left on ice for one hour to allow the homogeneous diffusion of the Matrigel and the medium and then incubated again at the same conditions to allow the jellification of the matrix around the aggregates. After one hour, new medium was added to the jellified wells and pictures were taken immediately after and every 24 hours for 2-4 days (according to the invasive ability of the cell line under examination).

The analysis of the 2D grey scale projection pictures was obtained by the use of a customizable script in FIJI, reported in the appendix 5 (Moriconi et al., 2017).

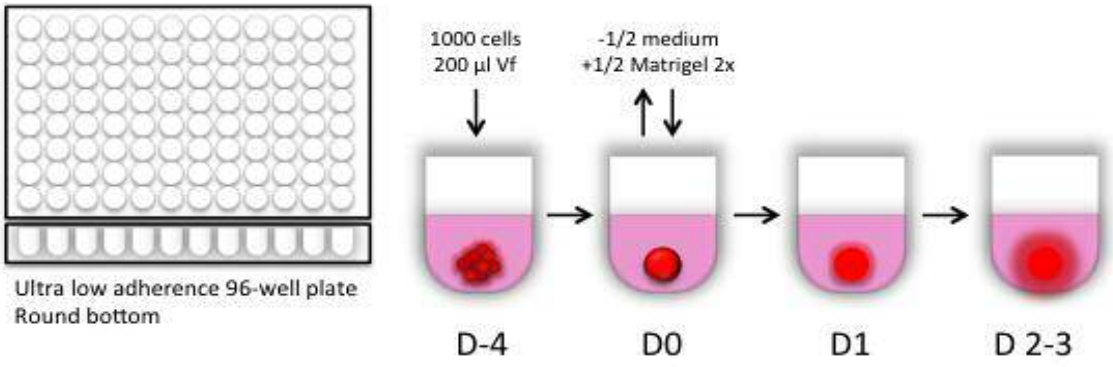

Figure 4.9 Invasion assay- experimental procedure. Cells are seeded in a low-adherence round bottom multi-well plate and after four days one single sphere per well can be observed. Half of the medium is then replaced with Matrigel and the cells can be followed in time.

Figure 4.10 Invasion assay. Acquisition of images procedure. After the gelification (D0) of Matrigel, each well is imaged at 5x magnification and stored in separate folders. Every day and at the end of the assay (D2-4) the procedure is repeated, and images are stored in the corresponding folders.

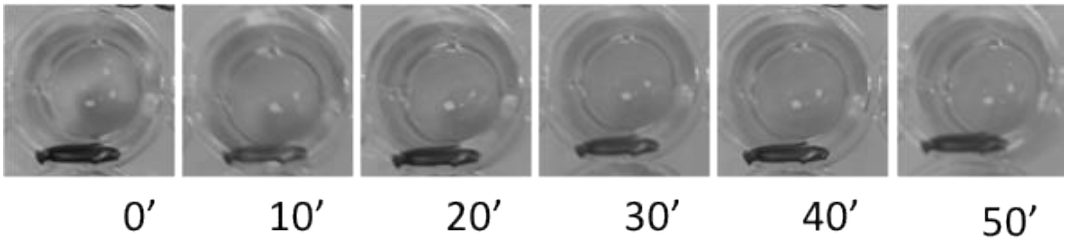

Figure 4.11 Matrigel diffusion study. Half of the spheroid phenol red-free medium was replaced with matrigel, as described in previous protocols (Vinci et al., 2012) and the plates were kept on ice until a homogeneous distribution of colour was achieved. Time reported in the pictures is in minutes.

4.4 RESULTS AND DISCUSSION

4.4.1 ASSAY SETTINGS

From a qualitative point of view, many features can be observed, like single cell leaving the spheroid (Figure 4.12A), starting replicating in the MATRIGEL™ (Figure 4.12B) and collective invasion (Figure 4.12C).

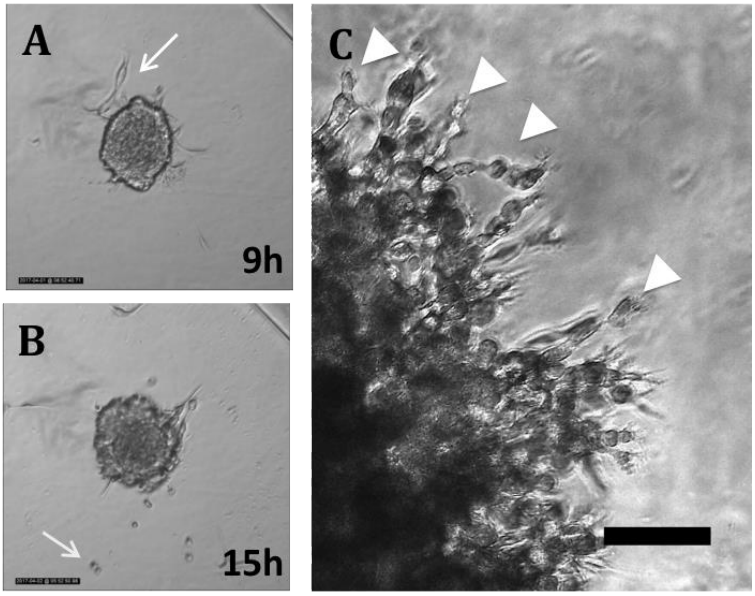

Figure 4.12 Time lapse pictures of spheroid embedded in Matrigel with single cells leaving to invade (white arrow in A) and starting to divide outside the spheroid (grey arrow in B). In C it is possible to observe chains of cells (white arrows) leaving the spheroid in an organized structure.

In this chapter, we focused on the 3D invasion assay of wild-type GBM cells and their quantification.

4.4.2 INSIDIA

Considering all the efforts formulated in the past for the quantification of the invasion that have been described in the introduction section, we decided to elaborate a new tool for the purpose that would be free to use, would use the useful features from past attempts and that would allow quantifying invasion in the most efficient, automatized and quick way. To do that we chose FIJI, the

new version of ImageJ, an open-source platform with a user-friendly interface, and the help of Dr Valentina Palmieri, as an expert in FIJI coding language.

We wrote a script with the ImageJ language, that we called INSIDIA (Invasion SpheoID Invasion Analysis) and published in 2017 on Biotechnology journal (Moriconi et al., 2017). INSIDIA code is reported on Appendix 5.

As mentioned before, two steps are important for the quantification of invasive or non-invasive spheroids. The first is the distinguishing of the cellular mass from the background, the so-called **spheroid segmentation**, while the second one is the ability to establish the point of transition between the core and the invasive edges, the **Core thresholding**. Both can be done manually and arbitrarily, or with the help of software tools.

4.4.2.1 PRE-ANALYSIS: SEGMENTATION

As shown in Figure 4.13, and as described in the introduction for the spheroid segmentation, a classic ImageJ thresholding method (not to be mistaken with the Core thresholding, described later), based on pixel density is not able to include all the invasive ramifications (Figure 4.13 middle). On the contrary, the Frangi filter, described by Blacher et al. (Blacher et al., 2014) is able to capture effectively all of them, as shown in Figure 4.13 (right). Since this filter is available for the ImageJ platform, we decided to use it as our tool for spheroid segmentation.

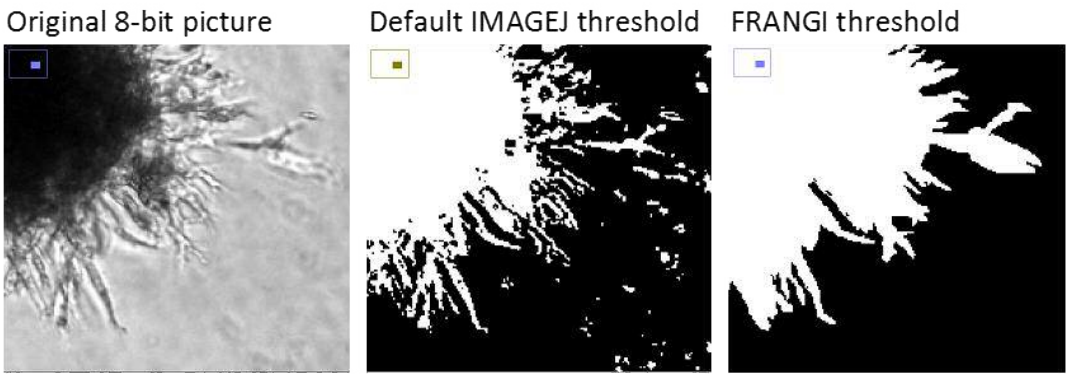

Figure 4.13 Comparison between two thresholds (middle and right), on the same picture (left).

4.4.2.2 PRE-ANALYSIS: CORE THRESHOLDING

As for the core selection, we had to understand how to establish the thresholding. We tried first arbitrarily to select a pixel density value but there was a necessity for a more universal method that would be adequate for different illumination methods and different cell lines. We then tried to select a pixel density that would represent a percentage of decrease of pixel density from the darkest pixel, that in theory is in the centre of the core (an example in Figure 4.14). However, this method doesn't take into consideration the heterogeneity in core pixel density displayed by some cell lines. For those cell lines, the resulting possible cores are very fragmented, and it is not possible to find a core threshold that is unequivocally mirror of the real Core.

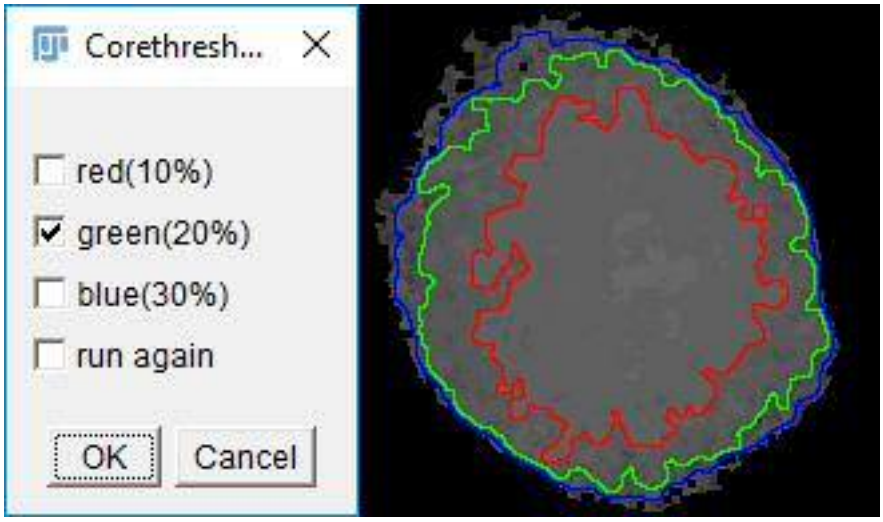

Figure 4.14 3D spheroid image segmented for three possible cores based on pixel density percentage decrease. Each line represents a possible core outline. Red 10%, Green 20% and Blue 30% from the maximum pixel intensity.

We applied both the arbitrary pixel density value and the percentage of decrease of the Blacher Core thresholding method (Blacher et al., 2014). As reported before the method consists in drawing concentric circles on a 2D picture from the spheroid (Figure 4.15B). Each circle is bigger than the previous one of 1 pixel. The recorded average pixel density is then plot for each circle against the distance from the centroid of that specific circle. The result is a density profile (Figure 4.15C) where the pixel density starts from the maximum value, which represents the core and then goes down when the circles pass

from the core to the invasive edges and the to the lower point when they reach the background.

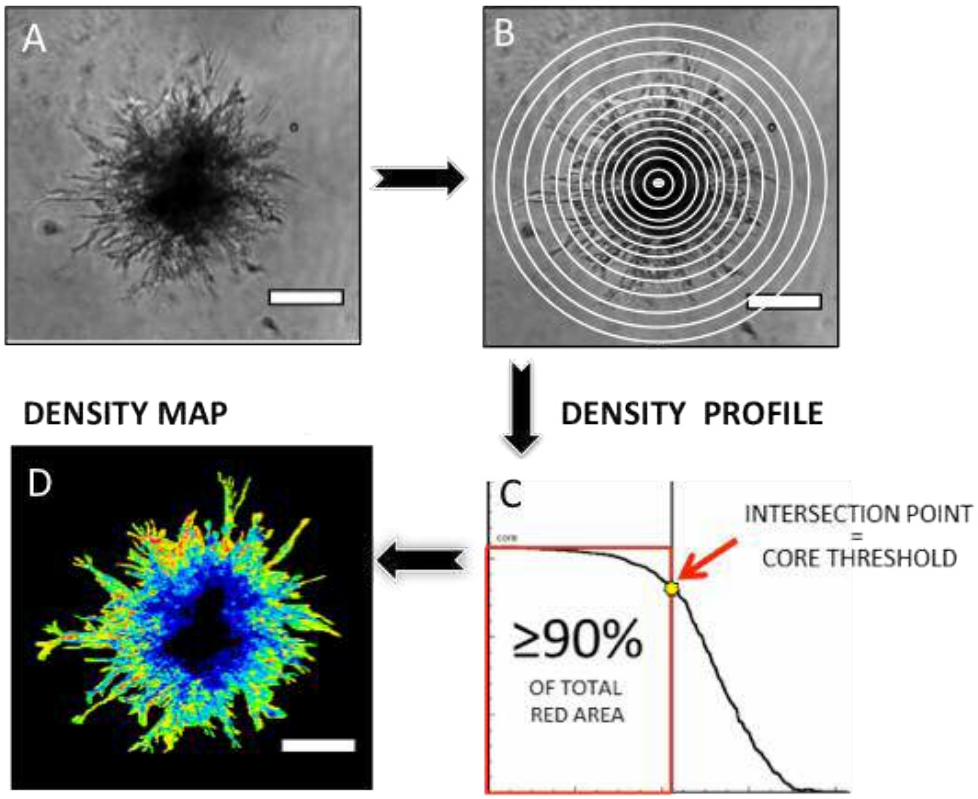

Figure 4.15 Core thresholding method. A- original 8-bit picture. B- Concentric circles are drawn from the centroid for recording average pixel density. C- Circle average pixel density plotted against distance from the centroid to get density profile, for the calculation of parameters, among which the Core thresholding density value, that is used to differentiate Core and Invasive edges on both the profile and the density map (D).

We then studied the best way to calculate the point in the density profile where the core was transforming in invasive edges. Blacher et al (Blacher et al., 2014) set the pixel scale as a max density of 1 and a minimum density as 0 (Figure 4.17A) and then decided that the Core would have ended when the pixel density would reach on the plot the value of 0.8. After manually studying several pictures at day 0, we established that at the transition the pixel values are decreasing rapidly but as an intermediate point in our scale (255 to 0) 100 could be chosen as an arbitrary point.

4.4.2.3 PRE-ANALYSIS: NORMALIZATION

in order to normalize and allow comparison of images acquired with different illumination settings we needed to adopt a new normalization standard. The

classic normalization process consists in stretching the pixel density so the darkest pixel is 255 (black in the pixel intensity value scale- Figure 4.16D) and the lightest 0 (white- Figure 4.16B). This resulted in the flattening of differences between spheroids with different core densities, which reflects the compactness of the cellular material. Our solution was to normalize only on the lightest pixel. The lightest pixel density value was then subtracted to all the image pixels (Figure 4.16C). This resulted in images that can be compared because they have the same value of background, but their core differences are maintained (Figure 4.16F).

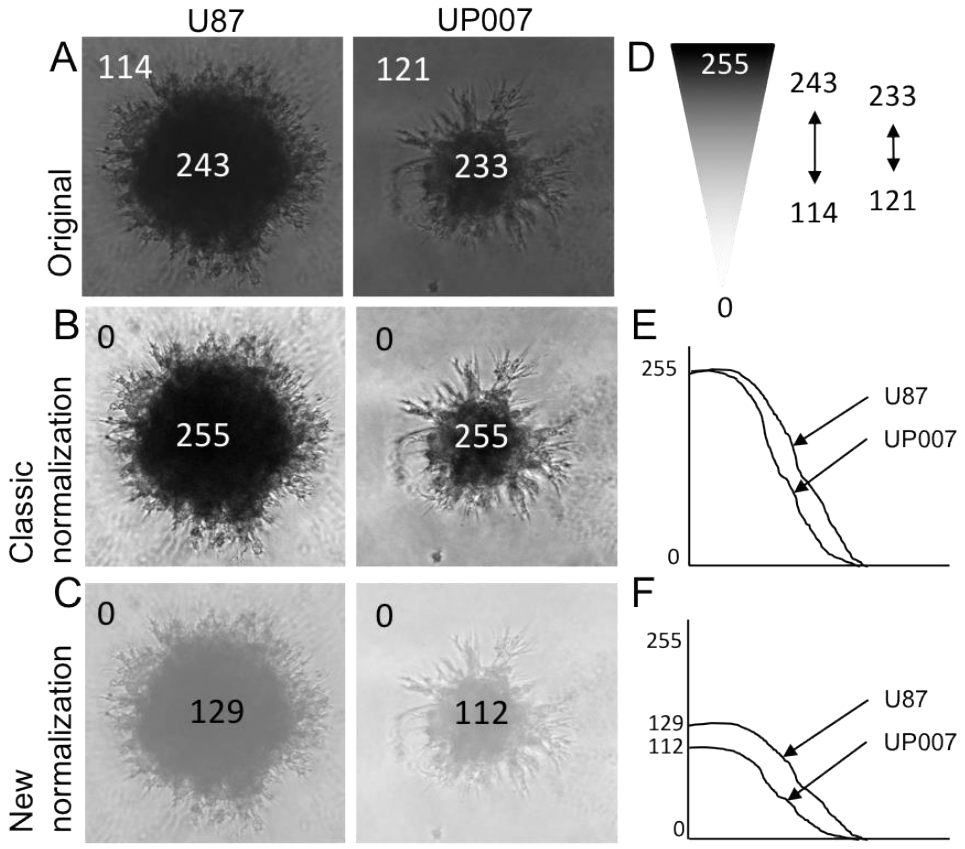

Figure 4.16 Image normalization options. A- Original pictures with values representing darkest and lighter pixel density. B- Classic normalization. Pixels area stretched to 255 and 0, black and white. C- New normalization. Only the lightest pixel is subtracted to all pixels. D- Pixel density scale with the values of the two original pictures. E- Density profile after classical normalization. F- Density profile after new normalization.

4.4.2.4 ANALYSIS: CORE THRESHOLDING

After the new normalization, however, the use of an arbitrary value was not possible anymore, because some spheroids with light cores do not reach a density of 100 after the normalization process. So, we used a value of

decreased pixel density (Figure 4.17C). In the beginning, we thought it would be better to have a user-customizable method and we decided to let the user decide the percentage of pixel density decrease to be used for all spheroids (an example in Figure 4.14). But that posed two problems, of which the most important was again the heterogeneous cores. They can indeed reach the designated pixel density decrease because of a reflection phenomenon and not because the invasive edges already started; that would result in a core thresholding that is valid for some replicates but not for others. And from this, it derived the second problem, which is that all the system was becoming time-consuming, the decision of the most suitable Core thresholding.

The final method we adopted (Figure 4.17D) is based on the software drawing a square that encapsulates the two axes on the left and bottom, touches the maximum pixel density on the top and starts from the end of the density profile on the right. By moving to the left until the area under the curve of the density profile corresponds to at least the 90% of total area of the square, the value of pixel intensity that intercepts the square is set as core thresholding value. This guarantees that the software can capture the darkest part of the profile, without the interference of lightest aberrations in the core. This can also be customised in the code, for users that have very dense (>90%) or light (<90%) replicates.

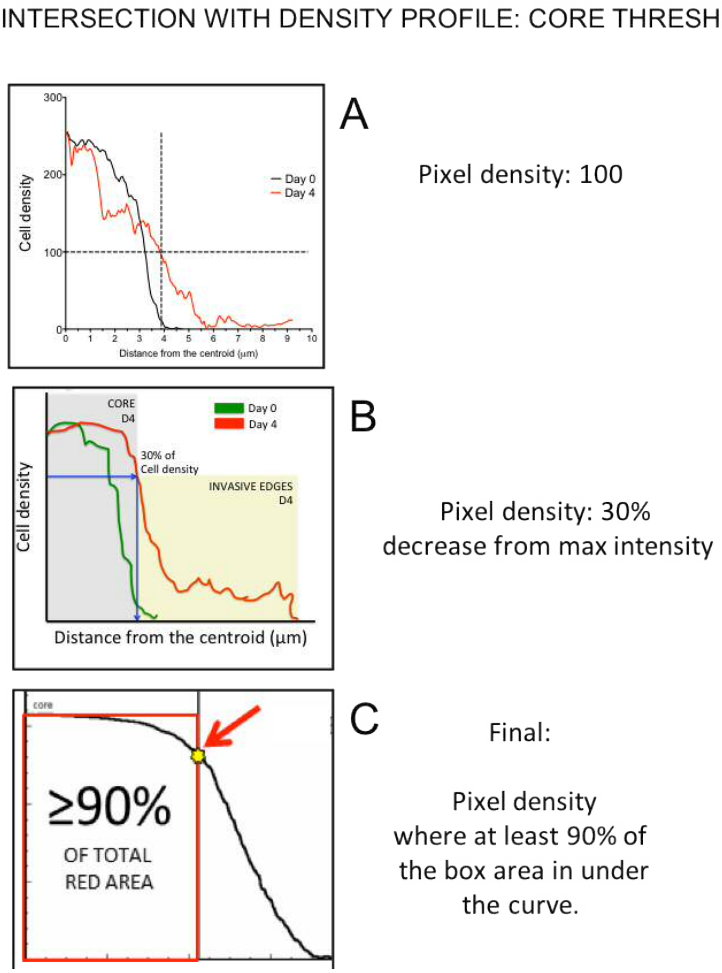

Figure 4.17 Core thresholding attempts in chronological order. A- Core threshold is established when pixel density reaches 100. B- Core threshold is set when pixel density decreases of 30% from the maximum pixel density. C- Core threshold is set as the pixel density of a box encasing the two axes, the maximum pixel density and the point of the profile that makes the area under the curve occupying at least 90% of the box area.

4.4.2.5 ANALYSIS: DENSITY MAP

Finally, once established the Core thresholding, the pixel intensity value is applied to the segmented picture (cellular mass without background) and the area corresponding to the range of pixels with an intensity higher than the core thresholding intensity value is considered as the Core of the Spheroid, while the remaining part is considered the Invasive edges (Figure 4.15D). The area in pixel^2 is then converted in μm^2. Here the technical issue to be solved involves the size of the Cores, which has been demonstrated earlier in the Introduction (Figure 4.2), as a determinant of misinterpretation of the net invasion. We solved this issue by normalizing the area of the invasive edges on the perimeter of the core.

4.4.2.6 SUMMARY OF OVERCOME TECHNICAL ISSUES

In Table 4.2 the main technical issues for the analysis of 2D images of 3D invading spheroids have been summarized.

Table 4.2 Technical issues related to the computed analysis of the 2D pictures of 3D invading spheroids.

N°	CATEGORY	ISSUE	SOLUTION	FIG.
1	Image processing	Large number of images. Laborious.	Batch mode	
2	Image processing	Intercellular differences depending on patterns of invasion	Customizability	
3	Image normalization	The classic 225-0 normalization method flattens the differences of the cores, which are due not only on illumination but also on actual cellular density.	New method in which the lightest pixel intensity value is subtracted from every other pixel value.	Figure 4.16
4	Image segmentation	The classic pixel intensity ImageJ threshold is not able to capture completely the invasive edge, resulting in an underestimation of the invasion area.	Frangi filter	Figure 4.13
5	Density profile	A single pixel intensity value for all the images is not able to reflect the real end of the core. The result can be a core that is too big (e.g. part of the core in the invasive edge)	“Red box” method: a box is drawn around the plot. The right side is intercepting the coordinate with which the box area is represented by at least 90% of the area under the curve of the plot. The pixel intensity value of that coordinate is used then as core threshold in both density profile and map.	Figure 4.17
6	Density map	Invasive edge area is different in spheroids with same invasive capacity but with different core sizes.	Normalization of invasion area on perimeter core derived from density map.	

4.4.2.7 INSIDIA PARAMETERS

The analysis of INSIDIA can calculate and make available 3 categories of parameters, summarized in Table 4.3:

- The **segmentation parameters** are essentially geometrical parameters that can be derived from the geometric analysis of the image after the segmentation. As already described in the previous works presented in the introduction they can give a rough tool of comparison for highly invading cell lines versus poorly invading ones, like the total area, and the shape-specific parameters (such as Circularity, SpecSurf, ShapeF and Env Area). However, they can be also used for the derivation of other categories' parameters, like the centre of mass and the maxRadius for the density profile.
- The **density map parameters** are the ones derived from the pixels highlighted after the Core thresholding. They are represented by the area of the core and the invasive edges, the percentage of the total area represented by those areas and the perimeter of the core after the density map, that serves as normalization tool for the net invasion area.
- The **density profile parameters** consist of the parameters derived from the analysis of the density profile and the Core thresholding. They are represented by the distances between the Centre of mass and the end of the Core and the one from the end of the core and the end of the invasive edges, and the areas under the curves (obtained by integrals) that belong to one or the other cellular compartment. They give not only information about the distance of invasion but also information about the density of that invasion, since cells invading for the same length may invade in few strings or in large numbers, as mentioned previously.

Table 4.3 INSIDIA parameters

VARIABLE	SEGMENTATION PARAMETERS
Areatotal	Area of the Spheroid
Perimeter	Perimeter of the Spheroid
Xc, Yc	Centre of Mass Coordinates
maxRadius	Maximum Radius of the Spheroid, calculated as half of max Feret's diameter (The longest distance between any two points along the selection boundary, also known as maximum calliper)
minRadius	Minimum Radius of the spheroid, this is calculated as half of the min Feret's diameter (minimum calliper)
Circularity	The circularity of the SS calculated with the formula 4π*Area/Perimeter^2 with a value of 1.0 indicates a perfect circle. As the value approaches 0.0, it indicates an increasingly elongated shape.
RadiusE	Radius calculated using the best fit ellipse (half of the major axis)
SpecSurf	Specific surface: the ratio of the perimeter over its total area, is employed to quantify the degree of "fingering" of the growing tumour. For a perfectly circular shape with radius R, the associated s is given by 2/R, which is the minimum value among all shapes with the same area. The specific surface of a tumour in excess of that of a circle provides a measurement of the roughness of the tumour surface and thus, the degree of "fingering". The formula used is s/(2/maxRadius).
ShapeF	The shape factor is calculated using the following formula (perimeter)^2/4π(area). It gives a minimum value of 1 for a perfect circle and larger values for shapes having a higher ratio of perimeter to area.
EnvArea	the envelope area, defined as the area of the minimal convex polygon containing the whole spheroid
	DENSITY MAP PARAMETERS
AreaCore	Area of pixel with intensity>CT
AreaInvasion	Area of pixel with intensity<CT
PercCore	AreaCore /AreaTotal*100
PercInvasion	AreaInvasion /AreaTotal*100
PeriMap	Perimeter of DensityMap Core
	DENSITY PROFILE PARAMETERS
Profiles.txt	Coordinates of the profiles, conversion is applied to the X coordinates. Y coordinates represent normalized intensities
ACMtotal	Area under the density profile curve (arbitrary units)
ACMcore	Area under the density profile curve below the CT (arbitrary units)
ACMinvasion	Area under the density profile curve over the CT (arbitrary units)
ACMPercCore	(ACMcore/ACMtotal)*100
ACMPercInvasion	(ACMinvasion/ACMtotal)*100
RadiusCore	Core Radius obtained with CT

4.4.3 GLIOMA CELL LINES INVASION INHIBITION MEDIATED BY SRC INHIBITOR, SARACATINIB

To test the new script, before applying it to the analysis of Cav-1 influence over GBM cell lines invasion in a 3D system, we tested two of the cell lines for their invasion, under the influence of the treatment with an inhibitor of Src, Saracatinib-AZD0530. Src has been proved as a mediator of cancer aggressiveness, both in terms of proliferation and invasion, with a particular role in adhesion, cytoskeletal reorganization and EMT (Green et al., 2009; Guarino, 2010; Nam et al., 2013). Three concentrations of the drug were tested (500nM, 1μM and 2μM). Representative pictures can be observed in Figure 4.18.

The observed consistent decrease of the invasive edges, especially with the UP007 where this change was significant (Figure 4.18), proved the reliability of this assay in the invasion observation.

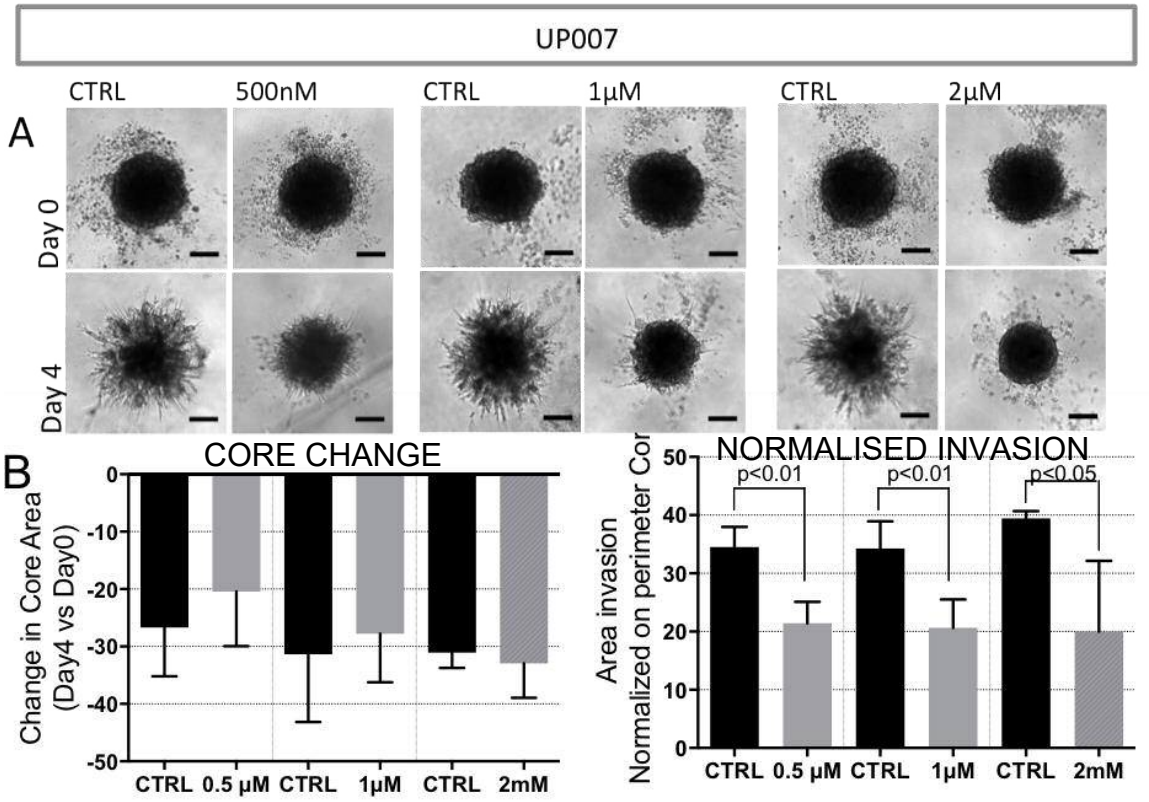

Figure 4.18 Src inhibition leads to a decrease in the invasion capacity in UP007. A: Representative pictures of UP007 at D0 and D4 treated or not with Src inhibitor at 3 three different concentrations, 500nM, 1µM and 2µM. The experiment was performed three times with n=3 replicates each time. CTRL represents cells treated with the same concentration of DMSO as the corresponding treatment. Scale bar 100µm. Graphs in B show the change of the Core, in terms of AUC of the Density profile, between D0 and D4 in all the conditions. Samples were compared using T-TEST between each corresponding CTRL and treatment.

The UP029, on the other hand, showing a very small invasion propensity, make the observation of significant differences difficult (Figure 4.19). Interestingly when UP029 were treated with the Src inhibitor, they stopped invading and the formation of a cloudy material around the aggregates was observed. This material was thought to be the result of the production of other components of the ECM by the cells in the aggregate. Further studies may unravel interesting phenomena and mechanisms.

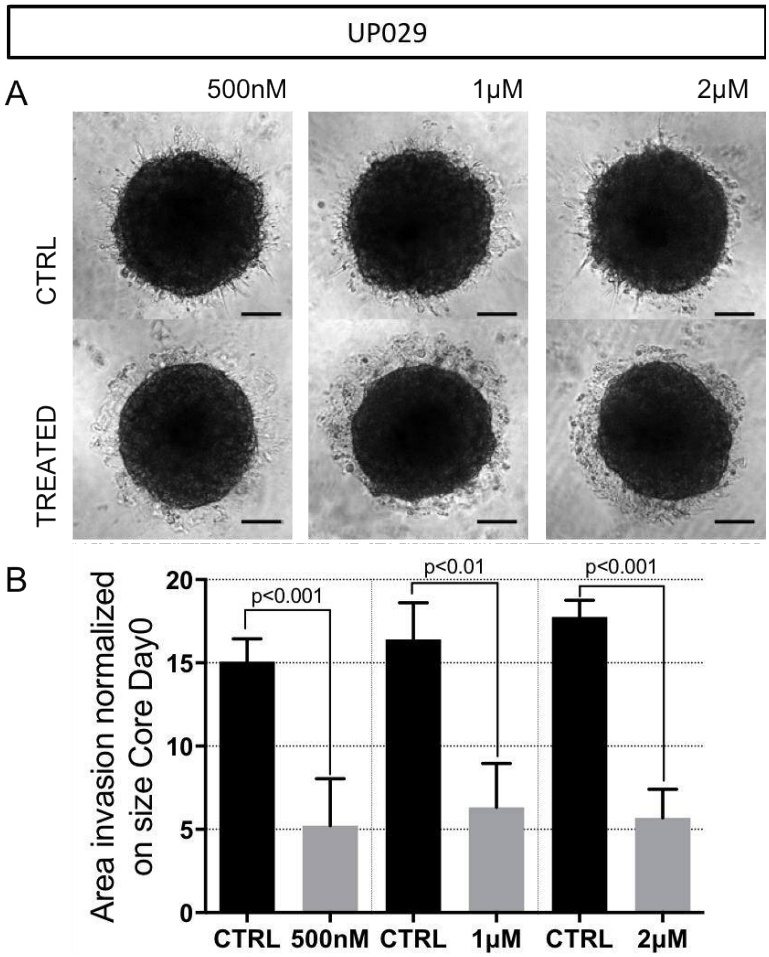

Figure 4.19 Src inhibition leads to a decrease in the invasion capacity in UP029. A: Representative pictures of UP029 at D0 and D4 treated or not with Src inhibitor at 3 three different concentrations, 500nM, 1µM and 2µM. The experiment was performed three times with n=3 replicates each time. CTRL represents cells treated with the same concentration of DMSO as the corresponding treatment. Scale bar 100µm. Graphs in B show the change of the Core, in terms of AUC of the Density profile, between D0 and D4 in all the conditions. Samples were compared using T-TEST between each corresponding CTRL and treatment.

4.5 CONCLUSIONS

The 3D invasion assay has been proven hard to quantify in a shared and unequivocal way. The necessity to compare experiments from different laboratories, with different cell lines and different imaging resources was addressed in this chapter.

We developed a script, INSIDIA (INvasion SpheroIDImageJ Analysis), on the freeware software FIJI for the accurate high-throughput high-content analysis of 3D cancer cell or organoid/spheroid invasion assays. This represents a step towards the collection of the analysis methods, that can be shared and implemented by the users, being the code made available (see Appendix 5). The macro can provide quantitative parameters about spheroids' growth and invasive behaviour, and it can be easily adapted for both fluorescent and bright-field greyscale images.

Despite its efforts, INSIDIA is still not able to quantify the degree of invasion patterns, like single cells or collective invasion. This may need further research in the field, in order to get more information that can guide the implementation.

Possible future applications could be the use of the assay, and therefore the INSIDIA tool, for the study of freshly-resected brain tumours samples, as a personalized tool for the therapeutical decision that can take into consideration also the invasive behaviour of the patients' cancer.

5 CHAPTER 5- MOLECULAR SIGNALING INVOLVED IN CAV-1 ROLE IN INVASION

5.1 INTRODUCTION

Cell movement is an important factor in the neural stem cell niche since quiescent cells can receive the signals to produce new neurons or new macroglia components and, after activation, start moving to restore the functionality of the damaged area.

Invasion in cancer is tightly related to an aberrant EMT, the embryonic process during which cells pass from an epithelial to a mesenchymal phenotype, losing contact with the surrounding cells and breaking through different tissue components for the formation of new sub-tissues and, later on, organs (J. Zhang et al., 2015). Several distinct molecular processes are required to initiate an EMT as discussed in the introductory chapter.

The invasion mechanism can differ from tissue to tissue, and from tumour stage to stage. For this reason understanding the patterns of invasion can help the understanding of the aggressiveness of the tumour, the patients' prognosis and the therapeutical choices (Friedl et al., 2012). Cancer cells can invade as single or groups of cells and with an amoeboid or mesenchymal movement. Every pattern has specific molecular pathways involved, like the production of proteases or the cell-environment/cell contacts or the cytoskeletal rearrangements.

Cancer invasion patterns are particularly relevant for high-grade gliomas, and in particular GBM, Glioma cells display a highly invasive behaviour that leads to the quick spreading of a tumour throughout both hemispheres (Brösicke & Faissner, 2015). This feature causes a dramatically shortening of glioma patients lifespan (Adamson et al., 2009), making it an important prognostic factor.

The challenge for the surgical teams during GBM resection relies in the ability of cancer cells to migrate as single cells even to distant parts of the brain, following the perivascular niche or the white matter tracts. Despite precise and accurate surgical procedures, the removal of all malignant cells is impossible and the relapsing tumours exhibit high resistance to chemotherapy and radiation approaches (Bao et al., 2006; Giese et al., 2003).

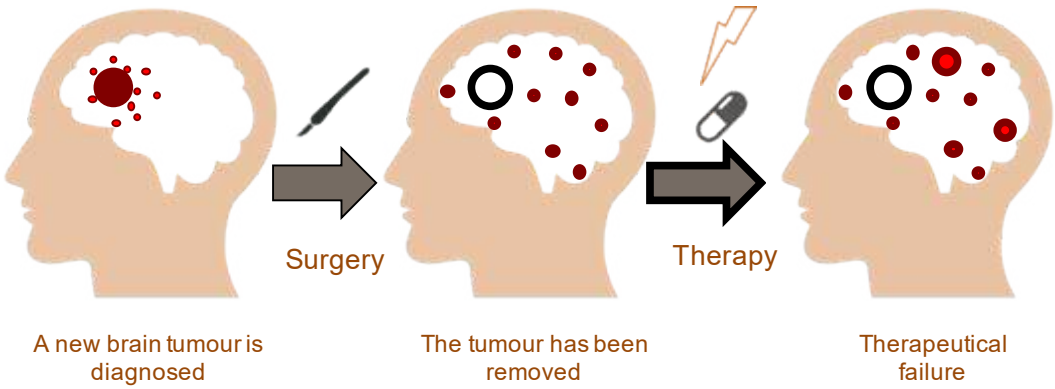

Figure 5.1 The challenge of invasive brain tumours

Invading cells contact both extracellular matrix and other cells and, according to the environment (the white matter tracts and the perivascular niche differ greatly in cellular and extracellular composition), different migration and invasion strategies are adopted for each barrier that have to be overcome. For example, the production of proteases for the digestion of the ECM, rearrangement of the cytoskeleton for the passage into narrow spaces, production and expression of adhesion molecules for the “grabbing” and “pulling” interactions necessary to move to distant sites.

Cav-1 is believed to be part of all these processes since it is involved as a regulator of invasion major components, like proteases activation (Senetta et al., 2013), signal molecules (Y. N. Kim et al., 2000), anchorage-independent growth and migration (H Lee et al., 2000).

5.2 SCOPE OF THE CHAPTER

In this chapter, the analysis on migratory capacity (scratch assay) and the 3D invasion assay based on INSIDIA, are extended to the lentiviral-mediated Cav-1 KD (U87, U373, UP007 and UP029) and the U87 CRIPSR knockdown (KO), for the exploration of the impact of Cav-1.

Molecular mechanisms causing the phenotype modifications were also studied, using several tools, including protein arrays, PCR, Western blot and Immunofluorescence cells grown on plastic, on Matrigel and inside Matrigel, as single cells or invading spheres embedded in the ECM-mimicking material.

5.3 MATERIAL AND METHODS

5.3.1 EXPERIMENTAL CONDITIONS USED FOR EACH APPLICATION

Cells were tested under different culture conditions, as shown in Figure 5.2. For Cav-1 modulation, both Lentiviral KD and CRISPR KO were tested on 2D plastic and in 3D spheres embedded in Growth growth factorreduced (GFR) Matrigel (Corning- cat. 354230). The CRISPR cell lines were also tested after growing on the top of 100% Matrigel or embedded as single cells in a layer of Matrigel 50%.

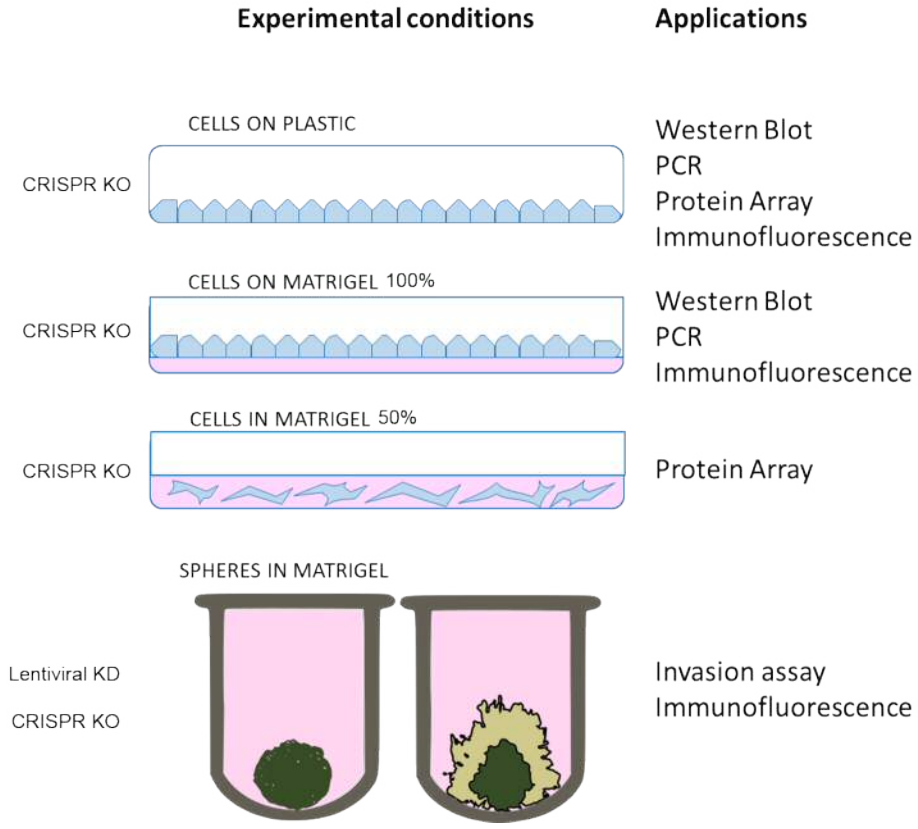

Figure 5.2 Experimental conditions of cell lines adopted for each application described on the side. Cells have been grown in 2D plastic or on the top of a layer of undiluted Matrigel. In 3D cells were cultured as single cells embedded in 1:1 Matrigel:culture medium or as spheres in the ULA round bottom 96-well plates.

5.3.2 PROTEIN ARRAY

Protein arrays kits (R&D Systems, Abingdon, UK) were used to explore the protein expression of human Oncology-related panel (Table 5.1), Angiogenesis-related panel (Table 5.2), and human Phospho-kinases panel (Table 5.3). On each nitrocellulose membrane, antibodies directed against the target proteins were spotted in duplicate, together with positive (reference Spot) and negative control antibodies.

Table 5.1 Proteome Profiler Human XL Oncology Array kit: Detectable proteins. The names of the proteins are accompanied by the duplicate coordinates of their targeting antibodies on the membranes. Reference spots are used as positive controls.

ONCOLOGY ARRAY: DETECTABLE PROTEINS					
Coordinate	Analyte/Control	Coordinate	Analyte/Control	Coordinate	Analyte/Control
A1-2	Reference Spot	D1-2	FoxC2	F17-18	Osteopontin
A3-4	AFP	D3-4	FKHR	F19-20	p27/Kip1
A5-6	Amphiregulin	D5-6	Galectin-3	F21-22	p53
A7-8	Angiopoietin-1	D7-8	GM-CSF	F23-24	PDGF-AA
A9-10	ANGPTL4	D9-10	HCG	G1-2	CD31/PECAM-1
A11-12	ENPP-2/Autotaxin	D11-12	HGF R/c-Met	G3-4	Progesterone R
A13-14	AXL	D13-14	HIF-1alpha	G5-6	Progranulin
A15-16	BCL-X	D15-16	HNF-3beta	G7-8	Prolactin
A17-18	CA125/MUC-16	D17-18	HO-1/HMOX1	G9-10	Prostasin
A19-20	E-Cadherin	D19-20	ICAM-1/CD54	G11-12	E-Selectin
A21-22	VE-Cadherin	D21-22	CD25/IL-2 R alpha	G13-14	Maspin
A23-24	Reference Spot	D23-24	IL-6	G15-16	PAI-1/Serpin E1
B3-4	CAP-G	E1-2	CXCL8/IL-8	G17-18	SNAIL
B5-6	CA-9	E3-4	IL-18 Bpa	G19-20	SPARC
B7-8	Cathepsin B	E5-6	KLK-3/PSA	G21-22	Survivin
B9-10	Cathepsin D	E7-8	KLK-5	G23-24	Tenascin-C
B11-12	Cathepsin S	E9-10	KLK-6	H1-2	THBS-1
B13-14	CEACAM-5	E11-12	Leptin (OB)	H3-4	TIE-2
B15-16	Decorin	E13-14	Lumican	H5-6	UPA-1
B17-18	DKK-1	E15-16	CCL2/MCP-1	H7-8	VCAM-1
B19-20	DLL-1	E17-18	CCL8/MCP-2	H9-10	VEGF
B21-22	EGF R/ErbB1	E19-20	CCL7/MCP-3	I1-2	Reference Spot
C3-4	Endoglin/CD105	E21-22	M-CSF	I23-24	Negative Control
C5-6	Endostatin	E23-24	Mesothelin		
C7-8	Enolase 2	F1-2	CCL3/MIP-1alpha		
C9-10	eNOS	F3-4	CCL20/MIP-3alpha		
C11-12	EpCAM	F5-6	MMP-2		
C13-14	ER-alpha	F7-8	MMP-3		
C15-16	ErbB2	F9-10	MMP-9		
C17-18	ErbB3	F11-12	MSP/MST1		
C19-20	ErbB4	F13-14	MUC-1		
C21-22	FGF basic	F15-16	Nectin-4		

Table 5.2 Proteome Profiler Human Angiogenesis Array kit: Detectable proteins. The names of the proteins are accompanied by the duplicate coordinates of their targeting antibodies on the membranes. Reference spots are used as positive controls.

ANGIOGENESIS: DETECTABLE PROTEINS					
Coordinate	Analyte/Control	Coordinate	Analyte/Control	Coordinate	Analyte/Control
A1-2	Reference Spot	C1-2	GDNF	D21-22	PIGF
A5-6	Activin A	C3-4	GM-CSF	D23-24	Prolactin
A7-8	ADAMTS-1	C5-6	HB-EGF	E1-2	Serpin B5/Maspin
A9-10	Angiogenin	C7-8	HGF	E3-4	Serpin E1/PAI-1
A11-12	Angiopoietin-1	C9-10	IGFBP-1	E5-6	Serpin F1/PEDF
A13-14	Angiopoietin-2	C11-12	IGFBP-2	E7-8	TIMP-1
A15-16	Angiostatin/Plasminogen	C13-14	IGFBP-3	E9-10	TIMP-4
A17-18	Amphiregulin	C15-16	IL-1 beta	E11-12	Thrombospondin-1
A19-20	Artemin	C17-18	CXCL8/IL-8	E13-14	Thrombospondin-2
A23-24	Reference Spot	C19-20	LAP (TGF-beta 1)	E15-16	uPA
B1-2	Tissue Factor/Factor III	C21-22	Leptin	E17-18	Vasohibin
B3-4	CXCL16	C23-24	CCL2/MCP-1	E19-20	VEGF
B5-6	DPPIV/CD26	D1-2	CCL3/MIP-1 alpha	E21-22	VEGF-C
B7-8	EGF	D3-4	MMP-8	F1-2	Reference Spot
B9-10	EG-VEGF	D5-6	MMP-9	F23-24	Negative Control
B11-12	Endoglin/CD105	D7-8	NRG1-beta 1		
B13-14	Endostatin/Collagen XVIII	D9-10	Pentraxin 3		
B15-16	Endothelin-1	D11-12	PD-ECGF		
B17-18	FGF acidic	D13-14	PDGF-AA		
B19-20	FGF basic	D15-16	PDGF-AB/PDGF-BB		
B21-22	FGF-4	D17-18	Persephin		
B23-24	FGF-7/KGF	D19-20	CXCL4/PF4		

Table 5.3 Proteome Profiler Human Phospho-Kinase Array kit: Detectable proteins. The names of the proteins are accompanied by the duplicate coordinates of their targeting antibodies on the membranes. Reference spots are used as positive controls.

PHOSPHO-KINASES: DETECTABLE PROTEINS					
Coordinate	Analyte/Control	Coordinate	Analyte/Control	Coordinate	Analyte/Control
A1-2	Reference Spot	C7-8	AMPK alpha2 (T172)	E9-10	STAT5b (Y699)
A3-4	p38 alpha (T180/Y182)	C9-10	beta-Catenin	E11-12	STAT3 (Y705)
A5-6	ERK1/2 (T202/Y204, T185/Y187)	C11-12	p70 S6 Kinase (T389	E13-14	p27 (T198)
A7-8	JNK pan (T183/Y185, T221/Y223)	C13-14	p53 (S15)	E15-16	PLC gamma-1 (Y783)
A9-10	GSK-3 alpha/beta (S21/S9)	C15-16	c-Jun (S63)	F1-2	Hck (Y411)
A13-14	p53 (S392)	D1-2	Src (Y419)	F3-4	Chk-2 (T68)
A17-18	Reference Spot	D3-4	Lyn (Y397)	F5-6	FAK (Y397)
B3-4	EGF R (Y1086)	D5-6	Lck (Y394)	F7-8	PDGF R beta (Y751)
B5-6	MSK1/2 (S376/S360)	D7-8	STAT2 (Y689)	F9-10	STAT5a/b (Y694/Y699)
B7-8	AMPK alpha1 (T174)	D9-10	STAT5a (Y694)	F11-12	STAT3 (S727)
B9-10	Akt (S473)	D11-12	p70 S6 Kinase (T421/S424)	F13-14	WNK-1 (T60)
B11-12	Akt (T308)	D13-14	RSK1/2/3 (S380/S386/S377)	F15-16	Pyk2 (Y402)
B13-14	p53 (S46)	D15-16	eNOS (S1177)	G1-2	Reference Spot
C1-2	TOR (S2448)	E1-2	Fyn (Y420)	G3-4	PRAS40 (T246)
C3-4	CREB (S133)	E3-4	Yes (Y426)	G9-10	Negative Control
C5-6	HSP27 (S78/S82)	E5-6	Fgr (Y412)	G11-12	HSP60
		E7-8	STAT6 (Y641)	G17-18	Negative Control

The U87 CRISPR KO were cultured in 2D plastic and embedded in GFR Matrigel (Matrigel) as single cells, to select only cells interacting with the ECM.

After four days, cells in 2D were lysed directly following the procedure already described in Chapter 2 (Western Blot section) and total protein amount was quantified, whilst Matrigel surrounding the 3D cell cultures was dispersed using Cell Recovery solution (Corning, REF. 354253). Wells were washed with ice-cold PBS and the solution was applied for the resuspension of the cells/aggregates and the transfer in appropriate tubes. The suspension of

cellular material and Matrigel in the recovery solution was left on ice for one hour, with shaking, then cells were centrifuged at 200g for 10 minutes, washed with ice-cold PBS and centrifuged again. After recovering from Matrigel, cells were lysed, and total protein amount was quantified.

A total amount of 200µg of protein lysate was loaded on each membrane and incubated on a rocking shaker over night at 4°C. The following day membranes were washed to remove the unbound material and incubated with the second set of biotinylated antibodies. Detection was mediated by Streptavidin-HRP incubation and chemiluminescent detection reagents application. The resulting signals in each spot were proportional to the protein expression of the markers under examination. Signals were detected and recorded by the same procedure as the Western Blot section in Chapter 2, following the kit instructions.

Each signal was normalized to the negative and the positive control and only signals significantly higher than the negative control (>2 fold) were further used for the analysis. A fold-change value was derived by the ratio CAV+/CAV-, and ratios comprised between 0 and 1 were converted in a negative signal by the formula y=-1/x, where ‘x’ is the original ratio and ‘y’ the converted one. Only fold changes >1.25 and <-1.25 were then taken in further consideration.

Fold changes were plotted in a heat map using Graph Pad Prism.

Further studies about pathway and clustering of the significantly modulated proteins were conducted via KEGG Pathway (http://www.genome.jp/kegg/pathway.html), DAVID (https://david.ncifcrf.gov/), and MINT (http://mint.bio.uniroma2.it/HomoMINT/Welcome.do).

Confirmation of protein expression data was obtained with Western Blot (described in Chapter 2 and in the following section).

5.3.3 WESTERN BLOT ANALYSIS

U87 carrying the CRISPR-mediated Cav-1 KO were collected and processed following the procedure explained in Chapter 2.

To assess the ability of cells to respond to stress, we obtained samples from serum-stimulated cells. Cell lines were seeded in normal conditions until they reached 80% confluence. Then the full medium was replaced with a serum-deprived one. After 16 hrs serum was reintroduced for 10 minutes before collecting and lysing the cells, as usual. The serum stimulation procedure was used to test the expression of phospho-proteins in cells grown on plastic.

Table 5.4 shows the antibody used for the protein expression detection and their dilution.

The luminescent bands detected were quantified by FIJI software and plotted for comparison. Phospho-proteins were always normalized on their total form, while the total forms were normalised on the Housekeeping gene, like GAPDH, Beta-Actin or Vinculin.

Table 5.4 Antibodies for the detection of target proteins and their use across applications, Western Blots (WB), Immunofluorescence (IF) on 2D plastic and on 2D Matrigel and in 3D Matrigel-embedded spheroids. Suppliers for each antibody are indicated in the table.

CAT	PROTEIN	WB DILUTION	IF 2D DILUTION	IF 3D DILUTION
		CELL SIGNALING		
9272	AKT	1:1000		
9271	AKT SER473	1:1000		
9275	AKT THR308	1:1000		
3238	CAV1	1:1000	1:250	
3267	CAV1 XP	1:1000	1:800	1:400
3195	E CADHERIN	1:1000	1:400	
3570	CD44	1:1000	1:50	1:20
3285	FAK	1:1000		
8556	FAK TYR397	1:1000		
2402	HSP27	1:1000		
2401	HSP27 S82	1:1000		
2123	SRC	1:1000		
2101	SRC TYR418	1:1000		
12713	UPAR	1:1000	1:50	1:25
2118	GAPDH	1:1000	1:100	1:50
		ABCAM		
ab58802	CATHEPSIN B	0.25 µg/ml	1:200	1:100
ab6313	CATHEPSIN D	1:1000	1:200	1:100
ab33333	CORTACTIN		1:1000	1:500
ab38929	MMP1	1:5000	1:100	1:50
ab192033	PVRL4 (NECTIN-4)	1:1000		
ab85762	THROMBOSPONDIN-1 (TSP1)	1 µg/ml		
ab169754	UPA	1:1000		
		SIGMA		
V9131	VINCULIN	1:400	1:400	1:200
A5441	BETA ACTIN		1:100	1:100

5.3.4 RT-PCR FOR GENE EXPRESSION ANALYSIS

The RT-PCR analysis was performed on CRIPSR-mediate Cav-1 KO U87 cell line and its positive control on cells growing in 2D on plastic and on a layer of Matrigel, as shown in Figure 5.2.

5.3.4.1 TOTAL RNA EXTRACTION

RNA extraction was obtained using TRIzol® Reagent (Life Technologies). Cells were collected in microcentrifuge tubes and resuspended in ice-cold PBS to eliminate any residual presence of medium. After pelleting at 300g for five minutes, cells were resuspended in TRIzol reagent and lysis was performed by repetitive pipetting.

200µL of chloroform every 1mL of TRIzol were then added, samples were mixed by vortexing and then let incubate at room temperature (RT) for few minutes. After centrifugation (12,000g for 15 minutes at 4˚C), the aqueous top phase, containing RNA, was collected and combined with 500µL of isopropyl alcohol. Incubation at RT for 10 minutes was followed by a centrifugation step (12,000g for 10 min at 4˚C) for the precipitation of the isolated RNA.

The supernatant was removed, and the RNA pellet was washed with 75% ethanol (1mL) and centrifuged (7500g for five minutes at 4˚). The last two steps were repeated twice.

RNA was let dry for 5-10 minutes at RT and then dissolved in DEPC-treated water.

Isolated RNA was quantified by diluting it 1:40 in DEPC-treated water and analysing the solution with a spectrophotometer using absorbance at 260 and 280. The ration 260/280 was considered acceptable when over 1.6, while the RNA concentration was derived by considering that 1OD at 260 equals 40µg/mL of RNA. Extracted RNA was labelled and stored at -80˚C.

5.3.4.2 REVERSE-TRANSCRIPTION

The reverse-transcription step was performed using the High-Capacity cDNA Reverse Transcription Kit (Applied Biosystems). This is based on the preparation of a 2x RT master mix that is diluted 1:1 with the RNA and amplifies the RNA using Random Primers.

Before the reverse-transcription samples and kit components were defrosted on ice.

The 2x RT master mix for the reaction was prepared as follow:

Component	Volume/Reaction (µL)
10x RT Buffer	5
25x dNTP Mix (100mM)	2
10x RT Random Primers	5
Multiscribe Reverse Transcriptase	2.5
RNase Inhibitor	2.5
Nuclease-free H_2O	8
Total per reaction	25

RNA was diluted to achieve 5µg each 25µL sample. The cDNA RT reaction was then prepared by pipetting 25µL of 2x RT Master mix in PCR tubes and adding 25µL of RNA sample. After pipetting, tubes were sealed and placed in the thermal cycler for the following protocol:

	Step 1	Step 2	Step 3	Step 4
Temperature (˚C)	25	37	85	4
Time (min)	10	120	5	∞

Reverse-transcribed samples were stored at -20˚C.

5.3.4.3 PCR FOR THE ANALYSIS OF GENE EXPRESSION

PCR was performed using a Hot-Start Taq DNA Polymerase (QIAGEN- cat. 203205). A low amount of cycles doesn't allow the amplicons to reach the plateau, therefore it is possible to compare gene expression in different samples.

The PCR mix was assembled as follow:

Component	Volume (µL)
10 PCR Buffer	2
dNTPs (10mM)	0.4
Hot-Start Taq Pol	0.1
Forward-primer (10mM)	1
Reverse-primer (10mM)	1
cDNA	1
Molecular Biology Grade Water	14.5
Total Volume	20

The PCR mix freshly assembled is put on a thermocycler for the following steps:

	STEP		TEMPERATURE (˚C)	TIME
	Step 1	Enzyme Activation	95	15 minutes
33 CYCLES	Step 2	DNA denaturing	94	30 seconds
	Step 3	Primers Annealing	56	45 seconds
	Step 4	Amplification	72	90 seconds
	Step 5	Final Amplification	72	10 minutes
	Step 6	Until analysis	4	

After the amplification samples were run on a 2% agarose gel. 2g of agarose (Thermo Fisher Scientific- cat. 16500500) was dissolved in 100 mL TBE (Thermo Fisher Scientific- cat. 15581044) by rapid heating. During cooling, 30µL of Ethidium Bromide (Thermo Fisher Scientific- cat. 15585011) were added and the solution was poured in a preformed cassette, with the appropriate gel comb, for the formation of the gelatinised block and the loading wells.

After the complete set of the gel, this was removed from the cast, placed in an electrophoresis tank and submerged in TBE. PCR products were mixed with an appropriate amount of 5x Gel Loading Buffer (Thermo Fisher Scientific- cat. 10482028) and loaded into the wells. One lane was reserved for the DNA ladder (Thermo Fisher Scientific- 10787018).

The gel was allowed to run for 40 minutes at 90V to allow separation of the DNA bands.

As soon as the electrophoresis run is complete, gels were imaged by ChemiDoc Scanner (Biorad), after applying a filter for Ethidium Bromide (580 nm).

Bands were quantified for their integrated density with FIJI and plotted in Graph Pad.

In Table 5.5 it is reported all the genes of interest that have been investigated by PCR.

Table 5.5 Genes whose expression has been investigated by PCR, and their main involvement in cellular processes.

NUMBER	GENE	PROTEIN	FUNCTION
1	ITGAV	Integrin Subunit Alpha V	Adhesion
2	ITGA3	Integrin Subunit Alpha 3	Adhesion
3	ITGA5	Integrin Subunit Alpha 5	Adhesion
4	ITGB1	Integrin Subunit Beta 1	Adhesion
5	ITGB3	Integrin Subunit Beta 3	Adhesion
6	ITGB5	Integrin Subunit Beta 5	Adhesion
7	MMP2	Matrix Metallopeptidase 2	Invasion
8	MMP9	Matrix Metallopeptidase 9	Invasion
9	MMP14	Membrane-Type-1 Matrix Metalloproteinase	Invasion
10	MMP7	Matrix Metallopeptidase 7	Invasion
11	MMP10	Matrix Metallopeptidase 10	Invasion
12	MMP1	Matrix Metallopeptidase 1	Invasion
13	MMP8	Matrix Metallopeptidase 8	Invasion
14	MMP3	Matrix Metallopeptidase 3	Invasion
15	CTSK	Cathepsin K	Invasion
16	CTSB	Cathepsin B	Invasion
17	CTSL	Cathepsin L	Invasion
18	CTSS	Cathepsin S	Invasion
19	CTSH	Cathepsin H	Invasion
20	CTSD	Cathepsin D	Invasion
21	PLAU	Urokinase Plasminogen Activator (UPA)	Invasion
22	PLAUR	Urokinase Plasminogen Activator Receptor (UPAR)	Adhesion/invasion
23	TIMP1	TIMP Metallopeptidase Inhibitor 1	Inhibitor of invasion (MMPs)
24	TIMP3	TIMP Metallopeptidase Inhibitor 3	Inhibitor of invasion (MMPs)
25	SERPINE1	Plasminogen Activator Inhibitor 1 (PAI1)	Inhibitor of invasion (UPA)
26	CD44	CD44	Adhesion (HA)
27	VIM	Vimentin	Mesenchymal Phenotype
28	CDH1	E-Cadherin	Adhesion/Epitelial Phenotype
29	GAPDH	Glyceraldehyde-3-Phosphate Dehydrogenase	Positive control

Primers were designed using the NCBI tool “Pick Primers” (https://www.ncbi.nlm.nih.gov/tools/primer-blast/index.cgi). Primers requisites were:

- A melting temperature range between 57 and 63˚C;
- A GC content between 45 and 60%;
- A primer length between 18-25 bases;
- A maximum product size of 1000 base pairs.

Among the available resulting options, primers with an amplicon size between 300 and 700 kb were selected and then blasted again on NCBI (https://blast.ncbi.nlm.nih.gov/Blast.cgi) to detect eventual cross-matches that could allow non-specific amplification. The annealing temperature was obtained by a Thermo Fisher Scientific tool, Tm Calculator[1] (Allawi & Santalucia, 1997).

At the end of the validation process, final primers for the gene expression analysis were selected and are reported in Table 5.6 together with their predicted amplicon size and their annealing temperature.

Other primers used during the validation properties are reported in Appendix 4.

[1] https://www.thermofisher.com/uk/en/home/brands/thermo-scientific/molecular-biology/molecular-biology-learning-center/molecular-biology-resource-library/thermo-scientific-web-tools/tm-calculator.html

Table 5.6 List of validated pairs of primers for post-invasion analysis

GENE	FORWARD SEQUENCE	REVERSE SEQUENCE	PREDICTED SIZE (Kb)	T°a
ITGAV	GGGAAGCAAAGGACCGTCTG	ATGGTACAATGGGGCACAGG	671	54
ITGA3	CAAGGATGACTGTGAGCGGA	TTTTGGGGTGCAGGATGAAG	497	52.1
ITGA5	CCTATGAGGCTGAGCTTCGG	GGTGCAGTTGAGTCCCGTAA	548	54
ITGB1	CCGCGCGGAAAAGATGA	ATGTCATCTGGAGGGCAACC	252	53
ITGB3	ATGACGGGCAGTGTCATGTT	TTAGGTTCAGCTTGGGCCTG	526	53
ITGB5	TACTCCAGACTGCAGCTTGTC	CCAGCATGAGATGGGGTCTT	504	53.3
MMP2	CGCATCTGGGGCTTTAAACATA	CTGTCTGGGGCAGTCCAAAG	503	51.9
MMP9	CAGTCCACCCTTGTGCTCTTC	TGCCACCCGAGTGTAACCAT	102	55
MT1-MMP	GGAAAATGAGGACGTGCAGC	ACTGGGTCTCACTCTCCCAA	466	53.9
MMP7	CTACAGTGGGAACAGGCTCA	GTGAGCATCTCCTCCGAGAC	486	53.1
MMP10	AGATCCCACTGGAACCCTGA	ATCCTGGCATTGGGGTCAAA	443	53.5
MMP1	ATGCACAGCTTTCCTCCACT	GTTGTCCCGATGATCTCCCC	513	53
MMP8	TCCCTGAAGACGCTTCCATTT	TTTTCCAGGTAGTCCTGAACAGT	110	51.9
MMP3	CCTAGGTTTCCCTCCAACCG	AGCCCATTTGAATGCCCTGTA	491	53.3
CATK	GAGGCTTCTCTTGGTGTCCA	CATTGGTCATGTAGCCCCCT	367	53.6
CATB	GTCTTCAGGCCTATGGAGAGC	CAGATCCGGTCAGAGATGGC	462	54.5
CATL	CGTCTACCCCGAACTCTGC	CCTTCCTGGGCTTACGGTTT	436	54.3
CATS	TCCACTTTGTCCCCAAGACC	GGAACTCTCAGGGAACTCATCA	524	52.8
CATH	CACCAGTGCATGTGCTTTTGA	GCATCATCCGTCTCTTGTGG	538	52.5
CATD	CTCTAGTTCCCAAGGCGTCC	CCGGGACACTGAACAGGTAG	496	54.2
UPA	GCGACTCCAAACGAACTGTG	ATGCACCATGCACTCTTGGA	373	53.3
UPAR1	GCTGGTGGAGAAAAGCTGTA	CCTTCTTCACCTTCCTGGAT	291	50.5
TIMP-1	TTCTGCAATTCCGACCTCGT	CGGGACTGGAAGCCCTTTT	452	53.2
TIMP-3	GGAGGGCCGATGAGGTAATG	CGGATCACGATGTCGGAGTT	543	53.6
PAI-1	ATACTGAGTTCACCACGCCC	CACTTGGCCCATGAAAAGGAC	500	53.4
CD44	GACACATATTGCTTCAATGCTTCAGC	GATGCCAAGATGATCAGCCATTCTGGAAT	419	53.4
VIMENTIN	GTGGACCAGCTAACCAACGA	CCACTTCACAGGTGAGGGAC	511	54
CDH1	GAACTGCAAAGCACCTGTGA	TCAGCGTGACTTTGGTGGAA	463	52.3
GAPDH	CTCTGCTCCTCCTGTTCGAC	GCGCCCAATACGACCAAATC	121	54.1

5.3.5 IMMUNOFLUORESCENCE

Immunofluorescence analysis was performed implementing the protocol described in Ylivinkka at al. (Ylivinkka et al., 2017).

After the 3D invasion assay (day 2 for the U87 cell lines), blocks of Matrigel containing invading/non-invading spheroids were transferred into 24-well plates, using a 1000mL pipette with a resected tip, to avoid damaging the 3D structure. This allowed an easier approach in the washing and staining process with a reduced risk of touching the samples and thus compromising their integrity.

After transferring into the 24-well plate, blocks were washed with PBS and fixed with 4% formaldehyde for 30 minutes at room temperature. After fixation, formaldehyde was removed and blocks washed again with PBS twice. Blocking and permeabilization were performed simultaneously by incubating blocks in PBS 3% BSA 0.3% Tween-20 (Blocking Buffer) for one hour at room temperature and with a gentle shake.

Incubation with primary antibodies was performed in Blocking Buffer overnight at 4˚C with a gentle shake. The antibodies used and their dilutions for this technique are reported in Table 5.4.

The blocks were then washed with PBS 0,1%Tween-20 three times for 10 minutes at room temperature with a gentle shake and then incubated for one hour at room temperature with secondary antibody, Hoechst 33342 (Thermo Fisher Scientific- cat. 62249) and Alexa Fluor 647 phalloidin (Life Technologies- cat. A22287) all diluted in Blocking Buffer.

After a further three PBS washings, the blocks were washed briefly with milli-Q water and then transferred onto the imaging slides.

The imaging was achieved using Multispot Microscope Slides (Thermo Fisher Scientific- cat. 9991095). As shown in Figure 5.3, blocks were positioned at the centre of each spot and Matrigel was cut away with a scalpel as much as possible, until only the Matrigel containing the cellular material was left (Figure 5.3B). This was a crucial step because an excess of Matrigel results in a sample thickness unsuitable for confocal imaging. The multispot slides were

chosen because the thickness provided by the extra step created by the edge of the spot onto the glass provides help for the preservation of the spheroids 3D structure, while also allowing an easier localization of the samples during imaging.

After this step samples were covered with ProLong™ Gold Antifade Mountant (Thermo Fisher Scientific- cat. P10144), covered with a coverslip and sealed with nail polish.

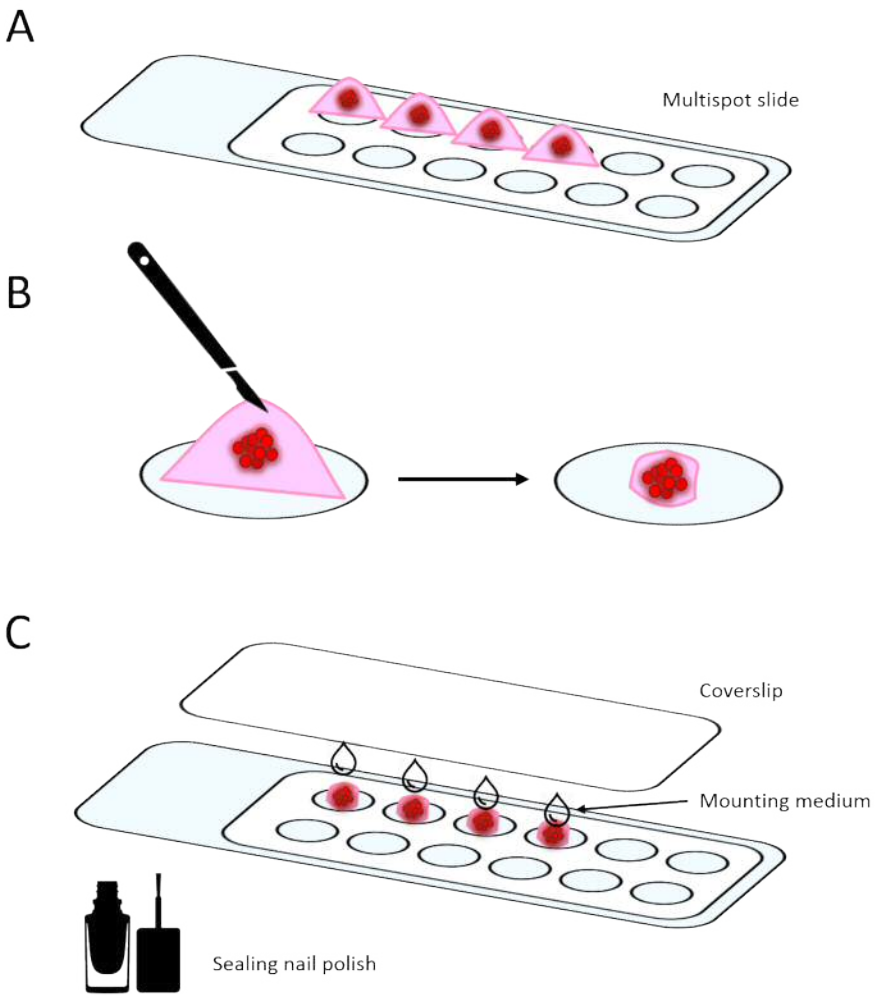

Figure 5.3 Mounting steps for 3D spheres embedded in Matrigel. A: Matrigel blocks were transferred onto a Multispot slide, one every spot. B: Extra Matrigel was trimmed with a scalpel. C: Mounting medium was applied to each block before covering with Coverslip and sealing with nail polish.

For the immunofluorescence of 2D cells growing on plastic, cells were seeded, fixed, washed and stained on Black Clear Bottom 96-Well Polystyrene Microplates (Corning- cat. 3610), then imaged directly from the plates. Cells

growing on Matrigel were seeded on Chamber slides with a removable 12 well silicone chamber (IBIDI, cat. 81201) previously coated with 100% Matrigel. After four days, cells were washed, fixed and stained as previously described. Before imaging the silicon chamber was removed, mounting medium applied and slides were covered with a coverslip and sealed with nail polish.

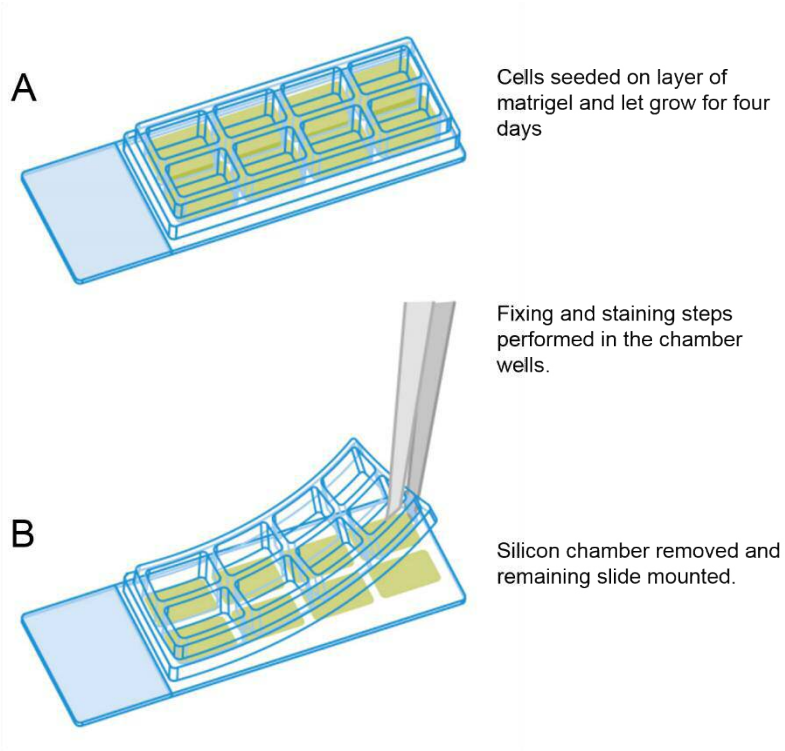

Figure 5.4 Procedure for Immunofluorescence staining of cells growing on Matrigel. A: Cell lines were seeded on the top of the Matrigel-coated wells formed by the silicon chamber. Fixation, permeabilization and staining were performed in the chamber wells as well. B: Before imaging, the silicon chamber was removed, Matrigel layers coated with stained cells were covered with mounting medium, coverslip was applied, and nail polish was used for sealing Adapted from https://ibidi.com/img/cms/products/labware/open_removable/E_8XXXX_Chamber_removable/IN_80841_8Well_Chamber.pdf.

The imaging was performed with a Leica SP5 inverted confocal laser scanning microscope. 40x and 63x oil-immersion objectives were used. Excitations of 405 nm (Hoescht), 488 nm (mouse), 453 nm (rabbit) and 633 nm (647-Phalloidin) nm were chosen for each fluorophore under examination while gain and offset settings were optimized for each fluorescent channel within an experiment. Images were recorded and captured using two sequential scans to avoid fluorescence channel crosstalk. Images were scanned with a line average of three to reduce noise (100 Hz).

5.3.6 IMMUNOHISTOCHEMISTRY

The immunohistochemistry protocol was prepared with the help of Christopher Von Ruhland PhD, from the School of Medicine, as an expert in sample processing for both optical and electron microscopy.

After the invasion assay (2 days for the U87), Matrigel blocks were washed and fixed in formaldehyde 4% glutaraldehyde 0.1% for one hour at room temperature. After the fixation blocks were transferred in 1.5 mL tubes, where a layer of liquified low-melting agarose had just been deposited. They were then covered with extra low melting agarose, to allow total embedding, and let gelify at room temperature overnight. After resuspension in PBS the newly formed blocks were processed as normal tissue samples:

DEHYDRATION STEPS			
Solution	Incubation Time (min)	Solution	Incubation Time (min)
50% Ethanol	10	2:1 Ethanol: Xylene	10
70% Ethanol	10	1:1 Ethanol: Xylene	10
80% Ethanol	10	1:2 Ethanol: Xylene	10
95% Ethanol	10	100% Xylene	10
100% Ethanol	10	100% Xylene	10
100% Ethanol	10	100% Xylene	10
100% Ethanol	10	100% Xylene	10

After all the incubations samples were embedded in Paraffin Wax overnight. Then the sample was positioned, and the paraffin was let harden in each block.

To enhance the outcome of the sectioning, the blocks were cut by ultramicrotome ad transferred onto slides and incubated overnight at 37˚C to allow the spreading of the paraffin and the firm adhesion to the microscope slides.

Before proceeding with the staining protocol, slides were deparaffinized and rehydrated with the steps resumed in the following table.

DEPARAFFINATION STEPS	
Solution	Incubation Time (min)
Xylene 100%	3
Xylene 100%	3
1:1 Ethanol: Xylene	3
95% Ethanol	3
70% Ethanol	3
50% Ethanol	3
Running cold tap water	rinse

Slides were kept in water until ready to perform antigen retrieval.

Slides were placed in a beaker with Sodium Citrate pH 6.0, which was brought to boil, with a Bunsen flame. Once boiling, the flame was lowered, and the slides were left inside for 30 minutes.

After 30 minutes, tap water was let run into the Becker to simultaneously cool down the solution and block the reaction.

Once slides have been washed in Optimax washing buffer (Biogenex Laboratories- cat. HK5835K), they were partially dried with absorbing paper towel and samples areas were isolating using pap-pen (Abcam- cat. ab2601). Primary antibody diluted in 0.6% BSA in Optimax (Reagent diluent) were applied

on the samples and an incubation overnight at 4˚C in a humid chamber followed. Primary antibody was Beta-Actin (Sigma) diluted 1:100.

The following day, slides were re-equilibrated at room temperature for one hour before washing again and applying the secondary antibody diluted in reagent diluent. After an incubation of one hour at room temperature, slides were washed again and then incubated in DAB solution. DAB solution is a mix of Diaminobenzidine dihydrochloride (DAB) and Hydrogen Peroxide (for the DAB activation). 10 ml of DAB 5g/L were dissolved in 90mL of Optimax washing buffer and the 8 drops of hydrogen peroxide were added before mixing. Incubation with DAB solution was performed for 5 minutes before blocking the reaction by transferring the slides into a container with tap water.

Counterstain with Haematoxylin (Sigma- cat. GHS1128) was achieved by incubating a drop of the solution on each sample for 1 minute and then was in running tap water.

After the counterstain slides were dehydrated again as follow:

DEHYDRATION STEP	
Solution	Incubation Time (min)
50% Ethanol	3
70% Ethanol	3
80% Ethanol	3
95% Ethanol	3
100% Ethanol	3
100% Ethanol	3
1:1 Ethanol: Xylene	3
100% Xylene	Until ready for mounting

Slides were mounted on coverslips using DPX mounting medium (Sigma- cat. 06552) and left overnight to dry in the dark.

Images of the slides were taken using a Leica DMI6000 inverted microscope.

5.4 RESULTS AND DISCUSSION

5.4.1 CAV-1 DRIVES INVASIVE PHENOTYPE ON 3D INVASION ASSAY MODEL

As reported in Chapter 3, the scratch assay of the lentiviral transfected GBM cell lines revealed that Cav-1 can drive a migratory phenotype. In chapter 4 we developed a quantitative tool to measure invasion within a 3D matrix.

Here, we explored the impact of Cav-1 genetic KD and KO upon invasion in the 3D model. We tested the ability of the cells to move through an extracellular matrix using the 3D invasion assay, described in the previous chapter, and quantified results with INSIDIA (Moriconi et al., 2017). Typical images and the quantification of the invasion assay are reported in Figure 5.5 for U87 and U373, and Figure 5.6 for UP007 and UP029, these experiments conducted in cells carrying a lentiviral-mediated inhibition of Cav-1 expression.

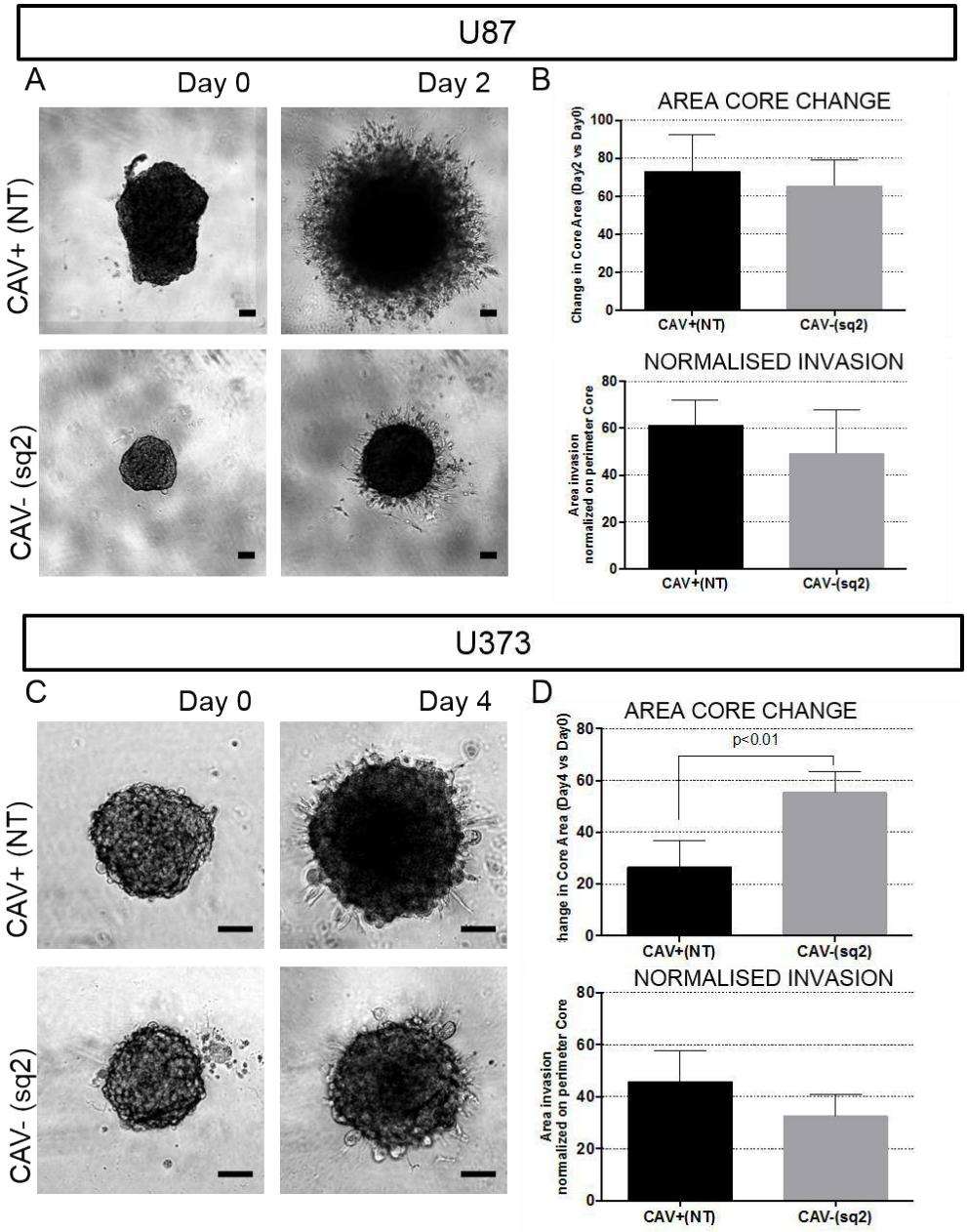

Figure 5.5 Invasion assay on two cell lines transfected for the down-regulation of Cav-1. Seeding density: 1000 cells/well for the U87 (A, B), 5000 cells/well for the U373 (C, D). Experiments were repeated three times and replicates were analysed according to both density profile and density map. A, C: Scale bar 100μm. B, D: Graphs represent the Change in the Core and the amount of invasive edges according to the density map analysis, normalised on the perimeter of the Core. Statistical analysis unpaired two-tailed T-Test (p-value is indicated when relevant).

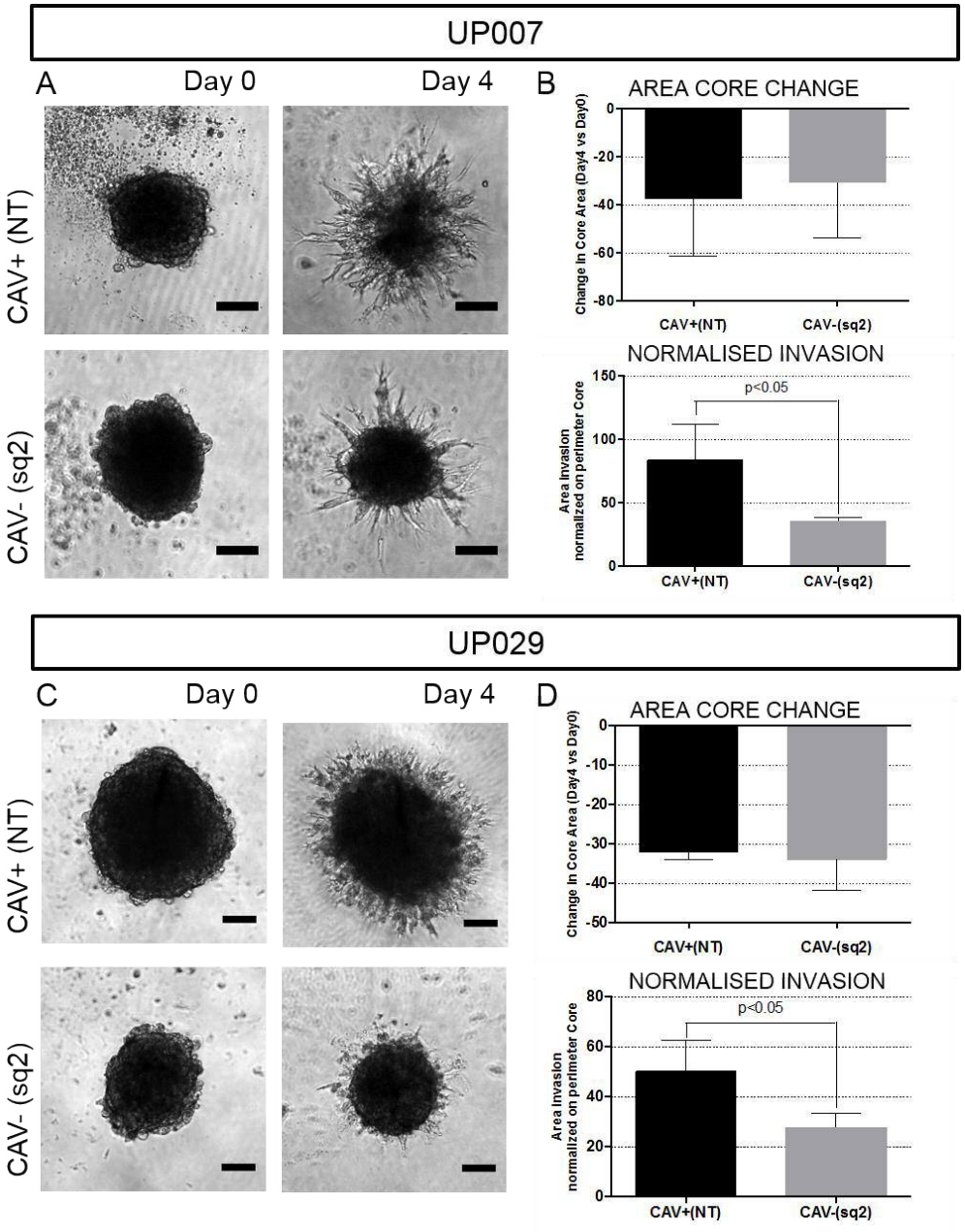

Figure 5.6 Invasion assay on two cell lines transfected for the down-regulation of Cav-1. Seeding density: 5000 cells/well for both UP007 (A, B) and U373 (C,D). Experiments were repeated three times and replicates were analysed according to both density profile and density map. A, C: Scale bar 100µm. B-D: Graphs represent the Change in the Core and the amount of invasive edges according to the density map analysis, normalised on the perimeter of the Core. Statistical analysis unpaired two-tailed T-Test (p-value is indicated when relevant).

In agreement with the scratch assay data, the 3D invasion data show UP007 and UP029 to have a decreased invasion when Cav-1 is knocked down, while the U373 does not present a high invasive capacity and does not show a significant difference when Cav-1 is inhibited. The U87 CAV-(KD) on the other hand showed an apparent much-reduced invasion ability in comparison with their NT control. However, when the area of the invasion (density map data) normalized on the perimeter of the core (as justified and explained in Chapter 4), the difference in invasion is not significant. Nevertheless, it is interesting to observe that Cav+(NT) cells are still able to travel farther into the Matrigel from the edge of the Core (Figure 5.7), and this is evident, also for the other cell lines, the higher the invasive ability of the cell line is.

The difference in the core areas at Day 0 for the U87 appears to be annulled when spheroids are surrounded by Matrigel. In fact, the ratio of the Core Area D2/D0 is similar between CAV+ and CAV- cells (Figure 5.5B). This suggests that CAV+ cells can survive and replicate better in an attachment-free environment than the CAV- ones, while when they are surrounded by the extracellular matrix, their ability to replicate is restored.

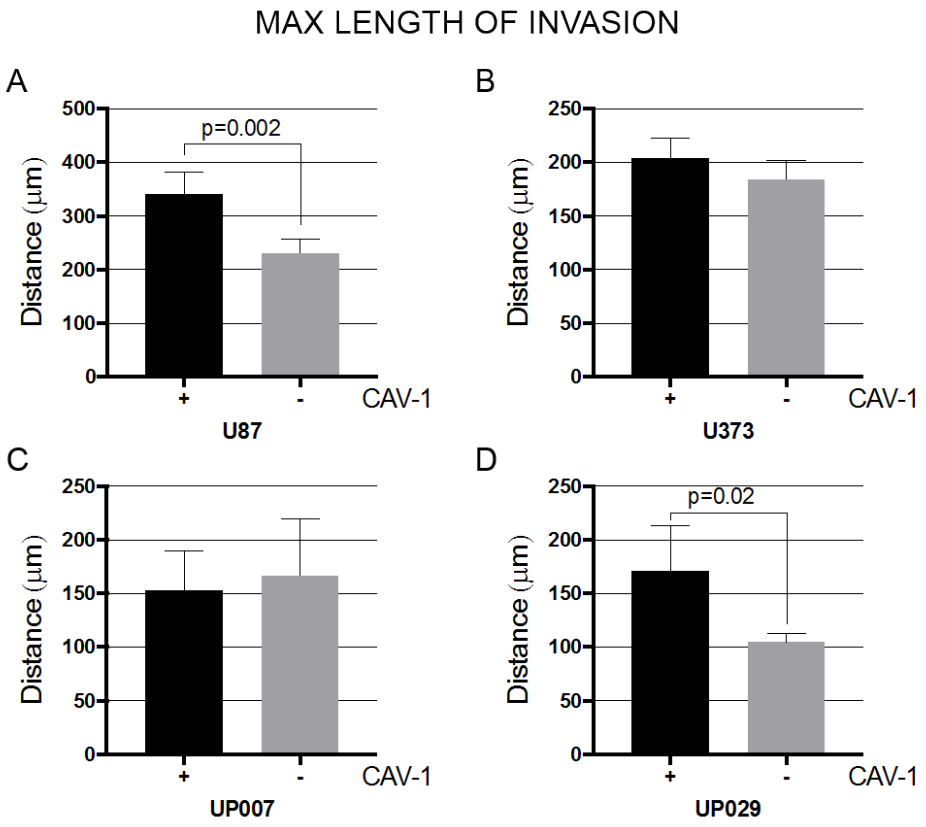

Figure 5.7 Maximum length reached by the invading/non-invading spheroids from the edge of the spheroid during 3D invasion assay on Matrigel for U87 (A), U373 (B), UP007 (C) and UP029(D) carrying the lentiviral-mediated KD of Cav-1. Parameters have been calculated with INSIDIA. Statistical analysis: unpaired T-Test (p-value is indicated when relevant).

During experiments with the lentiviral-transfected cells, there was a loss in the consistency of the experimental outcomes. This was considered to reflect the polyclonal nature of the lentiviral cell lines and a change in the repression of Cav-1. As a result, the laboratory pursued the knockout of Cav-1 using a CRISPR approach.

Figure 5.8 shows the 3D invasive characteristics of the CRISPR Cav-1 modulated U87 cells. Figure 5.8A shows the Cav-1 KO confirmed by Western Blot. Figure 5.8B shows the 3D invasion in Matrigel for the CAV+ and the CAV- (KO) cells. Figure 5.8C shows the INSIDIA analysis of the invasion assay of Figure 5.8B with the KO cells displaying essentially no expansion of the cells in the core of the sphere and also an essentially complete loss of invasion.

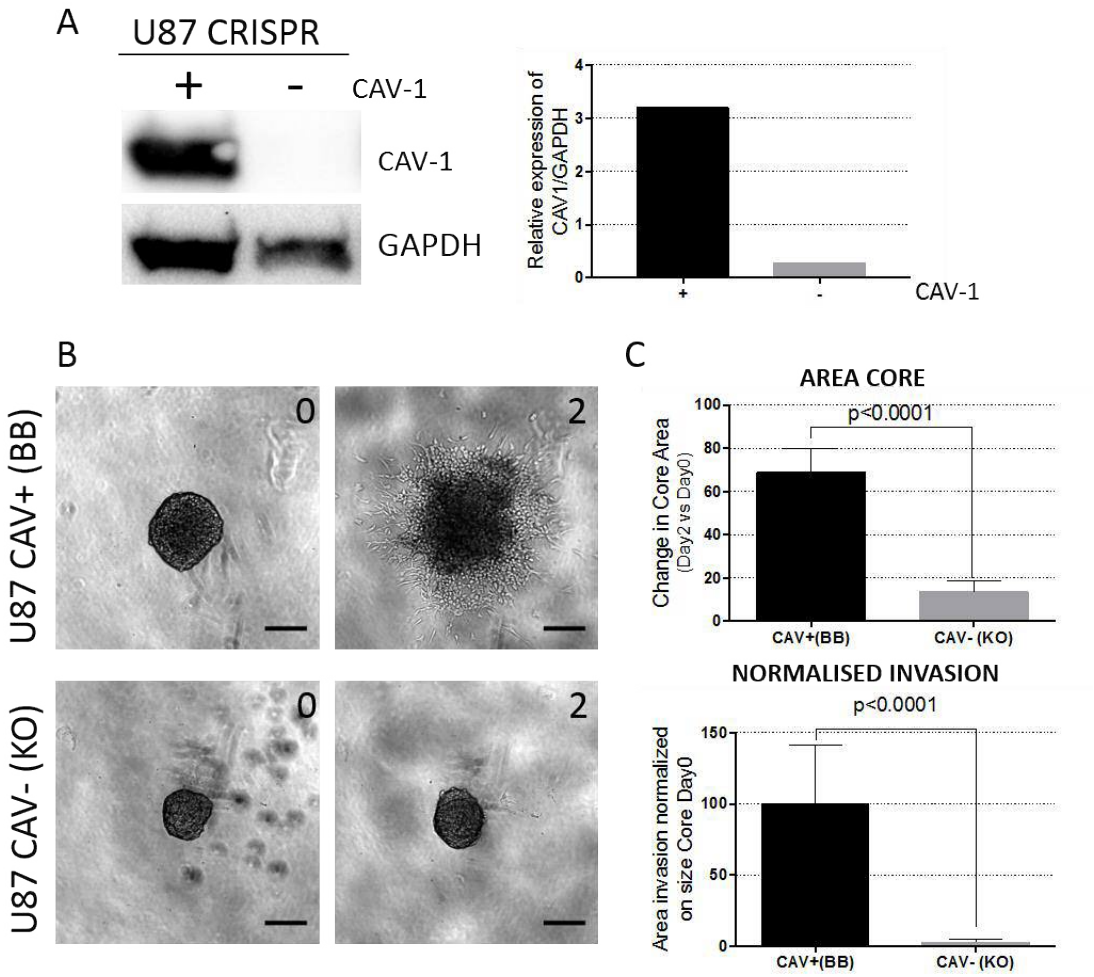

Figure 5.8 A- Western Blot analysis of U87 CRISPR expression of Cav-1. B U87 CRISPR Invasion assay on U87 cell lines transfected for the knockout of Cav-1. Seeding density: 1000 cells/well. U87. Experiments were repeated three times and replicates were analysed according to both density profile and density map. Scale bar 100µm. C- Graphs represent the Change in the Core between Day 0 and Day 2 and the amount of invasive edges according to the density profile analysis. Statistical analysis unpaired two-tailed T-Test (p-value is indicated when relevant).

In order to understand why the Cav-1 KO and its positive control presented different Core growth rate and motility, we tested if Cav-1 KO was affecting cells viability in 3D. We stained live floating spheroids with Hoescht for the visualization of all cell nuclei and Propidium Iodide (PI) for the identification of dead cells. The motionless of the KO spheroids was not related to an increased death (Figure 5.9), indicating that cells with the Cav-1 KO are not able to grow at high rates or to interact/ invade the extracellular matrix, but they are still able to survive. This suggests a less aggressive phenotype for the cells not expressing Cav-1.

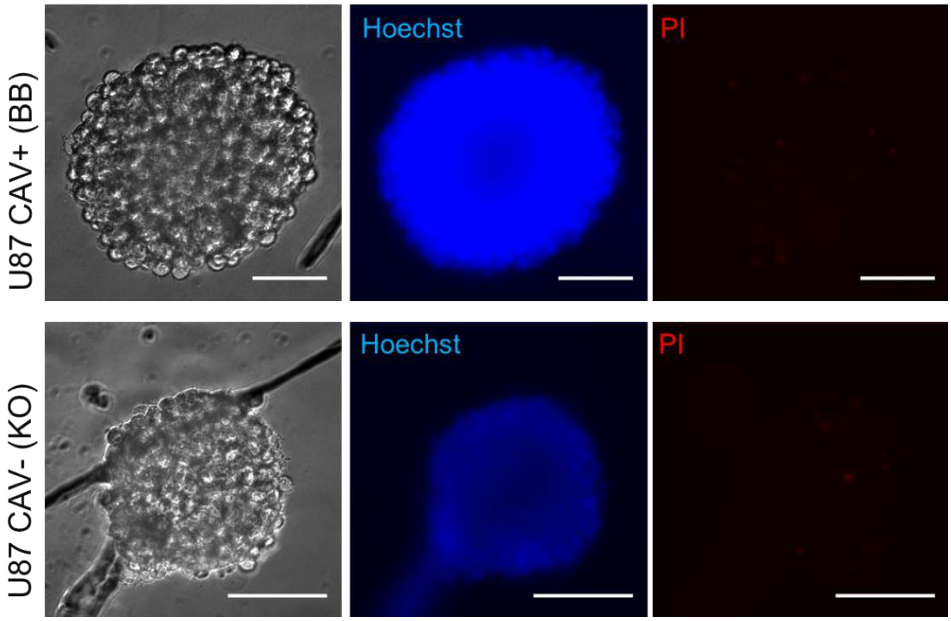

Figure 5.9 Live cell imaging on spheroids after four days in floating conditions. U87 CRISPR (CAV+ on the top, CAV- on the bottom) were stained with cell-permeable nuclei staining Hoechst 33342 1µg/ml (blue), and membrane impermeable dead cells staining Propidium Iodide 20µg/ml (PI- red). Scale bar 100µm.

We next sought to develop an immunofluorescence approach that could allow the study of signalling molecules within the 3D invading spheres.

Immunofluorescent staining for Cav-1 reveals that invading cells expressed a significant Level of Cav-1 (Figure 5.10B- green), while the KO spheroids in contact with the matrix do not show any expression of Cav-1, confirming the success of the KO and also corroborating the hypothesis that Cav-1 plays a role in invasion.

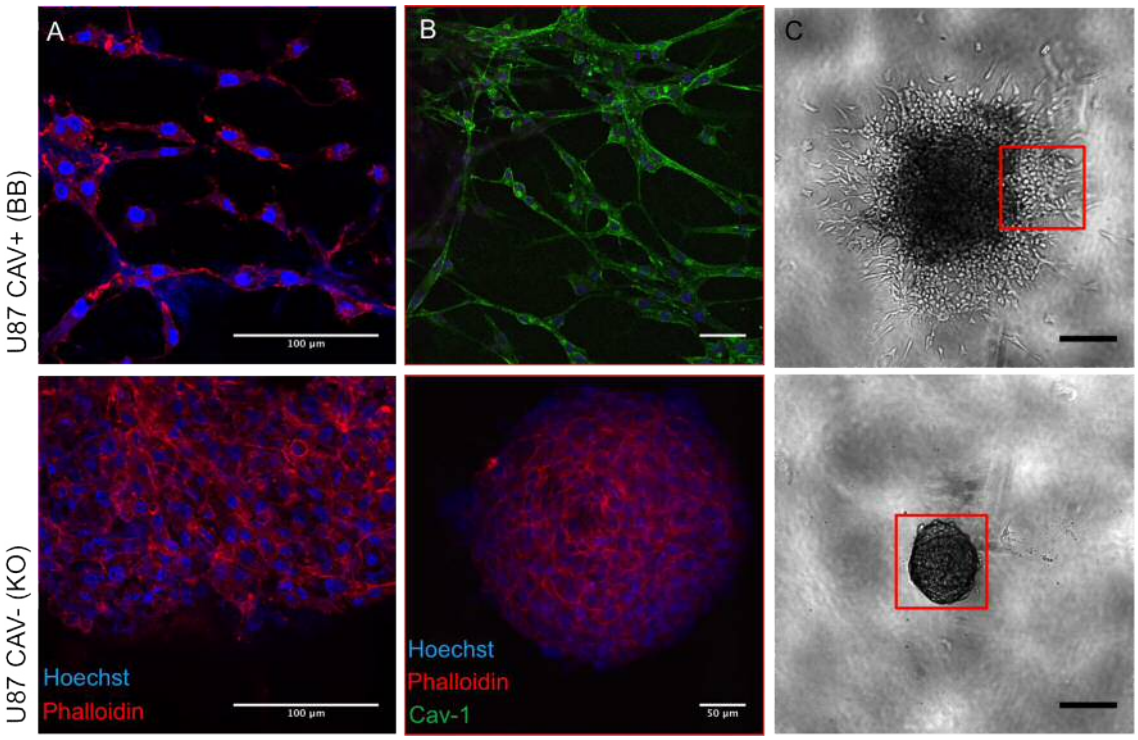

Figure 5.10 3D Immunofluorescence analysis of U87 CRISPR expression of Cav-1. A. U87 CAV+ and CAV- spheres embedded in Matrigel stained with Hoechst 33342 (blue: nuclei) and Phalloidin-Alexa647 (Red: Cytoskeleton). Scale bar 100µm. B- U87 CAV+ and CAV- spheres embedded in Matrigel stained with Hoechst 33342 (blue), Phalloidin-Alexa647 (Red) and Cav-1 (Green). Scale bar 50µm. C: indicative position (red square) of the pictures in B over whole sized bright field images of the invading/non-invading spheres. Scale bar 100µm.

From the immunostaining for Cav-1 in CAV+ vs CAV- spheroids, no signal of Cav-1 could be detected in the spheroid core, while Hoechst (nuclei- blue) and Phalloidin (F-actin- red) could still be detected. The average size of an antibody (i.e. IgG2a) is 150'000 g/mole while Phalloidin is roughly 100 times smaller

(1528 g/mole). This led to the question of whether the antibody was physically able, despite the permeabilization step, to penetrate the spheroid and stain the core. In an attempt to address this, we stained U87 CAV+ and CAV- spheres with antibodies directed against housekeeping genes, including β-Actin, GAPDH and Vinculin.

First, we optimized the housekeeping genes staining on 2D cell cultures grown on plastic (Figure 5.11).

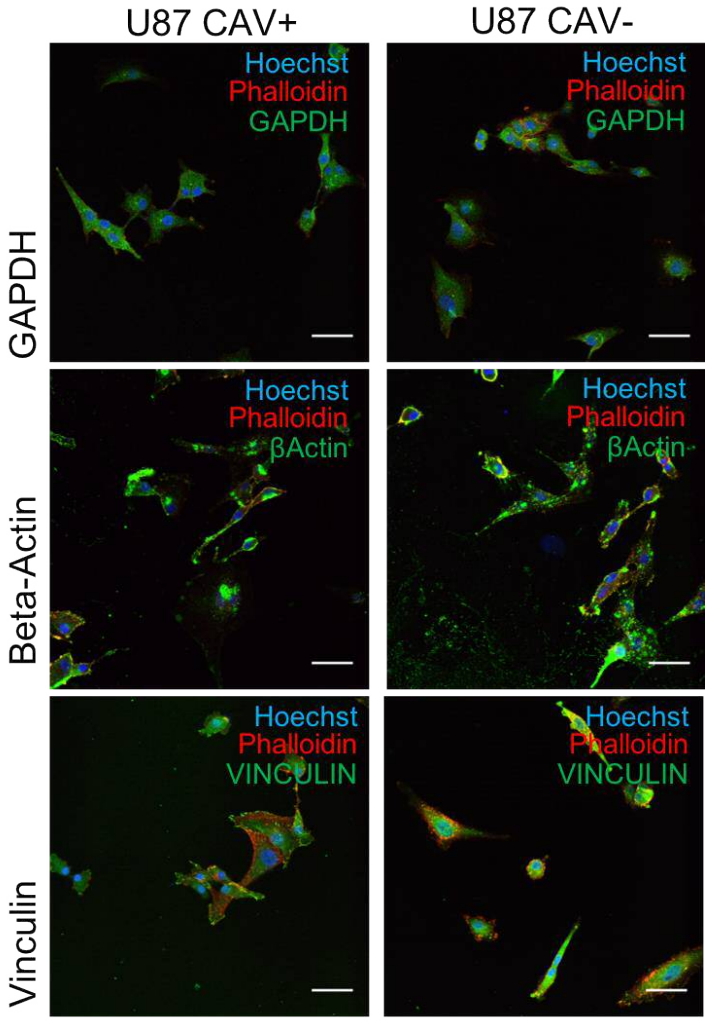

Figure 5.11 2D Immunofluorescence analysis of U87 CRISPR expression of Cytoskeletal proteins. U87 CAV+ and CAV- grown on plastic and stained with Hoechst 33342 (blue: nuclei), Phalloidin-Alexa647 (Red: Cytoskeleton) and, when indicated, GAPDH, Beta Actin and Vinculin (Cytoskeleton: Green). Scale bar 50µm.

After optimizing in 2D, we tested the housekeeping antibodies in 3D spheroids.

The U87 CAV+ showed a signal for the antibodies in the invading edges and partially in the core (shown in Figure 5.12) while the CAV- spheroids, being more compact and lacking invasive edges, were stained only on their outer layers. This can be seen in comparing the confocal sections at the spheroid surface (Figure 5.12C) to the sections deep in the spheroid core (Figure 5.12D). Vinculin showed a higher signal in both CAV+ and CAV- cells, but it showed also several non-specific signals that make its use unreliable (despite its validation via western blot).

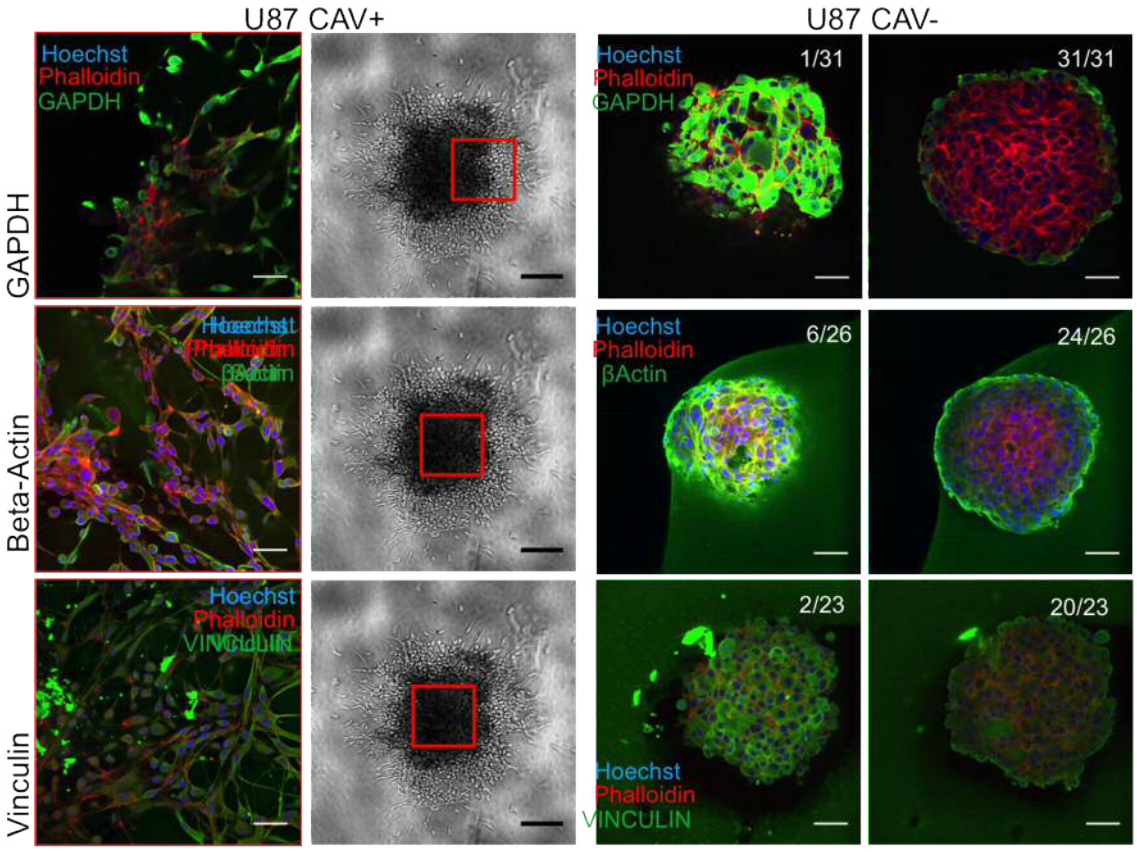

Figure 5.12 3D Immunofluorescence analysis of U87 CRISPR expression of Cytoskeletal proteins. U87 CAV+ (A-B) and CAV- spheres (C-D), embedded in Matrigel and stained with Hoechst 33342 (blue: nuclei), Phalloidin-Alexa647 (Red: Cytoskeleton) and, when indicated, GAPDH, Beta Actin and Vinculin (Cytoskeleton: Green). B indicates the location of the correspondent picture in A. Images of the KO spheroids stained for the selected housekeeping antibodies are shown, representing their outer layer (C) and their core-level layer (D). Scale bar 50µm.

Given the challenge of antibody penetration into the spheroid core, we explored the fixing and embedding of the spheroids in paraffin wax, followed by physical sectioning and immunohistochemistry staining. However, while the sectioning was able to preserve the compact nature of the non-invading CAV- spheroids, the invasive edges of the CAV+ spheroids were not maintained (Figure 5.13).

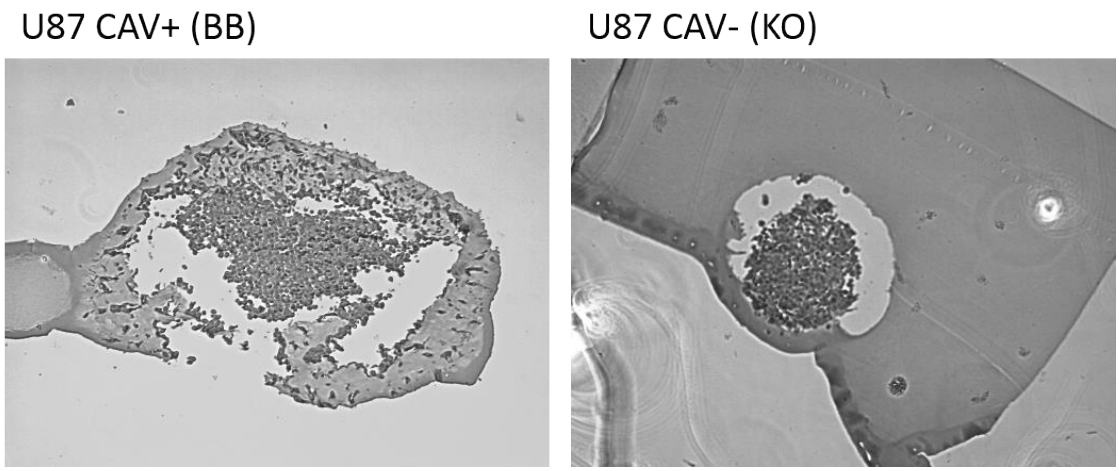

Figure 5.13 Paraffin-embedded sections of U87 CAV+ and CAV-. Spheroids embedded in Matrigel were fixed in formaldehyde 4% glutaraldehyde, washed, dehydrated and embedded in paraffin wax, then sectioned.

Due to the inefficiency of the antibody penetration in the intact spheroids, and the fragility of the paraffin-embedded sections, we decided to continue immunofluorescence investigations on 3D matrix-embedded spheroids only for the CAV+ cell lines and in particular their invasion projections. Any comparisons between CAV+ and CAV- cells were performed on cells in 2D growing on plastic or in 2D with cells growing upon a layer of Matrigel.

We found the growth on Matrigel particularly interesting because cells are interacting with matrix which may cause different effects. For example, Figure 5.14A and B shows the U87 CAV+ and CAV- cells grown on plastic. The images confirm similar morphology. In contrast, Figure 5.14C and D show CAV+ and CAV- cells grown on Matrigel. Here, the CAV+ cells started interacting with the matrix, sending projections and connecting with distant groups of cells. The CAV- cells, on the other side, grew as clusters with limited migratory movement and only after a four day delay small projections outside the clusters observable. The difference in matrix effects are thus exemplified, and the results with the cells grown on the matrix consistent with the observations seen in the 3D invasion assays (Figure 5.8B). Since the clusters of CAV- cells are much smaller than the spheroids, it was possible to overcome the difficulty of the antibody penetration.

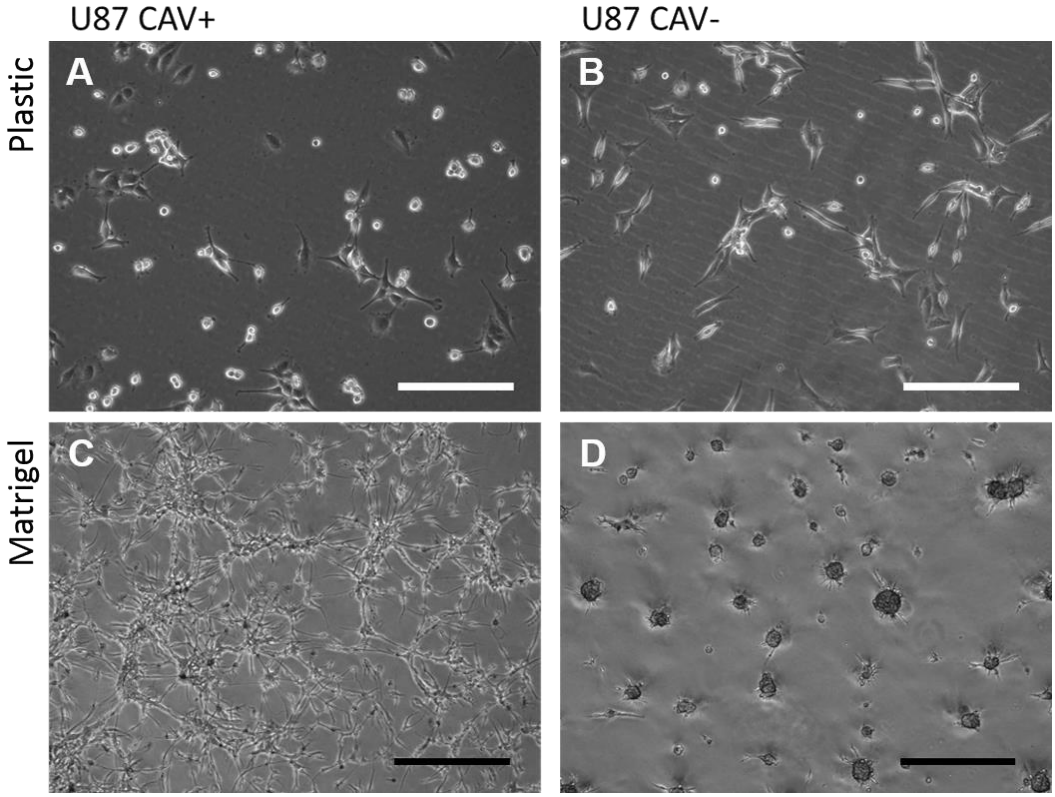

Figure 5.14 Culture conditions of U87 CRISPR. Both CAV+ and CAV- were cultured on 2D plastic (A and B) and on upon a layer of 100% Matrigel (C and D). Scale bar 250 μm.

Figure 5.15 shows the staining of cells grown upon plastic or Matrigel in the 2D format. As expected Cav-1 staining is clearly observed in the CAV+ cells but not the CRISPR knockout cells. The CAV+ cells expressed a high and distributed level of the protein confirming the validity of the 2D Matrigel culture condition (Figure 5.15).

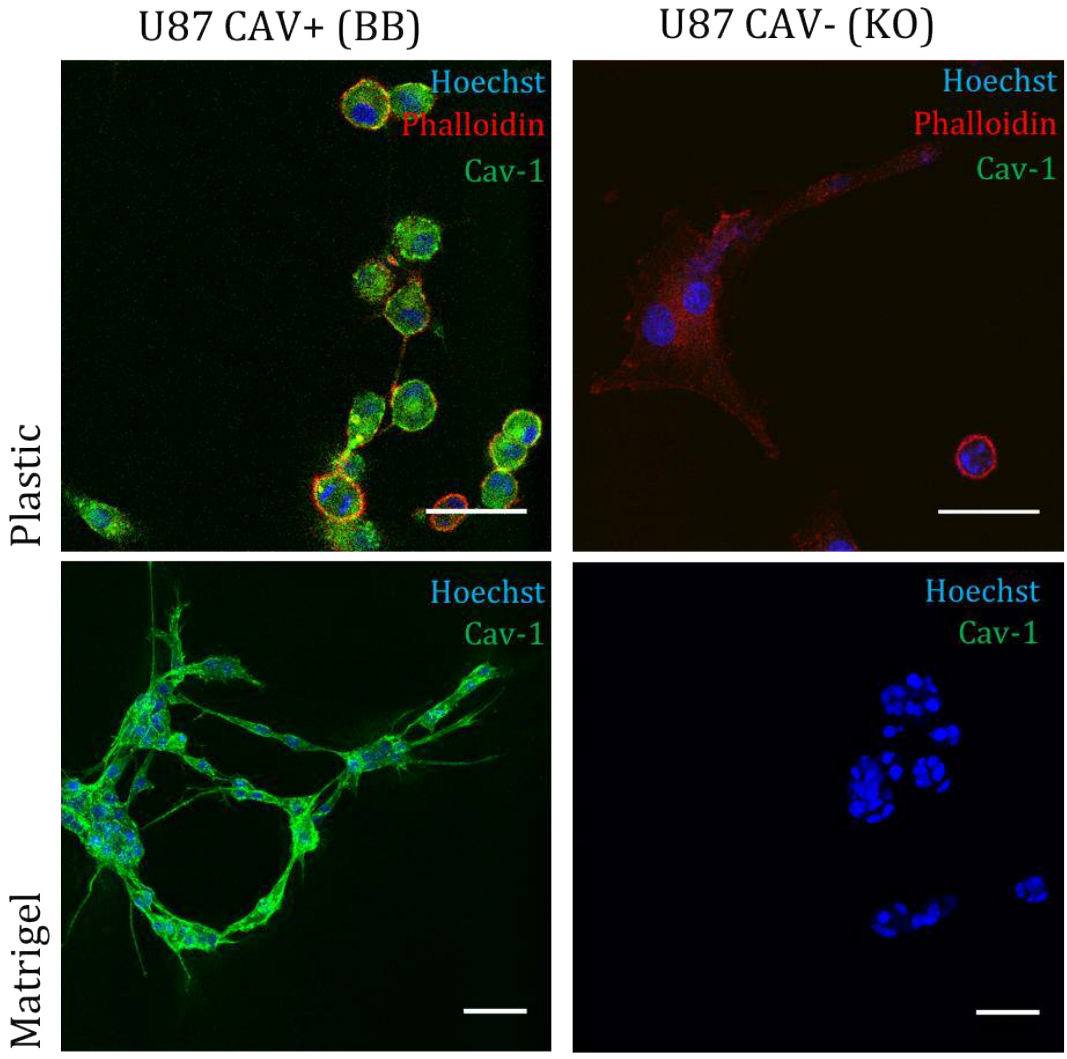

Figure 5.15 2D Immunofluorescence analysis of U87 CRISPR knockout cells for the expression of Cav-1. The U87 CAV+ and CAV- cells grown on plastic (top) were stained with Hoechst 33342 (blue: nuclei), Phalloidin-Alexa647 (Red: Cytoskeleton) and, Cav-1 (Green). The U87 CAV+ and CAV- cells grown on Matrigel (bottom) were similarly stained except Phalloidin-Alexa647. Scale bar in all images 50µm.

To investigate invadopodia capacity in the 2D growth conditions we stained for cortactin, a marker of invadopodia (Kirkbride, Sung, Sinha, & Weaver, 2011; MacGrath & Koleske, 2012; Weaver, 2008). This staining is able to highlight membranes and cell projections. The expression of cortactin in glioma specimens has been reported to be significantly higher than in normal brain tissues (Spandidos et al., 1994). On 2D plastic (Figure 5.16A), cortactin expression appeared to be more diffuse in CAV+ cells while more localized in CAV- cells, with focal points on the membrane (Figure 5.16A). On 2D Matrigel again the protein was expressed by both cell lines, with a diffuse distribution of signal in both, even if for the small clusters of CAV- cells it was difficult to interpret localisation as they were in a compact multicellular cluster. Intense staining in the invadopodia arising from the CAV+ cells (Figure 5.16B) was evident. Similarly, for the 3D spheroid growth in Matrigel we saw for cells invading the matrix a high level of expression of cortactin throughout the cell body (Figure 5.16C).

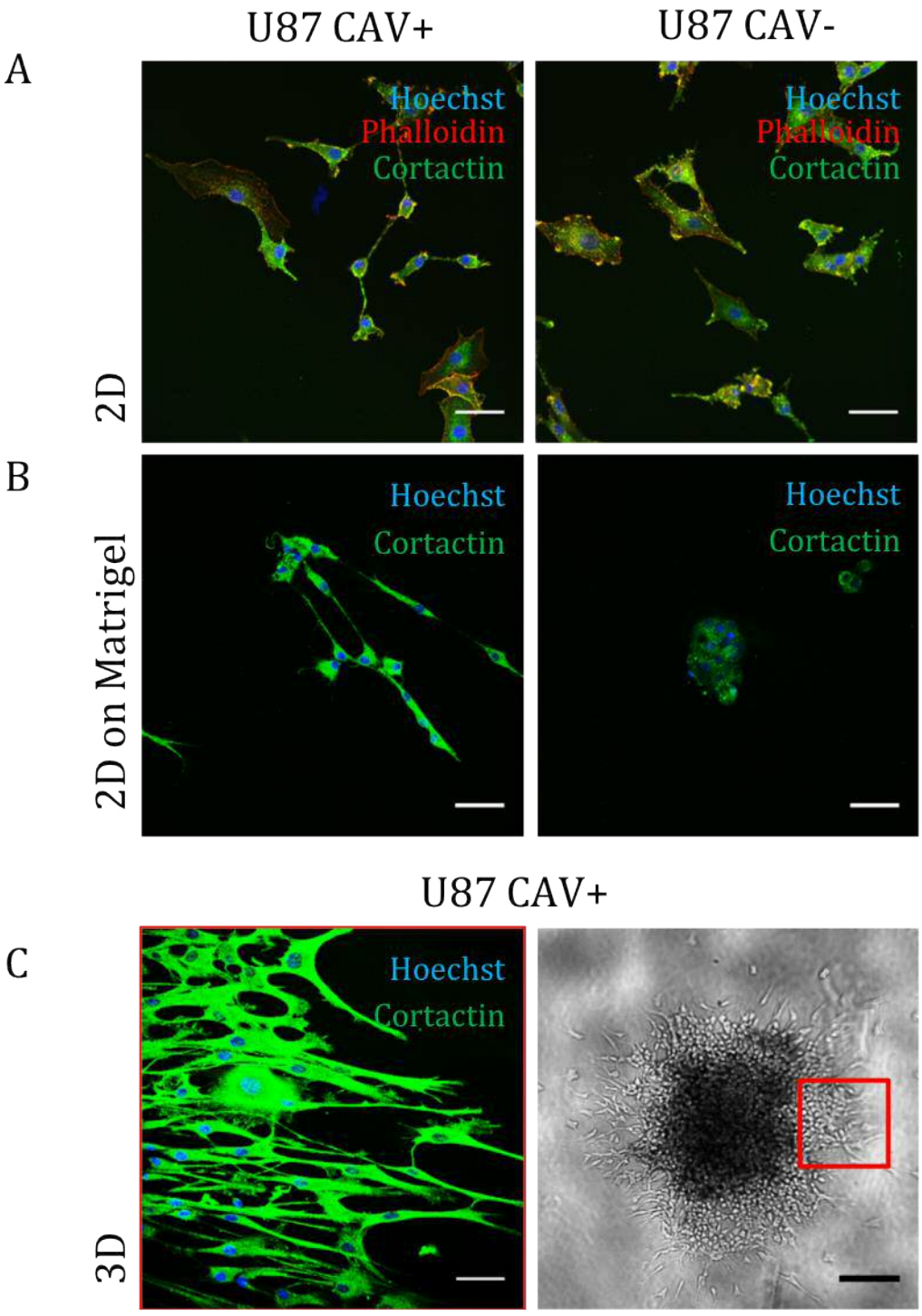

Figure 5.16 Immunofluorescence analysis of U87 CRISPR cells for the expression of the cytoskeletal protein, cortactin. A: U87 CAV+ and CAV- grown on plastic and stained with Hoechst 33342 (blue: nuclei), Phalloidin-Alexa647 (Red: Cytoskeleton) and, Cortactin (Cytoskeleton: Green). B: U87 CAV+ and CAV- grown on Matrigel and stained as previously. C: U87 CAV+ spheroids embedded in Matrigel and stained as previously. Scale bar 50µm for all of above. Shown in the bright-field image (bottom right) the indicative position (red square) for the spheroid staining. Scale bar 100µm.

Another approach to staining invadopodia within the 3D spheroid model was undertaken using Concanavalin A. It is a lectin that binds glycoproteins and glycolypids on the cell plasma membrane. *In vitro* use of Concanavalin A has been shown in GBM cells to promote the activation of MT1MMP and consequently MMP2 (Annabi et al., 2001).

In this current work the staining gave rise to significant signal of the Matrigel (Figure 5.17). However penetration of the matrix was sufficent to stain some of the cells, but interestlngly an absence of staining (Figure 5.17) the projections (red) into the Matrigel network.

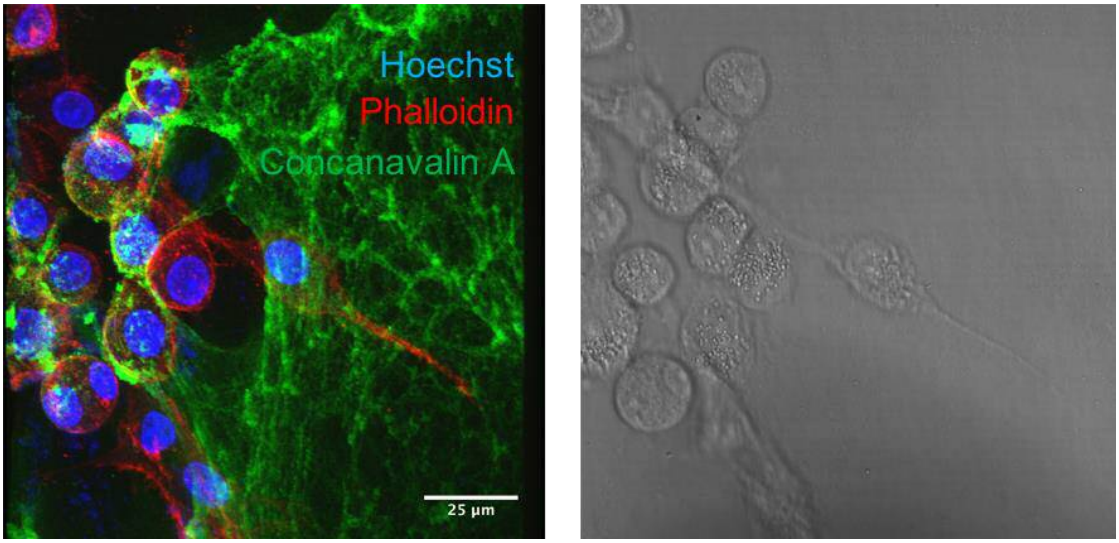

Figure 5.17 Immunofluorescence analysis of U87 CRISPR cell lines using ConcanavalinA. U87 CAV+ sphere embedded in Matrigel and stained with Hoechst 33342 (blue: nuclei), Phalloidin-Alexa647 (Red: Cytoskeleton) and, Concanavalin A (Green). Scale bar 25 µm.

5.4.2 RT-PCR ANALYSIS FOR GENES ASSOCIATED WITH INVASION

In order to explore the mechanisms involved in the Cav-1 pro-invasive phenotype, we examined by RT-PCR levels of transcripts for genes involved in adhesion, digestion of matrix and epithelial to mesenchymal transition. A list of all these genes and their main role is reported in Materials and Methods (Table 5.5).

Gene expression was compared between U87 CAV+ and CAV- cells grown in 2D format on both plastic (Figure 5.18) and on Matrigel (Figure 5.19) with the results summarised in (Figure 5.20).

Primers were first validated for their specificity with a high number of PCR cycles PCR (50, as shown in Appendix 4) to allow every band to eventually appear and determine if the primers were specific for the target. After the validation the PCR was run on 33 cycles, to allow comparison of gene expression between CAV+ and CAV- cells.

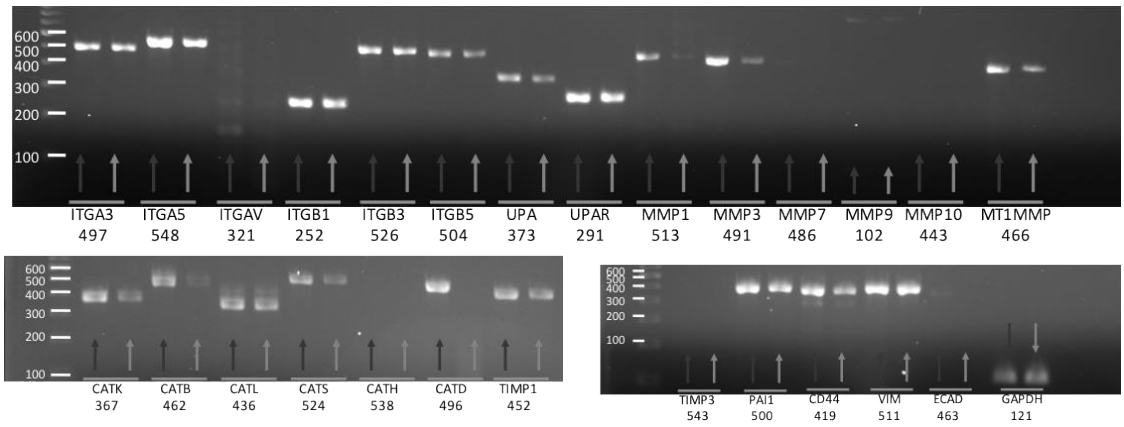

Figure 5.18 RT-PCR analysis of 26 genes using validated primers on lysates from U87 CAV+ and CAV- cells grown on normal plastic culture conditions.

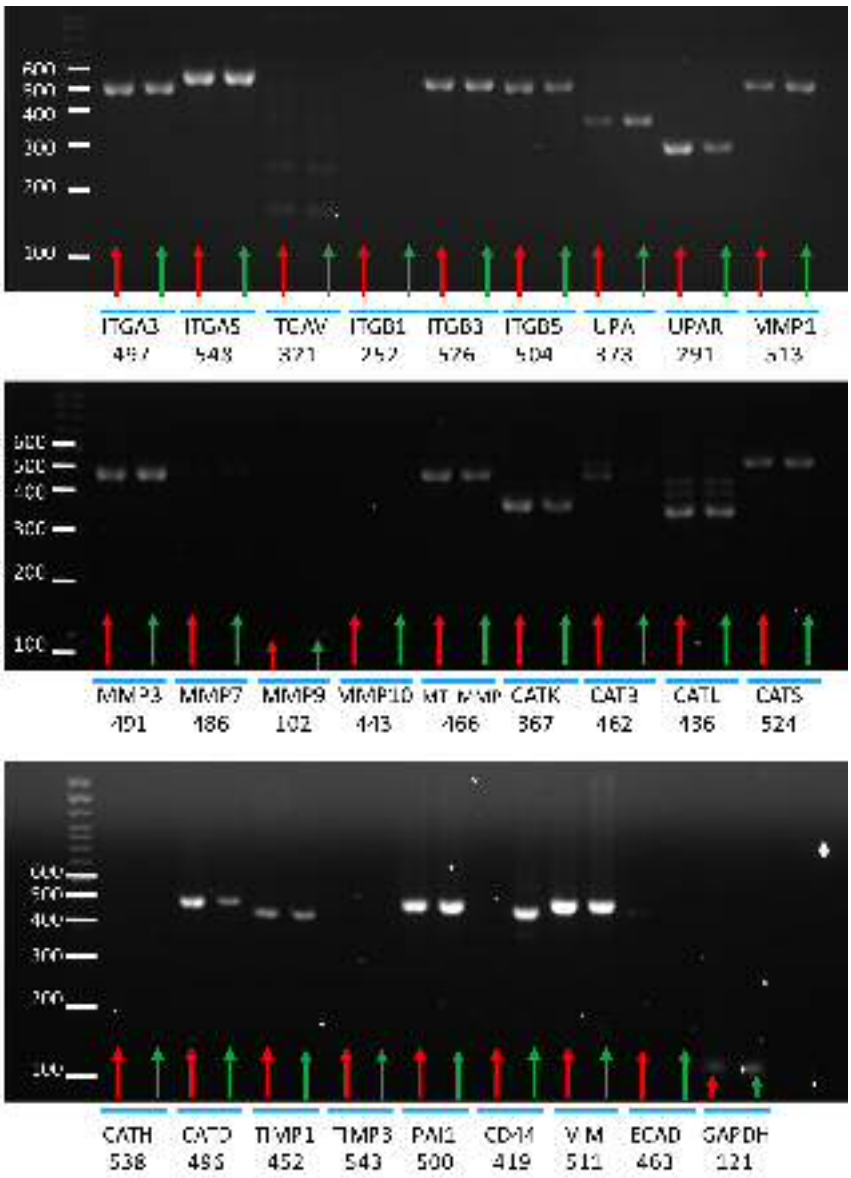

Figure 5.19 PCR analysis of 26 pairs of validated primers on U87 CAV+ (Dark Grey) and CAV- (Light Grey) grown on a Matrigel layer.

Figure 5.20 is a summary of the RT-PCR study results for cells grown on plastic and on Matrigel. The expression comparison was reported as a fold-change between the CAV+ and CAV- cells, with the fold-change values ranked in decreasing order by the Matrigel data.

Despite acknowledging that cells grown on plastic will synthesise their own ECM, the results with Matrigel maybe more pertinent since the immediate contact with Matrigel could stimulate earlier those pathways closer to the physiological conditions.

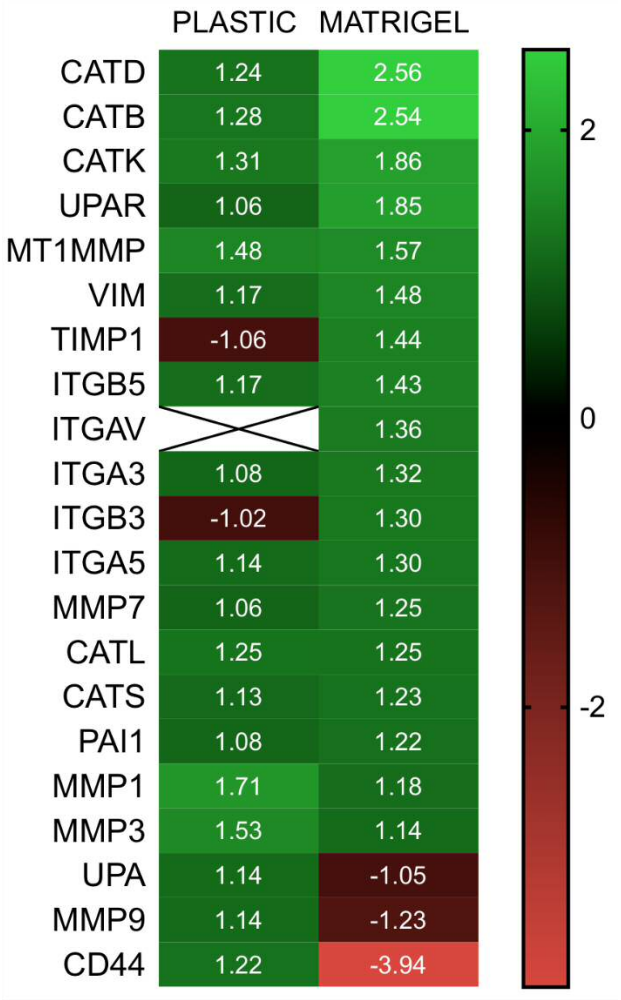

Figure 5.20 Summary of results of RT-PCR analysis on lysates from U87 CAV+ and CAV- cells on cells grown on plastic (left) and on Matrigel (right). Values represent the fold-change of CAV+/CAV- gene expression. Results are ordered from higher to lower in respect to the Matrigel condition. Colour code bar is reported on the side.

A selection of molecules from the RT-PCR was chosen for further investigation by Western blot and immunofluorescence. These molecules are acknowledged to have relevance to GBM pathophysiology and showed some significant fold-changes in the RT-PCR data, cathepsins D (CATD/CTSD) and B (CATB/CTSB), UPAR and CD44. Further MMP1, a molecule related to pathology of GBM showed disparate outcomes on plastic and Matrigel, which warranted further study.

5.4.3 WESTERN BLOT AND IMMUNOFLUORESCENCE OF SELECT MOLECULES FROM THE RT-PCR ANALYSIS

The PCR results for the four most modulated markers was achieved by Western blot and immunofluorescence of cells in 2D plastic, 2D on Matrigel and 3D in Matrigel. The Western blot analysis was used to confirm the differences in the proteins expression both in plastic and on 2D Matrigel, while the immunofluorescence studies were useful to compare qualitatively the intensity of the signal (and thus of the protein expression), as well as the localization and distribution of the marker. In 3D spheroids embedded in Matrigel, the expression signal was evaluated only on invading cells, for the U87 CAV+.

In particular, we analysed the expression of the matrix-digesting CTSB, CTSD, MMP1 and the adhesion UPAR and CD44. As a control, we also chose to analyse E-Cadherin (CDH1).

5.4.3.1 MATRIX-DIGESTING ENZYMES

The first protein analysed was CTSB (Figure 5.21, Figure 5.22, Figure 5.23). Cathepsin B is a lysosomal cysteine protease involved in intracellular proteolysis. In cancer it may increase the activity of other proteases, including CTSD, UPA and MMPs.

Despite the inter-experimental variation, on Matrigel CATB is always more expressed in CAV+ than in Cav- cells, while on plastic the results of different experiments were not consistent (Figure 5.21). The results of the Western blot

showing increased CTSB in CAV+ cells when grown on Matrigel are consistent with the PCR analysis for similarly growth conditions (Figure 5.20).

The immunofluorescence analysis for both CAV+ and CAV- cell lines grown in 2D on plastic show that some cells displayed a high level of CTSB, while others could be observed displaying a low level of expression or indeed a complete absence (Figure 5.22A). In contrast, on 2D Matrigel, all cells expressed CTSB with peaks of intensity in CAV+ cells projections (Figure 5.22B). This latter point was further substantiated for the immunofluorescence of the invading spheroids which revealed CAV+ cells in the outer rim of the invasive edges to express high levels of CTSB, suggesting the molecule is at the forefront of the migratory/invasive process (Figure 5.23).

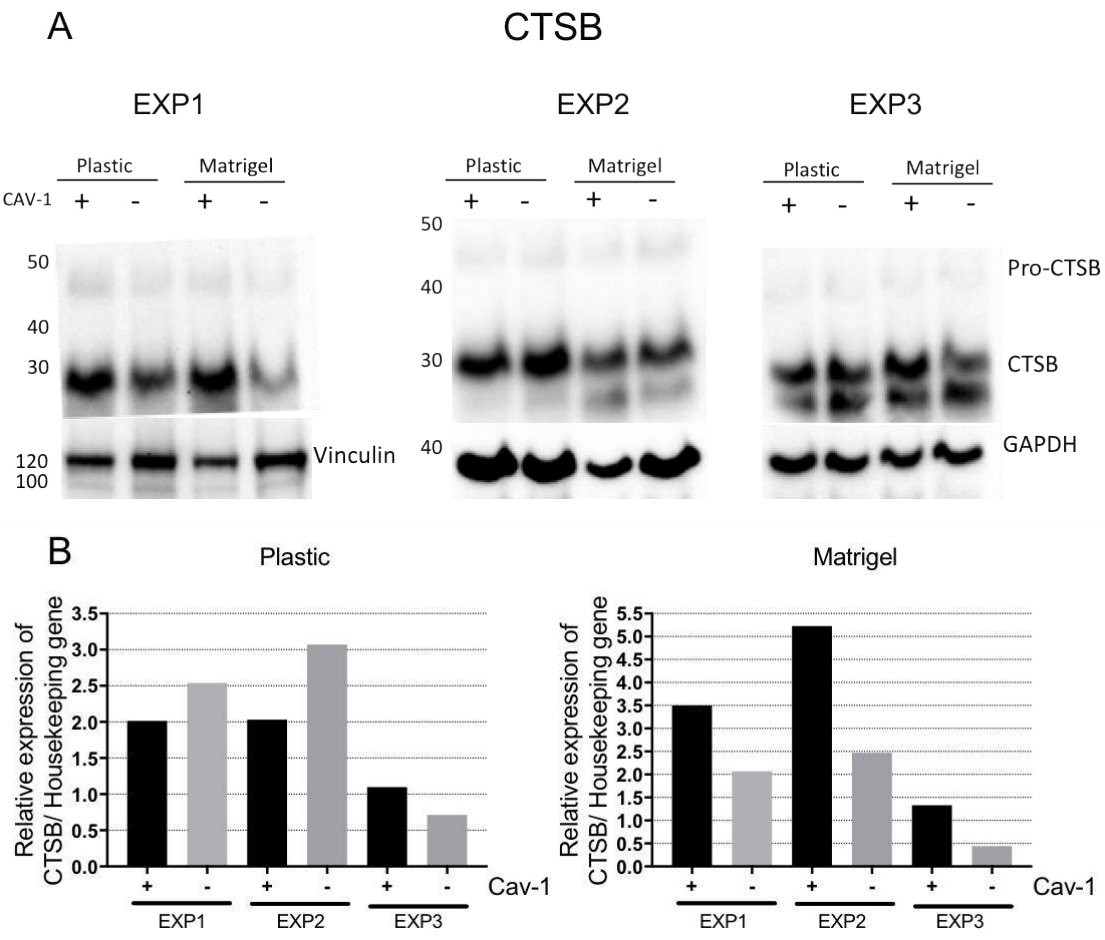

Figure 5.21 A: Western blot analysis for the expression of Cathepsin B (CTSB) in U87 CAV+ and CAV- grown on plastic or on Matrigel. The antibody recognizes a mature form at 31kDa and a pro-form at 43kDa. GAPDH (EXP 2 and 3) or Vinculin (EXP 1) were used as a housekeeping gene and the normalized quantification is reported in B. Three separate experiments are reported, each one from three different sets of samples.

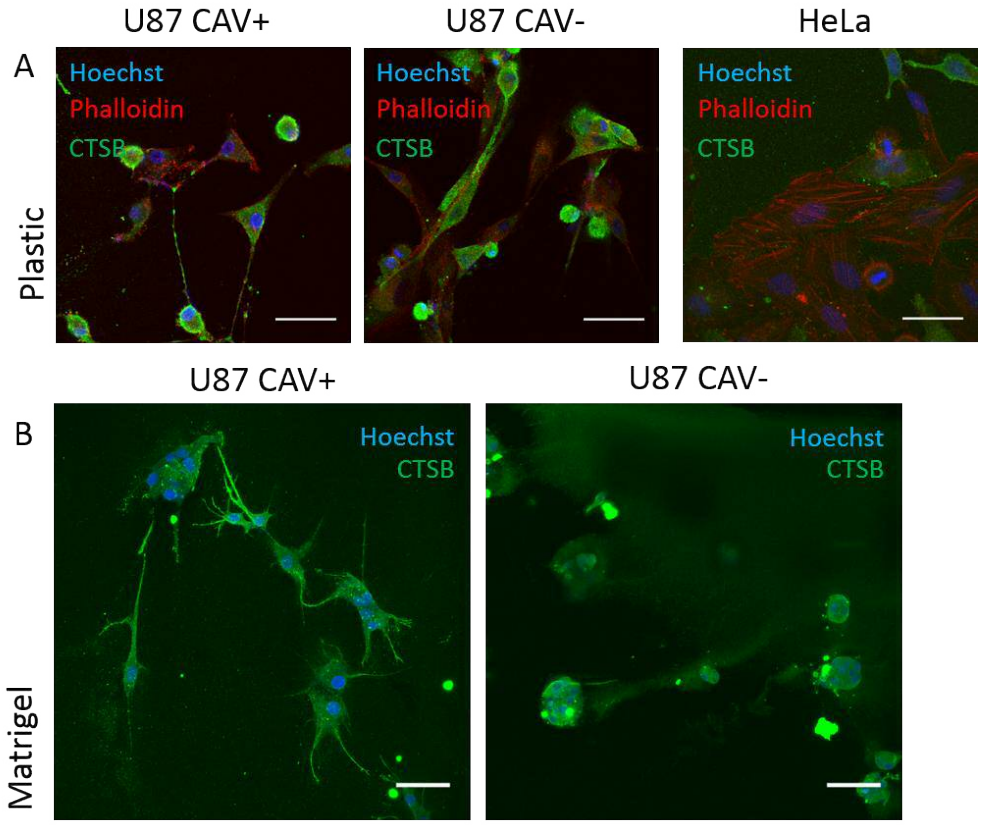

Figure 5.22 Immunofluorescence of 2D cultures of U87 CRISPR and HeLa cell lines for the expression of Cathepsin B (CTSB). U87 CAV+ and CAV- grown on plastic (A) and on Matrigel (B) and stained with Hoechst 33342 (blue: nuclei), Phalloidin-Alexa647 (Red: Cytoskeleton) and, CTSB (Green). HeLa in A were used as a control. Scale bar 50µm.

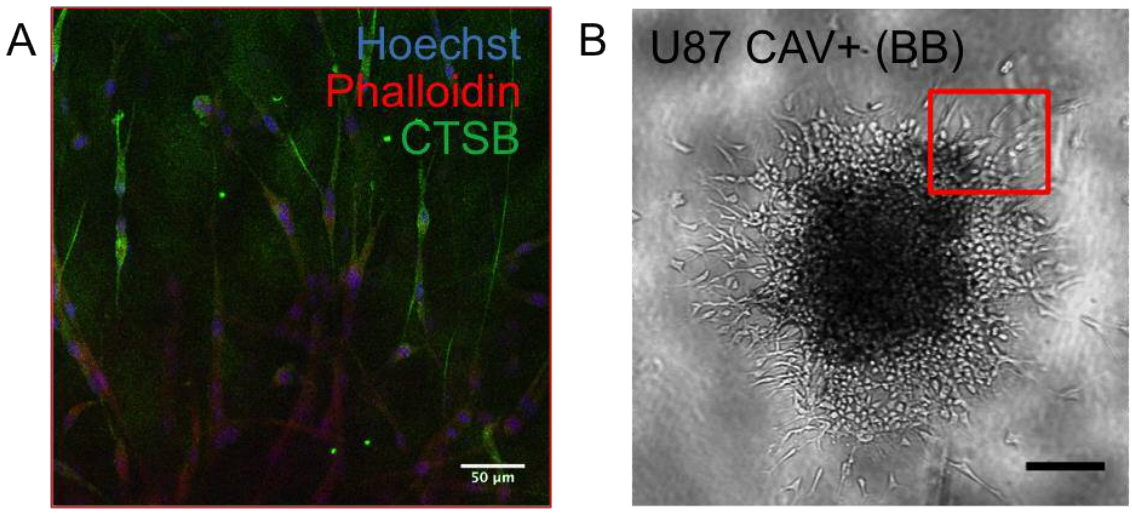

Figure 5.23 Immunofluorescence of 3D-spheroids (U87 CAV+ cell lines) embedded in Matrigel for the expression of Cathepsin B (CTSB). A: Spheres were embedded in Matrigel and stained with Hoechst 33342 (blue: nuclei), Phalloidin-Alexa647 (Red: Cytoskeleton) and CTSB (Green). Scale bar 50µm. B: Bright-field image of the indicative position (red square) for the spheroid staining. Scale bar 100µm.

We next analysed for CTSD (Figure 5.24, Figure 5.25, Figure 5.26). CTSD is an aspartyl-protease that appears to cleave a variety of substrates such as fibronectin and laminin.

Here, CTSD Western blot analysis did not provide any consistent outcome, particularly when the cells were grown upon Matrigel, and certainly not demonstrating significantly higher expression for the CAV+ cells over CAV- cells (Figure 5.24).

The immunofluorescence analysis for both 2D plastic and 2D Matrigel failed to show any difference between the CAV+ and CAV- cells, with a diffuse (distributed throughout the cell body) signal present in all. However, of note is the staining present in the membrane projections seen for CAV+ cells grown on Matrigel (Figure 5.25). This is consistent with the signals seen for CTSD in the invadopodia for CAV+ cells arising from 3D invading spheroids (Figure 5.26).

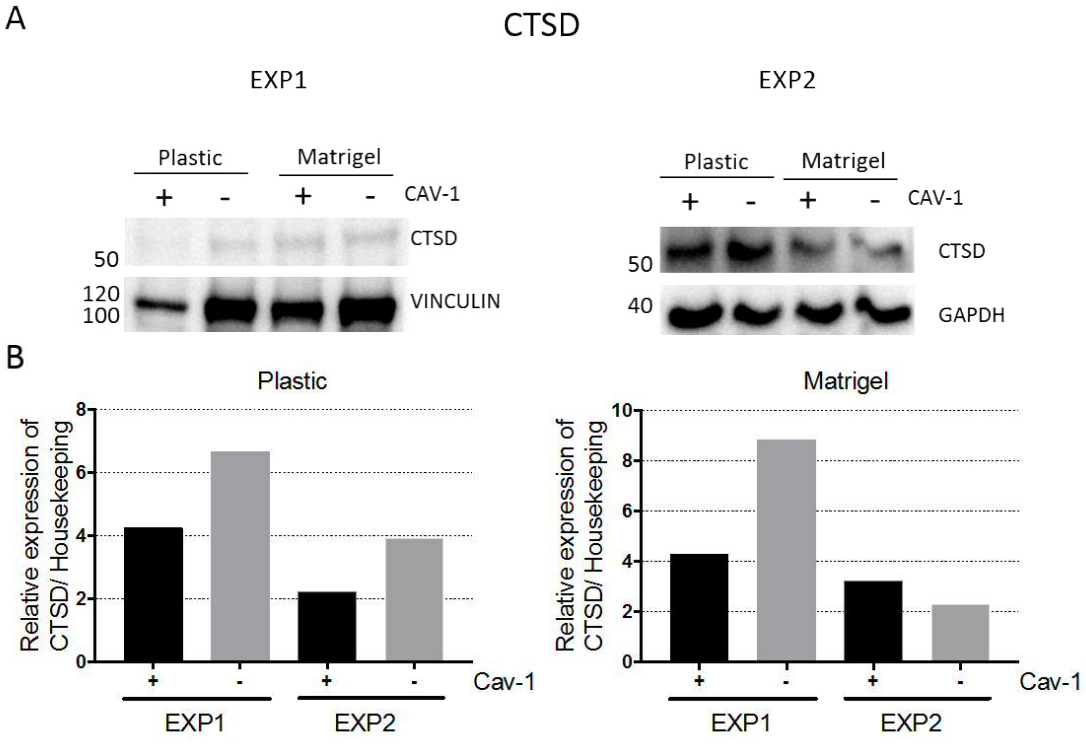

Figure 5.24 A: Western blot analysis for the expression of Cathepsin D (CTSD) in U87 CAV+ and CAV- cell lines grown upon 2D plastic or upon 2D Matrigel. GAPDH or Vinculin were used as housekeeping genes and the normalized quantification is reported in B. Three separate experiments are reported, each one from three different sets of samples.

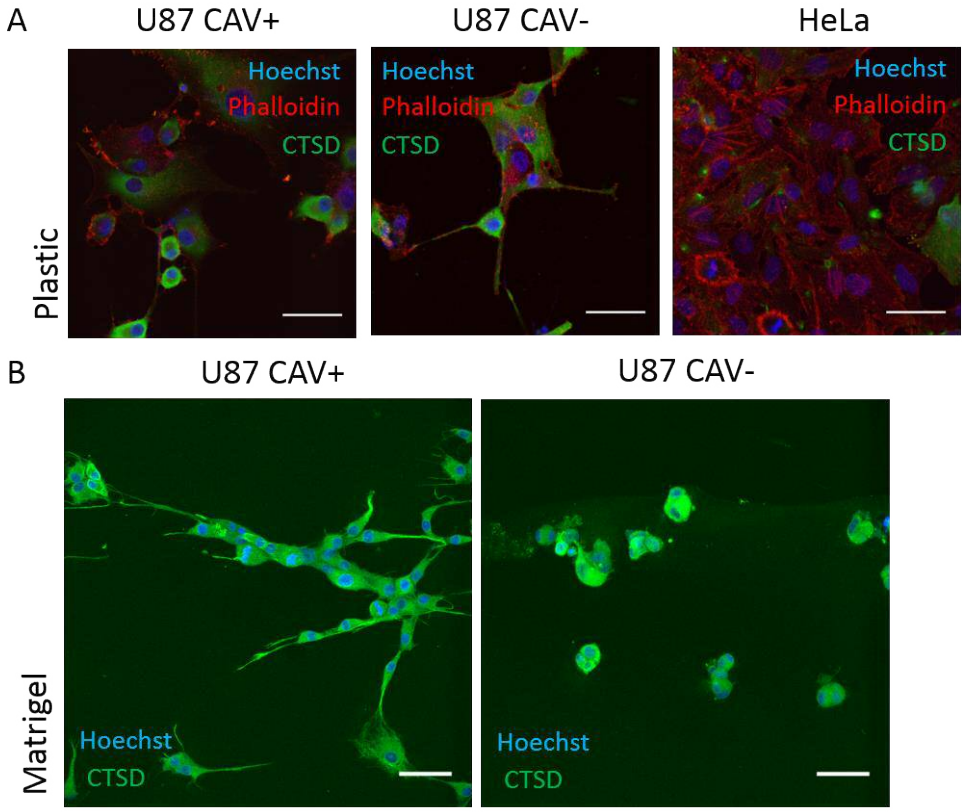

Figure 5.25 Immunofluorescence of 2D cultures of U87 CRISPR and HeLa cell lines for the expression of Cathepsin D (CTSD). U87 CAV+ and CAV- grown on plastic (A) and on Matrigel (B) and stained with Hoechst 33342 (blue: nuclei), Phalloidin-Alexa647 (Red: Cytoskeleton) and, CTSD (Green). HeLa in A were used as a control. Scale bar 50µm

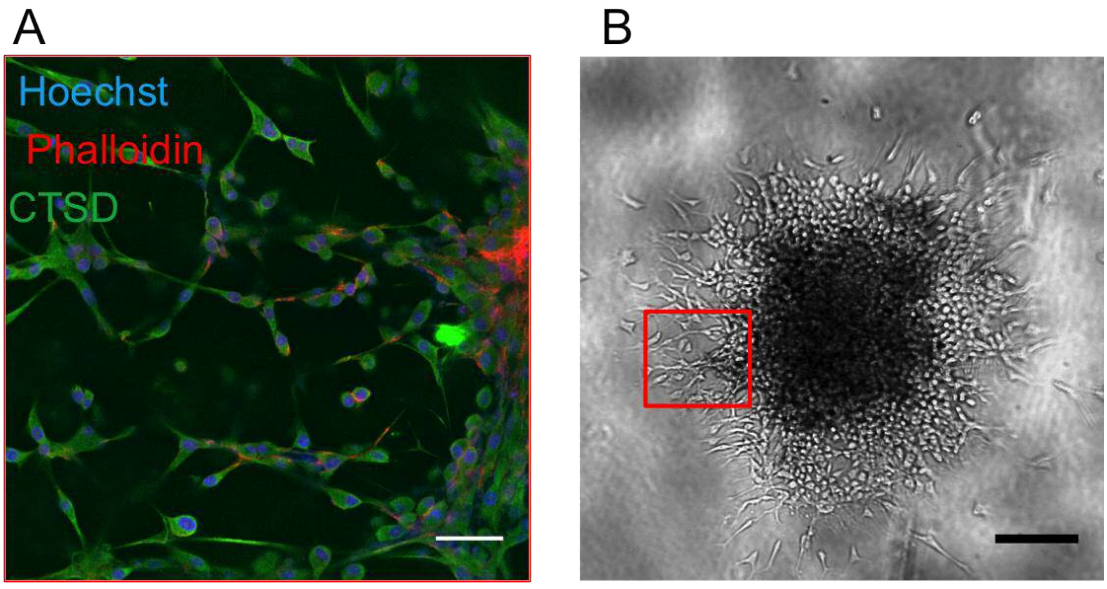

Figure 5.26 Immunofluorescence of 3D-spheroids (U87 CAV+ cell lines) embedded in Matrigel for the expression of Cathepsin D (CTSD). A: Sphere was embedded in Matrigel and stained with Hoechst 33342 (blue: nuclei), Phalloidin-Alexa647 (Red: Cytoskeleton) and CTSD (Green). Scale bar 50µm. B: Bright-field image of the indicative position (red square) for the spheroid staining. Scale bar 100µm.

We next analysed for MMP1 (Figure 5.27, Figure 5.28, Figure 5.29). MMP1 is involved in the breakdown of extracellular matrix, in particular interstitial collagens.

The Western blot analysis of MMP1 was difficult to interpret because the signal from the MMP1 antibody was very weak, even when adjustments for the increase of sensitivity were made (Figure 5.27A). According to the quantification results on Matrigel, however, MMP1 appeared to some extent to be inhibited by Cav-1. This contrasts with the RT-PCR results, although the results for Matrigel were not clearly indicative of an up-regulation, whereas on plastic MMP1 appeared to positively correlate with high Cav-1 levels. (Figure 5.27B and Figure 5.20).

Intriguingly, immunofluorescence staining for MMP1 in cells grown upon 2D Matrigel showed that MMP1 is expressed only by the Cav+ cells (Figure 5.28). The simultaneous conduct of these immunofluorescence studies gives some assurance that this result is real and not a technical artefact. The immunofluorescence results reinforced concerns of the suitability of the MMP1 antibody for Western blot applications.

The staining for MMP1 was also evident by immunofluorescence in the invading spheroids, which revealed CAV+ cells in the outer rim of the invasive edges to express levels of MMP1, again indicative that the molecule is important for migratory/invasive function in these cells (Figure 5.29).

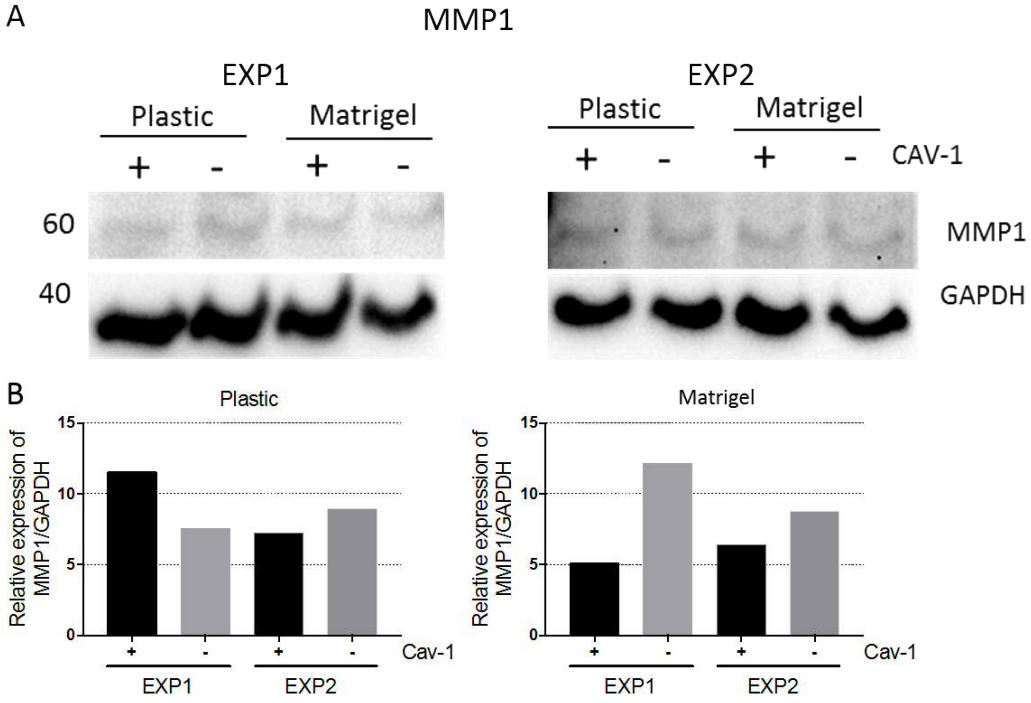

Figure 5.27 A: Western blot analysis for the expression of MMP1 in U87 CAV+ and CAV- grown upon 2D plastic or upon 2D Matrigel. GAPDH was used as a housekeeping gene and the normalized quantification is reported in B. Three separate experiments are reported, each one from three different sets of samples.

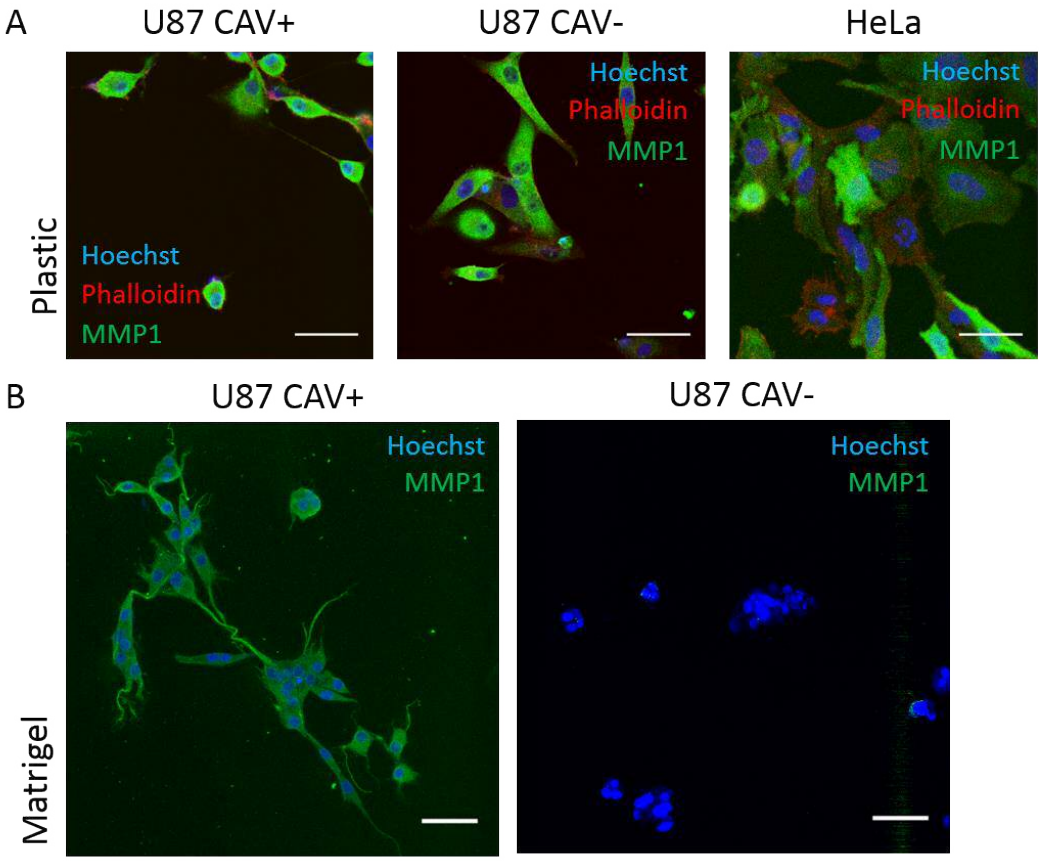

Figure 5.28 Immunofluorescence of 2D cultures of U87 CRISPR and HeLa cell lines for the expression of MMP1. U87 CAV+ and CAV- grown on plastic (A) and on Matrigel (B) and stained with Hoechst 33342 (blue: nuclei), Phalloidin-Alexa647 (Red: Cytoskeleton) and, MMP1 (Green). HeLa in A were used as a control. Scale bar 50µm

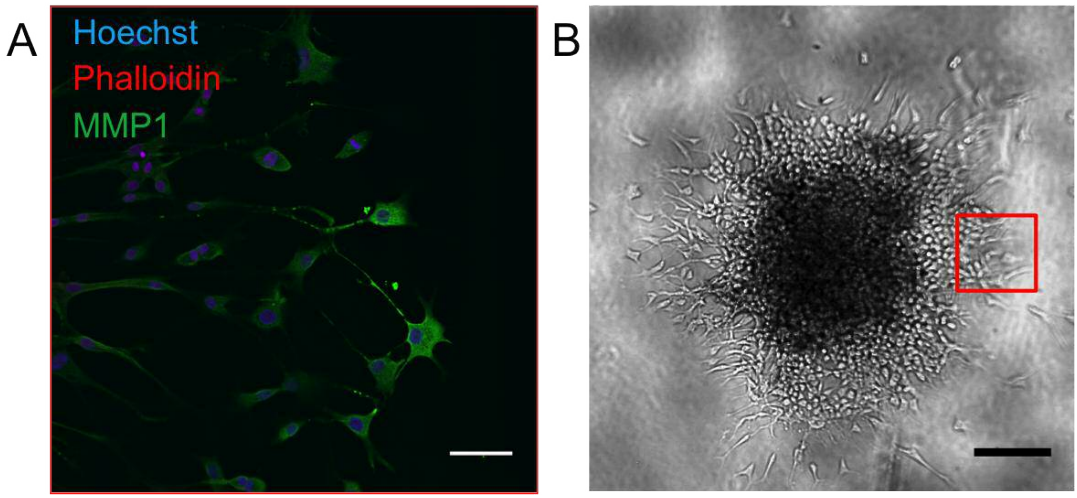

Figure 5.29 I Immunofluorescence of 3D-spheroids (U87 CAV+ cell lines) embedded in Matrigel for the expression of MMP1. A: Sphere was embedded in Matrigel and stained with Hoechst 33342 (blue: nuclei), Phalloidin-Alexa647 (Red: Cytoskeleton) and MMP1 (Green). Scale bar 50µm. B: Bright-field image of the indicative position (red square) for the spheroid staining. Scale bar 100µm.

5.4.3.2 ADHESION MARKERS

We next analysed for UPAR (Figure 5.30, Figure 5.31, Figure 5.32). UPAR is the primary ligand of UPA but is also able to interact with a variety of proteins such as vitronectin in the ECM and integrins.

Western blot for UPAR showed more consistent results, particularly when cells were grown on Matrigel (Figure 5.30). The results here showed the expression of UPAR to correlate with the expression of Cav-1, UPAR being higher in the CAV+ cells. These findings are consistent with the RT-PCR data (Figure 5.20). The data for cells growing on plastic showed essentially no difference in UPAR expression between CAV+ and CAV- cells. Again, this is entirely consistent with the respective RT-PCR results.

Immunofluorescence staining for UPAR in cells grown upon 2D Matrigel showed that UPAR is highly expressed only by the CAV+ cells (Figure 5.31) while CAV- cells a weaker signal. Similarly to the studies with MMP1, the simultaneous conduct of these immunofluorescence studies gives some assurance that this result is real and not a technical artefact.

The staining for UPAR was also evident by immunofluorescence in the invading spheroids, which revealed CAV+ cells in the outer rim of the invasive edges to express levels of UPAR, again indicative that the molecule is important for migratory/invasive function in these cells (Figure 5.32).

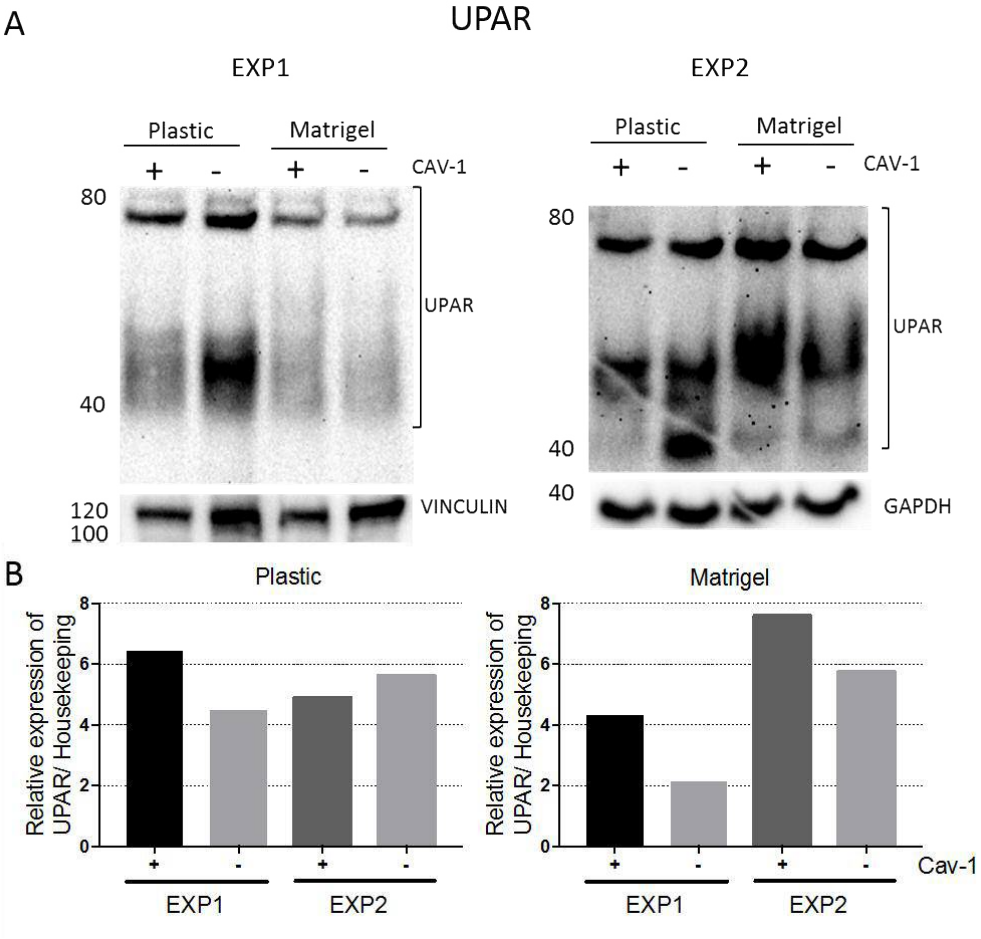

Figure 5.30 A: Western blot analysis for the expression of UPAR in U87 CAV+ and CAV- grown upon 2D plastic or upon 2D Matrigel. GAPDH or Vinculin were used as a housekeeping gene and the normalized quantification is reported in B. three separate experiments are reported, each one from three different sets of samples.

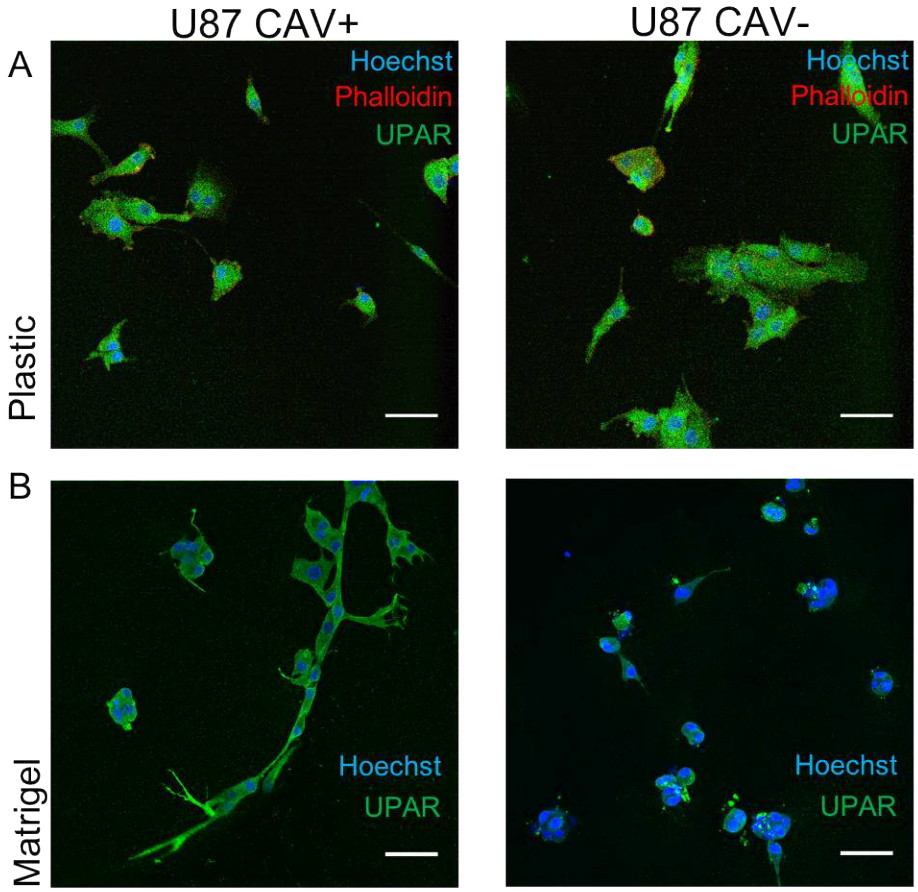

Figure 5.31 Immunofluorescence of 2D cultures of U87 CRISPR cell lines for the expression of UPAR. U87 CAV+ and CAV- grown on plastic (A) and on Matrigel (B) and stained with Hoechst 33342 (blue: nuclei), Phalloidin-Alexa647 (Red: Cytoskeleton) and, UPAR (Green). Scale bar 50µm

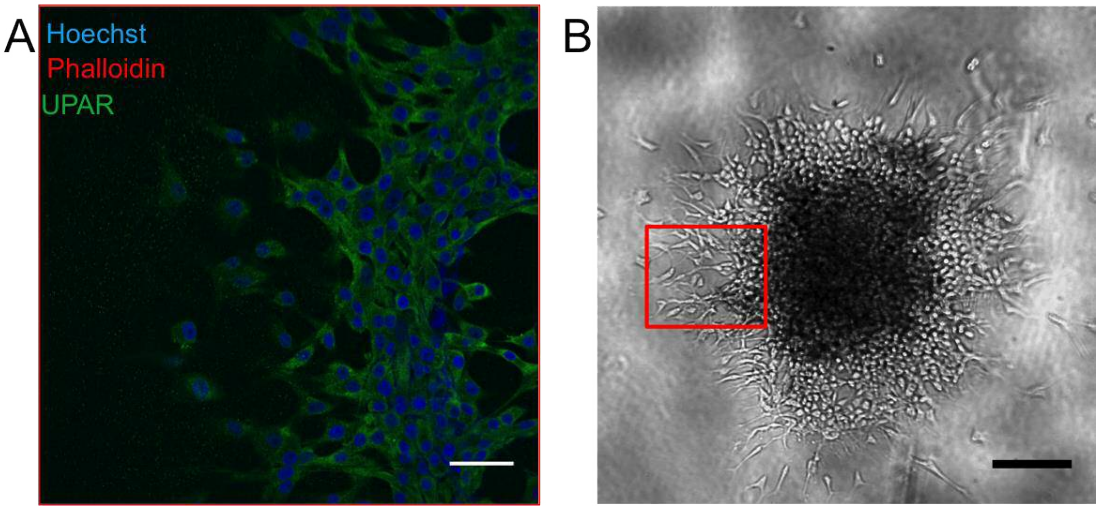

Figure 5.32 Immunofluorescence of 3D-spheroids (U87 CAV+ cell lines) embedded in Matrigel for the expression of UPAR. A: Sphere was embedded in Matrigel and stained with Hoechst 33342 (blue: nuclei), Phalloidin-Alexa647 (Red: Cytoskeleton) and UPAR (Green). Scale bar 50µm. B: Bright-field image of the indicative position (red square) for the spheroid staining. Scale bar 100µm.

We next analysed for CD44 (Figure 5.33, Figure 5.34, Figure 5.35). CD44 is the primary ligand of Hyaluronic acid, involved in cell–cell interactions, cell adhesion and migration.

The results for CD44 represents an anomalous finding in that the RT-PCR data (Figure 5.20), indicated that cells growing on 2D Matrigel showed significant reduction in CD44 transcript in the CAV+ phenotype.

The Western blot analysis showed a very strong signal for CD44 expression in all samples, with a slight increase in CD44 expression in the CAV+ cells when growing on Matrigel (Figure 5.33). Interestingly, Experiment 2 showed a shift in the CD44 signal from a molecular weight of ca. 80 kDa to 220 kDa. This molecular weight shift was not replicated in the signals for other antibodies run simultaneneously on the same gel, such as GAPDH. A possiblility is that the boiling of the samples didn't completely denature the 3D structure of the proteins and some glycosylation sites were still in their native conformation, making more difficult for CD44 to travel along the electrophoresis gel.

The immunofluorescence on 2D showed no difference in CD44 expression, both on plastic and on Matrigel, with the images showing a strong and well-defined signal (Figure 5.34). CD44 was also abundantly expressed by CAV+ cells invading from spheroids embedded in the 3D Matrigel (Figure 5.35).

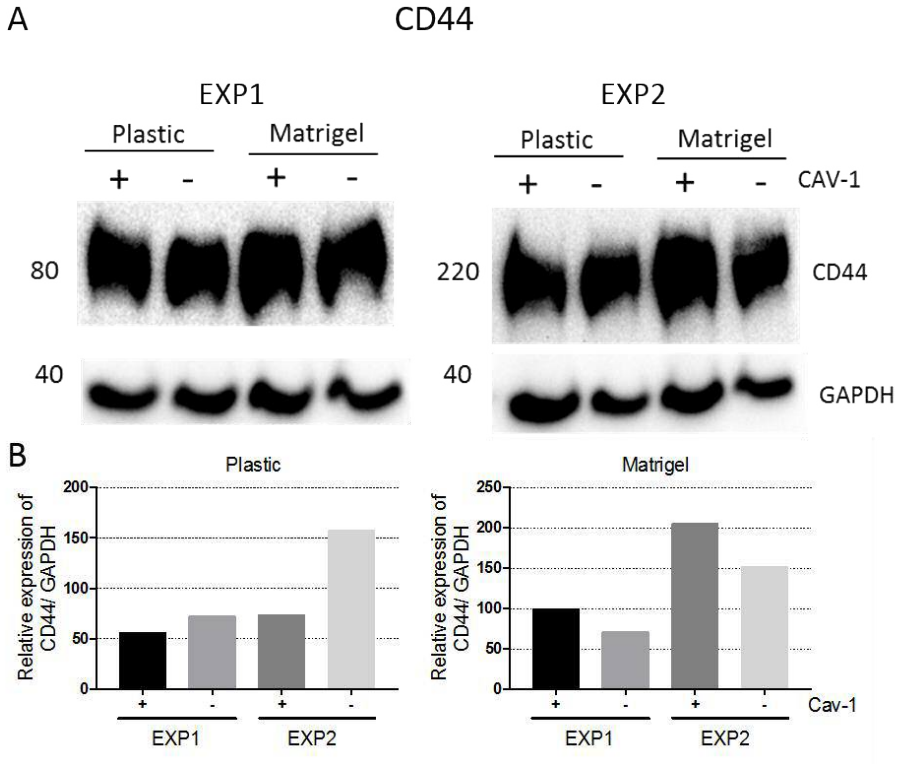

Figure 5.33 A: Western blot analysis for the expression of CD44 in U87 CAV+ and CAV- grown upon 2D plastic or upon 2D Matrigel. GAPDH was used as a housekeeping gene and the normalized quantification is reported in B. three separate experiments are reported, each one from three different sets of samples.

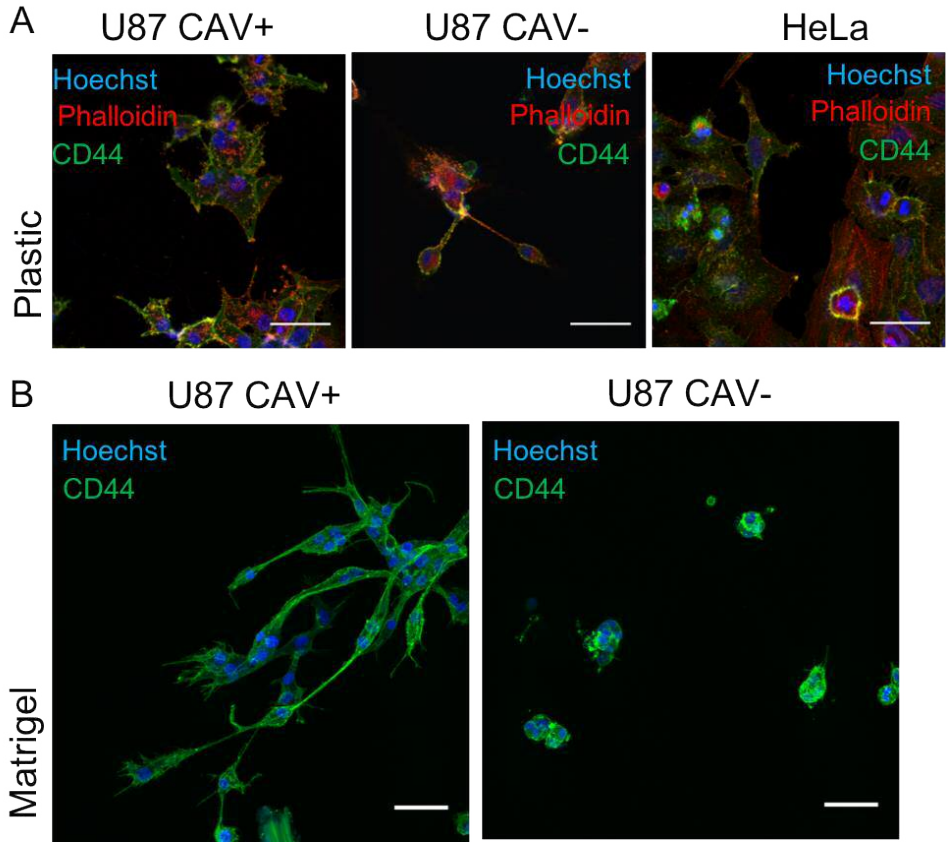

Figure 5.34 Immunofluorescence of 2D cultures of U87 CRISPR and HeLa cell lines for the expression of CD44. U87 CAV+ and CAV- grown on plastic (A) and on Matrigel (B) and stained with Hoechst 33342 (blue: nuclei), Phalloidin-Alexa647 (Red: Cytoskeleton) and, CD44 (Green). HeLa in A were used as a control. Scale bar 50µm

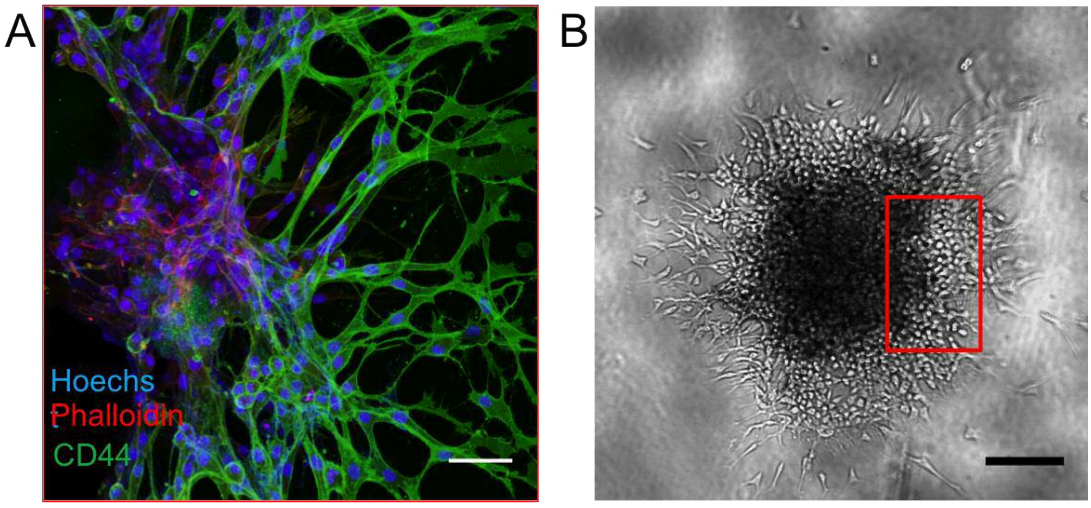

Figure 5.35 Immunofluorescence of 3D-spheroids (U87 CAV+ cell lines) embedded in Matrigel for the expression of C44. A: Sphere was embedded in Matrigel and stained with Hoechst 33342 (blue: nuclei), Phalloidin-Alexa647 (Red: Cytoskeleton) and CD44 (Green). Scale bar 50µm. B: Indicative position (red square) of the picture in A over whole sized bright field images of the invading sphere. Scale bar 100µm.

Finally, we analysed for ECAD (Figure 5.36, Figure 5.37). ECAD is a cell-cell adhesion glycoprotein recognised as marker of epithelial differentiation and as a tumour suppressor.

E-Cadherin displayed no signal in the RT-PCR but is a molecule of potential interest in terms of interaction with Cav-1. Hence, the correlation with Cav-1 was examined here by Western blot and Immunofluorescence (Figure 5.20).

The Western blot data failed to reveal any further information, as ECAD appeared to be variously expressed depending on the experiment (Figure 5.36). Perhaps, the studies on Matrigel would indicate that Cav-1 has little effect on the expression of ECAD, but clearly further studies would be required to confirm this (Figure 5.36). On 2D plastic, we failed to obtain a signal, even with an increase in the primary antibody concentration (Figure 5.37); no staining for ECAD was perform in cells grown on 2D Matrigel or within Matrigel-embedded 3D spheres.

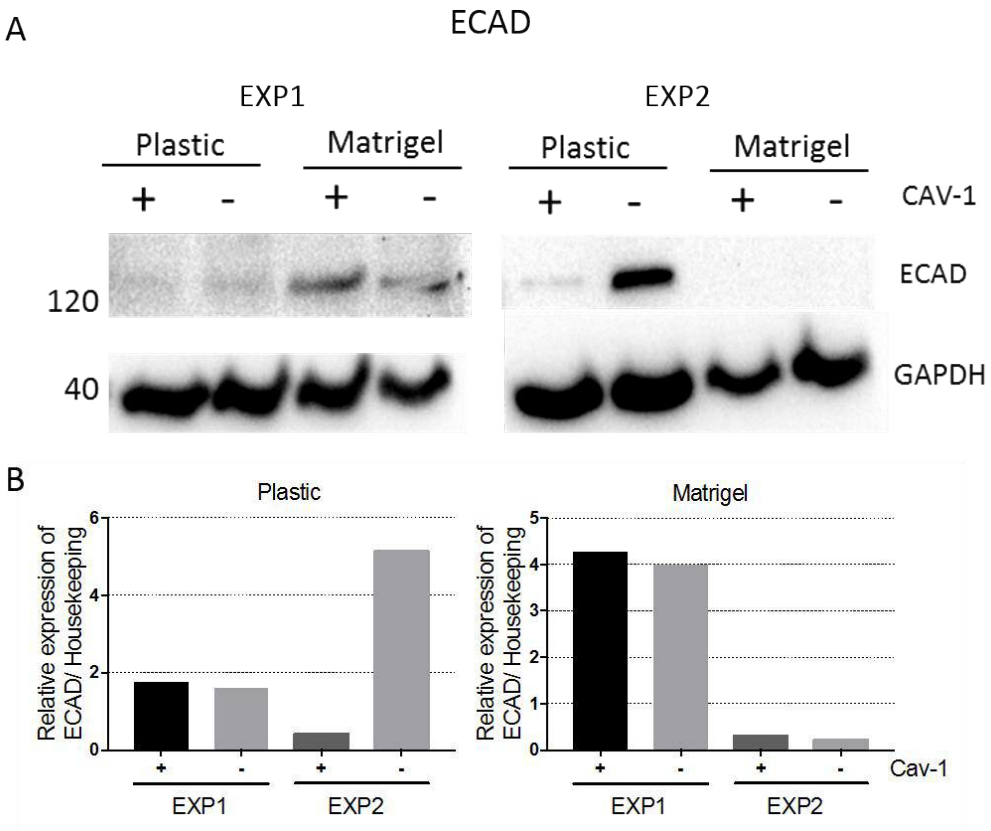

Figure 5.36 A: Western blot analysis for the expression of E Cadherin (ECad) in U87 CAV+ (BB) and CAV- (KO) grown on plastic or on Matrigel. GAPDH was used as a housekeeping gene and the normalized quantification is reported in B. three separate experiments are reported, each one from three different sets of samples.

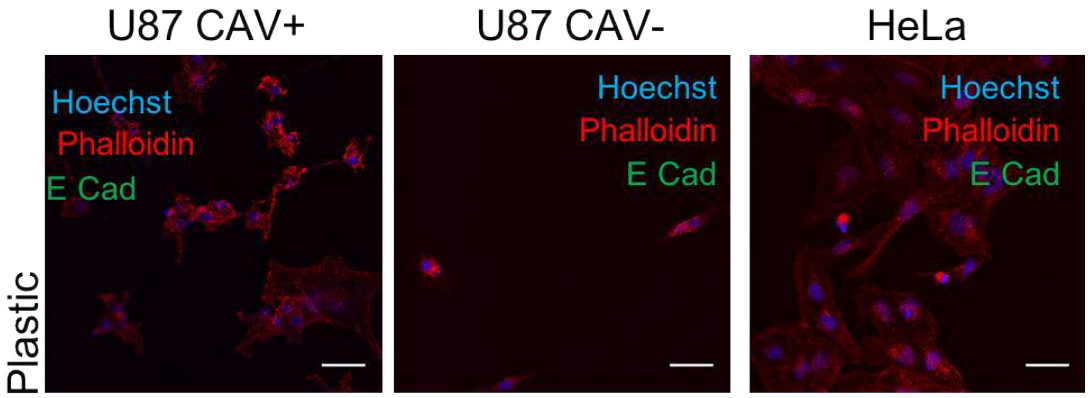

Figure 5.37 Immunofluorescence of 2D cultures of U87 CRISPR and HeLa cell lines for the expression of E Cadherin (E Cad). U87 CAV+ and CAV- grown on plastic and stained with Hoechst 33342 (blue: nuclei), Phalloidin-Alexa647 (Red: Cytoskeleton) and, ECad (Green). HeLa in A were used as a control. Scale bar 50µm

5.4.4 PROTEIN ARRAY ON CELLS INTERACTING WITH MATRIGEL: BUILDING A PUTATIVE SIGNALLING PATHWAY

Given the findings from RT-PCR, Western blot and immunofluorescence studies for both cells grown on 2D Matrigel and for 3D spheroids embedded on Matrigel we next utilised a proteomic approach to examine molecules that may correlate with the changes in Cav-1 levels resulting from our CRISPR knockout model. In particular this section of the work utlised an intermediate matrix model, i.e. intermediate between the 2D Matrigel and 3D spheroids, whereby individual cells were embedded in Matrigel for 4 days prior to using for proteomic array analysis. The advantages of this approach for the proteomic analysis over both the 3D spheroid model and the 2D model, are that all cells are interacting with the Matrigel rather than just the invading edge and hence bulk biochemical analysis may produce more consistent and meaningful data.

The proteomic data also includes analysis of cells grown on 2D plastic, the comparisons between the plastic and Matrigel formats will not be the subject of extensive discussion but rather the focus will be what the collective findings may mean for potential hypotheses around Cav-1 interactions that promote invasion.

Figure 5.38 shows the results of the proteomic array analysis for U87 CAV+ and CAV- grown upon plastic and importantly embedded within Matrigel, and using commercially obtained oncology, angiogenesis and protein kinases platforms. From the combined platforms a selection of 16 molecules are shown in the heatmap (Figure 5.38C). These 16 molecules were the ones which showed a level of expression signficantly greater to background irrespective of the growth format, i.e. plastic or Matrigel.

The molecules that showed a significant fold-change in expression as a function of ratio be CAV+/CAV- included UPA, HSP27 S78/S82, IL8 all of which were positively correlated with Cav-1 expression in cells grown within Matrigel. Those molecules whose expression appeared negatively correlated with Cav-1 expression included, TSP-1 and Coagulation Factor III.

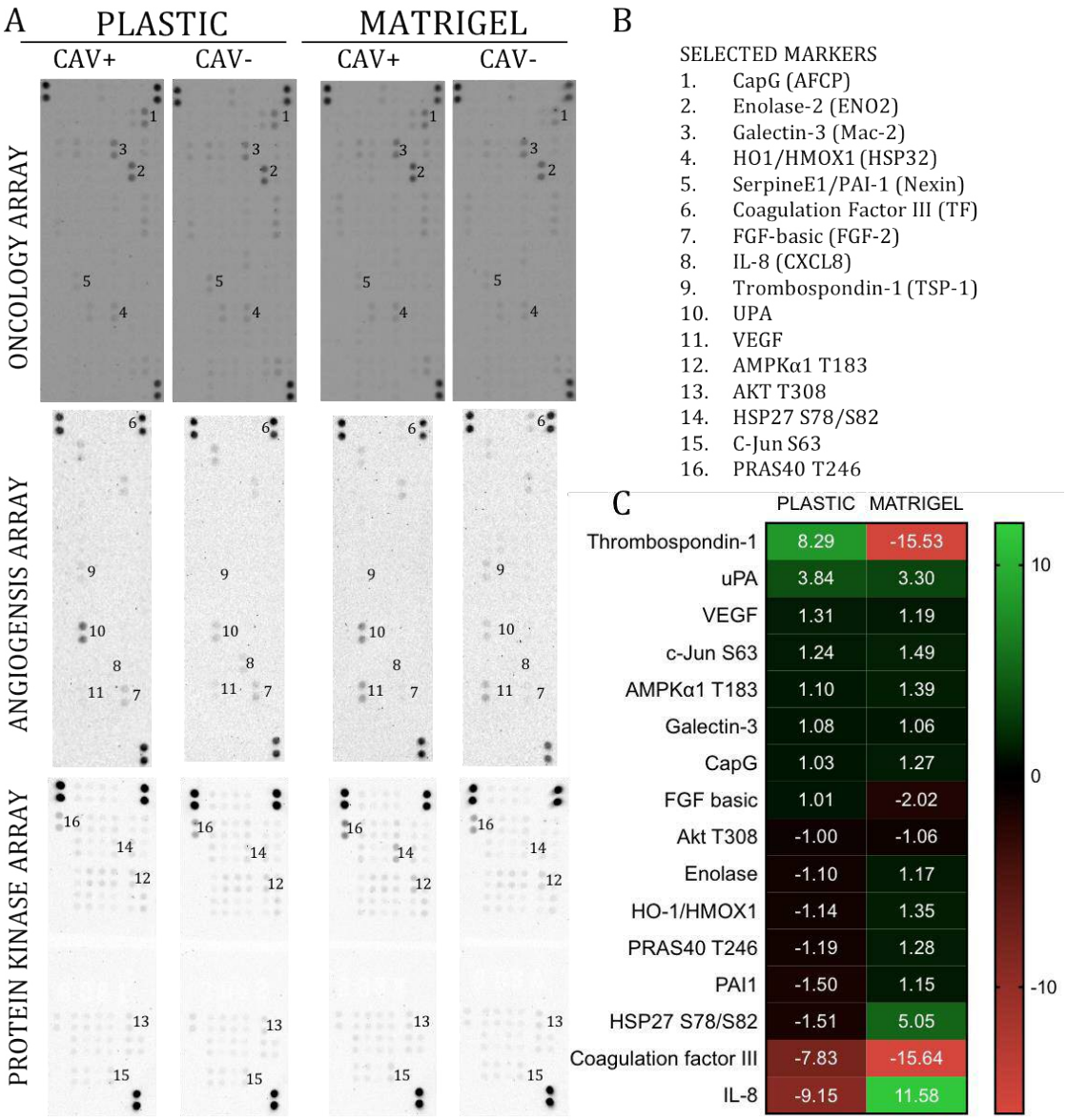

Figure 5.38 A: Oncology, angiogenesis and protein kinases array analysis on U87 CAV+ and CAV- grown upon plastic and within Matrigel. Resulting pictures of the exposed Arrays for each cell line. B: Legend of the markers indicated in A. C: Heat map of the significant protein expression modifications. Each value represents the fold change ratio CAV+/CAV-.

Some of the markers evidenced as correlating with Cav-1 from the protein array data have previously been linked with GBM invasion and/or with Cav-1 signalling. A schematic summarizing the putative interactions that involve some of our examined molecules shown in Figure 5.39, with a more simplified scheme presented in Figure 5.40. In constructing the schemes showing putative Cav-1 interactions we have brought information from the literature and focussed from the array on UPA, HSP27 S78/S82 and TSP-1 interactions in particular.

Interesting is the connection between TSP-1 and UPA (H. Li et al., 2017) since they inhibit each other but at the same time, they promote the activation of TGF-β1. The latter is able in return to promote the activation of TSP1 and indirectly inhibit the activation of PLS, through activation of PAI1, which inhibits UPA, consequently blocking the conversion from plasminogen (PLG) to plasmin (PLS).

Cav-1 would have a role in this process since it is known to block TGF-β1 (Cosset et al., 2012). This would promote the activation of the proteases cascade and the enhancing of the invasion process (red circle in Figure 5.39B).

TSP1 is also known for being able to behave as a tumour suppressor (Huang, Sun, Yuan, & Qiu, 2017) with the ability, against VEGF, to induce apoptosis (Figure 5.39C). When TSP1 overcomes VEGF, it allows the recruitment of FYN by CD36 and this activates the cascade for apoptosis, while when VEGF is higher CD36 recruits SRC and promotes survival.

TSP1 expression has been related to increased survival (Elstner et al., 2011), but it has also been demonstrated that tumours can adapt to high levels of TSP1 and bypass its inhibitory action (Filleur et al., 2001).

Kinases HSP27 and AKT participate in the invasive process by activating UPA (Malinowsky et al., 2012).

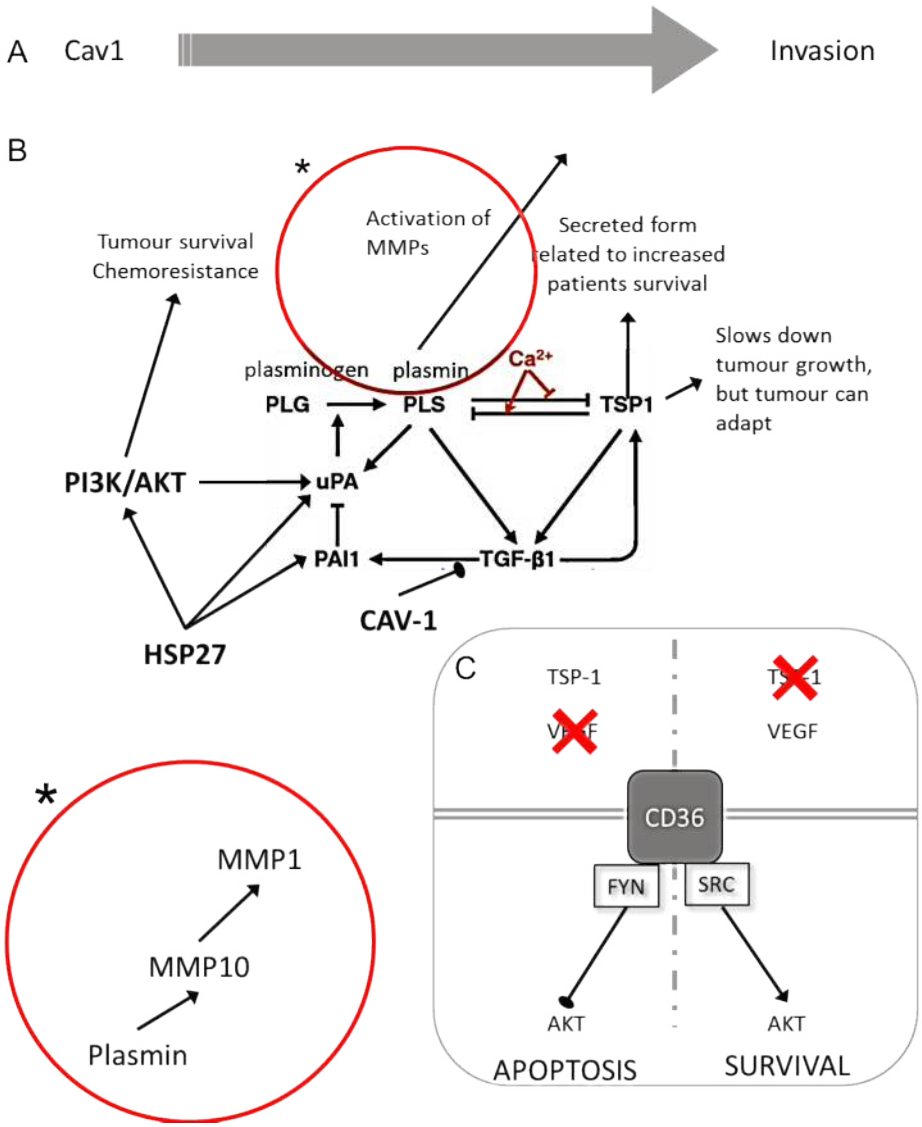

Figure 5.39. Literature analysis of protein array. A. Main result of the invasion analysis. Cav-1 appears to drive invasion in Matrigel in GBM cell lines. B: Connections between differentially expressed markers in the protein array, reviewed from the literature. The circle with the asterisk is reported enlarged in the bottom to show the activation cascade of the MMPs. C. Differential activation of CD36 by TSP-1 or VEGF leads to the recruitment of FYN or SRC and results in two phenotypical outcomes, apoptosis or survival.

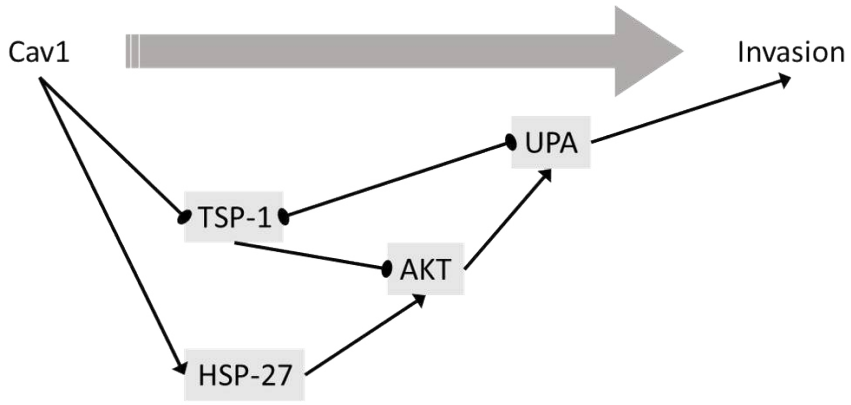

Figure 5.40 Simplified conjectured pathway explaining the mechanism under Cav-1 stimulating invasion of GBM cell lines.

The integration of the protein array results with the information provided by the literature allowed us to create a putative pathway that explains the mechanism according to which Cav-1 regulates 3D invasion (Figure 5.40). In CAV+ cells, Cav-1 activates HSP27 that promotes the activation of UPA through AKT. UPA converts PLG in PLS and activates the cascade of the proteases that leads to invasion. At the same time, Cav-1 inhibits TSP1, which is not able to inhibit both AKT, UPA and consequently invasion.

To test our hypothesis, we decided to validate the markers selected in Figure 5.40 via Western blot. Together with UPA, HSP27 and TSP1, we also decided to examine:

- Activation of AKT, a key molecule in the putative scheme (Figure 5.40)
- SRC, which is involved in the activation of AKT and it has been related to Cav-1 in the literature (Goetz, Lajoie, et al., 2008);
- FAK, which is present at the focal adhesions (FAs) and it has been reported as stabilized by Cav-1, thus promoting FAs disassembling and cell movement (Goetz, Joshi, et al., 2008).

5.4.5 PROTEIN ARRAY PATHWAY VALIDATION

The phosphokinases protein array analysis of U87 CAV+ and CAV- showed that on plastic the activation of HSP27 was inhibited to some extent by Cav-1 and on Matrigel driven by Cav-1 (Figure 5.38). The Western blot analysis was consistent with the results for plastic, but showed for cells on Matrigel that contrary to the proteomic array results Cav-1 appeared to inhibit the activation (phosphorylation) of HSP27 (Figure 5.41) when the quantification of the phosphorylated form was normalised on the total expression of HSP27. While the readout for the protein array was solely on the phosphorylated HSP27, examining the Western blot in Figure 5.41A for the Matrigel lanes fails to show a positive correlation with Cav-1 even based on the phosphorylated HSP27 form alone. A further point of note is that while the proteomic array was conducted with cells embedded within the Matrigel, the Western blot data was undertaken on cells growing on the surface of Matrigel in a simlar format to that described as the 2D Matrigel format in previous sections. The approach for the Western blot was out of necessity to harvest sufficient protein for the gel loading. The more intimate interactions of all of the cells when embedded in the matrix could well have impacts upon the signalling molecules. A future study to consider is the use of the p38 MAPK inhibitor, SB202190 to see if effects on invasion can be seen to be mediated via HSP27. p38 MAPK is one of the kinases responsible for the phosphorylation and activation of HSP27 (Malinowsky et al., 2012) and has been used experimentally in cell culture at effective concentrations of 5μM (Chen, Xie, & Xu, 2010; Nemoto, Xiang, Huang, & Lin, 1998). Although any data from such experiment needs to be considered carefully as phosphorylation of HSP27 may be carried out by other kinases, not only p38 MAPK, e.g. PDK (Stetler et al., 2012).

On the protein array we found TSP1 to be positively correleated with Cav-1 levels in cells grown on plastic but signficantly downregulated in CAV+ cells embedded Matrigel (Figure 5.38). The Western blot analysis presented challenges in interpretation since the signals were very weak despite the use of ultra-sensitive developing agents and extended exposure times. Based on the

technical issues alone it was not so surprising that the Western blot did not reveal TSP1 to be influenced by changing Cav-1 levels (Figure 5.42).

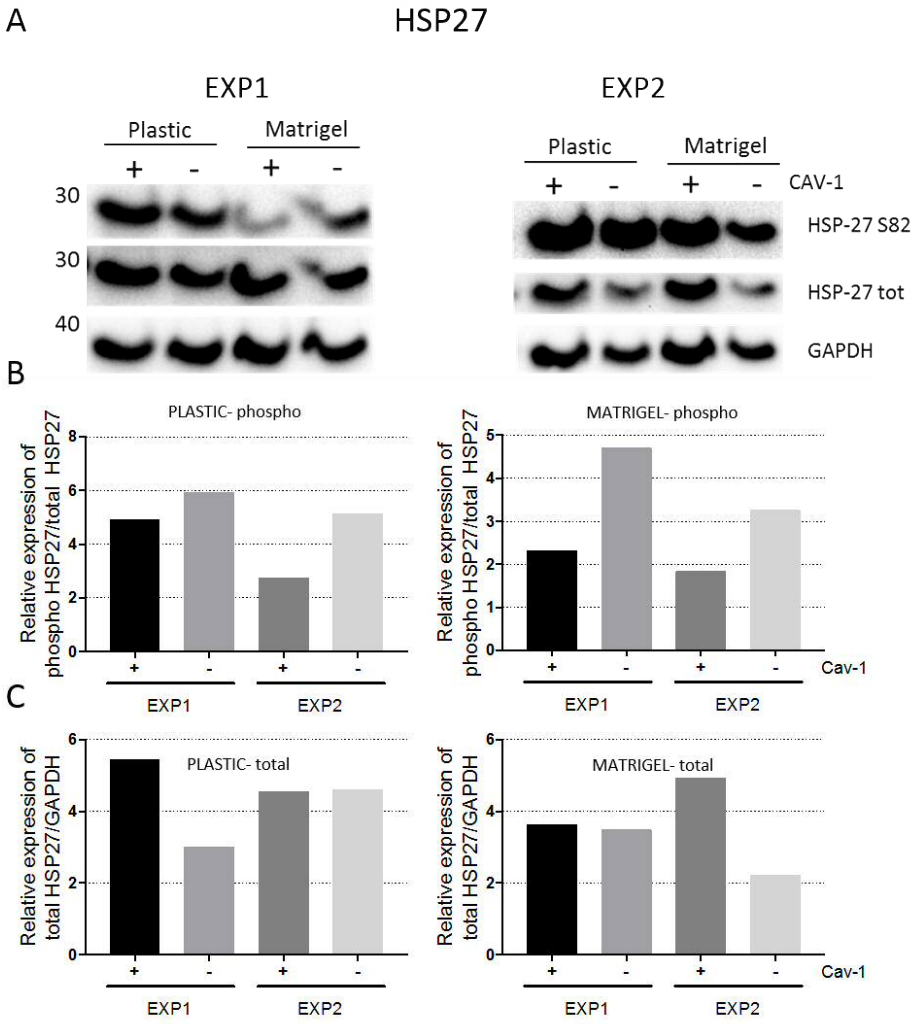

Figure 5.41 Western blot analysis for the expression of phospho HSP27 (Ser82) in U87 CAV+ and CAV- cells grown on plastic or on Matrigel. GAPDH was used as a housekeeping. The phosphorylated forms were normalized on their total form (B), while the total forms were normalised on GAPDH (C).

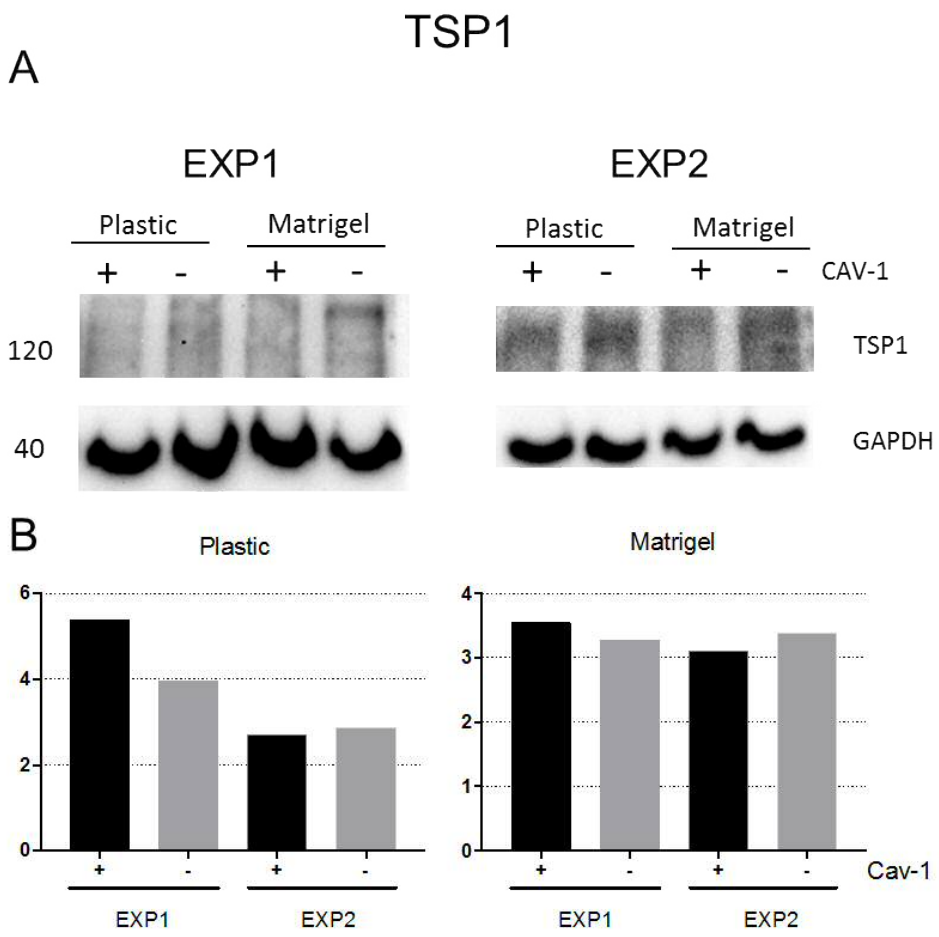

Figure 5.42 A: Western blot analysis for the expression of Thrombospondin-1 (TSP1) in U87 CAV+ and CAV- grown on plastic or on Matrigel. GAPDH was used as a housekeeping gene and the normalized quantification is reported in B. three separate experiments are reported, each one from three different sets of samples.

UPA in the protein array was shown upregulated in CAV+ cells, both in cells growing on plastic and in cells embedded in Matrigel (Figure 5.38). Despite some interexperimental variation, two from three Western blot experiments on cells grown on Matrigel showed an upregulation of UPA in CAV+ cells (Figure 5.43), a result concordant with the protein array findings. The Western blot data for cells grown on plastic did not indicate any dependence as such for UPA expression upon Cav-1.

To further clarify the relationship of UPA and Cav-1 in cells grown on Matrigel we undertook immunofluorescence for UPA (Figure 5.44) which revealed that UPA is ubiquitously expressed by CAV+ cells, while only some of the KO cells express the marker, with some groups of CAV- cells not showing any signal for UPA. This was in agreement with the protein array and western blot analyses.

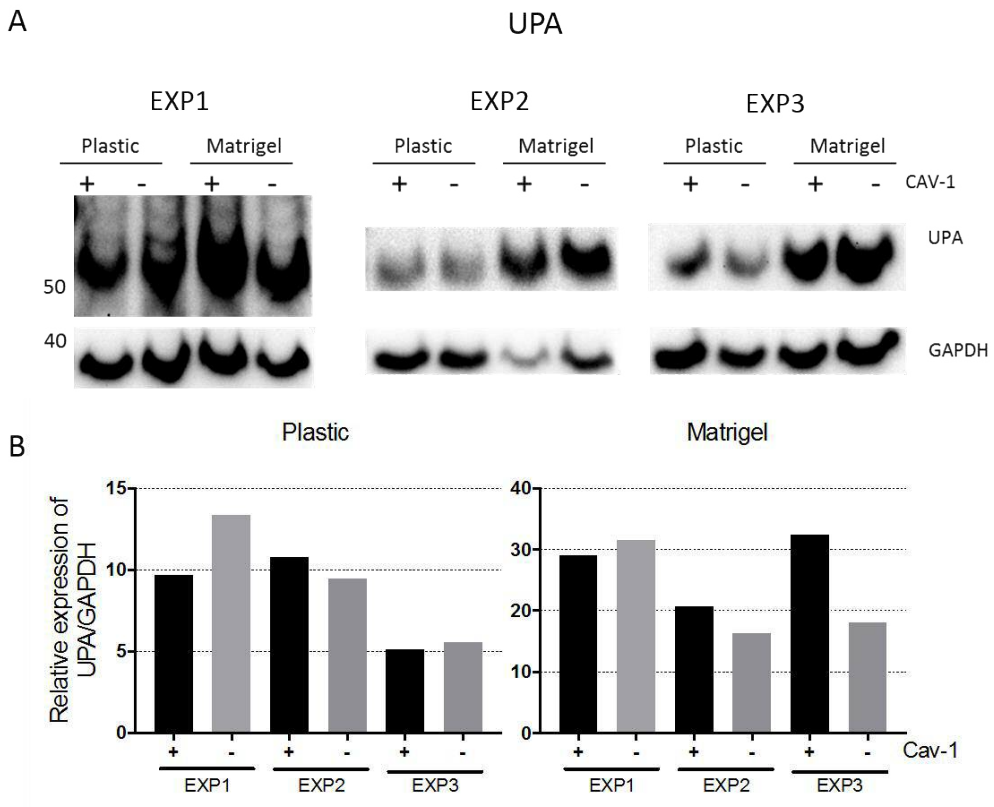

Figure 5.43 A: Western blot analysis for the expression of UPA in U87 CAV+ and CAV- grown on plastic or on Matrigel. GAPDH was used as a housekeeping gene and the normalized quantification is reported in B. three separate experiments are reported, each one from three different sets of samples.

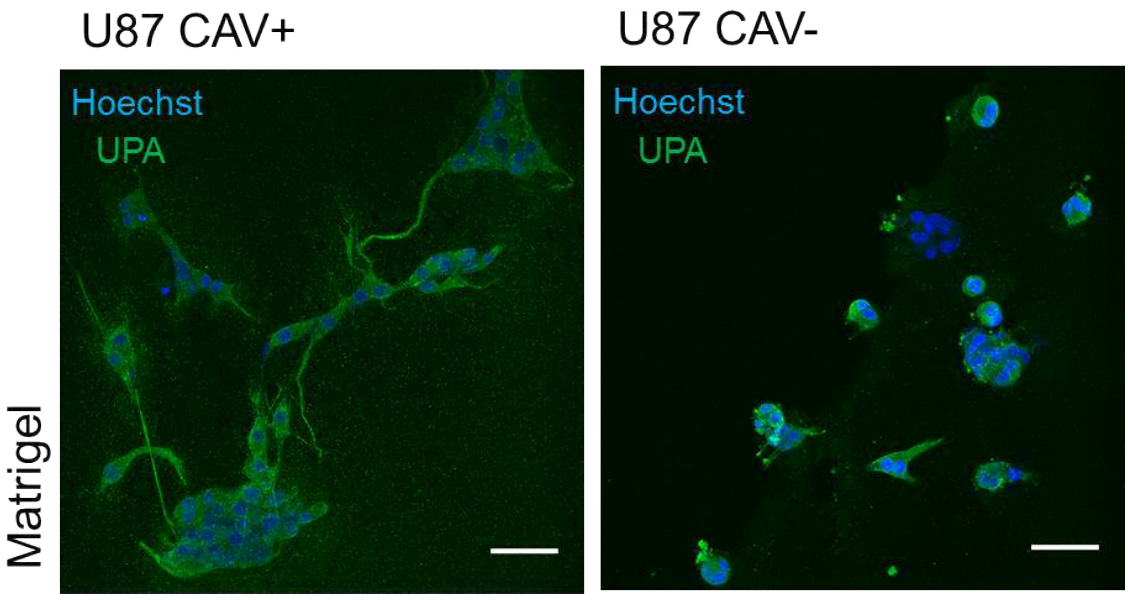

Figure 5.44 Immunofluorescence analysis of U87 CRISPR expression of UPA. U87 CAV+ and CAV- grown on Matrigel and stained with Hoechst 33342 (blue: nuclei), Phalloidin-Alexa647 (Red: Cytoskeleton) and, UPA (Green). Scale bar 50µm

In an attempt to further understand the connection of Cav-1 with the markers studied in this chapter, we explored intracellular kinases involved in GBM aggressiveness and reported to be correlated with Cav-1 and their expression. These are AKT, SRC and FAK.

In GBM, UPAR drives invasion also via key intracellular pathways, including PI3K/AKT. A large scale genomic analysis of GBM has demonstrated that this pathway is mutated in the majority of GBMs, with consequent high levels of phospho AKT. AKT can be phosphorylated in two sites, S473 and T308, both required for its activation. The phosphorylated form of AKT , detected at high levels in the majority of GBM samples, has been shown to help glioma cells to grow, evade apoptosis and enhance tumour invasion.

AKT was analysed for two of its activated phosphorylation forms, Ser473 and Thr308. The samples on plastic were obtained from both normal culture conditions or from samples undergone serum stimulation. Serum stimulation consisted of removing the serum from the culture medium for 16 hrs and then reintroducing it for 10 minutes before lysing the samples. The procedure allows examination of how able the cells can react under stress conditions, and is a common manipulation when observing phospho-proteins (Levin et al., 2010;

Levin, Panchabhai, Shen, & Baggerly, 2012). Serum stimulation is not a straight forward procedure for cells grown on Matrigel, as by the nature of the matrix itself growth factors will be present even in 'growth factor reduced' Matrigel. Experiments conducted in serum stimulation conditions are indicated as appropriate in the following series of figures. Quantification shows the phosphorylated forms normalised on the total expression of AKT.

For AKT S473 two out of three experiments conducted on plastic showed CAV+ cells to be associated with a greater degree of AKT phophorylation. The single experiment on Matrigel also showed the proportion of total protein that is phosphorylated on AKT Ser473 to be higher in the CAV+ cells (Figure 5.45).

For AKT Thr308 we found upon serum stimulation the phosphorylation response in CAV+ cells to be very noticable indicating, as for the S483 site, a role of Cav-1 in facilitating AKT activation (Figure 5.44). Under the other conditions conducted in normal growth medium conditions, the signal for AKT T308 was very weak, although quantification where possible suggested that CAV+ cells even here worked to facilitate AKT Thr308 (Figure 5.46).

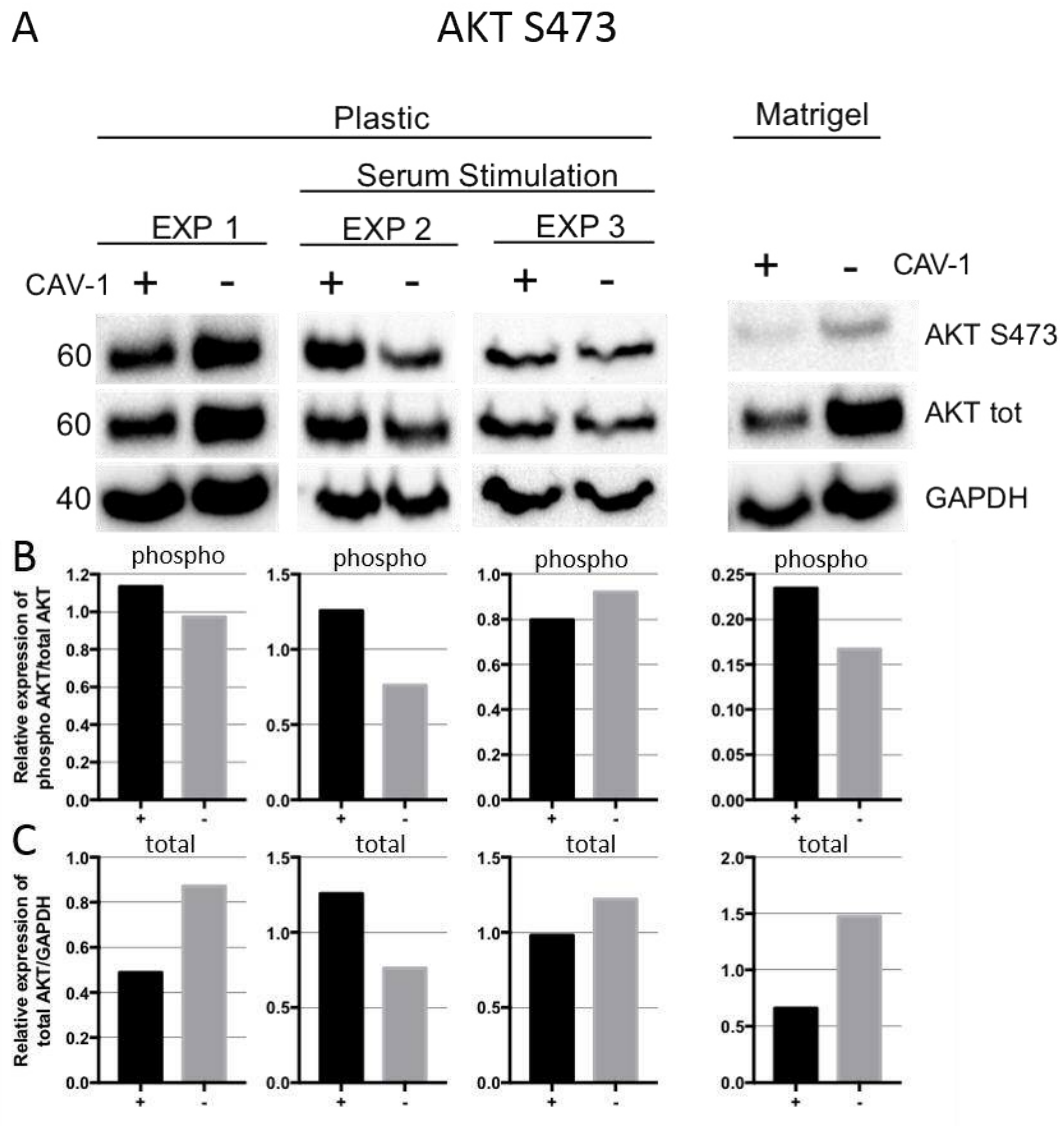

Figure 5.45 Western blot analysis for the expression of phospho AKT (Ser473) in U87 CAV+ and CAV- grown on plastic or on Matrigel. GAPDH was used as housekeeping. Three experiments are reported for the plastic condition, two of whom were conducted in serum reintroduction conditions. The phosphorylated forms were normalized on their total form (B), while the total forms were normalised on GAPDH (C).

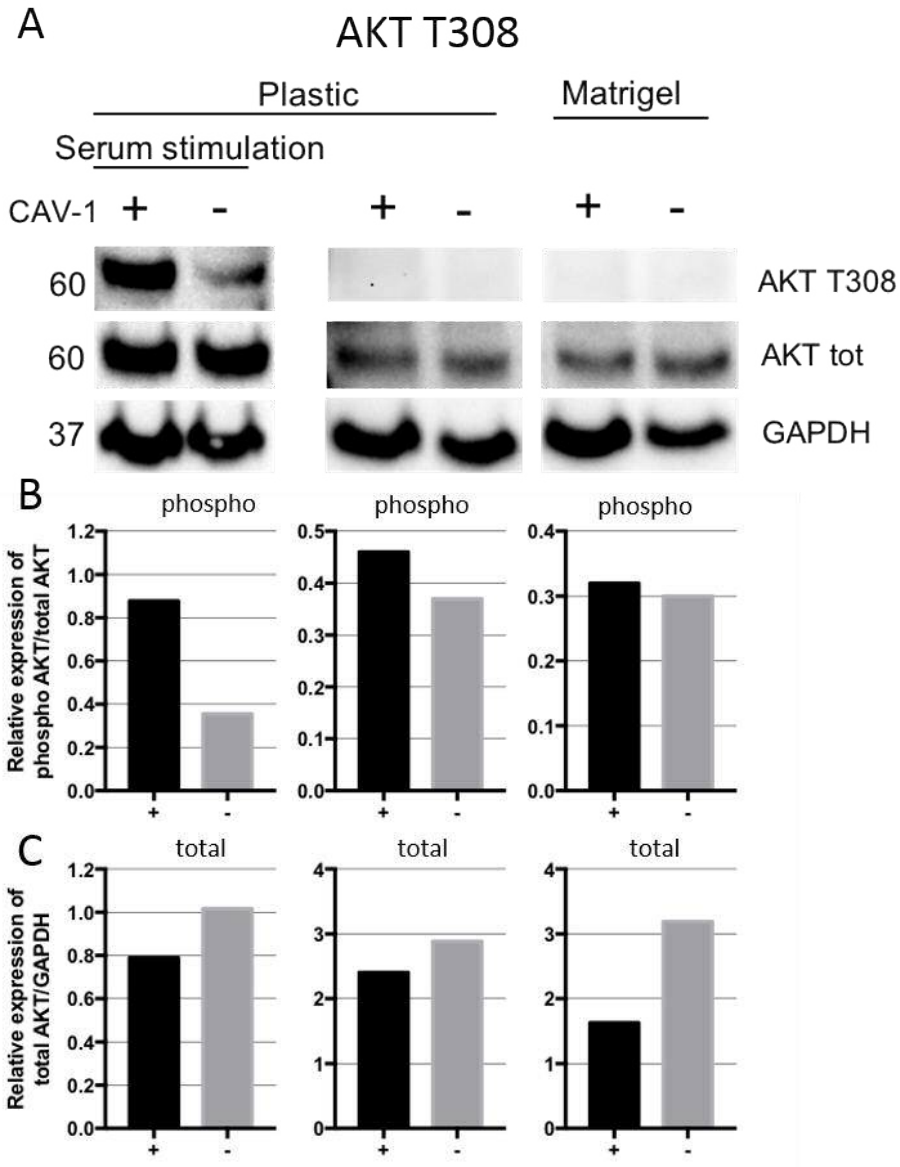

Figure 5.46 Western blot analysis for the expression of phospho AKT (Thr 308) in U87 CAV+ and CAV- grown on plastic or on Matrigel. GAPDH was used as housekeeping. Two experiments are reported for the plastic condition, one of whom was conducted in serum reintroduction conditions. The phosphorylated forms were normalized on their total form (B), while the total forms were normalised on GAPDH (C).

Src is reported as a promising target for anti-cancer therapy. Elevated Src activity has been detected in GBM samples in comparison with normal brain tissue. Our pilot studies for the validation of INSIDIA (Chapter 4) showed that Src inhibition has an impact on the ability of GBM cell lines to invade in the 3D invasion model.

Activated phosphoSrc (Tyr418) is able to phosphorylate Cav-1 on its Tyr14.

The Src signal in the Western blot was extremely weak, consistent with the phospho protein array data for this molecule (not shown). For this reason, a quantification of the phosphorylated form was not performed and only the total Src is shown in Figure 5.47. Specifically, in Matrigel cav-1 apperas not to have any influence on total Src levels, whereas disparate effects on total Src could be seen on cells grown on plastic, with or without serum stimulation.

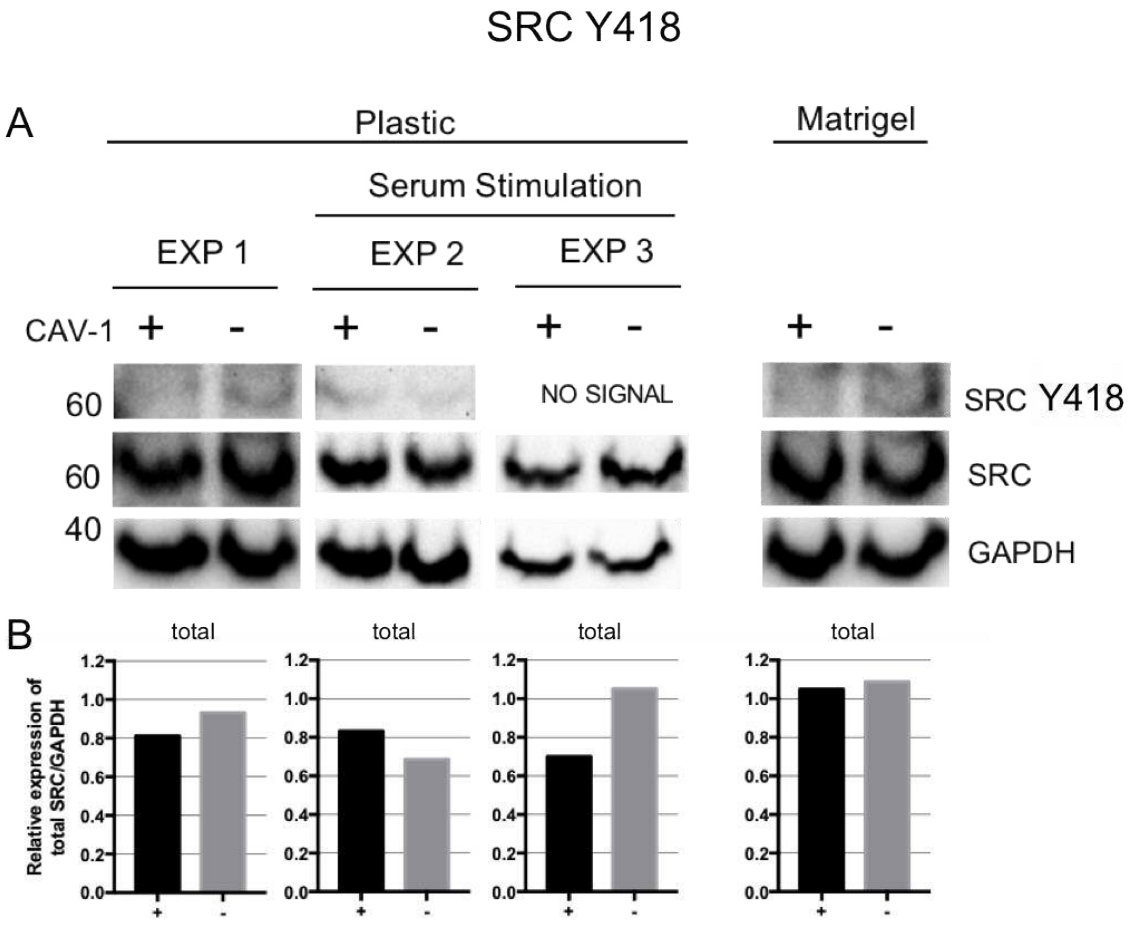

Figure 5.47 Western blot analysis for the expression of phospho Src (Tyr417) in U87 CAV+ and CAV- grown on plastic or on Matrigel. GAPDH was used as housekeeping. Three experiments are reported for the plastic condition, two of which were conducted in serum reintroduction conditions (A). The total forms were normalised on GAPDH (B).

FAK, together with Src, regulate the focal adhesion turnover, migration and proliferation in GBM. As mentioned, Src phosphorylates Cav-1 on its Tyr14. The phosphorylated form of Cav-1 is required to stabilize the localization of FAK within focal adhesions.

In the protein array the signal of phospho-FAK was very weak (data not shown). However, in Western blot experiments here we found that when cells underwent serum stimulation (plastic), a significant difference between CAV+ and CAV- cells was evident, with CAV+ cells having a higher proportion of FAK Tyr397. On Matrigel, under normal serum conditions, this difference in regulating the activity of FAK disappeared (Figure 5.48).

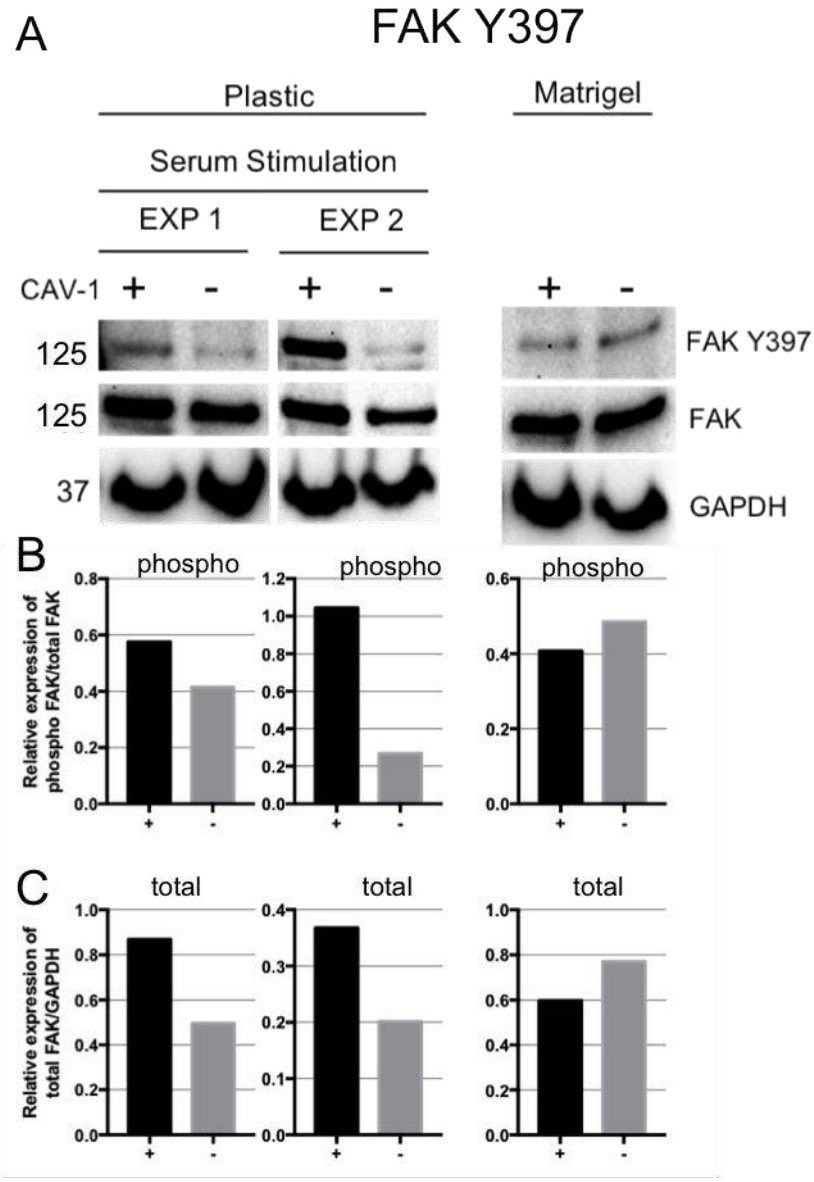

Figure 5.48 Western blot analysis for the expression of phospho FAK (Tyr397) in U87 CAV+ and CAV- grown on plastic or on Matrigel. GAPDH was used as a housekeeping. Two experiments are reported for the plastic condition, one of whom was conducted in serum reintroduction conditions. The phosphorylated forms were normalized on their total form (B), while the total forms were normalised on GAPDH (C).

5.5 SUMMARY AND CONCLUSIONS

Despite several decades of intensive research and improved diagnostic technology, the prognosis for patients with high-grade gliomas remains very poor.

One of the main reasons for the lack of improvements is the highly invasive behaviour of glioma cells able to effectively spread from the tumour to both

hemispheres of the brain, along white matter tracts, subependymal layers and blood vessel basement membranes. Despite more precise surgery, the elimination of all malignant cells is improbable. Recurrent tumours exhibit resistance to both chemotherapy and radiotherapy.

To initiate this migration process, glioma cells have to be able to degrade the extracellular matrix for the creation of a migration space. They also have to be able to detach from the tumour bulk, attach to the single components of the extracellular environment and modify their cytoskeletal structure to allow the movement.

In this chapter we have shown that Cav-1 influences positively the invasive ability of GBM cell lines growing in spheroids surrounded by an extracellular matrix. When Cav-1 expression was inhibited by different techniques, cells all displayed a reduction of their invasive ability. The reduction in invasion was not related to an increase in cellular death, suggesting that cells with no or low expression of Cav-1 may not be able to interact effectively with the extracellular environment. This is consistent with reports in the literature relating to caveolae regulating communication between the extracellular and the intracellular environment, undertaking vesicular transport as well as cholesterol homeostasis, facilitating cell migration and cell cycle progression (Parat & Riggins, 2012). It also appears that Cav-1 itself is able to function outside the caveolae compartments, being secreted into the extracellular environment as part of membrane vesicles which are able to advance prostate cancer aggressiveness (Watanabe et al., 2009).

In this work, the mechanistic insight of the Cav-1- driven invasion included the use of transcriptional (RT-PCR) and protein expression analysis (Protein array) with validation of the results by Western Blot and immunofluorescence studies.

Most of the investigations we undertook in this chapter involved 2D model platforms, with cells growing on plastic, on Matrigel or, for the protein array work, as single cells embedded in Matrigel. The latter model more likely to align to the 3D spheroid model we used in Chapter 4 and earlier parts of chapter 5 for the quantitative measure of invasion. The 3D spheroid model itself while excellent for the study of quantitative aspects of invasion did not lend itself to discreet measurements of biology happening at the cell-matrix interphase. Specifically,

the one approach we pursued to explore this, immunofluorescence investigations, presented significant technical challenges on the embedded 3D spheroid model.

A summary of the results obtained for each of the molecules of interest and for each technique used is shown in Table 5.7. While CTSB and UPAR show consistent results among the experiments, with both of them being driven by Cav-1 in their expression, the other markers expression is less clear. One of the most interesting among them is MMP1, with Cav-1 driving its expression according to the PCR and the immunofluorescence on 2D Matrigel, as well as with a good expression in the CAV+ invading cells in 3D. The other interesting one is UPA, whose results on protein array, western blot and immunofluorescence on Matrigel confirm its expression to be concordant with Cav-1.

Table 5.7 Integrated results on markers expression from different techniques. The arrows indicate if the marker expression is concordant (↑) or discordant (↓) with the one of Cav-1.

	CTSB	**CTSD**	**MMP1**
PCR	Cav1 ↑	Cav1 ↑	Cav1 ↑
Protein Array	No difference	No difference	-
Western Blot	Cav1 ↑ on Matrigel	Cav1 ↓	Cav1 ↓ on Matrigel
IF 2D Plastic	No difference	No difference	No difference
IF 2D Matrigel	Cav1 ↑	No difference	Cav1 ↑
IF 3D	Invading cells	Invading cells	Invading cells
	CD44	**UPAR**	**UPA**
PCR	Cav1 ↓ on Matrigel	Cav1 ↑	Cav1 ↓ on Matrigel
Protein Array	-	-	Cav1 ↑
Western Blot	Cav1 ↑ on Matrigel	Cav1 ↑ on Matrigel	Cav1 ↑ on Matrigel
IF 2D Plastic	No difference	No difference	-
IF 2D Matrigel	Cav1 ↑	Cav1 ↑	Cav1 ↑
IF 3D	Invading cells	All spheroid	-
	TSP1	**HSP27 S82**	**FAK Y397**
PCR	-	-	-
Protein Array	Cav1 ↓ on Matrigel	Cav1 ↑ on Matrigel	No difference
Western Blot	No difference	Cav1 ↓	Cav1 ↑ on Plastic
	AKT S473	**AKT T308**	**SRC Y417**
PCR	-	-	-
Protein Array	No difference	No difference	No difference
Western Blot	Cav1 ↑	Cav1 ↑	No signal

In 2010, a work published on the Annals of Biomedical Engineering (Demou, 2010) connected Cav-1 as the orchestrator of the increased invasiveness of U87 after increased compressive pressure. The work reported that, when compression is applied to GBM cells growing in 3D gels, invasion and cells detachment are enhanced. Cav-1 would be the first responder, by activating CD44, the complex UPAR-UPA, CTSB and MMP1, all promoting adhesion to contact and degradation of the extracellular matrix. Its action would also result in the activation, through integrins, of Src and FAK signalling and the regulation of cell cycle by the activation of the PI3K/AKT pathway (Figure 5.49). At the same

time, Cav-1 would stimulate the production of ITGβ1 and inhibit the expression of CDH1 (ECAD), leading to tumour progression.

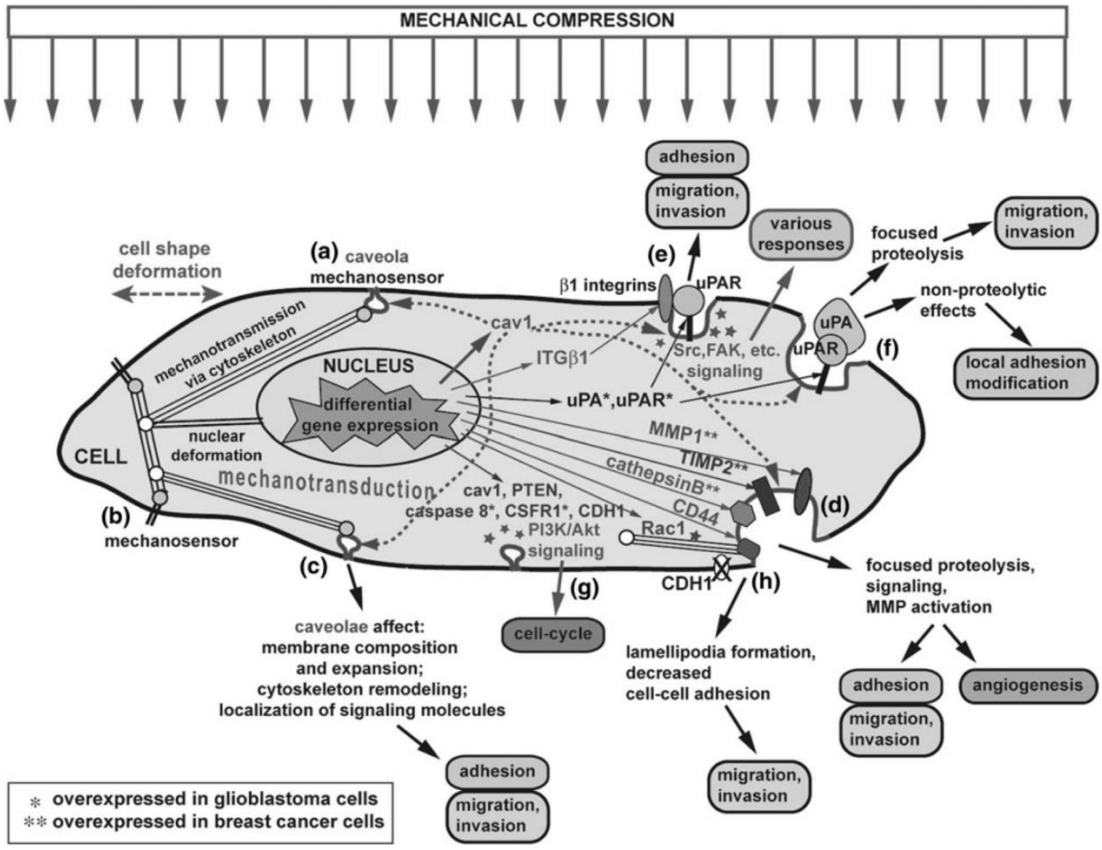

Figure 5.49 Figure from Demou et al 2010, with pathway led by Cav-1 after mechano-compression is applied to GBM cells. A. Cav-1 senses compression, together with other mechanosensors (B) and induces differential upregulation of Cav-1, which could affect adhesion, migration, and invasion (C). Molecules involved can localize at caveolae and enhance proteolysis, adhesion, migration, and invasion via: recruitment and activation of MMPs and cathepsins (D), involvement of UPA (E), or integrin-mediated pathways, like Src, FAK, and PI3k/ Akt (F). PI3K/Akt pathway is involved in the control of cell cycle (G). CD44 localized in the caveolae of the invasive cells could promote recruitment of MMPs and other molecules that enhance migration and invasion (H). Image is reported with permission.

This work is consistent with our findings. Cav.1 appears to drive UPAR, UPA, CTSB and partially MMP1 and CD44, which were all upregulated in Demou et al after compression. AKT phosphorylation forms and FAK were also upregulated in CAV+ cells. The influence of the PI3K/AKT pathway over cell cycle could be in the future investigated by the use of proliferation-specific staining, like Ki67 on invading spheroids or on cells on Matrigel.

To be more specific on the single molecules that Cav-1 appears to modulate:

- UPAR is a negative prognostic factor for aggressive gliomas. It interacts with integrins and vitronectin and mediates a link between cell adhesion and chemotaxis (N. Levicar, Nutall, & Lah, 2003).
- UPA when bound to UPAR in the caveolae, converts plasminogen to active plasmin, and induces the degradation of various ECM components such as fibronectin and laminin, while also contributing to the activation of the adhesive and invasive properties of glioblastoma cells (Vehlow & Cordes, 2013).
- CTSB is physiologically an intra-lysosomal protease. In GBM it is secreted and helps degrading laminin and collagen. It activates UPA from its precursor (J. S. Rao, 2003). It is a negative prognostic factor for GBM patients (Natasa Levicar et al., 2002).
- MMP1 is a collagenase that enhances both GBM tumorigenicity and tumour-related angiogenesis (Pullen, Anand, Cooper, & Fillmore, 2012) MMP1 has been shown to be upregulated in glioma specimens and to be related to increased invasiveness (McCready, Broaddus, Sykes, & Fillmore, 2005).
- CD44 is the receptor for Hyaluronic acid. It is also overexpressed in GBM. Cells positive for CD44 are usually localized at the normal tissue-tumour interface, suggesting that it causes them to be more efficient at invading the brain parenchyma (Rape, Ananthanarayanan, & Kumar, 2014). CD44 has also been reported to activate intracellular signals that lead to the increase of glioma proliferation and invasion (Ponta, Sherman, & Herrlich, 2003; Xu, Stamenkovic, & Yu, 2010).
- AKT is the downstream player of many pathways, among which CD44 (Rape et al., 2014), EGFR and other receptors (Majewska & Szeliga, 2017). It stimulates secretion of MMP2 and MMP9 (Claes et al., 2007) especially in cells at invasive edges, giving these cells enhanced proteolytic capacity. It has been reported that in breast cancer AKT is activated by Cav-1 and promotes invadopodia formation and metastasis (H. Yang et al., 2016).

In summary, Cav-1 drives invasion in GBM cell lines, through the activation of UPA/UPAR, localized in the caveolae, which activate MMP1. At the same time, it induces the production of cathepsin B which contributes to the dismantling of

the extracellular matrix, and CD44, which helps cells recognizing hyaluronic acid and pathways triggered by the binding. AKT activation stimulates the regulation of cell cycle and contributes at different levels to GBM aggressiveness.

Experiments such as chemical inhibition of these pathways would allow to confirm if Cav-1 is indeed responsible for driving the expression of these molecules and consequenty invasion or if a more complex relatioship is needed, with iother interactors and feedback loops.

6 CHAPTER 6- THE CLINICAL IMPACT OF CAV-1 AND ASSOCIATED SIGNAL MOLECULES IN GBM

6.1 INTRODUCTION

6.1.1 The study of survival in GBM- The Cancer Genome Atlas (TCGA)

As mentioned in Chapter 1, high-grade gliomas present a very poor patient survival, which has not been improved in many decades of research (Ostrom et al., 2017).

The high tumour heterogeneity among patients and even among different parts of the same tumour increases immeasurably the difficulty of finding common pathways and mechanisms that can be used as a therapeutical target (Inda et al., 2014). This is why GBM, in particular, was the first cancer to be adopted and studied by the Cancer Genome Atlas Project (McLendon et al., 2008). The Cancer Genome Atlas (TCGA) is a project that collected data from genomic, epigenomic, expression (microarray and recently RPPA) studies and combined them with the clinical information about the patients involved. TCGA started with GBM but it actually now comprises 33 different cancer types.

In six years from the publication of the data in TCGA, the group has published significant results on GBM (Brennan et al., 2013; McLendon et al., 2008).

These results included the establishment of new GBM subgroups that are characterized by different molecular expression profiles (Huse et al., 2011) and varying patient survival rates. They also included the identification of mutations that can lead to GBM development and Temozolomide resistance (Yip et al., 2009), as well as the association of different mutations by chromosomal proximity. They confirmed the implication of five mutations (NF1, ERBB2, TP53, PIK3R1 and TERT) in GBM (Andersson et al., 2010; Verhaak et al., 2010b), and the definition of a pattern of methylation predicting GBM aggressiveness (Noushmehr et al., 2010).

At the same time, with the database currently available, researchers are able to verify if their genes of interest are related to GBM survival or other specific clinical features by comparing their expression across large datasets.

6.1.2 Cav-1 and GBM clinical samples

The understanding of Cav-1 biology in glioma is by comparison to other tumour types poorly understood. There are only a few limited studies of Cav-1 expression in clinical material. These have reported positive correlations between Cav-1 expression and increased tumour histological grade (Barresi et al., 2009; Cassoni et al., 2007). Cav-1 expression has also been reported to independently predict shorter survival in oligodendrogliomas (Senetta et al., 2009), although this finding is equivocal (Barresi et al., 2009). It is clear however, that Cav-1 positive and negative tumour cells co-exist in high-grade glioma.

6.2 SCOPE OF THE CHAPTER

In this chapter, we investigated the relationship between Cav-1 transcriptional levels in GBM clinical samples and patient survival.

Specifically, if Cav-1 served as an independent marker of survival and how Cav-1 may interact with other molecules associated with invasion to impact upon patient prognosis.

The invasion-associated molecules explored in combination with Cav-1 in this chapter were those identified from Chapter 5 in the *in vitro* studies, and included molecules active in adhesion and digestion of the ECM and the EMT.

We used two different platforms for the interrogation of the database. The first one is R, a software for statistical analysis, whereas the second one is R2, a web tool for the analysis of TCGA databases for scientists without programming experience, both described in the materials and methods section.

6.3 MATERIALS AND METHODS

6.3.1 The Cancer Genome Atlas (TCGA)

The Cancer Genome Atlas (TCGA) is provided by https://portal.gdc.cancer.gov/.

The dataset used in this work is “Tumor Glioblastoma - TCGA - 540 - MAS5.0 - u133a”. It comprises information about 540 patients, including 85 samples sub-classified in classical (n = 17), mesenchymal (n = 27), neural (n = 17) and proneural (n = 24) GBM.

Whilst the number of the patients present in the dataset is quite large (540), only 152 patients’ samples have been analysed for gene expression.

6.3.2 R2 Genomic platform for the analysis of TCGA database

The R2 Genomics Platform is a free platform, where publicly accessible genomics can be analysed and visualized. This allows biomedical researchers without bioinformatics training, to study clinical and genomics data and to compare their own results to larger databases (Koster, 2016; Valentijn, Koster, & Versteeg, 2006). From 2006 the number of publications using the tool has increased exponentially up to reaching, in July 2018, 778 publications in different scientific journals.

The dataset “Tumor Glioblastoma - TCGA - 540 - MAS5.0 - u133a” was added to R2 in 2011. It was used for Overall survival analysis and gene expression correlation using the scan cut-off mode based on median target gene expression and specifying different track subsets.

R2 allows generating Kaplan Meier plots and provides a statistical comparison, expressed in p-value, based on the Log-Rank Scale. It does not provide Cox regression analysis nor median survival.

6.3.3 R project

R Project 3.5.0 (RCoreTeam, 2018) and RStudio, Version 1.1.423 (RStudioTeam, 2018) were used for this study.

The survival statistical analysis was performed by the use of Survminer package (Kassambara & Kosinski, 2017). The Survminer package provides functions for facilitating survival analysis and visualization.

The optimal cut off point was calculated by maximally selected rank statistics (Delgado, Pereira, Villamor, López-Guillermo, & Rozman, 2014). This test can be easily applied using R (maxstat package- (Hassen et al., 2015)) and has two main advantages. The first is that there is no need for the time-dependent endpoint transformation, whilst the second is that the test calculates an exact cut-off point with a P value (type I error). (Lausen & Schumacher, 1992)

The scripts used on R are available in the Appendix 6. The maxstat cutoffs for each gene analysed are in Appendix 9.

6.3.4 Kaplan Meyer survival visualization and analysis

Kaplan-Meier (KM) estimates represent effective measures of survival analysis and prognostic factors identification, thanks to their ability to analyse patients independently from their follow up (Kaplan & Meier, 1958). This method excludes (censors) patients whose survival status is unknown. This is the reason why KM is appropriate for the evaluation of the impact of a gene expression/mutation/epigenetic modification on the prognosis of patients with a determined disease. Disease-free or progression-free survival can also be calculated. Several tests can be used to compare different KMs, with the log-rank test as the most popular (Klein, Rizzo, Zhang, & Keiding, 2001).

The log-rank test verifies if the difference between two groups (or more) in terms of survival times is statistically significant or not. It does not allow us to test the impact of other independent variables (Kishore, Goel, & Khanna, 2010). The smaller the p-value, the more significant and reliable the difference between the groups.

6.3.5 COX regression and survival analysis

The Cox proportional hazard regression model is very popular because allows evaluating continuous variables (e.g. age) without having to convert them into categorical variables, like when using the KM method. Furthermore, it is possible to evaluate variables that are unknown at Time 0 but become known later, in a time-dependent manner (Cox, 1972).

The Cox regression elaborates a Hazard Ratio (exp(coeff)) that equals to 1 when the expression of a marker has no effect on survival (no difference between the two groups) and increases or decreases together with the risk that the group in consideration will die in a determined time. For example, if the expression of a marker correlates with a positive prognosis and a delayed survival curve, the Hazard Ratio (HR) will be smaller than 1. Vice versa, if the marker increases the chances of those patients to die sooner, the hazard ration will be bigger than 1. To give a practical idea, if the HR is 0.5 only half of the patients will be likely to die at a certain time-point in comparison with the baseline (groups combined). On the other hand, if the HR is 2, at every time-point the double number of patients will die in comparison with the baseline.

6.3.6 Median Survival

Median survival (in R, returned by Surv_median) provides data about the time by which it is more probable that a half of the group under examination will be still alive. It is coupled with a 95% confidence interval (95CI), which allows the comparison of different groups by verifying if the respective 95CIs present overlapping areas.

6.4 RESULTS AND DISCUSSION

6.4.1 GBM survival and The Cancer Genome Atlas (TCGA)

GBM survival has been extensively reviewed in the literature (D. N. Louis et al., 2016a) but the impact of Cav-1 on GBM patient survival has not. Due to lack of surgical material, for this analysis, we decided to use a TCGA dataset, the TCGA 540-MAS 5.0- U133a. We chose this dataset, which is the largest of the TCGA datasets and it has been extensively studied (Y. W. Kim et al., 2013; Q. Wang et al., 2017).

We first interrogated the TCGA database for Glioblastoma patients' overall survival (Figure 6.1). It is clear from this analysis that the prognosis for the patients is not favourable, with as little as 20% of the whole GBM population achieving the 24-months survival and only 10% survival at 48 months. According to other sources, less than 3% of patients are still alive five years after diagnosis (Ohgaki & Kleihues, 2005).

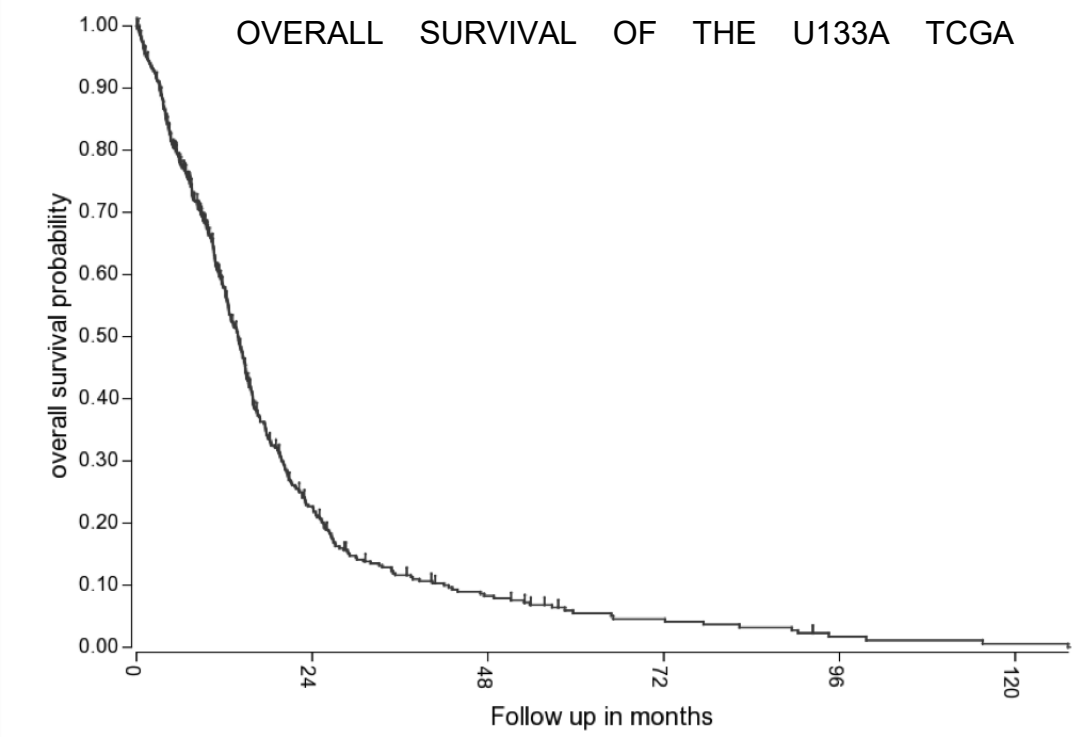

Figure 6.1 Overall survival curves for GBM patients. Plot represents all 540 patients present in the dataset and was obtained through the R2 web tool.

6.4.2 Impact of Cav-1 on GBM survival

What is absent from the literature is the role that Cav-1 has in GBM patients' survival. From the TCGA database analysis, it resulted that Cav-1 impacts significantly on survival (Figure 6.2). In particular, patients with a high expression of Cav-1 present a significantly shorter median survival (4.7 months for high Cav-1 expression whereas 14.2 months for low Cav-1 expression).

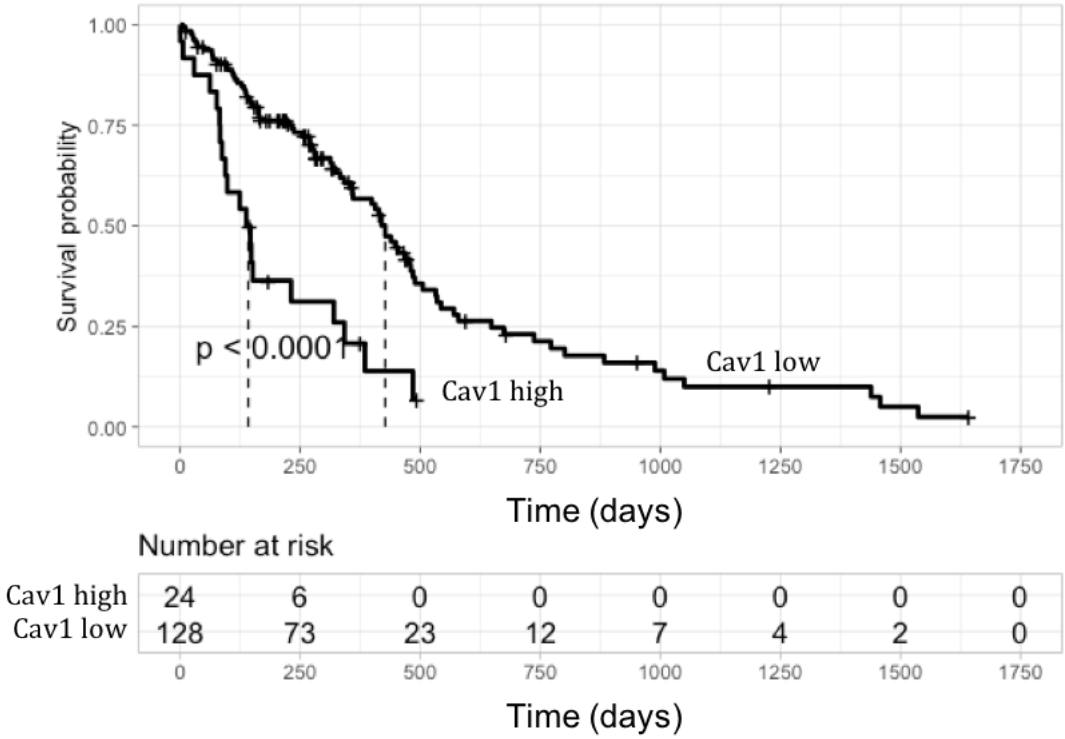

	Log Rank p-value	Median survival	95 CI	Cox- Hazard ratio	Cox p-value
CAV1=high	1e-05	142	94-342	2.985	2.9e-05
CAV1=low		427	359-485		

Figure 6.2 Overall survival curves for GBM patients with a high and low expression of Cav-1. Vertical lines connect median survival time. The number of patients alive at each time-point is reported under the plot. The table shows Log Rank p-value for the evaluation of the curves statistical difference; median survival for each group is reported together with the confidence interval (CI), whilst Cox hazard ratio for the referring group is coupled with its p-value. Plot and analysis were obtained through R project.

This finding is in line with the previous chapter results, where Cav-1 was shown to drive invasion in GBM cell spheroids (Chapter 5).

When looking at the overall survival the data showed no difference in gender (Figure 6.3A). When Cav-1 was introduced in the analysis, however, it emerged that this gene impacts on patients' survival more significantly in female patients than in male ones (Figure 6.3B). Indeed, the median survival for female patients with a high expression of Cav-1 is of only three months - compared to 14 for the low-Cav-1 expressing female population. The male group survival, on the other side, is influenced by Cav-1 in a less significant way, having the MaleCav-1^{high} subgroup 11 months median survival, versus the 14 months of the MaleCav^{low} subgroup.

A quick analysis showed that the worst prognosis of Cav-1^{high} female patients, compared to the Cav-1^{high} male patients, was not due to a significant difference in age between the groups.

However, differences in the degree of surgical resection (complete vs. partial) or performance status of patients cannot be ruled out.

Furthermore, it may be possible that the worse overall survival in females whose tumours expressed Cav-1 has a biological basis. It is well established that Cav-1 is a regulator of ER signalling (Goetz, Lajoie, et al., 2008). More recent work has revealed that certain isotypes of ERβ, when activated, drive disease progression. Namely, ERβ1 is shown to be a tumour suppressor, whilst the ERβ5 isotype is oncogenic (Jinyou Liu et al., 2018). Therefore, the possibility exists that Cav-1 is driving disease progression in females through its potentiation of ERβ5 signalling.

Further mechanistic studies to explore this possibility are necessary. It has not been done here because it would have been beyond the scope of this thesis.

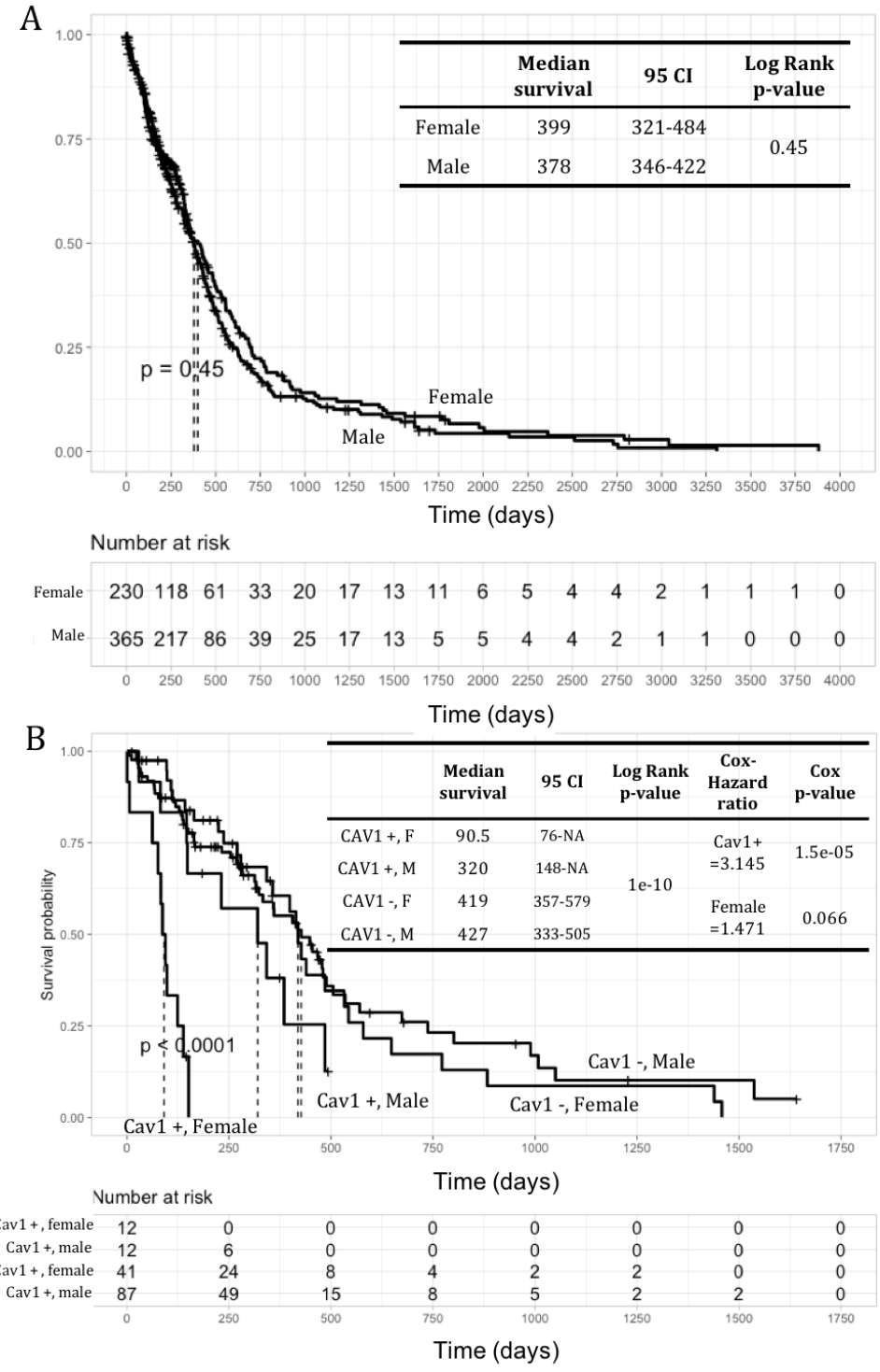

Figure 6.3 Overall survival, gender and Cav-1. A. Survival curves for GBM patients belonging to the two different gender groups. B. Survival curves for GBM patients with high (Cav+) and low (Cav-) expression of Cav-1 in the two gender groups. Vertical lines connect median survival times. The number of patients alive at each time-point is reported under the plots. Tables show Log Rank p-value for the evaluation of the curves statistical difference; median survival for each group is reported together with the confidence interval (CI), whereas Cox hazard ratio for the referring group is coupled with its p-value. Plot and analysis were achieved through R project.

Patients appear to express an average higher Level of Cav-1 in the mesenchymal group, compared with the other molecular subgroups (Figure 6.4). Despite the distribution is statistically different, the low number of patients in each group does not allow to draw conclusive results. The TCGA database indeed provides information about the molecular subtypes only for a limited number of patients (85 in total). An analysis of a larger group of classified patients would allow the confirmation of the different distribution of Cav-1 expressing patients within the molecular subtypes.

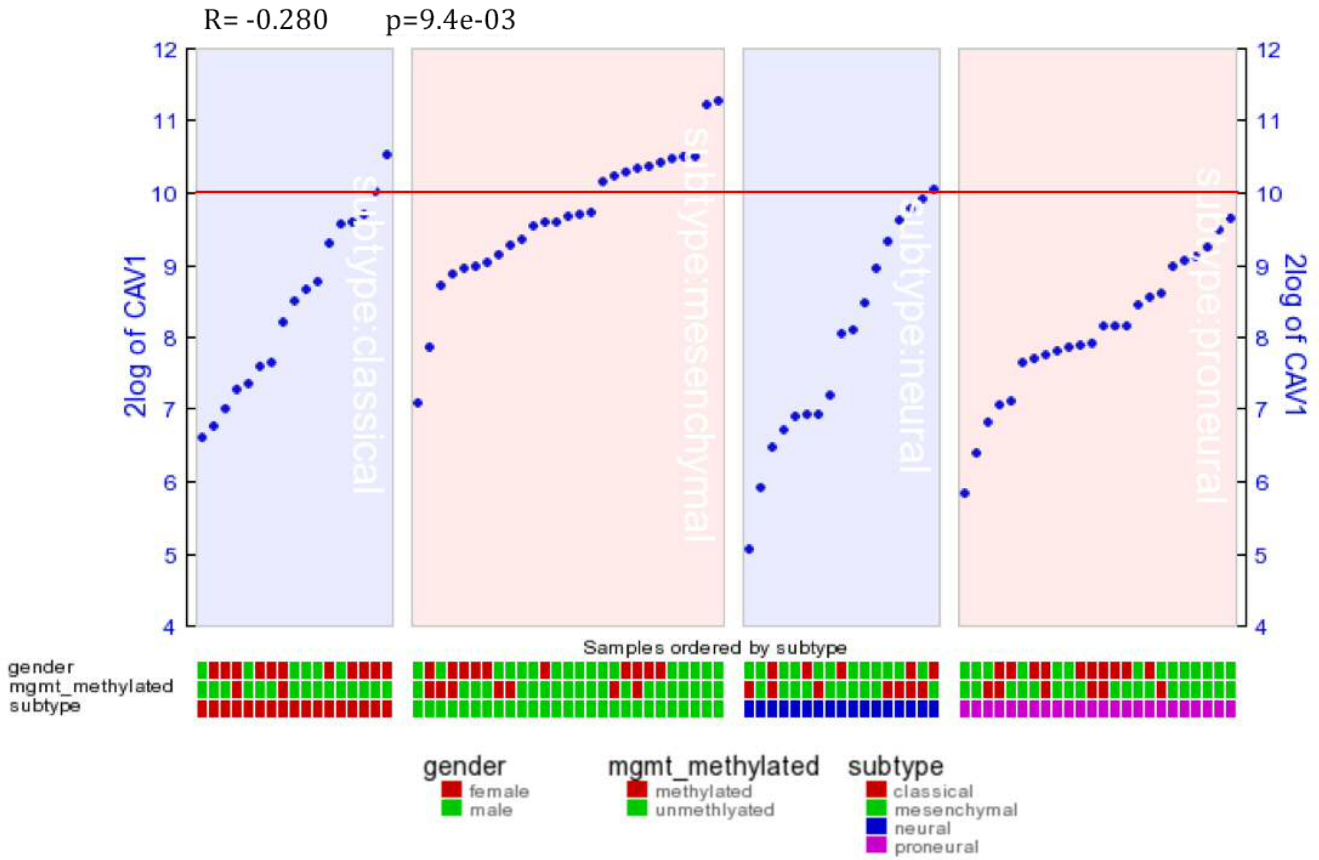

Figure 6.4 Cav-1 expression in GBM subgroups (from left to right: classical, mesenchymal, neural, proneural). Patients are ordered within each group by their Level of expression of Cav-1. Expression scale is 2Log, with each increment representing the double value of the precedent one. Red line represents cut off between Cav-1 high and low in Figure 6.2. R-value and p-value are reported on the top left. Gender is indicated in the bottom (female: red, male: green), together with MGMT methylation (methylated: red, un-methylated: green) and subtype (classical: red, mesenchymal: green, neural: blue, proneural: fuchsia). Plots were obtained through R2.

The same patients have been also tested separately to understand if Cav-1 expression has an impact on survival in different subgroups. Again, in the mesenchymal group, a higher expression of Cav-1 leads to a shorter patients' survival (Figure 6.5).

Interestingly, it appears also that in the proneural group a low expression of Cav-1 is related to a lower median survival. In Figure 6.4 the same proneural group was represented only by patients with an expression of Cav-1 that is under the cut off established for the general population. This could mean that in proneural GBMs Cav-1 has a different role in comparison with the mesenchymal ones. In a recently published thesis, it was reported that Cav-1 was found inversely correlated with proneural markers in peri-necrotic areas of patients' samples and that hypoxia was possibly related to the shift in Cav-1 expression (Kundu, 2018). This would confirm the low expression of Cav-1 that we observed in the TCGA patients belonging to the proneural group and also the increased hazard of the Cav^{low} subgroup in comparison with Cav^{high} in the same subtype.

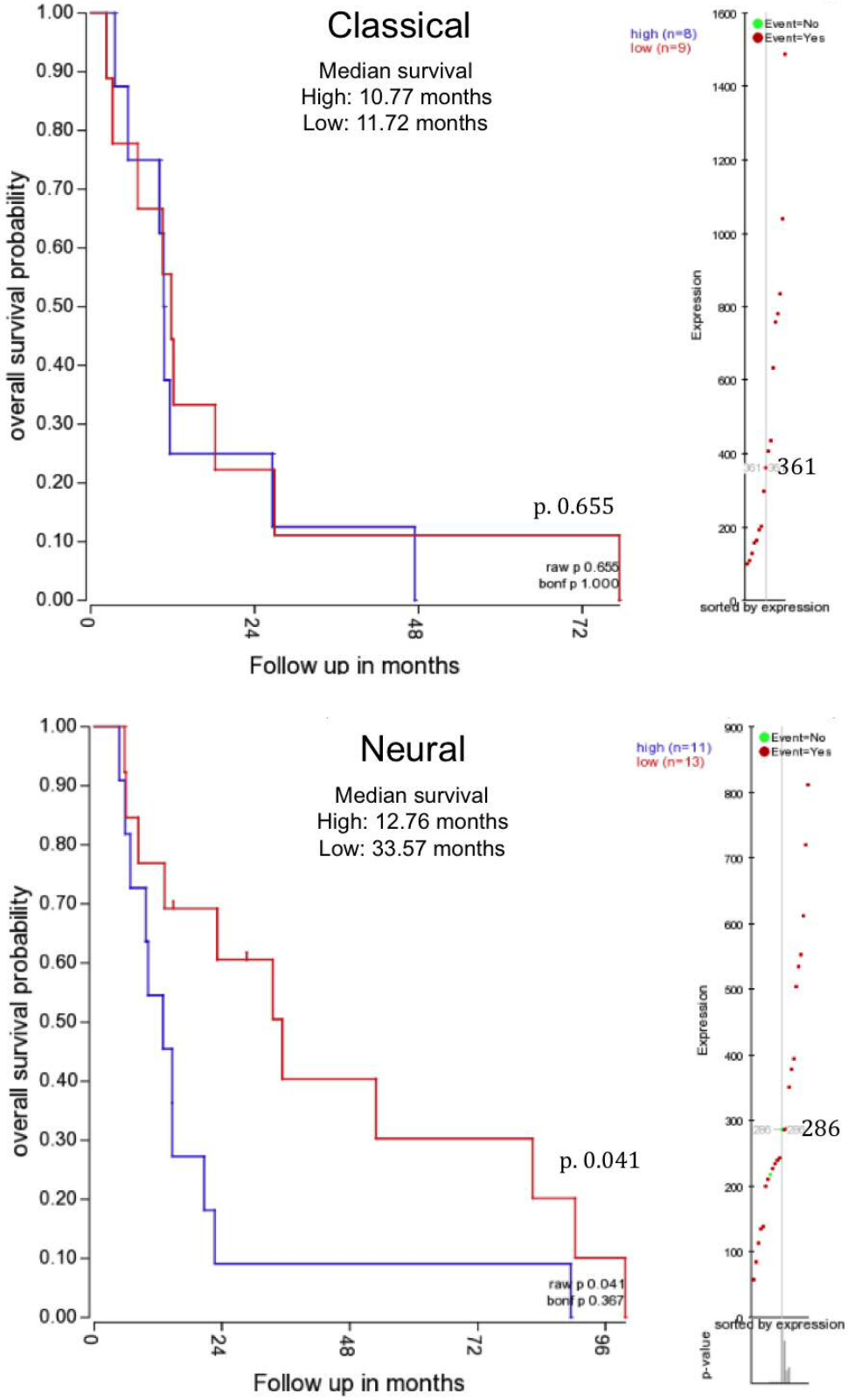

Figure 6.5 Overall survival curves for GBM patients belonging to the four different GBM subgroups and divided into high (blue) and low (red) Cav-1 expression groups. Median survival for each group is reported. Log Rank p-value is reported on the bottom right of the plots. Each plot is coupled with the distribution of Cav-1 expression and the cut-off established by the software (R2).

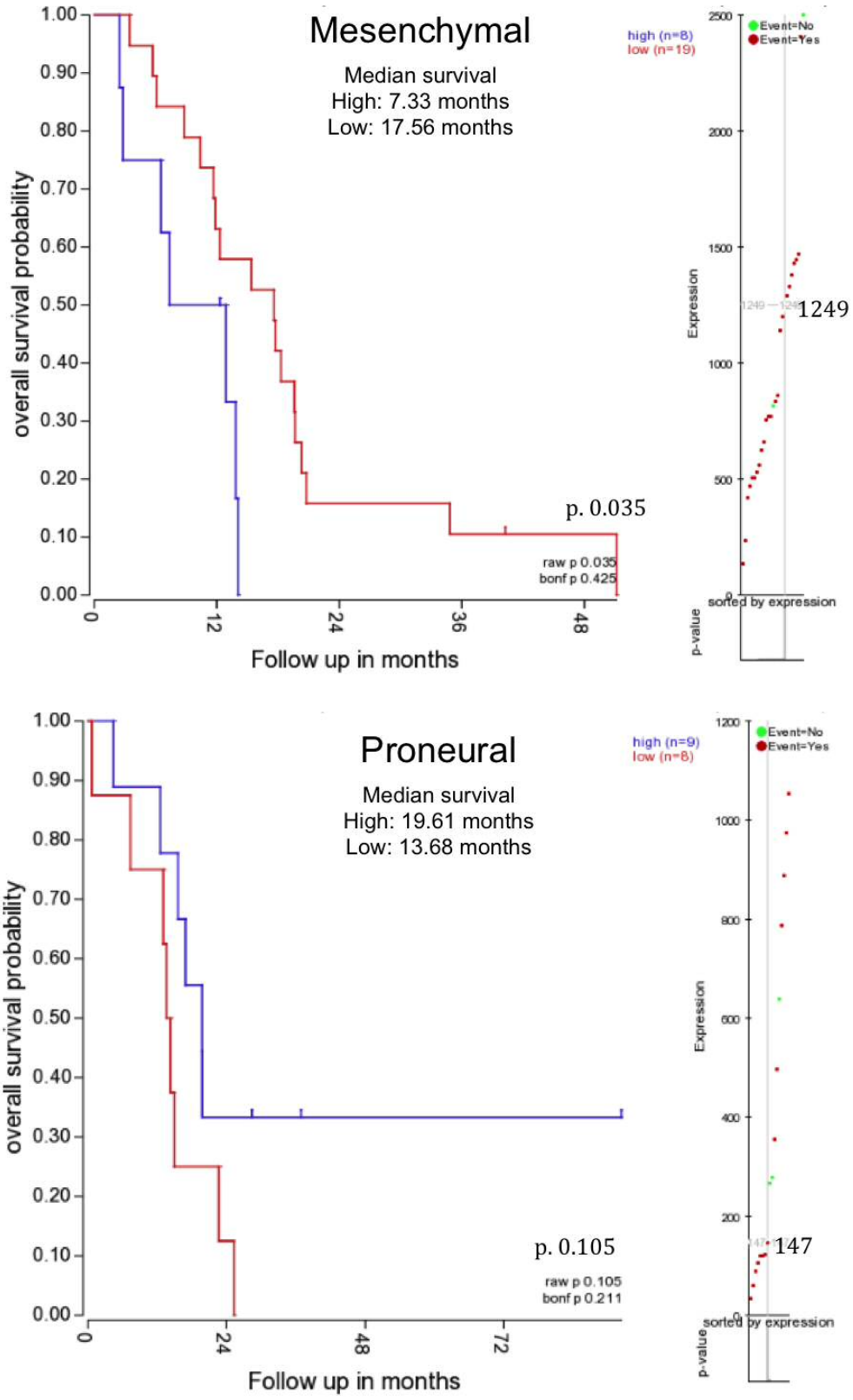

Figure 6.6 Overall survival curves for GBM patients belonging to the four different GBM subgroups and divided into high (blue) and low (red) Cav-1 expression groups. Median survival for each group is reported. Log Rank p-value is reported on the bottom right of the plots. Each plot is coupled with the distribution of Cav-1 expression and the cut-off established by the software (R2).

Being the mesenchymal group the GBM subtype with a highest aggressive feature, Cav-1 higher expression and shorter survival supports the hypothesis of its oncogene function. This may be achieved by influencing invasion and facilitating relapse.

6.4.3 Invasion-associated genes, Cav-1 expression and GBM

In order to explore further the hypothesis generated in the previous section, we interrogated the database to understand if genes known to be related to invasion in GBM are related to Cav-1 expression. Results are reported in Table 6.1. The XY expression correlation plots are reported in the appendix 8, while the highest 500-ranked proteins related to Cav-1 expression in GBM are in the Appendix 7.

Table 6.1 Genes previously of interest (CH.5) related to invasion: statistically significant relationship to Cav-1 expression in GBM TCGA dataset. The analysis was conducted through R2 web tool.

Rank	HUGO	R-value	R-p value
Positive correlation with Cav1			
3	PAI1	0.639	8.96E-60
8	CD44	0.555	8.70E-42
11	ITGB1	0.547	1.97E-40
19	UPAR	0.529	1.80E-37
25	ITGA5	0.518	1.09E-35
43	CTSB	0.488	3.00E-31
50	UPA	0.482	1.83E-30
126	TIMP1	0.428	1.45E-23
139	CTSL1	0.42	1.24E-22
213	ITGA3	0.384	1.10E-18
262	ITGB5	0.37	2.12E-17
275	TSP1	0.368	3.19E-17
288	VIM	0.363	1.06E-16
416	ITGAV	0.33	7.12E-14
564	CTSS	0.301	1.30E-11
566	MMP1	0.301	1.42E-11
572	MMP7	0.3	1.50E-11
593	CTSD	0.296	3.02E-11
775	MT1MMP	0.265	3.55E-09
1093	MMP9	0.226	7.30E-07
1315	MMP10	0.201	1.23E-05
1768	CTSH	0.158	0.00074103
1936	CTSK	0.143	0.00243346
2131	MMP3	0.128	0.00743621
2317	TIMP3	0.115	0.01658755
2552	ITGB3	0.1	0.03983414
2625	MMP2	0.096	0.04943577
Negative correlation with Cav1			
604	PVRL4	-0.247	4.93E-08
1625	ECAD	-0.172	0.0002088

ITGAV: Integrin Subunit Alpha V	**ITGA3**: Integrin Subunit Alpha 3
ITGA5: Integrin Subunit Alpha 5	**ITGB1**: Integrin Subunit Beta 1
ITGB3: Integrin Subunit Beta 3	**ITGB5**: Integrin Subunit Beta 5
MMP2: Matrix Metallopeptidase 2	**MMP9**:Matrix Metallopeptidase 9
MT1MMP: Membrane-Type-1 MMP	**MMP7**:Matrix Metallopeptidase 7
MMP10: Matrix Metallopeptidase 10	**MMP1**:Matrix Metallopeptidase 1
MMP8: Matrix Metallopeptidase 8	**MMP3**:Matrix Metallopeptidase 3
CTSK: Cathepsin K	**CTSB**: Cathepsin B
CTSL: Cathepsin L	**CTSS**: Cathepsin S
CTSH: Cathepsin H	**CTSD**: Cathepsin D
UPA: Urokinase Plasminogen Activator	**UPAR**: UPA Receptor

TIMP family - through the inhibition of enzymes such as MMPs - are positively correlated to Cav-1 as well.

To test whether the correlation showed in Table 6.1 translates into an impact for patients we first interrogated the database for the impact of the single genes on GBM patients' survival (Level 1). After which, we then examined the combined expression of both Cav-1 and the target genes upon patient survival (Level 2 and Level 3).

The aim of Level 1 analysis is to understand if the selected markers are independent prognostic markers in the selected GBM patient dataset. Level 2 and Level 3 provide information regarding the correlation between the markers, Cav-1 and patient survival. Specifically, Level 2 is useful to determine if the two combined markers are correlated, i.e. acting in synergy. This would be the case if, for example, the median survival of the combined biomarkers would be shorter than the median survival of the single biomarkers analysis (Level 1). Level 3 clear further the relatioship between the two markers and the role that one marker could have in one of the subpopulations of the other marker. For example, whether Cav-1 acts as a tumour suppressor or oncogene in the subpopulation of patients expressing low levels of UPAR and vice-versa.

The resulting analysis has been summarized in Figure 6.7.

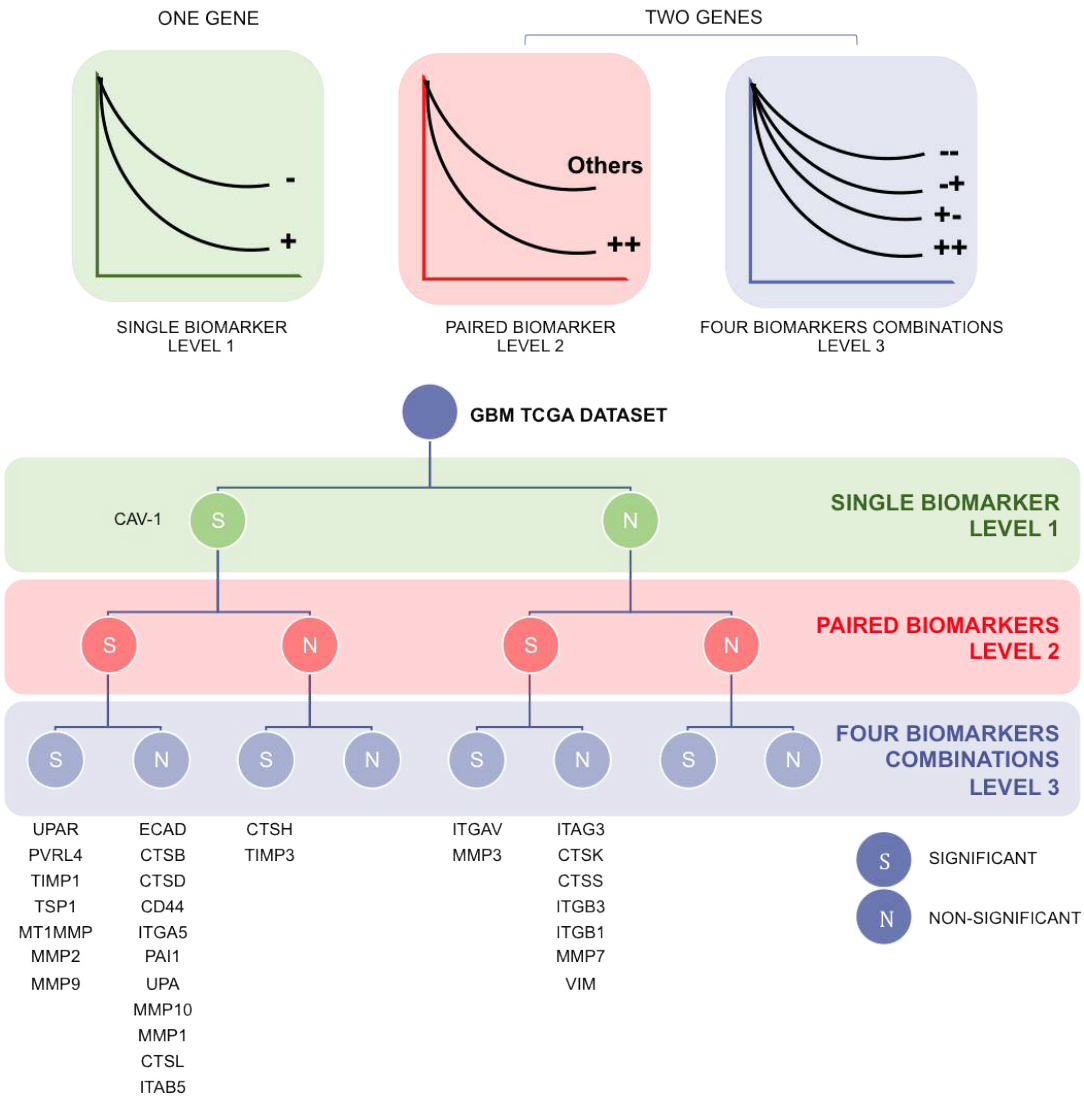

Figure 6.7 Summarizing figure of the workflow of the three analyses conducted on the selected markers. Level 1 overall survival analysis was followed by the combination of patients with high levels of both Cav-1 and target genes. The split of the four possible combinations was performed as last. Analysis revealed differences that were significant (S) or non-significant (N). Genes belonging to each group of results are listed at the bottom.

When commenting each of the genes analyses, the terms “drive” and “inhibit” indicate not a direct activation or inhibition of the target, but a positive or negative influence over the target expression.

Figure 6.8 shows the impact of UPAR expression levels on survival. Figure 6.8A shows $UPAR^{high}$ tumours (UPAR+) to have a reduced survival (316 days vs 480 for the $UPAR^{low}$ group), paired with a significant HR of 2.457, suggesting that UPAR may be an independent negative prognostic biomarker. Figure 6.8B shows survival curves corresponding to the portion of the patients with high

levels of both Cav-1 and UPAR (CAV+UPAR+) and the remaining population (Others). The combination of the two biomarkers determines a shorter survival median time (146 days) than the others (419 days), indicating that the subpopulation of patients with $UPAR^{high}CAV^{high}$ have a significantly worse outcome than the patients with $UPAR^{high}$ but not a different outcome than the CAV^{high} alone, whose median survival is 142 days. This could exclude a synergistic effect of Cav-1 and UPAR expression. Figure 6.8C shows the single stratifications with the two biomarkers reported as a significant negative prognostic factors (HR for Cav-1^{high} is 2.294 and for UPAR ^{high} 2.123). Figure 6.8C shows that, when Cav-1 is low expressed, UPAR drives the disease progression however, when Cav-1 expression is high, the $UPAR^{low}CAV^{high}$ condition is met only by one patient so in this case, it is not possible to explore the relationship further, by checking if Cav-1 has more impact on survival than UPAR.

Figure 6.9 shows the impact of CD44 expression levels on survival. Figure 6.9A shows $CD44^{high}$ tumours (CD44+) to have a reduced survival (320 days vs 419 for the $CD44^{low}$ group), paired with a significant HR of 1.536, suggesting that CD44 may be an independent negative prognostic biomarker. Figure 6.9B shows survival curves corresponding to the portion of the patients with high levels of both Cav-1 and CD44 (CAV+CD44+) and the remaining population (Others). The combination of the two biomarkers determines a shorter survival median time (142 days) than the others (427 days). This value corresponds to the median survival of Cav-1, suggesting that a synergistic effect in this case is not present. Figure 6.9C shows the single stratifications with only Cav-1 confirmed as a significant negative prognostic factor (HR for Cav-1 ^{high} is 2.688). All patients with high levels of Cav-1 are also $CD44^{high}$, while $CD44^{high}$ patients can be CAV^{low}, suggesting that CD44 is a pre-requisite for Cav-1 expression. Moreover, when Cav-1 is low there is no difference between $CD44^{high}$ and $CD44^{low}$, whilst Cav-1 high expression in the $CD44^{high}$ subpopulation drives disease progression. This suggests that CD44 is able to drive disease progression, and thus act as an oncogene, only when Cav-1 is highly expressed as well.

Figure 6.10 shows the impact of ITGA3 expression levels on survival. Figure 6.10A shows ITGA3^{high} tumours (ITGA3+) to have no significant impact upon patient survival (360 days vs 427 for the ITGA3^{low} group), paired with a non-significant HR of 1.527. This suggests that ITGA3 is not a prognostic marker for GBM. Figure 6.10B shows survival curves corresponding to the portion of the patients with high levels of both Cav-1 and ITGA3 (CAV+ITGA3+) and the remaining population (Others). The combination of the two biomarkers determines a shorter survival median time (142 days) than the others (427 days). This value corresponds to the median survival of Cav-1, suggesting that a synergistic effect in this case is not present. Figure 6.10C shows that the group Cav^{high}ITGA3^{low} is not present, suggesting that all Cav^{high} patients are also ITGA3^{high}. The Level 3 stratifications confirmed Cav-1 as a significant negative prognostic factor (HR for Cav-1 ^{high} is 2.747) while ITGA3 is not. This is because, when Cav-1 is low, there is no difference between patients with high or low levels of ITGA3. However, in the subpopulation of ITGA3^{high}CAV^{high} the survival is greatly reduced. This indicates that is able to shorten patient survival only when it is co-expressed with Cav-1, and that Cav-1 can be highly expressed only when ITGA3 is highly expressed as well, thus ITGA3 is a pre-requisite for Cav-1 expression.

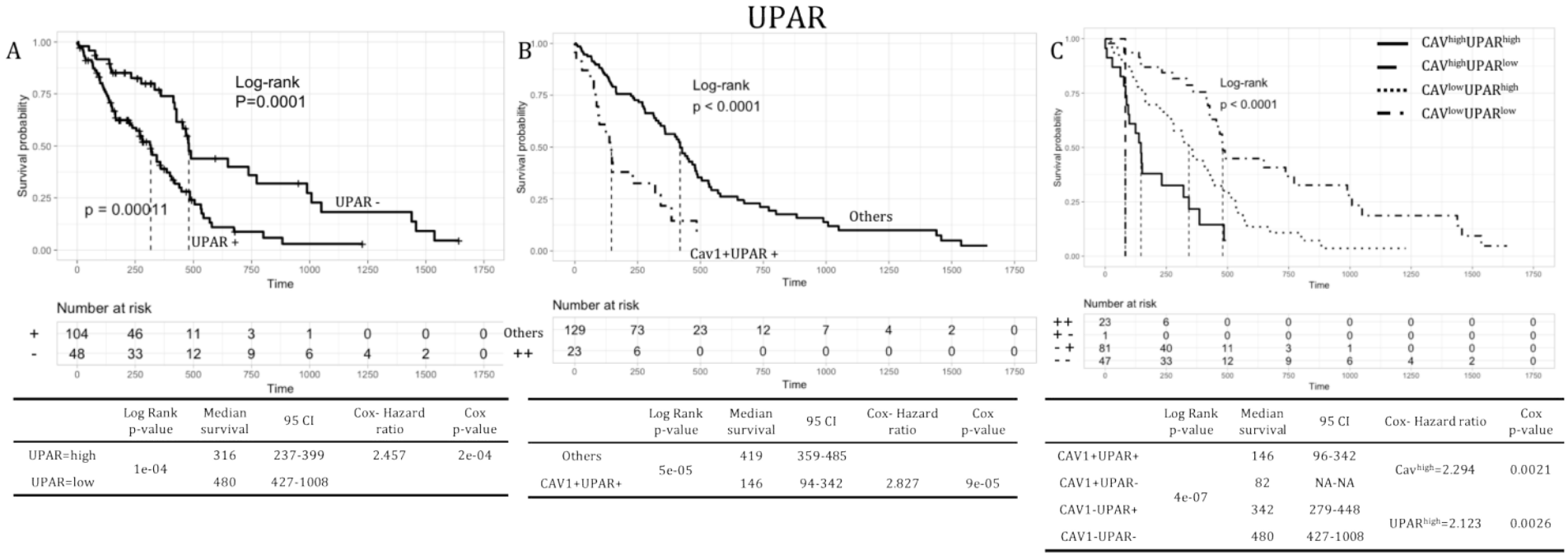

	Log Rank p-value	Median survival	95 CI	Cox- Hazard ratio	Cox p-value
UPAR=high	1e-04	316	237-399	2.457	2e-04
UPAR=low		480	427-1008		

	Log Rank p-value	Median survival	95 CI	Cox- Hazard ratio	Cox p-value
Others	5e-05	419	359-485		
CAV1+UPAR+		146	94-342	2.827	9e-05

	Log Rank p-value	Median survival	95 CI	Cox- Hazard ratio	Cox p-value
CAV1+UPAR+	4e-07	146	96-342	Cav^{high}=2.294	0.0021
CAV1+UPAR-		82	NA-NA		
CAV1-UPAR+		342	279-448	$UPAR^{high}$=2.123	0.0026
CAV1-UPAR-		480	427-1008		

Figure 6.8 Cav-1 and UPAR (adhesion 1). Overall survival curves of UPAR for GBM patients. A. Impact of high and low expression on survival (Level 1). B. Survival curve for patients with high expression of both Cav-1 and UPAR was compared to the rest of the patients (Level 2). High or low expressions have been abbreviated to +/-. C. Comparison between the single combinations of a high and low expression of Cav-1 and the target gene (Level 3). Vertical lines connect median survival time. Tables show for each plot: Log Rank p-value for the evaluation of the curves statistical difference; median survival for each group, reported together with the con fidence interval (CI); Cox hazard ratio for the referring group, coupled with its p-value. Plot and analysis were achieved through R project.

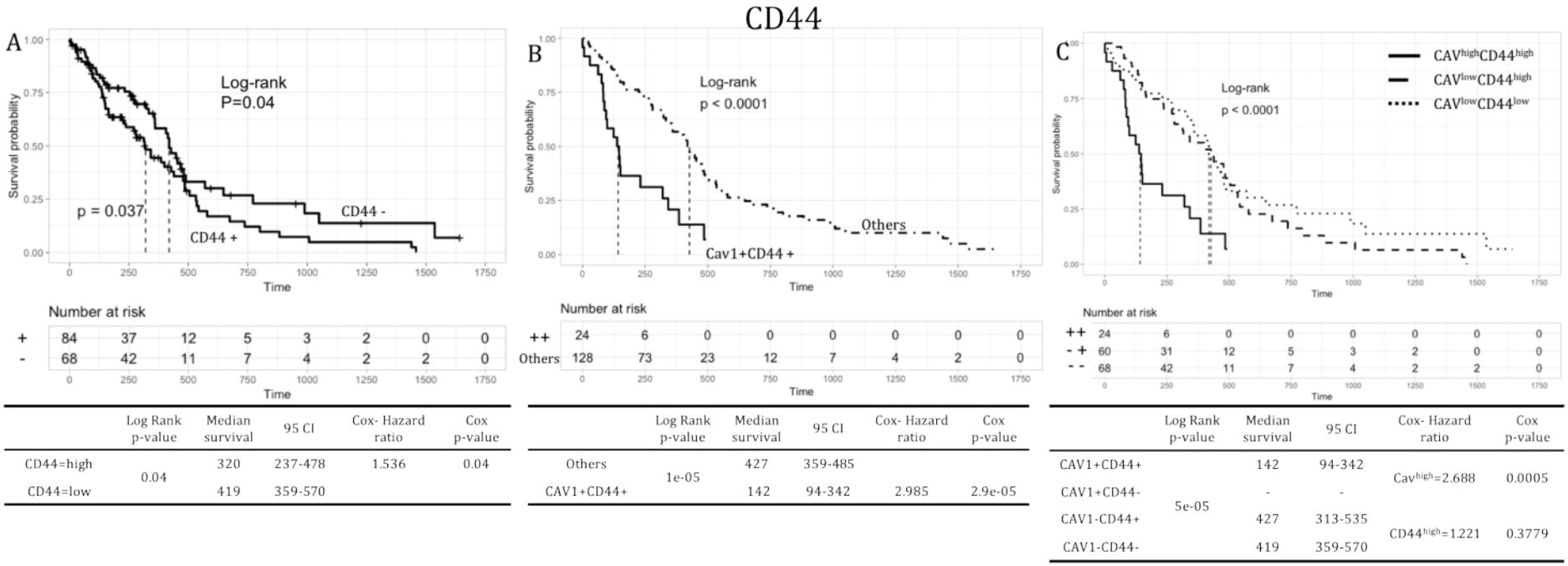

	Log Rank p-value	Median survival	95 CI	Cox- Hazard ratio	Cox p-value
CD44=high	0.04	320	237-478	1.536	0.04
CD44=low		419	359-570		

	Log Rank p-value	Median survival	95 CI	Cox- Hazard ratio	Cox p-value
Others	1e-05	427	359-485		
CAV1+CD44+		142	94-342	2.985	2.9e-05

	Log Rank p-value	Median survival	95 CI	Cox- Hazard ratio	Cox p-value
CAV1+CD44+	5e-05	142	94-342	Cav^{high}=2.688	0.0005
CAV1+CD44-		-	-		
CAV1-CD44+		427	313-535	$CD44^{high}$=1.221	0.3779
CAV1-CD44-		419	359-570		

Figure 6.9 Cav-1 and CD44 (adhesion 2). Overall survival curves of CD44 for GBM patients. A. Impact of a high and low expression on survival (Level 1). B. Survival curve for patients with high expression of both Cav-1 and CD44 was compared to the rest of the patients (Level 2). High or low expressions have been abbreviated to +/- . C. Comparison between the single combinations of a high and low expression of Cav-1 and the target gene (Level 3). Vertical lines connect median survival time. Tables show for each plot: Log Rank p-value for the evaluation of the curves statistical difference; median survival for each group, reported together with the con fidence interval (CI); Cox hazard ratio for the referring group, coupled with its p-value. Plot and analysis were achieved through R project.

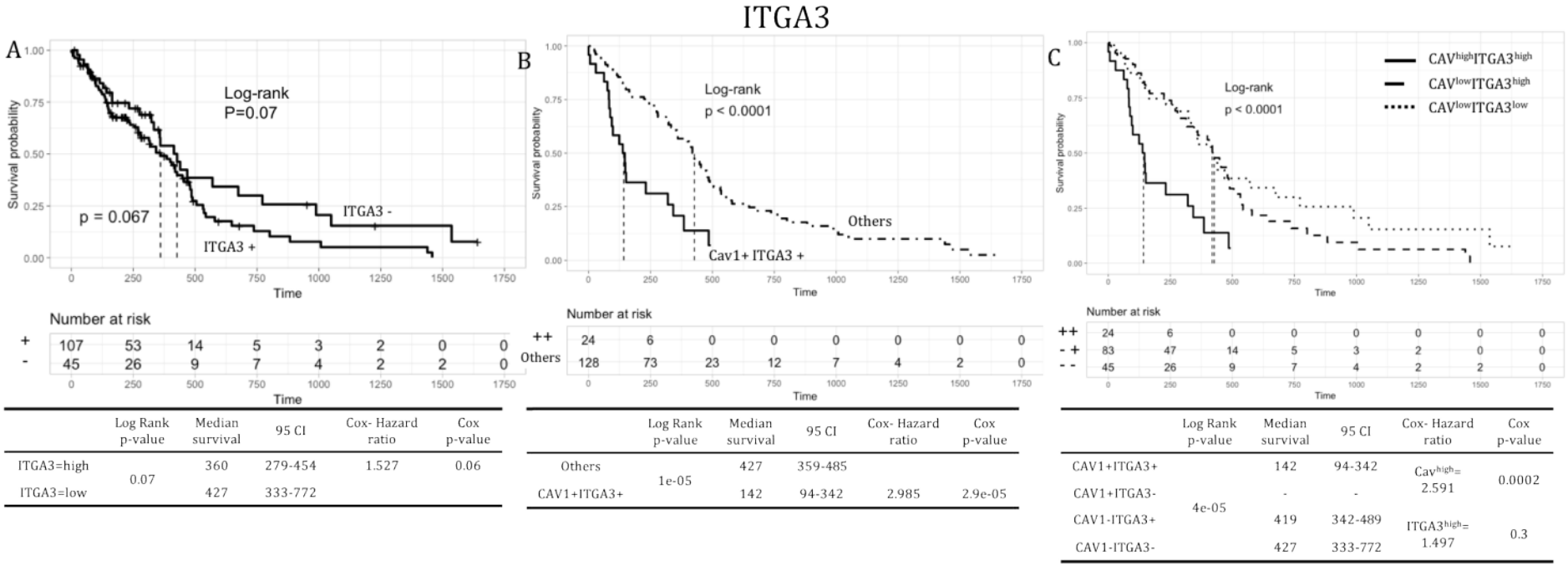

	Log Rank p-value	Median survival	95 CI	Cox- Hazard ratio	Cox p-value
ITGA3=high	0.07	360	279-454	1.527	0.06
ITGA3=low		427	333-772		

	Log Rank p-value	Median survival	95 CI	Cox- Hazard ratio	Cox p-value
Others	1e-05	427	359-485		
CAV1+ITGA3+		142	94-342	2.985	2.9e-05

	Log Rank p-value	Median survival	95 CI	Cox- Hazard ratio	Cox p-value
CAV1+ITGA3+	4e-05	142	94-342	Cav^{high}= 2.591	0.0002
CAV1+ITGA3-		-	-		
CAV1-ITGA3+		419	342-489	$ITGA3^{high}$= 1.497	0.3
CAV1-ITGA3-		427	333-772		

Figure 6.10 Cav-1 and ITGA3 (adhesion 3). Overall survival curves of ITGA3 for GBM patients. A. Impact of a high and low expression on survival (Level 1). B. Survival curve for patients with high expression of both Cav-1 and ITGA3 was compared to the rest of the patients (Level 2). High or low expressions have been abbreviated to +/-. C. Comparison between the single combinations of a high and low expression of Cav-1 and the target gene (Level 3). Vertical lines connect median survival time. Tables show for each plot: Log Rank p-value for the evaluation of the curves statistical difference; median survival for each group, reported together with the confidence interval (CI); Cox hazard ratio for the referring group, coupled with its p-value. Plot and analysis were achieved through R project.

Figure 6.11 shows the impact of ITGA5 expression levels on survival. Figure 6.11A shows ITGA5^{high} tumours (ITGA5+) to have a reduced survival (316 days vs 419 for the ITGA5^{low} group), paired with a significant HR of 1.757, suggesting that ITGA5 is an independent prognostic biomarker for GBM. Figure 6.11B shows survival curves corresponding to the portion of the patients with high levels of both Cav-1 and ITGA5 (CAV+ITGA5+) and the remaining population (Others). The combination of the two biomarkers determines a shorter survival median time (148 days) than the others (419 days), indicating that the subpopulation of patients with ITGA5^{high}CAV^{high} have a significantly worse outcome than the patients with ITGA5^{high} but not a different outcome than the CAV^{high} alone, whose median survival is 142 days. This could exclude a synergistic effect of Cav-1 and ITGA5 expression. Figure 6.11C shows the single stratifications with only Cav-1 reported as a significant negative prognostic factor (HR for Cav-1 ^{high} is 2.591). This suggests that ITGA5 is a poor driver of disease progression and that its oncogene properties are reduced in comparison with Cav-1.

Figure 6.12 shows the impact of ITGAV expression levels on survival. Figure 6.12A shows ITGAV^{high} tumours (ITGAV+) to have no significant impact upon patient survival (427 days vs 342 for the ITGAV^{low} group), with a non-significant HR of 1.484 for ITGAV^{low}. This suggests that ITGAV is not an independent prognostic marker for GBM. Figure 6.12B shows survival curves corresponding to the portion of the patients with high levels of both Cav-1 and ITGAV (CAV+ITGAV+) and the remaining population (Others). The combination of the two biomarkers determines a shorter survival median time (138 days) than the others (419 days). The median survival for the combined biomarkers in this case is shorter than both the median survival times of ITGAV^{high} (342 days) and CAV^{high} alone (142 days), suggesting that some synergy may be present between them. Figure 6.12C for the Level 3 stratification shows, however, that Cav-1 is a significant negative prognostic factor (HR for Cav-1 ^{high} is 3.155) while ITGAV as a positive prognostic factor (HR for ITGAV^{low} is 1.589). This is because, whilst Cav-1 expression drives disease progression and shortens median survival, a high expression of ITGAV correlates with a longer survival,

even if the effect is not powerful enough to annul the oncogene effect of Cav-1 high expression. This suggests that ITGAV is a tumour suppressor in GBM, but also that Cav-1 is able to override its action.

Figure 6.13 shows the impact of ITGB1 expression levels on survival. Figure 6.13A shows $ITGB1^{high}$ tumours (ITGB1+) to have no significant impact upon survival (342 days vs 419 for the $ITGB1^{low}$ group), paired with a non-significant HR of 1.344. this suggests that ITGB1 is not an independent prognostic marker for GBM. Figure 6.13B shows survival curves corresponding to the portion of the patients with high levels of both Cav-1 and ITGB1 (CAV+ITGB1+) and the remaining population (Others). The combination of the two biomarkers determines a shorter median survival time (146 days) than the others (419 days), indicating that the subpopulation of patients with $ITGB1^{high}CAV^{high}$ have a significantly worse outcome than the patients with $ITGB1^{high}$ but not a different outcome than the CAV^{high} alone, whose median survival is 142 days. Figure 6.13C shows the single stratifications with Cav-1 reported as a significant negative prognostic factor (HR for Cav-1 ^{high} is 2.865). when Cav-1 is low expressed, there is no difference between $ITGB1^{high}$ and $ITGB1^{low}$ patients. When Cav-1 is high the survival time decreases drastically, but the difference between $ITGB1^{high}$ and $ITGB1^{low}$ is not reliable. This is because the group $Cav^{high}ITGB1^{low}$ is comprised of only two patients, making a reliable statistical analysis for the impact of ITGB1 upoon CAV^{high} patients impossible. A larger cohort would allow the unequivocal understanding of the role of ITGB1 in GBM patient survival.

Figure 6.14 shows the impact of ITGB3 expression levels on survival. Figure 6.14A shows $ITGB3^{high}$ tumours (ITGB3+) to have no significant impact upon survival (485 days vs 359 for the $ITGB3^{low}$ group), paired with a non-significant HR of 1.460. this suggests that ITGB3 is not an independent biomarker for GBM. Figure 6.14B shows survival curves corresponding to the portion of the patients with high levels of both Cav-1 and ITGB3 (CAV+ITGB3+) and the remaining population (Others). The combination of the two biomarkers determines a shorter survival median time (146 days) than the others (419

days), indicating that the subpopulation of patients with ITGB3^{high}CAV^{high} have a significantly worse outcome than the patients with ITGB3^{high} but not a different outcome than the CAV^{high} alone, whose median survival is 142 days. Figure 6.14C shows the single stratifications with Cav-1 reported as a significant negative prognostic factor (HR for Cav-1 ^{high} is 2.710). The group Cav^{high}ITGB3^{low} is comprised of only two patients, making a reliable statistical analysis impossible. A larger cohort would allow the unequivocal understanding of the role of ITGB1 in GBM patient survival.

Figure 6.15 shows the impact of ITGB5 expression levels on survival. Figure 6.15A shows ITGB5^{high} tumours (ITGB5+) to have a reduced survival (316 days vs 439 for the ITGB5^{low} group), paired with an HR of 1.715. this suggests that ITGB5 is an independent prognostic marker for GBM. Figure 6.15B shows survival curves corresponding to the portion of the patients with high levels of both Cav-1 and ITGB5 (CAV+ITGB5+) and the remaining population (Others). The combination of the two biomarkers determines a shorter survival median time (138 days) than the others (419 days). The median survival for the combined biomarkers in this case is shorter than both the median survival times of ITGB5^{high} (316 days) and CAV^{high} alone (142 days), suggesting that some synergy may be present between them. Figure 6.15C shows the single stratifications with only Cav-1 reported as a significant negative prognostic factor (HR for Cav-1 ^{high} is 2.611). This indicated that ITGB5 is a poor driver of disease progression.

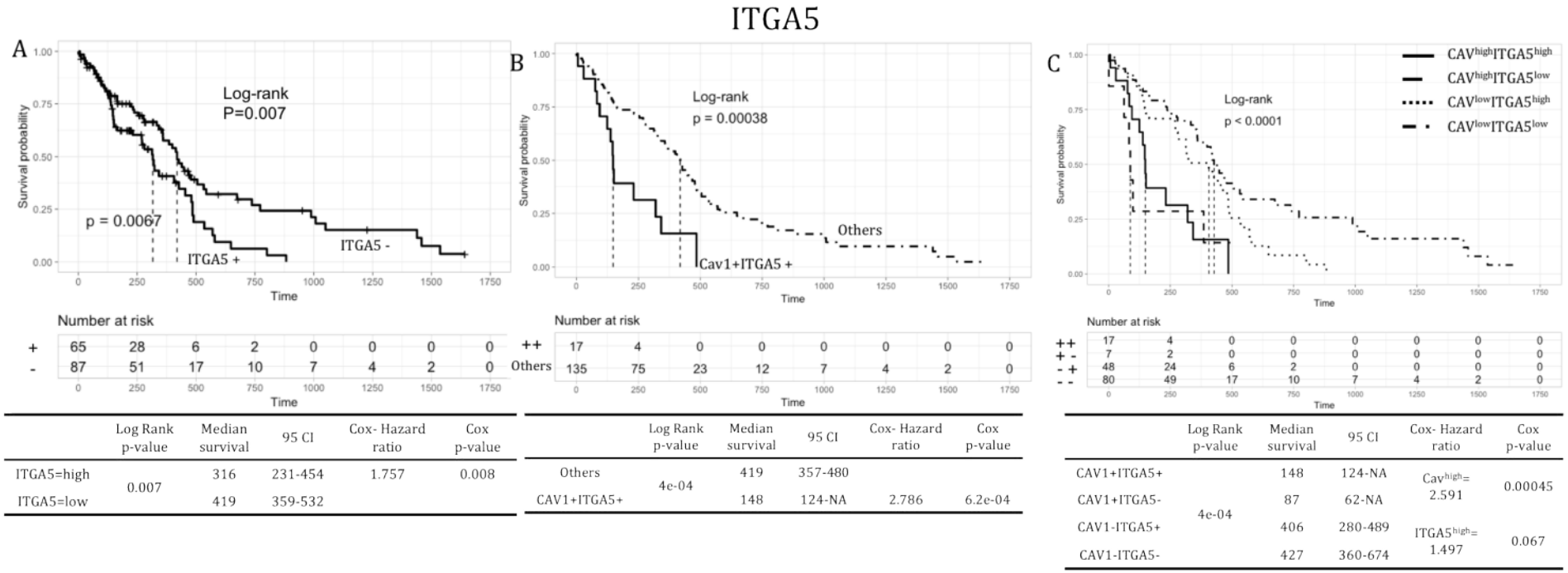

	Log Rank p-value	Median survival	95 CI	Cox- Hazard ratio	Cox p-value
ITGA5=high	0.007	316	231-454	1.757	0.008
ITGA5=low		419	359-532		

	Log Rank p-value	Median survival	95 CI	Cox- Hazard ratio	Cox p-value
Others	4e-04	419	357-480		
CAV1+ITGA5+		148	124-NA	2.786	6.2e-04

	Log Rank p-value	Median survival	95 CI	Cox- Hazard ratio	Cox p-value
CAV1+ITGA5+	4e-04	148	124-NA	Cav^{high}= 2.591	0.00045
CAV1+ITGA5-		87	62-NA		
CAV1-ITGA5+		406	280-489	$ITGA5^{high}$= 1.497	0.067
CAV1-ITGA5-		427	360-674		

Figure 6.11 Cav-1 and ITGA5 (adhesion 4). Overall survival curves of ITGA5 for GBM patients. A. Impact of a high and low expression on survival (Level 1). B. Survival curve for patients with high expression of both Cav-1 and ITGA5 was compared to the rest of the patients (Level 2). High or low expressions have been abbreviated to +/. C. Comparison between the single combinations of a high and low expression of Cav-1 and the target gene (Level 3). Vertical lines connect median survival time. Tables show for each plot: Log Rank p-value for the evaluation of the curves statistical difference; median survival for each group, reported together with the confidence interval (CI); Cox hazard ratio for the referring group, coupled with its p-value. Plot and analysis were achieved through R project.

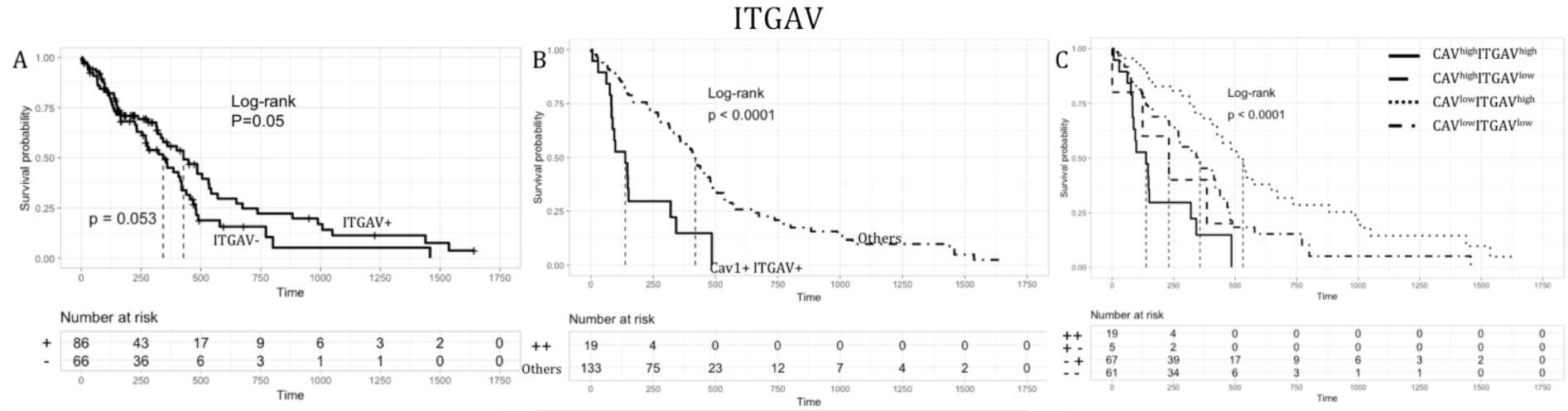

	Log Rank p-value	Median survival	95 CI	Cox- Hazard ratio	Cox p-value
ITGAV=high	0.05	427	333-543		
ITGAV=low		342	269-419	1.484	0.06

	Log Rank p-value	Median survival	95 CI	Cox- Hazard ratio	Cox p-value
Others	7e-06	419	357-480		
CAV1+ITGAV+		138	87-342	3.367	2e-05

	Log Rank p-value	Median survival	95 CI	Cox- Hazard ratio	Cox p-value
CAV1+ITGAV+	2e-06	138	87-342	$Cav^{high=}$ 3.155	1e-05
CAV1+ITGAV-		231	124-NA		
CAV1-ITGAV+		532	427-737	$ITGAV^{low=}$ 1.589	0.025
CAV1-ITGAV-		357	269-439		

Figure 6.12 Cav-1 and ITGAV (adhesion 5). Overall survival curves of ITGAV for GBM patients. A. Impact of a high and low expression on survival (Level 1). B. Survival curve for patients with high expression of both Cav-1 and ITGAV was compared to the rest of the patients (Level 2). High or low expressions have been abbreviated to +/-. C. Comparison between the single combinations of a high and low expression of Cav-1 and the target gene (Level 3). Vertical lines connect median survival time. Tables show for each plot: Log Rank p-value for the evaluation of the curves statistical difference; median survival for each group, reported together with the confidence interval (CI); Cox hazard ratio for the referring group, coupled with its p-value. Plot and analysis were achieved through R project.

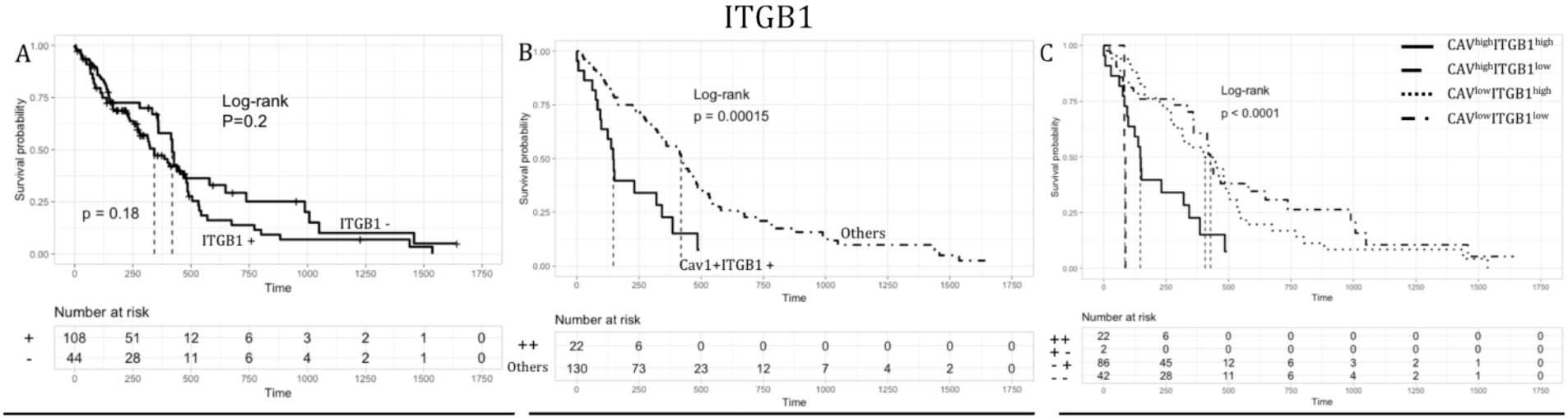

	Log Rank p-value	Median survival	95 CI	Cox- Hazard ratio	Cox p-value
ITGB1=high	0.2	342	275-478	1.344	0.2
ITGB1=low		419	359-648		

	Log Rank p-value	Median survival	95 CI	Cox- Hazard ratio	Cox p-value
Others	2e-04	419	357-485	2.681	2.6e-04
CAV1+ITGB1+		146	98-395		

	Log Rank p-value	Median survival	95 CI	Cox- Hazard ratio	Cox p-value
CAV1+ITGB1+	6e-06	146	98-385	Cav^{high}= 2.865	0.0001
CAV1+ITGB1-		84	82-NA		
CAV1-ITGB1+		406	316-505	$ITGB1^{high}$= 1.135	0.5828
CAV1-ITGB1-		427	360-737		

Figure 6.13 Cav-1 and ITGB1 (adhesion 6). Overall survival curves of ITGB1 for GBM patients. A. Impact of a high and low expression on survival (Level 1). B. Survival curve for patients with high expression of both Cav-1 and ITGB1 was compared to the rest of the patients (Level 2). High or low expressions have been abbreviated to +/-. C. Comparison between the single combinations of a high and low expression of Cav-1 and the target gene (Level 3). Vertical lines connect median survival time. Tables show for each plot: Log Rank p-value for the evaluation of the curves statistical difference; median survival for each group, reported together with the confidence interval (CI); Cox hazard ratio for the referring group, coupled with its p-value. Plot and analysis were achieved through R project.

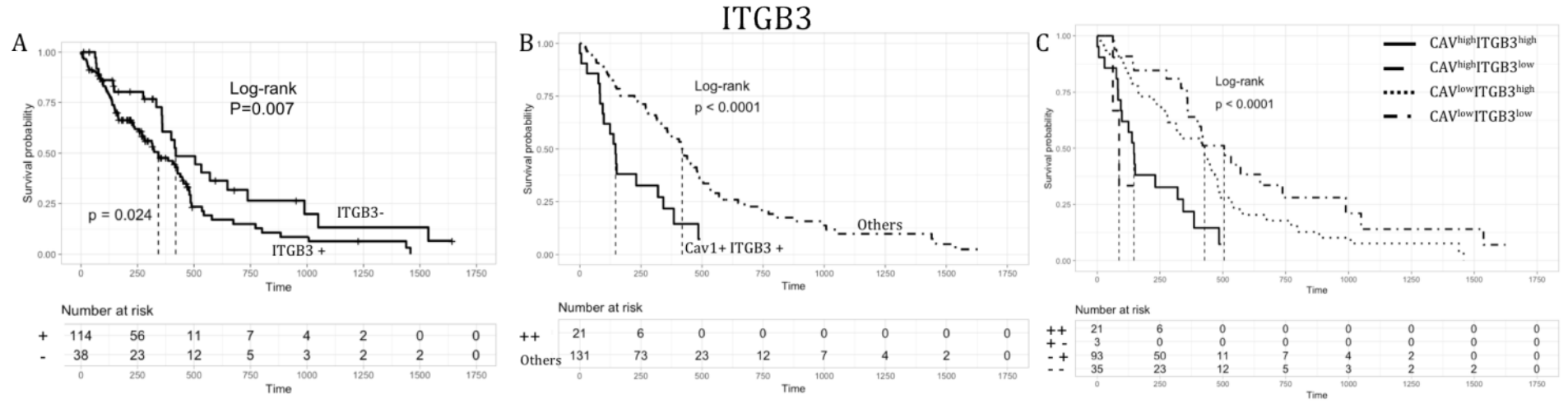

	Log Rank p-value	Median survival	95 CI	Cox- Hazard ratio	Cox p-value
ITGB3=high	0.07	485	313-737		
ITGB3=low		359	279-427	1.460	0.07

	Log Rank p-value	Median survival	95 CI	Cox- Hazard ratio	Cox p-value
Others	9e-05	419	357-485		
CAV1+ITGB3+		146	94-385	2.762	1.6e-04

	Log Rank p-value	Median survival	95 CI	Cox- Hazard ratio	Cox p-value
CAV1+ITGB3+	3e-05	146	94-385	Cav^{high}= 2.710	0.00017
CAV1+ITGB3-		87	62-NA		
CAV1-ITGB3+		427	313-480	$ITGB3^{high}$= 1.531	0.09
CAV1-ITGB3-		505	360-1050		

Figure 6.14 Cav-1 and ITGB3 (adhesion 7). Overall survival curves of ITGB3 for GBM patients. A. Impact of a high and low expression on survival (Level 1). B. Survival curve for patients with high expression of both Cav-1 and ITGB3 was compared to the rest of the patients (Level 2). High or low expressions have been abbreviated to +/-. C. Comparison between the single combinations of a high and low expression of Cav-1 and the target gene (Level 3). Vertical lines connect median survival time. Tables show for each plot: Log Rank p-value for the evaluation of the curves statistical difference; median survival for each group, reported together with the confidence interval (CI); Cox hazard ratio for the referring group, coupled with its p-value. Plot and analysis were achieved through R project.

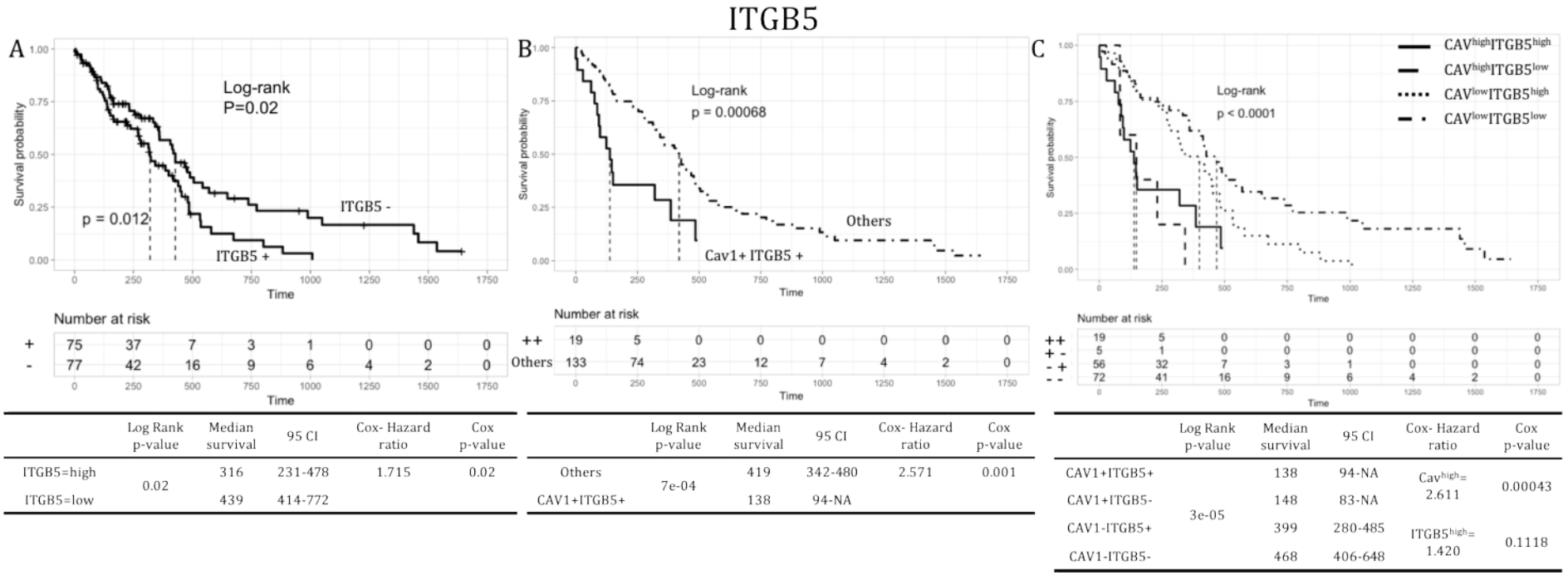

	Log Rank p-value	Median survival	95 CI	Cox- Hazard ratio	Cox p-value
ITGB5=high	0.02	316	231-478	1.715	0.02
ITGB5=low		439	414-772		

	Log Rank p-value	Median survival	95 CI	Cox- Hazard ratio	Cox p-value
Others	7e-04	419	342-480	2.571	0.001
CAV1+ITGB5+		138	94-NA		

	Log Rank p-value	Median survival	95 CI	Cox- Hazard ratio	Cox p-value
CAV1+ITGB5+	3e-05	138	94-NA	Cav^{high}= 2.611	0.00043
CAV1+ITGB5-		148	83-NA		
CAV1-ITGB5+		399	280-485	$ITGB5^{high}$= 1.420	0.1118
CAV1-ITGB5-		468	406-648		

Figure 6.15 Cav-1 and ITGB5 (adhesion 8). Overall survival curves of ITGB5 for GBM patients. A. Impact of a high and low expression on survival (Level 1). B. Survival curve for patients with high expression of both Cav-1 and ITGB5 was compared to the rest of the patients (Level 2). High or low expressions have been abbreviated to +/-. C. Comparison between the single combinations of a high and low expression of Cav-1 and the target gene (Level 3). Vertical lines connect median survival time. Tables show for each plot: Log Rank p-value for the evaluation of the curves statistical difference; median survival for each group, reported together with the confidence interval (CI); Cox hazard ratio for the referring group, coupled with its p-value. Plot and analysis were achieved through R project.

Figure 6.16 shows the impact of ECAD expression levels on survival. Figure 6.16A shows ECAD ^{high} tumours (ECAD +) to have an increased survival (441 days vs 231 for the ECAD ^{low} group), paired with an HR for ECAD^{low} of 2.431. This suggests that ECAD is and independent positive prognostic marker for GBM. Figure 6.16B shows survival curves corresponding to the portion of the patients with high levels of both Cav-1 and ECAD (CAV+ ECAD +) and the remaining population (Others). The combination of the two biomarkers determines a shorter survival median time (135 days) than the others (414 days). The median survival for the combined biomarkers in this case is shorter than both the median survival times of ECAD^{high} (441 days) and CAV^{high} alone (142 days), suggesting that some synergy may be present between them. Figure 6.16C shows the single stratifications with Cav-1 reported as a significant negative prognostic factor (HR for Cav-1 ^{high} is 2.674) while ECAD is a positive prognostic factor (HR for ECAD^{low} is 1.652) even if not significant. Specifically, when Cav-1 is high, there is no difference between ECAD^{high} and ECAD^{low}, while when Cav-1 is low ECAD inhibits disease progression, thus not allowing a significant statistical difference. This suggests that ECAD acts as a tumour suppressor, but also that Cav-1 is able to override its tumour suppressor abilities.

Figure 6.17 shows the impact of VIM expression levels on survival. Figure 6.17A shows VIM^{high} tumours (VIM+) to have no significant impact upon patient survival (342 days vs 468 for the VIM^{low} group), paired with a non-significant HR of 1.328. This suggests that VIM is not a prognostic marker for GBM. Figure 6.17B shows survival curves corresponding to the portion of the patients with high levels of both Cav-1 and VIM (CAV+VIM+) and the remaining population (Others). The combination of the two biomarkers determines a shorter survival median time (142 days) than the others (427 days). This value corresponds to the median survival of Cav-1, suggesting that a synergistic effect in this case is not present. Figure 6.17C shows the single stratifications. The group Cav^{high}VIM^{low} is not present, indicating that all Cav^{high} patients are also VIM^{high}. Only Cav-1 reported as a significant negative prognostic marker (HR for Cav-1 ^{high} is 2.890), while VIM is not. This is because, when Cav-1 is low, there is no

difference between patients with high or low levels of VIM. However, in the subpopulation of $VIM^{high}CAV^{high}$ the survival is greatly reduced. This indicates that is able to shorten patient survival only when it is co-expressed with Cav-1, and that Cav-1 can be highly expressed only when VIM is highly expressed as well, thus VIM is a pre-requisite for Cav-1 expression.

Figure 6.18 shows the impact of PVRL4 expression levels on survival. Figure 6.18Figure 6.14A shows $PVRL4^{high}$ tumours (PVRL4+) to have a reduced survival (231 days vs 419 for the $PVRL4^{low}$ group), paired with a significant HR of 2.695. This indicates that PVRL4 is an independent negative prognostic marker for GBM. Figure 6.18B shows survival curves corresponding to the portion of the patients with high levels of both Cav-1 and PVRL4 (CAV+PVRL4+) and the remaining population (Others). The combination of the two biomarkers determines a shorter survival median time (83 days) than the others (406 days). Figure 6.18C shows the single stratifications with both biomarkers reported as a significant negative prognostic factors (HR for Cav-1 ^{high} is 2.833 and for PVRL4 ^{high} 2.494). The median survival of Level 1 $PVRL4^{high}$ and Level 1 CAV^{high} are both longer than the $PVRL4^{high}CAV^{high}$ group in Level 2, suggesting that Cav-1 and PVRL4 may sinergetically drive disease progression.

Figure 6.19 shows the impact of CTSB expression levels on survival. Figure 6.19Figure 6.14A shows $CTSB^{high}$ tumours (CTSB+) to have a reduced survival (333 days vs 478 for the $CTSB^{low}$ group), paired with an HR of 2.155, suggesting that CTSB may be an independent prognostic marker. Figure 6.19B shows survival curves corresponding to the portion of the patients with high levels of both Cav-1 and CTSB (CAV+CTSB+) and the remaining population (Others). The combination of the two biomarkers determines a shorter survival median time (142 days) than the others (427 days). This value corresponds to the median survival of Cav-1, suggesting that a synergistic effect in this case is not present. Figure 6.19Figure 6.14C shows that the group $Cav^{high}CTSB^{low}$ is not present, suggesting that all Cav^{high} patients are also $CTSB^{high}$. The Level 3 stratifications confirmed Cav-1 reported as a significant negative prognostic factor (HR for Cav-1 ^{high} is 2.681) while CTSB wass not. This is because, when

Cav-1 is low, there is no significant difference between patients with high or low levels of CTSB. However, in the subpopulation of $CTSB^{high}CAV^{high}$ the survival is greatly reduced. This indicates that is able to shorten patient survival only when it is co-expressed with Cav-1, and that Cav-1 can be highly expressed only when ITGA3 is highly expressed as well, thus ITGA3 is a pre-requisite for Cav-1 expression.

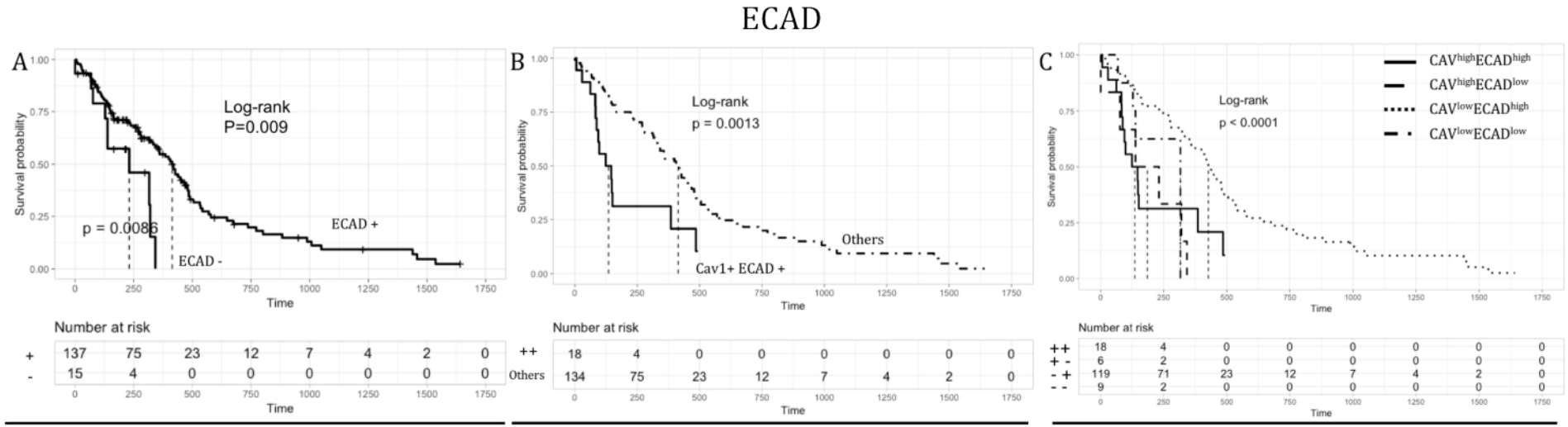

	Log Rank p-value	Median survival	95 CI	Cox- Hazard ratio	Cox p-value
ECAD=high	0.009	441	342-478		
ECAD=low		231	138-NA	2.431	0.02

	Log Rank p-value	Median survival	95 CI	Cox- Hazard ratio	Cox p-value
Others	0.001	414	342-478		
CAV1+ECAD+		135	87-NA	2.519	0.0018

	Log Rank p-value	Median survival	95 CI	Cox- Hazard ratio	Cox p-value
CAV1+ECAD+	7e-05	135	87-NA	$Cav^{high=}$ 2.674	0.0004
CAV1+ECAD-		184	76-NA		
CAV1-ECAD+		427	360-489	$ECAD^{low=}$ 1.652	0.1736
CAV1-ECAD-		316	138-NA		

Figure 6.16 Cav-1 and ECAD (EMT 1). Overall survival curves of ECAD for GBM patients. A. Impact of a high and low expression on survival (Level 1). B. Survival curve for patients with high expression of both Cav-1 and ECAD was compared to the rest of the patients (Level 2). High or low expressions have been abbreviated to +/-. C. Comparison between the single combinations of a high and low expression of Cav-1 and the target gene (Level 3). Vertical lines connect median survival time. Tables show for each plot: Log Rank p-value for the evaluation of the curves statistical difference; median survival for each group, reported together with the con fidence interval (CI); Cox hazard ratio for the referring group, coupled with its p-value. Plot and analysis were achieved through R project.

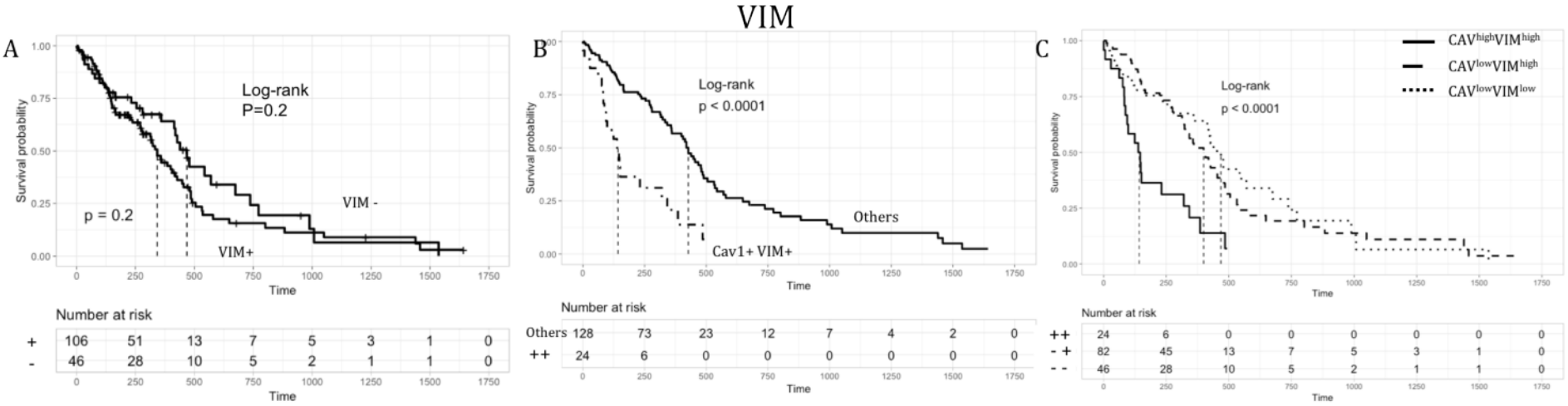

	Log Rank p-value	Median survival	95 CI	Cox- Hazard ratio	Cox p-value
VIM=high	0.2	342	279-427	1.328	0.2
VIM=low		468	414-737		

	Log Rank p-value	Median survival	95 CI	Cox- Hazard ratio	Cox p-value
Others	7e-04	427	359-485		
CAV1+VIM+		142	94-342	2.985	2.9e-05

	Log Rank p-value	Median survival	95 CI	Cox- Hazard ratio	Cox p-value
CAV1+VIM+	6e-05	142	94-342	Cav^{high}= 2.890	0.00011
CAV1+VIM-		-	-		
CAV1-VIM+		399	323-485	VIM^{high}= 1.094	0.70307
CAV1-VIM-		468	414-737		

Figure 6.17 Cav-1 and VIM (EMT 2). Overall survival curves of VIM for GBM patients. A. Impact of a high and low expression on survival (Level 1). B. Survival curve for patients with high expression of both Cav-1 and VIM was compared to the rest of the patients (Level 2). High or low expressions have been abbreviated to +/-. C. Comparison between the single combinations of a high and low expression of Cav-1 and the target gene (Level 3). Vertical lines connect median survival time. Tables show for each plot: Log Rank p-value for the evaluation of the curves statistical difference; median survival for each group, reported together with the confidence interval (CI); Cox hazard ratio for the referring group, coupled with its p-value. Plot and analysis were achieved through R project.

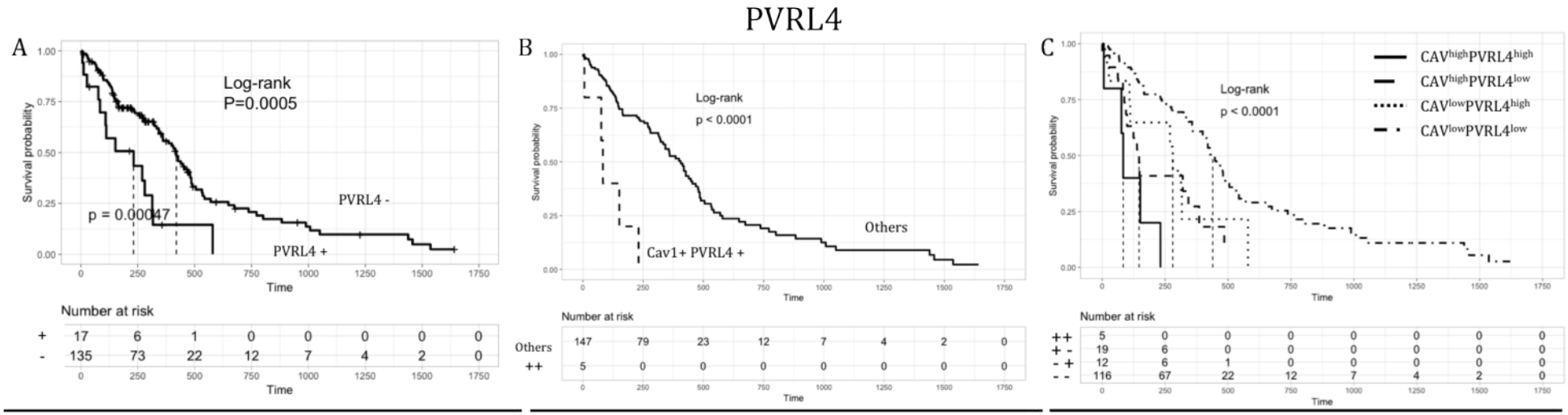

	Log Rank p-value	Median survival	95 CI	Cox- Hazard ratio	Cox p-value
PVRL4=high	5e-04	231	108-NA	2.695	0.003
PVRL4=low		419	357-480		

	Log Rank p-value	Median survival	95 CI	Cox- Hazard ratio	Cox p-value
Others	3e-05	406	333-468		
CAV1+PVRL4+		83	76-NA	5.729	2.5e-04

	Log Rank p-value	Median survival	95 CI	Cox- Hazard ratio	Cox p-value
CAV1+PVRL4+	3e-07	83	76-NA	Cav^{high}= 2.833	7.6e-05
CAV1+PVRL4-		146	98-NA		
CAV1-PVRL4+		280	111-NA	$PVRL4^{high}$= 2.494	0.0022
CAV1-PVRL4-		439	399-505		

Figure 6.18 Cav-1 and PVRL4 (cell-cell adhesion). Overall survival curves of PVRL4 for GBM patients. A. Impact of a high and low expression on survival (Level 1). B. Survival curve for patients with high expression of both Cav-1 and PVRL4 was compared to the rest of the patients (Level 2). High or low expressions have been abbreviated to +/-. C. Comparison between the single combinations of a high and low expression of Cav-1 and the target gene (Level 3). Vertical lines connect median survival time. Tables show for each plot: Log Rank p-value for the evaluation of the curves statistical difference; median survival for each group, reported together with the confidence interval (CI); Cox hazard ratio for the referring group, coupled with its p-value. Plot and analysis were achieved through R project.

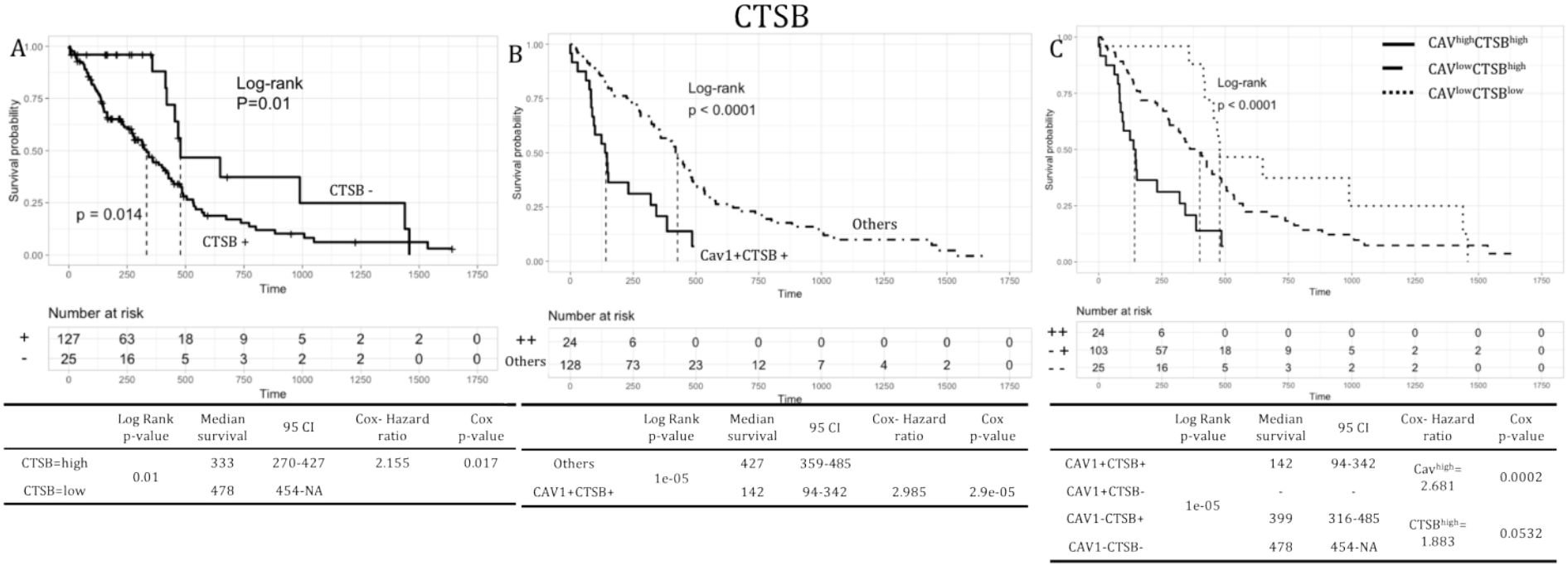

	Log Rank p-value	Median survival	95 CI	Cox- Hazard ratio	Cox p-value
CTSB=high	0.01	333	270-427	2.155	0.017
CTSB=low		478	454-NA		

	Log Rank p-value	Median survival	95 CI	Cox- Hazard ratio	Cox p-value
Others	1e-05	427	359-485		
CAV1+CTSB+		142	94-342	2.985	2.9e-05

	Log Rank p-value	Median survival	95 CI	Cox- Hazard ratio	Cox p-value
CAV1+CTSB+	1e-05	142	94-342	Cav^{high}= 2.681	0.0002
CAV1+CTSB-		-	-		
CAV1-CTSB+		399	316-485	$CTSB^{high}$= 1.883	0.0532
CAV1-CTSB-		478	454-NA		

Figure 6.19 Cav-1 and CTSB (invasion 1). Overall survival curves of CTSB for GBM patients. A. Impact of a high and low expression on survival (Level 1). B. Survival curve for patients with high expression of both Cav-1 and CTSB was compared to the rest of the patients (Level 2). High or low expressions have been abbreviated to +/-. C. Comparison between the single combinations of a high and low expression of Cav-1 and the target gene (Level 3). Vertical lines connect median survival time. Tables show for each plot: Log Rank p-value for the evaluation of the curves statistical difference; median survival for each group, reported together with the confidence interval (CI); Cox hazard ratio for the referring group, coupled with its p-value. Plot and analysis were achieved through R project.

Figure 6.20 shows the impact of CTSD expression levels on survival. Figure 6.20A shows $CTSD^{high}$ tumours (CTSD+) to have a reduced survival (269 days vs 427 for the $CTSD^{low}$ group), paired with an HR of 1.848, indicating that CTSD is an independent negative prognostic biomarker. Figure 6.20B shows survival curves corresponding to the portion of the patients with high levels of both Cav-1 and CTSD (CAV+CTSD+) and the remaining population (Others). The combination of the two biomarkers determines a shorter survival median time (151 days) than the others (414 days), indicating that the subpopulation of patients with $CTSD^{high}CAV^{high}$ have a significantly worse outcome than the patients with $CTSD^{high}$ but not a worse outcome than the CAV^{high} alone, whose median survival is 142 days. This could exclude a synergistic effect of Cav-1 and CTSD expression. Figure 6.20C shows the single stratifications with only Cav-1 reported as a significant negative prognostic factor (HR for Cav-1 ^{high} is 2.451). The Level 3 analysis reveals that there is no difference in in survival rate between $CTSD^{high}$ and $CTSD^{low}$ when Cav-1 is high as well. However, when Cav-1 expression is low, $CTSD^{high}$ drives disease progression. This suggests that CTSD is an independent negative prognostic biomarker but also that its effect is relatively small in comparison with the impact of Cav-1.

Figure 6.21 shows the impact of CTSH expression levels on survival. Figure 6.21A shows $CTSH^{high}$ tumours (CTSH+) to have a increased survival (543 days vs 360 for the $CTSH^{low}$ group), paired with an HR for $CTSH^{low}$ of 2.059, suggesting that CTSH is an independent positive prognostic biomarker. Figure 6.21B shows survival curves corresponding to the portion of the patients with high levels of both Cav-1 and CTSH (CAV+CTSH+) and the remaining population (Others). The combination of the two biomarkers determines a shorter survival median time (233 days) than the others (399 days) but the hazard is not significant. Figure 6.21C shows the single stratifications with Cav-1 reported as a significant negative prognostic factor (HR for Cav-1 ^{high} is 3.311) and CTSH as a positive prognostic factor (HR for CTSH ^{low} is 2.332). Whilst Cav-1 high expression drives disease progression and shortens median survival, $CTSH^{high}$ correlates with a longer survival, even if not enough to

counterbalance the negative effect of Cav-1 (in fact CTSH HR is lower than Cav-1). This suggests that CTSH acts as a tumour suppressor but also that Cav-1 is able to partially override its tumour suppressor potential.

Figure 6.22 shows the impact of CTSK expression levels on survival. Figure 6.22 shows $CTSK^{high}$ tumours (CTSK+) to have no significant impact upon patient survival (323 days vs 427 for the $CTSK^{low}$ group), paired with a non-significant HR of 1.418. Figure 6.22B shows survival curves corresponding to the portion of the patients with high levels of both Cav-1 and CTSK (CAV+CTSK+) and the remaining population (Others). The combination of the two biomarkers determines a shorter survival median time (138 days) than the others (419 days). The median survival for the combined biomarkers in this case is shorter than both the median survival times of $CTSK^{high}$ (323 days) and CAV^{high} alone (142 days), suggesting that some synergy may be present between them. Figure 6.22C shows the single stratifications with only Cav-1 reported as a significant negative prognostic factor (HR for Cav-1 ^{high} is 3.096). This indicates that CTSK is not a driver of disease progression.

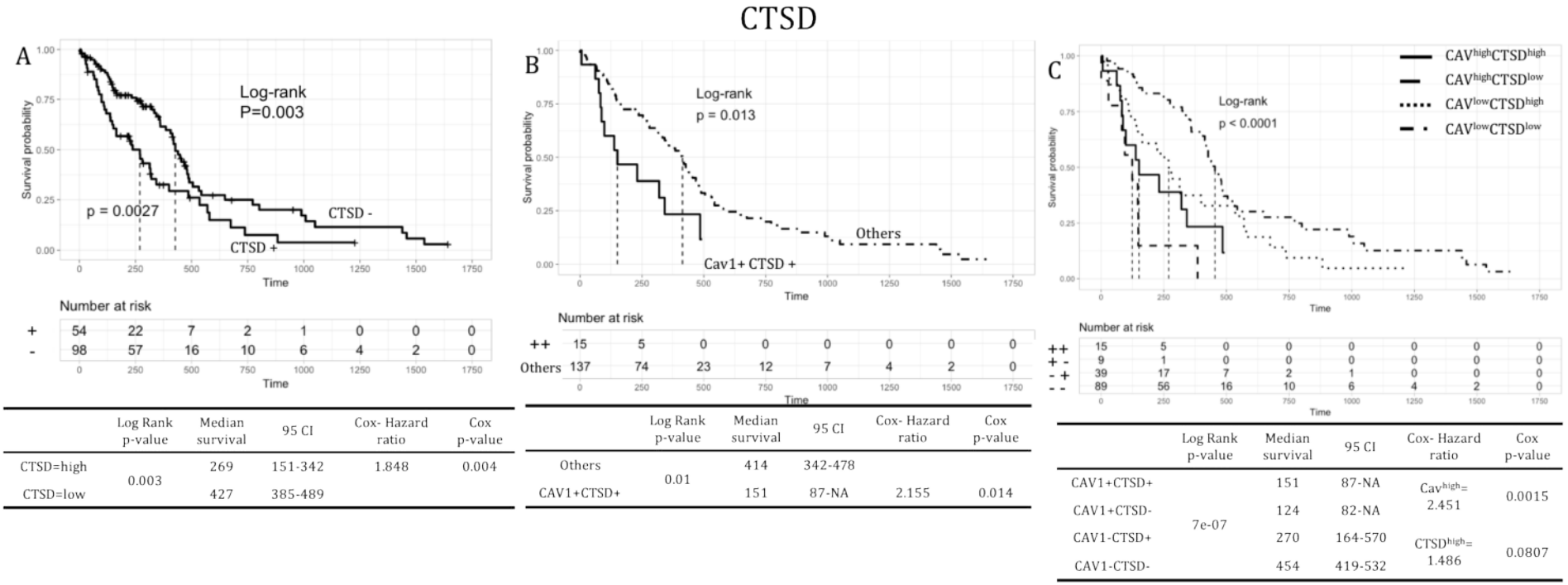

	Log Rank p-value	Median survival	95 CI	Cox- Hazard ratio	Cox p-value
CTSD=high	0.003	269	151-342	1.848	0.004
CTSD=low		427	385-489		

	Log Rank p-value	Median survival	95 CI	Cox- Hazard ratio	Cox p-value
Others	0.01	414	342-478		
CAV1+CTSD+		151	87-NA	2.155	0.014

	Log Rank p-value	Median survival	95 CI	Cox- Hazard ratio	Cox p-value
CAV1+CTSD+	7e-07	151	87-NA	Cav^{high}= 2.451	0.0015
CAV1+CTSD-		124	82-NA		
CAV1-CTSD+		270	164-570	$CTSD^{high}$= 1.486	0.0807
CAV1-CTSD-		454	419-532		

Figure 6.20 Cav-1 and CTSD (invasion 2). Overall survival curves of CTSD for GBM patients. A. Impact of a high and low expression on survival (Level 1). B. Survival curve for patients with high expression of both Cav-1 and CTSD was compared to the rest of the patients (Level 2). High or low expressions have been abbreviated to +/-. C. Comparison between the single combinations of a high and low expression of Cav-1 and the target gene (Level 3). Vertical lines connect median survival time. Tables show for each plot: Log Rank p-value for the evaluation of the curves statistical difference; median survival for each group, reported together with the confidence interval (CI); Cox hazard ratio for the referring group, coupled with its p-value. Plot and analysis were achieved through R project.

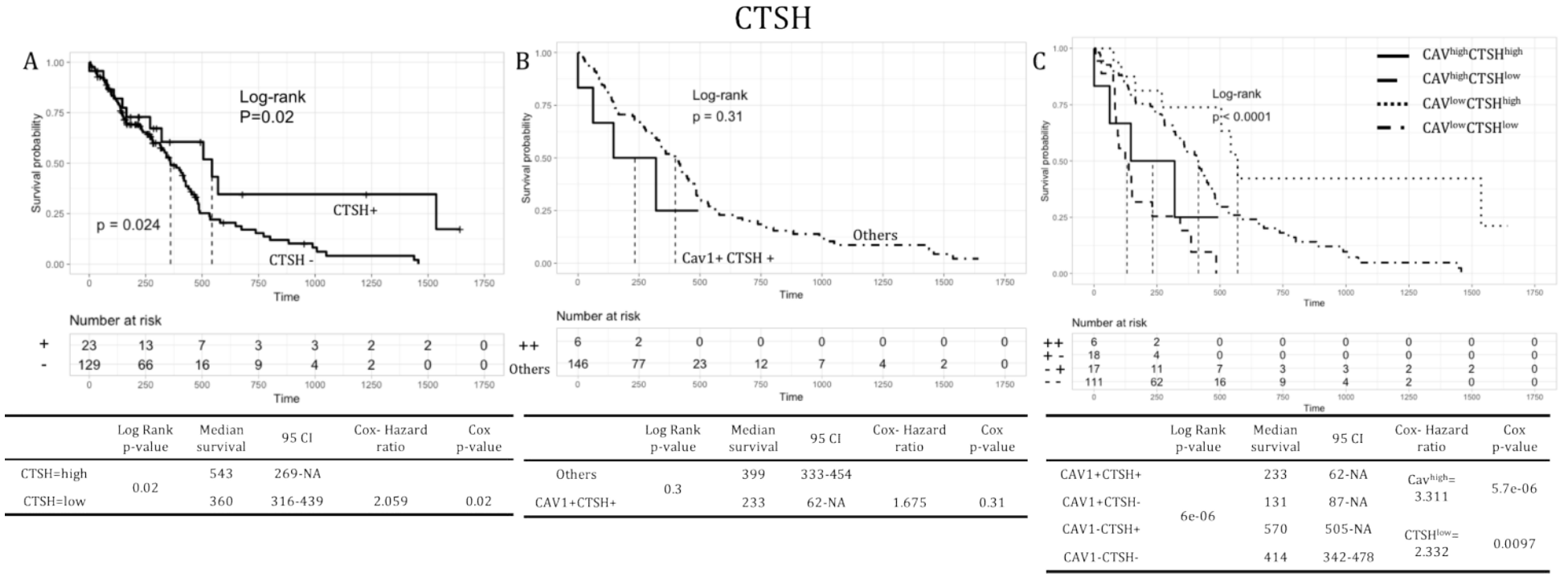

	Log Rank p-value	Median survival	95 CI	Cox- Hazard ratio	Cox p-value
CTSH=high	0.02	543	269-NA		
CTSH=low		360	316-439	2.059	0.02

	Log Rank p-value	Median survival	95 CI	Cox- Hazard ratio	Cox p-value
Others	0.3	399	333-454		
CAV1+CTSH+		233	62-NA	1.675	0.31

	Log Rank p-value	Median survival	95 CI	Cox- Hazard ratio	Cox p-value
CAV1+CTSH+	6e-06	233	62-NA	Cav^{high}= 3.311	5.7e-06
CAV1+CTSH-		131	87-NA		
CAV1-CTSH+		570	505-NA	$CTSH^{low}$= 2.332	0.0097
CAV1-CTSH-		414	342-478		

Figure 6.21 Cav-1 and invasion 3. Overall survival curves of CTSH for GBM patients. A. Impact of a high and low expression on survival (Level 1). B. Survival curve for patients with high expression of both Cav-1 and CTSH was compared to the rest of the patients (Level 2). High or low expressions have been abbreviated to +/-. C. Comparison between the single combinations of a high and low expression of Cav-1 and the target gene (Level 3). Vertical lines connect median survival time. Tables show for each plot: Log Rank p-value for the evaluation of the curves statistical difference; median survival for each group, reported together with the confidence interval (CI); Cox hazard ratio for the referring group, coupled with its p-value. Plot and analysis were achieved through R project.

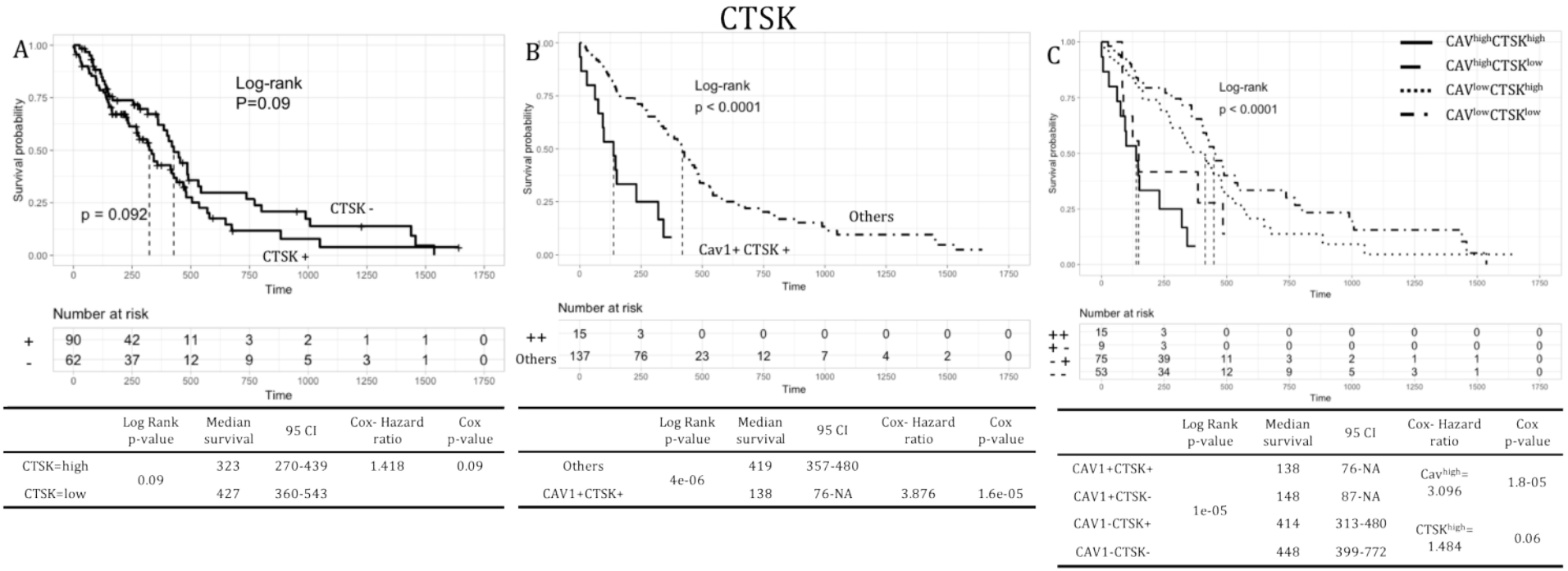

	Log Rank p-value	Median survival	95 CI	Cox- Hazard ratio	Cox p-value
CTSK=high	0.09	323	270-439	1.418	0.09
CTSK=low		427	360-543		

	Log Rank p-value	Median survival	95 CI	Cox- Hazard ratio	Cox p-value
Others	4e-06	419	357-480		
CAV1+CTSK+		138	76-NA	3.876	1.6e-05

	Log Rank p-value	Median survival	95 CI	Cox- Hazard ratio	Cox p-value
CAV1+CTSK+	1e-05	138	76-NA	Cav^{high}= 3.096	1.8-05
CAV1+CTSK-		148	87-NA		
CAV1-CTSK+		414	313-480	$CTSK^{high}$= 1.484	0.06
CAV1-CTSK-		448	399-772		

Figure 6.22 Cav-1 and invasion 4. Overall survival curves of CTSK for GBM patients. A. Impact of a high and low expression on survival (Level 1). B. Survival curve for patients with high expression of both Cav-1 and CTSK was compared to the rest of the patients (Level 2). High or low expressions have been abbreviated to +/-. C. Comparison between the single combinations of a high and low expression of Cav-1 and the target gene (Level 3). Vertical lines connect median survival time. Tables show for each plot: Log Rank p-value for the evaluation of the curves statistical difference; median survival for each group, reported together with the confidence interval (CI); Cox hazard ratio for the referring group, coupled with its p-value. Plot and analysis were achieved through R project.

Figure 6.23 shows the impact of CTSL expression levels on survival. Figure 6.23A shows $CTSL^{high}$ tumours (CTSL+) to have a reduced survival (316 days vs 439 for the $CTSL^{low}$ group), paired with an HR of 1.418, suggesting that it is an independent negative prognostic biomarker. Figure 6.23B shows survival curves corresponding to the portion of the patients with high levels of both Cav-1 and CTSL (CAV+CTSL+) and the remaining population (Others). The combination of the two biomarkers determines a shorter survival median time (142 days) than the others (427 days). This value corresponds to the median survival of Cav-1, suggesting that a synergistic effect in this case is not present. Figure 6.23C shows the single stratifications with only Cav-1 reported as a significant negative prognostic factor (HR for Cav-1 ^{high} is 2.632). The group $CAV^{high}CTSL^{low}$ is not present, indicating that all Cav^{high} patients are also $CTSL^{high}$. All patients with high levels of Cav-1 are also $CTSL^{high}$, while $CTSL^{high}$ patients can be CAV^{low}, suggesting that CTSL is a pre-requisite for Cav-1 expression.

Figure 6.24 shows the impact of CTSS expression levels on survival. Figure 6.24A shows $CTSS^{high}$ tumours (CTSS+) to have no significant impact upon patient survival (342 days vs 468 for the $CTSS^{low}$ group), paired with a non-significant HR of 1.506. This suggests that CTSS is not an independent prognostic biomarker for GBM. Figure 6.24B shows survival curves corresponding to the portion of the patients with high levels of both Cav-1 and CTSS (CAV+CTSS+) and the remaining population (Others). The combination of the two biomarkers determines a shorter survival median time (146 days) than the others (419 days), indicating that the subpopulation of patients with $CTSS^{high}CAV^{high}$ have a significantly worse outcome than the patients with $CTSS^{high}$ but not a different outcome than the CAV^{high} alone, whose median survival is 142 days. This could exclude a synergistic effect of Cav-1 and CTSS expression. Figure 6.24C shows the single stratifications with only Cav-1 reported as a significant negative prognostic factor (HR for Cav-1 ^{high} is 2.762). Figure 6.24 that, when Cav-1 is low expressed, CTSS drives the disease progression however, when Cav-1 expression is high, the $CTSS^{low}CAV^{high}$ condition is met only by three patients so in this case, it is not possible to

explore the relationship further, by checking if Cav-1 has more impact on survival than CTSS.

Figure 6.25 shows the impact of MMP1 expression levels on survival. Figure 6.25A shows $MMP1^{high}$ tumours (MMP1+) to have a reduced survival (313 days vs 419 for the $MMP1^{low}$ group), paired with an HR of 1.672, suggesting that MMP1 may be an independent negative prognostic biomarker. Figure 6.25B shows survival curves corresponding to the portion of the patients with high levels of both Cav-1 and MMP1 (CAV+ MMP1+) and the remaining population (Others). The combination of the two biomarkers determines a shorter survival median time (149 days) than the others (414 days), indicating that the subpopulation of patients with $MMP1^{high}CAV^{high}$ have a significantly worse outcome than the patients with $MMP1^{high}$ but not a different outcome than the CAV^{high} alone, whose median survival is 142 days. This could exclude a synergistic effect of Cav-1 and MMP1 expression. Figure 6.25C shows the single stratifications with only Cav-1 reported as a significant negative prognostic factor (HR for Cav-1 ^{high} is 2.667). This indicated that MMP1 is a poor driver of disease progression.

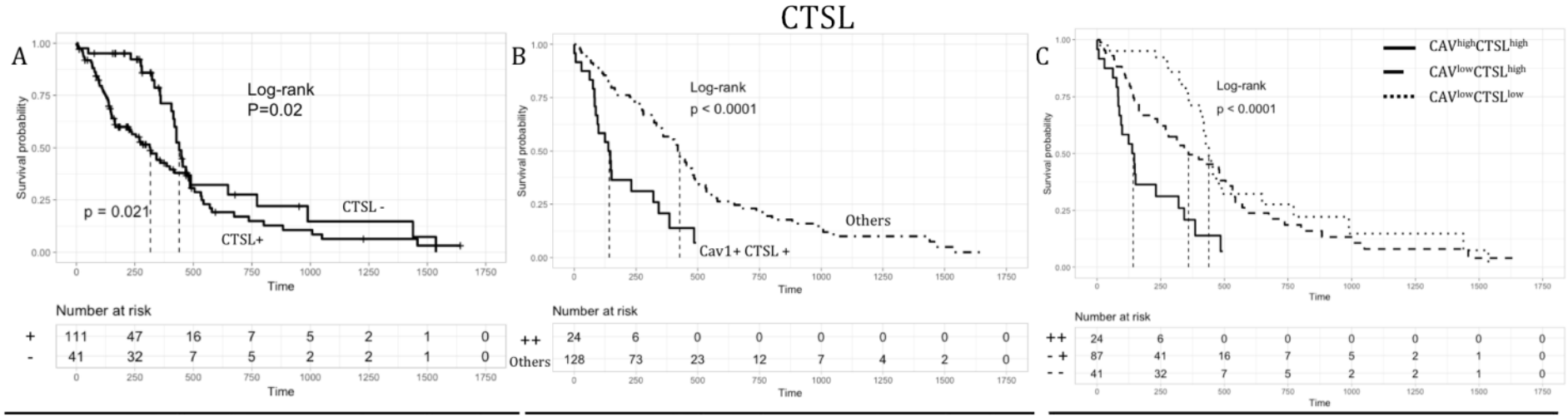

	Log Rank p-value	Median survival	95 CI	Cox- Hazard ratio	Cox p-value
CTSL=high	0.02	316	231-478	1.715	0.02
CTSL=low		439	414-772		

	Log Rank p-value	Median survival	95 CI	Cox- Hazard ratio	Cox p-value
Others	1e-05	427	359-485		
CAV1+CTSL+		142	94-342	2.985	2.9e-05

	Log Rank p-value	Median survival	95 CI	Cox- Hazard ratio	Cox p-value
CAV1+CTSL+	3e-05	142	94-342	Cav^{high}= 2.632	0.00036
CAV1+CTSL-		-	-		
CAV1-CTSL+		359	270-532	$CTSL^{high}$= 1.443	0.13576
CAV1-CTSL-		439	414-772		

Figure 6.23 Cav-1 and invasion 5. Overall survival curves of CTSL for GBM patients. A. Impact of a high and low expression on survival (Level 1). B. Survival curve for patients with high expression of both Cav-1 and CTSL was compared to the rest of the patients (Level 2). High or low expressions have been abbreviated to +/-. C. Comparison between the single combinations of a high and low expression of Cav-1 and the target gene (Level 3). Vertical lines connect median survival time. Tables show for each plot: Log Rank p-value for the evaluation of the curves statistical difference; median survival for each group, reported together with the confidence interval (CI); Cox hazard ratio for the referring group, coupled with its p-value. Plot and analysis were achieved through R project.

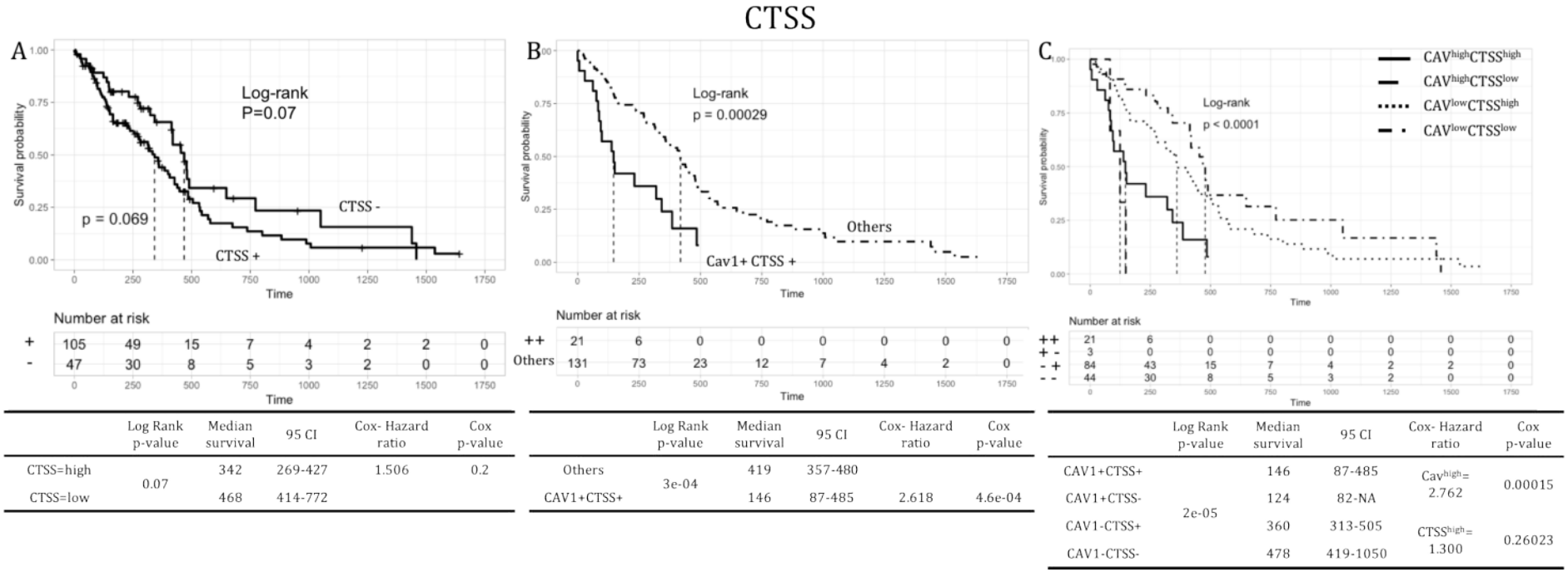

	Log Rank p-value	Median survival	95 CI	Cox- Hazard ratio	Cox p-value
CTSS=high	0.07	342	269-427	1.506	0.2
CTSS=low		468	414-772		

	Log Rank p-value	Median survival	95 CI	Cox- Hazard ratio	Cox p-value
Others	3e-04	419	357-480		
CAV1+CTSS+		146	87-485	2.618	4.6e-04

	Log Rank p-value	Median survival	95 CI	Cox- Hazard ratio	Cox p-value
CAV1+CTSS+	2e-05	146	87-485	Cav^{high}= 2.762	0.00015
CAV1+CTSS-		124	82-NA		
CAV1-CTSS+		360	313-505	$CTSS^{high}$= 1.300	0.26023
CAV1-CTSS-		478	419-1050		

Figure 6.24 Cav-1 and invasion 6. Overall survival curves of CTSS for GBM patients. A. Impact of a high and low expression on survival (Level 1). B. Survival curve for patients with high expression of both Cav-1 and CTSS was compared to the rest of the patients (Level 2). High or low expressions have been abbreviated to +/-. C. Comparison between the single combinations of a high and low expression of Cav-1 and the target gene (Level 3). Vertical lines connect median survival time. Tables show for each plot: Log Rank p-value for the evaluation of the curves statistical difference; median survival for each group, reported together with the confidence interval (CI); Cox hazard ratio for the referring group, coupled with its p-value. Plot and analysis were achieved through R project.

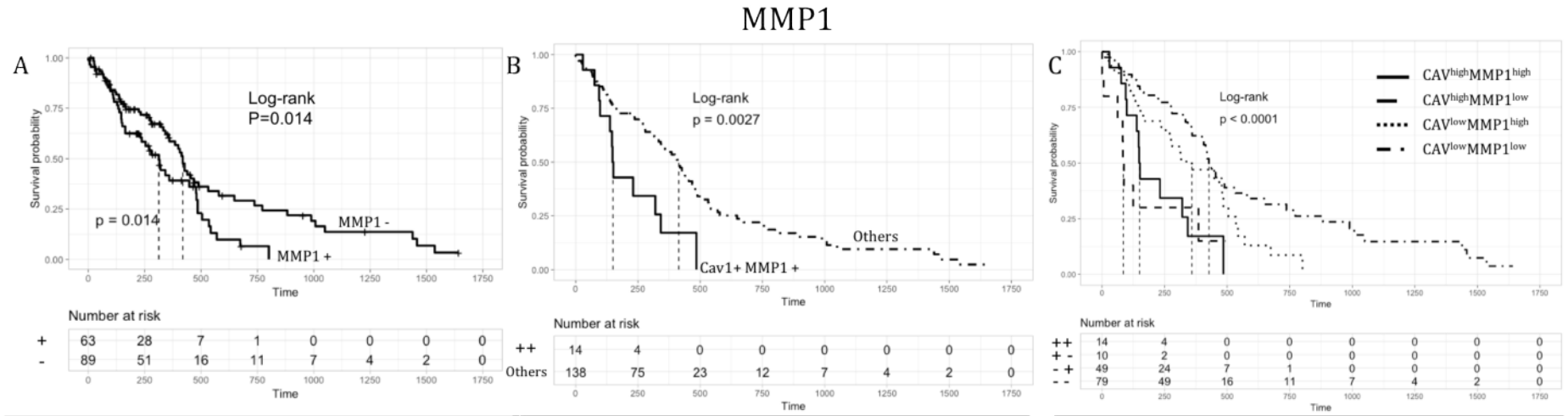

	Log Rank p-value	Median survival	95 CI	Cox- Hazard ratio	Cox p-value
MMP1=high	0.01	313	231-480	1.672	0.02
MMP1=low		419	360-532		

	Log Rank p-value	Median survival	95 CI	Cox- Hazard ratio	Cox p-value
Others	0.003	414	342-478		
CAV1+MMP1+		149	138-NA	2.519	0.0036

	Log Rank p-value	Median survival	95 CI	Cox- Hazard ratio	Cox p-value
CAV1+MMP1+	3e-05	150	138-NA	Cav^{high}= 2.667	0.00027
CAV1+MMP1-		85	62-NA		
CAV1-MMP1+		359	270-505	$MMP1^{high}$= 1.445	0.09427
CAV1-MMP1-		427	399-648		

Figure 6.25 Cav-1 and invasion 7. Overall survival curves of MMP1 for GBM patients. A. Impact of a high and low expression on survival (Level 1). B. Survival curve for patients with high expression of both Cav-1 and MMP1 was compared to the rest of the patients (Level 2). High or low expressions have been abbreviated to +/-. C. Comparison between the single combinations of a high and low expression of Cav-1 and the target gene (Level 3). Vertical lines connect median survival time. Tables show for each plot: Log Rank p-value for the evaluation of the curves statistical difference; median survival for each group, reported together with the confidence interval (CI); Cox hazard ratio for the referring group, coupled with its p-value. Plot and analysis were achieved through R project.

Figure 6.26 shows the impact of MMP2 expression levels on survival. Figure 6.26A shows $MMP2^{high}$ tumours (MMP2+) to have a reduced survival (357 days vs 543 for the $MMP2^{low}$ group), paired with an HR of 1.984, suggesting that MMP2 may be an independent negative prognostic biomarker. Figure 6.26B shows survival curves corresponding to the portion of the patients with high levels of both Cav-1 and MMP2 (CAV+ MMP2+) and the remaining population (Others). The combination of the two biomarkers determines a shorter survival median time (138 days) than the others (419 days). The median survival for the combined biomarkers in this case is shorter than both the median survival times of $MMP2^{high}$ (357 days) and CAV^{high} alone (142 days), suggesting that some synergy may be present between them. Figure 6.26C shows the single stratifications with both markers reported as a significant negative prognostic factors (HR for Cav-1^{high} is 3.356 whilst for $MMP2^{high}$ 2.320). MMP2 impact upon survival is irrespective of Cav-1, suggesting that MMP2 is an independent prognostic marker.

Figure 6.27 shows the impact of MMP3 expression levels on survival. Figure 6.27A shows $MMP3^{high}$ tumours (MMP3+) to have no significant impact upon patient survival (485 days vs 359 for the $MMP3^{low}$ group), paired with a non-significant HR of 1.460 for $MMP3^{low}$. This suggests that MMP3 is not an independent prognostic marker for GBM. Figure 6.27B shows survival curves corresponding to the portion of the patients with high levels of both Cav-1 and MMP3 (CAV+ MMP3+) and the remaining population (Others). The combination of the two biomarkers determines a shorter survival median time (146 days) than the others (406 days), indicating that the subpopulation of patients with $MMP3^{high}CAV^{high}$ have a significantly worse outcome than the patients with $MMP3^{high}$ but not a different outcome than the CAV^{high} alone, whose median survival is 142 days. This could exclude a synergistic effect of Cav-1 and MMP3 expression. Figure 6.27C shows the single stratifications with Cav-1 reported as a significant negative prognostic factor (HR for Cav-1^{high} is 3.322) whereas MMP3 is a positive prognostic marker (HR for $MMP3^{low}$ is 1.641). This is because, whilst Cav-1 expression drives disease progression and shortens median survival, a high expression of MMP3 correlates with a longer survival,

even if the effect is not powerful enough to annul the oncogene effect of Cav-1 high expression. This suggests that MMP3 is a tumour suppressor in GBM, but also that Cav-1 is able to override its action.

Figure 6.28 shows the impact of MMP7 expression levels on survival. Figure 6.28A shows $MMP7^{high}$ tumours (MMP7+) to have a reduced survival (316 days vs 468 for the $MMP7^{low}$ group), paired with an HR of 1.645, suggesting that MMP7 may be an independent negative prognostic biomarker. Figure 6.28B shows survival curves corresponding to the portion of the patients with high levels of both Cav-1 and MMP7 (CAV+ MMP7+) and the remaining population (Others). The combination of the two biomarkers determines a shorter survival median time (146 days) than the others (419 days), indicating that the subpopulation of patients with $MMP7^{high}CAV^{high}$ have a significantly worse outcome than the patients with $MMP7^{high}$ but not a different outcome than the CAV^{high} alone, whose median survival is 142 days. This could exclude a synergistic effect of Cav-1 and MMP7 expression. Figure 6.28C shows the single stratifications with only Cav-1 reported as a significant negative prognostic factor (HR for Cav-1^{high} is 2.625). ,When Cav-1 is low expressed, MMP7 drives the disease progression however, when Cav-1 is high almost all patients are $MMP7^{high}$ as well. A larger cohort would allow to include more patients $CAV^{high}MMP7^{low}$ and determine if MMP7 is actually a prognostic factor for gliomas.

Figure 6.29 shows the impact of MMP9 expression levels on survival. Figure 6.29A shows $MMP9^{high}$ tumours (MMP9+) to have a reduced survival (359 days vs 737 for the $MMP9^{low}$ group), paired with an HR of 1.789, suggesting that MMP9 may be an independent negative prognostic biomarker. Figure 6.29B shows survival curves corresponding to the portion of the patients with high levels of both Cav-1 and MMP9 (CAV+ MMP9+) and the remaining population (Others). The combination of the two biomarkers determines a shorter survival median time (139 days) than the others (419 days). The median survival for the combined biomarkers in this case is shorter than both the median survival times of $MMP9^{high}$ (359 days) and CAV^{high} alone (142 days),

suggesting that some synergy may be present between them. Figure 6.29C shows the single stratifications with both markers reported as a significant negative prognostic factors (HR for Cav-1^{high} is 3.086 and for MMP9^{high} 1.869). MMP9 impact upon survival is irrespective of Cav-1, suggesting that MMP9 is an independent prognostic marker.

Figure 6.30 shows the impact of MMP10 expression levels on survival. Figure 6.30A shows MMP10^{high} tumours (MMP10+) to have a reduced survival (320 days vs 427 for the MMP10^{low} group), paired with an HR of 1.653, suggesting that MMP10 may be an independent negative prognostic biomarker. Figure 6.30B shows survival curves corresponding to the portion of the patients with high levels of both Cav-1 and MMP10 (CAV+ MMP10+) and the remaining population (Others). The combination of the two biomarkers determines a shorter survival median time (142 days) than the others (419 days). This value corresponds to the median survival of Cav-1, suggesting that a synergistic effect in this case is not present. Figure 6.30C shows the single stratifications with only Cav-1 reported as a significant negative prognostic factor (HR for Cav-1^{high} is 2.703). When Cav-1 is low there is no difference between MMP10^{high} and MMP10^{low} patients. When the expression of Cav-1 increases, however, only two patients corresponds to the phenotype CAV^{high}MMP10^{low}. This makes not possible to explore the relationship further, by checking if Cav-1 has more impact on survival than MMP10.

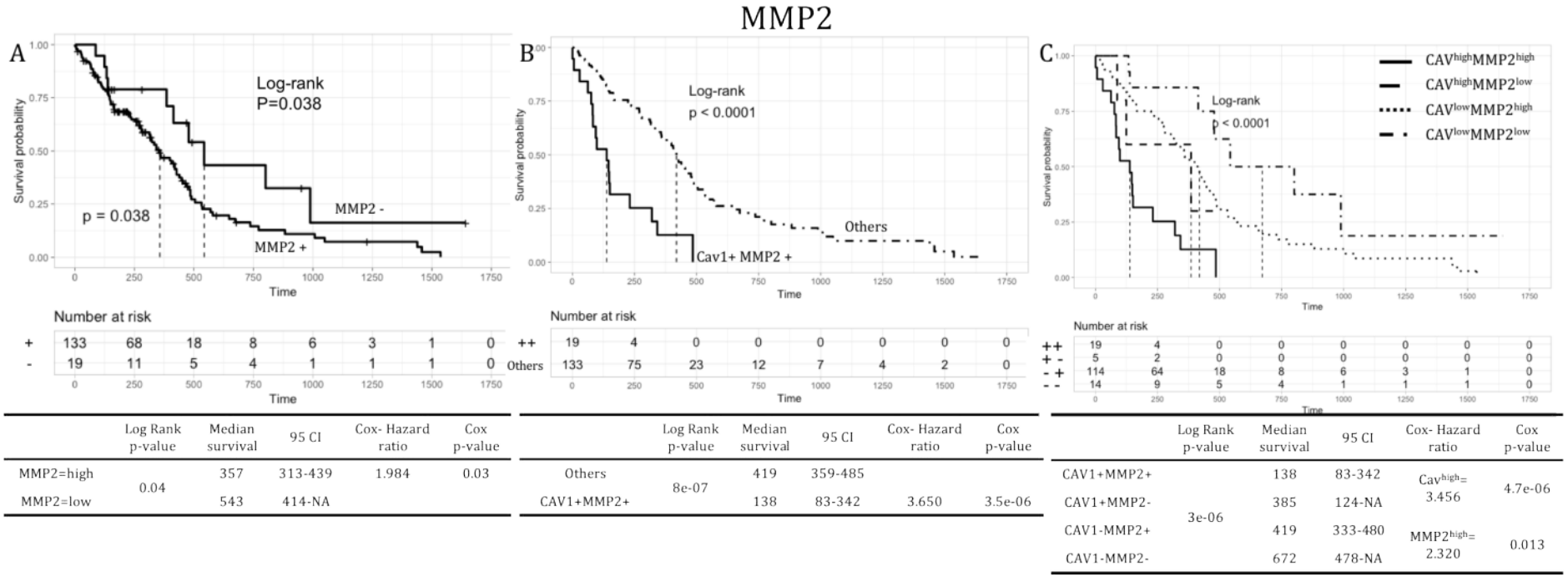

	Log Rank p-value	Median survival	95 CI	Cox- Hazard ratio	Cox p-value
MMP2=high	0.04	357	313-439	1.984	0.03
MMP2=low		543	414-NA		

	Log Rank p-value	Median survival	95 CI	Cox- Hazard ratio	Cox p-value
Others	8e-07	419	359-485		
CAV1+MMP2+		138	83-342	3.650	3.5e-06

	Log Rank p-value	Median survival	95 CI	Cox- Hazard ratio	Cox p-value
CAV1+MMP2+	3e-06	138	83-342	$Cav^{high=}$ 3.456	4.7e-06
CAV1+MMP2-		385	124-NA		
CAV1-MMP2+		419	333-480	$MMP2^{high=}$ 2.320	0.013
CAV1-MMP2-		672	478-NA		

Figure 6.26 Cav-1 and invasion 8. Overall survival curves of MMP2 for GBM patients. A. Impact of a high and low expression on survival (Level 1). B. Survival curve for patients with high expression of both Cav-1 and MMP2 was compared to the rest of the patients (Level 2). High or low expressions have been abbreviated to +/-. C. Comparison between the single combinations of a high and low expression of Cav-1 and the target gene (Level 3). Vertical lines connect median survival time. Tables show for each plot: Log Rank p-value for the evaluation of the curves statistical difference; median survival for each group, reported together with the confidence interval (CI); Cox hazard ratio for the referring group, coupled with its p-value. Plot and analysis were achieved through R project.

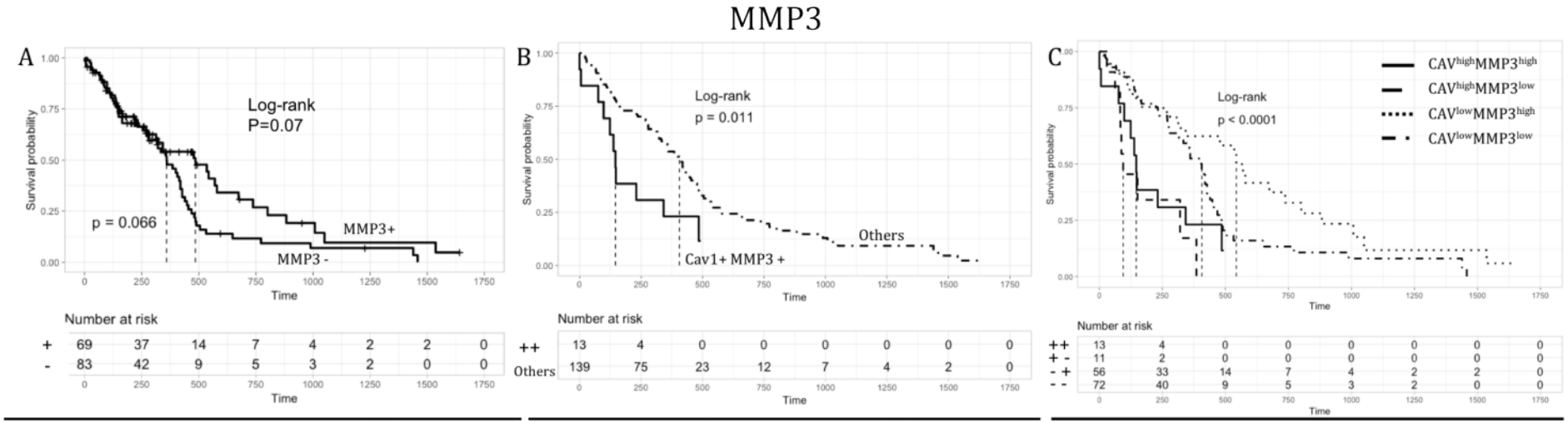

	Log Rank p-value	Median survival	95 CI	Cox- Hazard ratio	Cox p-value
MMP3=high	0.07	485	313-737		
MMP3=low		359	279-427	1.460	0.07

	Log Rank p-value	Median survival	95 CI	Cox- Hazard ratio	Cox p-value
Others	0.01	406	333-478		
CAV1+MMP3+		146	98-NA	3.774	0.013

	Log Rank p-value	Median survival	95 CI	Cox- Hazard ratio	Cox p-value
CAV1+MMP3+	1e-05	146	98-NA	$Cav^{high=}$ 2.625	6.5e-06
CAV1+MMP3-		94	83-NA		
CAV1-MMP3+		543	342-883	$MMP3^{low=}$ 1.641	0.019
CAV1-MMP3-		406	333-448		

Figure 6.27 Cav-1 and invasion 9. Overall survival curves of MMP3 for GBM patients. A. Impact of a high and low expression on survival (Level 1). B. Survival curve for patients with high expression of both Cav-1 and MMP3 was compared to the rest of the patients (Level 2). High or low expressions have been abbreviated to +/-. C. Comparison between the single combinations of a high and low expression of Cav-1 and the target gene (Level 3). Vertical lines connect median survival time. Tables show for each plot: Log Rank p-value for the evaluation of the curves statistical difference; median survival for each group, reported together with the confidence interval (CI); Cox hazard ratio for the referring group, coupled with its p-value. Plot and analysis were achieved through R project.

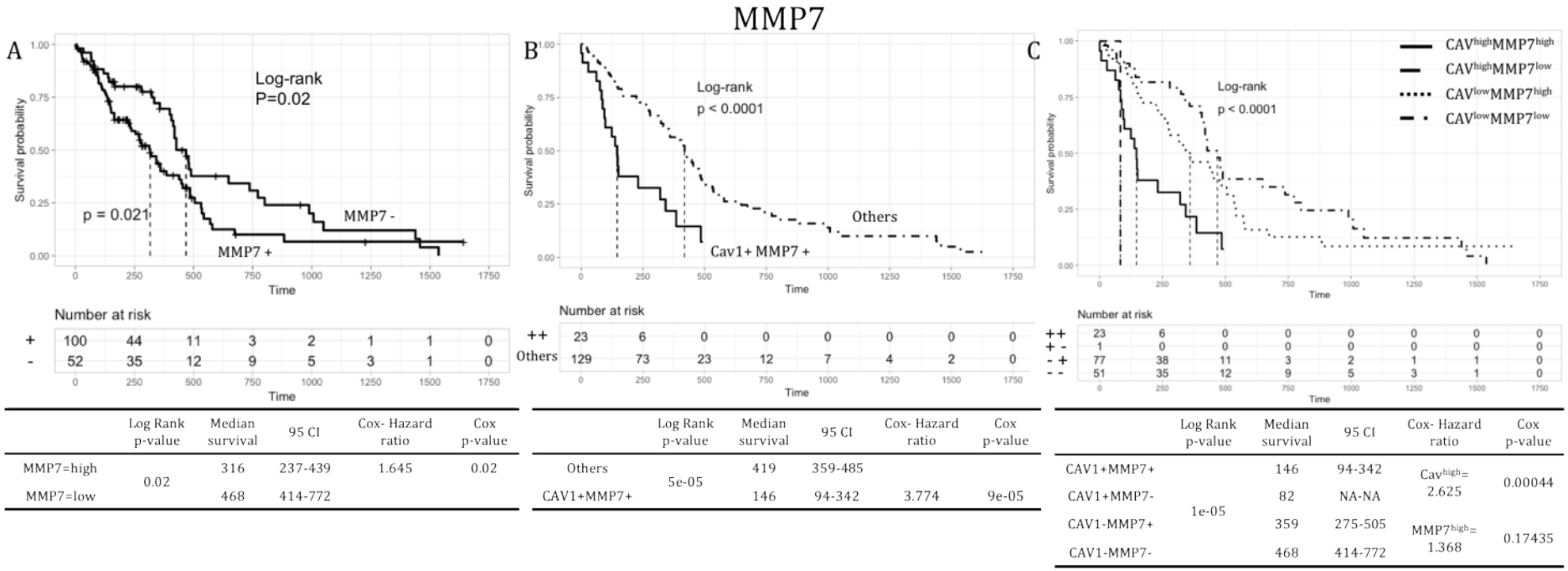

	Log Rank p-value	Median survival	95 CI	Cox- Hazard ratio	Cox p-value
MMP7=high	0.02	316	237-439	1.645	0.02
MMP7=low		468	414-772		

	Log Rank p-value	Median survival	95 CI	Cox- Hazard ratio	Cox p-value
Others	5e-05	419	359-485		
CAV1+MMP7+		146	94-342	3.774	9e-05

	Log Rank p-value	Median survival	95 CI	Cox- Hazard ratio	Cox p-value
CAV1+MMP7+	1e-05	146	94-342	$Cav^{high=}$ 2.625	0.00044
CAV1+MMP7-		82	NA-NA		
CAV1-MMP7+		359	275-505	$MMP7^{high=}$ 1.368	0.17435
CAV1-MMP7-		468	414-772		

Figure 6.28 Cav-1 and invasion 10. Overall survival curves of MMP7 for GBM patients. A. Impact of a high and low expression on survival (Level 1). B. Survival curve for patients with high expression of both Cav-1 and MMP7 was compared to the rest of the patients (Level 2). High or low expressions have been abbreviated to +/-. C. Comparison between the single combinations of a high and low expression of Cav-1 and the target gene (Level 3). Vertical lines connect median survival time. Tables show for each plot: Log Rank p-value for the evaluation of the curves statistical difference; median survival for each group, reported together with the confidence interval (CI); Cox hazard ratio for the referring group, coupled with its p-value. Plot and analysis were achieved through R project.

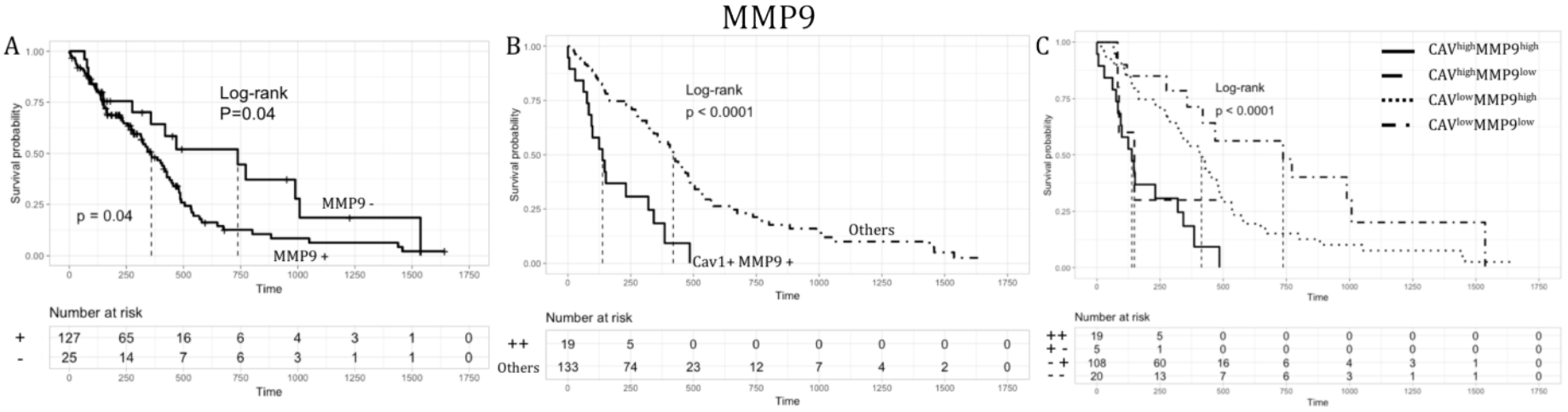

	Log Rank p-value	Median survival	95 CI	Cox- Hazard ratio	Cox p-value
MMP9=high	0.04	359	313-439	1.789	0.03
MMP9=low		737	357-NA		

	Log Rank p-value	Median survival	95 CI	Cox- Hazard ratio	Cox p-value
Others	5e-06	419	357-485		
CAV1+MMP9+		138	94-342	3.311	1.6e-05

	Log Rank p-value	Median survival	95 CI	Cox- Hazard ratio	Cox p-value
CAV1+MMP9+	2e-05	138	94-342	Cav^{high}= 3.086	1.7e-05
CAV1+MMP9-		148	87-NA		
CAV1-MMP9+		414	333-480	$MMP9^{high}$= 1.869	0.029
CAV1-MMP9-		737	419-NA		

Figure 6.29 Cav-1 and invasion 11. Overall survival curves of MMP9 for GBM patients. A. Impact of a high and low expression on survival (Level 1). B. Survival curve for patients with high expression of both Cav-1 and MMP9 was compared to the rest of the patients (Level 2). High or low expressions have been abbreviated to +/-. C. Comparison between the single combinations of a high and low expression of Cav-1 and the target gene (Level 3). Vertical lines connect median survival time. Tables show for each plot: Log Rank p-value for the evaluation of the curves statistical difference; median survival for each group, reported together with the confidence interval (CI); Cox hazard ratio for the referring group, coupled with its p-value. Plot and analysis were achieved through R project.

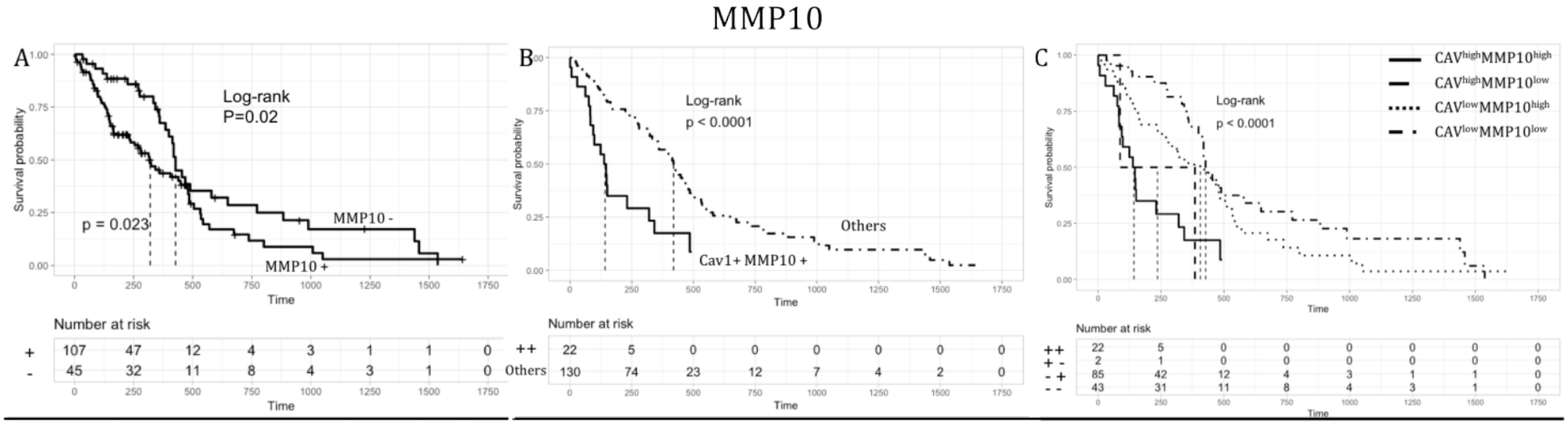

	Log Rank p-value	Median survival	95 CI	Cox- Hazard ratio	Cox p-value
MMP10=high	0.02	320	237-478	1.653	0.02
MMP10=low		427	399-648		

	Log Rank p-value	Median survival	95 CI	Cox- Hazard ratio	Cox p-value
Others	3e-05	419	359-480		
CAV1+MMP10+		142	94-342	2.924	7.4e-05

	Log Rank p-value	Median survival	95 CI	Cox- Hazard ratio	Cox p-value
CAV1+MMP10+	7e-05	142	94-342	$Cav^{high=}$ 2.703	0.00019
CAV1+MMP10-		236	87-NA		
CAV1-MMP10+		406	280-505	$MMP10^{high=}$ 1.456	0.10277
CAV1-MMP10-		427	414-772		

Figure 6.30 Cav-1 and invasion 12. Overall survival curves of MMP10 for GBM patients. A. Impact of a high and low expression on survival (Level 1). B. Survival curve for patients with high expression of both Cav-1 and MMP10 was compared to the rest of the patients (Level 2). High or low expressions have been abbreviated to +/-. C. Comparison between the single combinations of a high and low expression of Cav-1 and the target gene (Level 3). Vertical lines connect median survival time. Tables show for each plot: Log Rank p-value for the evaluation of the curves statistical difference; median survival for each group, reported together with the confidence interval (CI); Cox hazard ratio for the referring group, coupled with its p-value. Plot and analysis were achieved through R project.

Figure 6.31 shows the impact of MT1MMP expression levels on survival. Figure 6.31A shows MT1MMP^{high} tumours (MT1MMP+) to have a reduced survival (359 days vs 772 for the MT1MMP^{low} group), paired with an HR of 2.451, suggesting that MT1MMP is a negative prognostic biomarker. Figure 6.31B shows survival curves corresponding to the portion of the patients with high levels of both Cav-1 and MT1MMP (CAV+MT1MMP+) and the remaining population (Others). The combination of the two biomarkers determines a shorter survival median time (142 days) than the others (427 days). This value corresponds to the median survival of Cav-1, suggesting that a synergistic effect in this case is not present. Figure 6.31C shows the single stratifications with both biomarkers reported as a significant negative prognostic factors (HR for Cav-1^{high} is 2.762 and MT1MMP^{high} 2.212). All CAV^{high} patients are also MT1MMP^{high} whilst not all MT1MMP^{high} patients were also CAV^{high}. This suggests that MT1MMP is a pre-requisite for Cav-1 expression. Finally MT1MMP has an impact upon survival irrespective of Cav-1 expression, suggesting that MT1MMP is also an independent prognostic biomarker.

Figure 6.32 shows the impact of UPA expression levels on survival. Figure 6.32A shows UPA^{high} tumours (UPA+) to have a reduced survival (320 days vs 427 for the UPA^{low} group), paired with an HR of 1.580, suggesting that UPA is an independent negative prognostic biomarker. Figure 6.32B shows survival curves corresponding to the portion of the patients with high levels of both Cav-1 and UPA (CAV+ UPA+) and the remaining population (Others). The combination of the two biomarkers determines a shorter survival median time (146 days) than the others (419 days), indicating that the subpopulation of patients with UPA^{high}CAV^{high} have a significantly worse outcome than the patients with UPA^{high} but not a different outcome than the CAV^{high} alone, whose median survival is 142 days. This could exclude a synergistic effect of Cav-1 and UPA expression. Figure 6.32C shows the single stratifications with only Cav-1 reported as a significant negative prognostic factor (HR for Cav-1^{high} is 2.667). this indicates that UPA is a poor driver of disease progression.

Figure 6.33 shows the impact of TIMP1 expression levels on survival. Figure 6.33A shows $TIMP1^{high}$ tumours (TIMP1+) to have a reduced survival (342 days vs 989 for the $TIMP1^{low}$ group), paired with an HR of 3.425, suggesting that TIMP1 may be an independent negative prognostic biomarker. Figure 6.33B shows survival curves corresponding to the portion of the patients with high levels of both Cav-1 and TIMP1 (CAV+TIMP1+) and the remaining population (Others). The combination of the two biomarkers determines a shorter survival median time (142 days) than the others (427 days). This value corresponds to the median survival of Cav-1, suggesting that a synergistic effect in this case is not present. Figure 6.33C shows the single stratifications with both biomarkers reported as a significant negative prognostic factors (HR for $Cav\text{-}1^{high}$ is 2.681 and $TIMP1^{high}$ 3.086). All CAV^{high} patients were also $TIMP1^{high}$ whilst not all $TIMP1^{high}$ patients were also CAV^{high}. This suggests that TIMP1 is a pre-requisite for Cav-1 expression. Finally TIMP1 has an impact upon survival irrespective of Cav-1 expression, suggesting that TIMP1 s also an independent prognostic biomarker.

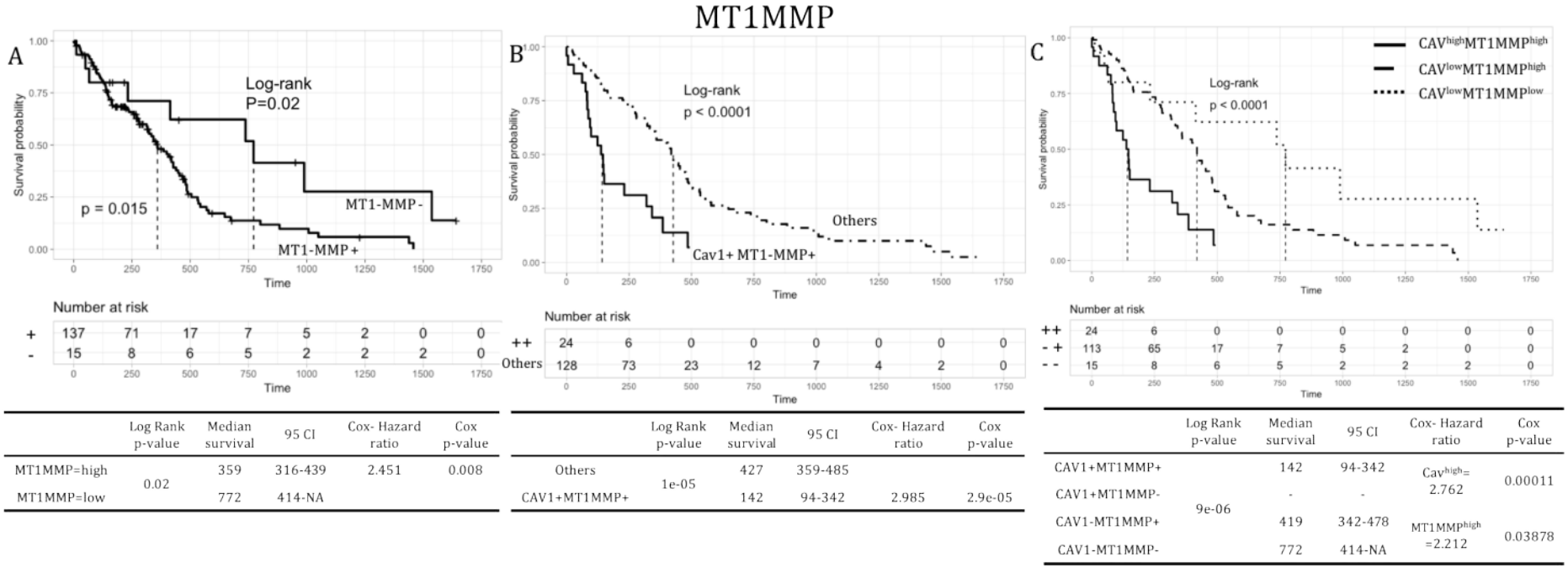

	Log Rank p-value	Median survival	95 CI	Cox- Hazard ratio	Cox p-value
MT1MMP=high	0.02	359	316-439	2.451	0.008
MT1MMP=low		772	414-NA		

	Log Rank p-value	Median survival	95 CI	Cox- Hazard ratio	Cox p-value
Others	1e-05	427	359-485		
CAV1+MT1MMP+		142	94-342	2.985	2.9e-05

	Log Rank p-value	Median survival	95 CI	Cox- Hazard ratio	Cox p-value
CAV1+MT1MMP+	9e-06	142	94-342	Cav^{high}= 2.762	0.00011
CAV1+MT1MMP-		-	-		
CAV1-MT1MMP+		419	342-478	$MT1MMP^{high}$ =2.212	0.03878
CAV1-MT1MMP-		772	414-NA		

Figure 6.31 Cav-1 and invasion 13. Overall survival curves of MT1MMP for GBM patients. A. Impact of a high and low expression on survival (Level 1). B. Survival curve for patients with high expression of both Cav-1 and MT1MMP was compared to the rest of the patients (Level 2). High or low expressions have been abbreviated to +/-. C. Comparison between the single combinations of a high and low expression of Cav-1 and the target gene (Level 3). Vertical lines connect median survival time. Tables show for each plot: Log Rank p-value for the evaluation of the curves statistical difference; median survival for each group, reported together with the confidence interval (CI); Cox hazard ratio for the referring group, coupled with its p-value. Plot and analysis were achieved through R project.

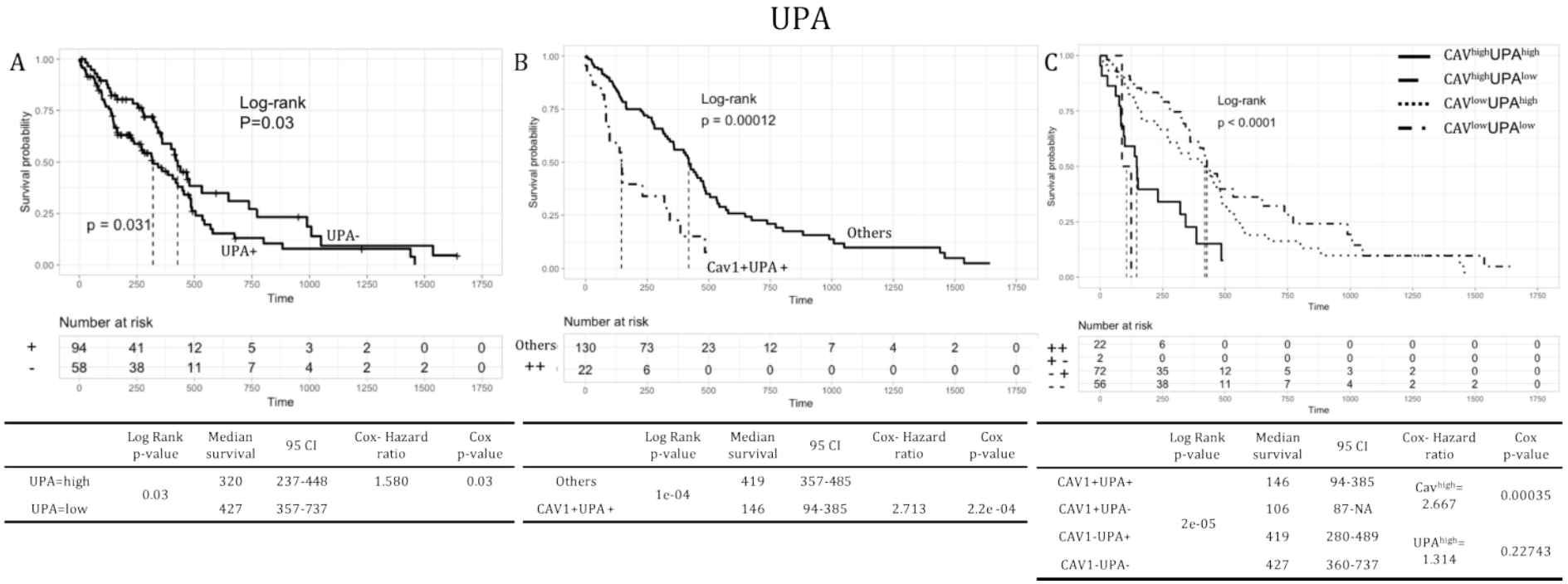

	Log Rank p-value	Median survival	95 CI	Cox- Hazard ratio	Cox p-value
UPA=high	0.03	320	237-448	1.580	0.03
UPA=low		427	357-737		

	Log Rank p-value	Median survival	95 CI	Cox- Hazard ratio	Cox p-value
Others	1e-04	419	357-485		
CAV1+UPA+		146	94-385	2.713	2.2e-04

	Log Rank p-value	Median survival	95 CI	Cox- Hazard ratio	Cox p-value
CAV1+UPA+	2e-05	146	94-385	$Cav^{high=}$ 2.667	0.00035
CAV1+UPA-		106	87-NA		
CAV1-UPA+		419	280-489	$UPA^{high=}$ 1.314	0.22743
CAV1-UPA-		427	360-737		

Figure 6.32 Cav-1 and invasion 14. Overall survival curves of UPA for GBM patients. A. Impact of a high and low expression on survival (Level 1). B. Survival curve for patients with high expression of both Cav-1 and UPA was compared to the rest of the patients (Level 2). High or low expressions have been abbreviated to +/-. C. Comparison between the single combinations of a high and low expression of Cav-1 and the target gene (Level 3). Vertical lines connect median survival time. Tables show for each plot: Log Rank p-value for the evaluation of the curves statistical difference; median survival for each group, reported together with the confidence interval (CI); Cox hazard ratio for the referring group, coupled with its p-value. Plot and analysis were achieved through R project.

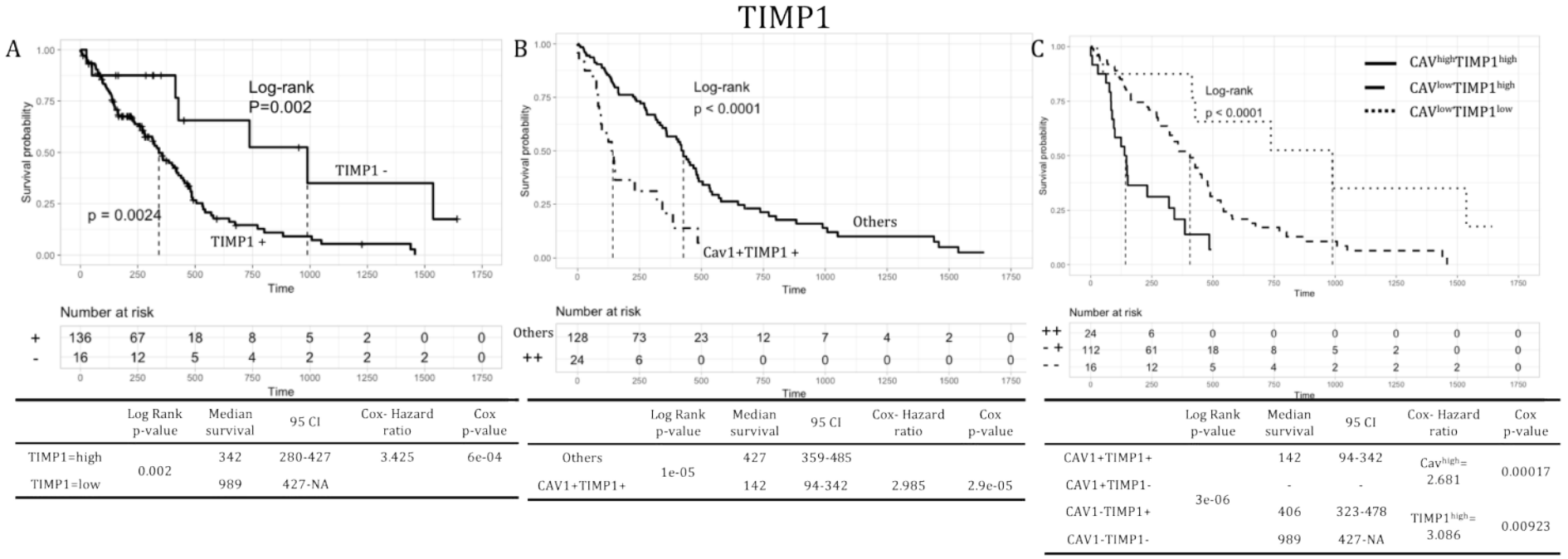

	Log Rank p-value	Median survival	95 CI	Cox- Hazard ratio	Cox p-value
TIMP1=high	0.002	342	280-427	3.425	6e-04
TIMP1=low		989	427-NA		

	Log Rank p-value	Median survival	95 CI	Cox- Hazard ratio	Cox p-value
Others	1e-05	427	359-485		
CAV1+TIMP1+		142	94-342	2.985	2.9e-05

	Log Rank p-value	Median survival	95 CI	Cox- Hazard ratio	Cox p-value
CAV1+TIMP1+	3e-06	142	94-342	Cav^{high}= 2.681	0.00017
CAV1+TIMP1-		-	-		
CAV1-TIMP1+		406	323-478	$TIMP1^{high}$= 3.086	0.00923
CAV1-TIMP1-		989	427-NA		

Figure 6.33 Cav-1 and invasion inhibition 1. Overall survival curves of TIMP1 for GBM patients. A. Impact of a high and low expression on survival (Level 1). B. Survival curve for patients with high expression of both Cav-1 and TIMP1 was compared to the rest of the patients (Level 2). High or low expressions have been abbreviated to +/-. C. Comparison between the single combinations of a high and low expression of Cav-1 and the target gene (Level 3). Vertical lines connect median survival time. Tables show for each plot: Log Rank p-value for the evaluation of the curves statistical difference; median survival for each group, reported together with the confidence interval (CI); Cox hazard ratio for the referring group, coupled with its p-value. Plot and analysis were achieved through R project.

Figure 6.34 shows the impact of TIMP3 expression levels on survival. Figure 6.34A shows $TIMP3^{high}$ tumours (TIMP3+) to have a delayed survival (480 days vs 357 for the $TIMP3^{low}$ group), paired with an HR of 1.967, indicating that TIMP3 is an independent positive prognostic marker in GBM. Figure 6.34B shows survival curves corresponding to the portion of the patients with high levels of both Cav-1 and TIMP3 (CAV+ TIMP3+) and the remaining population (Others). The combination of the two biomarkers was present only in one patient (median survival NA days) so no statistical conclusions could be inferred. Figure 6.34C shows the single stratifications with Cav-1 reported as a significant negative prognostic factor (HR for $Cav\text{-}1^{high}$ is 2.825) and TIMP3 as a significant positive prognostic factor (HR for $TIMP3^{low}$ is 1.838). The Level 3 analysis indicates that TIMP3 is a tumour suppressor in patients with low expression of Cav-1, whereas Cav-1 still drives disease progression in the $TIMP3^{low}$ patients. TIMP3 and Cav-1 appear to be mutually exclusive, with the exception of the only patient in the cohort that expressed high levels of both markers.

Figure 6.35 shows the impact of PAI1 expression levels on survival. Figure 6.35A shows $PAI1^{high}$ tumours (PAI1+) to have a reduced survival (231 days vs 419 for the $PAI1^{low}$ group), paired with an HR of 1.715, suggesting that PAI1 may be an independent negative prognostic factor for GBM. Figure 6.35B shows survival curves corresponding to the portion of the patients with high levels of both Cav-1 and PAI1 (CAV+ PAI1+) and the remaining population (Others). The combination of the two biomarkers determines a shorter survival median time (149 days) than the others (414 days), indicating that the subpopulation of patients with $PAI1^{high}CAV^{high}$ have a significantly worse outcome than the patients with $PAI1^{high}$ but not a different outcome than the CAV^{high} alone, whose median survival is 142 days. This could exclude a synergistic effect of Cav-1 and PAI1 expression. Figure 6.35C shows the single stratifications with Cav-1 reported as a significant negative prognostic factor (HR for $Cav\text{-}1^{high}$ is 3.215). The Level 3 analysis reveals that there is no difference in in survival rate between $PAI1^{high}$ and $PAI1^{low}$ when Cav-1 is high as well. However, when Cav-1 expression is low, $PAI1^{high}$ drives disease progression. This suggests that PAI1

is an independent negative prognostic biomarker but also that its effect is relatively small in comparison with the impact of Cav-1.

Figure 6.36 shows the impact of TSP1 expression levels on survival. Figure 6.36A shows $TSP1^{high}$ tumours (TSP1+) to have a reduced survival (323 days vs 648 for the $TSP1^{low}$ group), paired with an HR of 2.597, suggesting that TSP1 may be an independent negative prognostic biomarker. Figure 6.36B shows survival curves corresponding to the portion of the patients with high levels of both Cav-1 and TSP1 (CAV+TSP1+) and the remaining population (Others). The combination of the two biomarkers determines a shorter survival median time (142 days) than the others (427 days). This value corresponds to the median survival of Cav-1, suggesting that a synergistic effect in this case is not present. Figure 6.36C shows the single stratifications with both biomarkers reported as a significant negative prognostic factors (HR for $Cav\text{-}1^{high}$ is 2.591 and $TSP1^{high}$ 2.268). All CAV^{high} patients were also $TSP1^{high}$ whilst not all $TSP1^{high}$ patients were also CAV^{high}. This suggests that TSP1 is a pre-requisite for Cav-1 expression. Finally TSP1 has an impact upon survival irrespective of Cav-1 expression, suggesting that TSP1 s also an independent prognostic biomarker.

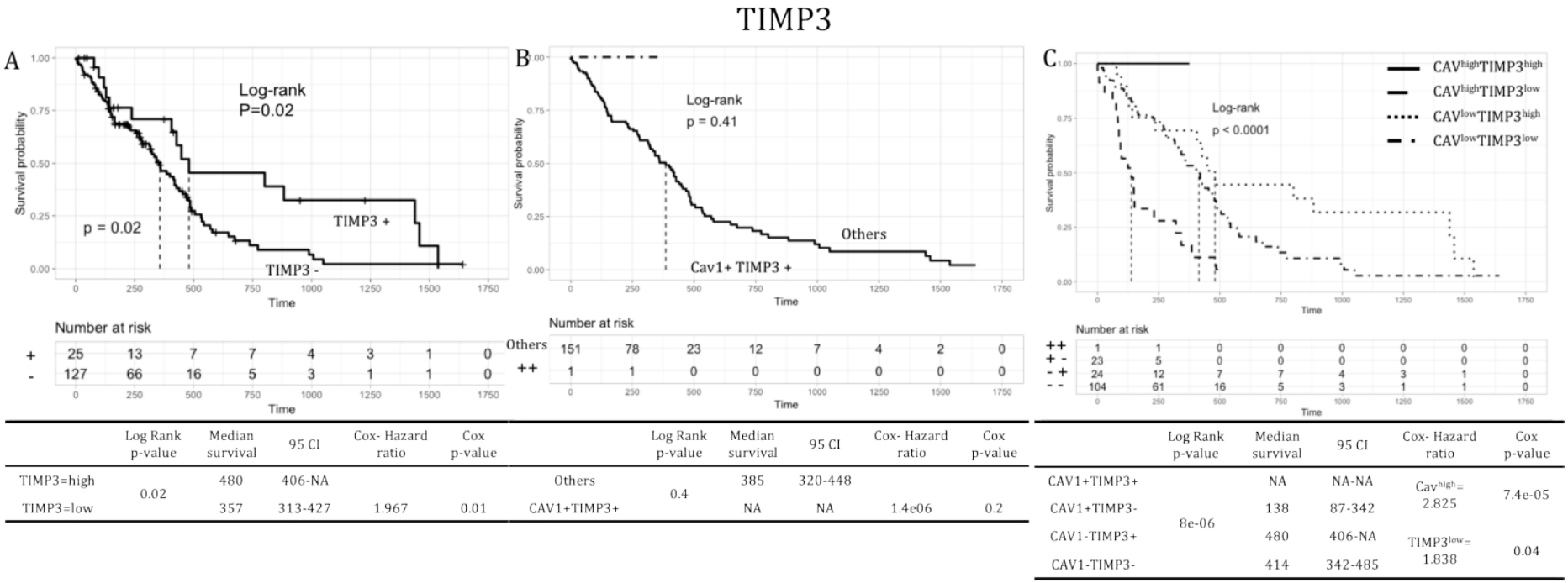

	Log Rank p-value	Median survival	95 CI	Cox- Hazard ratio	Cox p-value
TIMP3=high	0.02	480	406-NA		
TIMP3=low		357	313-427	1.967	0.01

	Log Rank p-value	Median survival	95 CI	Cox- Hazard ratio	Cox p-value
Others	0.4	385	320-448		
CAV1+TIMP3+		NA	NA	1.4e06	0.2

	Log Rank p-value	Median survival	95 CI	Cox- Hazard ratio	Cox p-value
CAV1+TIMP3+	8e-06	NA	NA-NA	Cav^{high}= 2.825	7.4e-05
CAV1+TIMP3-		138	87-342		
CAV1-TIMP3+		480	406-NA	$TIMP3^{low}$= 1.838	0.04
CAV1-TIMP3-		414	342-485		

Figure 6.34 Cav-1 and invasion inhibition 2. Overall survival curves of TIMP3 for GBM patients. A. Impact of a high and low expression on survival (Level 1). B. Survival curve for patients with high expression of both Cav-1 and TIMP3 was compared to the rest of the patients (Level 2). High or low expressions have been abbreviated to +/-. C. Comparison between the single combinations of a high and low expression of Cav-1 and the target gene (Level 3). Vertical lines connect median survival time. Tables show for each plot: Log Rank p-value for the evaluation of the curves statistical difference; median survival for each group, reported together with the confidence interval (CI); Cox hazard ratio for the referring group, coupled with its p-value. Plot and analysis were achieved through R project.

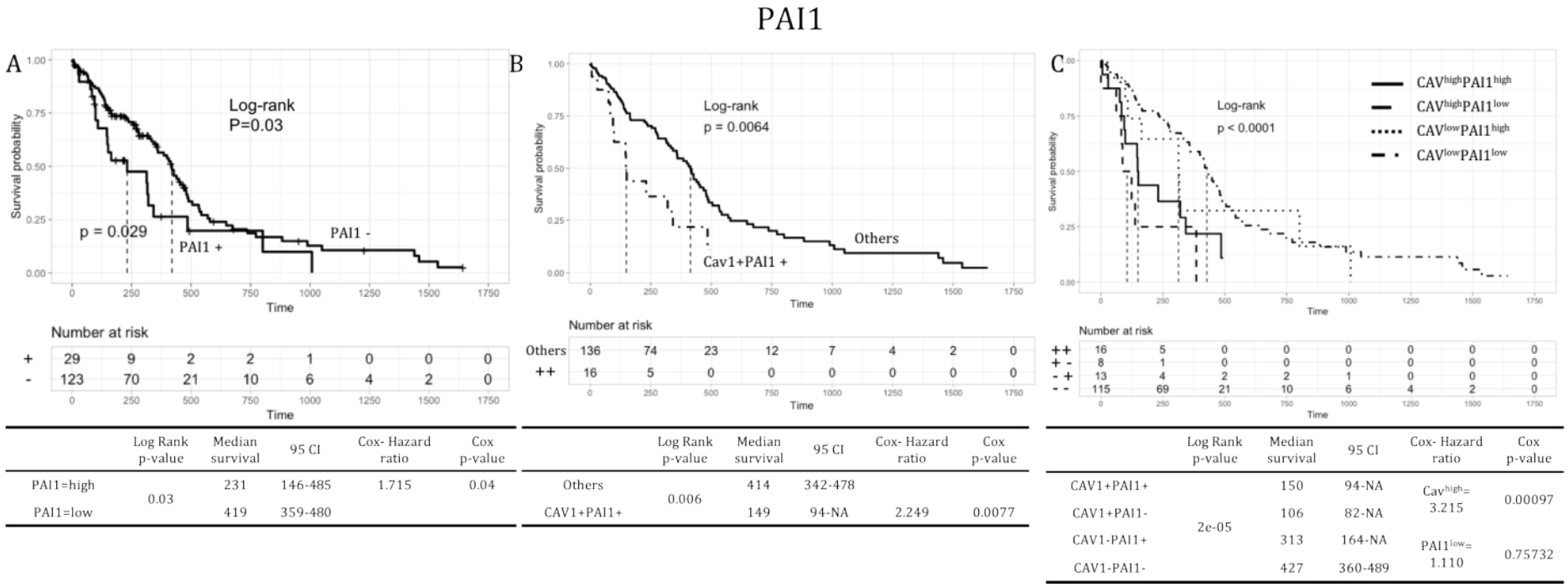

	Log Rank p-value	Median survival	95 CI	Cox- Hazard ratio	Cox p-value
PAI1=high	0.03	231	146-485	1.715	0.04
PAI1=low		419	359-480		

	Log Rank p-value	Median survival	95 CI	Cox- Hazard ratio	Cox p-value
Others	0.006	414	342-478		
CAV1+PAI1+		149	94-NA	2.249	0.0077

	Log Rank p-value	Median survival	95 CI	Cox- Hazard ratio	Cox p-value
CAV1+PAI1+	2e-05	150	94-NA	$Cav^{high=}$ 3.215	0.00097
CAV1+PAI1-		106	82-NA		
CAV1-PAI1+		313	164-NA	$PAI1^{low=}$ 1.110	0.75732
CAV1-PAI1-		427	360-489		

Figure 6.35 Cav-1 and invasion inhibition 3. Overall survival curves of PAI1 for GBM patients. A. Impact of a high and low expression on survival (Level 1). B. Survival curve for patients with high expression of both Cav-1 and PAI1 was compared to the rest of the patients (Level 2). High or low expressions have been abbreviated to +/-. C. Comparison between the single combinations of a high and low expression of Cav-1 and the target gene (Level 3). Vertical lines connect median survival time. Tables show for each plot: Log Rank p-value for the evaluation of the curves statistical difference; median survival for each group, reported together with the confidence interval (CI); Cox hazard ratio for the referring group, coupled with its p-value. Plot and analysis were achieved through R project.

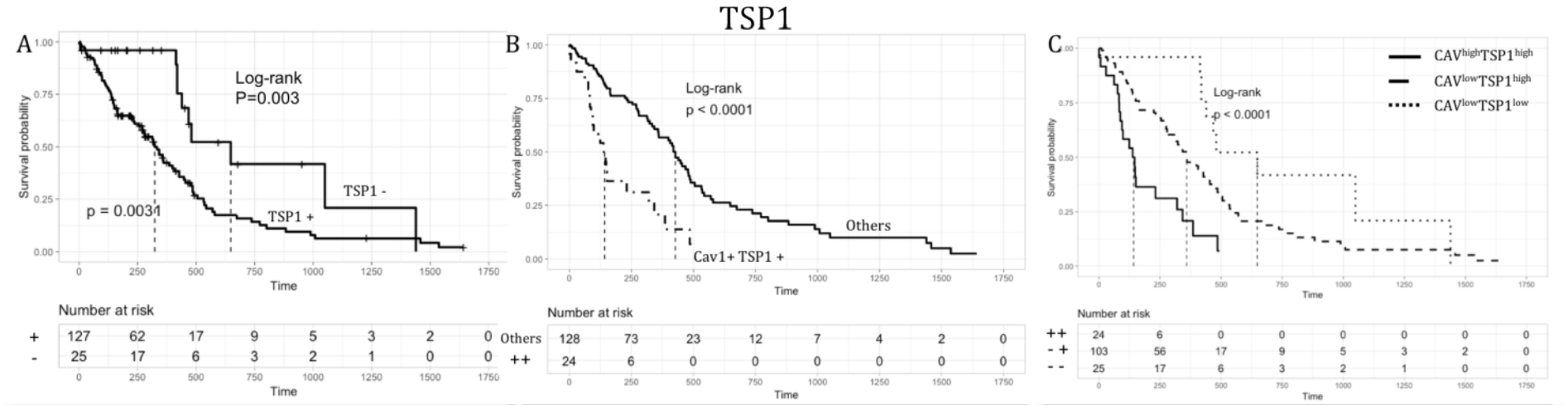

	Log Rank p-value	Median survival	95 CI	Cox- Hazard ratio	Cox p-value
TSP1=high	0.003	323	270-406	2.597	0.001
TSP1=low		648	439-NA		

	Log Rank p-value	Median survival	95 CI	Cox- Hazard ratio	Cox p-value
Others	1e-05	427	359-485		
CAV1+TSP1+		142	94-342	2.982	2.9e-05

	Log Rank p-value	Median survival	95 CI	Cox- Hazard ratio	Cox p-value
CAV1+TSP1+	5e-06	142	94-342	Cav^{low}= 2.591	0.00031
CAV1+TSP1-		-	-		
CAV1-TSP1+		359	313-478	$TSP1^{low}$= 2.268	0.01615
CAV1-TSP1-		648	439-NA		

Figure 6.36 Cav-1 and invasion inhibition 4. Overall survival curves of TSP1 for GBM patients. A. Impact of a high and low expression on survival (Level 1). B. Survival curve for patients with high expression of both Cav-1 and TSP1 was compared to the rest of the patients (Level 2). High or low expressions have been abbreviated to +/-. C. Comparison between the single combinations of a high and low expression of Cav-1 and the target gene (Level 3). Vertical lines connect median survival time. Tables show for each plot: Log Rank p-value for the evaluation of the curves statistical difference; median survival for each group, reported together with the confidence interval (CI); Cox hazard ratio for the referring group, coupled with its p-value. Plot and analysis were achieved through R project.

6.4.4 Level 1 analysis

Refer to Figure 6.7.

From the survival analysis of the studied biomarkers, Cav-1 is one of the strongest prognostic indicators. Only TIMP1 had a higher HR when analysed at Level 1 with TIMP1^{high} having a median survival of 342 days, while Cav-1^{high} median survival was 142 days.

The analysis at the single-molecule level (Level 1) revealed that some of them are independent prognostic biomarkers. Specifically, as single biomarkers UPAR, PVRL4, TIMP1, TSP1, MT1MMP, MMP2, MMP9, CTSB, CTSD, CD44, ITGA5, ITGB5, PAI1, UPA, MMP10, MMP1 and CTSL were all independent negative prognostic biomarkers, i.e. predictors of poor outcome, while ECAD, CTSH and TIMP3 were all independent positive prognostic biomarkers, i.e. predictors of improved outcome.

6.4.5 Level 2 and 3 analysis

Refer to Figure 6.7.

Level 2 and Level 3 analysis seek to explore those biomarkers combined with Cav-1 in predicting poor outcome, and if such molecules have a positive relationship with Cav-1.

Level 2 analysis indicated if the expression of high levels of Cav-1 together with the selected markers correlates with differences in survival in comparison with the rest of the population. This could indicate if specific genes are correlated with Cav-1 expression and may act in synergy with it (i.e. TIMP1 and PVRL4).

Eight genes displayed coexpression pattern whereby Cav^{high} only occurs in situations where the respective paired gene itself shows high expression, i.e. low expression of those genes was never co-present with Cav^{high}. These genes were CD44, ITGA3, VIM, CTSB, CTSL, MT1MMP, TIMP1 and TSP1. This data strongly suggests that these eight genes are all upstream of Cav-1 with Cav-1 serving as a downstream effector molecule.

In this context, Cav-1 may serve as a critical organization centre for multiple genes that make the biology of GBM more aggressive with respect to tumour invasion and spread, ultimately impacting upon patient survival. Consistent with this, is that none of the above genes appears to be interacting with Cav-1 to bring synergy in the survival data.

Several genes present a shorter median survival when combined with CAV^{high} than their high expression alone or CAV^{high} alone, although not statistically significant. They are ITGAV, ITGB5, ECAD, CTSK, MMP2, MMP9. MMP2 and MMP9 displayed oncogene functions and therefore may be proposed to be Cav-1 synergistic partners. It is, however, important to remember that the differences in the median survival are not significant. A study with a larger cohort of patients could be helpful in understanding if the connection is real.

Both ECAD and ITGAV appear to be tumour suppressors when Cav-1 expression is low, while CTSK and ITGB5 have no significant impact in the Level 3 analysis.

6.4.6 Biological implications of the survival analysis

Figure 6.37 represents a hypothetical schematic derived from the current TCGA analysis that shows a putative relationship between Cav-1 and different gene sets studied.

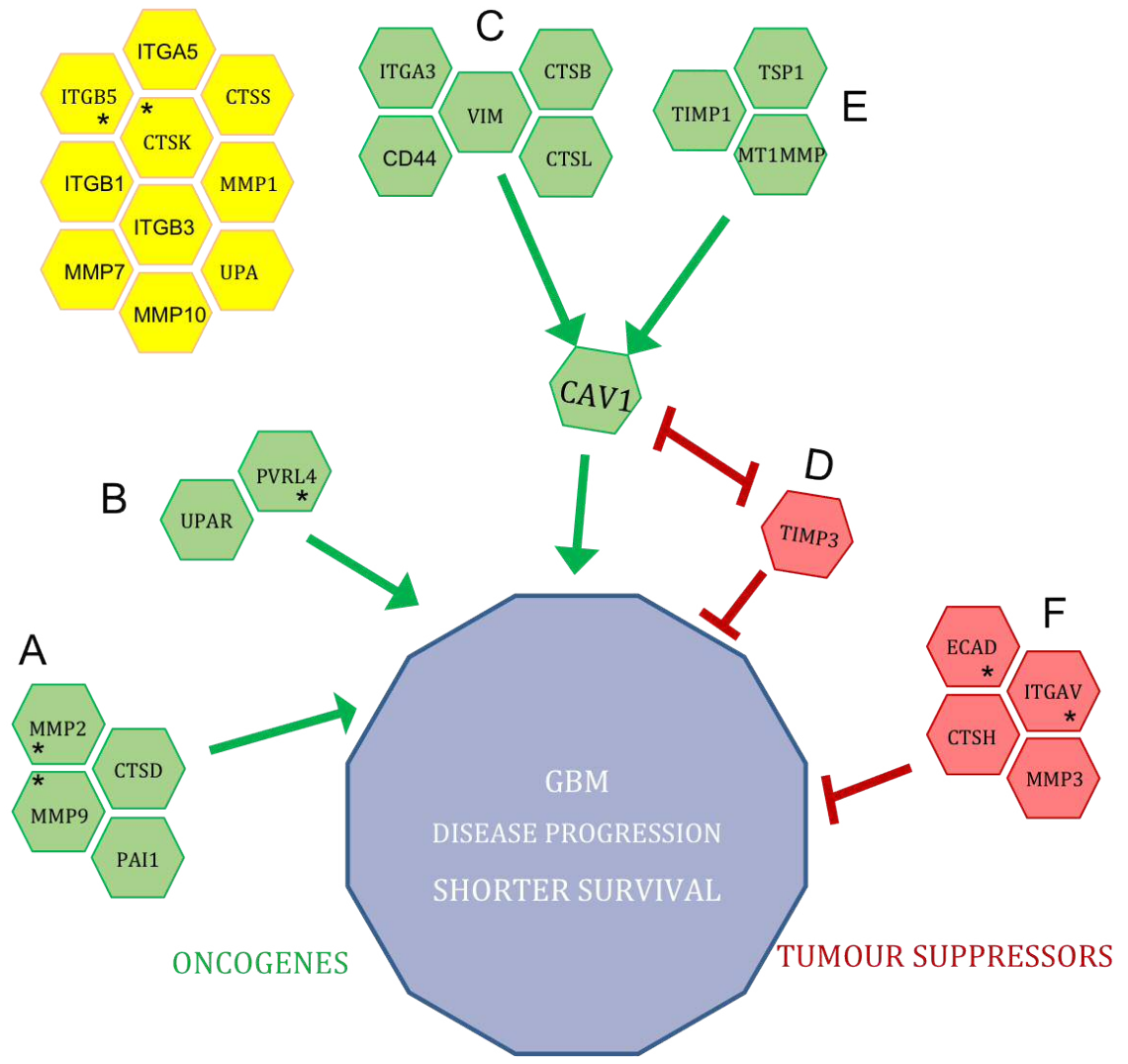

Figure 6.37 Conclusive summary of the chapter findings. A. Oncogenes minimised by Cav-1. B. Oncogene independently driving GBM progression. C. Oncogene whose expression is driven by Cav-1. D. Oncogenes able to drive disease progression only when co-expressed with Cav-1. E. Oncogenes expressed by patients with high levels of Cav-1, whose tumour promoter activity is enhanced by Cav-1 expression. Tumour suppressor TIMP1 and Cav-1 are mutually exclusive and able to inhibit each other. G. Tumour suppressors over-ridden by Cav-1. Markers not significant and not correlated with Cav-1 are reported in yellow. Green arrows indicate positive correlation. Red diamonds indicate negative correlation. Different arrow sizes indicate high or low correlation. Asterisks indicate a possible synergistic cooperation with Cav-1.

From the survival analysis, it can be concluded that (Refer to Figure 6.37):

[A]. Genes comprising CTSD, MMP2, MMP9 and PAI1 may serve as oncogenes. They drive disease progression, although not as effectively as Cav-1

[B]. The receptor for UPA, UPAR, and the cell-cell adhesion marker PVRL4 are powerful and independent negative prognostic factor. PVRL4 may act also in synergy with Cav-1 in driving disease progression.

[C]. Genes represented in group C (ITGA3, CD44, VIM, CTSB and CTSL) only have an adverse impact on survival when co-expressed with Cav-1 in a double-high phenotype. Cav-1 is not highly expressed when these genes are low or absent. Collectively, this data shows that Cav-1 is a critical downstream effector molecule for the genes present in group C.

[D]. Genes represented in group D (MT1MMP, TIMP1 and TSP1) are similar to those in group C, in that is no high expression of Cav-1 when these genes are low/absent. These genes are also upstream of Cav-1. The survival analysis shows that these three genes adversely impact overall survival without the presence of Cav-1, i.e. independent biomarker of poor outcome. Although it must be stressed that the outcome is much worse when Cav-1 is co-expressed. Collectively, these data suggest that these three genes drive aggressiveness mainly through Cav-1, but may also activate other oncogene pathways independently of Cav-1.

[E]. TIMP3 is a tumour suppressor. Cav-1 and TIMP3 are mutually exclusive.

[F]. ECAD, ITGAV, CTSH and MMP3 are tumour suppressors that Cav-1 is able to override and overcome the tumour suppressor actions.

6.4.6.1 Groups A-B (Figure 6.37)

In vitro, *in vivo* and clinical studies, UPAR and MMP9 (Veeravalli & Rao, 2012), CTSD (Mallawaaratchy et al., 2017) and MMP2 (Ramachandran, Sørensen, Aaberg-Jessen, Hermansen, & Kristensen, 2017) have all been recognised as negative prognostic markers for GBM, confirming the results of the analysis in this current chapter. UPAR and CTSB have also been positively related to glioma-initiating cells and self-renewal (Gopinath et al., 2013).

From the current TCGA analysis, both PAI1 and UPAR serve as negative prognostic markers, whereas UPA does not. It is surprising that UPA does not serve as a negative prognostic marker in this dataset. UPA is a serine protease able to activate plasminogen in plasmin, which can then degrade the extracellular matrix (Irigoyen, Muñoz-Cánoves, Montero, Koziczak, & Nagamine, 1999). Its catalytic-independent binding to UPAR triggers an intracellular pathway that leads to increased migration, growth and survival (Andreasen, Kjoller, Christensen, & Duffy, 1997). As PAI1 is the main inhibitor of UPA, it is similarly surprising that PAI1 in this analysis serves as a negative prognostic biomarker. PAI1 is an inhibitor of UPA catalytic activity, preventing plasmin activation while still allowing UPA to bind to UPAR. One possible reason for UPA not serving as a negative prognostic marker could be that the UPAR-UPA system can also be activated by other molecules, such as vitronectin in the extracellular space and integrins (Blasi & Carmeliet, 2002). It is not clear though if the presence of UPA is still required for this activation mechanism.

Among the reported integrins interacting with UPAR, is the product of ITGA3 and ITGB1, Integrin $\alpha 3\beta 1$ (Supurna Ghosh et al., 2006). Indeed, UPAR is mostly localized with clustered- Integrin $\alpha 3\beta 1$, in caveolae (Parat & Riggins, 2012). Integrin $\alpha 3$ has also been found overexpressed in glioma stem-like cells in vitro and acts as a promoter of invasion (Nakada et al., 2013). This is consistent with ITGA3 being a negative prognostic marker. Moreover, Cav-1 has been linked to the Integrin $\beta 1$ subunit for the regulation of signalling and endocytosis (Hwang et al., 2016; F. Shi & Sottile, 2008).

Cav-1 has also been reported to activate the UPAR-mediated activation of other Integrins, like Integrin $\alpha 5\beta 1$ (Hwang et al., 2016), which is the integrin studied in relation to Cav-1 in GBM cells by Martin et al. (Martin et al., 2009). The *in vitro* interaction of Cav-1 and Integrin $\alpha 5\beta 1$ is reported by these authors to prevent cell invasion and migration *in vitro*. Our clinical analysis does not confirm these studies in that ITGA5 and ITGB1 have no significant impact on GBM.

PVRL4 has been described elsewhere as being highly expressed in lung, breast, colon, and ovarian tumours (Noyce & Richardson, 2012), but it has not been demonstrated in brain tumours. According to our analysis, PVRL4 is a powerful negative prognostic marker in GBM, that acts in synergy with Cav-1

expression. Nectin-4 is the product of the PVRL4 gene and is a cell-cell adhesion molecule, but also the receptor for the measles virus, which is being used in clinical trials against several types of cancer, including GBM. Moreover, PVRL4 is not expressed in the normal brain. Our data might suggest therefore that an in-situ therapy with a modified measles virus could be successful in targeting Cav-1 positive GBM cells.

Of note, in early pilot proteomic studies with lentiviral-mediated Cav-1 KD of GBM cell lines, we did find Nectin-4 to be positively correlated with Cav-1 in UP007 and UP029.

6.4.6.2 Group C and D (Figure 6.37)

Of note, an extraordinary finding is that it is only when all eight genes in Groups C and D display high expression, will there be a high expression of Cav-1 and decreased survival. This may involve these markers clustering together and promoting Cav-1 expression. Cav-1 in return would allow the cross-activation of the markers and allow disease progression.

CD44, together with Vimentin, is a molecular marker of the mesenchymal phenotype, which is the most aggressive GBM subtype (Phillips et al., 2006). Our analysis identified them as both negative prognostic markers, able to influence disease progression only when co-expressed with high levels of Cav-1.

CTSD and CTSB are shuttled from the endoplasmic reticulum to the caveolae where CTSD activates CTSB (Aghdassi et al., 2018) which in turn activates UPA (Kobayashi et al., 1993), MMPs and induces angiogenesis (Yanamandra et al., 2004). In Inflammatory Breast Cancer, Cav-1 and CTSB co-expression has been reported, with Cav-1 unlocking CTSB proteolytic properties (Nouh et al., 2011). Our analysis in GBM shows CTSD to be an independent prognostic factor, and CTSB being able to promote disease progression only when co-expressed with Cav-1.

CTSL has previously been reported as an independent negative prognostic marker promoting hepatocellular carcinoma aggressiveness (Ruan et al., 2014). Others have reported that CTSL expression is increased in GBM cell lines after

induction by VEGF (Keerthivasan, Keerthivasan, Mittal, & Chauhan, 2007). But the role of CTSL in GBM and its relationship with Cav-1 has not been previously described. Here we suggest that CTSL is able to promote tumour aggressiveness when co-expressed with Cav-1.

Parat and Riggins published in 2012 a comprehensive review about Cav-1 in GBM (Parat & Riggins, 2012). This includes the description of molecules that cluster within the caveolae and their interactions. According to their work, Cav-1 interacts directly and stabilizes not only UPAR but also MT1-MMP, which activates in turn other MMPs. MMPs can also be activated by Plasmin, whose activation from Plasminogen is catalysed by UPA. In our analysis, MT1MMP appears to serve as an oncogene whose tumour promoter effect is enhanced by Cav-1. This is consistent with the necessity of MT1MMP to be within the caveolae, in contact with Cav-1, in order to be activated by UPA and to activate the MMPs.

MT1MMP has also the ability to cleave CD44, thus increasing cell motility. This shedding of CD44 allows to disconnect with degraded hyaluronic acid fibres and connect with new ones and is crucial for the CD44-dependent tumour migration process (Ulasov, Yi, Guo, Sarvaiya, & Cobbs, 2014).

TSP1 expression and secretion are highly increased in GBM when compared to normal tissue (Naganuma et al., 2004). This protein is a known inhibitor of tumour growth and angiogenesis. However, it has also been reported that tumours are able to acquire a resistance to high levels of TSP1 (Filleur et al., 2001). In pulmonary hypertension, it has also been reported that TSP1 is able to induce the expression of Cav-1 (Rogers, Ghimire, Calzada, & Isenberg, 2017). This is consistent with our analysis, which shows Cav-1 is only expressed in $TSP1^{high}$ patients meaning TSP1 is upstream and is able to drive the high expression of Cav-1. TSP1 could be then able to shorten patient survival, both in a Cav-mediated and -independent way.

TIMP1 has already been described in the literature associated with a shortened survival in GBM (Aaberg-Jessen et al., 2009). According to our analysis, and consistent with what was reported, TIMP1 is a strong marker of aggressiveness, with 89% of the patients expressing high levels of the biomarker (Figure 6.33). The analysis also shows that co-expression of TIMP1 and Cav-1 further

shortens survival and that TIMP1 is pre-required for the expression of Cav-1. TIMP1, however, has been described as a bland inhibitor of MMP9 and that its overexpression in mice determines a reduction in cancer occurrence. At the same time, we also know that TIMP1 is not as an efficient inhibitor as the other TIMP family members, i.e. it is unable to inhibit MT1MMP or MMP2 (Sternlicht & Werb, 2009). Moreover, in patients samples, a positive correlation between MMP2 and TIMP1 expression has been reported, and the combination of high levels of MMP2 together with TIMP1 had a stronger prognostic value than MMP2 alone (Ramachandran et al., 2017). Further studies are needed in order to explain the controversial reports.

6.4.6.3 Group E (Figure 6.37F)

Unlike TIMP1, TIMP3 is a strong inhibitor of MMP9, but also of MT1MMP and the ADAMs/ADAMTs family (Sternlicht & Werb, 2009). TIMP3 is also able to bind directly to heparan-sulfate proteoglycans, thus concentrating its action on basement membranes (Langton, Barker, & McKie, 1998). TIMP3 activity has also been correlated in GBM with respect to the activity of MGMT (Saraiva-Esperón, Ruibal, & Herranz, 2014). According to our analysis, TIMP3 serves as a tumour suppressor with only 4% of the patients (1/24) expressing both high levels of Cav-1 and TIMP3. To date, no studies have been conducted to investigate whether Cav-1 and TIMP3 functionally interact.

6.4.6.4 Group F (Figure 6.37G)

The most important epithelial-differentiation marker, E-Cadherin, is rarely expressed in glioma (Iwadate, 2016). Consistently, our analysis concluded that ECAD is a tumour suppressor, whose activity appears to be over-ridden by Cav-1 oncogene activity. Collectively the Cav-1 data, when considered alongside with ECAD and VIM, suggest that Cav-1 may be important for the epithelial to mesenchymal transition process.

Integrin αV has been reported in GBM to help tumour cells to escape senescence (Franovic et al., 2015). According to our analysis, when Cav-1 is not expressed ITGAV acts as a tumour suppressor, possibly through the binding of

vitronectin and the anchorage to the basal membranes. However, this data interestingly shows that Cav-1 switches ITGAV from tumour suppressor to oncogene when co-expressed. This could be because Cav-1 is a strong driver of aggressiveness, overriding ITGAV tumour suppressor activity. Alternatively and consistently with published literature, when Cav-1 is expressed, ITGAV clusters in the caveolae and helps tumour cells to escape senescence (Franovic et al., 2015). Further studies would be needed to confirm that.

In pancreatic cancer, CTSH is reported to be a tumour promoter (Gocheva, Chen, Peters, Reinheckel, & Joyce, 2010). However, there are no studies about its role in GBM, with the exception of an *in vitro* study from 1996, where it has been reported that an antibody anti-CTSH was inhibiting invasion through Matrigel in three cell lines (Sivaparvathi, Sawaya, Gokaslan, Chintala, & Rao, 1996). In our analysis, CTSH is a statistically significant tumour suppressor both alone and in combination with Cav-1. Further studies will be needed to identify the actual function of CTSH in GBM and its connection to Cav-1.

A protective role of MMP3 has been reported in squamous carcinomas, in terms of papillomas insurgence and tumour growth (Shay, Lynch, Fingleton, & Moffitt, 2015). Even if not reported in GBM, this finding is in line with our analysis. In the TCGA dataset indeed MMP3 displays a tumour suppressor activity when Cav-1 is not expressed.

6.5 CONCLUSIONS

- In this chapter, we interrogated the TCGA database to understand if Cav-1 has an impact on the survival of patient suffering from GBM, and whether Cav-1 is related to any other biomarkers of tumour aggressiveness.
- Significantly, in a population of 540 patients we found that a high expression of Cav-1 is related to a shorter survival, with a decrease from 14.2 to 4.7 months (Figure 6.2).
- Certain subgroups of patients were differentially affected. For example:
    - median survival in females displaying high Cav-1 levels was only 3 months, whereas males displaying high Cav-1 had a median survival of 10.5 months; median survival for both male and females expressing low Cav-1 were not different from each other, ca. 14 months (Figure 6.3B).
    - for 87 patients we had information on GBM molecular subtypes. Here we found high expression of Cav-1 appears to be more common in mesenchymal GBMs, a GBM subtype recognised to be one of the most aggressive forms (Figure 6.4) with a 7.3 months median survival for Cav-1^{high} versus 17.6 months for Cav-1^{low} (Figure 6.6). In the proneural subgroup of patients the expression of high Cav-1 appeared to be associated with better prognosis. This may be in line with the theory that Cav-1 can have different roles in cancer progression.
    - Unfortunately, the TCGA dataset accessed via R project does not allow to discriminate between different subtypes, so it was not possible to verify if the markers selected were differentially related to Cav-1 and survival in specific molecular subtypes. This could be implemented in the future.
- We then investigated whether Cav-1 expression is related to other aggressiveness markers (Table 6.1). We found that a high expression of Cav-1 is always associates with a high expression of certain markers of adhesion (CD44, ITGA3), certain markers of invasion (Vimentin,

Cathepsin B, Cathepsin L, MT1MMP) but also recognized inhibitors of invasion (TIMP1, TSP1) (Figure 6.37 C and D).

- While CD44, ITAG3, VIM, CTSB and CTSL were able to serve as oncogenes only when Cav-1 was also highly co-expressed, TSP1, TIMP1 and MT1MMP displayed oncogenic functions independently but also in synergy with Cav-1.
- Some other markers, like UPAR, PVRL4, CTSD, MMP2, MMP9, PAI1 predict poor survival independently of Cav-1 (Figure 6.37A and B).
- We found the effect of some genes (ECAD, ITGAV, MMP3, CTSH) to act as tumour suppressors could only be observed when Cav-1 is not highly expressed. When Cav-1 is highly expressed the suppressor actions of these genes are no longer evident (ECAD, MMP3, CTSH) or indeed there appears to be a reversal of actions, with the molecule displaying oncogenic properties (ITGAV).
- TIMP3 serves as a tumour suppressor mutually exclusive of Cav-1 (Figure 6.37E).
- The TCGA results in this chapter implicate Cav-1 as a potentially important therapeutic target in GBM.

.

7 CHAPTER 7- SUMMARISING DISCUSSION

CHAPTER 7- SUMMARISING DISCUSSION

The overall aim of the thesis was to explore the role of Cav-1 in the cancer-stem like properties, i.e. aggressiveness, of GBM. Cav-1 is at the centre of the interaction between signals coming from the environment and their receptors, the consequent activation of intracellular pathways for the adaptation to the environment and the cell structure modification. For this reason, it could potentially be a major player in GBM aggressiveness (Parat & Riggins, 2012).

The functional work was undertaken using in vitro cell lines, while work exploring the role of Cav-1 as an independent prognostic marker driving poor survival in GBM was undertaken using The Cancer Genome Atlas (TCGA) database, a repository of clinical data linking genomic patient information to clinical outcome.

One of the major problems with the treatment of GBM is that cells can detach from the tumour bulk, as singles or small groups, and travel along the perivascular niche or the white matter tracts. These cells can reach other areas of the patients' brain and form new tumours. This capacity reflects the ability of the cells to display invasive and self-renewal properties. Further, the re-established tumours often become chemo and radio-resistant.

We initially tested two key properties that are related to tumour aggressiveness, clonogenicity and invasion.

Clonogenic assays (Chapter 3) showed a general trend with Cav-1 driving clonogenicity in a range of different models: cells bearing lipid-based shRNA knockdown of Cav-1, lentiviral-based shRNA knockdown of Cav-1 and CRISPR-mediated knockout of Cav-1; and different model platforms, i.e. 2D colony formation, 3D free floating sphere formation, 3D soft agar sphere formation.

The knockdown/knockout approaches partially showed that Cav-1 has a positive impact on in vitro GBM cell lines clonogenicity and enhanced their cell cycle progression.

In Chapter 4, we developed a custom ImageJ-based script - INSIDIA - for the analysis of 3D spheroid invasion. The script represents a novel tool for the cancer biology community, enabling customizable quantitative processing of a large number of images for the quantification of 3D invasion assays undertaken

in vitro. Using this tool, together with other approaches we found (Chapter 5) that in a number of different GBM cell lines Cav-1 is unequivocally a factor in driving the invasion of the GBM model cells from a preformed spheroid through the extracellular matrix. Given the unequivocal data for the invasion studies, we focused attention, in the later part of Chapter 5, upon the biological mechanisms in respect to this particular phenotypic trait.

From the *in vitro* studies, it appears that Cav-1 drives the expression of enzymes for the digestion of the matrix, i.e. Cathepsin B (CTSB), MMP1 and urokinase-type plasminogen activator (UPA) and also expression of receptors i.e. UPAR and CD44, as well as increases in AKT activation. The context of these findings to the literature was discussed in detail in Chapter 5.

A schematic showing how Cav-1 interactions with these components may give rise to altered function is shown in Figure 7.1.

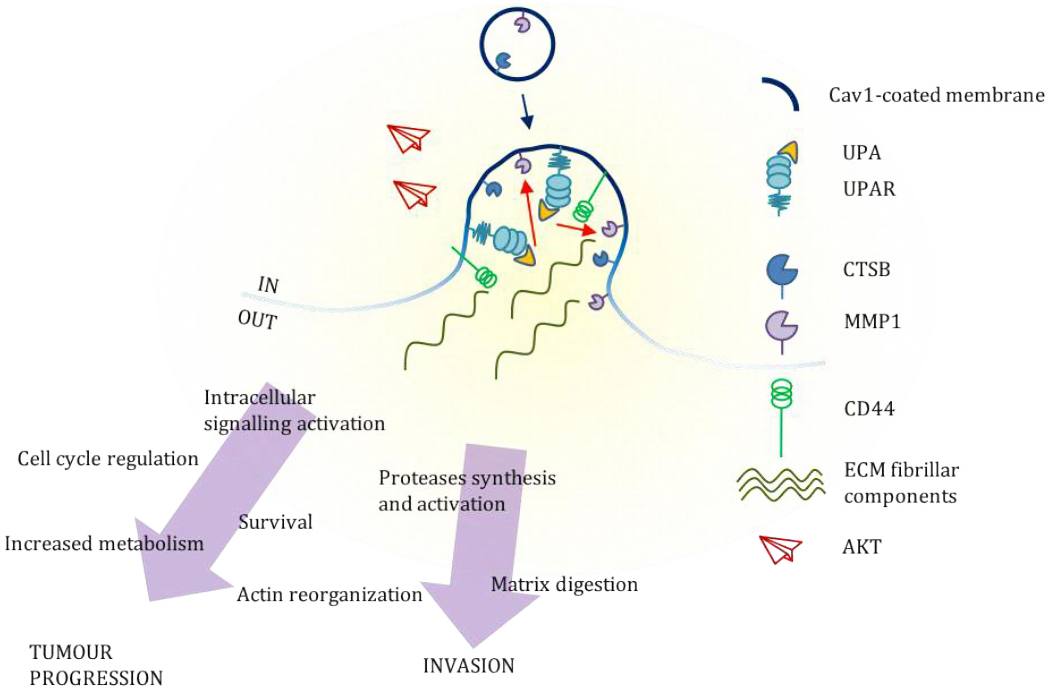

Figure 7.1 Markers putatively related to Cav-1-mediated increases in GBM invasion. Cav-1 regulates the synthesis or turnover of UPA and UPAR, which together activate the collagenase MMP1. Cav-1 promotes the synthesis of CTSB, which is exposed inside the caveolae and contributes to the degradation of the matrix. An increased CD44 allows the activation of intracellular pathways, among which AKT, promoting overall tumour progression.

Future in vitro studies to explore the mechanisms by which Cav-1 may be modulating the invasive phenotype should include:

- Selective and sequential manipulation of molecules in the putative pathway(s) using genetic or chemical knockouts of, for example potential downstream molecules, e.g. MMP1. This would help to address whether the relationship with Cav-1 is direct or indirect in nature.
- To support the above studies exploring if any physical interaction exists between Cav-1 with the respective molecules should be undertaken, using immunoprecipitation and immunofluorecence microscopy approaches.
- Expanding the molecular biology knockout studies to include a broader range of GBM cell lines, including those with a known molecular-subtype. Ideally studies in primary tumour cells or at least lower-passage cells should be undertaken. Where genetic manipulations my not be possible to accommodate this, the use of siRNA or chemical inhibitors (notably for molecules other than Cav-1) should be explored.
- The study of Cav-1 relationship with these molecules in an hypoxic environment, and in presence of endothelial cells for the study of neo-angiogenesis.
- The developing of a methodology that would allow the study of molecular expression in both core and invasive edges of a Matrigel-embedded spheroid, in an immunofluorescence context or using tools like micro-dissectors for the isolation of the spheroid components and then a transcriptomic (PCR) or phosphoproteomic (WB) analysis.
- The use of the 3D spheroid *in vitro* invasion assay for the study of the invasive behaviour of freshly resected GBM samples, in order to help the therapeutical decision.
- To develop INSIDIA: Increasing of the power of INSIDIA by, for instance, allowing the detection of single cells invasion. Adapt INSIDIA script for the study of MRI scans, where the M1 and M2 projection, whose juxtaposition is commonly used to determine the rough tumour invasion, could be used to better quantify and study the invasive behaviour of every

single tumour before the surgical resection. This would allow to gain precious time that could help the prognosis of the patients.

Reports about Cav-1 are conflicting, with different suggested roles attributed to the caveolae major component (Cerezo et al., 2009; Hnasko & Lisanti, 2003). Some reported that Cav-1 plays a tumour suppressor role, while others suggested Cav-1 to be an oncogene, according to cancer/tissue type and the patients (Senetta et al., 2013). As for GBM, the few studies published report Cav-1 as a tumour suppressor (Cosset et al., 2012; Martin et al., 2009; Quann et al., 2013; Shimato et al., 2013). An interesting hypothesis describes Cav-1 as playing a double role as a tumour suppressor in the early cancer stages and as an oncogene in the later aggressive and resistant stages (Quest et al., 2013).

Due to GBM inter and intra-heterogeneity, the identification of a single unequivocal therapeutic target represents a significant challenge (Xie et al 2014). Indeed, an effective therapeutic approach may have to involve targeting of multiple proteins simultaneously. Further, an understanding of the underlying molecular pathway physiology by patient subgroups will be critical.

In Chapter 6, we interrogated “The Cancer Genome Atlas” (TCGA) and found that Cav-1 is a strong independent prognostic biomarker indicative of poor survival in GBM patients, i.e. median survival 4.7 months for patients expressing high levels of Cav-1 vs. 14.2 months for the general GBM population. We also noted a potential gender bias in that median survival in females displaying high Cav-1 levels was only 3 months, whereas males displaying high Cav-1 have a median survival of 10.5 months. At the same time, high expression of Cav-1 appears to be more common in mesenchymal GBMs, a GBM subtype recognised to be one of the most aggressive forms.

In Chapter 5, we explored the correlation between Cav-1 KO and the expression of a range of transcripts and proteins, that are associated with the invasion process per se, that are adhesion molecules, proteases, and receptors. Encouraged by some of the findings we then further interrogated the TCGA database to see if the selected genes were correlated to Cav-1 expression and ultimately GBM survival in the clinical material (Figure 7.2).

The findings (Figure 7.2) were that markers comprising CD44, ITGA3, VIM, CTSB, CTSL, MT1MMP, TIMP1, TSP1 appeared to drive Cav-1 expression and

thus disease progression. While the high expression of CD44, ITAG3, VIM, CTSB and CTSL serves an oncogenic function only when Cav-1 was itself highly expressed. The molecules TSP1, TIMP1 and MT1MMP, when highly expressed, display oncogenic functions independently of Cav-1 but, when Cav-1 itself is also highly expressed, these molecular pairings display synergistic outcomes. We also found Cav-1 to override the tumour suppressor ability of ECAD, CTSH, MMP3 and ITGAV.

Further, TIMP3 appears to serve as a tumour suppressor mutually exclusive with Cav-1.

Finally, UPAR and PVRL4 appear to drive disease progression independently from Cav-1, while MMP2, CTSD and MMP9 are independent negative prognostic biomarkers whose oncogenic effect is relatively minor compared to that attributed to Cav-1.

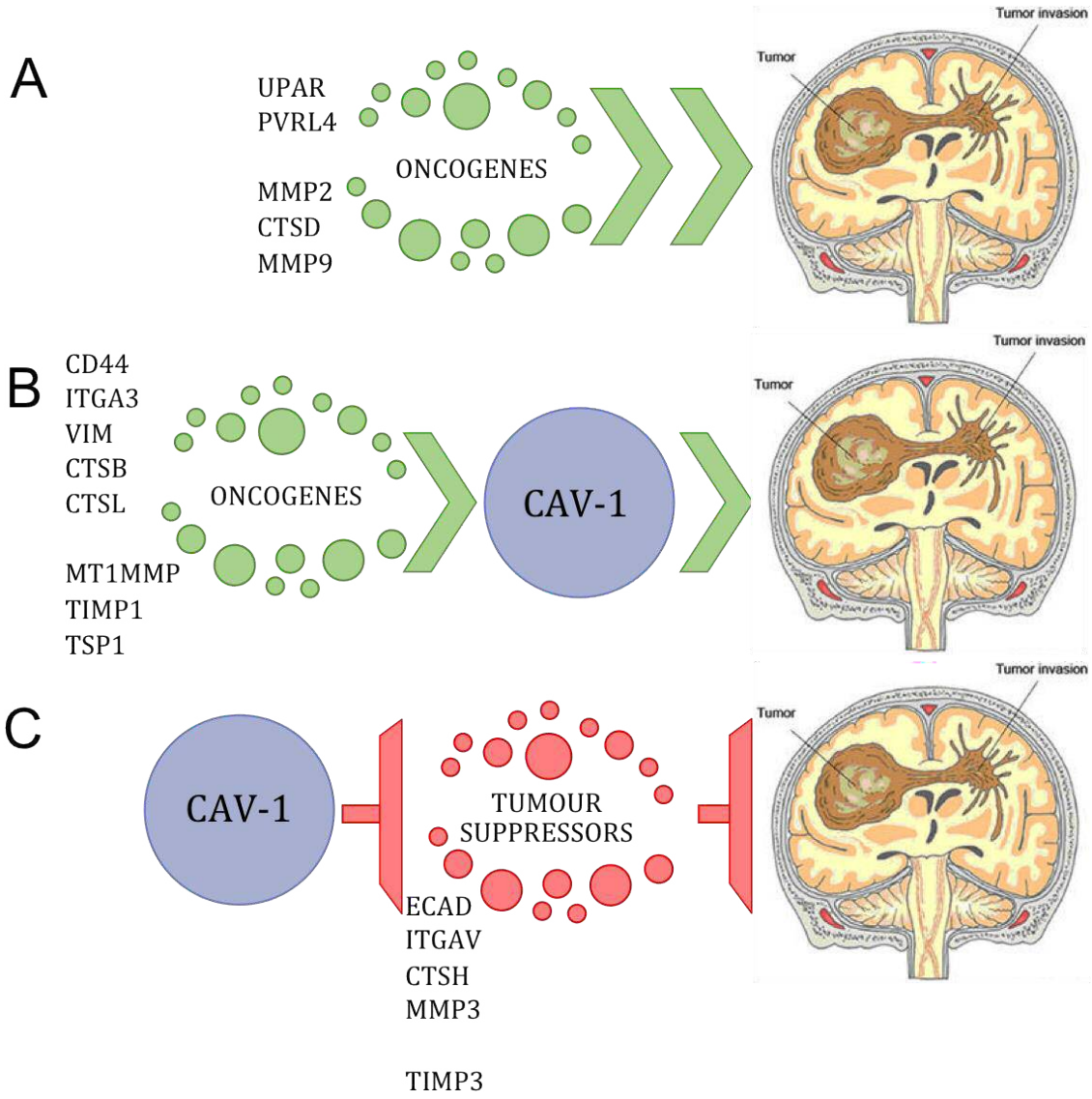

Figure 7.2 Summary of key findings in Chapter 6. A. Oncogenes independently driving disease progression. B Oncogenes driving disease progression and Cav-1 expression, which itself drives PVRL-4 and a shorter survival. C. Tumour suppressors inhibited by Cav-1 expression.

Future studies exploiting the TCGA database and/or the use of clinical material in biomarker investigations would comprise:

- Testing further the correlation between Cav-1 and the markers by combining multiple genes in the same survival analysis, e.g. high expression of three markers versus the rest of the population.
- Testing the role on Cav-1 in a dataset containing more information about the molecular subtype of each tumour, in order to verify if Cav-1 has an impact on mesenchymal and proneural subtypes.

- Expanding the study of molecules that may interact with Cav-1 to include ones involved in processes such as survival, self-renewal and hypoxic responses.

The most significant finding of this thesis is that from both the database analysis, and from the *in vitro* findings, Cav-1 is a molecule that strongly drives GBM aggressiveness through enhancing cell invasion. This includes the ability to establish contact and react to the extracellular environment, the production of matrix-degrading enzymes and the movement through the newly formed passages. Cav-1 appears to represent a good candidate for the targeting of invasion in high-grade gliomas.

APPENDIX

APPENDIX 1: BUFFERS AND SOLUTIONS

7.1.1 PBS (PHOSPATE BUFFER SALINE), 10mM

NaCl	8 g
KCl	0.2 g
Na_2HPO_4	1.44 g
KH_2PO_4	0.24 g
ddH_2O	to 2 L

pH 7.4

7.1.2 LYSIS BUFFER

5M NaCl	70 μL
Proteases inhibitor cocktail	10 μL
(Thermo Fisher Scientific cat. 1861281)	
0.5M EDTA	10 μL
(Thermo Fisher Scientific cat. 1861274)	
T-PER buffer	to 1 mL
(Thermo Fisher Scientific cat. 78510)	

7.1.3 ELCTROPHORESIS RUNNING BUFFER

0.25M TRIS	6.06 g
GLYCINE	28.8 g

pH TO 8.3

SDS	2 g
ddH_2O	to 2 L

7.1.4 BLOTTING BUFFER

TRIS	6.06 g
GLYCINE	28.8 g
SDS	2 g
METHANOL	400 mL
ddH_2O	to 2 L

7.1.5 WESTERNBLOT WASHING BUFFER

TRIS	2.42 g

pH TO 7.5

NaCl	11.688 g
Tween 20	2 mL
ddH_2O	to 2 L

7.1.6 BLOCKING BUFFER

Washing buffer	100 mL		
Powdered milk	5 g (5%)	or	1g (1%)

7.1.7 ANTIBODY DILUENT FOR WESTERN BLOT

Washing buffer	100 mL		
BSA	5 g (5%)	or	1g (1%)

Filter before use

7.1.8 PONCEAU

Glacial acetic acid	0.5 mL
Ponceau S	0.05 g
ddH_2O	to 50 mL

7.1.9 IMMUNOHISTOCHEMISTRY REAGENT DILUENT

0.6% BSA in Supersentisitive Wash Buffer 1x (BioGenex- cat. HK583-5KE)

7.1.10 IMMUNOHISTOCHEMISTRY SODIUM CITRATE BUFFER

10mM SODIUM CITRATE 1.47 g

pH 6

7.1.11 IMMUNOHISTOCHEMISTRY ACTIVE DAB SOLUTION

5 g/L DAB (diaminobenzidine dihydrochloride)	10 mL
Optimax 1x	90 mL
H_2O_2	8 drops

7.1.12 IMMUNOFLUORESCENCE BLOCKING BUFFER

3% BSA

0.3% TWEEN 20

PBS

7.1.13 IMMUNOFLUORESCENCE WASHING BUFFER

0.1% TWEEN 20

PBS

APPENDIX 2: SCRATCH ASSAY ANALYSIS PROCEDURE

- Open pictures with ImageJ FiJi;
- Image->type->8-bit;
- Process-> Sharpen
- Process -> find edges
- Process -> make binary
- Edit -> Invert
- Process ->Binary ->Options
    - in "Options" select:
        - interations: 6
        - Do: dilate
        - Select "preview"
- Select background picture with Magic wand
- Analyse -> Measure (Area to be selected in "Analyse -> set measurements")

After analysing all the areas (A) at t_0 and t_8, they have been compared, with A t_0 =100%, with the formula:

$$A\ t_8(\%) = 100 - ((A\ t_8/A\ t_0)*100)$$

The result is the percentage of area occupied by the migrated cells.

APPENDIX 3: IF SECONDARY ANTIBODIES

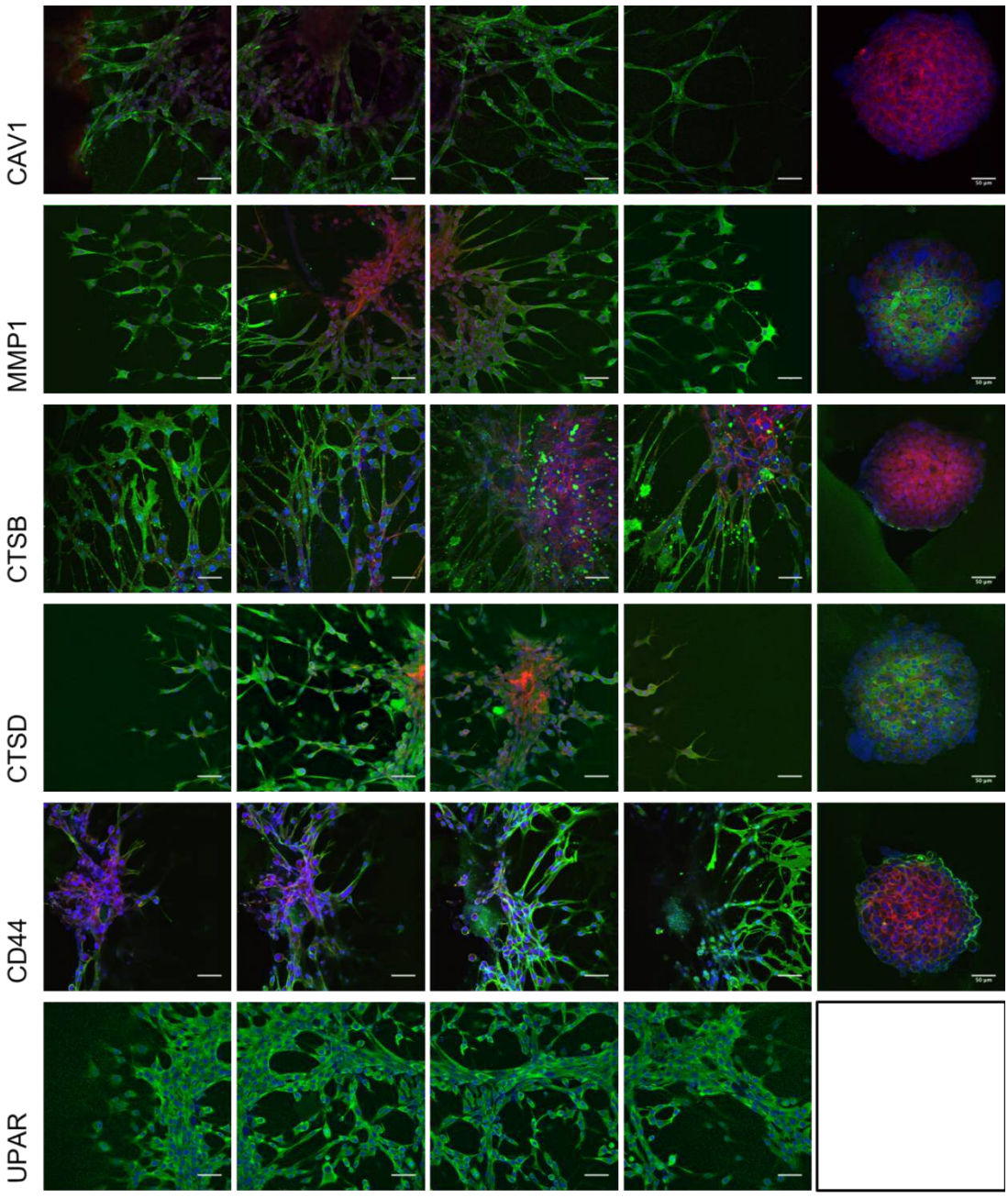

Figure 8.13D Immunofluorescence analysis of U87 CAV+(BB- first four images) and CAV- (KO- last image) expression of Cav-1, MMP1, CTSB, CTSD, CD44 and UPAR. Sphere was embedded in Matrigel and stained with Hoechst 33342 (blue: nuclei), Phalloidin-Alexa647 (Red: Cytoskeleton) and target genes (Green). Scale bar 50µm.

APPENDIX 4: PRIMERS VALIDATION

Table 8. 1 Primers pairs sequences for primers validation 1 (Refer to Figure 8.2 Primers validation 1- 25 pairs of primers were tested on U87 CAV+ (grey arrow) and MDA-231 (white arrow) isolated and retro-transcribed mRNA. PCR was conducted for 50 cycles at 56°C annealing temperature (sequences at Table 5.2).)

GENE	FORWARD SEQUENCE	REVERSE SEQUENCE	PREDICTED SIZE (Kb)	Ta (°C)
GAPDH	CTC TGC TCC TCC TGT TCG AC	GCG CCC AAT ACG ACC AAA TC	121	54.1
ITGAV	GGG AAG CAA AGG ACC GTC T	TCA CAT TTG AGG ACC TGC CC	511	54.3
ITGA3	CAA GGA TGA CTG TGA GCG GA	TTT TGG GGT GCA GGA TGA AG	497	52.1
ITGA5	CCT ATG AGG CTG AGC TTC GG	GGT GCA GTT GAG TCC CGT AA	548	54
MMP2	GCA TCT GGG GCT TTA AAC ATA CAA	TCA GGT ATT GCA CTG CCA ACT	406	52.1
MMP9	GCA ATG CTG ATG GGA AAC CC	GCA CAG TAG TGG CCG TAG AA	681	53.7
MT1-MMP	GGA AAA TGA GGA CGT GCA GC	ACT GGG TCT CAC TCT CCC AA	466	53.9
MMP7	CTA CAG TGG GAA CAG GCT CA	GTG AGC ATC TCC TCC GAG AC	486	53.1
MMP10	AGA TCC CAC TGG AAC CCT GA	ATC CTG GCA TTG GGG TCA AA	443	53.5
MMP1	ATG CAC AGC TTT CCT CCA CT	GTT GTC CCG ATG ATC TCC CC	513	53
MMP8	AGA AAG CCA GGA GGG GTA GA	TTC CCA CTT GGG GTT TCC TG	363	54.3
MMP3	CCT AGG TTT CCC TCC AAC CG	AGC CCA TTT GAA TGC CCT GTA	491	53.3
CATK	GAG GCT TCT CTT GGT GTC CA	CAT TGG TCA TGT AGC CCC CT	367	53.6
CATB	GTC TTC AGG CCT ATG GAG AGC	CAG ATC CGG TCA GAG ATG GC	462	54.5
CATL	CGT CTA CCC CGA ACT CTG C	CCT TCC TGG GCT TAC GGT TT	436	54.3
CATS	TCC ACT TTG TCC CCA AGA CC	GGA ACT CTC AGG GAA CTC ATC A	524	52.8
CATH	CAC CAG TGC ATG TGC TTT TGA	GCA TCA TCC GTC TCT TGT GG	538	52.5
CATD	CTC TAG TTC CCA AGG CGT CC	CCG GGA CAC TGA ACA GGT AG	496	54.2
UPA	GCG ACT CCA AAC GAA CTG TG	ATG CAC CAT GCA CTC TTG GA	373	53.3
UPAR	ATG CAC CAT GCA CTC TTG GA	CAC ACA ACC TCG GTA AGG CT	502	53.3
TIMP1	TTC TGC AAT TCC GAC CTC GT	CGG GAC TGG AAG CCC TTT T	452	53.2
TIMP3	GGA GGG CCG ATG AGG TAA TG	CGG ATC ACG ATG TCG GAG TT	543	53.6
PAI-1	ATA CTG AGT TCA CCA CGC CC	CAC TTG GCC CAT GAA AAG GAC	500	53.4
CD44	TTT ACA GCC TCA GCA GAG CA	CAT TGG GCA GGT CTG TGA CT	737	52.9
VIM	GTG GAC CAG CTA ACC AAC GA	CCA CTT CAC AGG TGA GGG AC	511	54
CDH1	GAA CTG CAA AGC ACC TGT GA	TCA GCG TGA CTT TGG TGG AA	463	52.3

Table 8. 2 Primers' pairs sequences for primers validation 3 (Refer to Figure 8.4)

GENE	FORWARD SEQUENCE	REVERSE SEQUENCE	PREDICTED SIZE (Kb)	Ta (°C)
ITGB1	CCG CGC GGA AAA GAT GA	ATG TCA TCT GGA GGG CAA CC	252	53
ITGB3	ATG ACG GGC AGT GTC ATG TT	TTA GGT TCA GCT TGG GCC TG	526	53
ITGB5	TAC TCC AGA CTG CAG CTT GTC	CCA GCA TGA GAT GGG GTC TT	504	53.3
MMP9	CAG TCC ACC CTT GTG CTC TTC	TGC CAC CCG AGT GTA ACC AT	102	55
UPAR1	GCT GGT GGA GAA AAG CTG TA	CCT TCT TCA CCT TCC TGG AT	291	50.5
CD44	GAC ACA TAT TGC TTC AAT GCT TCA GC	GAT GCC AAG ATG ATC AGC CAT TCT GGA AT	419	53.4
MMP2	CGC ATC TGG GGC TTT AAA CAT A	CTG TCT GGG GCA GTC CAA AG	503	51.9
ITGAV	GGG AAG CAA AGG ACC GTC TG	ATG GTA CAA TGG GGC ACA GG	671	54
MMP8	TCC CTG AAG ACG CTT CCA TTT	TTT TCC AGG TAG TCC TGA ACA GT	110	51.9

.

Table 8. 3 Primers' pairs remixed (Refer to Figure 8.5).

GENE	FORWARD SEQUENCE	REVERSE SEQUENCE	PREDICTED SIZE (Kb)	Ta (°C)
ITGAV-1	GGG AAG CAA AGG ACC GTC T	ATG GTA CAA TGG GGC ACA GG	671	54
ITGAV-2	GGG AAG CAA AGG ACC GTC TG	TCA CAT TTG AGG ACC TGC CC	511	54.3
MMP2-1	GCA TCT GGG GCT TTA AAC ATA CAA	CTG TCT GGG GCA GTC CAA AG	502	52.1
MMP2-2	CGC ATC TGG GGC TTT AAA CAT A	TCA GGT ATT GCA CTG CCA ACT	407	51.9
MMP8-1	AGA AAG CCA GGA GGG GTA GA	TTT TCC AGG TAG TCC TGA ACA GT	152	51.9
MMP8-2	TCC CTG AAG ACG CTT CCA TTT	TTC CCA CTT GGG GTT TCC TG	321	53.1

Table 8. 4 Alternative primers for CDH1 (Refer to Figure 8.3)

GENE	FORWARD SEQUENCE	REVERSE SEQUENCE	PREDICTED SIZE (Kb)	Ta (°C)
CDH1-alt 1	GAA CTG CAA AGC ACC TGT GA	TCA GCG TGA CTT TGG TGG AA	463	52.3
CDH1-alt 2	GGTGCTCTTCCAGGAACCTC	GGTGTATACAGCCTCCCACG	423	54.4
CDH1-alt 3	GGG GTC TGT CAT GGA AGG TG	CGA CGT TAG CCT CGT TCT CA	371	56.3

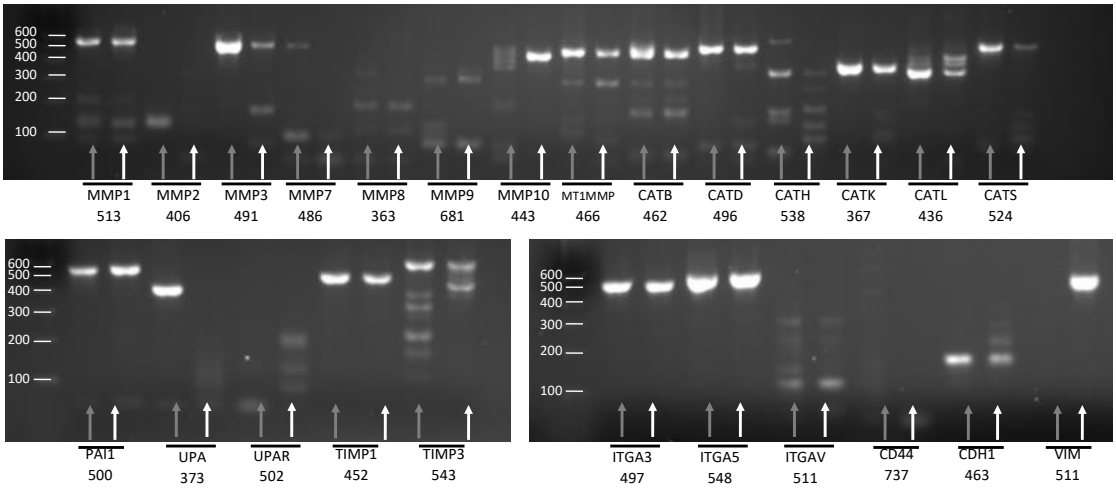

Figure 8.2 Primers validation 1- 25 pairs of primers were tested on U87 CAV+ (grey arrow) and MDA-231 (white arrow) isolated and retro-transcribed mRNA. PCR was conducted for 50 cycles at 56°C annealing temperature (sequences at Table 5.2).

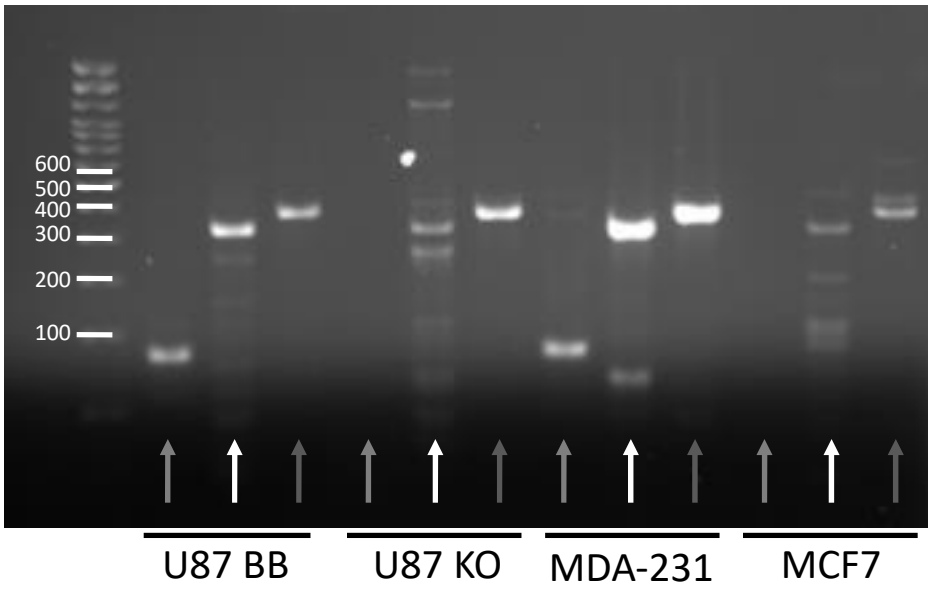

Figure 8.3 Primers validation 2- Three pairs of primers directed to ECAD transcript were tested on mRNA isolated and retro-transcribed from U87 CAV+, U87 CAV-, MDA-231 and MCF-7 cell lines. PCR was conducted at 56°C annealing temperature for 40 cycles. Light grey arrow: alt1; white arrow: alt2; dark grey arrow: alt3 (Table 5.4).

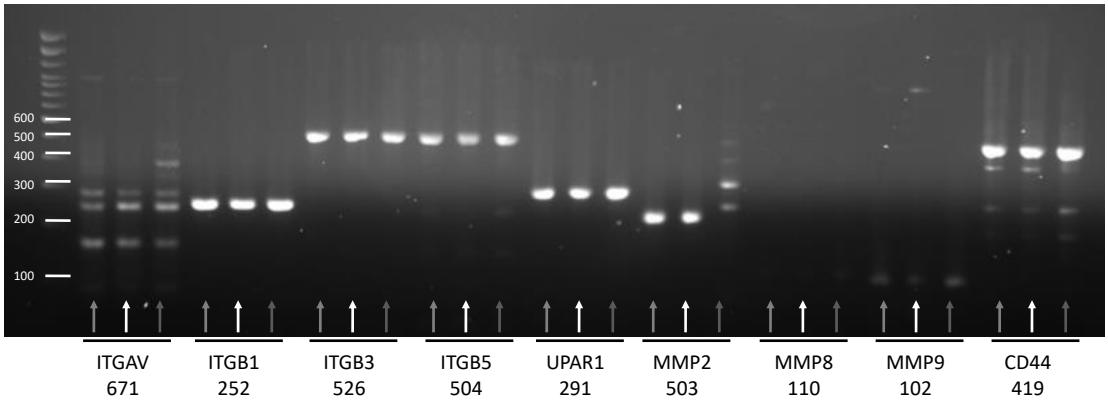

Figure 8.4 Primers validation 3- Nine pairs of primers were tested on U87 CAV+ (light grey arrow) U87 CAV- (KO- white arrow) and MDA-231 (dark grey arrow) isolated and retro-transcribed mRNA. PCR was conducted for 40 cycles at 56°C annealing temperature (Table 5.3).

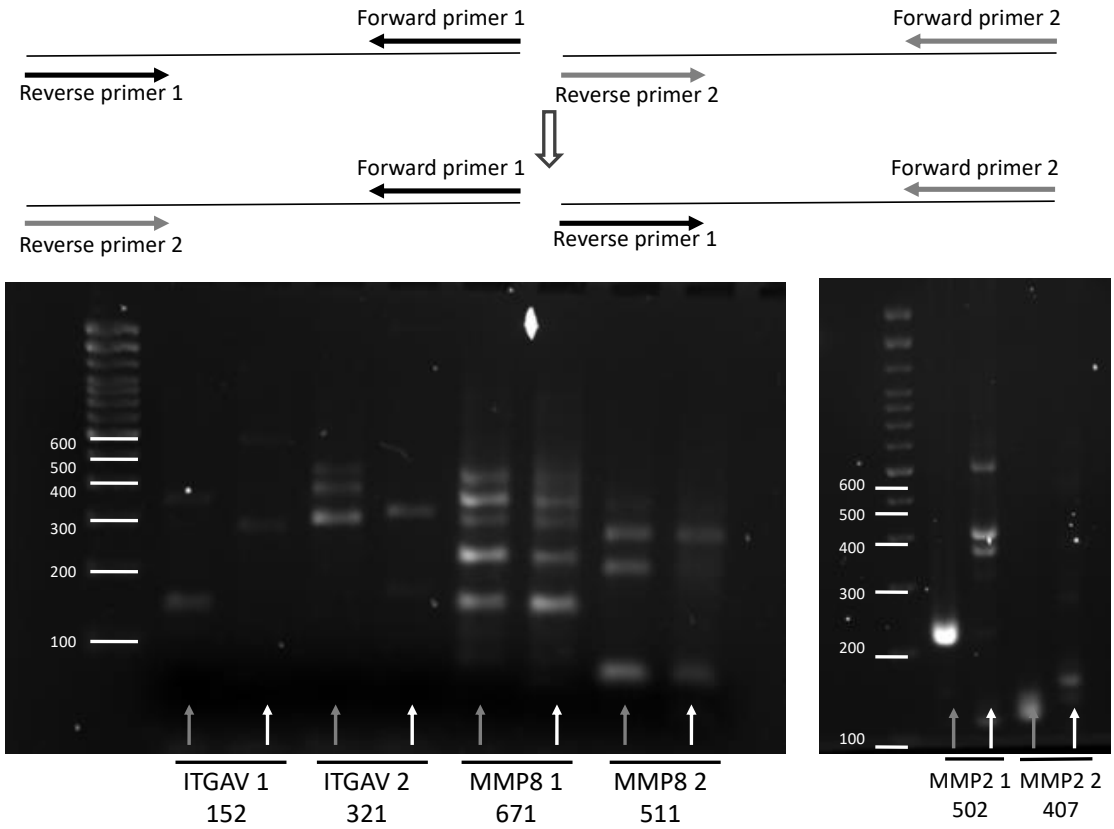

Figure 8.5 Primers validation 4- ITGAV, MMP" and MMP8 primers from validation 1 and 3 were mixed. PCR conditions: 40 cycles, T°a 56°C. Sequences on Table 5.4

APPENDIX 5: INSIDIA CODE

```
////////////////////////////////////////

////////////// FUNCTIONS/////////////////

////////////////////////////////////////

////note: do not modify this part

function closing(a) {

run("8-bit");

run("Auto Threshold", "method=Default white");

run("Dilate");

run("Dilate");

run("Erode");

run("Erode");

run("Dilate");

run("Dilate");

run("Erode");

run("Erode");

run("Fill Holes");

run("Erode");

}

function SSdialog(franginum,frangimin,frangimax){

label=newArray(3);

default=newArray(3);

label[0]="accept segmentation";

label[1]="manual threshold";

label[2]="Frangi filter";

default[0]=true;

default[1]=false;

default[2]=false;

Dialog.create("Spheroid segmentation");

Dialog.addCheckboxGroup(3,1,label,default);

Dialog.addNumber("number", franginum);

Dialog.addNumber("minimum", frangimin);

Dialog.addNumber("maximum", frangimax);

Dialog.show();

}

function printArray(a) {

print("");

for (i=0; i<a.length; i++)

print(a[i]);

}

function error(err) {

Dialog.create("Error");

Dialog.addMessage(err);
```

```
Dialog.show();
}
function largest(input,X,xc,yc){
run("Analyze Particles...", "size=0-Infinity circularity=0.00-1.00 show=Nothing display clear");
totalArea=0;
for(j=0; j<nResults; j++){
current=getResult("Area",j);
if(current>totalArea){
totalArea=current;
xc[X]=round(getResult("XM",j));
yc[X]=round(getResult("YM",j));
}
}
run("Analyze Particles...", "size="+totalArea+"-Infinity show=Masks display clear");
run("Dilate");
run("Clear Results", "");
run("Grays");
run("Select None");}
////////////////////////////////////////
////////////////////////////////////////
////////////////////////////////////////
////////////////////////////////////////
```

```
/////IMAGEJ SETTINGS//////////////////
/////////&ERRORS//////////////////////
////////////////////////////////////
////note: do not modify this part
run("Close All");
run("Set Measurements...", "area mean min centroid center perimeter fit shape feret's redirect=None decimal=3");
setForegroundColor(0, 0, 0);
run("Options...", "iterations=1 count=1 black");
roiManager("reset");
getDateAndTime(year, month, dayOfWeek, dayOfMonth, hour, minute, second, msec);
single="Please select a single option";
instr="Please follow the instructions to prepare your folders";
////////////////////////////////////////
////////////////////////////////////////
//////////////////////////////////
//////MENU 1 CHOOSE DIR///////////
/////MENU 2 SS Y/N/////////////////
//////////////////////////////////
////note: do not modify this part
```

```
maindir = getDirectory("Choose main folder");
do{
mode=newArray(2);
Dialog.create("Are your spheroids segmented?");
Dialog.addCheckbox("Yes, proceed to density map & density profile",false);
Dialog.addCheckbox("No, I want to do spheroid segmentation",true);
Dialog.show();
mode[0]=Dialog.getCheckbox();
mode[1]=Dialog.getCheckbox();
mainlist = getFileList(maindir);
nfolder=0;/// number of folder in the mainfolder
for (i=0; i<mainlist.length; i++) {
if (endsWith(mainlist[i], "/")){
nfolder=nfolder+1;
}
else
mainlist[i] =""; ///removes image files from list
}
numbdir=0;
for(G=0; G<nfolder;G++){
dir = maindir+mainlist[G];
list = getFileList(dir);
c=list.length;
tof=tof+c;
for (i=0; i<c; i++){
if (File.isDirectory(dir+list[i])==true){
numbdir=numbdir+1;}
}}
tof=tof-numbdir;
if (mode[1]==mode[0] ) {
error(single);
r=0;}
else
if(((mode[0]==true)&(numbdir!=nfolder))||((mode[1]==true)&(numbdir>0))|| (mainlist.length!=nfolder)){
error(instr);
r=0;
}
else
r=1;
} while (r==0);
////////////////////////////////////////
////////////////////////////////////////
/////FLUORESCENCE MENU//////////////////
```

```
////////////////////////////////////////

Dialog.create("Do you work with fluorescence images?");

Dialog.addCheckbox("Yes",false);

Dialog.addMessage("if you check Yes your images will be inverted");

Dialog.show();

fluo=Dialog.getCheckbox();

////////////////////////////////////

//////////INSIDIA PART 1//////////

//////SPHEROID SEGMENTATION///////

////////////////////////////////

if ((mode[1]==true) & (mode[0]==false)) {

for(G=0; G<nfolder;G++){

dir = maindir+mainlist[G];

list = getFileList(dir);

c=list.length;

if (G==0) {

xc=newArray(tof);

yc=newArray(tof);

}

myDir = dir+"000results"+File.separator;

File.makeDirectory(myDir);

name=newArray(c);

res=newArray(c);

for (i=0; i<c; i++) {

X=c*G+i;

name[i]=replace(list[i],".tif","res");

res[i]=myDir+name[i];

open(dir+list[i]);

run("Set Scale...", "distance=0 known=0 pixel=1 unit=pixel");

run("8-bit");

if (fluo==true)

run("Invert");

h=getHeight();

w=getWidth();

run("Select None");

selectWindow(list[i]);

run("Duplicate...", "Duplicate.tif");

run("Auto Threshold", "method=[Default]");

rename(list[i]+"bw");

selectWindow(list[i]+"bw");

run("Fill Holes");////////////NEW

largest((list[i]+"bw"),X,xc,yc);

selectWindow("Mask of "+list[i]+"bw");

rename("Mask of "+list[i]);
```

```
selectWindow(list[i]+"bw");
run("Close");
selectWindow("Mask of "+list[i]);
doWand(round(xc[X]), round(yc[X]));
roiManager("Add");
selectWindow(list[i]);
roiManager("Select",0);
listisempty=0;
menu=true;
check=false;
while (menu==true){
SSdialog(4,0.6,1);
franginum=Dialog.getNumber();
frangimin=Dialog.getNumber();
frangimax=Dialog.getNumber();
check=Dialog.getCheckbox();
manual=Dialog.getCheckbox();
frang=Dialog.getCheckbox();
if(listisempty==0 &&
roiManager("count")!=0){
roiManager("delete");}
segmcheck=check+manual+frang;
if (segmcheck!=1){
error(single);
listisempty=1;
}
else
menu=false;
if (check==false){
selectWindow("Mask of "+list[i]);
run("Close");
selectWindow(list[i]);
run("Select None");
/////frangi thresholding
if (frang==true){
run("Frangi Vesselness (imglib,
experimental)",
"number="+franginum+"
minimum="+frangimin+"
maximum="+frangimax+"");
closing("vesselness of "+list[i]);
selectWindow("vesselness of
"+list[i]);
rename("Mask of "+list[i]);}
////////manual thresholding
else if (manual==true){
selectWindow(list[i]);
run("Duplicate...", "title=Mask of
"+list[i]);
rename("Mask of "+list[i]);
run("Threshold...");
```

```
setOption("BlackBackground", true);
title = "ManualThreshold";
msg = "Use the \"Threshold\" tool to\nadjust the threshold,click apply then click OK\".";
waitForUser(title, msg);
run("Invert");
run("Fill Holes");////////////NEW
}
selectWindow("Mask of "+list[i]);
largest(("Mask of "+list[i]),X,xc,yc);
roicheck=roiManager("count");
if (roicheck!=0){
roiManager("reset");
}
selectWindow("Mask of Mask of "+list[i]);
doWand(xc[X], yc[X]);
run("Clear Outside");
run("ROI Manager...");
roiManager("Add");
selectWindow("Mask of Mask of "+list[i]);
run("Close");
selectWindow(list[i]);
roicheck=roiManager("count");
if (roicheck!=0){
roiManager("Select", 0);
}
menu=true;
listisempty=0;
}}
selectWindow(list[i]);
run("Close");
roicheck=roiManager("count");
if (roicheck!=0){
roiManager("reset");}
///// segmented images saving /////
selectWindow("Mask of "+list[i]);
doWand(xc[X], yc[X]);
run("Clear Outside");
run("Select None");
saveAs(".tif",res[i]);
}
run("Close All");
selectWindow("Results");
run("Close");
}
}
////////////////////////////////////////////////////////
/
```

APPENDIX

```
//////////////////SS PARAMETERS//////////////////////
////////////////////////////////////////////////////
/
setBatchMode(true);
for(G=0; G<nfolder;G++){
dir = maindir+mainlist[G];
analysisdir=maindir+"analysis"+dayOfMonth+"_"+month+1+"h"+hour+"-"+minute+File.separator;
File.makeDirectory(analysisdir);
anSubdir=analysisdir+mainlist[G];
File.makeDirectory(anSubdir);
list = getFileList(dir); ////list contains results folder in the first line
c=list.length-1;
name=newArray(c);
res=newArray(c);
myDir = dir+"000results"+File.separator;
if (G==0){
xc=newArray(tof);
yc=newArray(tof);
AreaTotal=newArray(tof);
Perimeter=newArray(tof);
maxRadius=newArray(tof);
minRadius=newArray(tof);
coordinates=newArray(tof);
circularity=newArray(tof);
RadiusE=newArray(tof);
SpecSurf=newArray(tof);
ShapeF=newArray(tof);
EnvArea=newArray(tof);
//DM//
AreaCore=newArray(tof);
AreaInvasion=newArray(tof);
PercCore=newArray(tof);
PercInvasion=newArray(tof);
PeriMap=newArray(tof);
startx=newArray(tof);
starty=newArray(tof);
printnames=newArray(tof);
//DP
RadiusCore=newArray(tof);
RadiusCoreII=newArray(tof);
INTENSE=newArray(tof);
ACMtotal=newArray(tof);
ACMcore=newArray(tof);
ACMinvasion=newArray(tof);
ACMpercCore=newArray(tof);
ACMpercInvasion=newArray(tof);
```

```
}
for (i=0; i<c; i++) { ////for all the images in each folder
roicheck=roiManager("count");
if (roicheck!=0){
roiManager("reset");
}
X=c*G+i;
name[i]=replace(list[i+1],".tif","res.tif");
res[i]=myDir+name[i];
open(dir+list[i+1]);
if (fluo==true)
run("Invert");
run("Set Scale...", "distance=0 known=0 pixel=1 unit=pixel");
printnames[X]=list[i+1];
printnames[X]=replace(printnames[X]," ","_");
run("8-bit");
h=getHeight();
w=getWidth();
run("Select None");
image="current"+i;
bw="bw"+i;
selectWindow(list[i+1]);
rename(image);
open(res[i]);
run("Select None");
rename(bw);
run("Set Scale...", "distance=0 known=0 pixel=1 unit=pixel");
run("Analyze Particles...", "size=0-Infinity circularity=0.00-1.00 show=Nothing display clear");
totalArea=0;
for(j=0; j<nResults; j++){
current=getResult("Area",j);
if(current>totalArea){
totalArea=current;
AreaTotal[X]=getResult("Area",j);
Perimeter[X]=getResult("Perim.",j);
xc[X]=round(getResult("XM",j));
yc[X]=round(getResult("YM",j));
maxRadius[X]=(round(getResult("Feret",j)))/2;
minRadius[X]=(round(getResult("MinFeret",j)))/2;
RadiusE[X]=(round(getResult("Major",j)))/2;
circularity[X]=(getResult("Circ.",j));
}
```

```
}
run("Clear Results", "");
run("Set Scale...", "distance=0 known=0 pixel=1 unit=pixel");
run("Analyze Particles...", "size="+totalArea+"-Infinity show=Masks display clear");
run("Grays");
run("Select None");
doWand(xc[X],yc[X]);
doWand(xc[X],yc[X]);
run("Convex Hull");
run("Measure");
EnvArea[X]=getResult("Area",0);
run("Clear Results", "");
run("Select None");
selectWindow(bw);
run("Close");
selectWindow("Mask of "+bw);
rename(bw);RadiusCore=newArray(tof);
RadiusCoreII=newArray(tof);
INTENSE=newArray(tof);
ACMtotal=newArray(tof);
ACMcore=newArray(tof);
ACMinvasion=newArray(tof);
ACMpercCore=newArray(tof);
ACMpercInvasion=newArray(tof);

////////////////////////////////////////////////////////
//
////////////////////////////////////
//////////INSIDIA PART 2//////////
////////////////////////////////
////IMAGE NORMALISATION/////////
//////////////////////////////
selectWindow(image);
run("Macro...", "code=v=(-v+255)");
/////////image inverted
selectWindow(bw);
run("Select None");
doWand(xc[X],yc[X]);
doWand(xc[X],yc[X]);
roiManager("Add");
selectWindow(image);
run("Select None");
roiManager("Select",0);
run("Make Inverse");///area external to spheroid selected
run("Measure");
bg=getResult("Mean",0);
run("Clear Results", "");
```

```
roiManager("reset");
selectWindow(image);
run("Select None");
run("Subtract...", "value="+bg+"");
//////////////////////////
selectWindow(bw);
run("Select None");
run("Divide...", "value=255");
imageCalculator("Multiply create", image,bw);///only greyscale spheroid in the image
selectWindow(image);
run("Close");
///////////density file//////////////////
selectWindow("Result of "+image);
run("Select None");
run("Duplicate...", "Duplicate.tif");
saveAs(".tif",anSubdir+"density"+i);
selectWindow("density"+i+".tif");
run("Close");
selectWindow(bw);
run("Close");
selectWindow("Result of "+image);
run("Close");
}
////////////////////////////////
//////Pixel Conversion Menu//////
////////////////////////////////
Dialog.create("Convert values in microns?");
Dialog.addNumber("pixel to micron", 2.09);
Dialog.addCheckbox("convert",true);
Dialog.show();
pixel=Dialog.getNumber();
convert=Dialog.getCheckbox();
xaxisunits="(um)";
if (convert==false) {
xaxisunits="(pixel)";
pixel=1;}
run("Close All");
selectWindow("Results");
run("Close");
////////////////////////////////
////////////////////////////////
////////INSIDIA PART 3/////////
/////////DENSITY PROFILE//////////
////////////////////////////
//Profile Table//
```

```
title1 = "Profiles";
f="["+title1+"]";
run("New... ", "name="+f+" type=Table");
////////////////
for(G=0; G<nfolder;G++){
dir = maindir+mainlist[G];
list = getFileList(dir);
c=list.length-1;
myDir = dir+"000results"+File.separator;
profileth=newArray(c);
anSubdir=analysisdir+mainlist[G];
for (i=0; i<c; i++) {
X=c*G+i;
densitysave=anSubdir+"density"+i+".tif";
//////////////////DM file ////////////////////////
open(densitysave);
run("Median...", "radius=4");//////////////////
rename("density"+i+".tif");
run("Duplicate...", "Duplicate.tif");
rename("profile"+i);
sumy=0; /// to calculate the integral of the whole curve
selectWindow("profile"+i);
run("Concentric Circles", "circles="+maxRadius[X]+" line=1 x="+xc[X]+" y="+yc[X]+ " inner=1 outer="+maxRadius[X]+" measure");
y=newArray(nResults);
for(a=0; a<nResults; a++){
y[a]=getResult("Mean",a);
sumy=sumy+y[a];
}
////x coordinates for plot////
Xplot=newArray(y.length);
for(xx=0;xx<Xplot.length; xx++){
Xplot[xx]=(xx+1)*pixel;
}
print(f,printnames[X]);
for (p=0; p<y.length; p++){
print(f,y[p]);
}
print(f," ");
ACMtotal[X]=pixel*sumy;  ////integral of the curve
max=(y[3]+y[5]+y[7]+y[9])/4;
ylength=y.length;
counter=0;
if(i!=0){
```

```
for (inte=5;inte<ylength; inte+=5){
sumapp=0;
for(in=0; in<y.length-inte; in++){
sumapp=sumapp+y[in];
}
THEORY=max*(y.length-inte);
delta=sumapp/THEORY*100;
counter=counter+1;
if (delta>89){
RadiusCoreII[X]=ylength-inte;
CT=(ylength-(counter*5));
INTENSE[X]=round(y[CT]);
inte=ylength;
}
}
}
else
RadiusCoreII[X]=maxRadius[X];
////////////////////////////////////////////////
////////////Profile Plot Creation/////////////////
//plot creation
xaxis="Distance from centre of mass"+xaxisunits;
Plot.create("Circle profile", xaxis, "Intensity");
Plot.setLimits(0, 1000, 0, 255);
Plot.setFormatFlags("11001100001111");
Plot.setLineWidth(i+1.5);
Plot.add("line",Xplot, y);
Plot.show();
///plot legend
setColor(0, 0, 0);
drawString(printnames[X],350,50+11*i);
run("Set Scale...", "distance=0 known=0 pixel=1 unit=pixel");
setLineWidth(i*1);
drawLine(330,40+11*i,340,40+11*i);
rename("plot"+i);
////create empty plot////
if (i==0){
hp=getHeight();
wp=getWidth();
newImage("Plot", "8-bit white", wp, hp, 1);}
///sum the two plots before drawing the line
imageCalculator("AND", "Plot", "plot"+i);
////draw the line /////
```

```
selectWindow("plot"+i);///axis origin is 60,510
saveAs("tiff",anSubdir+"plot"+i);
open(anSubdir+"plot"+i+".tif");
rename("plot"+i+".tif");
selectWindow("plot"+i+".tif");
run("Clear Results");
run("Select None");
//////////////////
run("16 colors");
if(i!=0){
setLineWidth(2);
newnumberII=(((9*RadiusCoreII[X])/10)+60);
setColor(255, 0, 0);
drawLine(newnumberII, hp, newnumberII, 0);
setColor(0, 0, 0);
///integral of curve below core
for (gg=0;gg<RadiusCoreII[X];gg++){
ACMcore[X]=ACMcore[X]+pixel*y[gg];
}
}
else{
ACMcore[X]=ACMtotal[X];
}
ACMinvasion[X]=ACMtotal[X]-ACMcore[X];
ACMpercCore[X]=((ACMcore[X])/(ACMtotal[X]))*100;
ACMpercInvasion[X]=((ACMinvasion[X])/(ACMtotal[X]))*100;
drawString("core",70,200);
selectWindow("plot"+i+".tif");
saveAs("tiff",anSubdir+"plot"+i);
//////////NEW DENSITY MAP//////////////////
selectWindow("density"+i+".tif");
run("Duplicate...", "Duplicate.tif");
rename("green"+i);
selectWindow("green"+i);
for(sss=0;sss<w;sss++){
for(jjj=0;jjj<h;jjj++){
test=getPixel(sss,jjj);
if(test>INTENSE[X]){
setPixel(sss,jjj,255); //pixel is set in white
}
}
}
run("Subtract...", "value=254");
```

```
run("Multiply...", "value=255.000");
setOption("BlackBackground", true);
run("Make Binary");
run("Dilate");
run("Fill Holes");
run("Erode");
run("Analyze Particles...", "size=0-Infinity circularity=0.00-1.00 show=Nothing display clear");
apptotalArea=0;
for(jjj=0; jjj<nResults; jjj++){
current=getResult("Area",jjj);
if(current>apptotalArea){
apptotalArea=current;
}
}
run("Analyze Particles...", "size="+apptotalArea+"-Infinity show=Masks display clear");
AreaCore[X]=getResult("Area",0);
PeriMap[X]=getResult("Perim.",0);
AreaInvasion[X]=AreaTotal[X]-AreaCore[X];
run("Clear Results", "");
run("Dilate");
run("Clear Results", "");
run("Grays");
run("Select None");
imageCalculator("Add create", "Mask of green"+i,"density"+i+".tif");
selectWindow("Mask of green"+i);
run("Close");
selectWindow("green"+i);
run("Close");
selectWindow("density"+i+".tif");
run("Close");
selectWindow("Result of Mask of green"+i);
rename("density"+i+".tif");
doWand(xc[X],yc[X]);
run("Measure");
selectWindow("density"+i+".tif");
run("Red/Green");
saveAs(".tif",anSubdir+"density"+i);
run("Close");
}
selectWindow("Plot");
saveAs("tiff",anSubdir+"Plot");
run("Close All");
}
//////////////
```

APPENDIX

```
//montage///
////////////
run("Close All");
for(G=0; G<nfolder;G++){
dir=maindir+mainlist[G];
list=getFileList(dir);
c=list.length;
newImage("HyperStack", "RGB color-mode", w, h, 1, 1, 4);
open(dir+list[1]);
selectWindow(list[1]);
run("Select None");
run("Copy");
selectWindow("HyperStack");
Stack.setFrame(1);
run("Paste");
close(list[1]);
open(dir+list[c-1]);
selectWindow(list[c-1]);
run("Select None");
run("Copy");
selectWindow("HyperStack");
Stack.setFrame(2);
run("Paste");
close(list[c-1]);
anSubdir=analysisdir+mainlist[G]+"/";
open(anSubdir+"density0.tif");
selectWindow("density0.tif");
run("Select None");
run("Copy");
selectWindow("HyperStack");
Stack.setFrame(3);
run("Paste");
close("density0.tif");
open(anSubdir+"density"+(c-2)+".tif");
selectWindow("density"+(c-2)+".tif");
run("Select None");
run("Copy");
selectWindow("HyperStack");
Stack.setFrame(4);
run("Paste");
close("density0.tif");
run("Make Montage...", "columns=2 rows=2 scale=1 first=1 last=4 increment=1 border=0 font=12");
selectWindow("Montage");
saveAs("tiff",anSubdir+"Montage");
run("Close All");
}
```

```
////////////////////////////

////////INSIDIA PART 6/////////

////////OUTPUT////////////////

////////////////////////////

for(G=0; G<nfolder;G++){

anSubdir=analysisdir+mainlist[G];}

print("This macro has been run on "+dayOfMonth+"/"+month+1+"/"+year+" at "+hour+":"+minute+" with");

if (mode[0]==true){

print("thresholded images.");

} else

{

print("unthresholded images.");

}

print("The pixel value conversion used is "+pixel);

print("SS Parameters");

print("\\file AreaTotal Perimeter MaxRadius MinRadius Circularity RadiusE SpecificSurf ShapeF EnvArea ");

for (b=0; b<tof; b++){

////////pixel conversion////////

///SS parameters///////

coordinates[b]=maxRadius[b];

maxRadius[b]=maxRadius[b]*pixel;

minRadius[b]=minRadius[b]*pixel;

RadiusE[b]=RadiusE[b]*pixel;

AreaTotal[b]=AreaTotal[b]*pixel;

Perimeter[b]=Perimeter[b]*pixel;

EnvArea[b]=EnvArea[b]*pixel;

SpecSurf[b]=(Perimeter[b]/AreaTotal[b])/(2/maxRadius[b]);

ShapeF[b]=(Perimeter[b]*Perimeter[b])/(4*PI*AreaTotal[b]);

/////density profile parameters////

RadiusCoreII[b]=RadiusCoreII[b]*pixel;

////density map parameters///////

AreaCore[b]=AreaCore[b]*pixel;

PeriMap[b]=PeriMap[b]*pixel;

AreaInvasion[b]=AreaInvasion[b]*pixel;

PercCore[b]=(AreaCore[b]/AreaTotal[b])*100;

PercInvasion[b]=(AreaInvasion[b]/AreaTotal[b])*100;

print(printnames[b]+" "+AreaTotal[b]+" "+Perimeter[b]+" "+maxRadius[b]+" "+minRadius[b]+" "+circularity[b]+" "+RadiusE[b]+" "+SpecSurf[b]+" "+ShapeF[b]+" "+EnvArea[b]);
```

```
}
b=0;
print("DM and DP parameters");
print("\\file PeriMap AreaCore AreaInvasion %Core %Invasion ACMTotal ACMCore ACMInvasion %ACMcore %ACMinvasion RadiuscoreII");
for (b=0; b<tof; b++){
print(printnames[b]+" "+PeriMap[b]+" "+AreaCore[b]+" "+AreaInvasion[b]+" "+PercCore[b]+" "+PercInvasion[b]+" "+ACMtotal[b]+" "+ACMcore[b]+" "+ACMinvasion[b]+" "+ACMpercCore[b]+" "+ACMpercInvasion[b]+" "+RadiusCoreII[b]);
}
///search for largest maxradius and print x coordinates for profiles, if conversion is not selected values are in pixel
largR=0;
for(iii=0; iii<tof; iii++){
current=coordinates[iii]; ///in pixel
if(current>largR){
largR=current;
}}
XCoord=newArray(round(largR));
print(f,"X coordinates");
for(i=0;i<XCoord; i++){
XCoord[i]=(1+i)*pixel;
print(f,XCoord[i]);
}
////////////////////////////////
/////////CLOSE&EXIT////////////
////////////////////////////////
setBatchMode(false);
selectWindow("Results");
run("Close");
selectWindow("Log");
saveAs("Text", analysisdir+"output");
run("Close");
selectWindow(title1);
saveAs("Text", analysisdir+"Profiles");
run("Close");
waitForUser("Finish","Click OK to exit");
exit();
```

APPENDIX 6: R CODE

7.1.14 SURVIVAL

SINGLE GENE

```
# installation
source("https://bioconductor.org/biocLite.R")
biocLite("RTCGA.clinical")
biocLite("RTCGA.rnaseq")
install.packages("devtools")
library(devtools)



library(tidyverse) # pipes (%>%) and dplyr data munging
library(RTCGA.clinical) # survival times
library(RTCGA.rnaseq) # genes' expression
library(RTCGA) ##access library
library(devtools)
infoTCGA()  ##see names of cohorts (brca, gbm, etc)

GBM.surv<-survivalTCGA(GBM.clinical)


#head(GBM.surv)
GBM.expressions<-expressionsTCGA(GBM.rnaseq)
#head(colnames(GBM.expressions[,3021], 50))


#head(GBM.expressions)
#nrow(GBM.expressions)


expressionsTCGA(
  GBM.rnaseq,
  extract.cols = c("CAV-1|857")) %>%
  rename(cohort = dataset,
         CAV-1 = `CAV-1|857`) %>%
  filter(substr(bcr_patient_barcode, 14, 15) == "01") %>%
  # only cancer samples
  mutate(bcr_patient_barcode =
           substr(bcr_patient_barcode, 1, 12)) -> GBM.rnaseq_v2


GBM.surv %>%
```

```
  left_join(GBM.rnaseq_v2,
            by = "bcr_patient_barcode") -
>
  GBM.surv_rnaseq



GBM.surv_rnaseq                    <-
GBM.surv_rnaseq %>%
  filter(!is.na(cohort))



library(survminer)


GBM.surv_rnaseq.cut                <-
surv_cutpoint(
  GBM.surv_rnaseq,
  time = "times",
  event = "patient.vital_status",
  variables = c("CAV-1", "cohort")
)
summary(GBM.surv_rnaseq.cut)


plot(GBM.surv_rnaseq.cut,  "CAV-1",
palette = c("#000000","#000000"))
```

```
GBM.surv_rnaseq.cat                <-
surv_categorize(GBM.surv_rnaseq.c
ut)



library(survival)


fit          <-          survfit(Surv(times,
patient.vital_status)  ~  ITGB1  +
cohort ,
             data                  =
GBM.surv_rnaseq.cat)


ggsurvplot(
  fit,                  # survfit object with
calculated statistics.
  risk.table = TRUE,        # show risk
table.
  pval = TRUE,                # show p-
value of log-rank test.
  conf.int = FALSE,             # show
confidence intervals for
  # point estimaes of survival curves.
  xlim = c(0,1750),             # present
narrower X axis, but not affect
  # survival estimates.
  break.time.by = 250,      # break X
axis in time intervals by 500.
```

```
  surv.median.line = "v",

  ggtheme = theme_light(), # customize plot and risk table with a theme.

  palette = c("#000000","#000000"),

  risk.table.y.text.col = T, # colour risk table text annotations.

  risk.table.y.text = FALSE # show bars instead of names in text annotations

  # in legend of risk table

)


surv_median(fit) #returns median survival with upper and lower for each curve

survdiff(Surv(times,
patient.vital_status) ~ CAV-1, data = GBM.surv_rnaseq.cat) #log rank test

coxph(Surv(times,
patient.vital_status) ~ CAV-1, data = GBM.surv_rnaseq.cat)
```

7.1.15 SURVIVAL DOUBLE POSITIVE VS OTHER

```
# installation
source("https://bioconductor.org/biocLite.R")
biocLite("RTCGA.clinical")
biocLite("RTCGA.rnaseq")
install.packages("devtools")
library(devtools)



library(tidyverse) # pipes (%>%) and dplyr data munging
library(RTCGA.clinical) # survival times
library(RTCGA.rnaseq) # genes' expression
library(RTCGA) ##access library
library(devtools)
infoTCGA()  ##see names of cohorts (brca, gbm, etc)

GBM.surv<-survivalTCGA(GBM.clinical)


#head(GBM.surv)
GBM.expressions<-expressionsTCGA(GBM.rnaseq)
#head(colnames(GBM.expressions[, 3021], 50))


#head(GBM.expressions)
#nrow(GBM.expressions)


expressionsTCGA(
  GBM.rnaseq,
  extract.cols = c("SPP1|6696", "CAV-1|857")) %>%
  rename(cohort = dataset,
         TSP1 = `SPP1|6696`,
         CAV-1 = `CAV-1|857`) %>%
  filter(substr(bcr_patient_barcode, 14, 15) == "01") %>%
  # only cancer samples
  mutate(bcr_patient_barcode =
           substr(bcr_patient_barcode, 1, 12)) -> GBM.rnaseq_v2
```

```
GBM.surv %>%
  left_join(GBM.rnaseq_v2,
            by = "bcr_patient_barcode") ->
  GBM.surv_rnaseq



GBM.surv_rnaseq <- GBM.surv_rnaseq %>%
  filter(!is.na(cohort))




library(survminer)


GBM.surv_rnaseq.cut <- surv_cutpoint(
  GBM.surv_rnaseq,
  time = "times",
  event = "patient.vital_status",
  variables = c("TSP1", "cohort", "CAV-1")
)
summary(GBM.surv_rnaseq.cut)
```

```
GBM.surv_rnaseq.cat <- surv_categorize(GBM.surv_rnaseq.cut)
GBM.surv_rnaseq.cat <- GBM.surv_rnaseq.cat %>%
  mutate(group = ifelse(TSP1 == 'high' & CAV-1 == 'high', 'TSP1+/CAV-1+', 'other'))


library(survival)


fit <- survfit(Surv(times, patient.vital_status) ~ group,
               data = GBM.surv_rnaseq.cat)


ggsurvplot(
  linetype = c(1,4),          # change linetypes, the first element is for first group, the second for the 2nd group
  pval.coord = c(470, 0.7),   # coordinates of the p-value apperance
  censor = FALSE,             # should censoring be included in survival plots
  pval.method = TRUE,         # should the p-value method name be plotted
```

pval.method.coord = c(470, 0.8), # coordinates for the test for which the p-value was calculated

fit, # survfit object with calculated statistics.

risk.table = TRUE, # show risk table.

pval = TRUE, # show p-value of log-rank test.

conf.int = FALSE, # show confidence intervals for

point estimaes of survival curves.

xlim = c(0,1750), # present narrower X axis, but not affect

survival estimates.

break.time.by = 250, # break X axis in time intervals by 500.

surv.median.line = "v",

ggtheme = theme_light(), # customize plot and risk table with a theme.

palette = c("#000000","#000000"),

risk.table.y.text.col = T, # colour risk table text annotations.

risk.table.y.text = FALSE # show bars instead of names in text annotations

in legend of risk table

)

surv_median(fit) #returns median survival with upper and lower for each curve

survdiff(Surv(times, patient.vital_status) ~ group, data = GBM.surv_rnaseq.cat) #log rank test

coxph(Surv(times, patient.vital_status) ~ group, data = GBM.surv_rnaseq.cat)

7.1.16 SURVIVAL FOUR GROUPS

```
# installation
source("https://bioconductor.org/biocLite.R")
biocLite("RTCGA.clinical")
biocLite("RTCGA.rnaseq")
install.packages("devtools")
library(devtools)



library(tidyverse) # pipes (%>%) and dplyr data munging
library(RTCGA.clinical) # survival times
library(RTCGA.rnaseq) # genes' expression
library(RTCGA) ##access library
library(devtools)
infoTCGA()  ##see names of cohorts (brca, gbm, etc)



GBM.surv<-survivalTCGA(GBM.clinical)
#head(GBM.surv)
GBM.expressions<-expressionsTCGA(GBM.rnaseq)
#head(colnames(GBM.expressions[, 3021], 50))


#head(GBM.expressions)
#nrow(GBM.expressions)


expressionsTCGA(
  GBM.rnaseq,
  extract.cols = c("SPP1|6696", "CAV-1|857")) %>%
  rename(cohort = dataset,
         TSP1 = `SPP1|6696`,
         CAV-1 = `CAV-1|857`) %>%
  filter(substr(bcr_patient_barcode, 14, 15) == "01") %>%
  # only cancer samples
  mutate(bcr_patient_barcode =
           substr(bcr_patient_barcode, 1, 12)) -> GBM.rnaseq_v2


GBM.surv %>%
  left_join(GBM.rnaseq_v2,
```

```
        by = "bcr_patient_barcode") ->
 GBM.surv_rnaseq

GBM.surv_rnaseq <- GBM.surv_rnaseq %>%
 filter(!is.na(cohort))

library(survminer)

GBM.surv_rnaseq.cut <- surv_cutpoint(
 GBM.surv_rnaseq,
 time = "times",
 event = "patient.vital_status",
 variables = c("TSP1", "cohort", "CAV-1")
)
summary(GBM.surv_rnaseq.cut)

GBM.surv_rnaseq.cat <- surv_categorize(GBM.surv_rnaseq.cut)

GBM.surv_rnaseq.cat <- GBM.surv_rnaseq.cat %>%
 mutate(group = ifelse(TSP1 == 'high' & CAV-1 == 'high', 'TSP1+/CAV-1+', 'other'))

library(survival)

fit <- survfit(Surv(times, patient.vital_status) ~ CAV-1 + TSP1,
        data = GBM.surv_rnaseq.cat)

ggsurvplot(
 linetype = c(1, 2, 3, 4), # change linetypes, the first element is for first group, the second for the 2nd group
 pval.coord = c(470, 0.7), # coordinates of the p-value apperance
 censor = FALSE, # should censoring be included in survival plots
```

```
  pval.method = TRUE,          # should the p-value method name be plotted

  pval.method.coord = c(470, 0.8),  # coordinates for the test for which the p-value was calculated

  fit,                 # survfit object with calculated statistics.

  risk.table = TRUE,       # show risk table.

  pval = TRUE,             # show p-value of log-rank test.

  conf.int = FALSE,        # show confidence intervals for

  # point estimaes of survival curves.

  xlim = c(0,1750),        # present narrower X axis, but not affect

  # survival estimates.

  break.time.by = 250,     # break X axis in time intervals by 500.

  surv.median.line = "v",

  ggtheme = theme_light(), # customize plot and risk table with a theme.

  palette = c("#000000","#000000","#000000","#000000"),

  risk.table.y.text.col = T, # colour risk table text annotations.

  risk.table.y.text = FALSE # show bars instead of names in text annotations

  # in legend of risk table

)


surv_median(fit) #returns median survival with upper and lower for each curve

survdiff(Surv(times, patient.vital_status) ~ CAV-1 + TSP1, data = GBM.surv_rnaseq.cat) #log rank test

coxph(Surv(times, patient.vital_status) ~ CAV-1 + TSP1, data = GBM.surv_rnaseq.cat)
```

APPENDIX 7: TOP 500 GENES POSITIVELY CORRELATED TO CAV-1 IN GBM

	HUGO	R-value	R-pvalue		HUGO	R-value	R-pvalue
1	PRSS23	0.69	1.16E-73	126	TIMP1	0.428	1.45E-23
2	CAV2	0.645	3.10E-61	127	PTRF	0.428	1.67E-23
3	SERPINE1	0.639	8.96E-60	128	EHD2	0.428	1.59E-23
4	MYOF	0.617	1.83E-54	129	DUSP1	0.427	2.14E-23
5	P4HA2	0.583	3.58E-47	130	STC2	0.426	2.80E-23
6	GBE1	0.576	9.89E-46	131	MET	0.426	2.56E-23
7	BACE2	0.564	2.08E-43	132	ARPC1B	0.425	3.52E-23
8	CD44	0.555	8.70E-42	133	TGFB1I1	0.425	3.87E-23
9	UPP1	0.549	8.68E-41	134	RBM47	0.425	3.45E-23
10	ANXA2P2	0.547	1.91E-40	135	LMNA	0.424	4.47E-23
11	ITGB1	0.547	1.97E-40	136	REXO2	0.422	7.29E-23
12	CSDA	0.546	2.58E-40	137	DSE	0.422	8.01E-23
13	LOX	0.545	4.26E-40	138	CHSY1	0.421	1.15E-22
14	SRPX2	0.544	4.98E-40	139	CTSL1	0.42	1.24E-22
15	GPRC5A	0.542	1.17E-39	140	SYNPO	0.42	1.48E-22
16	MMP19	0.54	2.67E-39	141	TNFRSF1B	0.42	1.48E-22
17	EMP1	0.536	1.01E-38	142	MAFF	0.42	1.48E-22
18	LOXL2	0.536	1.23E-38	143	SPAG4	0.419	1.73E-22
19	PLAUR	0.529	1.80E-37	144	RGS2	0.417	3.50E-22
20	CFI	0.528	2.31E-37	145	WBP5	0.416	4.51E-22
21	NAMPT	0.526	4.98E-37	146	C1RL	0.416	3.70E-22

22	CA12	0.521	3.51E-36	147	CAST	0.415	4.98E-22
23	PROS1	0.521	3.69E-36	148	SERPINH1	0.414	6.00E-22
24	ANXA2	0.519	7.42E-36	149	WWTR1	0.413	8.03E-22
25	ITGA5	0.518	1.09E-35	150	POLD4	0.413	8.97E-22
26	TREM1	0.517	1.40E-35	151	S100A6	0.413	7.72E-22
27	COL5A1	0.515	3.05E-35	152	FSTL1	0.409	2.21E-21
28	MVP	0.51	1.49E-34	153	TPM4	0.409	2.67E-21
29	DPYD	0.509	2.72E-34	154	DAB2	0.407	4.39E-21
30	VCL	0.507	4.59E-34	155	PTP4A2	0.406	4.92E-21
31	TNC	0.507	4.79E-34	156	CHPF2	0.406	5.98E-21
32	CA9	0.504	1.33E-33	157	NDRG1	0.405	7.00E-21
33	C5AR1	0.503	2.15E-33	158	IGFBP6	0.405	7.13E-21
34	FOSL1	0.502	2.77E-33	159	LY96	0.405	6.08E-21
35	FLNA	0.496	2.61E-32	160	MFSD1	0.405	7.70E-21
36	LAMB1	0.496	2.33E-32	161	LDHA	0.404	8.03E-21
37	CEBPB	0.494	4.55E-32	162	BHLHE40	0.404	8.02E-21
38	GFPT2	0.491	1.09E-31	163	TNFAIP3	0.404	8.06E-21
39	P4HA1	0.491	1.36E-31	164	TRAM2	0.403	1.19E-20
40	THBS1	0.489	2.12E-31	165	FAM129A	0.403	1.03E-20
41	IL1R1	0.489	2.19E-31	166	IBSP	0.402	1.27E-20
42	FAM114A1	0.489	2.35E-31	167	MYLK	0.401	1.79E-20
43	CTSB	0.488	3.00E-31	168	ABCA1	0.401	1.63E-20
44	ADM	0.488	3.67E-31	169	FNDC3B	0.401	1.85E-20
45	GEM	0.486	6.65E-31	170	RAB13	0.4	2.19E-20
46	TGFBI	0.485	7.11E-31	171	ANPEP	0.4	2.49E-20

47	C1R	0.485	8.28E-31	172	FCGR2B	0.399	2.79E-20
48	CALD1	0.485	7.69E-31	173	VKORC1	0.399	2.73E-20
49	SHC1	0.483	1.33E-30	174	CLCF1	0.399	2.77E-20
50	PLAU	0.482	1.83E-30	175	LUM	0.398	3.37E-20
51	GLIPR1	0.482	2.35E-30	176	ATF3	0.398	4.03E-20
52	HK2	0.481	2.72E-30	177	MSR1	0.398	4.14E-20
53	SLC39A14	0.481	3.30E-30	178	COL3A1	0.398	3.64E-20
54	FN1	0.48	3.45E-30	179	MYL9	0.397	4.39E-20
55	ANXA1	0.479	5.89E-30	180	FCGR2A	0.397	5.22E-20
56	ADAM9	0.479	5.11E-30	181	PDIA5	0.397	5.24E-20
57	TMEM43	0.478	6.74E-30	182	FAS	0.397	4.74E-20
58	PLP2	0.477	1.04E-29	183	GSN	0.396	5.96E-20
59	PLOD2	0.476	1.22E-29	184	TCIRG1	0.396	5.72E-20
60	C8orf4	0.474	3.01E-29	185	RALA	0.396	6.07E-20
61	S100A11	0.473	3.90E-29	186	BIRC3	0.395	6.77E-20
62	ABCC3	0.473	4.00E-29	187	SLC11A1	0.394	1.01E-19
63	TAGLN	0.472	4.85E-29	188	MYH9	0.394	1.03E-19
64	C1S	0.472	4.45E-29	189	PCOLCE	0.393	1.09E-19
65	PLOD1	0.469	1.19E-28	190	CXCR4	0.393	1.33E-19
66	MBD2	0.468	1.89E-28	191	KYNU	0.393	1.18E-19
67	CD163	0.468	1.68E-28	192	COL5A2	0.393	1.22E-19
68	PTPN12	0.467	2.45E-28	193	GYS1	0.392	1.58E-19
69	ANGPTL4	0.467	2.46E-28	194	CCL20	0.392	1.58E-19
70	ACTN1	0.464	4.91E-28	195	RCAN1	0.392	1.51E-19
71	S100A10	0.463	8.79E-28	196	LOXL1	0.391	1.88E-19

72	IQGAP1	0.462	1.19E-27	197	HILPDA	0.391	2.19E-19
73	TNFRSF12A	0.459	2.85E-27	198	SLC2A3	0.39	2.55E-19
74	ACTA2	0.455	1.00E-26	199	DCBLD2	0.39	2.68E-19
75	PTX3	0.455	7.97E-27	200	TPM2	0.389	3.03E-19
76	LIF	0.454	1.31E-26	201	TGFBR2	0.389	2.82E-19
77	ICAM1	0.453	1.68E-26	202	SERPINA1	0.389	2.96E-19
78	F13A1	0.453	1.49E-26	203	NNMT	0.388	3.62E-19
79	LTBP2	0.452	2.20E-26	204	ARHGAP29	0.387	5.55E-19
80	CTSC	0.451	2.73E-26	205	NFKBIA	0.386	6.67E-19
81	LIMS1	0.451	2.56E-26	206	EFEMP1	0.386	6.92E-19
82	IL1R2	0.45	3.52E-26	207	FBN1	0.386	7.19E-19
83	RNASE4	0.45	3.31E-26	208	TNFAIP8	0.386	6.60E-19
84	COL1A1	0.449	5.33E-26	209	GLB1	0.385	8.34E-19
85	STC1	0.449	4.42E-26	210	STEAP3	0.385	8.15E-19
86	AIM1	0.449	5.44E-26	211	P4HB	0.384	9.97E-19
87	FOSL2	0.449	5.37E-26	212	LRP10	0.384	9.11E-19
88	SAT1	0.448	6.57E-26	213	ITGA3	0.384	1.10E-18
89	GNS	0.448	5.86E-26	214	FHL2	0.384	1.08E-18
90	SLC16A3	0.447	7.63E-26	215	NFIL3	0.384	1.06E-18
91	PYGL	0.447	8.62E-26	216	KLF6	0.383	1.19E-18
92	TMEM45A	0.445	1.64E-25	217	RBMS1	0.383	1.18E-18
93	IL13RA1	0.444	2.20E-25	218	EDNRA	0.382	1.77E-18
94	COL6A2	0.444	1.96E-25	219	VEGFA	0.382	1.57E-18
95	SH3BGRL3	0.444	2.19E-25	220	B4GALT1	0.381	2.00E-18
96	ELL2	0.443	2.65E-25	221	IFI16	0.381	2.15E-18

97	TNFRSF1A	0.442	3.78E-25	222	RND3	0.381	2.01E-18
98	RAB27A	0.442	4.08E-25	223	SLC39A8	0.38	2.32E-18
99	COL6A1	0.442	3.55E-25	224	SLC2A1	0.379	3.37E-18
100	GBP2	0.441	4.59E-25	225	SRGN	0.379	3.22E-18
101	BCL3	0.441	4.33E-25	226	TNIP1	0.379	3.39E-18
102	ALDH3B1	0.441	4.59E-25	227	IL10RB	0.379	3.00E-18
103	NRP1	0.441	4.58E-25	228	ZFP36L1	0.379	2.83E-18
104	COL1A2	0.439	7.15E-25	229	FXYD5	0.379	3.40E-18
105	HEXB	0.438	1.15E-24	230	CD93	0.378	4.07E-18
106	PLOD3	0.437	1.46E-24	231	SLAMF8	0.378	4.35E-18
107	HSPA5	0.437	1.61E-24	232	S100A4	0.377	5.06E-18
108	MAFB	0.437	1.26E-24	233	SH2B3	0.377	4.93E-18
109	RRAS	0.436	1.77E-24	234	GADD45A	0.377	5.24E-18
110	CEBPD	0.435	2.50E-24	235	OLFML2B	0.377	5.26E-18
111	ANG	0.435	2.40E-24	236	ELF4	0.376	5.80E-18
112	CYR61	0.433	4.49E-24	237	EHD4	0.375	7.12E-18
113	PALLD	0.432	6.60E-24	238	GRN	0.374	1.05E-17
114	AHNAK2	0.432	5.50E-24	239	CD14	0.374	1.01E-17
115	NPC2	0.431	7.35E-24	240	RAI14	0.374	1.06E-17
116	COL6A3	0.431	7.66E-24	241	STAB1	0.374	9.87E-18
117	ADAM12	0.431	7.59E-24	242	CLIC1	0.374	1.03E-17
118	THBD	0.431	7.27E-24	243	FTH1P5	0.374	1.03E-17
119	SOCS3	0.431	8.36E-24	244	IGFBP7	0.373	1.26E-17
120	ARL4C	0.43	9.78E-24	245	SDC1	0.373	1.19E-17
121	ELK3	0.43	9.77E-24	246	MAPKAPK2	0.373	1.14E-17

122	CALU	0.429	1.26E-23	247	MAN2A1	0.373	1.35E-17
123	CNN2	0.429	1.39E-23	248	ERP44	0.373	1.19E-17
124	HSPB1	0.429	1.24E-23	249	ERO1L	0.373	1.34E-17
125	TIPARP	0.429	1.34E-23	250	HMOX1	0.372	1.65E-17

APPENDIX 8: CAV-1/TARGET GENES EXPRESSION CORRELATION

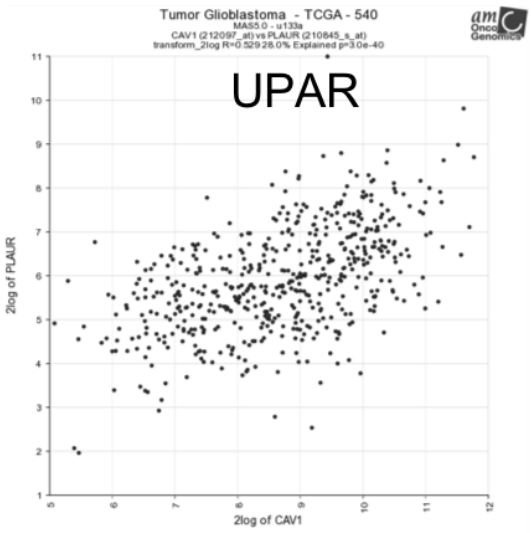

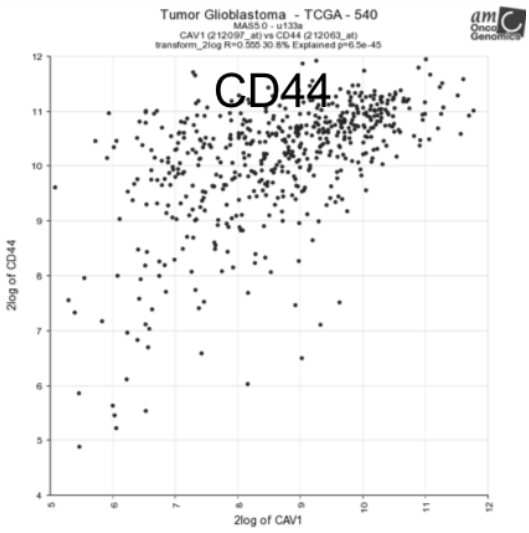

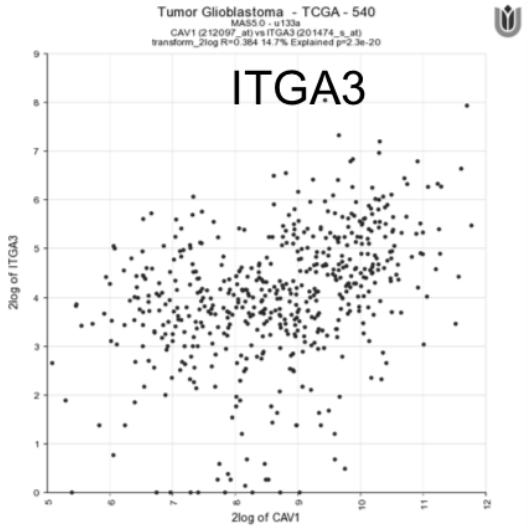

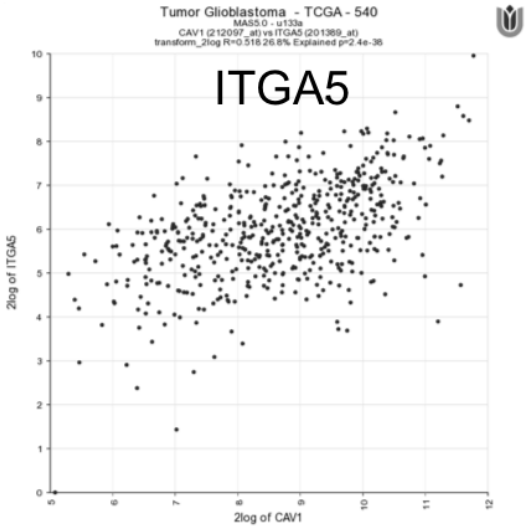

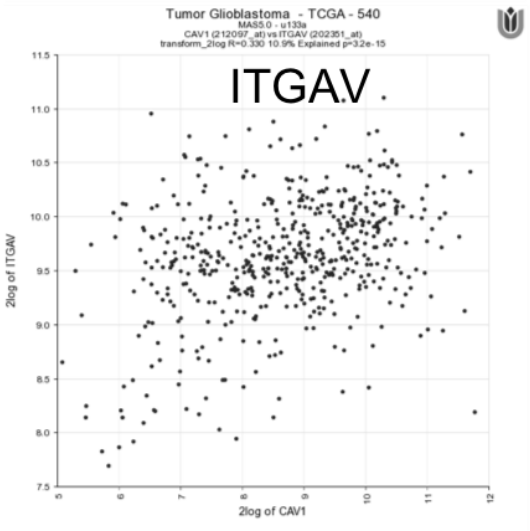

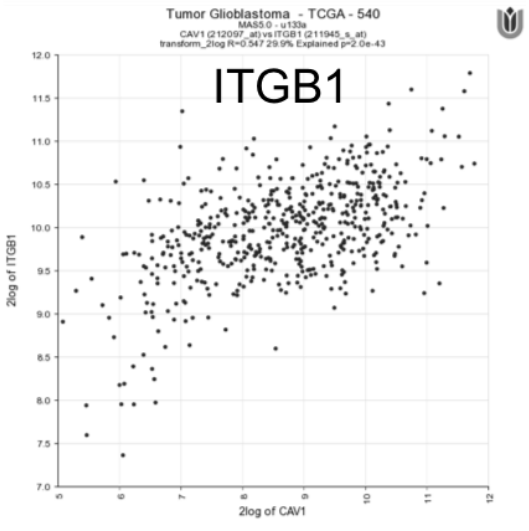

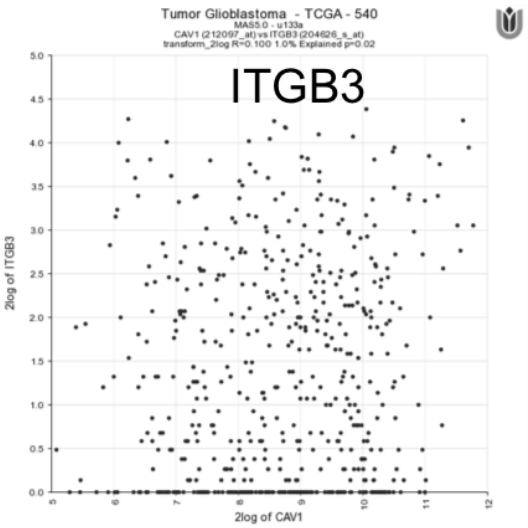
Tumor Glioblastoma - TCGA - 540
MAS5.0 - u133a
CAV1 (212097_at) vs ITGB3 (204626_s_at)
transform_2log R=0.100 1.0% Explained p=0.02
ITGB3
2log of ITGB3
2log of CAV1

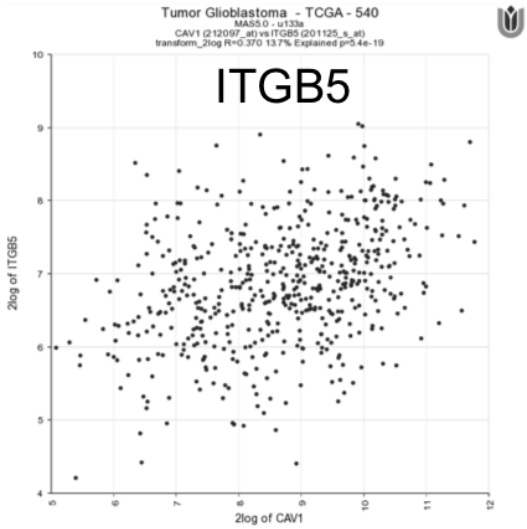
Tumor Glioblastoma - TCGA - 540
MAS5.0 - u133a
CAV1 (212097_at) vs ITGB5 (201125_s_at)
transform_2log R=0.370 13.7% Explained p=5.4e-19
ITGB5
2log of ITGB5
2log of CAV1

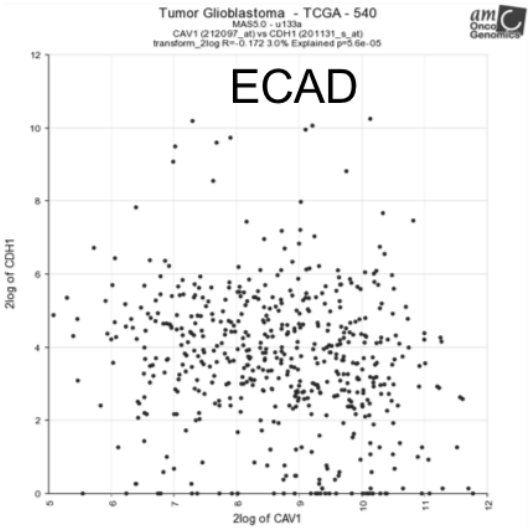
Tumor Glioblastoma - TCGA - 540
MAS5.0 - u133a
CAV1 (212097_at) vs CDH1 (201131_s_at)
transform_2log R=-0.172 3.0% Explained p=5.6e-05
ECAD
2log of CDH1
2log of CAV1

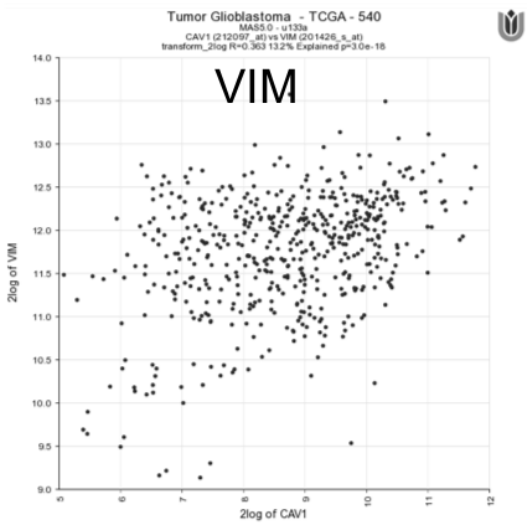
Tumor Glioblastoma - TCGA - 540
MAS5.0 - u133a
CAV1 (212097_at) vs VIM (201426_s_at)
transform_2log R=0.363 13.2% Explained p=3.0e-16
VIM
2log of VIM
2log of CAV1

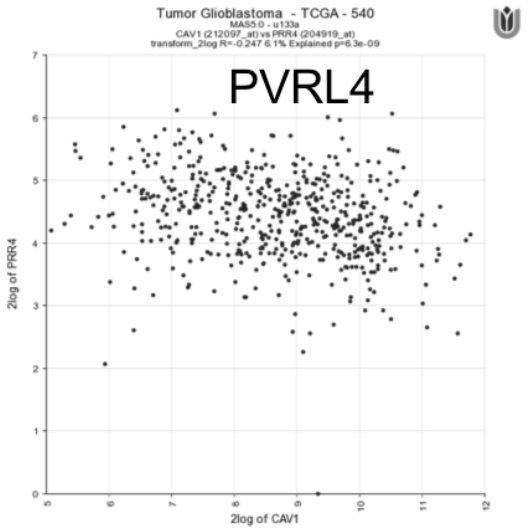
Tumor Glioblastoma - TCGA - 540
MAS5.0 - u133a
CAV1 (212097_at) vs PRR4 (204919_at)
transform_2log R=-0.247 6.1% Explained p=6.3e-09
PVRL4
2log of PRR4
2log of CAV1

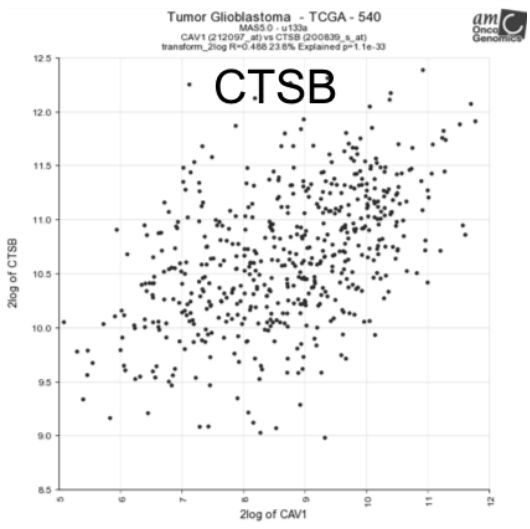
Tumor Glioblastoma - TCGA - 540
MAS5.0 - u133a
CAV1 (212097_at) vs CTSB (200839_s_at)
transform_2log R=0.488 23.8% Explained p=1.1e-33
CTSB
2log of CTSB
2log of CAV1

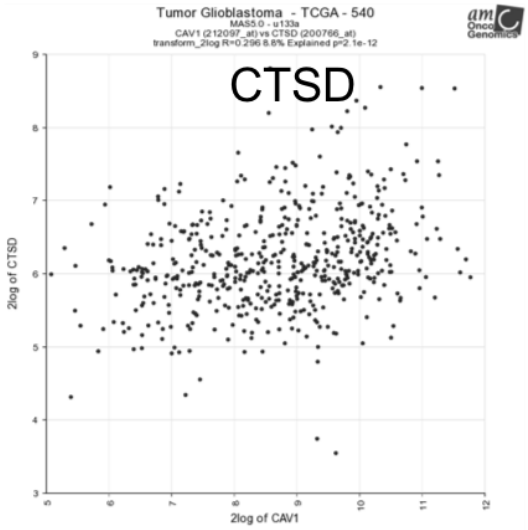
Tumor Glioblastoma - TCGA - 540
MAS5.0 - u133a
CAV1 (212097_at) vs CTSD (200766_at)
transform_2log R=0.296 8.8% Explained p=2.1e-12
CTSD
2log of CTSD
2log of CAV1

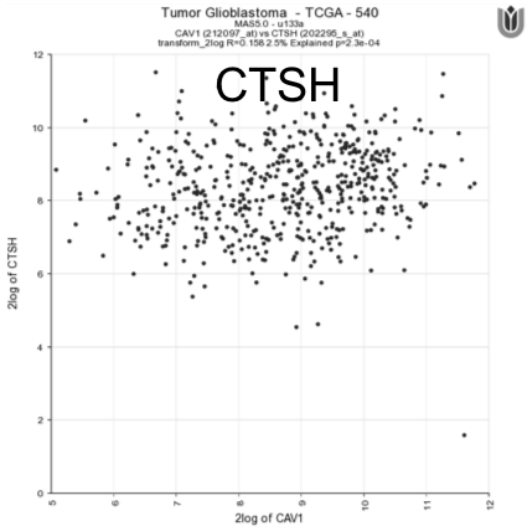
Tumor Glioblastoma - TCGA - 540
MAS5.0 - u133a
CAV1 (212097_at) vs CTSH (202295_s_at)
transform_2log R=0.158 2.5% Explained p=2.3e-04
CTSH
2log of CTSH
2log of CAV1

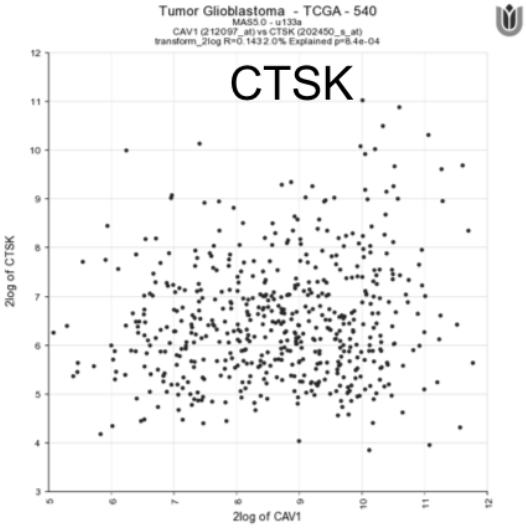
Tumor Glioblastoma - TCGA - 540
MAS5.0 - u133a
CAV1 (212097_at) vs CTSK (202450_s_at)
transform_2log R=0.143 2.0% Explained p=8.4e-04
CTSK
2log of CTSK
2log of CAV1

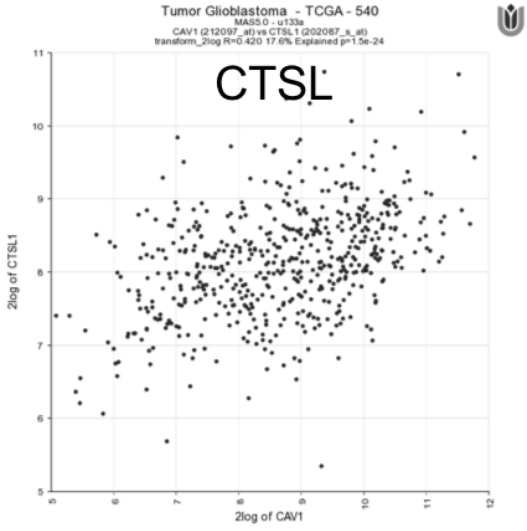
Tumor Glioblastoma - TCGA - 540
MAS5.0 - u133a
CAV1 (212097_at) vs CTSL1 (202087_s_at)
transform_2log R=0.420 17.6% Explained p=1.5e-24
CTSL
2log of CTSL1
2log of CAV1

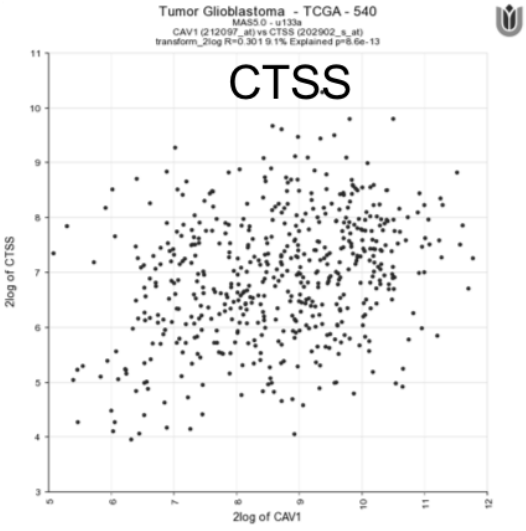
Tumor Glioblastoma - TCGA - 540
MAS5.0 - u133a
CAV1 (212097_at) vs CTSS (202902_s_at)
transform_2log R=0.301 9.1% Explained p=8.6e-13
CTSS
2log of CTSS
2log of CAV1

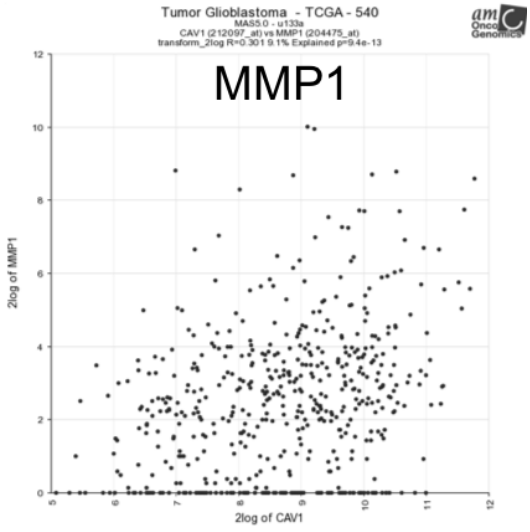
Tumor Glioblastoma - TCGA - 540
MAS5.0 - u133a
CAV1 (212097_at) vs MMP1 (204475_at)
transform_2log R=0.301 9.1% Explained p=9.4e-13
MMP1
2log of MMP1
2log of CAV1

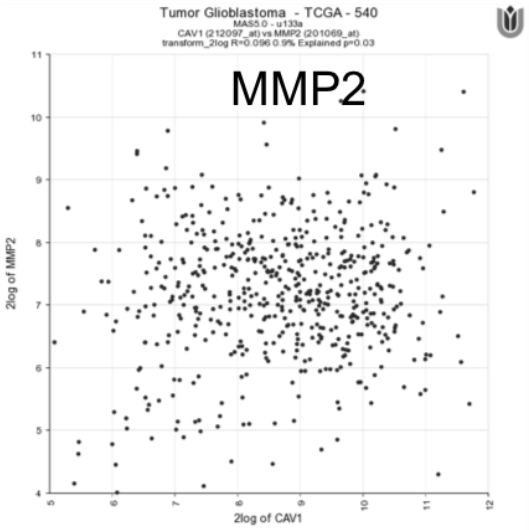
Tumor Glioblastoma - TCGA - 540
MAS5.0 - u133a
CAV1 (212097_at) vs MMP2 (201069_at)
transform_2log R=0.096 0.9% Explained p=0.03
MMP2
2log of MMP2
2log of CAV1

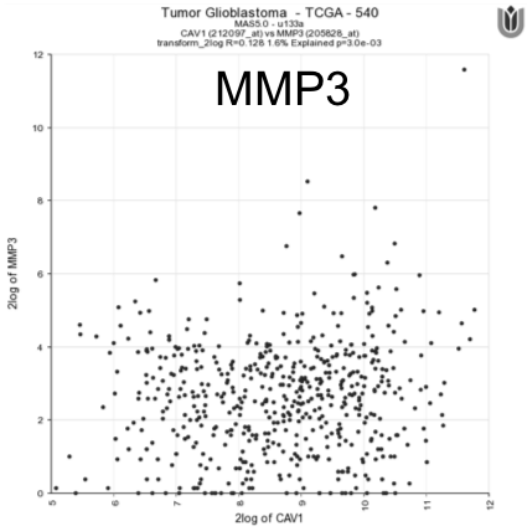
Tumor Glioblastoma - TCGA - 540
MAS5.0 - u133a
CAV1 (212097_at) vs MMP3 (205828_at)
transform_2log R=0.128 1.6% Explained p=3.0e-03
MMP3
2log of MMP3
2log of CAV1

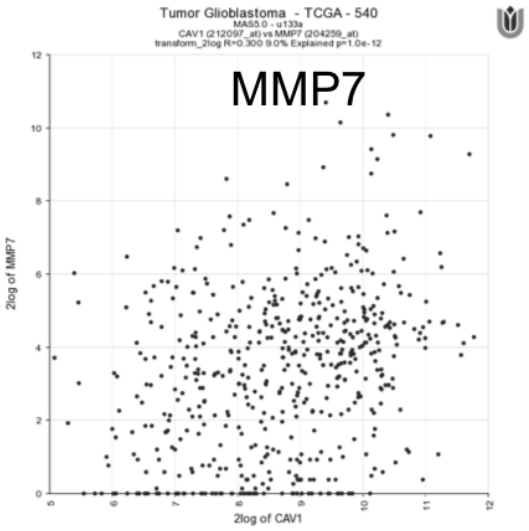
Tumor Glioblastoma - TCGA - 540
MAS5.0 - u133a
CAV1 (212097_at) vs MMP7 (204259_at)
transform_2log R=0.300 9.0% Explained p=1.0e-12
MMP7
2log of MMP7
2log of CAV1

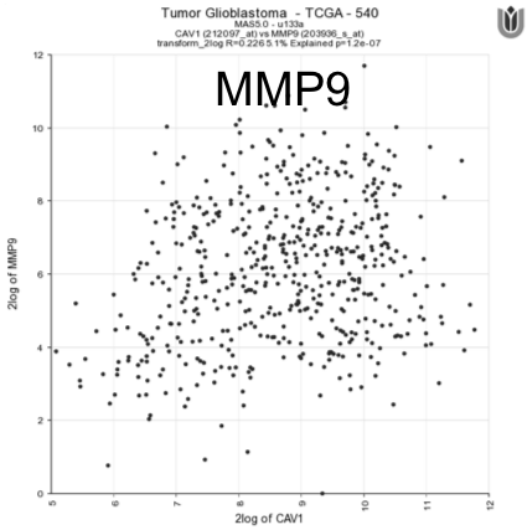
Tumor Glioblastoma - TCGA - 540
MAS5.0 - u133a
CAV1 (212097_at) vs MMP9 (203936_s_at)
transform_2log R=0.226 5.1% Explained p=1.2e-07
MMP9
2log of MMP9
2log of CAV1

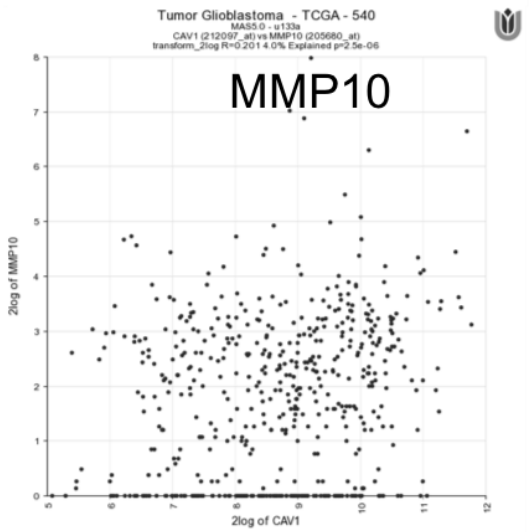
Tumor Glioblastoma - TCGA - 540
MAS5.0 - u133a
CAV1 (212097_at) vs MMP10 (205680_at)
transform_2log R=0.201 4.0% Explained p=2.5e-06
MMP10
2log of MMP10
2log of CAV1

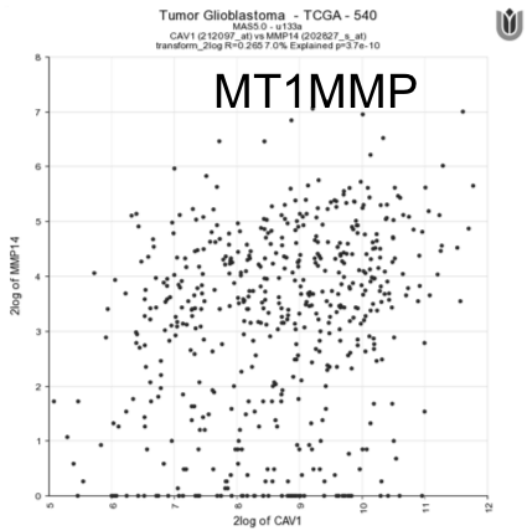
Tumor Glioblastoma - TCGA - 540
MAS5.0 - u133a
CAV1 (212097_at) vs MMP14 (202827_s_at)
transform_2log R=0.265 7.0% Explained p=3.7e-10
MT1MMP
2log of MMP14
2log of CAV1

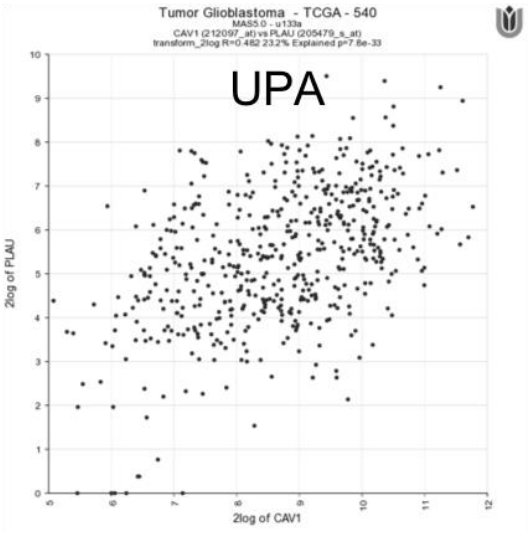
Tumor Glioblastoma - TCGA - 540
MAS5.0 - u133a
CAV1 (212097_at) vs PLAU (205479_s_at)
transform_2log R=0.482 23.2% Explained p=7.8e-33
UPA
2log of PLAU
2log of CAV1

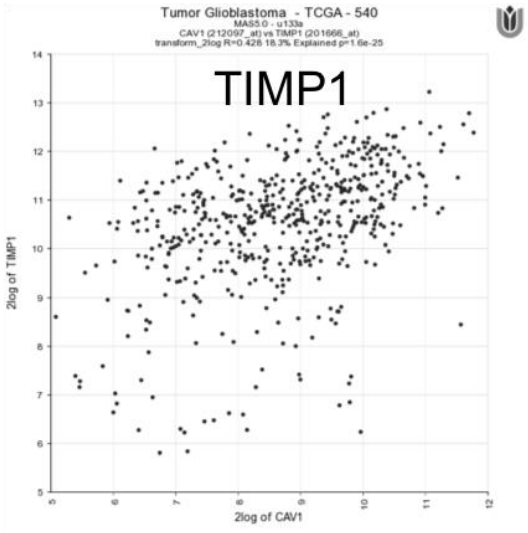
Tumor Glioblastoma - TCGA - 540
MAS5.0 - u133a
CAV1 (212097_at) vs TIMP1 (201666_at)
transform_2log R=0.426 18.3% Explained p=1.6e-25
TIMP1
2log of TIMP1
2log of CAV1

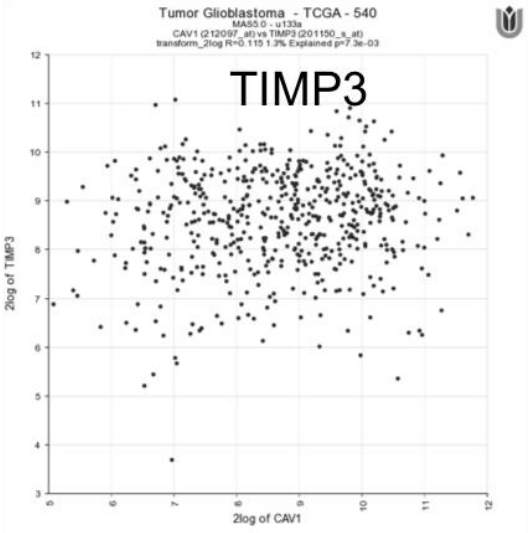
Tumor Glioblastoma - TCGA - 540
MAS5.0 - u133a
CAV1 (212097_at) vs TIMP3 (201150_s_at)
transform_2log R=0.115 1.3% Explained p=7.3e-03
TIMP3
2log of TIMP3
2log of CAV1

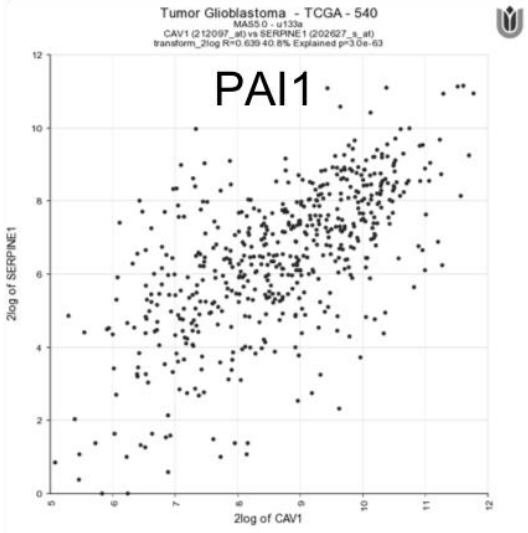
Tumor Glioblastoma - TCGA - 540
MAS5.0 - u133a
CAV1 (212097_at) vs SERPINE1 (202627_s_at)
transform_2log R=0.639 40.8% Explained p=3.0e-63
PAI1
2log of SERPINE1
2log of CAV1

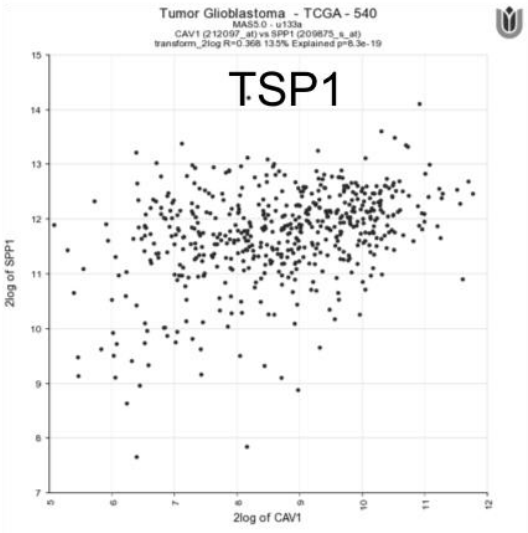
Tumor Glioblastoma - TCGA - 540
MAS5.0 - u133a
CAV1 (212097_at) vs SPP1 (209875_s_at)
transform_2log R=0.368 13.5% Explained p=8.3e-19
TSP1
2log of SPP1
2log of CAV1

APPENDIX 9: GENE EXPRESSION MAX_STAT CUT OFF

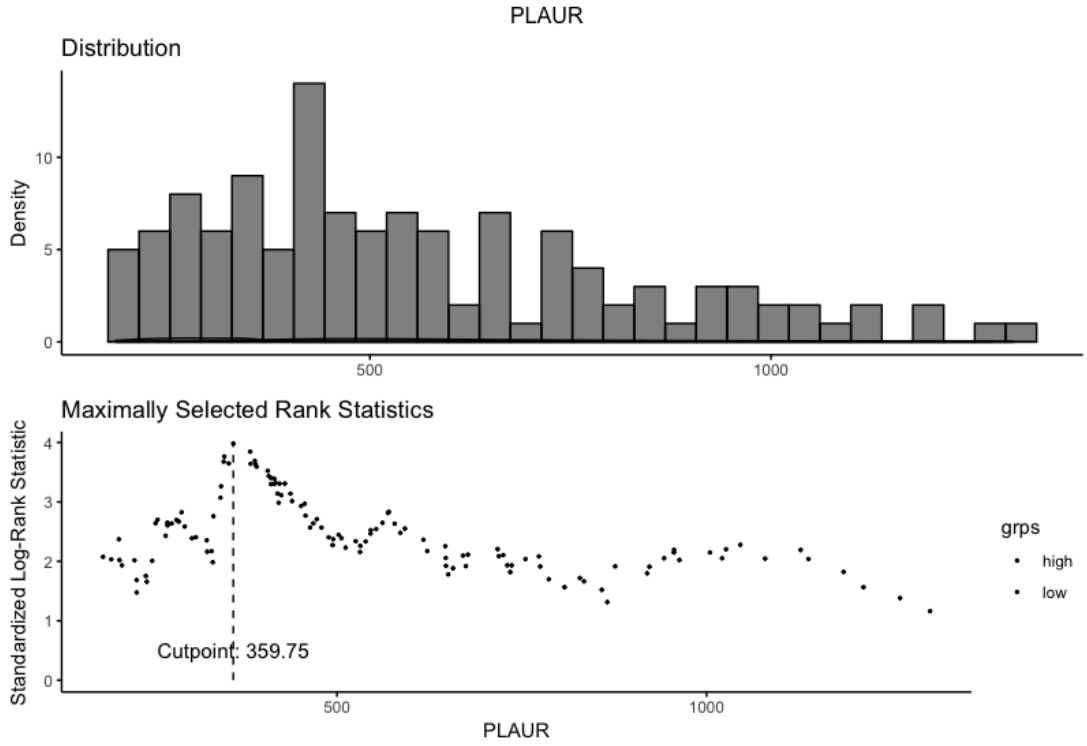

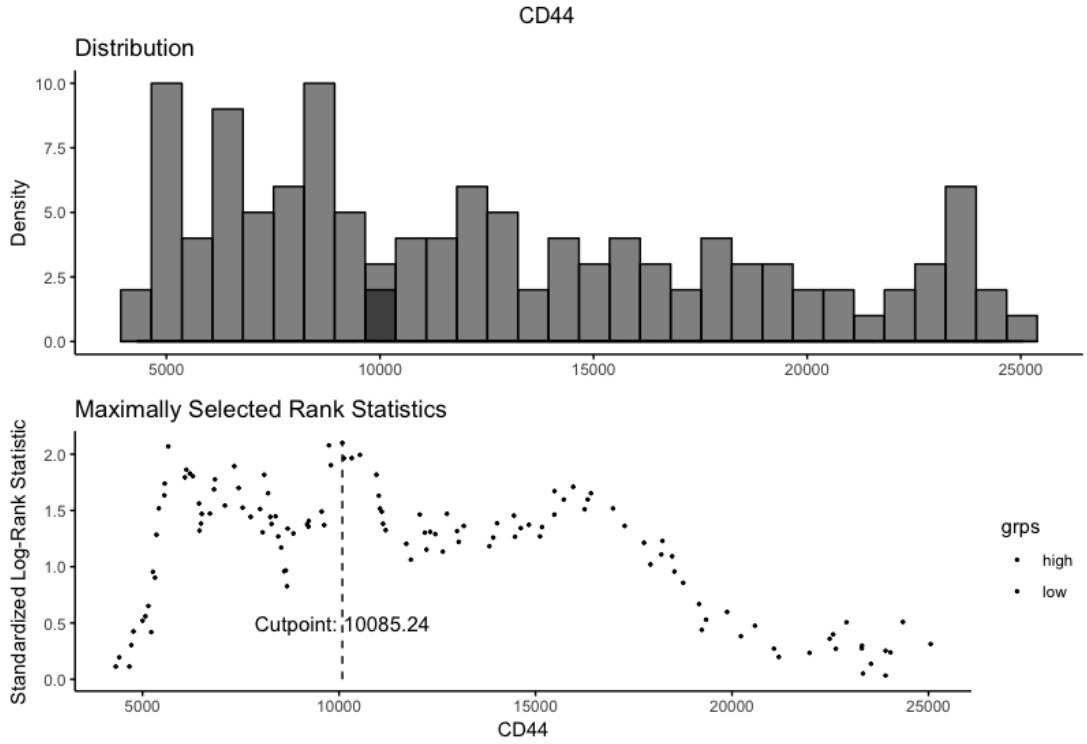

APPENDIX

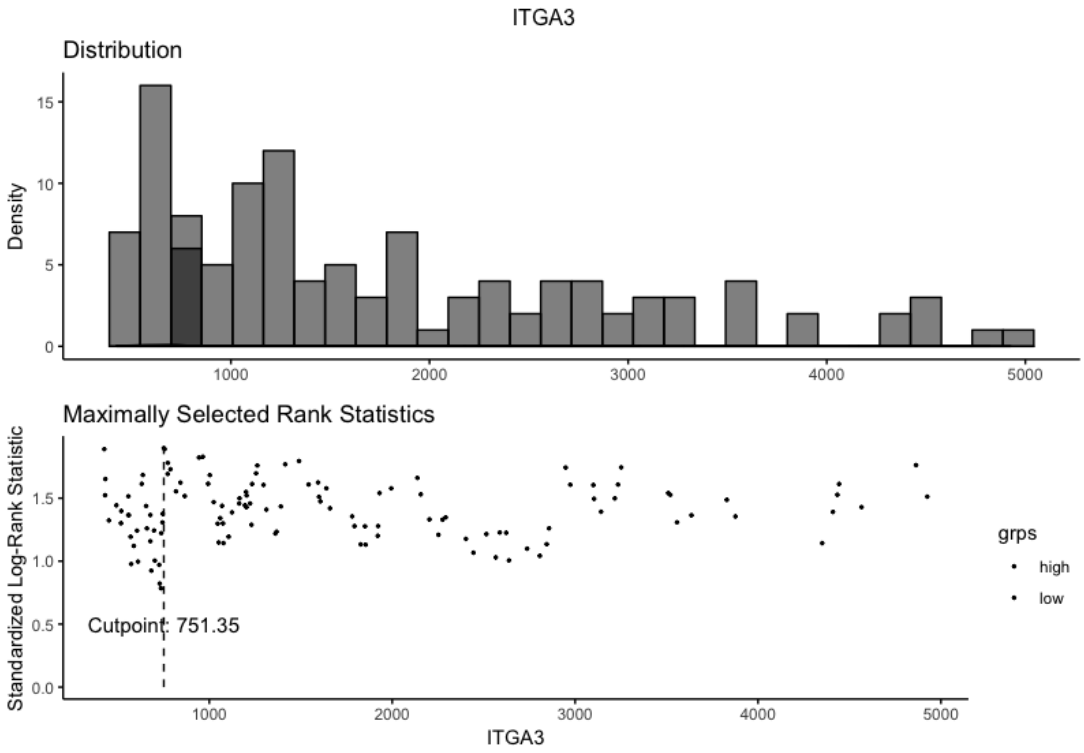
ITGA3
Distribution
Density
15
10
5
0
1000
2000
3000
4000
5000
Maximally Selected Rank Statistics
Standardized Log-Rank Statistic
1.5
1.0
0.5
0.0
Cutpoint: 751.35
grps
high
low
1000
2000
3000
4000
5000
ITGA3

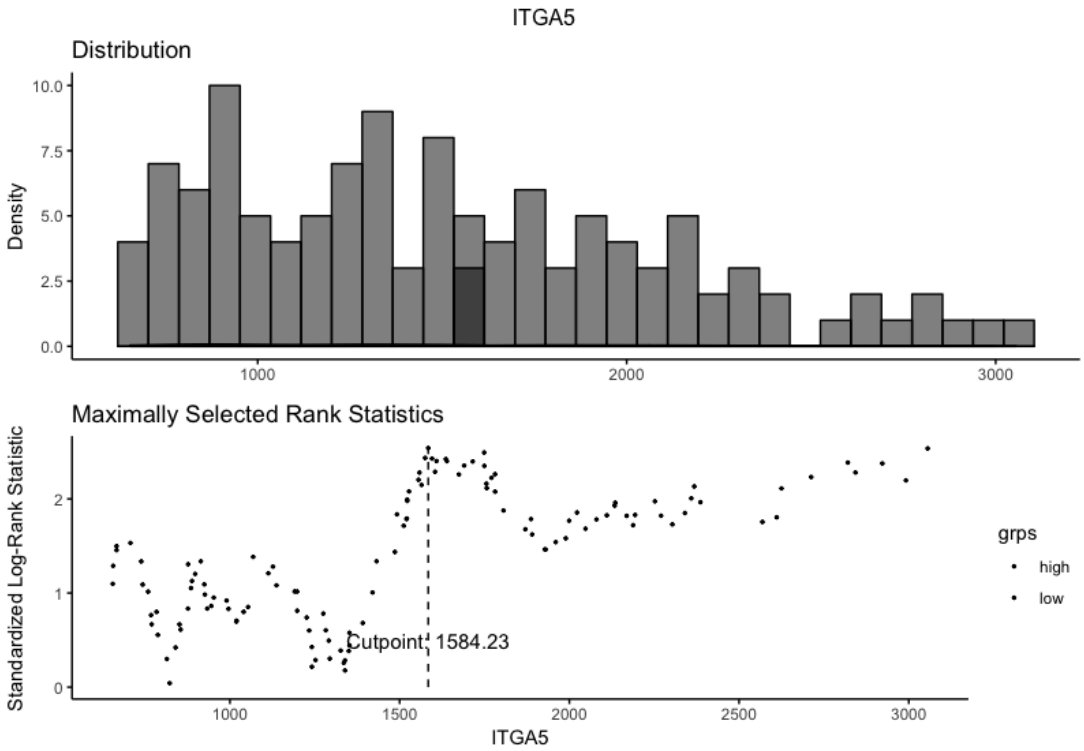
ITGA5
Distribution
Density
10.0
7.5
5.0
2.5
0.0
1000
2000
3000
Maximally Selected Rank Statistics
Standardized Log-Rank Statistic
2
1
0
Cutpoint: 1584.23
grps
high
low
1000
1500
2000
2500
3000
ITGA5

APPENDIX

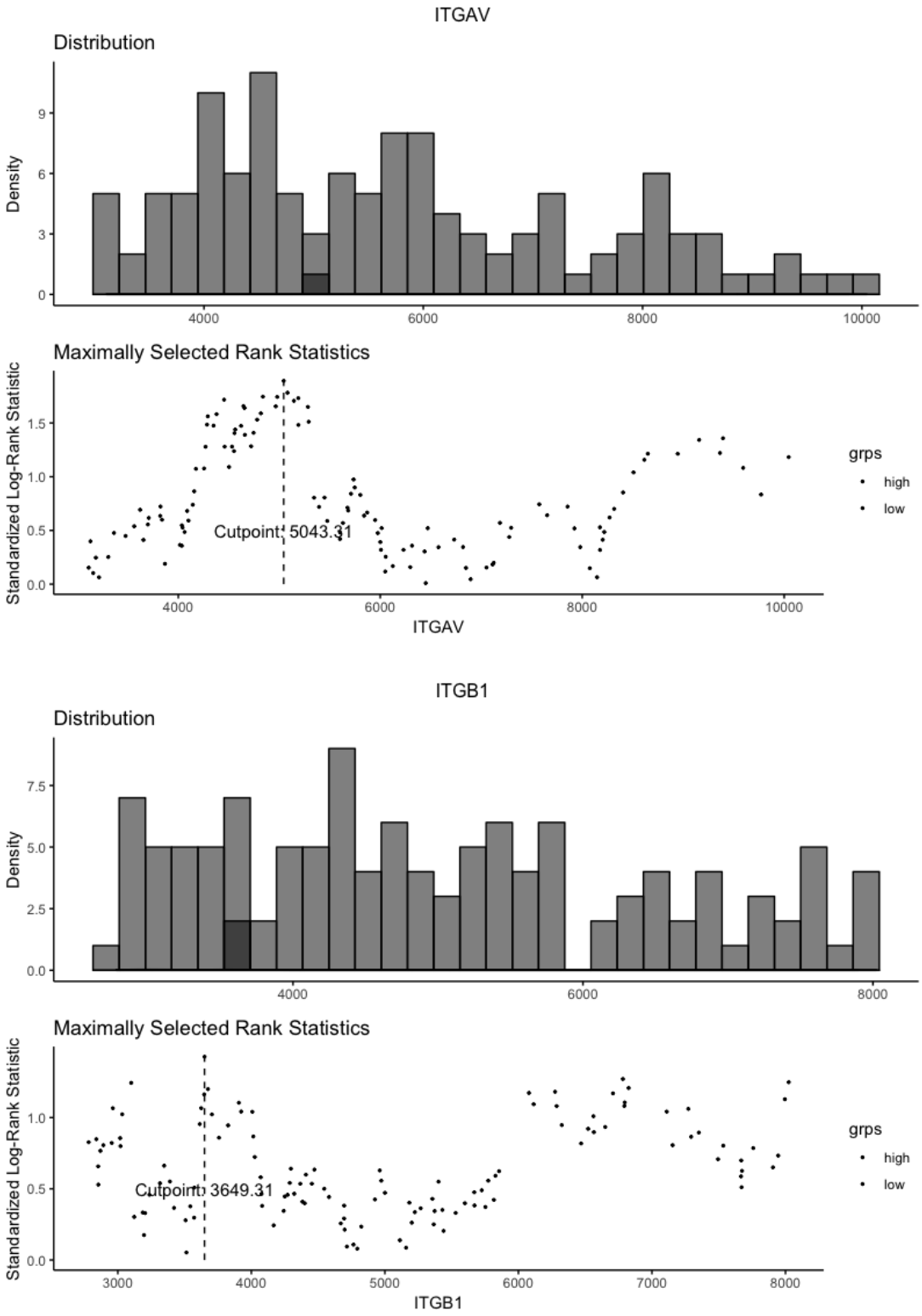
ITGAV
Distribution
Density
9
6
3
0
4000
6000
8000
10000
Maximally Selected Rank Statistics
Standardized Log-Rank Statistic
1.5
1.0
0.5
0.0
Cutpoint: 5043.31
4000
6000
8000
10000
ITGAV
grps
high
low
ITGB1
Distribution
Density
7.5
5.0
2.5
0.0
4000
6000
8000
Maximally Selected Rank Statistics
Standardized Log-Rank Statistic
1.0
0.5
0.0
Cutpoint: 3649.31
3000
4000
5000
6000
7000
8000
ITGB1
grps
high
low

APPENDIX

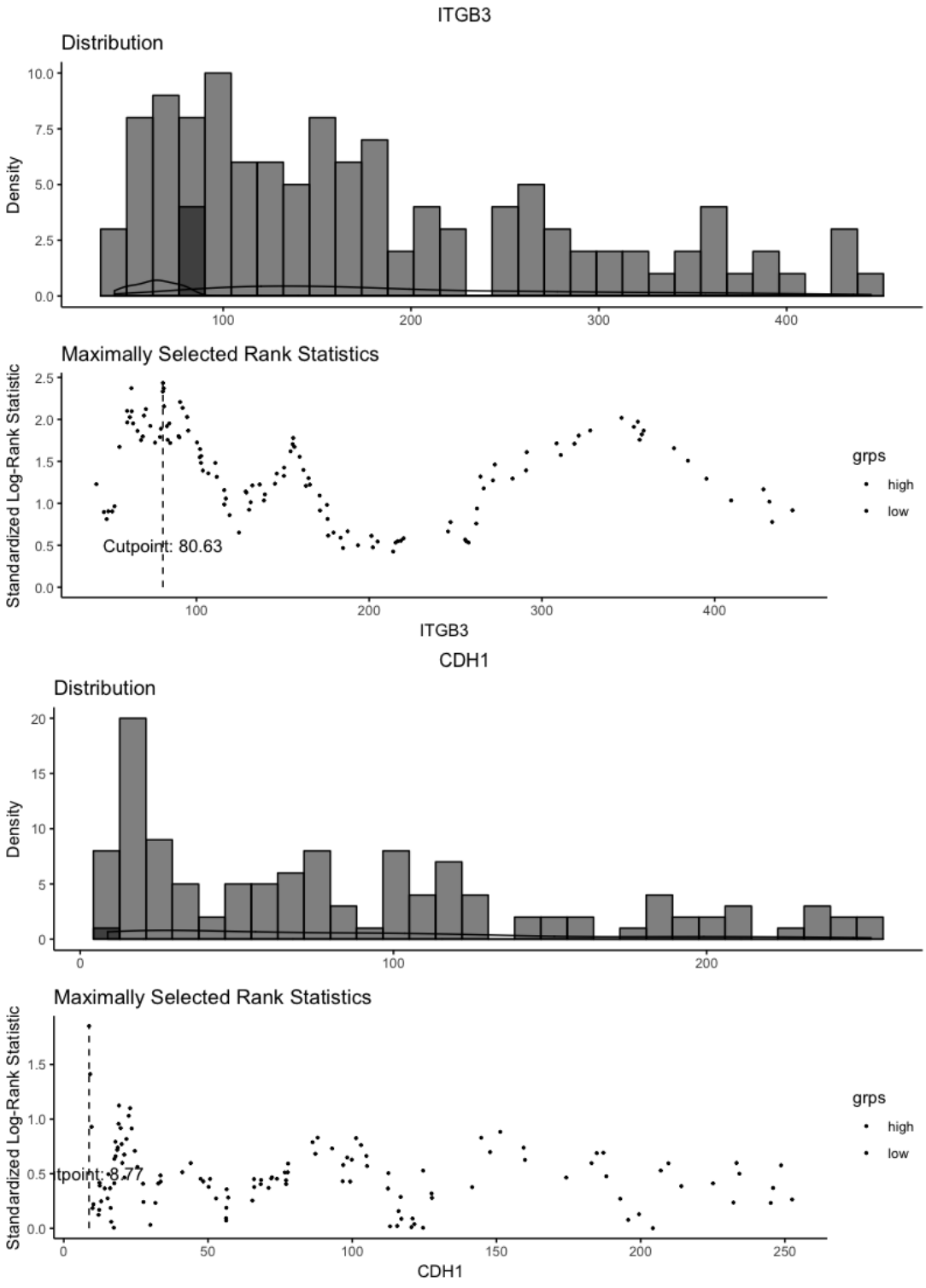
ITGB3
Distribution
Density
10.0
7.5
5.0
2.5
0.0
100
200
300
400
Maximally Selected Rank Statistics
Standardized Log-Rank Statistic
2.5
2.0
1.5
1.0
0.5
0.0
Cutpoint: 80.63
100
200
300
400
ITGB3
grps
high
low
CDH1
Distribution
Density
20
15
10
5
0
0
100
200
Maximally Selected Rank Statistics
Standardized Log-Rank Statistic
1.5
1.0
0.5
0.0
tpoint: 8.77
0
50
100
150
200
250
CDH1
grps
high
low

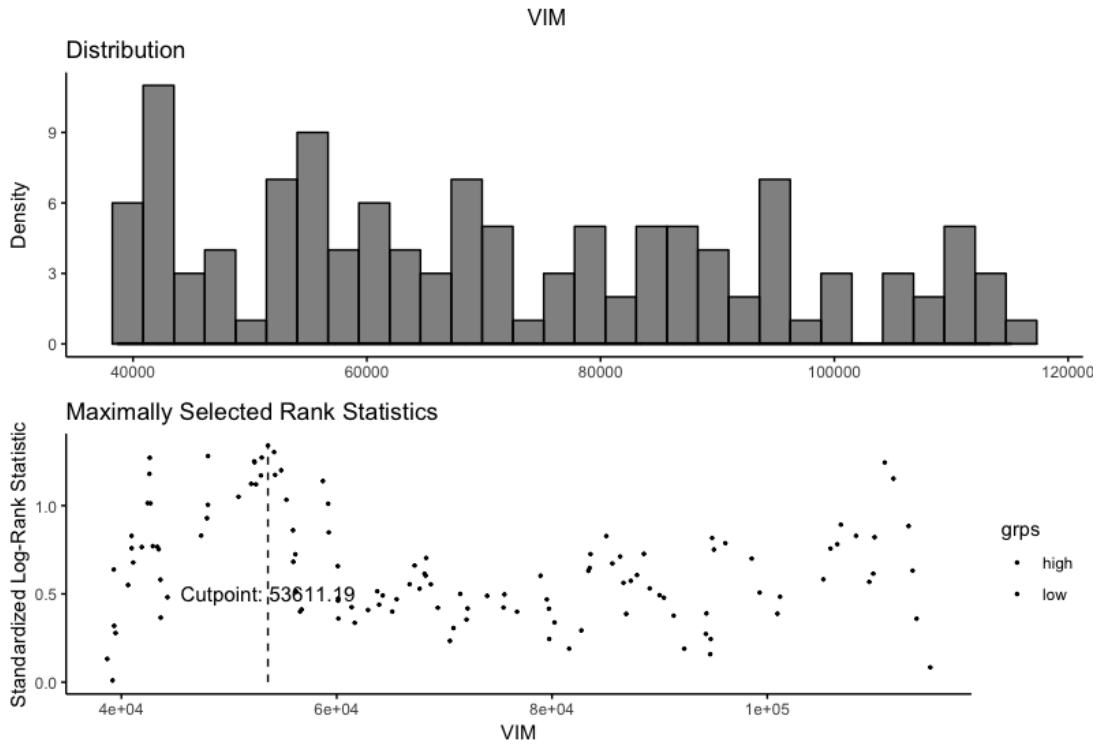
VIM
Distribution
Density
9
6
3
0
40000
60000
80000
100000
120000
Maximally Selected Rank Statistics
Standardized Log-Rank Statistic
1.0
0.5
0.0
Cutpoint: 53611.19
4e+04
6e+04
8e+04
1e+05
VIM
grps
high
low

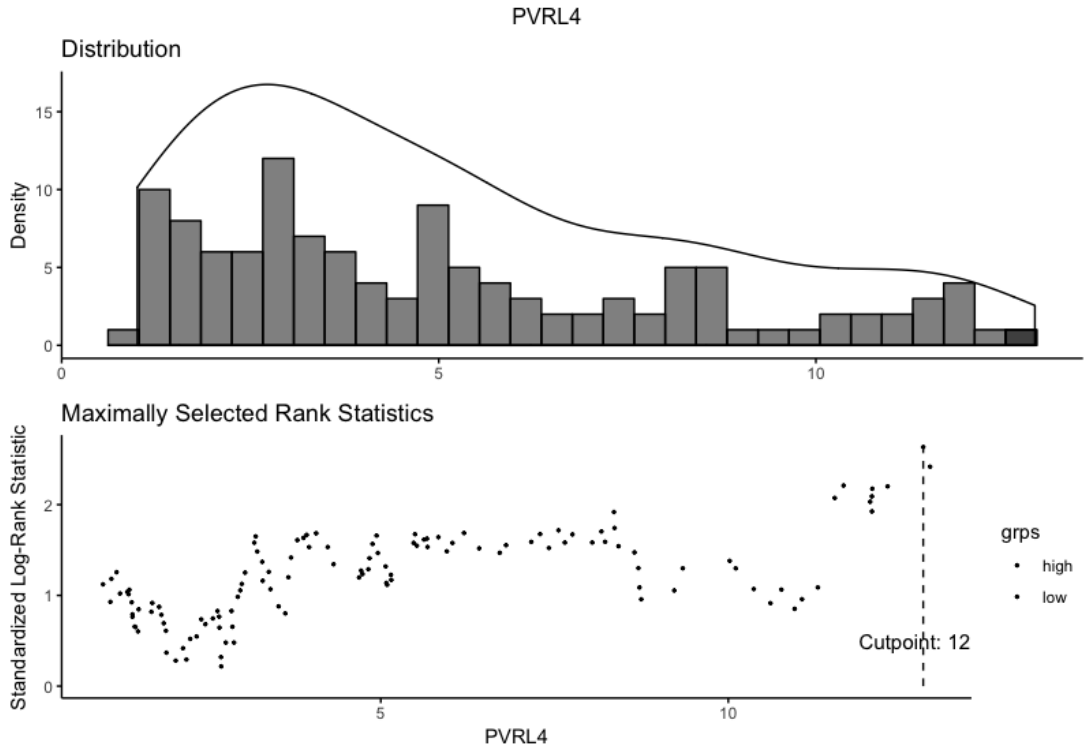
PVRL4
Distribution
Density
15
10
5
0
0
5
10
Maximally Selected Rank Statistics
Standardized Log-Rank Statistic
2
1
0
Cutpoint: 12
5
10
PVRL4
grps
high
low

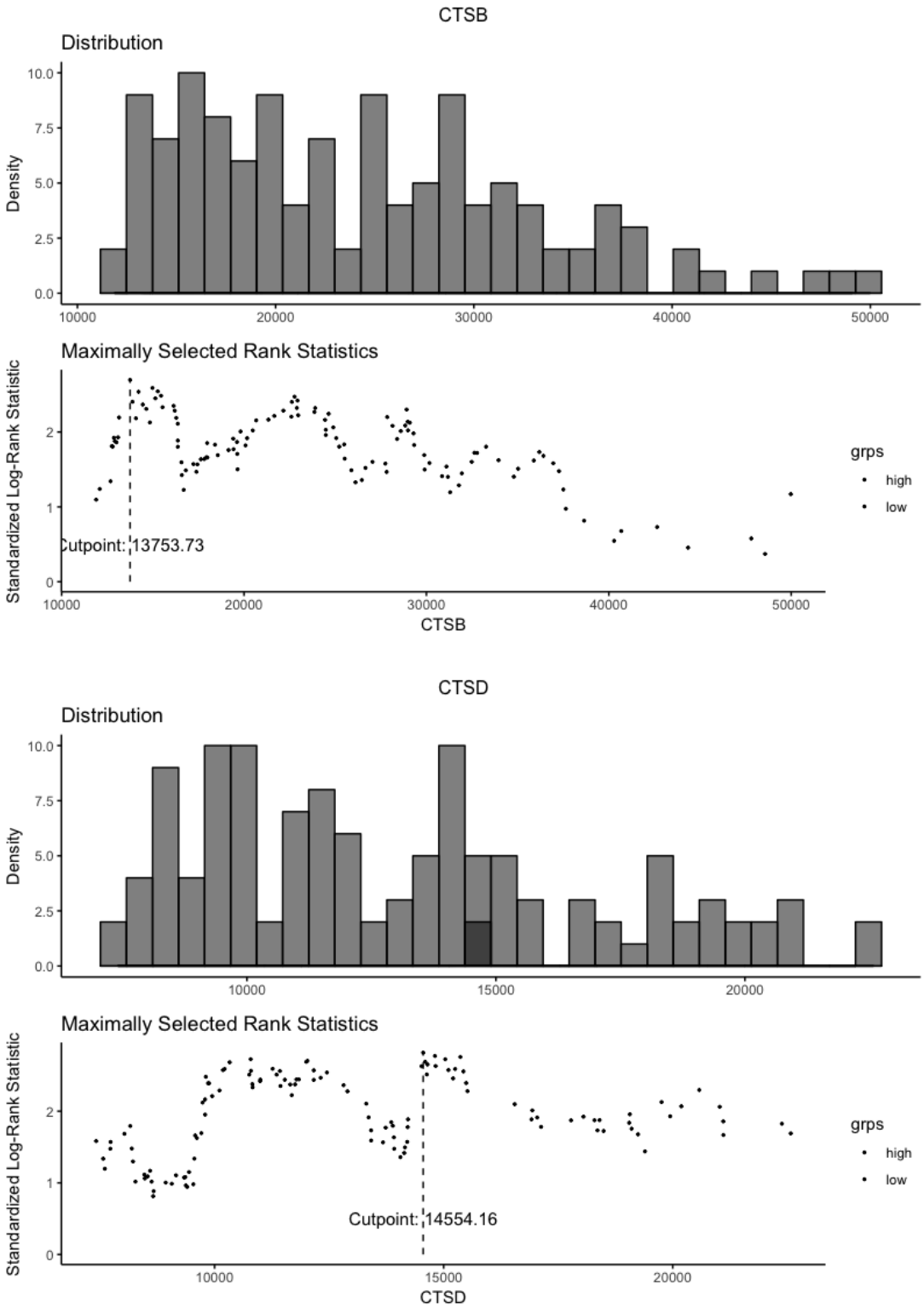
CTSB
Distribution
Density
10.0
7.5
5.0
2.5
0.0
10000
20000
30000
40000
50000
Maximally Selected Rank Statistics
Standardized Log-Rank Statistic
2
1
0
Cutpoint: 13753.73
grps
high
low
CTSB
CTSD
Distribution
Density
10.0
7.5
5.0
2.5
0.0
10000
15000
20000
Maximally Selected Rank Statistics
Standardized Log-Rank Statistic
2
1
0
Cutpoint: 14554.16
grps
high
low
CTSD

APPENDIX

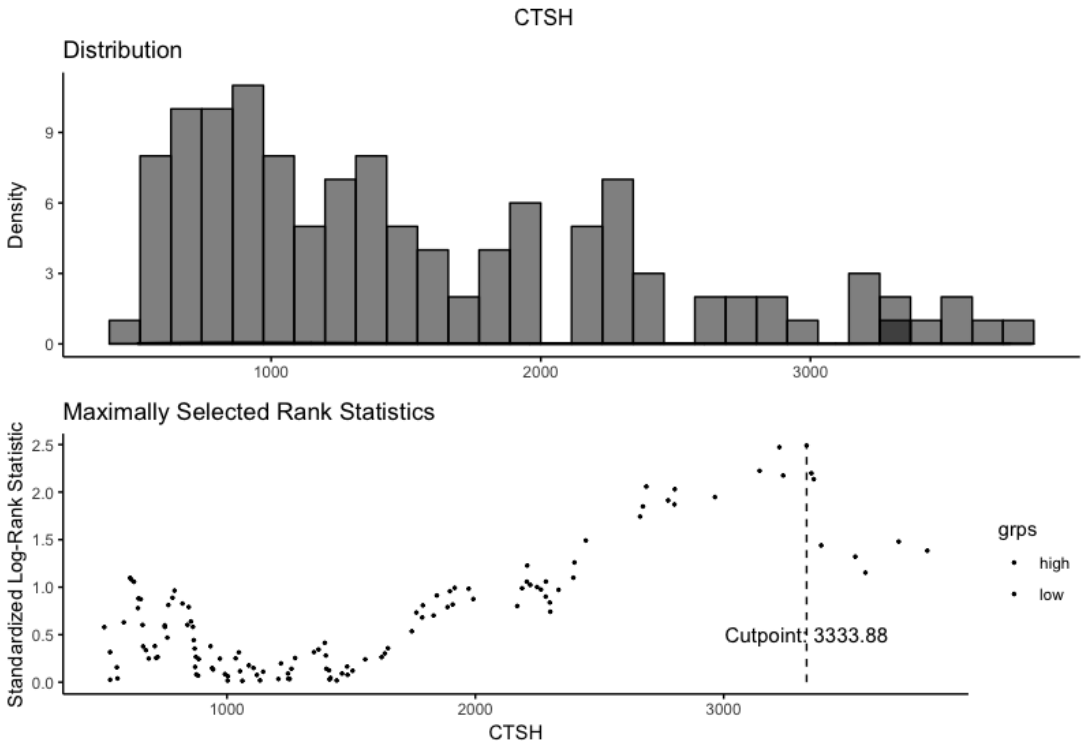
CTSH
Distribution
Density
0
3
6
9
1000
2000
3000
Maximally Selected Rank Statistics
Standardized Log-Rank Statistic
0.0
0.5
1.0
1.5
2.0
2.5
Cutpoint: 3333.88
grps
high
low
CTSH

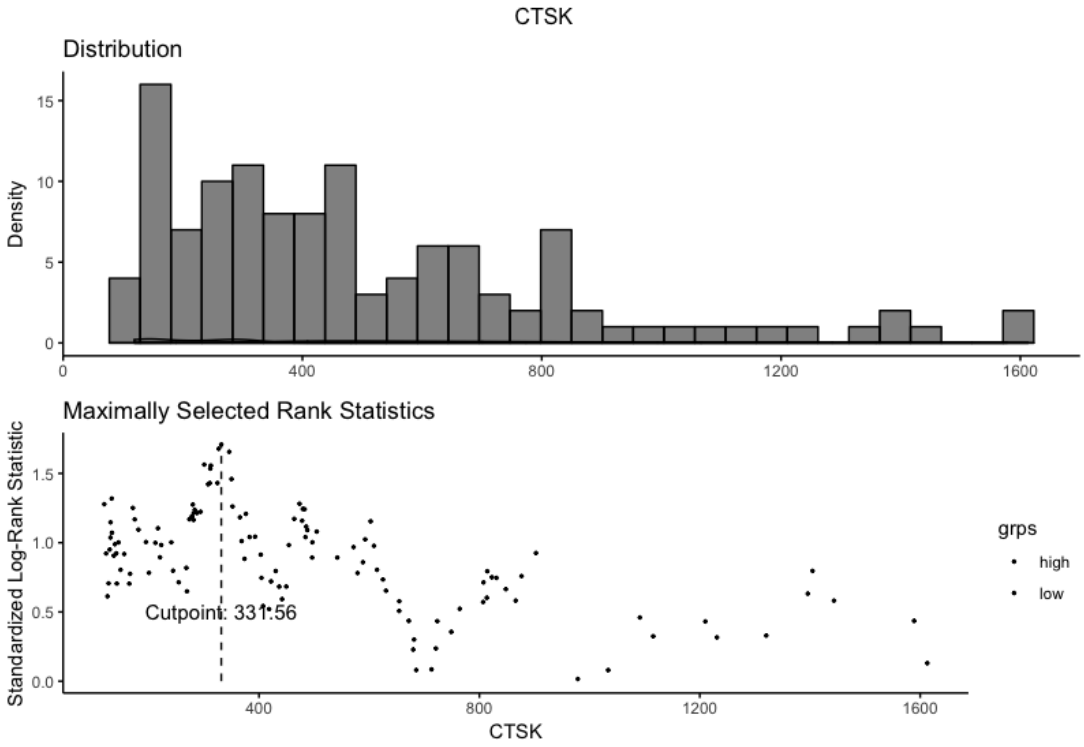
CTSK
Distribution
Density
0
5
10
15
0
400
800
1200
1600
Maximally Selected Rank Statistics
Standardized Log-Rank Statistic
0.0
0.5
1.0
1.5
Cutpoint: 331.56
grps
high
low
CTSK

APPENDIX

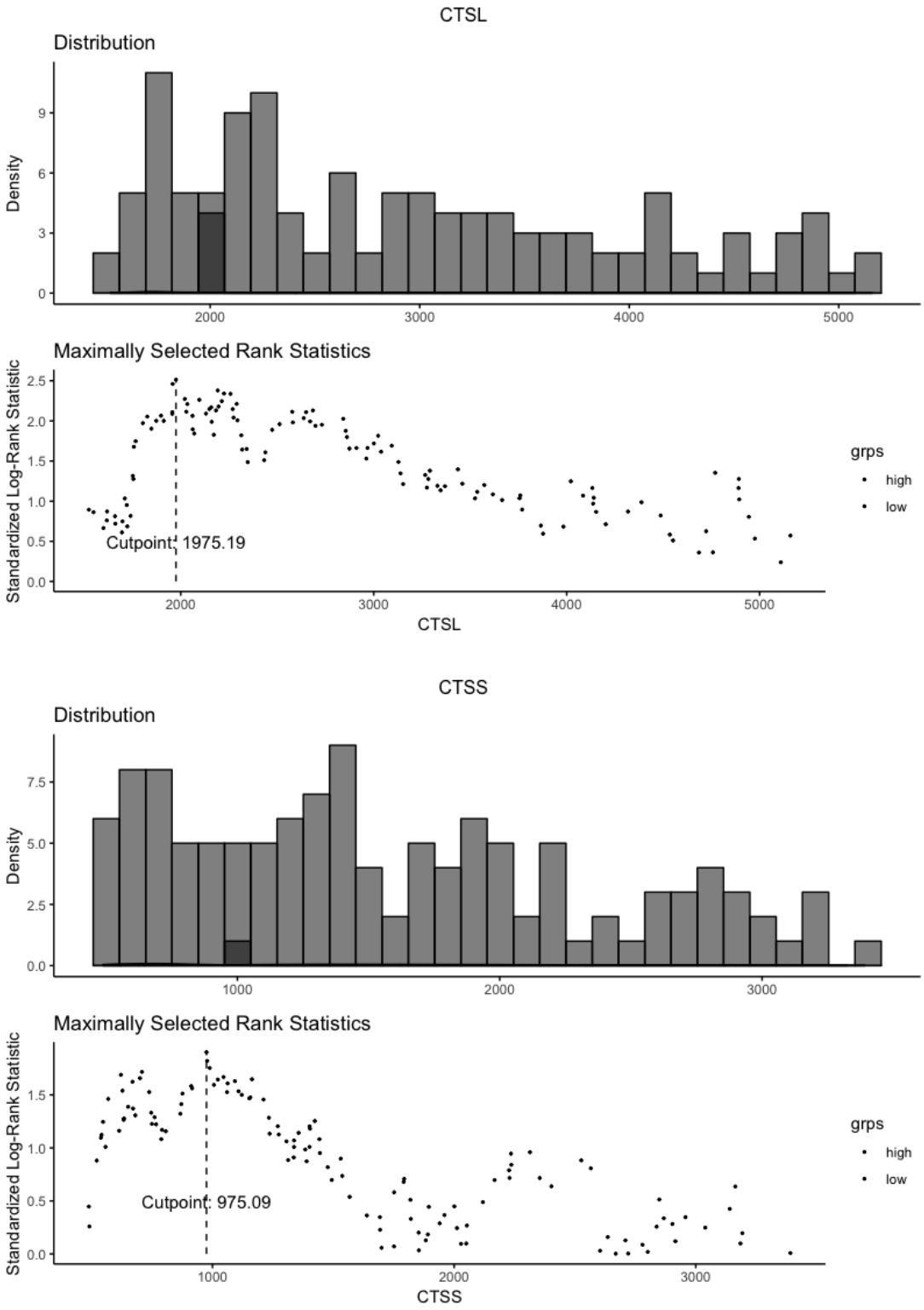
CTSL
Distribution
Density
9
6
3
0
2000
3000
4000
5000
Maximally Selected Rank Statistics
Standardized Log-Rank Statistic
2.5
2.0
1.5
1.0
0.5
0.0
Cutpoint: 1975.19
2000
3000
4000
5000
CTSL
grps
high
low
CTSS
Distribution
Density
7.5
5.0
2.5
0.0
1000
2000
3000
Maximally Selected Rank Statistics
Standardized Log-Rank Statistic
1.5
1.0
0.5
0.0
Cutpoint: 975.09
1000
2000
3000
CTSS
grps
high
low

APPENDIX

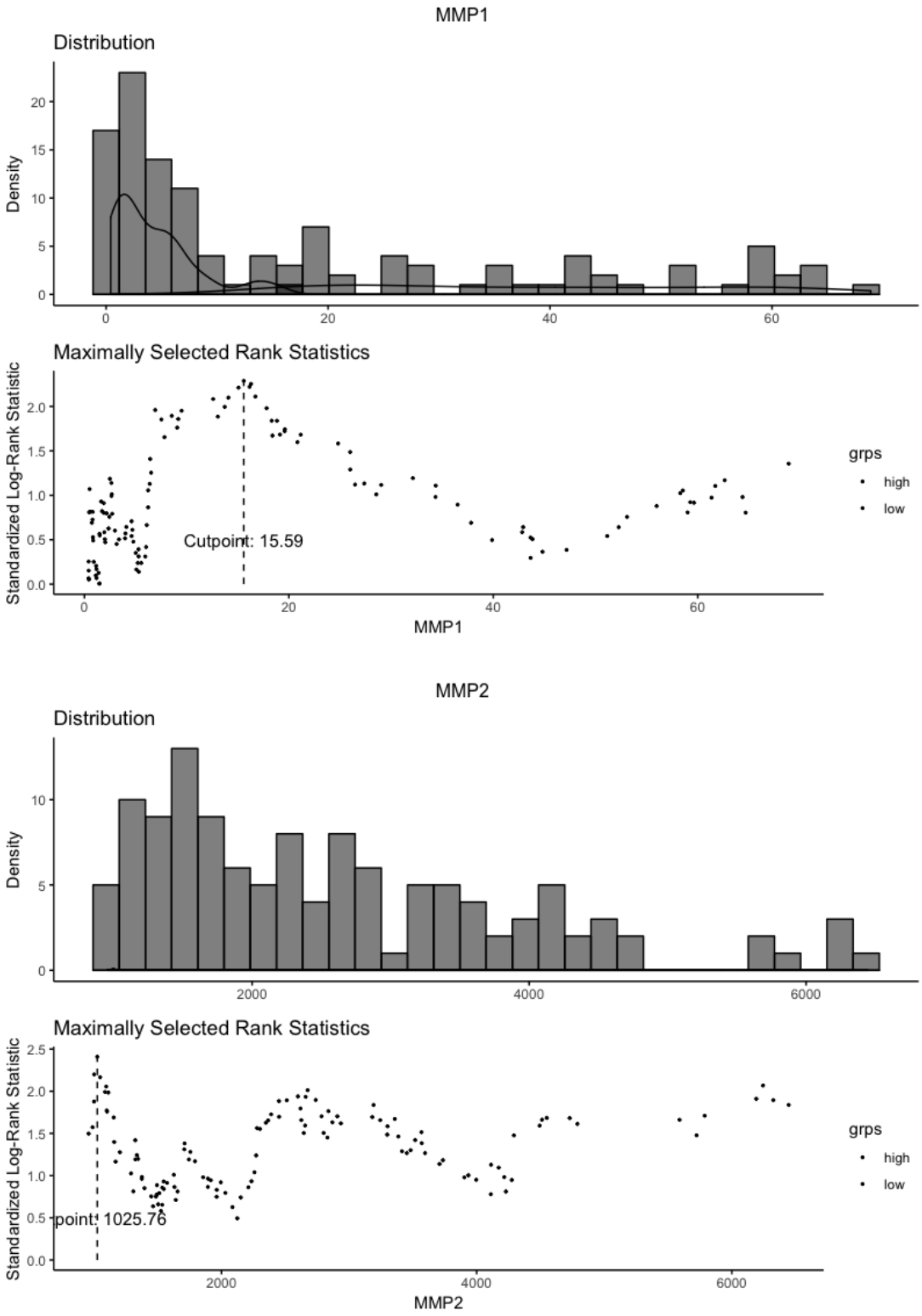
MMP1
Distribution
Density
0
5
10
15
20
0
20
40
60
Maximally Selected Rank Statistics
Standardized Log-Rank Statistic
0.0
0.5
1.0
1.5
2.0
Cutpoint: 15.59
0
20
40
60
MMP1
grps
high
low
MMP2
Distribution
Density
0
5
10
2000
4000
6000
Maximally Selected Rank Statistics
Standardized Log-Rank Statistic
0.0
0.5
1.0
1.5
2.0
2.5
point: 1025.76
2000
4000
6000
MMP2
grps
high
low

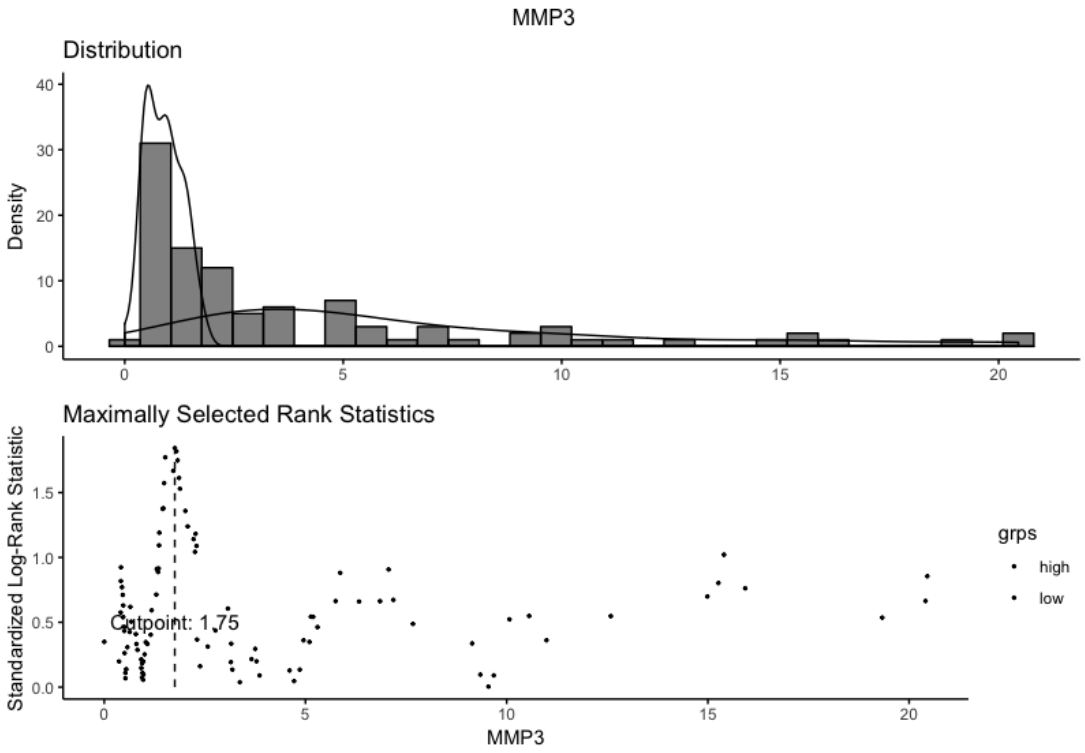
MMP3
Distribution
Density
Maximally Selected Rank Statistics
Standardized Log-Rank Statistic
Cutpoint: 1.75
MMP3
grps
high
low

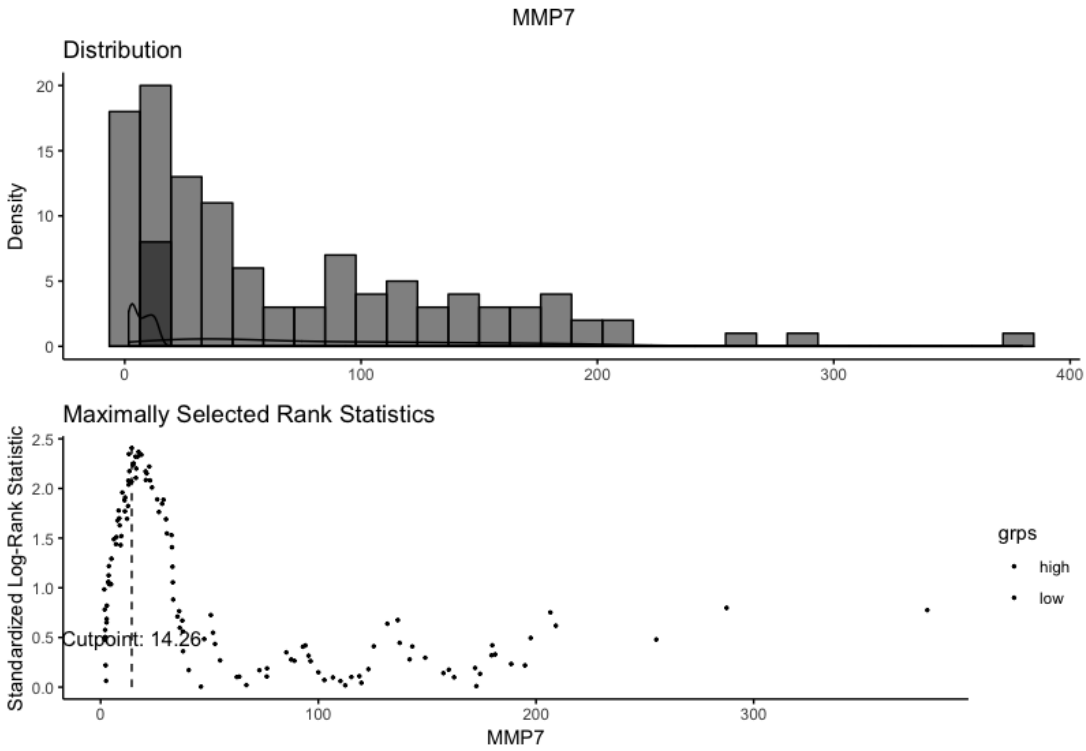
MMP7
Distribution
Density
Maximally Selected Rank Statistics
Standardized Log-Rank Statistic
Cutpoint: 14.26
MMP7
grps
high
low

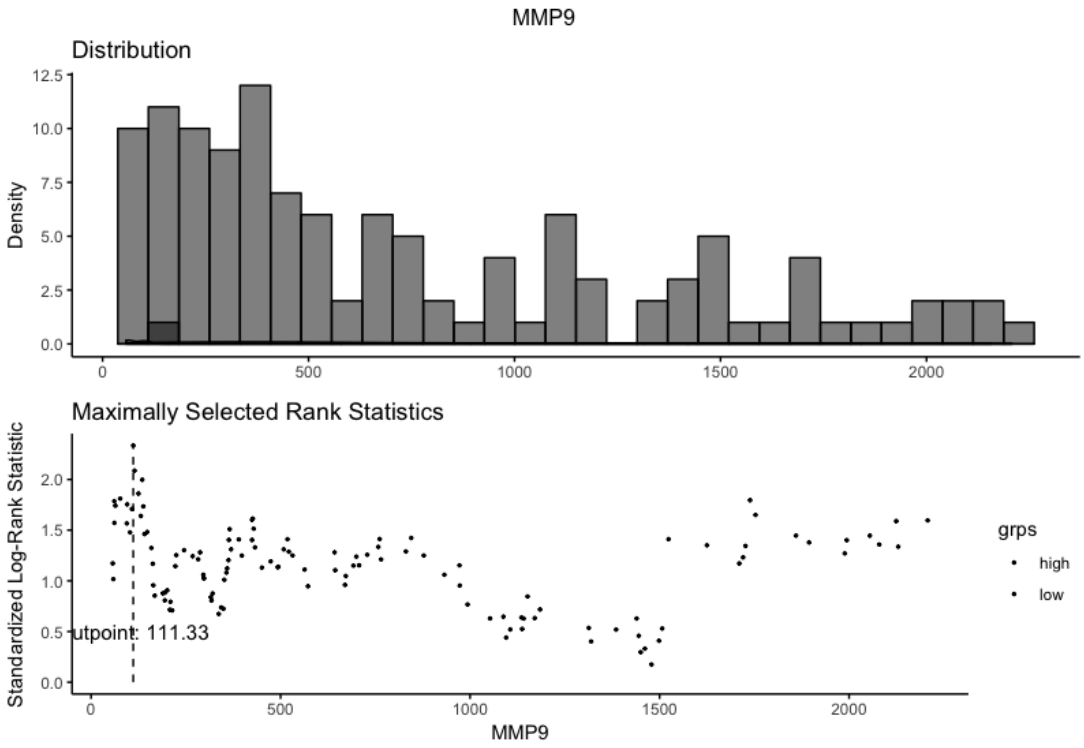
MMP9
Distribution
Density
12.5
10.0
7.5
5.0
2.5
0.0
0
500
1000
1500
2000
Maximally Selected Rank Statistics
Standardized Log-Rank Statistic
2.0
1.5
1.0
0.5
0.0
utpoint: 111.33
0
500
1000
1500
2000
MMP9
grps
high
low

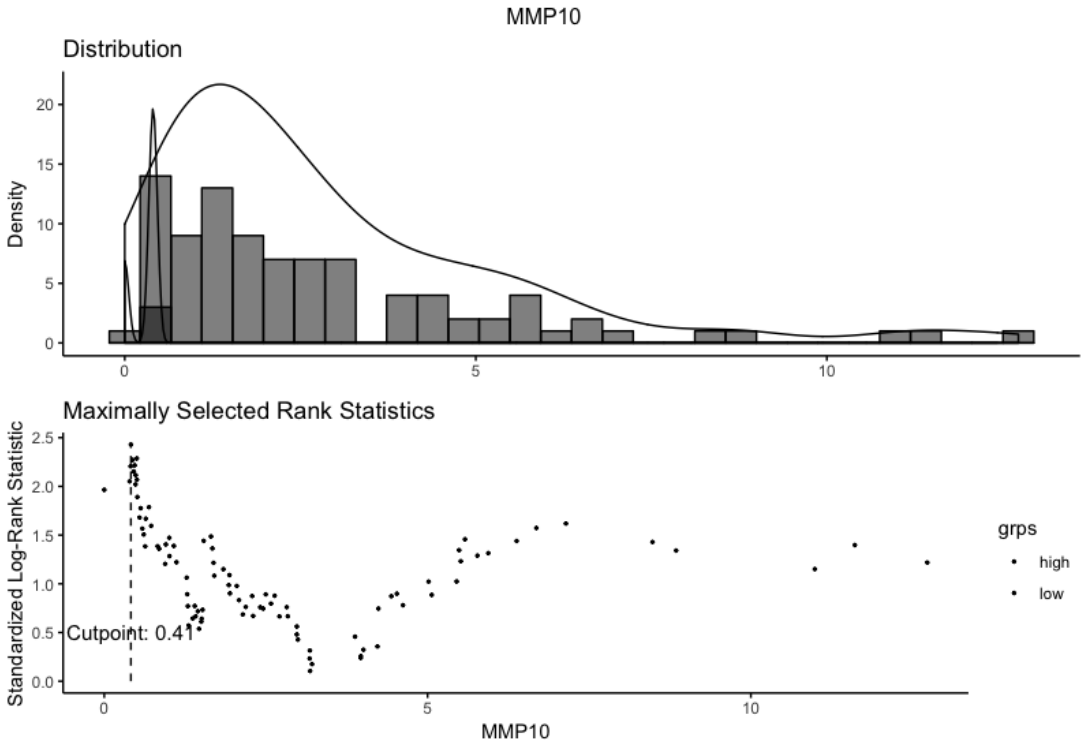
MMP10
Distribution
Density
20
15
10
5
0
0
5
10
Maximally Selected Rank Statistics
Standardized Log-Rank Statistic
2.5
2.0
1.5
1.0
0.5
0.0
Cutpoint: 0.41
0
5
10
MMP10
grps
high
low

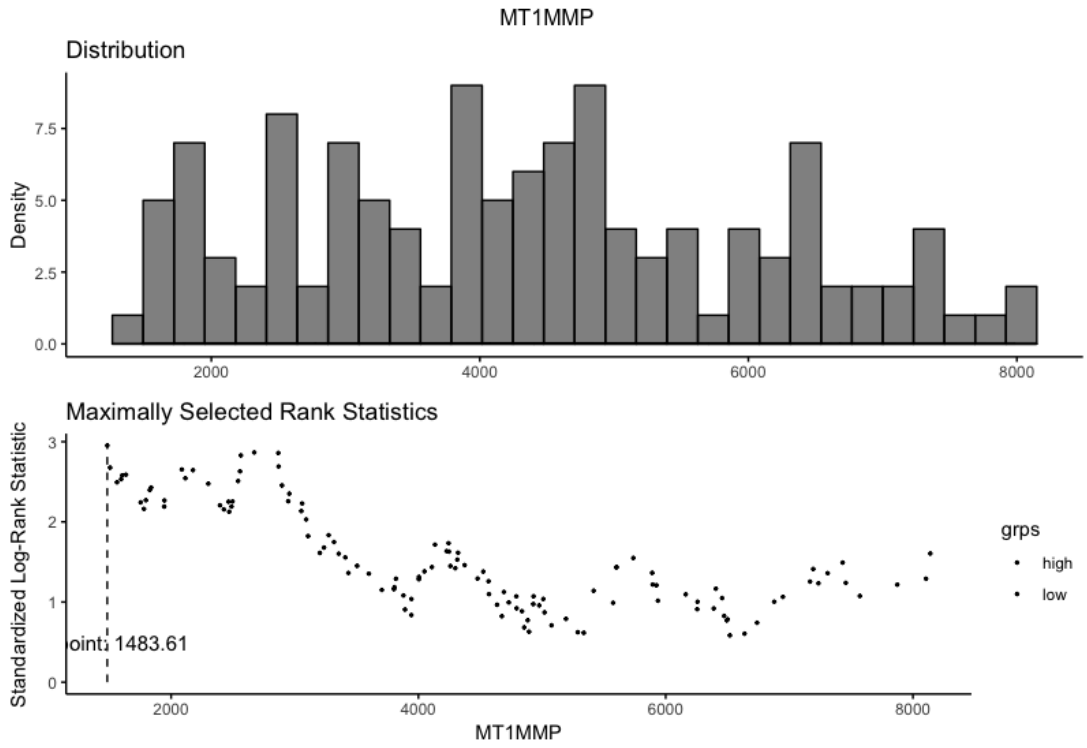
MT1MMP
Distribution
Density
7.5
5.0
2.5
0.0
2000
4000
6000
8000
Maximally Selected Rank Statistics
Standardized Log-Rank Statistic
3
2
1
0
oint: 1483.61
2000
4000
6000
8000
MT1MMP
grps
high
low

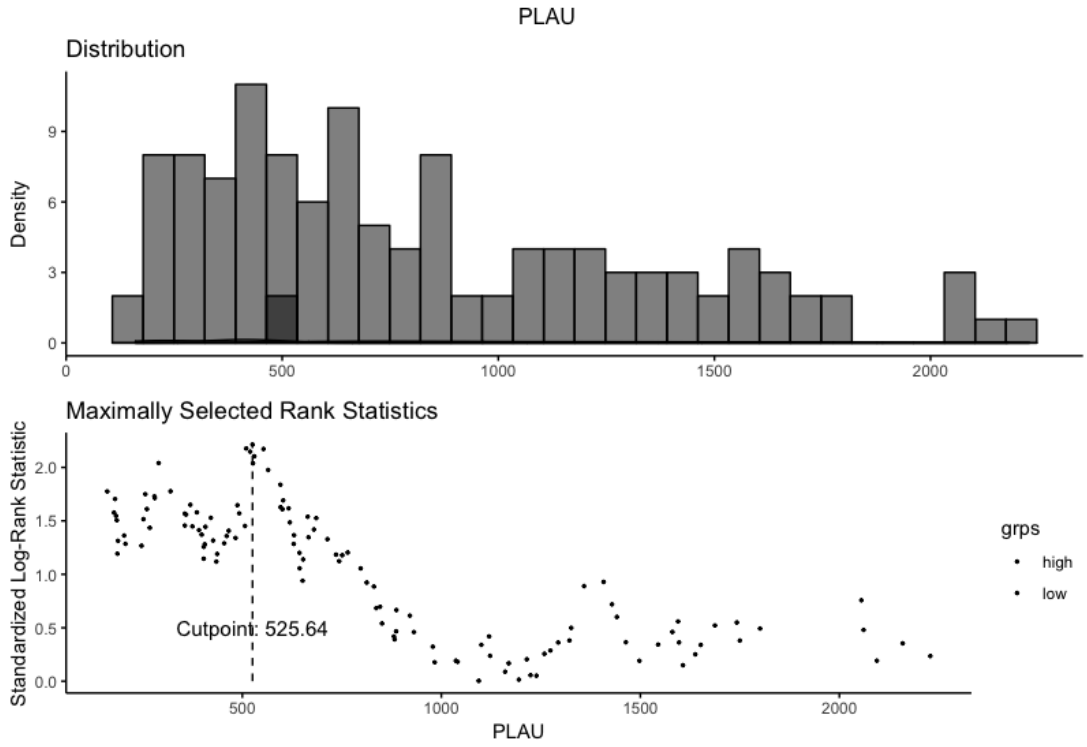
PLAU
Distribution
Density
9
6
3
0
0
500
1000
1500
2000
Maximally Selected Rank Statistics
Standardized Log-Rank Statistic
2.0
1.5
1.0
0.5
0.0
Cutpoint: 525.64
500
1000
1500
2000
PLAU
grps
high
low

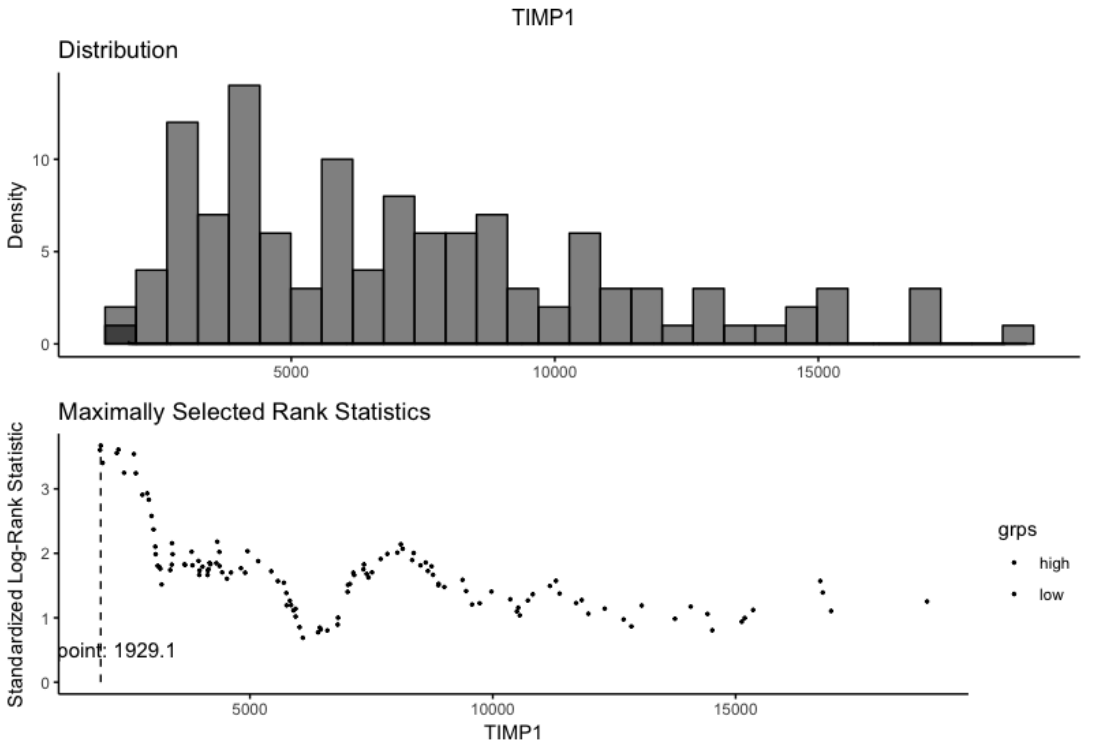
TIMP1
Distribution
Density
10
5
0
5000
10000
15000
Maximally Selected Rank Statistics
Standardized Log-Rank Statistic
3
2
1
0
oint: 1929.1
5000
10000
15000
TIMP1
grps
high
low

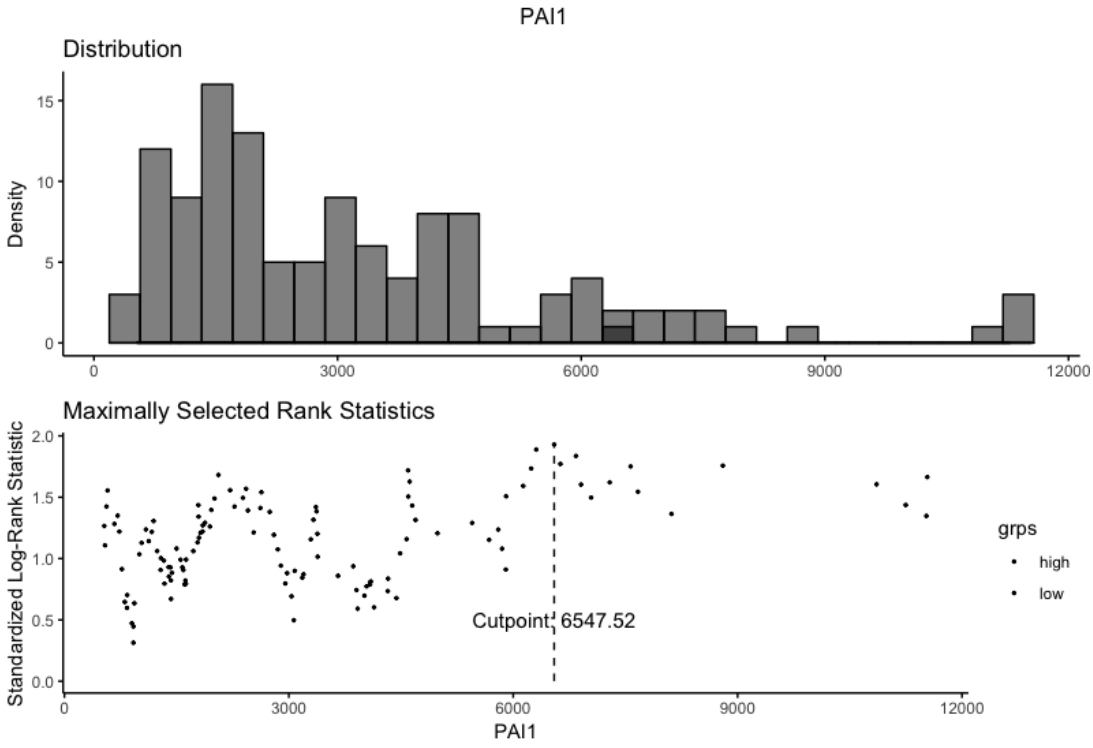
PAI1
Distribution
Density
15
10
5
0
0
3000
6000
9000
12000
Maximally Selected Rank Statistics
Standardized Log-Rank Statistic
2.0
1.5
1.0
0.5
0.0
Cutpoint: 6547.52
0
3000
6000
9000
12000
PAI1
grps
high
low

APPENDIX

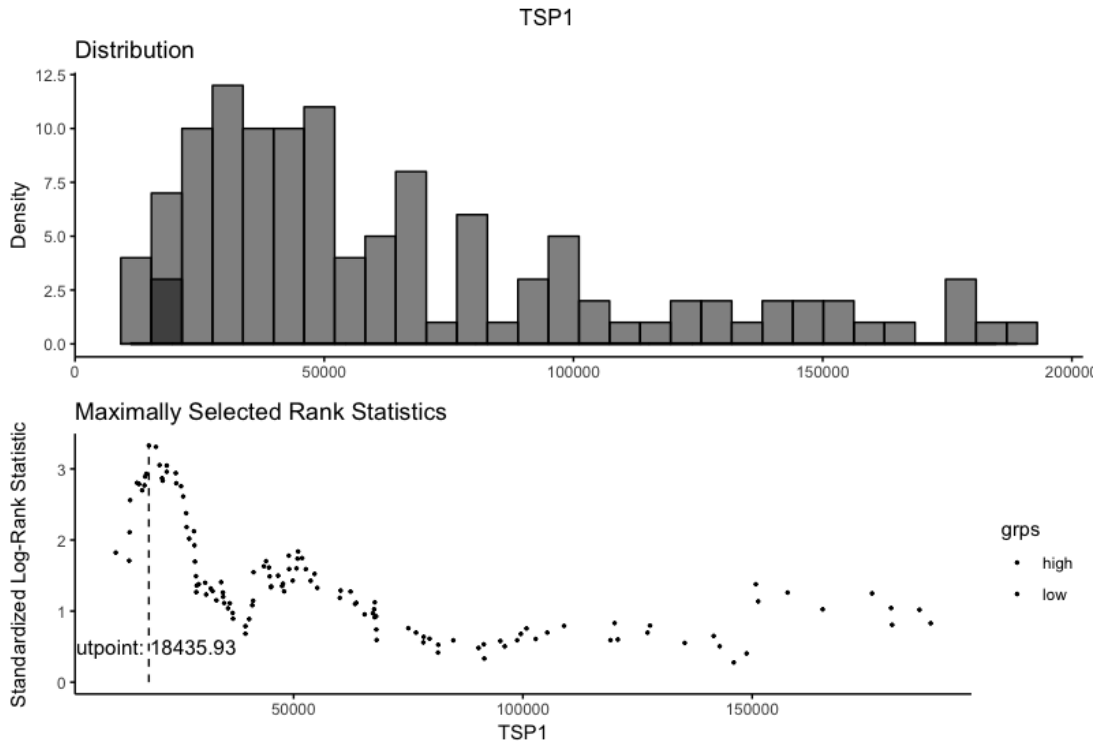
TSP1
Distribution
Density
12.5
10.0
7.5
5.0
2.5
0.0
0
50000
100000
150000
Maximally Selected Rank Statistics
Standardized Log-Rank Statistic
3
2
1
0
utpoint: 18435.93
50000
100000
150000
TSP1
grps
high
low

APPENDIX 10: COPYRIGHT PERMISSIONS

Figure no.	Authors	Year	DOI.	Permission
1.1	Gervasio	2011	10.1242/jcs.084376	Yes
1.7	Huse	2011	10.1002/glia.21165	Yes
1.8	De Sousa	2013	10.1038/embor.2013.92	Yes
1.9	Parker	2015	10.3389/fonc.2015.00055	Yes
1.12	Goldberg	2013	10.5772/54980	Yes
1.14	Friedl	2012	10.1038/ncb2548	Yes
1.15	Lau	2013	10.1038/nrn3550	Yes
1.19	Box	2013	10.1016/J.EJCA.2013.03.011	Yes
1.20	Kramer	2013	10.1016/j.mrrev.2012.08.001	Yes
4.3	Stein	2007	10.1529/biophysj.106.093468	Yes
4.4	Friedrich	2009	10.1038/nprot.2008.226	Yes
4.5	De Wever	2010	10.1387/ijdb.092948ow	Yes
4.6	Naber	2011	10.3791/3337	Yes
4.7	Vinci	2012	10.1186/1741-7007-10-29	Yes
4.8	Blacher	2014	10.1371/journal.pone.0097019	Yes
5.57	Demou	2010	10.1007/s10439-010-0097-0	Yes

APPENDIX 11: LIST OF PUBLICATIONS, ORAL PRESENTATIONS AND AWARDS

7.1.17

7.1.18 PUBLICATIONS

Moriconi, C, Palmieri, V, Tornillo, G, Fillmore H, Pilkington, G, Gumbleton, M . Caveolin-1, a driver of invasive phenotype in in-vitro 3D-spheroid assays comprised of high grade GBM cells association with an AKT-inhibited phenotype. January 2018 Neuro-Oncology 20(suppl_1):i13-i13.DOI10.1093/neuonc/nox238.058

Moriconi, C, Palmieri, V, Di Santo, R, Tornillo, G, Papi, M, Pilkington, G, De Spirito, M & Gumbleton, M 2017, 'INSIDIA: a FIJI macro delivering high-throughput and high-content spheroid invasion analysis' Biotechnology Journal. DOI: 10.1002/biot.201700140.

Moriconi, C, Palmieri, V, Tornillo, G, Fillmore H, Pilkington, G, Gumbleton, M . Pp80. Caveolin-1 implicated as a pro-invasive gene in high-grade glioma cell models: implementation of a 3d spheroid matrix invasion assay. January 2017 Neuro-Oncology 19(suppl_1):i21-i22. DOI10.1093/neuonc/now293.080

7.1.19 AWARDS

Best Poster Award at the BNOS2016 Conference. Leeds, UK. Poster title: Caveolin-1 implicated as a pro-invasive gene in high-grade glioma cell models: Implementation of a 3D spheroid matrix invasion assay.

Best Poster Award at the Research Day 2016, School of Pharmacy and Pharmaceutical Sciences, Cardiff University, UK. Poster title: Caveolin-1 implicated as a pro-invasive gene in high-grade glioma cell models: Implementation of a 3D spheroid matrix invasion assay.

7.1.20 CONFERENCES

BNOS 2017 “Engaging Science Enhancing Survival”, Edinburgh, UK (21-23 June 2017)

GIF 2017 “Glioma Invasion Forum”, with talk contribution, Piran, (23-25 April 2017)

BNOS 2016 “trials, technologies and T cells”, Leeds, UK (29 June-1 July 2016)

“Tumour Microenvironment and Signalling” EMBL Symposium (3-6 April 2016)

II International Symposium on Clinical and Basic Investigation in Glioblastoma (9-12 September 2015, Toledo, ES)

BNOS 2015 “Neuro-oncology across the ages” (1-3 July 2015 Nottingham, UK)

BIBLIOGRAPHY

Aaberg-Jessen, C., Christensen, K., Offenberg, H., Bartels, A., Dreehsen, T., Hansen, S., … Kristensen, B. W. (2009). Low expression of tissue inhibitor of metalloproteinases-1 (TIMP-1) in glioblastoma predicts longer patient survival. *Journal of Neuro-Oncology*, *95*(1), 117–128. https://doi.org/10.1007/s11060-009-9910-8

Abbracchio, M. P., & Ceruti, S. (2006). Roles of P2 receptors in glial cells: focus on astrocytes. *Purinergic Signalling*, *2*(4), 595–604. https://doi.org/10.1007/s11302-006-9016-0

Abulrob, A., Giuseppin, S., Andrade, M. F., McDermid, A., Moreno, M., & Stanimirovic, D. (2004). Interactions of EGFR and caveolin-1 in human glioblastoma cells: evidence that tyrosine phosphorylation regulates EGFR association with caveolae. *Oncogene*, *23*(41), 6967–6979. https://doi.org/10.1038/sj.onc.1207911

Adamson, C., Kanu, O. O., Mehta, A. I., Di, C., Lin, N., Mattox, A. K., & Bigner, D. D. (2009). Glioblastoma multiforme: a review of where we have been and where we are going. *Expert Opinion on Investigational Drugs*, *18*(8), 1061–1083. https://doi.org/10.1517/13543780903052764

Aghdassi, A. A., John, D. S., Sendler, M., Weiss, F. U., Reinheckel, T., Mayerle, J., & Lerch, M. M. (2018). Cathepsin D regulates cathepsin B activation and disease severity predominantly in inflammatory cells during experimental pancreatitis. *The Journal of Biological Chemistry*, *293*(3), 1018–1029. https://doi.org/10.1074/jbc.M117.814772

Aigner, A. (2006). Delivery Systems for the Direct Application of siRNAs to Induce RNA Interference (RNAi) In Vivo. *Journal of Biomedicine and Biotechnology*, *2006*(4), 1–15. https://doi.org/10.1155/JBB/2006/71659

Akiyama, Y., Jung, S., Salhia, B., Lee, S., Hubbard, S., Taylor, M., … Rutka, J. T. (2001). Hyaluronate receptors mediating glioma cell migration and proliferation. *Journal of Neuro-Oncology*, *53*(2), 115–127. Retrieved from http://www.ncbi.nlm.nih.gov/pubmed/11716065

Alberts, B., Johnson, A., Lewis, J., Raff, M., Roberts, K., & Walter, P. (2002). Molecular Biology of the Cell. Garland Science.

Allawi, H. T., & Santalucia, J. (1997). Thermodynamics and NMR of internal G·T

mismatches in DNA. *Biochemistry*, *36*(34), 10581–10594. https://doi.org/10.1021/bi962590c

Altschul, S. F., Gish, W., Miller, W., Myers, E. W., & Lipman, D. J. (1990). Basic local alignment search tool. *Journal of Molecular Biology*, *215*(3), 403–410. https://doi.org/10.1016/S0022-2836(05)80360-2

Andersson, U., Schwartzbaum, J., Wiklund, F., Sjöström, S., Liu, Y., Tsavachidis, S., … Melin, B. (2010). A comprehensive study of the association between the EGFR and ERBB2 genes and glioma risk. *Acta Oncologica*, *49*(6), 767–775. https://doi.org/10.3109/0284186X.2010.480980

Andreasen, P., Kjoller, L., Christensen, L., & Duffy, M. (1997). The urokinase-type plasminogen activator system in cancer metastasis: A review. *International Journal of Cancer*, *72*(1), 1–22. https://doi.org/10.1002/(SICI)1097-0215(19970703)72:1<1::AID-IJC1>3.0.CO;2-Z

Annabi, B., Lachambre, M., Bousquet-Gagnon, N., Pagé, M., Gingras, D., & Béliveau, R. (2001). Localization of membrane-type 1 matrix metalloproteinase in caveolae membrane domains. *The Biochemical Journal*, *353*(Pt 3), 547–553. Retrieved from http://www.pubmedcentral.nih.gov/articlerender.fcgi?artid=1221600&tool=pmcentrez&rendertype=abstract

Annabi, B., Thibeault, S., Moumdjian, R., & Béliveau, R. (2004). Hyaluronan cell surface binding is induced by type I collagen and regulated by caveolae in glioma cells. *The Journal of Biological Chemistry*, *279*(21), 21888–21896. https://doi.org/10.1074/jbc.M313694200

Bao, S., Wu, Q., McLendon, R. E., Hao, Y., Shi, Q., Hjelmeland, A. B., … Rich, J. N. (2006). Glioma stem cells promote radioresistance by preferential activation of the DNA damage response. *Nature*, *444*(7120), 756–760. https://doi.org/10.1038/nature05236

Barrangou, R., Fremaux, C., Deveau, H., Richards, M., Boyaval, P., Moineau, S., … Horvath, P. (2007). CRISPR Provides Acquired Resistance Against

Viruses in Prokaryotes. *Science*, *315*(5819), 1709–1712. https://doi.org/10.1126/science.1138140

Barresi, V., Buttarelli, F. R., Vitarelli, E. E., Arcella, A., Antonelli, M., & Giangaspero, F. (2009). Caveolin-1 expression in diffuse gliomas: correlation with the proliferation index, epidermal growth factor receptor, p53, and 1p/19q status. *Human Pathology*, *40*(12), 1738–1746. https://doi.org/10.1016/j.humpath.2009.04.026

Beck, B., & Blanpain, C. (2013). Unravelling cancer stem cell potential. *Nature Reviews. Cancer*, *13*(10), 727–738. https://doi.org/10.1038/nrc3597

Behlke, M. A. (2006). Progress towards in Vivo Use of siRNAs. *Molecular Therapy*, *13*(4), 644–670. https://doi.org/10.1016/j.ymthe.2006.01.001

Bellail, A. C., Hunter, S. B., Brat, D. J., Tan, C., & Van Meir, E. G. (2004). Microregional extracellular matrix heterogeneity in brain modulates glioma cell invasion. *The International Journal of Biochemistry & Cell Biology*, *36*(6), 1046–1069. https://doi.org/10.1016/j.biocel.2004.01.013

Bignami, A., Hosley, M., & Dahl, D. (1993). Hyaluronic acid and hyaluronic acid-binding proteins in brain extracellular matrix. *Anatomy and Embryology*, *188*(5), 419–433. Retrieved from http://www.ncbi.nlm.nih.gov/pubmed/7508695

Blacher, S., Erpicum, C., Lenoir, B., Paupert, J., Moraes, G., Ormenese, S., … Noel, A. (2014). Cell invasion in the spheroid sprouting assay: A spatial organisation analysis adaptable to cell behaviour. *PLoS ONE*, *9*(5), 1–10. https://doi.org/10.1371/journal.pone.0097019

Blasi, F., & Carmeliet, P. (2002). uPAR: A versatile signalling orchestrator. *Nature Reviews Molecular Cell Biology*. https://doi.org/10.1038/nrm977

Boettcher, M., & McManus, M. T. (2015). Choosing the Right Tool for the Job: RNAi, TALEN, or CRISPR. *Molecular Cell*, *58*(4), 575–585. https://doi.org/10.1016/j.molcel.2015.04.028

Bosher, J. M., & Labouesse, M. (2000). RNA interference: genetic wand and genetic watchdog. *Nature Cell Biology*, *2*(2), E31–E36. https://doi.org/10.1038/35000102

Box, C., Mendiola, M., Gowan, S., Box, G. M., Valenti, M., Brandon, A. D. H., … Eccles, S. A. (2013). A novel serum protein signature associated with resistance to epidermal growth factor receptor tyrosine kinase inhibitors in head and neck squamous cell carcinoma. *European Journal of Cancer*, *49*(11), 2512–2521. https://doi.org/10.1016/j.ejca.2013.03.011

Brennan, C. W., Verhaak, R. G. W., McKenna, A., Campos, B., Noushmehr, H., Salama, S. R., … McLendon, R. (2013). The somatic genomic landscape of glioblastoma. *Cell*, *155*(2), 462–477. https://doi.org/10.1016/j.cell.2013.09.034

Brösicke, N., & Faissner, A. (2015). Role of tenascins in the ECM of gliomas. *Cell Adhesion & Migration*, *9*(1–2), 131–140. https://doi.org/10.1080/19336918.2014.1000071

Brouns, S. J. J., Jore, M. M., Lundgren, M., Westra, E. R., Slijkhuis, R. J. H., Snijders, A. P. L., … van der Oost, J. (2008). Small CRISPR RNAs Guide Antiviral Defense in Prokaryotes. *Science*, *321*(5891), 960–964. https://doi.org/10.1126/science.1159689

Burgener, R., Wolf, M., Ganz, T., & Baggiolini, M. (1990). Purification and characterization of a major phosphatidylserine-binding phosphoprotein from human platelets. *Biochemical Journal*, *269*(3), 729–734. Retrieved from http://www.scopus.com/inward/record.url?eid=2-s2.0-0025364470&partnerID=tZOtx3y1

Cahill, D. P., Levine, K. K., Betensky, R. A., Codd, P. J., Romany, C. A., Reavie, L. B., … Louis, D. N. (2007). Loss of the mismatch repair protein MSH6 in human glioblastomas is associated with tumor progression during temozolomide treatment. *Clinical Cancer Research : An Official Journal of the American Association for Cancer Research*, *13*(7), 2038–2045. https://doi.org/10.1158/1078-0432.CCR-06-2149

Campbell, L., Al-Jayyoussi, G., Gutteridge, R., Gumbleton, N., Griffiths, R., Gumbleton, S., … Gumbleton, M. (2013). Caveolin-1 in renal cell carcinoma promotes tumour cell invasion, and in co-operation with pERK predicts metastases in patients with clinically confined disease. *Journal of Translational Medicine*, *11*(1), 255. https://doi.org/10.1186/1479-5876-11-

Carte, J., Wang, R., Li, H., Terns, R. M., & Terns, M. P. (2008). Cas6 is an endoribonuclease that generates guide RNAs for invader defense in prokaryotes. *Genes & Development*, *22*(24), 3489–3496. https://doi.org/10.1101/gad.1742908

Cassoni, P., Senetta, R., Castellano, I., Ortolan, E., Bosco, M., Magnani, I., & Ducati, A. (2007). Caveolin-1 expression is variably displayed in astroglial-derived tumors and absent in oligodendrogliomas: concrete premises for a new reliable diagnostic marker in gliomas. *The American Journal of Surgical Pathology*, *31*(5), 760–769. https://doi.org/10.1097/01.pas.0000213433.14740.5d

Cech, T. R. (1986). The generality of self-splicing RNA: relationship to nuclear mRNA splicing. *Cell*, *44*(2), 207–210. Retrieved from http://www.ncbi.nlm.nih.gov/pubmed/2417724

Cekanova, M., & Rathore, K. (2014). Animal models and therapeutic molecular targets of cancer: utility and limitations. *Drug Design, Development and Therapy*, *8*, 1911. https://doi.org/10.2147/DDDT.S49584

Cerezo, A., Guadamillas, M. C., Goetz, J. G., Sánchez-Perales, S., Klein, E., Assoian, R. K., & del Pozo, M. A. (2009). The absence of caveolin-1 increases proliferation and anchorage- independent growth by a Rac-dependent, Erk-independent mechanism. *Molecular and Cellular Biology*, *29*(18), 5046–5059. https://doi.org/10.1128/MCB.00315-09

Chang, N., Sun, C., Gao, L., Zhu, D., Xu, X., Zhu, X., … Xi, J. J. (2013). Genome editing with RNA-guided Cas9 nuclease in Zebrafish embryos. *Cell Research*, *23*(4), 465–472. https://doi.org/10.1038/cr.2013.45

Chen, H.-F., Xie, L.-D., & Xu, C.-S. (2010). The signal transduction pathways of heat shock protein 27 phosphorylation in vascular smooth muscle cells. *Molecular and Cellular Biochemistry*, *333*(1–2), 49–56. https://doi.org/10.1007/s11010-009-0203-5

Chiu, Y.-L., Ali, A., Chu, C.-Y., Cao, H., & Rana, T. M. (2004). Visualizing a correlation between siRNA localization, cellular uptake, and RNAi in living

cells. *Chemistry & Biology*, *11*(8), 1165–1175. https://doi.org/10.1016/j.chembiol.2004.06.006

Cho, S. H., Park, Y. S., Kim, H. J., Kim, C. H., Lim, S. W., Huh, J. W., … Kim, H. R. (2012). CD44 enhances the epithelial-mesenchymal transition in association with colon cancer invasion. *International Journal of Oncology*, *41*(1), 211–218. https://doi.org/10.3892/ijo.2012.1453

Cho, S. W., Kim, S., Kim, Y., Kweon, J., Kim, H. S., Bae, S., & Kim, J.-S. (2014). Analysis of off-target effects of CRISPR/Cas-derived RNA-guided endonucleases and nickases. *Genome Research*, *24*(1), 132–141. https://doi.org/10.1101/gr.162339.113

Christopherson, K. S., Ullian, E. M., Stokes, C. C. A., Mullowney, C. E., Hell, J. W., Agah, A., … Barres, B. A. (2005). Thrombospondins are astrocyte-secreted proteins that promote CNS synaptogenesis. *Cell*, *120*(3), 421–433. https://doi.org/10.1016/j.cell.2004.12.020

Chunhacha, P., & Chanvorachote, P. (2012). Roles of caveolin-1 on anoikis resistance in non small cell lung cancer. *International Journal of Physiology, Pathophysiology and Pharmacology*, *4*(3), 149–155. Retrieved from http://www.pubmedcentral.nih.gov/articlerender.fcgi?artid=3466493&tool=pmcentrez&rendertype=abstract

Claes, A., Idema, A. J., & Wesseling, P. (2007). Diffuse glioma growth: A guerilla war. *Acta Neuropathologica*, *114*(5), 443–458. https://doi.org/10.1007/s00401-007-0293-7

Clarke, L. E., & Barres, B. A. (2013). Emerging roles of astrocytes in neural circuit development. *Nature Reviews. Neuroscience*, *14*(5), 311–321. https://doi.org/10.1038/nrn3484

Cong, L., Ran, F. A., Cox, D., Lin, S., Barretto, R., Habib, N., … Zhang, F. (2013). Multiplex Genome Engineering Using CRISPR/Cas Systems. *Science*, *339*(6121), 819–823. https://doi.org/10.1126/science.1231143

Cosset, E. C., Godet, J., Entz-Werlé, N., Guérin, E., Guenot, D., Froelich, S., … Martin, S. (2012). Involvement of the TGFβ pathway in the regulation of α5 β1 integrins by caveolin-1 in human glioblastoma. *International Journal of*

Cancer. Journal International Du Cancer, *131*(3), 601–611. https://doi.org/10.1002/ijc.26415

Cox, D. R. (1972). Regression Models and Life-Tables. *Journal of the Royal Statistical Society. Series B (Methodological)*. WileyRoyal Statistical Society. https://doi.org/10.2307/2985181

Cullen, B. R. (2004). Transcription and Processing of Human microRNA Precursors. *Molecular Cell*, *16*(6), 861–865. https://doi.org/10.1016/j.molcel.2004.12.002

Dalby, B., Cates, S., Harris, A., Ohki, E. C., Tilkins, M. L., Price, P. J., & Ciccarone, V. C. (2004). Advanced transfection with Lipofectamine 2000 reagent: primary neurons, siRNA, and high-throughput applications. *Methods (San Diego, Calif.)*, *33*(2), 95–103. https://doi.org/10.1016/j.ymeth.2003.11.023

Datsenko, K. A., Pougach, K., Tikhonov, A., Wanner, B. L., Severinov, K., & Semenova, E. (2012). Molecular memory of prior infections activates the CRISPR/Cas adaptive bacterial immunity system. *Nature Communications*, *3*, 945. https://doi.org/10.1038/ncomms1937

De Sousa E Melo, F., Vermeulen, L., Fessler, E., & Medema, J. P. (2013). Cancer heterogeneity--a multifaceted view. *EMBO Reports*, *14*(8), 686–695. https://doi.org/10.1038/embor.2013.92

De Wever, O., Hendrix, A., De Boeck, A., Westbroek, W., Braems, G., Emami, S., … Bracke, M. (2010). Modeling and quantification of cancer cell invasion through collagen type I matrices. *International Journal of Developmental Biology*, *54*(5), 887–896. https://doi.org/10.1387/ijdb.092948ow

De Witt Hamer, P. C. (2010). Small molecule kinase inhibitors in glioblastoma: a systematic review of clinical studies. *Neuro-Oncology*, *12*(3), 304–316. https://doi.org/10.1093/neuonc/nop068

Delgado, J., Pereira, A., Villamor, N., López-Guillermo, A., & Rozman, C. (2014). Survival analysis in hematologic malignancies: Recommendations for clinicians. *Haematologica*. https://doi.org/10.3324/haematol.2013.100784

Deltcheva, E., Chylinski, K., Sharma, C. M., Gonzales, K., Chao, Y., Pirzada, Z. A., … Charpentier, E. (2011). CRISPR RNA maturation by trans-encoded small RNA and host factor RNase III. *Nature*, *471*(7340), 602–607. https://doi.org/10.1038/nature09886

Demchik, L. L., Sameni, M., Nelson, K., Mikkelsen, T., & Sloane, B. F. (1999). Cathepsin B and glioma invasion. *International Journal of Developmental Neuroscience*, *17*(5–6), 483–494. https://doi.org/10.1016/S0736-5748(99)00011-8

Demou, Z. N. (2010). Gene expression profiles in 3D tumor analogs indicate compressive strain differentially enhances metastatic potential. *Annals of Biomedical Engineering*, *38*(11), 3509–3520. https://doi.org/10.1007/s10439-010-0097-0

Denayer, T., Stöhr, T., & Van Roy, M. (2014). Animal models in translational medicine: Validation and prediction. *New Horizons in Translational Medicine*, *2*(1), 5–11. https://doi.org/10.1016/j.nhtm.2014.08.001

Dolznig, H., Rupp, C., Puri, C., Haslinger, C., Schweifer, N., Wieser, E., … Garin-Chesa, P. (2011). Modeling Colon Adenocarcinomas in Vitro. *The American Journal of Pathology*, *179*(1), 487–501. https://doi.org/10.1016/j.ajpath.2011.03.015

Dontu, G., Al-Hajj, M., Abdallah, W. M., Clarke, M. F., & Wicha, M. S. (2003). Stem cells in normal breast development and breast cancer. *Cell Proliferation*, *36 Suppl 1*, 59–72. Retrieved from http://www.ncbi.nlm.nih.gov/pubmed/14521516

Drab, M., Verkade, P., Elger, M., Kasper, M., Lohn, M., Lauterbach, B., … Kurzchalia, T. V. (2001). Loss of caveolae, vascular dysfunction, and pulmonary defects in caveolin-1 gene-disrupted mice. *Science (New York, N.Y.)*, *293*(5539), 2449–2452. https://doi.org/10.1126/science.1062688

Duda, K., Lonowski, L. A., Kofoed-Nielsen, M., Ibarra, A., Delay, C. M., Kang, Q., … Frodin, M. (2014). High-efficiency genome editing via 2A-coupled co-expression of fluorescent proteins and zinc finger nucleases or CRISPR/Cas9 nickase pairs. *Nucleic Acids Research*, *42*(10), e84–e84.

https://doi.org/10.1093/nar/gku251

Eckes, B., Hunzelmann, N., Ziegler-Heitbrock, H.-W. L., Urbanski, A., Luger, T., Krieg, T., & Mauch, C. (1992). Interleukin-6 expression by fibroblasts grown in three-dimensional gel cultures. *FEBS Letters*, *298*(2–3), 229–232. https://doi.org/10.1016/0014-5793(92)80064-N

Edwards, D. R., Handsley, M. M., & Pennington, C. J. (2008). The ADAM metalloproteinases. *Molecular Aspects of Medicine*, *29*(5), 258–289. https://doi.org/10.1016/j.mam.2008.08.001

Elbashir, S. M., Harborth, J., Lendeckel, W., Yalcin, A., Weber, K., & Tuschl, T. (2001). Duplexes of 21-nucleotide RNAs mediate RNA interference in cultured mammalian cells. *Nature*, *411*(6836), 494–498. https://doi.org/10.1038/35078107

Elstner, A., Stockhammer, F., Nguyen-Dobinsky, T. N., Nguyen, Q. L., Pilgermann, I., Gill, A., … Kurtz, A. (2011). Identification of diagnostic serum protein profiles of glioblastoma patients. *Journal of Neuro-Oncology*, *102*(1), 71–80. https://doi.org/10.1007/s11060-010-0284-8

Engelman, J. A., Wykoff, C. C., Yasuhara, S., Song, K. S., Okamoto, T., & Lisanti, M. P. (1997). Recombinant expression of caveolin-1 in oncogenically transformed cells abrogates anchorage-independent growth. *The Journal of Biological Chemistry*, *272*(26), 16374–16381. Retrieved from http://www.ncbi.nlm.nih.gov/pubmed/9195944

Enzerink, A., Salmenperä, P., Kankuri, E., & Vaheri, A. (2009). Clustering of fibroblasts induces proinflammatory chemokine secretion promoting leukocyte migration. *Molecular Immunology*, *46*(8–9), 1787–1795. https://doi.org/10.1016/j.molimm.2009.01.018

Esiri. (2000). Russell and Rubinstein's pathology of tumors of the nervous system. Sixth edition. *Journal of Neurology, Neurosurgery, and Psychiatry*, *68*(4), 538D. Retrieved from http://www.ncbi.nlm.nih.gov/pubmed/10727500

Fielding, P. E., Chau, P., Liu, D., Spencer, T. A., & Fielding, C. J. (2004). Mechanism of Platelet-Derived Growth Factor-Dependent Caveolin-1 Phosphorylation: Relationship to Sterol Binding and the Role of Serine-80

†. *Biochemistry*, *43*(9), 2578–2586. https://doi.org/10.1021/bi035442c

Filatova, A., Acker, T., & Garvalov, B. K. (2013). The cancer stem cell niche(s): the crosstalk between glioma stem cells and their microenvironment. *Biochimica et Biophysica Acta*, *1830*(2), 2496–2508. https://doi.org/10.1016/j.bbagen.2012.10.008

Filleur, S., Volpert, O. V, Degeorges, A., Voland, C., Reiher, F., Clézardin, P., … Cabon, F. (2001). In vivo mechanisms by which tumors producing thrombospondin 1 bypass its inhibitory effects. *Genes and Development*, *15*(11), 1373–1382. https://doi.org/10.1101/gad.193501

Fiucci, G., Ravid, D., Reich, R., & Liscovitch, M. (2002). Caveolin-1 inhibits anchorage-independent growth, anoikis and invasiveness in MCF-7 human breast cancer cells. *Oncogene*, *21*(15), 2365–2375. https://doi.org/10.1038/sj.onc.1205300

Folkins, C., Man, S., Xu, P., Shaked, Y., Hicklin, D. J., & Kerbel, R. S. (2007). Anticancer therapies combining antiangiogenic and tumor cell cytotoxic effects reduce the tumor stem-like cell fraction in glioma xenograft tumors. *Cancer Research*, *67*(8), 3560–3564. https://doi.org/10.1158/0008-5472.CAN-06-4238

Foundation, C. B. C. (n.d.). About Brain Cancer. Retrieved from https://www.curebraincancer.org.au/page/7/about-brain-cancer

Frangi, A. F., Niessen, W. J., Vincken, K. L., & Viergever, M. a. (1998). Multiscale vessel enhancement filtering. *Medial Image Computing and Computer-Assisted Invervention - MICCAI'98. Lecture Notes in Computer Science, Vol 1496*, *1496*, 130–137. https://doi.org/10.1016/j.media.2004.08.001

Franken, N. A. P., Rodermond, H. M., Stap, J., Haveman, J., & van Bree, C. (2006). Clonogenic assay of cells in vitro. *Nature Protocols*, *1*(5), 2315–2319. https://doi.org/10.1038/nprot.2006.339

Franovic, A., Elliott, K. C., Seguin, L., Camargo, M. F., Weis, S. M., & Cheresh, D. A. (2015). Glioblastomas require integrin ??v??3/PAK4 signaling to escape senescence. *Cancer Research*, *75*(21), 4466–4473.

https://doi.org/10.1158/0008-5472.CAN-15-0988

Freyer, J. P., & Sutherland, R. M. (1986). Regulation of growth saturation and development of necrosis in EMT6/Ro multicellular spheroids by the glucose and oxygen supply. *Cancer Research*, *46*(7), 3504–3512. Retrieved from http://www.ncbi.nlm.nih.gov/pubmed/3708582

Friedl, P. (2004). Prespecification and plasticity: shifting mechanisms of cell migration. *Current Opinion in Cell Biology*, *16*(1), 14–23. https://doi.org/10.1016/j.ceb.2003.11.001

Friedl, P., Locker, J., Sahai, E., & Segall, J. E. (2012). Classifying collective cancer cell invasion. *Nature Cell Biology*, *14*(8), 777–783. https://doi.org/10.1038/ncb2548

Friedrich, J., Seidel, C., Ebner, R., & Kunz-Schughart, L. A. (2009). Spheroid-based drug screen: considerations and practical approach. *Nat. Protocols*, *4*(3), 309–324. https://doi.org/10.1038/nprot.2008.226

Frock, R. L., Hu, J., Meyers, R. M., Ho, Y.-J., Kii, E., & Alt, F. W. (2014). Genome-wide detection of DNA double-stranded breaks induced by engineered nucleases. *Nature Biotechnology*, *33*(2), 179–186. https://doi.org/10.1038/nbt.3101

Fu, Y., Foden, J. A., Khayter, C., Maeder, M. L., Reyon, D., Joung, J. K., & Sander, J. D. (2013). High-frequency off-target mutagenesis induced by CRISPR-Cas nucleases in human cells. *Nature Biotechnology*, *31*(9), 822–826. https://doi.org/10.1038/nbt.2623

Furnari, F. B., Fenton, T., Bachoo, R. M., Mukasa, A., Stommel, J. M., Stegh, A., … Cavenee, W. K. (2007). Malignant astrocytic glioma: genetics, biology, and paths to treatment. *Genes & Development*, *21*(21), 2683–2710. https://doi.org/10.1101/gad.1596707

Galbiati, F., Engelman, J. A., Volonte, D., Zhang, X. L., Minetti, C., Li, M., … Lisanti, M. P. (2001). Caveolin-3 null mice show a loss of caveolae, changes in the microdomain distribution of the dystrophin-glycoprotein complex, and t-tubule abnormalities. *The Journal of Biological Chemistry*, *276*(24), 21425–21433. https://doi.org/10.1074/jbc.M100828200

Galbiati, F., Volonté, D., Liu, J., Capozza, F., Frank, P. G., Zhu, L., … Lisanti, M. P. (2001). Caveolin-1 expression negatively regulates cell cycle progression by inducing G(0)/G(1) arrest via a p53/p21(WAF1/Cip1)-dependent mechanism. *Molecular Biology of the Cell*, *12*(8), 2229–2244. Retrieved from http://www.pubmedcentral.nih.gov/articlerender.fcgi?artid=58591&tool=pmcentrez&rendertype=abstract

Garneau, J. E., Dupuis, M.-V., Villion, M., Romero, D. A., Barrangou, R., Boyaval, P., … Moineau, S. (2010). The CRISPR/Cas bacterial immune system cleaves bacteriophage and plasmid DNA. *Nature*, *468*. https://doi.org/10.1038/nature09523

Gesner, E. M., Schellenberg, M. J., Garside, E. L., George, M. M., & MacMillan, A. M. (2011). Recognition and maturation of effector RNAs in a CRISPR interference pathway. *Nature Structural & Molecular Biology*, *18*(6), 688–692. https://doi.org/10.1038/nsmb.2042

Ghosh, S., Johnson, J. J., Sen, R., Mukhopadhyay, S., Liu, Y., Zhang, F., … Stack, M. S. (2006). Functional relevance of urinary-type plasminogen activator receptor-α3β1 integrin association in proteinase regulatory pathways. *Journal of Biological Chemistry*, *281*(19), 13021–13029. https://doi.org/10.1074/jbc.M508526200

Ghosh, S., Spagnoli, G. C., Martin, I., Ploegert, S., Demougin, P., Heberer, M., & Reschner, A. (2005). Three-dimensional culture of melanoma cells profoundly affects gene expression profile: A high density oligonucleotide array study. *Journal of Cellular Physiology*, *204*(2), 522–531. https://doi.org/10.1002/jcp.20320

Giaccone, G., Herbst, R. S., Manegold, C., Scagliotti, G., Rosell, R., Miller, V., … Johnson, D. H. (2004). Gefitinib in combination with gemcitabine and cisplatin in advanced non-small-cell lung cancer: a phase III trial--INTACT 1. *Journal of Clinical Oncology : Official Journal of the American Society of Clinical Oncology*, *22*(5), 777–784. https://doi.org/10.1200/JCO.2004.08.001

Giese, A., Bjerkvig, R., Berens, M. E., & Westphal, M. (2003). Cost of Migration:

Invasion of Malignant Gliomas and Implications for Treatment. *Journal of Clinical Oncology*, *21*(8), 1624–1636. https://doi.org/10.1200/JCO.2003.05.063

Gilbert, L. A., Horlbeck, M. A., Adamson, B., Villalta, J. E., Chen, Y., Whitehead, E. H., … Weissman, J. S. (2014). Genome-Scale CRISPR-Mediated Control of Gene Repression and Activation. *Cell*, *159*(3), 647–661. https://doi.org/10.1016/j.cell.2014.09.029

Gilbert, L. A., Larson, M. H., Morsut, L., Liu, Z., Brar, G. A., Torres, S. E., … Qi, L. S. (2013). CRISPR-Mediated Modular RNA-Guided Regulation of Transcription in Eukaryotes. *Cell*, *154*(2), 442–451. https://doi.org/10.1016/j.cell.2013.06.044

Glenney, J. R., & Soppet, D. (1992). Sequence and expression of caveolin, a protein component of caveolae plasma membrane domains phosphorylated on tyrosine in Rous sarcoma virus-transformed fibroblasts. *Proceedings of the National Academy of Sciences of the United States of America*, *89*(21), 10517–10521. Retrieved from http://www.pubmedcentral.nih.gov/articlerender.fcgi?artid=50370&tool=pmcentrez&rendertype=abstract

Gocheva, V., Chen, X., Peters, C., Reinheckel, T., & Joyce, J. A. (2010). Deletion of cathepsin H perturbs angiogenic switching, vascularization and growth of tumors in a mouse model of pancreatic islet cell cancer. In *Biological Chemistry* (Vol. 391, pp. 937–945). https://doi.org/10.1515/BC.2010.080

Goetz, J. G., Joshi, B., Lajoie, P., Strugnell, S. S., Scudamore, T., Kojic, L. D., & Nabi, I. R. (2008). Concerted regulation of focal adhesion dynamics by galectin-3 and tyrosine-phosphorylated caveolin-1. *The Journal of Cell Biology*, *180*(6), 1261–1275. https://doi.org/10.1083/jcb.200709019

Goetz, J. G., Lajoie, P., Wiseman, S. M., & Nabi, I. R. (2008). Caveolin-1 in tumor progression: the good, the bad and the ugly. *Cancer Metastasis Reviews*, *27*(4), 715–735. https://doi.org/10.1007/s10555-008-9160-9

Goggins, W. B., & Wong, G. (2009). Cancer among Asian Indians/Pakistanis

living in the United States: low incidence and generally above average survival. *Cancer Causes & Control : CCC*, *20*(5), 635–643. https://doi.org/10.1007/s10552-008-9275-x

Goldberg, J., & Hirschi, K. (2013). A Vascular Perspective on Neurogenesis. In *Neural Stem Cells - New Perspectives* (pp. 199–239). InTech. https://doi.org/10.5772/54980

Gopinath, S., Malla, R., Alapati, K., Gorantla, B., Gujrati, M., Dinh, D. H., & Rao, J. S. (2013). Cathepsin B and uPAR regulate self-renewal of glioma-initiating cells through GLI-regulated Sox2 and Bmi1 expression. *Carcinogenesis*, *34*(3), 550–559. https://doi.org/10.1093/carcin/bgs375

Gould, M. L., Williams, G., & Nicholson, H. D. (2010). Changes in caveolae, caveolin, and polymerase 1 and transcript release factor (PTRF) expression in prostate cancer progression. *The Prostate*, *70*(15), 1609–1621. https://doi.org/10.1002/pros.21195

Green, T. P., Fennell, M., Whittaker, R., Curwen, J., Jacobs, V., Allen, J., … Costello, G. F. (2009). Preclinical anticancer activity of the potent, oral Src inhibitor AZD0530. *Molecular Oncology*, *3*(3), 248–261. https://doi.org/10.1016/j.molonc.2009.01.002

Gridley, T. (2007). Notch signaling in vascular development and physiology. *Development (Cambridge, England)*, *134*(15), 2709–2718. https://doi.org/10.1242/dev.004184

Grossmann, J. (2002). Molecular mechanisms of “detachment-induced apoptosis--Anoikis”. *Apoptosis : An International Journal on Programmed Cell Death*, *7*(3), 247–260. Retrieved from http://www.ncbi.nlm.nih.gov/pubmed/11997669

Gu, Y., Fu, J., Lo, P-K., Wang, S., Wang, Q., Chen, H. (2011). The effect of B27 supplement on promoting in vitro propagation of Her2/neu-transformed mammary tumorspheres. *Journal of Biotech Research*, 7–18. Retrieved from http://scholarcommons.sc.edu/cgi/viewcontent.cgi?article=1059&context=biol_facpub

Guadamillas, M. C., Cerezo, A., & Del Pozo, M. A. (2011). Overcoming anoikis--pathways to anchorage-independent growth in cancer. *Journal of Cell Science*, *124*(Pt 19), 3189–3197. https://doi.org/10.1242/jcs.072165

Guarino, M. (2010). Src signaling in cancer invasion. *Journal of Cellular Physiology*. https://doi.org/10.1002/jcp.22011

Guizzetti, M., Zhang, X., Goeke, C., & Gavin, D. P. (2014). Glia and neurodevelopment: focus on fetal alcohol spectrum disorders. *Frontiers in Pediatrics*, *2*, 123. https://doi.org/10.3389/fped.2014.00123

Gupta, R., Toufaily, C., & Annabi, B. (2014). Caveolin and cavin family members: dual roles in cancer. *Biochimie*, *107 Pt B*, 188–202. https://doi.org/10.1016/j.biochi.2014.09.010

Haft, D. H., Selengut, J., Mongodin, E. F., & Nelson, K. E. (2005). A guild of 45 CRISPR-associated (Cas) protein families and multiple CRISPR/cas subtypes exist in prokaryotic genomes. *PLoS Computational Biology*, *1*(6), 0474–0483. https://doi.org/10.1371 /journal.pcbi.0010060

Hammond, S. M., Caudy, A. A., & Hannon, G. J. (2001). Post-transcriptional gene silencing by double-stranded RNA. *Nature Reviews Genetics*, *2*(2), 110–119. https://doi.org/10.1038/35052556

Hassen, W., Kassambara, A., Reme, T., Sahota, S., Seckinger, A., Vincent, L., … Klein, B. (2015). Drug metabolism and clearance system in tumor cells of patients with multiple myeloma. *Oncotarget*, *6*(8), 6431–6447. https://doi.org/10.18632/oncotarget.3237

Haurwitz, R. E., Jinek, M., Wiedenheft, B., Zhou, K., & Doudna, J. A. (2010). Sequence- and Structure-Specific RNA Processing by a CRISPR Endonuclease. *Science*, *329*(5997), 1355–1358. https://doi.org/10.1126/science.1192272

Hay, E. D. (1995). An Overview of Epithelio-Mesenchymal Transformation. *Cells Tissues Organs*, *154*(1), 8–20. https://doi.org/10.1159/000147748

Herbst, R. S., Giaccone, G., Schiller, J. H., Natale, R. B., Miller, V., Manegold, C., … Johnson, D. H. (2004). Gefitinib in combination with paclitaxel and carboplatin in advanced non-small-cell lung cancer: a phase III trial--

INTACT 2. *Journal of Clinical Oncology : Official Journal of the American Society of Clinical Oncology*, *22*(5), 785–794. https://doi.org/10.1200/JCO.2004.07.215

Herouy, Y. (2004). The role of matrix metalloproteinases (MMPs) and their inhibitors in venous leg ulcer healing. *Phlebolymphology*, (44), 231–243.

Higuchi, M., Ohnishi, T., Arita, N., Hiraga, S., & Hayakawa, T. (1993). Expression of tenascin in human gliomas: its relation to histological malignancy, tumor dedifferentiation and angiogenesis. *Acta Neuropathologica*, *85*(5), 481–487. Retrieved from http://www.ncbi.nlm.nih.gov/pubmed/7684178

Hill, M. M., Bastiani, M., Luetterforst, R., Kirkham, M., Kirkham, A., Nixon, S. J., … Parton, R. G. (2008). PTRF-Cavin, a Conserved Cytoplasmic Protein Required for Caveola Formation and Function. *Cell*, *132*(1), 113–124. https://doi.org/10.1016/j.cell.2007.11.042

Hirose, Y., Saijou, E., Sugano, Y., Takeshita, F., Nishimura, S., Nonaka, H., … Miyajima, A. (2012). Inhibition of Stabilin-2 elevates circulating hyaluronic acid levels and prevents tumor metastasis. *Proceedings of the National Academy of Sciences of the United States of America*, *109*(11), 4263–4268. https://doi.org/10.1073/pnas.1117560109

Hirschhaeuser, F., Menne, H., Dittfeld, C., West, J., Mueller-Klieser, W., & Kunz-Schughart, L. A. (2010). Multicellular tumor spheroids: An underestimated tool is catching up again. *Journal of Biotechnology*, *148*(1), 3–15. https://doi.org/10.1016/j.jbiotec.2010.01.012

Hnasko, R., & Lisanti, M. P. (2003). The biology of caveolae: lessons from caveolin knockout mice and implications for human disease. *Molecular Interventions*, *3*(8), 445–464. https://doi.org/10.1124/mi.3.8.445

Ho, C.-C., Huang, P.-H., Huang, H.-Y., Chen, Y.-H., Yang, P.-C., & Hsu, S.-M. (2002). Up-regulated caveolin-1 accentuates the metastasis capability of lung adenocarcinoma by inducing filopodia formation. *The American Journal of Pathology*, *161*(5), 1647–1656. https://doi.org/10.1016/S0002-9440(10)64442-2

Huang, T., Sun, L., Yuan, X., & Qiu, H. (2017). Thrombospondin-1 is a multifaceted player in tumor progression. *Oncotarget*, *8*(48), 84546–84558. https://doi.org/10.18632/oncotarget.19165

Huse, J. T., Phillips, H. S., & Brennan, C. W. (2011). Molecular subclassification of diffuse gliomas: Seeing order in the chaos. *GLIA*, *59*(8), 1190–1199. https://doi.org/10.1002/glia.21165

Hwang, I.-H., Kwon, Y.-K., Cho, C.-K., Lee, Y.-W., Sung, J.-S., Joo, J.-C., … Jang, I.-S. (2016). Modified *Panax ginseng* Extract Inhibits uPAR-Mediated α5β1-Integrin Signaling by Modulating Caveolin-1 to Induce Early Apoptosis in Lung Cancer Cells. *The American Journal of Chinese Medicine*, *44*(05), 1081–1097. https://doi.org/10.1142/S0192415X16500609

Ichim, T. E., Li, M., Qian, H., Popov, I. A., Rycerz, K., Zheng, X., … Min, W.-P. (2004). RNA interference: a potent tool for gene-specific therapeutics. *American Journal of Transplantation : Official Journal of the American Society of Transplantation and the American Society of Transplant Surgeons*, *4*(8), 1227–1236. https://doi.org/10.1111/j.1600-6143.2004.00530.x

Ihrie, R. A., Shah, J. K., Harwell, C. C., Levine, J. H., Guinto, C. D., Lezameta, M., … Alvarez-Buylla, A. (2011). Persistent Sonic Hedgehog Signaling in Adult Brain Determines Neural Stem Cell Positional Identity. *Neuron*, *71*(2), 250–262. https://doi.org/10.1016/j.neuron.2011.05.018

Inda, M.-D.-M., Bonavia, R., & Seoane, J. (2014). Glioblastoma multiforme: a look inside its heterogeneous nature. *Cancers*, *6*(1), 226–239. https://doi.org/10.3390/cancers6010226

Inder, K. L., Zheng, Y. Z., Davis, M. J., Moon, H., Loo, D., Nguyen, H., … Hill, M. M. (2012). Expression of PTRF in PC-3 Cells modulates cholesterol dynamics and the actin cytoskeleton impacting secretion pathways. *Molecular & Cellular Proteomics : MCP*, *11*(2), M111.012245. https://doi.org/10.1074/mcp.M111.012245

Irigoyen, J. P., Muñoz-Cánoves, P., Montero, L., Koziczak, M., & Nagamine, Y. (1999). The plasminogen activator system: Biology and regulation. *Cellular*

and Molecular Life Sciences. https://doi.org/10.1007/PL00000615

Ivanov, D. P., Parker, T. L., Walker, D. A., Alexander, C., Ashford, M. B., Gellert, P. R., & Garnett, M. C. (2014). Multiplexing spheroid volume, resazurin and acid phosphatase viability assays for high-throughput screening of tumour spheroids and stem cell neurospheres. *PLoS ONE*, *9*(8), 1–14. https://doi.org/10.1371/journal.pone.0103817

Iwadate, Y. (2016). Epithelial-mesenchymal transition in glioblastoma progression. *Oncology Letters*. https://doi.org/10.3892/ol.2016.4113

Iwao, T., Takaki, T., Kuramitsu, M., Nagasaka, S., Machi, T., Ogawa, H., … Kitamura, K. (1987). Characteristics of an established human glioma cell line, KNS-42. *Neurologia Medico-Chirurgica*, *27*(7), 581–587. https://doi.org/10.2176/nmc.27.581

Jäkel, S., & Dimou, L. (2017). Glial Cells and Their Function in the Adult Brain: A Journey through the History of Their Ablation. *Frontiers in Cellular Neuroscience*, *11*, 24. https://doi.org/10.3389/fncel.2017.00024

Jiang, W., & Marraffini, L. A. (2015). CRISPR-Cas: New Tools for Genetic Manipulations from Bacterial Immunity Systems. *Annual Review of Microbiology*, *69*(1), 209–228. https://doi.org/10.1146/annurev-micro-091014-104441

Jiménez, A. J., Domínguez-Pinos, M.-D., Guerra, M. M., Fernández-Llebrez, P., & Pérez-Fígares, J.-M. (2014). Structure and function of the ependymal barrier and diseases associated with ependyma disruption. *Tissue Barriers*, *2*(1), e28426. https://doi.org/10.4161/tisb.28426

Jinek, M., Chylinski, K., Fonfara, I., Hauer, M., Doudna, J. A., & Charpentier, E. (2012). A Programmable Dual-RNA-Guided DNA Endonuclease in Adaptive Bacterial Immunity. *Science*, *337*(6096), 816–821. https://doi.org/10.1126/science.1225829

Jui-Cheng Yen, J. C., Fu-Juay Chang, F. J., & Shyang Chang, S. (1995). A new criterion for automatic multilevel thresholding. *IEEE Transactions on Image Processing*, *4*(3), 370–378. https://doi.org/10.1109/83.366472

Kaplan, E. L., & Meier, P. (1958). Nonparametric Estimation from Incomplete

Observations. *Journal of the American Statistical Association*, *53*(282), 457. https://doi.org/10.2307/2281868

Karajannis, M., Allen, J. C., & Newcomb, E. W. (2008). Treatment of pediatric brain tumors. *Journal of Cellular Physiology*, *217*(3), 584–589. https://doi.org/10.1002/jcp.21544

Karcher, S., Steiner, H.-H., Ahmadi, R., Zoubaa, S., Vasvari, G., Bauer, H., … Herold-Mende, C. (2006). Different angiogenic phenotypes in primary and secondary glioblastomas. *International Journal of Cancer*, *118*(9), 2182–2189. https://doi.org/10.1002/ijc.21648

Kasai, M., Satoh, K., & Akiyama, T. (2005). Wnt signaling regulates the sequential onset of neurogenesis and gliogenesis via induction of BMPs. *Genes to Cells*, *10*(8), 777–783. https://doi.org/10.1111/j.1365-2443.2005.00876.x

Kassambara, A., & Kosinski, M. (2017). survminer: Survival Analysis and Visualization. Retrieved July 31, 2018, from https://cran.r-project.org/package=survminer

Katt, M. E., Placone, A. L., Wong, A. D., Xu, Z. S., & Searson, P. C. (2016). In Vitro Tumor Models: Advantages, Disadvantages, Variables, and Selecting the Right Platform. *Frontiers in Bioengineering and Biotechnology*, *4*(4), 123389–12. https://doi.org/10.3389/fbioe.2016.00012

Keerthivasan, S., Keerthivasan, G., Mittal, S., & Chauhan, S. S. (2007). Transcriptional upregulation of human cathepsin L by VEGF in glioblastoma cells. *Gene*, *399*(2), 129–136. https://doi.org/10.1016/j.gene.2007.05.002

Kelwick, R., Desanlis, I., Wheeler, G. N., Edwards, D. R., Porter, S., Clark, I., … Kumar, S. (2015). The ADAMTS (A Disintegrin and Metalloproteinase with Thrombospondin motifs) family. *Genome Biology*, *16*(1), 113. https://doi.org/10.1186/s13059-015-0676-3

Kerosuo, L., & Bronner-Fraser, M. (2012). What is bad in cancer is good in the embryo: importance of EMT in neural crest development. *Seminars in Cell & Developmental Biology*, *23*(3), 320–332. https://doi.org/10.1016/j.semcdb.2012.03.010

Khaitan, D., Chandna, S., Arya, M., & Dwarakanath, B. (2006). Establishment and characterization of multicellular spheroids from a human glioma cell line; Implications for tumor therapy. *Journal of Translational Medicine*, *4*(1), 12. https://doi.org/10.1186/1479-5876-4-12

Khaitan, D., & Dwarakanath, B. S. (2006). Multicellular spheroids as an *in vitro* model in experimental oncology: applications in translational medicine. *Expert Opinion on Drug Discovery*, *1*(7), 663–675. https://doi.org/10.1517/17460441.1.7.663

Kim, S. K., Nabekura, J., & Koizumi, S. (2017). Astrocyte-mediated synapse remodeling in the pathological brain. *Glia*. https://doi.org/10.1002/glia.23169

Kim, S., Kim, D., Cho, S. W., Kim, J., & Kim, J.-S. (2014). Highly efficient RNA-guided genome editing in human cells via delivery of purified Cas9 ribonucleoproteins. *Genome Research*, *24*(6), 1012–1019. https://doi.org/10.1101/gr.171322.113

Kim, W. J., Chang, C.-W., Lee, M., & Kim, S. W. (2007). Efficient siRNA delivery using water soluble lipopolymer for anti-angiogenic gene therapy. *Journal of Controlled Release*, *118*(3), 357–363. https://doi.org/10.1016/j.jconrel.2006.12.026

Kim, Y.-N., Dam, P., & Bertics, P. J. (2002). Caveolin-1 phosphorylation in human squamous and epidermoid carcinoma cells: dependence on ErbB1 expression and Src activation. *Experimental Cell Research*, *280*(1), 134–147. https://doi.org/S0014482702956235 [pii]

Kim, Y. N., Wiepz, G. J., Guadarrama, A. G., & Bertics, P. J. (2000). Epidermal growth factor-stimulated tyrosine phosphorylation of caveolin-1. Enhanced caveolin-1 tyrosine phosphorylation following aberrant epidermal growth factor receptor status. *The Journal of Biological Chemistry*, *275*(11), 7481–7491. Retrieved from http://www.ncbi.nlm.nih.gov/pubmed/10713051

Kim, Y. W., Koul, D., Kim, S. H., Lucio-Eterovic, A. K., Freire, P. R., Yao, J., … Yung, W. K. A. (2013). Identification of prognostic gene signatures of glioblastoma: A study based on TCGA data analysis. *Neuro-Oncology*, *15*(7), 829–839. https://doi.org/10.1093/neuonc/not024

Kirkbride, K. C., Sung, B. H., Sinha, S., & Weaver, A. M. (2011). Cortactin: a multifunctional regulator of cellular invasiveness. *Cell Adhesion & Migration*, *5*(2), 187–198. https://doi.org/10.4161/CAM.5.2.14773

Kishore, J., Goel, M., & Khanna, P. (2010). Understanding survival analysis: Kaplan-Meier estimate. *International Journal of Ayurveda Research*, *1*(4), 274. https://doi.org/10.4103/0974-7788.76794

Klapperich, C. M., & Bertozzi, C. R. (2004). Global gene expression of cells attached to a tissue engineering scaffold. *Biomaterials*, *25*(25), 5631–5641. https://doi.org/10.1016/j.biomaterials.2004.01.025

Klein, J., Rizzo, J., Zhang, M.-J., & Keiding, N. (2001). Mini-review Statistical methods for the analysis and presentation of the results of bone marrow transplants. Part I: Unadjusted analysis. *Bone Marrow Transplantation*, *28*, 909–915. Retrieved from https://www.nature.com/articles/1703260.pdf

Kleinstiver, B. P., Pattanayak, V., Prew, M. S., Tsai, S. Q., Nguyen, N. T., Zheng, Z., & Joung, J. K. (2016). High-fidelity CRISPR–Cas9 nucleases with no detectable genome-wide off-target effects. *Nature*, *529*(7587), 490–495. https://doi.org/10.1038/nature16526

Kobayashi, H., Moniwa, N., Sugimura, M., Shinohara, H., Ohi, H., & Terao, T. (1993). Effects of membrane-associated cathepsin B on the activation of receptor-bound prourokinase and subsequent invasion of reconstituted basement membranes. *BBA - Molecular Cell Research*, *1178*(1), 55–62. https://doi.org/10.1016/0167-4889(93)90109-3

Kogo, H., & Fujimoto, T. (2000). Caveolin-1 isoforms are encoded by distinct mRNAs. Identification Of mouse caveolin-1 mRNA variants caused by alternative transcription initiation and splicing. *FEBS Letters*, *465*(2–3), 119–123. Retrieved from http://www.ncbi.nlm.nih.gov/pubmed/10631317

Konermann, S., Brigham, M. D., Trevino, A. E., Joung, J., Abudayyeh, O. O., Barcena, C., … Zhang, F. (2014). Genome-scale transcriptional activation by an engineered CRISPR-Cas9 complex. *Nature*, *517*(7536), 583–588. https://doi.org/10.1038/nature14136

Korff, T., & Augustin, H. G. (1999). Tensional forces in fibrillar extracellular

matrices control directional capillary sprouting. *Journal of Cell Science*, *112 (Pt 19)*, 3249–3258. Retrieved from http://www.ncbi.nlm.nih.gov/pubmed/10504330

Koster, J. (2016). R2: Genomics Analysis and Visualization Platform. Retrieved July 31, 2018, from http://hgserver1.amc.nl/cgi-bin/r2/main.cgi

Kramer, N., Walzl, A., Unger, C., Rosner, M., Krupitza, G., Hengstschläger, M., & Dolznig, H. (2013). In vitro cell migration and invasion assays. *Mutation Research*, *752*(1), 10–24. https://doi.org/10.1016/j.mrrev.2012.08.001

Kucharzewska, P., Christianson, H. C., Welch, J. E., Svensson, K. J., Fredlund, E., Ringnér, M., … Belting, M. (2013). Exosomes reflect the hypoxic status of glioma cells and mediate hypoxia-dependent activation of vascular cells during tumor development. *Proceedings of the National Academy of Sciences of the United States of America*, *110*(18), 7312–7317. https://doi.org/10.1073/pnas.1220998110

Kundu, S. (2018). *Role of Caveolin-1 in Hypoxia and Proneural to Mesenchymal Transition of Glioblastoma*. Retrieved from http://bora.uib.no/bitstream/handle/1956/17969/Master_thesis2018_Kundu_Somdutta.pdf?sequence=1

Kuo, C.-H., Lu, Y.-C., Tseng, Y.-S., Shi, C.-S., Chen, S.-H., Chen, P.-T., … Lee, Y.-R. (2014). Reversine induces cell cycle arrest, polyploidy, and apoptosis in human breast cancer cells. *Breast Cancer*, *21*(3), 358–369. https://doi.org/10.1007/s12282-012-0400-z

Lakka, S. S., Gondi, C. S., Yanamandra, N., Olivero, W. C., Dinh, D. H., Gujrati, M., & Rao, J. S. (2004). Inhibition of cathepsin B and MMP-9 gene expression in glioblastoma cell line via RNA interference reduces tumor cell invasion, tumor growth and angiogenesis. *Oncogene*, *23*(27), 4681–4689. https://doi.org/10.1038/sj.onc.1207616

Langton, K. P., Barker, M. D., & McKie, N. (1998). Localization of the functional domains of human tissue inhibitor of metalloproteinases-3 and the effects of a Sorsby's fundus dystrophy mutation. *Journal of Biological Chemistry*, *273*(27), 16778–16781. https://doi.org/10.1074/jbc.273.27.16778

Lasky, J. L., & Wu, H. (2005). Notch signaling, brain development, and human disease. *Pediatric Research*, *57*(5 Pt 2), 104R–109R. https://doi.org/10.1203/01.PDR.0000159632.70510.3D

Lau, L. W., Cua, R., Keough, M. B., Haylock-Jacobs, S., & Yong, V. W. (2013). Pathophysiology of the brain extracellular matrix: a new target for remyelination. *Nature Reviews Neuroscience*, *14*(10), 722–729. https://doi.org/10.1038/nrn3550

Lausen, B., & Schumacher, M. (1992). Maximally Selected Rank Statistics. *Biometrics*, *48*(1), 73. https://doi.org/10.2307/2532740

Le Goff, C., & Cormier-Daire, V. (2011). The ADAMTS(L) family and human genetic disorders. *Human Molecular Genetics*, *20*(R2), R163-7. https://doi.org/10.1093/hmg/ddr361

Lee, H., Park, D. S., Razani, B., Russell, R. G., Pestell, R. G., & Lisanti, M. P. (2002). Caveolin-1 mutations (P132L and null) and the pathogenesis of breast cancer: caveolin-1 (P132L) behaves in a dominant-negative manner and caveolin-1 (-/-) null mice show mammary epithelial cell hyperplasia. *The American Journal of Pathology*, *161*(4), 1357–1369. https://doi.org/10.1016/S0002-9440(10)64412-4

Lee, H., Volonte, D., Galbiati, F., Iyengar, P., Lublin, D. M., Bregman, D. B., … Lisanti, M. P. (2000). Constitutive and growth factor-regulated phosphorylation of caveolin-1 occurs at the same site (Tyr-14) in vivo: identification of a c-Src/Cav-1/Grb7 signaling cassette. *Molecular Endocrinology (Baltimore, Md.)*, *14*(11), 1750–1775. https://doi.org/10.1210/mend.14.11.0553

Lee, J. M., Dedhar, S., Kalluri, R., & Thompson, E. W. (2006). The epithelial–mesenchymal transition: new insights in signaling, development, and disease. *The Journal of Cell Biology*, *172*(7), 973–981. https://doi.org/10.1083/jcb.200601018

Lee, S. W., Reimer, C. L., Oh, P., Campbell, D. B., & Schnitzer, J. E. (1998). Tumor cell growth inhibition by caveolin re-expression in human breast cancer cells. *Oncogene*, *16*(11), 1391–1397.

https://doi.org/10.1038/sj.onc.1201661

Lee, Y., Ahn, C., Han, J., Choi, H., Kim, J., Yim, J., … Kim, V. N. (2003). The nuclear RNase III Drosha initiates microRNA processing. *Nature*, *425*(6956), 415–419. https://doi.org/10.1038/nature01957

Lee, Y., Jeon, K., Lee, J.-T., Kim, S., & Kim, V. N. (2002). MicroRNA maturation: stepwise processing and subcellular localization. *The EMBO Journal*, *21*(17), 4663–4670. Retrieved from http://www.ncbi.nlm.nih.gov/pubmed/12198168

Lee, Y. S., Nakahara, K., Pham, J. W., Kim, K., He, Z., Sontheimer, E. J., & Carthew, R. W. (2004). Distinct roles for Drosophila Dicer-1 and Dicer-2 in the siRNA/miRNA silencing pathways. *Cell*, *117*(1), 69–81. Retrieved from http://www.ncbi.nlm.nih.gov/pubmed/15066283

Levicar, N., Nutall, R. K., & Lah, T. T. (2003). Proteases in brain tumour progression. *Acta Neurochirurgica*, *145*(9), 825–838. https://doi.org/10.1007/s00701-003-0097-z

Levicar, N., Strojnik, T., Kos, J., Dewey, R. A., Pilkington, G. J., & Lah, T. T. (2002). Lysosomal enzymes, cathepsins in brain tumour invasion. *Journal of Neuro-Oncology*, *58*(1), 21–32. Retrieved from http://www.ncbi.nlm.nih.gov/pubmed/12160137

Levin, V. A., Panchabhai, S. C., Shen, L., Kornblau, S. M., Qiu, Y., & Baggerly, K. A. (2010). Different Changes in Protein and Phosphoprotein Levels Result from Serum Starvation of High-Grade Glioma and Adenocarcinoma Cell Lines NIH Public Access. *J Proteome Res*, *9*(1), 179–191. https://doi.org/10.1021/pr900392b

Levin, V. A., Panchabhai, S., Shen, L., & Baggerly, K. A. (2012). Protein and phosphoprotein levels in glioma and adenocarcinoma cell lines grown in normoxia and hypoxia in monolayer and three-dimensional cultures. *Proteome Science*, *10*(1), 5. https://doi.org/10.1186/1477-5956-10-5

Lewis, K. M., & Petritsch, C. (2013). ASYMMETRIC CELL DIVISION: IMPLICATIONS FOR GLIOMA DEVELOPMENT AND TREATMENT. *Translational Neuroscience*, *4*(4), 484–503. https://doi.org/10.2478/s13380-

013-0148-8

Li, H., Venkatraman, L., Chakrapani Narmada, B., White, J. K., Yu, H., Tucker-Kellogg, L., … Tucker-Kellogg, L. (2017). Computational analysis reveals the coupling between bistability and the sign of a feedback loop in a TGF-β1 activation model. *BMC Systems Biology*, *11*. https://doi.org/10.1186/s12918-017-0508-z

Li, M., Chen, H., Diao, L., Zhang, Y., Xia, C., & Yang, F. (2010). Caveolin-1 and VEGF-C promote lymph node metastasis in the absence of intratumoral lymphangiogenesis in non-small cell lung cancer. *Tumori*, *96*(5), 734–743. Retrieved from http://www.scopus.com/inward/record.url?eid=2-s2.0-78650453708&partnerID=tZOtx3y1

Li, Y., Luo, J., Lau, W.-M., Zheng, G., Fu, S., Wang, T.-T., … Shen, J. (2011). Caveolin-1 plays a crucial role in inhibiting neuronal differentiation of neural stem/progenitor cells via VEGF signaling-dependent pathway. *PloS One*, *6*(8), e22901. https://doi.org/10.1371/journal.pone.0022901

Liang, X., Potter, J., Kumar, S., Zou, Y., Quintanilla, R., Sridharan, M., … Chesnut, J. D. (2015). Rapid and highly efficient mammalian cell engineering via Cas9 protein transfection. *Journal of Biotechnology*, *208*, 44–53. https://doi.org/10.1016/j.jbiotec.2015.04.024

Liebelt, B. D., Shingu, T., Zhou, X., Ren, J., Shin, S. A., & Hu, J. (2016). Glioma Stem Cells : Signaling , Microenvironment , and Therapy. *Stem Cells International*, *2016*. https://doi.org/10.1155/2016/7849890

Lin, Y., Cradick, T. J., Brown, M. T., Deshmukh, H., Ranjan, P., Sarode, N., … Bao, G. (2014). CRISPR/Cas9 systems have off-target activity with insertions or deletions between target DNA and guide RNA sequences. *Nucleic Acids Research*, *42*(11), 7473–7485. https://doi.org/10.1093/nar/gku402

Lisanti, M. P., Scherer, P. E., Tang, Z., & Sargiacomo, M. (1994). Caveolae, caveolin and caveolin-rich membrane domains: a signalling hypothesis. *Trends in Cell Biology*, *4*(7), 231–235. Retrieved from http://www.ncbi.nlm.nih.gov/pubmed/14731661

Liu, J., Carmell, M. A., Rivas, F. V, Marsden, C. G., Thomson, J. M., Song, J.-J., … Hannon, G. J. (2004). Argonaute2 Is the Catalytic Engine of Mammalian RNAi. *Science*, *305*(5689), 1437–1441. https://doi.org/10.1126/science.1102513

Liu, J., Sareddy, G. R., Zhou, M., Viswanadhapalli, S., Li, X., Lai, Z., … Vadlamudi, R. K. (2018). Differential effects of estrogen receptor beta isoforms on glioblastoma progression. *Cancer Research*, *78*(12), 3176–3189. https://doi.org/10.1158/0008-5472.CAN-17-3470

Liu, L., & Pilch, P. F. (2008). A critical role of cavin (polymerase I and transcript release factor) in caveolae formation and organization. *The Journal of Biological Chemistry*, *283*(7), 4314–4322. https://doi.org/10.1074/jbc.M707890200

Liu, P. C. C., Liu, X., Li, Y., Covington, M., Wynn, R., Huber, R., … Burn, T. C. (2006). Identification of ADAM10 as a major source of HER2 ectodomain sheddase activity in HER2 overexpressing breast cancer cells. *Cancer Biology & Therapy*, *5*(6), 657–664. https://doi.org/10.4161/cbt.5.6.2708

Liu, S., & Cheng, C. (2017). Akt Signaling Is Sustained by a CD44 Splice Isoform–Mediated Positive Feedback Loop. *Cancer Research*, *77*(14), 3791–3801. https://doi.org/10.1158/0008-5472.CAN-16-2545

Liu, Y., Zhou, Y., & Zhu, K. (2012). Inhibition of Glioma Cell Lysosome Exocytosis Inhibits Glioma Invasion. *PLoS ONE*, *7*(9). https://doi.org/10.1371/journal.pone.0045910

Llobet, L., Montoya, J., López-Gallardo, E., & Ruiz-Pesini, E. (2015). Side Effects of Culture Media Antibiotics on Cell Differentiation. *Tissue Engineering. Part C, Methods*, *21*(11), 1143–1147. https://doi.org/10.1089/ten.TEC.2015.0062

Lloyd, P. G., & Hardin, C. D. (2011). Caveolae in cancer: two sides of the same coin? Focus on “Hydrogen peroxide inhibits non-small cell lung cancer cell anoikis through the inhibition of caveolin-1 degradation”. *American Journal of Physiology. Cell Physiology*, *300*(2), C232-4. https://doi.org/10.1152/ajpcell.00483.2010

Louis, D. N. (International A. F. R. O. C. (2016). *WHO classification of tumours of the central nervous system*. International Agency For Research On Cancer. Retrieved from http://publications.iarc.fr/Book-And-Report-Series/Who-Iarc-Classification-Of-Tumours/Who-Classification-Of-Tumours-Of-The-Central-Nervous-System-2016

Louis, D. N., Ohgaki, H., Wiestler, O. D., Cavenee, W. K., Burger, P. C., Jouvet, A., … Kleihues, P. (2007). The 2007 WHO classification of tumours of the central nervous system. *Acta Neuropathologica*, *114*(2), 97–109. https://doi.org/10.1007/s00401-007-0243-4

Louis, D. N., Perry, A., Reifenberger, G., von Deimling, A., Figarella-Branger, D., Cavenee, W. K., … Ellison, D. W. (2016a). The 2016 World Health Organization Classification of Tumors of the Central Nervous System: a summary. *Acta Neuropathologica*, *131*(6), 803–820. https://doi.org/10.1007/s00401-016-1545-1

Louis, D. N., Perry, A., Reifenberger, G., von Deimling, A., Figarella-Branger, D., Cavenee, W. K., … Ellison, D. W. (2016b). The 2016 World Health Organization Classification of Tumors of the Central Nervous System: a summary. *Acta Neuropathologica*, *131*(6), 803–820. https://doi.org/10.1007/s00401-016-1545-1

Love, T. M., Moffett, H. F., & Novina, C. D. (2008). Not miR-ly small RNAs: Big potential for microRNAs in therapy. *Journal of Allergy and Clinical Immunology*, *121*(2), 309–319. https://doi.org/10.1016/j.jaci.2007.12.1167

Lund, E., Güttinger, S., Calado, A., Dahlberg, J. E., & Kutay, U. (2004). Nuclear Export of MicroRNA Precursors. *Science*, *303*(5654), 95–98. https://doi.org/10.1126/science.1090599

MacGrath, S. M., & Koleske, A. J. (2012). Cortactin in cell migration and cancer at a glance. *Journal of Cell Science*, *125*(7), 1621–1626. https://doi.org/10.1242/jcs.093781

Magnusson, J. P., & Frisen, J. (2016). Stars from the darkest night: unlocking the neurogenic potential of astrocytes in different brain regions. *Development*, *143*(7), 1075–1086. https://doi.org/10.1242/dev.133975

Majewska, E., & Szeliga, M. (2017). AKT/GSK3β Signaling in Glioblastoma. *Neurochemical Research*, *42*(3), 918–924. https://doi.org/10.1007/s11064-016-2044-4

Makarova, K. S., Haft, D. H., Barrangou, R., Brouns, S. J. J., Charpentier, E., Horvath, P., … Koonin, E. V. (2011). Evolution and classification of the CRISPR–Cas systems. *Nature Reviews Microbiology*, *9*(6), 467–477. https://doi.org/10.1038/nrmicro2577

Mali, P., Yang, L., Esvelt, K. M., Aach, J., Guell, M., DiCarlo, J. E., … Church, G. M. (2013). RNA-Guided Human Genome Engineering via Cas9. *Science*, *339*(6121), 823–826. https://doi.org/10.1126/science.1232033

Malinowsky, K., Wolff, C., Berg, D., Schuster, T., Walch, A., Bronger, H., … Becker, K.-F. (2012). uPA and PAI-1-Related Signaling Pathways Differ between Primary Breast Cancers and Lymph Node Metastases. *Translational Oncology*, *5*(2), 98-IN3. https://doi.org/10.1593/tlo.11268

Mallawaaratchy, D. M., Hallal, S., Russell, B., Ly, L., Ebrahimkhani, S., Wei, H., … Kaufman, K. L. (2017). Comprehensive proteome profiling of glioblastoma-derived extracellular vesicles identifies markers for more aggressive disease. *Journal of Neuro-Oncology*, *131*(2), 233–244. https://doi.org/10.1007/s11060-016-2298-3

Martin, S., Cosset, E. C., Terrand, J., Maglott, A., Takeda, K., & Dontenwill, M. (2009). Caveolin-1 regulates glioblastoma aggressiveness through the control of alpha(5)beta(1) integrin expression and modulates glioblastoma responsiveness to SJ749, an alpha(5)beta(1) integrin antagonist. *Biochimica et Biophysica Acta*, *1793*(2), 354–367. https://doi.org/10.1016/j.bbamcr.2008.09.019

Martinez, N. A., Ayala, A. M., Martinez, M., Martinez-Rivera, F. J., Miranda, J. D., & Silva, W. I. (2016). Caveolin-1 regulates the P2Y2 receptor signaling in human 1321N1 astrocytoma cells. *Journal of Biological Chemistry*, *291*(23), 12208–12222. https://doi.org/10.1074/jbc.M116.730226

McCready, J., Broaddus, W. C., Sykes, V., & Fillmore, H. L. (2005). Association of a single nucleotide polymorphism in the matrix metalloproteinase-1

promoter with glioblastoma. *International Journal of Cancer*, *117*(5), 781–785. https://doi.org/10.1002/ijc.21207

McKinney, P. A. (2004). Brain tumours: incidence, survival, and aetiology. *Journal of Neurology, Neurosurgery & Psychiatry*, *75*(suppl_2), ii12-ii17. https://doi.org/10.1136/jnnp.2004.040741

McLendon, R., Friedman, A., Bigner, D., Van Meir, E. G., Brat, D. J., M. Mastrogianakis, G., … Thomson, E. (2008). Comprehensive genomic characterization defines human glioblastoma genes and core pathways. *Nature*, *455*(7216), 1061–1068. https://doi.org/10.1038/nature07385

Mehta M, Vogelbaum MA, Chang S, et al. (2011). Neoplasms of the central nervous system. In L. W. & Wilkins (Ed.), *Cancer: Principles and Practice of Oncology* (9th ed., pp. 1700–1749). Philadelphia.

Mentlein, R., Hattermann, K., & Held-Feindt, J. (2012). Lost in disruption: role of proteases in glioma invasion and progression. *Biochimica et Biophysica Acta*, *1825*(2), 178–185. https://doi.org/10.1016/j.bbcan.2011.12.001

Mohanam, S., Jasti, S. L., Kondraganti, S. R., Chandrasekar, N., Lakka, S. S., Kin, Y., … Rao, J. S. (2001). Down-regulation of cathepsin B expression impairs the invasive and tumorigenic potential of human glioblastoma cells. *Oncogene*, *20*(28), 3665–3673. https://doi.org/10.1038/sj.onc.1204480

Monier, S., Dietzen, D. J., Hastings, W. R., Lublin, D. M., & Kurzchalia, T. V. (1996). Oligomerization of VIP21-caveolin in vitro is stabilized by long chain fatty acylation or cholesterol. *FEBS Letters*, *388*(2–3), 143–149. Retrieved from http://www.ncbi.nlm.nih.gov/pubmed/8690074

Mori, T., Abe, T., Wakabayashi, Y., Hikawa, T., Matsuo, K., Yamada, Y., … Hori, S. (2000). Up-regulation of urokinase-type plasminogen activator and its receptor correlates with enhanced invasion activity of human glioma cells mediated by transforming growth factor-alpha or basic fibroblast growth factor. *Journal of Neuro-Oncology*, *46*(2), 115–123. Retrieved from http://www.ncbi.nlm.nih.gov/pubmed/10894364

Moriconi, C., Palmieri, V., Di Santo, R., Tornillo, G., Papi, M., Pilkington, G., … Gumbleton, M. (2017, September 6). INSIDIA: A FIJI Macro Delivering

High-Throughput and High-Content Spheroid Invasion Analysis. *Biotechnology Journal*, p. 1700140. https://doi.org/10.1002/biot.201700140

Mueller-Klieser, W. (1984). Method for the determination of oxygen consumption rates and diffusion coefficients in multicellular spheroids. *Biophysical Journal*, *46*(3), 343–348. https://doi.org/10.1016/S0006-3495(84)84030-8

Mueller-Klieser, W., Freyer, J. P., & Sutherland, R. M. (1986). Influence of glucose and oxygen supply conditions on the oxygenation of multicellular spheroids. *British Journal of Cancer*, *53*(3), 345–353. https://doi.org/10.1038/bjc.1986.58

Murata, M., Peränen, J., Schreiner, R., Wieland, F., Kurzchalia, T. V, & Simons, K. (1995). VIP21/caveolin is a cholesterol-binding protein. *Proceedings of the National Academy of Sciences of the United States of America*, *92*(22), 10339–10343. Retrieved from http://www.pubmedcentral.nih.gov/articlerender.fcgi?artid=40792&tool=pmcentrez&rendertype=abstract

Naber, H. P. H., Wiercinska, E., Ten Dijke, P., & van Laar, T. (2011). Spheroid assay to measure TGF-β-induced invasion. *Journal of Visualized Experiments : JoVE*, (57). https://doi.org/10.3791/3337

Naber, H., Wiercinska, E., ten Dijke, P., & Laar, T. van. (2011). Spheroid Assay to Measure TGF-B-Induced Invasion. *Journal of Visualized Experiments*, (November), 1–7. https://doi.org/10.3791/3337

Naganuma, H., Satoh, E., Asahara, T., Amagasaki, K., Watanabe, A., Satoh, H., … Nukui, H. (2004). Quantification of thrombospondin-1 secretion and expression of ?v?3 and ?3?1 integrins and syndecan-1 as cell-surface receptors for thrombospondin-1 in malignant glioma cells. *Journal of Neuro-Oncology*, *70*(3), 309–317. https://doi.org/10.1007/s11060-004-9167-1

Nagase, H., Visse, R., Murphy, G., Newby, A. C., Spinale, F. G., Shah, P. K., … Carson, D. D. (2006). Structure and function of matrix metalloproteinases and TIMPs. *Cardiovascular Research*, *69*(3), 562–573. https://doi.org/10.1016/j.cardiores.2005.12.002

Naito, Y., & Ui-Tei, K. (2013). Designing Functional siRNA with Reduced Off-

Target Effects. In *Methods in molecular biology (Clifton, N.J.)* (Vol. 942, pp. 57–68). https://doi.org/10.1007/978-1-62703-119-6_3

Nakada, M., Nambu, E., Furuyama, N., Yoshida, Y., Takino, T., Hayashi, Y., … Hamada, J. (2013). Integrin α3 is overexpressed in glioma stem-like cells and promotes invasion. *British Journal of Cancer*, *108*(12), 2516–2524. https://doi.org/10.1038/bjc.2013.218

Nam, H.-J., Im, S.-A., Oh, D.-Y., Elvin, P., Kim, H.-P., Yoon, Y.-K., … Bang, Y.-J. (2013). Antitumor activity of saracatinib (AZD0530), a c-Src/Abl kinase inhibitor, alone or in combination with chemotherapeutic agents in gastric cancer. *Molecular Cancer Therapeutics*, *12*(January), 16–26. https://doi.org/10.1158/1535-7163.MCT-12-0109

Nemoto, S., Xiang, J., Huang, S., & Lin, A. (1998). Induction of apoptosis by SB202190 through inhibition of p38β mitogen- activated protein kinase. *Journal of Biological Chemistry*, *273*(26), 16415–16420. https://doi.org/10.1074/jbc.273.26.16415

Nicholson, C., & Syková, E. (1998). Extracellular space structure revealed by diffusion analysis. *Trends in Neurosciences*, *21*(5), 207–215. https://doi.org/10.1016/S0166-2236(98)01261-2

Nouh, M. A., Mohamed, M. M., El-Shinawi, M., Shaalan, M. A., Cavallo-Medved, D., Khaled, H. M., & Sloane, B. F. (2011). Cathepsin b: A potential prognostic marker for inflammatory breast cancer. *Journal of Translational Medicine*, *9*. https://doi.org/10.1186/1479-5876-9-1

Noushmehr, H., Weisenberger, D. J., Diefes, K., Phillips, H. S., Pujara, K., Berman, B. P., … Aldape, K. (2010). Identification of a CpG Island Methylator Phenotype that Defines a Distinct Subgroup of Glioma. *Cancer Cell*, *17*(5), 510–522. https://doi.org/10.1016/j.ccr.2010.03.017

Noyce, R. S., & Richardson, C. D. (2012). Nectin 4 is the epithelial cell receptor for measles virus. *Trends in Microbiology*. https://doi.org/10.1016/j.tim.2012.05.006

Oh, J.-W., Olman, M., & Benveniste, E. N. (2009). CXCL12-mediated induction of plasminogen activator inhibitor-1 expression in human CXCR4 positive

astroglioma cells. *Biological & Pharmaceutical Bulletin*, *32*(4), 573–577. Retrieved from http://www.ncbi.nlm.nih.gov/pubmed/19336886

Ohgaki, H., & Kleihues, P. (2005). Epidemiology and etiology of gliomas. *Acta Neuropathologica*. https://doi.org/10.1007/s00401-005-0991-y

Olar, A., & Aldape, K. D. (2014). Using the molecular classification of glioblastoma to inform personalized treatment. *Journal of Pathology*, *232*(2), 165–177. https://doi.org/10.1002/path.4282

Ostrom, Q. T., Gittleman, H., Liao, P., Vecchione-Koval, T., Wolinsky, Y., Kruchko, C., & Barnholtz-Sloan, J. S. (2017). Neuro-Oncology CBTRUS Statistical Report: Primary brain and other central nervous system tumors diagnosed in the United Introduction, (S5), 1–88. https://doi.org/10.1093/neuonc/nox158

Ottone, C., Krusche, B., Whitby, A., Clements, M., Quadrato, G., Pitulescu, M. E., … Parrinello, S. (2014). Direct cell-cell contact with the vascular niche maintains quiescent neural stem cells. *Nature Cell Biology*, *16*(11), 1045–1056. https://doi.org/10.1038/ncb3045

Palade, G. E. (1953). Fine Structure of Blood Capillaries. *J. Appl. Phys.*, *24*, 1424–1436.

Pancotti, F., Roncuzzi, L., Maggiolini, M., & Gasperi-Campani, A. (2012). Caveolin-1 silencing arrests the proliferation of metastatic lung cancer cells through the inhibition of STAT3 signaling. *Cellular Signalling*, *24*(7), 1390–1397. https://doi.org/10.1016/j.cellsig.2012.02.015

Paoli, P., Giannoni, E., & Chiarugi, P. (2013). Anoikis molecular pathways and its role in cancer progression. *Biochimica et Biophysica Acta*, *1833*(12), 3481–3498. https://doi.org/10.1016/j.bbamcr.2013.06.026

Parat, M.-O. (2009). The biology of caveolae: achievements and perspectives. *International Review of Cell and Molecular Biology*, *273*, 117–162. https://doi.org/10.1016/S1937-6448(08)01804-2

Parat, M.-O., & Riggins, G. J. (2012). Caveolin-1, caveolae, and glioblastoma. *Neuro-Oncology*, *14*(6), 679–688. https://doi.org/10.1093/neuonc/nos079

Park, J., Bae, E., Lee, C., Yoon, S.-S., Chae, Y. S., Ahn, K.-S., & Won, N. H. (2010). RNA interference-directed caveolin-1 knockdown sensitizes SN12CPM6 cells to doxorubicin-induced apoptosis and reduces lung metastasis. *Tumour Biology : The Journal of the International Society for Oncodevelopmental Biology and Medicine*, *31*(6), 643–650. https://doi.org/10.1007/s13277-010-0081-1

Parker, N. R., Khong, P., Parkinson, J. F., Howell, V. M., & Wheeler, H. R. (2015). Molecular Heterogeneity in Glioblastoma: Potential Clinical Implications. *Frontiers in Oncology*, *5*, 55. https://doi.org/10.3389/fonc.2015.00055

Parnas, O., Jovanovic, M., Eisenhaure, T. M., Herbst, R. H., Dixit, A., Ye, C. J., … Regev, A. (2015). A Genome-wide CRISPR Screen in Primary Immune Cells to Dissect Regulatory Networks. *Cell*, *162*(3), 675–686. https://doi.org/10.1016/j.cell.2015.06.059

Parolini, I., Sargiacomo, M., Galbiati, F., Rizzo, G., Grignani, F., Engelman, J. A., … Lisanti, M. P. (1999). Expression of caveolin-1 is required for the transport of caveolin-2 to the plasma membrane. Retention of caveolin-2 at the level of the golgi complex. *The Journal of Biological Chemistry*, *274*(36), 25718–25725. Retrieved from http://www.ncbi.nlm.nih.gov/pubmed/10464309

Pascual, O., Casper, K. B., Kubera, C., Zhang, J., Revilla-Sanchez, R., Sul, J.-Y., … Haydon, P. G. (2005). Astrocytic purinergic signaling coordinates synaptic networks. *Science (New York, N.Y.)*, *310*(5745), 113–116. https://doi.org/10.1126/science.1116916

Patchell, R. A. (2003). The management of brain metastases. *Cancer Treatment Reviews*, *29*(6), 533–540. Retrieved from http://www.ncbi.nlm.nih.gov/pubmed/14585263

Patil, M. L., Zhang, M., Betigeri, S., Taratula, O., He, H., & Minko, T. (2008). Surface-modified and internally cationic polyamidoamine dendrimers for efficient siRNA delivery. *Bioconjugate Chemistry*, *19*(7), 1396–1403. https://doi.org/10.1021/bc8000722

Paulus, W., Baur, I., Dours-Zimmermann, M. T., & Zimmermann, D. R. (1996). Differential expression of versican isoforms in brain tumors. *Journal of Neuropathology and Experimental Neurology*, *55*(5), 528–533. Retrieved from http://www.ncbi.nlm.nih.gov/pubmed/8627343

Pei, Y., Brun, S. N., Markant, S. L., Lento, W., Gibson, P., Taketo, M. M., … Wechsler-Reya, R. J. (2012). WNT signaling increases proliferation and impairs differentiation of stem cells in the developing cerebellum. *Development*, *139*(10), 1724–1733. https://doi.org/10.1242/dev.050104

Pelkmans, L., & Zerial, M. (2005). Kinase-regulated quantal assemblies and kiss-and-run recycling of caveolae. *Nature*, *436*(7047), 128–133. https://doi.org/10.1038/nature03866

Perna, A., Lucariello, A., Sellitto, C., Agliata, I., Carleo, M. A., Sangiovanni, V., … De Luca, A. (2017). Different Cell Cycle Modulation in SKOV-3 Ovarian Cancer Cell Line by Anti-HIV Drugs. *Oncology Research Featuring Preclinical and Clinical Cancer Therapeutics*, *25*(9), 1617–1624. https://doi.org/10.3727/096504017X14905635363102

Persano, L., Rampazzo, E., Basso, G., & Viola, G. (2013). Glioblastoma cancer stem cells: role of the microenvironment and therapeutic targeting. *Biochemical Pharmacology*, *85*(5), 612–622. https://doi.org/10.1016/j.bcp.2012.10.001

Phillips, H. S., Kharbanda, S., Chen, R., Forrest, W. F., Soriano, R. H., Wu, T. D., … Aldape, K. (2006). Molecular subclasses of high-grade glioma predict prognosis, delineate a pattern of disease progression, and resemble stages in neurogenesis. *Cancer Cell*, *9*(3), 157–173. https://doi.org/10.1016/j.ccr.2006.02.019

Piccirillo, S. G. M., Reynolds, B. a, Zanetti, N., Lamorte, G., Binda, E., Broggi, G., … Vescovi, a L. (2006). Bone morphogenetic proteins inhibit the tumorigenic potential of human brain tumour-initiating cells. *Nature*, *444*(7120), 761–765. https://doi.org/10.1038/nature05349

Pistollato, F., Chen, H.-L., Rood, B. R., Zhang, H.-Z., D'Avella, D., Denaro, L., … Panchision, D. M. (2009). Hypoxia and HIF1alpha repress the differentiative

effects of BMPs in high-grade glioma. *Stem Cells (Dayton, Ohio)*, *27*(1), 7–17. https://doi.org/10.1634/stemcells.2008-0402

Ponta, H., Sherman, L., & Herrlich, P. A. (2003). CD44: From adhesion molecules to signalling regulators. *Nature Reviews Molecular Cell Biology*, *4*(1), 33–45. https://doi.org/10.1038/nrm1004

Pontén, J., & Macintyre, E. H. (1968). Long term culture of normal and neoplastic human glia. *Acta Pathologica et Microbiologica Scandinavica*, *74*(4), 465–486. Retrieved from http://www.ncbi.nlm.nih.gov/pubmed/4313504

Preissner, K. T., Kanse, S. M., & May, A. E. (2000). Urokinase receptor: a molecular organizer in cellular communication. *Current Opinion in Cell Biology*, *12*(5), 621–628. Retrieved from http://www.ncbi.nlm.nih.gov/pubmed/10978899

Price, S. J., Whittle, I. R., Ashkan, K., Grundy, P., & Cruickshank, G. (2012). NICE guidance on the use of carmustine wafers in high grade gliomas: a national study on variation in practice. *British Journal of Neurosurgery*, *26*(3), 331–335. https://doi.org/10.3109/02688697.2012.673651

Pullen, N. A., Anand, M., Cooper, P. S., & Fillmore, H. L. (2012). Matrix metalloproteinase-1 expression enhances tumorigenicity as well as tumor-related angiogenesis and is inversely associated with TIMP-4 expression in a model of glioblastoma. *Journal of Neuro-Oncology*, *106*(3), 461–471. https://doi.org/10.1007/s11060-011-0691-5

Purow, B. W., Haque, R. M., Noel, M. W., Purow, B. W., Haque, R. M., Noel, M. W., … Fine, H. A. (2005). Expression of Notch-1 and Its Ligands , Delta-Like-1 and Jagged-1 , Is Critical for Glioma Cell Survival and Proliferation Is Critical for Glioma Cell Survival and Proliferation, (17), 2353–2363. https://doi.org/10.1158/0008-5472.CAN-04-1890

Qi, L. S., Larson, M. H., Gilbert, L. A., Doudna, J. A., Weissman, J. S., Arkin, A. P., & Lim, W. A. (2013). Repurposing CRISPR as an RNA-Guided Platform for Sequence-Specific Control of Gene Expression. *Cell*, *152*(5), 1173–1183. https://doi.org/10.1016/j.cell.2013.02.022

Quann, K., Gonzales, D. M., Mercier, I., Wang, C., Sotgia, F., Pestell, R. G., … Jasmin, J.-F. (2013). Caveolin-1 is a negative regulator of tumor growth in glioblastoma and modulates chemosensitivity to temozolomide. *Cell Cycle (Georgetown, Tex.)*, *12*(10), 1510–1520. https://doi.org/10.4161/cc.24497

Quest, A. F. G., Lobos-González, L., Nuñez, S., Sanhueza, C., Fernández, J.-G., Aguirre, A., … Torres, V. (2013). The caveolin-1 connection to cell death and survival. *Current Molecular Medicine*, *13*(2), 266–281. Retrieved from http://www.ncbi.nlm.nih.gov/pubmed/23228128

Ramachandran, R. K., Sørensen, M. D., Aaberg-Jessen, C., Hermansen, S. K., & Kristensen, B. W. (2017). Expression and prognostic impact of matrix metalloproteinase-2 (MMP-2) in astrocytomas. *PLOS ONE*, *12*(2), e0172234. https://doi.org/10.1371/journal.pone.0172234

Ran, F. A., Hsu, P. D., Lin, C.-Y., Gootenberg, J. S., Konermann, S., Trevino, A. E., … Zhang, F. (2013). Double Nicking by RNA-Guided CRISPR Cas9 for Enhanced Genome Editing Specificity. *Cell*, *154*(6), 1380–1389. https://doi.org/10.1016/j.cell.2013.08.021

Rao, D. D., Vorhies, J. S., Senzer, N., & Nemunaitis, J. (2009). siRNA vs. shRNA: similarities and differences. *Advanced Drug Delivery Reviews*, *61*(9), 746–759. https://doi.org/10.1016/j.addr.2009.04.004

Rao, J. S. (2003). Molecular mechanisms of glioma invasiveness: the role of proteases. *Nature Reviews. Cancer*, *3*(7), 489–501. https://doi.org/10.1038/nrc1121

Rape, A., Ananthanarayanan, B., & Kumar, S. (2014). Engineering strategies to mimic the glioblastoma microenvironment. *Advanced Drug Delivery Reviews*, *79–80*, 172–183. https://doi.org/10.1016/j.addr.2014.08.012

Razani, B., Engelman, J. A., Wang, X. B., Schubert, W., Zhang, X. L., Marks, C. B., … Lisanti, M. P. (2001). Caveolin-1 null mice are viable but show evidence of hyperproliferative and vascular abnormalities. *The Journal of Biological Chemistry*, *276*(41), 38121–38138. https://doi.org/10.1074/jbc.M105408200

RCoreTeam. (2018). R: A Language and Environment for Statistical Computing.

Vienna, Austria. https://doi.org/10.1038/sj.hdy.6800737

Régina, A., Jodoin, J., Khoueir, P., Rolland, Y., Berthelet, F., Moumdjian, R., … Béliveau, R. (2004). Down-regulation of caveolin-1 in glioma vasculature: modulation by radiotherapy. *Journal of Neuroscience Research*, *75*(2), 291–299. https://doi.org/10.1002/jnr.10865

Rivera, S., Khrestchatisky, M., Kaczmarek, L., Rosenberg, G. A., & Jaworski, D. M. (2010). Metzincin proteases and their inhibitors: foes or friends in nervous system physiology? *The Journal of Neuroscience : The Official Journal of the Society for Neuroscience*, *30*(46), 15337–15357. https://doi.org/10.1523/JNEUROSCI.3467-10.2010

Robb, G. B., & Rana, T. M. (2007). RNA helicase A interacts with RISC in human cells and functions in RISC loading. *Molecular Cell*, *26*(4), 523–537. https://doi.org/10.1016/j.molcel.2007.04.016

Rogers, N. M., Ghimire, K., Calzada, M. J., & Isenberg, J. S. (2017). Matricellular protein thrombospondin-1 in pulmonary hypertension: Multiple pathways to disease. *Cardiovascular Research*. https://doi.org/10.1093/cvr/cvx094

Roth V. (2006). Doubling Time Computing. Retrieved December 5, 2017, from http://www.doubling-time.com/compute.php

RStudioTeam. (2018). RStudio: Integrated development environment for R. RStudio, Inc., Boston, MA. Boston, MA. Retrieved from http://www.rstudio.com

Ruan, J., Zheng, H., Fu, W., Zhao, P., Su, N., & Luo, R. (2014). Increased expression of cathepsin L: A novel independent prognostic marker of worse outcome in hepatocellular carcinoma patients. *PLoS ONE*, *9*(11). https://doi.org/10.1371/journal.pone.0112136

Rutz, S., & Scheffold, A. (2004). Towards in vivo application of RNA interference - new toys, old problems. *Arthritis Research & Therapy*, *6*(2), 78. https://doi.org/10.1186/ar1168

Sabeh, F., Shimizu-Hirota, R., & Weiss, S. J. (2009, April 6). Protease-dependent versus-independent cancer cell invasion programs: Three-

dimensional amoeboid movement revisited. *Journal of Cell Biology*. The Rockefeller University Press. https://doi.org/10.1083/jcb.200807195

Sampetrean, O., & Saya, H. (2013). Characteristics of glioma stem cells. *Brain Tumor Pathology*, *30*(4), 209–214. https://doi.org/10.1007/s10014-013-0141-5

Sanguinetti, A. R., & Mastick, C. C. (2003). c-Abl is required for oxidative stress-induced phosphorylation of caveolin-1 on tyrosine 14. *Cellular Signalling*, *15*(3), 289–298. Retrieved from http://www.ncbi.nlm.nih.gov/pubmed/12531427

Sano, M., Sierant, M., Miyagishi, M., Nakanishi, M., Takagi, Y., & Sutou, S. (2008). Effect of asymmetric terminal structures of short RNA duplexes on the RNA interference activity and strand selection. *Nucleic Acids Research*, *36*(18), 5812–5821. https://doi.org/10.1093/nar/gkn584

Saraiva-Esperón, U., Ruibal, A., & Herranz, M. (2014). The contrasting epigenetic role of RUNX3 when compared with that of MGMT and TIMP3 in glioblastoma multiforme clinical outcomes. *Journal of the Neurological Sciences*, *347*(1–2), 325–331. https://doi.org/10.1016/j.jns.2014.10.043

Sargiacomo, M., Scherer, P. E., Tang, Z., Kübler, E., Song, K. S., Sanders, M. C., & Lisanti, M. P. (1995). Oligomeric structure of caveolin: implications for caveolae membrane organization. *Proceedings of the National Academy of Sciences of the United States of America*, *92*(20), 9407–9411. Retrieved from http://www.pubmedcentral.nih.gov/articlerender.fcgi?artid=40994&tool=pmcentrez&rendertype=abstract

Sato, T. N., Tozawa, Y., Deutsch, U., Wolburg-Buchholz, K., Fujiwara, Y., Gendron-Maguire, M., … Qin, Y. (1995). Distinct roles of the receptor tyrosine kinases Tie-1 and Tie-2 in blood vessel formation. *Nature*, *376*(6535), 70–74. https://doi.org/10.1038/376070a0

Savagner, P. (2010). The epithelial-mesenchymal transition (EMT) phenomenon. *Annals of Oncology : Official Journal of the European Society for Medical Oncology / ESMO*, *21 Suppl 7*(suppl_7), vii89-92.

https://doi.org/10.1093/annonc/mdq292

Schindelin, J., Arganda-Carreras, I., Frise, E., Kaynig, V., Longair, M., Pietzsch, T., … Cardona, A. (2012a). Fiji: an open-source platform for biological-image analysis. *Nature Methods*, *9*(7), 676–682. https://doi.org/10.1038/nmeth.2019

Schindelin, J., Arganda-Carreras, I., Frise, E., Kaynig, V., Longair, M., Pietzsch, T., … Cardona, A. (2012b). Fiji: an open-source platform for biological-image analysis. *Nature Methods*, *9*(7), 676–682. https://doi.org/10.1038/nmeth.2019

Schlegel, A., Schwab, R. B., Scherer, P. E., & Lisanti, M. P. (1999). A role for the caveolin scaffolding domain in mediating the membrane attachment of caveolin-1. The caveolin scaffolding domain is both necessary and sufficient for membrane binding in vitro. *The Journal of Biological Chemistry*, *274*(32), 22660–22667. Retrieved from http://www.ncbi.nlm.nih.gov/pubmed/10428847

Schumann, K., Lin, S., Boyer, E., Simeonov, D. R., Subramaniam, M., Gate, R. E., … Marson, A. (2015). Generation of knock-in primary human T cells using Cas9 ribonucleoproteins. *Proceedings of the National Academy of Sciences*, *112*(33), 10437–10442. https://doi.org/10.1073/pnas.1512503112

Semenova, E., Jore, M. M., Datsenko, K. A., Semenova, A., Westra, E. R., Wanner, B., … Severinov, K. (2011). Interference by clustered regularly interspaced short palindromic repeat (CRISPR) RNA is governed by a seed sequence. *Proceedings of the National Academy of Sciences*, *108*(25), 10098–10103. https://doi.org/10.1073/pnas.1104144108

Senetta, R., Stella, G., Pozzi, E., Sturli, N., Massi, D., & Cassoni, P. (2013). Caveolin-1 as a promoter of tumour spreading: when, how, where and why. *Journal of Cellular and Molecular Medicine*, *17*(3), 325–336. https://doi.org/10.1111/jcmm.12030

Senetta, R., Trevisan, E., Rudà, R., Maldi, E., Molinaro, L., Lefranc, F., … Cassoni, P. (2009). Caveolin 1 expression independently predicts shorter survival in oligodendrogliomas. *Journal of Neuropathology and*

Experimental Neurology, *68*(4), 425–431. https://doi.org/10.1097/NEN.0b013e31819ed0b7

Sequist, L. V, Martins, R. G., Spigel, D., Grunberg, S. M., Spira, A., Jänne, P. A., … Lynch, T. J. (2008). First-line gefitinib in patients with advanced non-small-cell lung cancer harboring somatic EGFR mutations. *Journal of Clinical Oncology : Official Journal of the American Society of Clinical Oncology*, *26*(15), 2442–2449. https://doi.org/10.1200/JCO.2007.14.8494

Shalem, O., Sanjana, N. E., & Zhang, F. (2015). High-throughput functional genomics using CRISPR–Cas9. *Nature Reviews Genetics*, *16*(5), 299–311. https://doi.org/10.1038/nrg3899

Shatz, M., & Liscovitch, M. (2008). Caveolin-1: a tumor-promoting role in human cancer. *International Journal of Radiation Biology*, *84*(3), 177–189. https://doi.org/10.1080/09553000701745293

Shay, G., Lynch, C. C., Fingleton, B., & Moffitt, H. L. (2015). Emerging roles for MMPs in Cancer Progression and Metastasis. *Matrix Biol.*, (615), 200–206. https://doi.org/10.1016/j.matbio.2015.01.019.Moving

Shi, F., & Sottile, J. (2008). Caveolin-1-dependent 1 integrin endocytosis is a critical regulator of fibronectin turnover. *Journal of Cell Science*, *121*(14), 2360–2371. https://doi.org/10.1242/jcs.014977

Shi, Y. (2003). Mammalian RNAi for the masses. *Trends in Genetics : TIG*, *19*(1), 9–12. Retrieved from http://www.ncbi.nlm.nih.gov/pubmed/12493242

Shimato, S., Anderson, L. M., Asslaber, M., Bruce, J. N., Canoll, P., Anderson, D. E., & Anderson, R. C. E. (2013). Inhibition of caveolin-1 restores myeloid cell function in human glioblastoma. *PloS One*, *8*(10), e77397. https://doi.org/10.1371/journal.pone.0077397

Sivaparvathi, M., Sawaya, R., Gokaslan, Z. L., Chintala, K. S., & Rao, J. S. (1996). Expression and the role of cathepsin H in human glioma progression and invasion. *Cancer Letters*, *104*(1), 121–126. https://doi.org/10.1016/0304-3835(96)04242-5

Sloan, E. K., Stanley, K. L., & Anderson, R. L. (2004). Caveolin-1 inhibits breast cancer growth and metastasis. *Oncogene*, *23*(47), 7893–7897.

https://doi.org/10.1038/sj.onc.1208062

Song, K. S., Tang, Z., Li, S., & Lisanti, M. P. (1997). Mutational analysis of the properties of caveolin-1. A novel role for the C-terminal domain in mediating homo-typic caveolin-caveolin interactions. *The Journal of Biological Chemistry*, *272*(7), 4398–4403. Retrieved from http://www.ncbi.nlm.nih.gov/pubmed/9020162

Sorek, R., Kunin, V., & Hugenholtz, P. (2008). CRISPR — a widespread system that provides acquired resistance against phages in bacteria and archaea. *Nature Reviews Microbiology*, *6*(3), 181–186. https://doi.org/10.1038/nrmicro1793

Spandidos, D., Ethnikon Hidryma Ereunōn (Greece), K., Ren, B., Zhu, M., Zhang, C., Zhao, P., … Yang, X. (1994). *Oncology reports. Oncology Reports* (Vol. 34). [National Hellenic Research Foundation]. Retrieved from https://www.spandidos-publications.com/or/34/4/1815?text=fulltext

Stein, A. M., Demuth, T., Mobley, D., Berens, M., & Sander, L. M. (2007). A Mathematical Model of Glioblastoma Tumor Spheroid Invasion in a Three-Dimensional In Vitro Experiment. *Biophysical Journal*, *92*(1), 356–365. https://doi.org/10.1529/biophysj.106.093468

Stein, C. A., & Cohen, J. S. (1988). Oligodeoxynucleotides as inhibitors of gene expression: a review. *Cancer Research*, *48*(10), 2659–2668. Retrieved from http://www.ncbi.nlm.nih.gov/pubmed/3282648

Sternlicht, M., & Werb, Z. (2009). How Matrix metalloproteinases regulate cell behavior. *Annu REv Cell Biol*, 463–516. https://doi.org/10.1146/annurev.cellbio.17.1.463.HOW

Stetler, R. A., Gao, Y., Zhang, L., Weng, Z., Zhang, F., Hu, X., … Chen, J. (2012). Phosphorylation of HSP27 by protein kinase D is essential for mediating neuroprotection against ischemic neuronal injury. *The Journal of Neuroscience : The Official Journal of the Society for Neuroscience*, *32*(8), 2667–2682. https://doi.org/10.1523/JNEUROSCI.5169-11.2012

Strale, P.-O., Clarhaut, J., Lamiche, C., Cronier, L., Mesnil, M., & Defamie, N. (2012). Down-regulation of Connexin43 expression reveals the involvement

of caveolin-1 containing lipid rafts in human U251 glioblastoma cell invasion. *Molecular Carcinogenesis*, *51*(11), 845–860. https://doi.org/10.1002/mc.20853

Strojnik, T., Kos, J., Zidanik, B., Golouh, R., & Lah, T. (1999). Cathepsin B immunohistochemical staining in tumor and endothelial cells is a new prognostic factor for survival in patients with brain tumors. *Clinical Cancer Research : An Official Journal of the American Association for Cancer Research*, *5*(3), 559–567. Retrieved from http://www.ncbi.nlm.nih.gov/pubmed/10100707

Stupp, R., Hegi, M. E., Mason, W. P., van den Bent, M. J., Taphoorn, M. J. B., Janzer, R. C., … Mirimanoff, R.-O. (2009). Effects of radiotherapy with concomitant and adjuvant temozolomide versus radiotherapy alone on survival in glioblastoma in a randomised phase III study: 5-year analysis of the EORTC-NCIC trial. *The Lancet Oncology*, *10*(5), 459–466. https://doi.org/10.1016/S1470-2045(09)70025-7

Stupp, R., Mason, W. P., van den Bent, M. J., Weller, M., Fisher, B., Taphoorn, M. J. B., … Mirimanoff, R. O. (2005). Radiotherapy plus concomitant and adjuvant temozolomide for glioblastoma. *The New England Journal of Medicine*, *352*(10), 987–996. https://doi.org/10.1056/NEJMoa043330

Suksuphew, S., & Noisa, P. (2015). Neural stem cells could serve as a therapeutic material for age-related neurodegenerative diseases. *World Journal of Stem Cells*, *7*(2), 502–511. https://doi.org/10.4252/wjsc.v7.i2.502

Swiech, L., Heidenreich, M., Banerjee, A., Habib, N., Li, Y., Trombetta, J., … Zhang, F. (2014). In vivo interrogation of gene function in the mammalian brain using CRISPR-Cas9. *Nature Biotechnology*, *33*(1), 102–106. https://doi.org/10.1038/nbt.3055

Tahir, S. A., Frolov, A., Hayes, T. G., Mims, M. P., Miles, B. J., Lerner, S. P., … Kadmon, D. (2006). Preoperative serum caveolin-1 as a prognostic marker for recurrence in a radical prostatectomy cohort. *Clinical Cancer Research : An Official Journal of the American Association for Cancer Research*, *12*(16), 4872–4875. https://doi.org/10.1158/1078-0432.CCR-06-0417

Tan, G.-J., Peng, Z.-K., Lu, J.-P., & Tang, F.-Q. (2013). Cathepsins mediate tumor metastasis. *World Journal of Biological Chemistry*, *4*(4), 91–101. https://doi.org/10.4331/wjbc.v4.i4.91

Thoma, C. R., Zimmermann, M., Agarkova, I., Kelm, J. M., & Krek, W. (2014). 3D cell culture systems modeling tumor growth determinants in cancer target discovery. *Advanced Drug Delivery Reviews*. https://doi.org/10.1016/j.addr.2014.03.001

Torres, V. A., Tapia, J. C., Rodríguez, D. A., Párraga, M., Lisboa, P., Montoya, M., … Quest, A. F. G. (2006). Caveolin-1 controls cell proliferation and cell death by suppressing expression of the inhibitor of apoptosis protein survivin. *Journal of Cell Science*, *119*(Pt 9), 1812–1823. https://doi.org/10.1242/jcs.02894

Trent, J., Meltzer, P., Rosenblum, M., Harsh, G., Kinzler, K., Mashal, R., … Vogelstein, B. (1986). Evidence for rearrangement, amplification, and expression of c-myc in a human glioblastoma. *Proceedings of the National Academy of Sciences of the United States of America*, *83*(2), 470–473. Retrieved from http://www.pubmedcentral.nih.gov/articlerender.fcgi?artid=322881&tool=pmcentrez&rendertype=abstract

Tso, C.-L., Freije, W. A., Day, A., Chen, Z., Merriman, B., Perlina, A., … Nelson, S. F. (2006). Distinct Transcription Profiles of Primary and Secondary Glioblastoma Subgroups. *Cancer Research*, *66*(1). Retrieved from http://cancerres.aacrjournals.org/content/66/1/159.long

Tsong, T. Y. (1991). Electroporation of cell membranes. *Biophysical Journal*, *60*(2), 297–306. https://doi.org/10.1016/S0006-3495(91)82054-9

Tsui, T. K. M., & Li, H. (2015). Structure Principles of CRISPR-Cas Surveillance and Effector Complexes. *Annual Review of Biophysics*, *44*(1), 229–255. https://doi.org/10.1146/annurev-biophys-060414-033939

Ui-Tei, K. (2013). Optimal choice of functional and off-target effect-reduced siRNAs for RNAi therapeutics. *Frontiers in Genetics*, *4*, 107. https://doi.org/10.3389/fgene.2013.00107

Ulasov, I., Yi, R., Guo, D., Sarvaiya, P., & Cobbs, C. (2014). The emerging role of MMP14 in brain tumorigenesis and future therapeutics. *Biochimica et Biophysica Acta (BBA) - Reviews on Cancer*, *1846*(1), 113–120. https://doi.org/10.1016/j.bbcan.2014.03.002

Unniyampurath, U., Pilankatta, R., & Krishnan, M. (2016). RNA Interference in the Age of CRISPR: Will CRISPR Interfere with RNAi? *International Journal of Molecular Sciences*, *17*(3), 291. https://doi.org/10.3390/ijms17030291

Valentijn, L. J., Koster, J., & Versteeg, R. (2006). Read-through transcript from NM23-H1 into the neighboring NM23-H2 gene encodes a novel protein, NM23-LV. https://doi.org/10.1016/j.ygeno.2005.11.004

van der Oost, J., Jore, M. M., Westra, E. R., Lundgren, M., & Brouns, S. J. J. (2009). CRISPR-based adaptive and heritable immunity in prokaryotes. *Trends in Biochemical Sciences*, *34*(8), 401–407. https://doi.org/10.1016/j.tibs.2009.05.002

van Golen, K. L. (2006). Is caveolin-1 a viable therapeutic target to reduce cancer metastasis? *Expert Opinion on Therapeutic Targets*, *10*(5), 709–721. https://doi.org/10.1517/14728222.10.5.709

Veeravalli, K. K., & Rao, J. S. (2012). MMP-9 and uPAR regulated glioma cell migration. *Cell Adhesion & Migration*, *6*(6), 509–512. https://doi.org/10.4161/cam.21673

Vehlow, A., & Cordes, N. (2013). Invasion as target for therapy of glioblastoma multiforme. *Biochimica et Biophysica Acta (BBA) - Reviews on Cancer*, *1836*(2), 236–244. https://doi.org/10.1016/j.bbcan.2013.07.001

Verbovšek, U., Van Noorden, C. J. F., & Lah, T. T. (2015). Complexity of cancer protease biology: Cathepsin K expression and function in cancer progression. *Seminars in Cancer Biology*, *35*, 71–84. https://doi.org/10.1016/j.semcancer.2015.08.010

Verhaak, R. G. W., Hoadley, K. A., Purdom, E., Wang, V., Qi, Y., Wilkerson, M. D., … Cancer Genome Atlas Research Network. (2010a). Integrated genomic analysis identifies clinically relevant subtypes of glioblastoma characterized by abnormalities in PDGFRA, IDH1, EGFR, and NF1. *Cancer*

Cell, *17*(1), 98–110. https://doi.org/10.1016/j.ccr.2009.12.020

Verhaak, R. G. W., Hoadley, K. A., Purdom, E., Wang, V., Qi, Y., Wilkerson, M. D., … Cancer Genome Atlas Research Network. (2010b). Integrated genomic analysis identifies clinically relevant subtypes of glioblastoma characterized by abnormalities in PDGFRA, IDH1, EGFR, and NF1. *Cancer Cell*, *17*(1), 98–110. https://doi.org/10.1016/j.ccr.2009.12.020

Vinci, M., Gowan, S., Boxall, F., Patterson, L., Zimmermann, M., Court, W., … Eccles, S. A. (2012). Advances in establishment and analysis of three-dimensional tumor spheroid-based functional assays for target validation and drug evaluation. *BMC Biology*, *10*(1), 29. https://doi.org/10.1186/1741-7007-10-29

Volonté, D., Galbiati, F., Pestell, R. G., & Lisanti, M. P. (2001). Cellular Stress Induces the Tyrosine Phosphorylation of Caveolin-1 (Tyr 14) via Activation of p38 Mitogen-activated Protein Kinase and c-Src kinase. *Journal of Biological Chemistry*, *276*(11), 8094–8103. https://doi.org/10.1074/jbc.M009245200

Wang, J., & Yu, R. K. (2013). Interaction of ganglioside GD3 with an EGF receptor sustains the self-renewal ability of mouse neural stem cells in vitro. *Proceedings of the National Academy of Sciences of the United States of America*, *110*(47), 19137–19142. https://doi.org/10.1073/pnas.1307224110

Wang, Q., Hu, B., Hu, X., Kim, H., Squatrito, M., Scarpace, L., … Verhaak, R. G. W. (2017). Tumor Evolution of Glioma-Intrinsic Gene Expression Subtypes Associates with Immunological Changes in the Microenvironment. *Cancer Cell*, *32*(1), 42–56.e6. https://doi.org/10.1016/j.ccell.2017.06.003

Wang, T., Birsoy, K., Hughes, N. W., Krupczak, K. M., Post, Y., Wei, J. J., … Sabatini, D. M. (2015). Identification and characterization of essential genes in the human genome. *Science*, *350*(6264), 1096–1101. https://doi.org/10.1126/science.aac7041

Wang, T., Wei, J. J., Sabatini, D. M., & Lander, E. S. (2014). Genetic Screens in Human Cells Using the CRISPR-Cas9 System. *Science*, *343*(6166), 80–84. https://doi.org/10.1126/science.1246981

Ward, S. J., Karakoula, K., Phipps, K. P., Harkness, W., Hayward, R., Thompson, D., … Warr, T. J. (2010). Cytogenetic analysis of paediatric astrocytoma using comparative genomic hybridisation and fluorescence in-situ hybridisation. *Journal of Neuro-Oncology*, *98*(3), 305–318. https://doi.org/10.1007/s11060-009-0081-4

Watanabe, M., Yang, G., Cao, G., Tahir, S. A., Naruishi, K., Tabata, K.-I., … Thompson, T. C. (2009). Functional analysis of secreted caveolin-1 in mouse models of prostate cancer progression. *Molecular Cancer Research : MCR*, *7*(9), 1446–1455. https://doi.org/10.1158/1541-7786.MCR-09-0071

Weaver, A. M. (2008). Cortactin in tumor invasiveness. *Cancer Letters*, *265*(2), 157–166. https://doi.org/10.1016/j.canlet.2008.02.066

Weigelt, B., Ghajar, C. M., & Bissell, M. J. (2014). The need for complex 3D culture models to unravel novel pathways and identify accurate biomarkers in breast cancer. *Advanced Drug Delivery Reviews*. https://doi.org/10.1016/j.addr.2014.01.001

Wiedenheft, B., van Duijn, E., Bultema, J. B., Bultema, J., Waghmare, S. P., Waghmare, S., … Doudna, J. A. (2011). RNA-guided complex from a bacterial immune system enhances target recognition through seed sequence interactions. *Proceedings of the National Academy of Sciences of the United States of America*, *108*(25), 10092–10097. https://doi.org/10.1073/pnas.1102716108

Williams, T. M., Medina, F., Badano, I., Hazan, R. B., Hutchinson, J., Muller, W. J., … Lisanti, M. P. (2004). Caveolin-1 gene disruption promotes mammary tumorigenesis and dramatically enhances lung metastasis in vivo. Role of Cav-1 in cell invasiveness and matrix metalloproteinase (MMP-2/9) secretion. *The Journal of Biological Chemistry*, *279*(49), 51630–51646. https://doi.org/10.1074/jbc.M409214200

Wolf, K., Wu, Y. I., Liu, Y., Geiger, J., Tam, E., Overall, C., … Friedl, P. (2007). Multi-step pericellular proteolysis controls the transition from individual to collective cancer cell invasion. *Nature Cell Biology*, *9*(8), 893–904. https://doi.org/10.1038/ncb1616

Woodman, S. E., Schlegel, A., Cohen, A. W., & Lisanti, M. P. (2002). Mutational analysis identifies a short atypical membrane attachment sequence (KYWFYR) within caveolin-1. *Biochemistry*, *41*(11), 3790–3795. Retrieved from http://www.ncbi.nlm.nih.gov/pubmed/11888297

Wu, H., Ma, H., Ye, C., Ramirez, D., Chen, S., Montoya, J., … Manjunath, N. (2011). Improved siRNA/shRNA functionality by mismatched duplex. *PloS One*, *6*(12), e28580. https://doi.org/10.1371/journal.pone.0028580

Wu, J., Armstrong, T. S., & Gilbert, M. R. (2016). Biology and management of ependymomas. *Neuro-Oncology*, *18*(7), 902–913. https://doi.org/10.1093/neuonc/now016

Wu, M., Frieboes, H. B., Chaplain, M. A. J., McDougall, S. R., Cristini, V., & Lowengrub, J. S. (2014). The effect of interstitial pressure on therapeutic agent transport: Coupling with the tumor blood and lymphatic vascular systems. *Journal of Theoretical Biology*, *355*, 194–207. https://doi.org/10.1016/j.jtbi.2014.04.012

Xie, Q., Mittal, S., & Berens, M. E. (2014). Targeting adaptive glioblastoma: an overview of proliferation and invasion. *Neuro-Oncology*, *16*(February), 1–10. https://doi.org/10.1093/neuonc/nou147

Xu, Y., Stamenkovic, I., & Yu, Q. (2010). CD44 attenuates activation of the hippo signaling pathway and is a prime therapeutic target for glioblastoma. *Cancer Research*, *70*(6), 2455–2464. https://doi.org/10.1158/0008-5472.CAN-09-2505

Yamada, E. (1955). The fine structure of the gall bladder epithelium of the mouse. *The Journal of Cell Biology*, *1*(5), 445–458. https://doi.org/10.1083/jcb.1.5.445

Yan, K., Wu, Q., Yan, D. H., Lee, C. H., Rahim, N., Tritschler, I., … Rich, J. N. (2014). Glioma cancer stem cells secrete Gremlin1 to promote their maintenance within the tumor hierarchy. *Genes and Development*, *28*(10), 1085–1100. https://doi.org/10.1101/gad.235515.113

Yanamandra, N., Gumidyala, K. V., Waldron, K. G., Gujrati, M., Olivero, W. C., Dinh, D. H., … Mohanam, S. (2004). Blockade of cathepsin B expression in

human glioblastoma cells is associated with suppression of angiogenesis. *Oncogene*, *23*(12), 2224–2230. https://doi.org/10.1038/sj.onc.1207338

Yang, H., Guan, L., Li, S., Jiang, Y., Xiong, N., Li, L., … Liu, Y. (2016). Mechanosensitive caveolin-1 activation-induced PI3K/Akt/mTOR signaling pathway promotes breast cancer motility, invadopodia formation and metastasis in vivo. *Oncotarget*, *7*(13), 16227–16247. https://doi.org/10.18632/oncotarget.7583

Yang, W., Xia, Y., Ji, H., Zheng, Y., Liang, J., Huang, W., … Lu, Z. (2011). Nuclear PKM2 regulates β-catenin transactivation upon EGFR activation. *Nature*, *478*(7375), 118–122. https://doi.org/10.1038/nature10598

Yi, R., Qin, Y., Macara, I. G., & Cullen, B. R. (2003). Exportin-5 mediates the nuclear export of pre-microRNAs and short hairpin RNAs. *Genes & Development*, *17*(24), 3011–3016. https://doi.org/10.1101/gad.1158803

Yilmaz, M., & Christofori, G. (2009). EMT, the cytoskeleton, and cancer cell invasion. *Cancer Metastasis Reviews*, *28*(1–2), 15–33. https://doi.org/10.1007/s10555-008-9169-0

Yip, S., Miao, J., Cahill, D. P., Iafrate, A. J., Aldape, K., Nutt, C. L., & Louis, D. N. (2009). MSH6 mutations arise in glioblastomas during temozolomide therapy and mediate temozolomide resistance. *Clinical Cancer Research : An Official Journal of the American Association for Cancer Research*, *15*(14), 4622–4629. https://doi.org/10.1158/1078-0432.CCR-08-3012

Ylivinkka, I., Sihto, H., Tynninen, O., Hu, Y., Laakso, A., Kivisaari, R., … Hyytiäinen, M. (2017). Motility of glioblastoma cells is driven by netrin-1 induced gain of stemness. *Journal of Experimental & Clinical Cancer Research*, *36*(1), 9. https://doi.org/10.1186/s13046-016-0482-0

Yosef, I., Goren, M. G., & Qimron, U. (2012). Proteins and DNA elements essential for the CRISPR adaptation process in Escherichia coli. *Nucleic Acids Research*, *40*(12), 5569–5576. https://doi.org/10.1093/nar/gks216

Zarrilli, R., Pignata, S., Apicella, A., Di Popolo, A., Memoli, A., Ricchi, P., … Acquaviva, A. M. (1999). Cell cycle block at G1-S or G2-M phase correlates with differentiation of Caco-2 cells: effect of constitutive insulin-like growth

factor II expression. *Gastroenterology*, *116*(6), 1358–1366. Retrieved from http://www.ncbi.nlm.nih.gov/pubmed/10348819

Zhang, C., Tang, N., Liu, X., Liang, W., Xu, W., & Torchilin, V. P. (2006). siRNA-containing liposomes modified with polyarginine effectively silence the targeted gene. *Journal of Controlled Release*, *112*(2), 229–239. https://doi.org/10.1016/j.jconrel.2006.01.022

Zhang, H., Kolb, F. A., Brondani, V., Billy, E., & Filipowicz, W. (2002). Human Dicer preferentially cleaves dsRNAs at their termini without a requirement for ATP. *The EMBO Journal*, *21*(21), 5875–5885. Retrieved from http://www.ncbi.nlm.nih.gov/pubmed/12411505

Zhang, J., Yao, H., Song, G., Liao, X., Xian, Y., & Li, W. (2015). Regulation of epithelial-mesenchymal transition by tumor-associated macrophages in cancer. *Am J Transl Res*, *7*(10), 1699–1711. Retrieved from www.ajtr.org

Zhang, N., Wei, P., Gong, A., Chiu, W. T., Lee, H. Te, Colman, H., … Huang, S. (2011). FoxM1 Promotes β-Catenin Nuclear Localization and Controls Wnt Target-Gene Expression and Glioma Tumorigenesis. *Cancer Cell*, *20*(4), 427–442. https://doi.org/10.1016/j.ccr.2011.08.016

Zheng, H., Ying, H., Wiedemeyer, R., Yan, H., Quayle, S. N., Ivanova, E. V, … DePinho, R. A. (2010). PLAGL2 Regulates Wnt Signaling to Impede Differentiation in Neural Stem Cells and Gliomas. *Cancer Cell*, *17*(5), 497–509. https://doi.org/10.1016/j.ccr.2010.03.020

Zong, H., Verhaak, R. G. W., & Canoll, P. (2012). The cellular origin for malignant glioma and prospects for clinical advancements. *Expert Review of Molecular Diagnostics*, *12*(4), 383–394. https://doi.org/10.1586/erm.12.30